Author:
Hilson, Gabrielle De Backer

Title:
The inter-relationship between surface condition and near surface residual stresses in engineering components

The Inter-Relationship between Surface Condition and Near Surface Residual Stresses in Engineering Components

Gabrielle De Backer Hilson

A dissertation submitted to the University of Bristol in accordance with the requirements of the degree of Ph.D. in the Faculty of Science, Interface Analysis Centre, October 2008.

67,498 words

Abstract

Supergen, Sustainable Power Generation and Supply, is an initiative lead and run by the Engineering and Physical Sciences Research Council with the aim of improving the sustainability of the UK's power generation and supply along with improving emission targets. Part of the initiative has involved a research into conventional power plant lifetime extension in order to maintain reliability and availability of power.

Integral to lifetime evaluation and extension is structural integrity assessment, in which knowledge of residual stresses plays a major role. This thesis discusses research undertaken to improve and understand residual stress measurements for power plant components. This was done using non-destructive/non-invasive techniques, as these techniques can reduce the otherwise costly need for machine down-time and the stripping-down of components. In the present work, emphasis has been placed on the role of oxides and the associated residual stresses.

Surface stresses were correlated with through-section stresses to obtain more detailed stress profiles of components. Stresses within surface "as grown" oxides were investigated, as was the relationship between these stresses with substrate stress/strain and the role of these oxides in the measurement of substrate stress was explored. Stresses formed in thermally grown oxides of turbine blades were monitored with time and temperature to investigate whether stress could be used to predict failure of the protective oxides. Research also was conducted into the applicability, calibration and sources of error of the surface techniques themselves, namely X-ray diffraction and Raman and photoluminescence spectroscopy.

Key outcomes were the reassessment of surface preparation requirements when undertaking X-ray diffraction on engineering components, the correlation of surface and through section residual stresses with finite element models and an indication of thermally grown oxide failure from their residual stresses.

In loving memory of Val Weinstein, friend and surrogate grandmother.

Acknowledgements

I would like to thank my first supervisor Prof. Peter Flewitt for giving me the opportunity to work on this project, for his guidance and enthusiasm, his encyclopaedic knowledge and his patience. Many thanks also to my second supervisor Prof. David Smith and to Prof. Martyn Pavier for their expert advice. I am grateful to Michael Parsley for his help with experimental technique. Thank you to Prof. Geoff Allen and Dr. John Day for their advice on spectroscopic techniques. Many thanks to Dr. Keith Hallam for finding out seemingly random pieces of information at incredibly short notice and more importantly for debugging my thesis. Thank you to the Physics and Mechanical Engineering workshops for their assistance with sample preparation along with teaching me Brizzle. I am grateful to the Engineering and Physical Sciences Research Council for funding and managing the project. I would like to thank family and friends for all they did. Thank you to Bernadette, Diana and Stefan for keeping an eye on my sanity. Finally, special thanks to Annegret, Harriet and Tim without whose encouragement and support I would never have got this far.

The following papers have resulted from this work:

A comparison between measured and modelled residual stresses in a circumferentially butt-welded P91 pipe, A.H. Yaghi, T.H. Hyde, A.A. Becker, W. Sun, G. Hilson, S. Simandjuntak, P.E.J. Flewitt, M. Pavier, D.J. Smith. To be submitted to the Journal of Pressure Vessel Technology.

Spatial variation of residual stresses in a welded pipe for high temperature applications, G. Hilson, S. Simunjuntak, P.E.J. Flewitt, K.R. Hallam, M.J. Pavier and D.J. Smith. Submitted to International Journal of Pressure Vessels and Piping, 2008.

The influence of surface oxide on the measurement of stresses in ferritic steel components, G. Hilson, M.C.J. Parsley, D. Smith, and P.E.J. Flewitt. Engineering Structural Integrity: Research Development and Application Vol. 1 (2007) pp. 452-455. (Presented at 9th International Conference on Engineering Structural Integrity Assessment conference in October 2007, Beijing.)

Through section measurements of residual stresses and their applications to repair welds. G. Hilson, C. Truman, D. Smith, and P. E. J. Flewitt. ESIA8 Throughlife Management of Structures and Components. (Presented at 8th International Conference on Engineering Structural Integrity Assessment, October 2006, Manchester.)

The measurement of stresses within oxides produced on austenitic and ferritic steels using Raman spectroscopy. G. Hilson, K.R. Hallam and P.E.J. Flewitt. Materials Science Forum, Vol. 524-525, (2006) pp.957-962. (Presented at 7th European Conference on Residual Stresses, September 2006, Berlin.)

I declare that the work in this dissertation was carried out in accordance with the Regulations of the University of Bristol. Where work or findings of others has been used, reference has been given and no part of the dissertation has been submitted for any other academic award. Any views expressed in the dissertation are those of the author:.

SIGNED: ....Gabrielle Hudson..... DATE: ..17/02/09

Contents

Symbols

The symbols employed in this thesis are shown below. All units are SI aside from temperature which is in degrees Celcius (°C) and wavenumber in centimetres to the minus one (cm^{-1}).

A	sample area
A_f	temperature at end of austenitic transformation
A_s	temperature at start of austenitic transformation
$\overline{A}, \overline{B}$	calibration constants
C_{ijkl}	stiffness tensor
E	Young's modulus, energy
F	load
G	shear modulus
G()	Gaussian
Hv	Vickers hardness
I	intensity of diffraction peaks
K	bulk modulus, stress intensity factor
K_{IC}	fracture toughness
K_r	proximity to fracture failure
L_r	proximity to ductile failure
L()	Lorentzian
M_s	temperature at start of martensitic transformation
M_f	temperature at end of martensitic transformation
Pr	pressure
P,Q,T	combination stresses
R_1, R_2	α-Al_2O_3 photoluminescence spectroscopic lines
S_{klij}	compliance tensor
S()	mixed Gaussian-Lorentzian
T	temperature
T_o	oxidation temperature
T_1	temperature of initial oxide scale or interface failure
T_2	temperature at which spalled oxide is released
V	lattice cell volume

V()	Voigt
W	width of individual Kα peaks
Z	atomic number
a,c	lattice cell parameters
c	speed of light
d	lattice spacing, depth
h	distance between focused diffractometer and sample, Planck constant
Δh	height displacement from Rowland circle
k	compliance value
k_l	linear kinetic constant
k_p	parabolic oxidation constant
l	length of specimen
Δl	change in length of specimen
m	molecular vibrational ground state
Δm	weight increase of component
n	integer, higher molecular vibrational state
p, q, t	combination strain variables
t	time
x	thickness, frequency or wavenumber
w	weight fraction
z	length of reference hole
z_l	through thickness position
Δ	negative dilation, change in value
Π_{ij}	piezospectroscopic tensor
α	linear coefficient of expansion
α_{th}	thermal expansion coefficient
γ	shear strain
ε	strain
ε_{ij}	strain tensor
ε_n	nominal strain
$\tilde{\varepsilon}_m$	measured distortions
ε_r	surface strain relief
ε_t	true strain

$\bar{\varepsilon}$	measured distortion
θ	Bragg angle
λ	wavelength
λ^2	lateral area of spalled oxide particle
μ	linear absorption coefficient
ν	Poisson's ratio, frequency
ξ	oxide thickness
ρ	density
σ	stress
σ_{ij}	stress tensor
σ_n	nominal stress
σ_{ox}	oxide stress
σ_{ref}	average stress in load bearing material
σ_t	true stress
σ_{th}	thermal stress
σ_y	yield stress
$\bar{\sigma}$	residual stress vector
$\tilde{\sigma}$	residual stress field
τ	shear stress
φ	angular separation of Kα peaks
ψ	Psi-angle
ω	wavenumber

Figures

Tables

1 Introduction

Sustainable Power Generation and Supply, Supergen, is an interdisciplinary initiative with several projects running in parallel [Supergen2], which aims to improve the sustainability of power generation and supply along with aiding the UK to meet its environmental emissions targets. The initiative is managed and led by the Engineering and Physical Sciences Research Council (EPSRC) in association with the Biotechnology and Biological Sciences Research Council (BBSRC), Economic and Social Research Council (ESRC), Natural Environment Research Council (NERC) and the Carbon Trust. It draws together partners from industry and universities.

More sustainable, yet variable, forms of power generation are being introduced in the UK [Supergen2]. Conventional forms of power generation must therefore continue to be employed to maintain reliability and availability of power. Fossil fuel technology is currently the predominant conventional form of power generation technology [Graus et al. 2007]. However, many of the fossil fired plants in use are reaching the end of their original design life and it is strategically and economically desirable for them to be safely employed beyond their original life specifications [Supergen2]. The work discussed in this thesis is part of the consortium for conventional power plant lifetime extension, addressing this issue.

Furthermore, although life assessment methodologies for high temperature plant were developed 20 to 30 years ago and could be employed in order to assess lifetime extension; for example by research programmes at EPRI [Viswanathan 1989] and CEGB [Gooch 1988], the ways in which power generation plants are operated are having to change in order to meet environmental and economic targets [Supergen2]. This complicates any lifetime predictions that may have previously been made. The aims of the Supergen work programme are to develop methods in order to help industry extend the lifetime of conventional fossil fuel fired power generation plants [Supergen2].

Historically, two strategies have been considered with regards to replacing components [Gooch 1988]. The first is to replace all major components after a specific time. The second is to replace each major component on their specific

predictive life criteria within a period of their safe and economic operating life. The second option has been preferred because components can be replaced as the need arises and replacement/refurbishment can take place during statutory outages.

It is necessary to have knowledge of the physical and mechanical properties of a component along with its stress state in order to evaluate its structural integrity [Gooch 1988]. Ideally, inspection methods should be used that are as non-invasive as possible, as machine down-time and the stripping-down of components can make the inspection of a power plant extremely costly [Supergen2]. However, many non-invasive methods only provide information on surface stresses and it is invasive techniques that can provide information on through-section stresses [Withers et al. 2008]. The aim of this work has been to improve understanding of the measurement of near surface residual stresses and the correlation between near surface and through section residual stresses in engineering components, including the behaviour of surface oxides. This has required addressing key issues relating to the application of non-destructive techniques used for plant inspection and monitoring.

The experiments undertaken had the following objectives. First, to explore the importance of calibration and sources of error in order to ensure repeatability of measurements. Second, to investigate the behaviour of "as grown" oxides in relation to substrate deformation and stress using Raman spectroscopy with a view to investigating the feasibility of using oxides as an "in-built" strain gauge. As oxides commonly form on power plant components [Viswanathan 1989], relating the oxide stresses to substrate strain/stress by Raman spectroscopy would provide a practical, non-destructive method of component monitoring. The third objective was to assess the correlation of surface X-ray stress measurements with through-section stress measurements and to compare these measurements to finite element models. The experimental and modelled stresses would then be related to a proposed repair weld procedure, which relies on the good correlation between experimentally measured surface and through-section stresses with modelled stresses. The final objective was to measure stresses in the thermally grown oxides of superalloy bond-coats using photoluminescence spectroscopy and relate these measurements to the lifetime of the oxides, thereby demonstrating a practical, in-situ method of assessing the lifetime of turbine blade coatings.

2 Literature Review

2.1 Conventional Power Plants

The main components of a conventional fossil fuelled power plant are the boiler, steam turbine, generator and condenser [Gooch 1988, Viswanathan 1989]. These are linked by pipework containing water, steam and gases. The following example is of the generation of power from a coal fired plant [Gooch 1988, Viswanathan 1989]. In one loop, water in the feedwater heaters is heated to a relatively low temperature before being pumped into the boiler tubes. Here the combustion of the pulverised coal in the boiler heats it to steam temperature. The steam is then superheated to temperature and pressure. The superheated and pressurised steam is then made to pass through the high pressure steam turbine where it causes the rotation of the turbine shaft. This process causes the steam to cool but it is then reheated and passed through an intermediate pressure turbine and then a low pressure turbine. The turbine shafts are connected to a generator or generators (the number of which depends on the plant), which convert the mechanical energy into electrical energy. After leaving the low pressure turbine, the steam is condensed and the cycle is repeated. The steam from the low pressure turbine is condensed by a second water loop from the cooling towers. The gases from the combusted pulverised coal in the boiler are used to heat the incoming air to the boiler in the heat exchangers. The gases are then cleaned in scrubbers and released into the environment via the stacks.

The components of a conventional electrical power plant therefore undergo extreme conditions, having to withstand high temperatures and pressures. In addition, components have to withstand different conditions, depending on the environment in which they are used [Viswanathan 1989]. They, therefore, have to be manufactured and monitored according to their specific function. Furthermore, since the lifetimes of conventional power plants are being extended and the plants are being made to work at higher efficiencies and therefore temperatures than they were originally designed for. Hence the components have to withstand harsher environments than considered in the original design.

Welded structures and components play a key role in the conventional power plant [Budden 1994]. Despite this, they are a potential source of failure and so developing an understanding of their structural integrity is of great importance.

In addition to the use of coal, gas has offered an important energy source [Haigh 1991]. In gas turbine plant another crucial component is the turbine blade [Layne 2000]. These blades are used in gas turbines and their properties govern the allowable inlet gas temperature [Çengel and Boles 1998]. The thermal efficiency of gas turbines can be described using the Carnot cycle, the efficiency of which is governed by the turbine inlet temperature [Çengel and Boles 1998]. In order to increase fuel efficiency, there has been a drive to increase the temperature of the gas [Layne 2000]. The fact that most failures in gas-turbine systems are associated with the components exposed to high temperatures [Layne 2000], illustrates the need for improved structural integrity evaluation methods for high temperature turbine blades in gas turbine systems. There is a significant difference in their mechanical requirements depending upon the place and function of turbine blades and vanes in generators [Viswanathan 1989]. Superalloys are used for the blades and vanes which have to withstand the highest temperatures [Layne 2000, Viswanathan 1989]. The melting point of these superalloys is of the order 1280°C and they can be used at temperatures of up to 850°C [Ashby and Jones 1996]. However, in order to raise the temperature at which they can be used, they can be coated with ceramic layers [Bressers et al. 2000, Callister 2000].

The components investigated, as well as their functions and therefore requirements, are discussed in Section 2.1.1.

2.1.1 Components

The components that this study concentrates on are welded steam pipework and gas turbine blades. The investigations therefore consider the materials from which they are manufactured. P91 martensitic steel is a candidate material for steam pipes and headers in future high temperature fossil fired plant [Viswanathan 1998]. Type 316 austenitic stainless steels have traditionally been used for boiler materials [Viswanathan 1989] and are candidate materials for the inner cylinder and nozzle box

of the next generation of advanced steam turbines [Viswanathan 1989, Viswanathan and Bakker 2001]. Although A533B ferritic steel is commonly used in the nuclear industry [Wu et al. 2006], it has similar properties to P91 steel [Klueh and Nelson] and so provides a viable alternative as a material for steam pipes and headers. In the case of gas turbine blade materials, nickel based superalloys, such as CMSX4, are used because of their good high temperature properties [McLean et al. 1995]. Additionally, they can be coated with a bond-coat and a thermal barrier coating in order to further improve their thermal properties [Meier et al. 1994, Padture et al. 2002]. The samples used in this investigation to replicate turbine blades had a CMSX4 substrate and an RT22 [Angenete and Stiller 2002, (a)Angenete and Stiller 2003 (b)Angenete and Stiller 2003] or CN91 [Saint-Ramond et al. 2004] bond-coat.

2.1.2 Life Extension

A large percentage of power plants in the U.K., as in many other parts of the world, are being operated for longer than the original design life [Gooch 1988, Viswanathan 1989]. There are several reasons why this is the case. The high construction costs and reduced investment, along with uncertainties with regards to future demand and increasing construction lead times means that it is more economical to increase the life of existing plants. There are also environmental considerations such as limited sites available for construction and tougher regulations with regards to environmental safety. Finally, there is an increasing awareness of the excess capacity of existing plants and of the technological methods with which life extension can be achieved. By re-assessing design codes, it is possible to explore the original conservative estimations of operating life and seek to reduce these based on an operating experience and current methodologies.

A major disadvantage of plant life extension is the risk that the efficiency of the plant could decrease [Viswanathan 1989]. However, the selective replacement of components with those of improved design and material properties has enabled plants to perform at higher efficiencies. Another issue is that conservatism in integrity calculations are difficult to validate, since plant failure cannot be permitted [Gooch 1988].

When extending plant life, it is necessary to be able to assess the remaining life of the plant and its components [Gooch 1988]. In order to be able to do this, the following considerations must be taken into account:

- The type of component and materials involved.
- Plant operating regimes.
- Failure mechanisms and ease of repair.
- Failure statistics
- Cost of repair and outages.

In addition to monitoring on line temperature, time and vibration, condition monitoring of components can be carried out periodically in-situ using a variety of non-destructive testing techniques including X-ray diffraction, radiography, ultrasonic testing, magnetic particle inspection and eddy current inspection [Coffey 1988, Doig and Flewitt 1978]. These techniques can be employed to measure various material characteristics, which in turn can be used to monitor their behaviour. During radiography, a source of high energy X-rays is placed on one side of the component and photographic film is placed on the other [Coffey 1988]. The differential attenuation of the radiation by flaws, crack cavities etc. and changes in section result in an intensity variation, which produces a shadow picture of defects on the film or detector. Ultrasonic testing uses megahertz frequency sound waves. A probe is used to convert electrical signals into sound waves and transmit the sound waves to the sample. The sound waves scatter from the surfaces and are then detected by the probe in an echo-like signal. This signal is then transmitted from to the probe in the form of an electrical signal which is analysed and used to assess whether defects are present and if so, to estimate the size. Magnetic particle inspection is a method of observing surface defects in ferromagnetic materials [Coffey 1988]. During magnetic particle inspection, a magnetic flux is introduced into the surface of the steel. Magnetite dust suspended in a liquid is sprayed over the surface of the component. The magnetite particles are then drawn to any leakage in flux, such as from a surface crack so that these features are seen. Eddy current inspection can be employed to find flaws in non-magnetic materials at depths of up to a few millimetres [Coffey 1988]. This is done by measuring the impedance of eddy currents into the surface of a metal. Near surface defects perturb the eddy currents and can thereby be detected. Other techniques are less widely used but are indeed employed to explore specific problems.

One such technique is X-ray diffraction, which is employed to measure both applied and residual stresses in crystalline materials [Cullity and Stock 2001, Doig and Flewitt 1978, (a)Withers and Bhadeshia 2001].

However, although the above mentioned testing methods can provide information as to the present state of the component, they cannot directly predict the component's behaviour in the future. Post exposure testing of components and materials removed from service can provide descriptions of behaviour over time [Lonsdale and Flewitt 1985]. In order to achieve results within an acceptable timescale, accelerated testing must be carried out. This has the disadvantage that the failure mechanism of the component or material may not be the same in the accelerated test as it would have been in service. Nonetheless, accelerated creep and thermal exposure tests have been carried out successfully enough to position specific casts of steel in a remaining life assessment.

2.1.3 Types of Load that a Plant Experiences

Power plant components are subject to various types of loadings and load cycles depending on their purpose. Thus components must be designed taking a range of factors into account and their structural health assessed accordingly.

Creep and fatigue are typically important factors when considering the requirements of turbine blades, as they are in a high cyclic stress and high temperature environment [Ashby et al. 2007, Viswanathan 1985]. The creep resistance of a component can be improved by increasing the yield strength of the material and reducing the susceptibility of grain boundary cavitation. One solution used for turbine blades is to manufacture them as single crystals which slows or stops diffusional flow and removes grain boundaries and therefore sites for the formation of cavitation [Ashby et al. 2007, Kassner and Hayes 2003, McLean et al. 1995]. The design of the blades must ensure that the stresses throughout the blades caused by the centripedal forces acting on them are kept to a minimum [Ashby et al. 2007]. Turbine blades must also have good oxidation and corrosion resistance so that the blade material is not lost to the environment [Ashby and Jones 1996, Viswanathan 1985]. The thermal and oxidation resistance of turbine blades is discussed further in Section 2.5.5.

However, other considerations must be taken when assessing, for example, the needs of boiler components. Although it is necessary for superheater/reheater tubes, headers and steam pipes to have good creep properties [Viswanathan 1985], they are not required to withstand the higher temperatures of turbine blades or the same cyclic loading and therefore can be manufactured from different materials. Flexible operation of power plants often leads to boiler temperatures peaking above those at which the boiler normally functions [Johnston et al. 2004]. This can lead to either creep, fatigue and oxidation damage or a combination of these. Nontheless, a key feature of these components is that they contain weldments and it is these features that contain potential flaws. In addition to being a main construction feature, welds can often be used to repair boiler components. If a welded component fails, it is commonly at the weld/parent material interface [Johnston et al. 2004, Viswanathan 1985]. In addition, it is recognised that weldments contain residual stresses [McDonald et al. 2002, McDonald et al. 2005 , (b)Withers and Bhadeshia 2001, Yaghi et al. 2005, Yaghi et al. 2007, Francis et al. 2007, Leggatt 2008] therefore, welded components must also be carefully assessed and/or monitored. Welding is discussed in more detail in Section 2.5.2.

2.2 Residual Stresses and Strains

2.2.1 Background

Knowledge of stresses is paramount to understanding the structural integrity of a component and therefore to avoiding failure of engineering plant [Akhurst 2008]. This requires both an understanding of both the materials involved and the operating environment [Akhurst 2008]. This section discusses the origins of different types of stresses, the relationship between stress and strain, the characterisation of stresses and ultimately, how stresses in components can lead to their failure. Particular emphasis is given to the discussion of residual stresses due to their effect on service life and their use as an indication of structural integrity [Banahan 2008, McDonald et al. 2005]. Finally, the types of load that a plant experiences are discussed, with a view to understanding the stresses generated in plant components.

2.2.2 Relationship between Stress and Strain

When analysing the strength of a body, it is assumed that it is in equilibrium [Dieter 1961]. Therefore, the sum of the external forces acting on the body must be equal (and opposite to) the sum of the resisting forces in the body. Stress is defined as the integral of these internal resisting forces divided by the area over which they are acting. However, this does not mean that the stresses in a body are necessarily uniformly distributed. In fact, this often not the case and there is a stress distribution throughout the body. It has been demonstrated, that all solid materials can experience some deformation, when an external load is applied [Ashby and Jones 1996]. The fraction of this deformation with respect to the original size of the body is known as strain. Strain can be elastic, such that when the external load is removed, the body returns to its original form; or it can be plastic, such that when the load is removed, the body is permanently deformed.

The relationship between stress and strain varies greatly depending upon whether the strain in elastic or plastic [Ashby and Jones 1996, Ashby et al. 2007]. As the load, F, and therefore strain, ε, increases, the relationship between stress, σ, and strain ceases to be linear and the rate of increase of stress with increased strain decreases. In general, this occurs because the material has deformed plastically. This means that the shear stress on the slip plane has caused the movement of dislocations and the material has yielded. This eventually causes the stress-relieving of the material and then failure. Figure 2.1 shows the relationship between stress and strain for a two types of material.

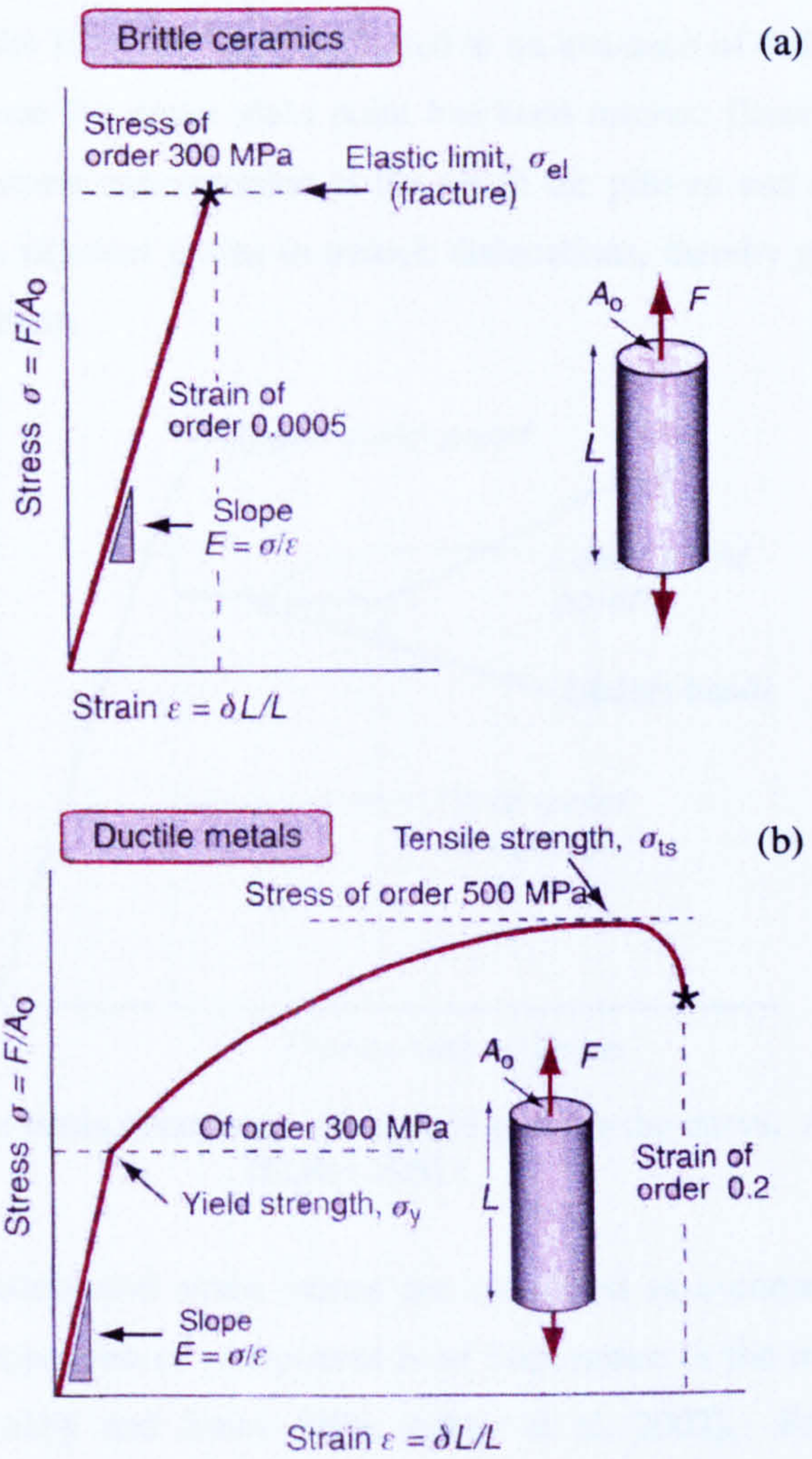

Figure 2.1. Stress/strain behaviour of (a) brittle ceramics and (b) ductile metals [Ashby et al. 2007].

Figure 2.1 shows that no plastic flow occurs in the brittle material such as a ceramic and as a consequence it fails at the elastic limit. However, the ductile metal does undergo plastic flow and so continues to deform after the elastic limit.

Additionally, many metals, in particular mild steel undergo an elastic to plastic transformation which results in an upper and lower yield point [Ananthakrishna 2007, Dieter 1961]. A front, which separates deformed from undeformed material is created after the upper yield point has been reached and propagates across the specimen. This results in the Lüders bands as shown on the stress-strain curve, as shown in Figure

2.2. Thereafter, the plastic strain proceeds as shown in Figure 2.1(b) until failure. The propagation of the front has been attributed to an avalanch of dislocations being released in grains once the upper yield point has been reached [Dieter 1961]. The combination of the stress concentration at the tip of the pile-up and the increase in applied stress causes adjacent grains to unlock dislocations, thereby propagating the front across the specimen.

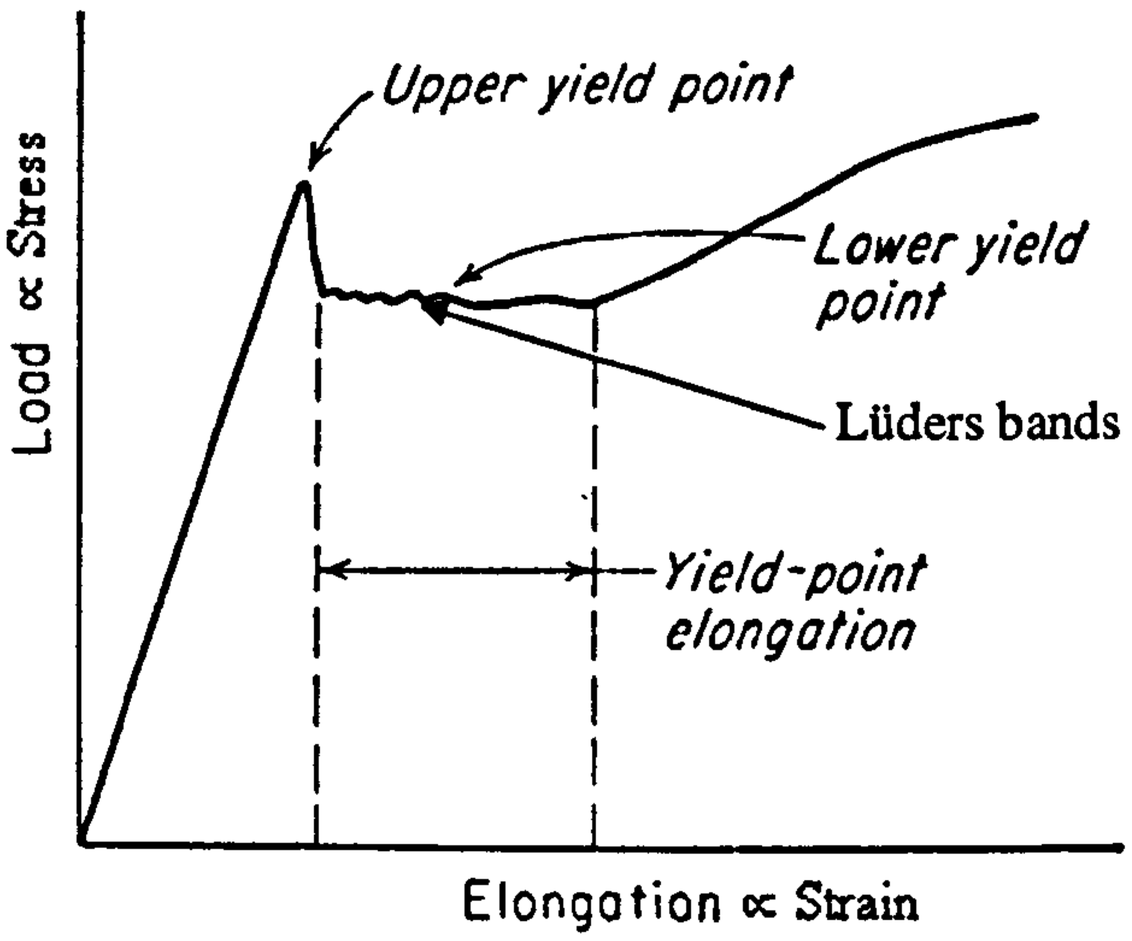

Figure 2.2. Stress strain behaviour with a yield point in the curve. After Dieter [Dieter 1961].

The way in which stress and strain values are calculated as a consequence of the deformation of the specimen or component is of importance in the measurement of stress and strain [Ashby and Jones 1996, Ashby et al. 2007]. For example, as previously mentioned in Section 2.2.2, the stress, σ, can be calculated as the nominal stress, σ_n, which is the applied force perpendicular to the sample surface, F, divided by the initial area of the sample, A, such that:

$$\sigma_n = \frac{F}{A} \qquad 2.1$$

Strain, ε, can be calculated as the nominal strain, ε_n, which is the change in length of the specimen, Δl, divided by its original length, l, and, when the material is undergoing linear elastic behaviour, the nominal strain can be related to the nominal stress, σ_n, divided by the Young modulus, E, of the material such that [Ashby and Jones 1996, Benham et al. 1996, Dugdale 1968]:

$$\varepsilon_n = \frac{\Delta l}{l} = \frac{\sigma_n}{E} \qquad 2.2$$

The true stress of a sample can be calculated by dividing the applied force to the sample surface by the area of the sample surface at the moment at which the force is applied, A_t. This means that the effects of Poisson's ratio on the specimen geometry are taken into account. Thus the true stress, σ_t, can be calculated as [Ashby and Jones 1996, Benham et al. 1996]:

$$\sigma_t = \frac{F}{A_t} \qquad 2.3$$

and true strain, ε_t, can be calculated as

$$\varepsilon_t = \frac{\Delta l}{l_t} = \frac{\sigma_t}{E} \qquad 2.4$$

where l_t is the true length of the sample.

In the above examples, the force is acting perpendicular to the discussed sample surface and the stresses and strains discussed are those acting in the direction of the force. However, stresses and strains can act in directions, which are not parallel to the applied force [Ashby and Jones 1996, Benham et al. 1996, Dugdale 1968]. Furthermore, the applied force need not act perpendicular to a surface in order to produce a deformation; it can also act parallel to it.

In the elastic region, strain and stress relationships can be generalised through the use of elastic constants [Ashby and Jones 1996, Benham et al. 1996, Dugdale 1968]. As mentioned previously, Young's modulus can relate nominal stress to nominal strain

$$E = \frac{\sigma_n}{\varepsilon_n} \qquad 2.5$$

The nominal lateral strain can be related to the nominal tensile strain through the Poisson ratio, ν, of the material such that

$$\nu = -\frac{\varepsilon_{n,lateral}}{\varepsilon_{n,tensile}} \qquad 2.6$$

The stress resulting from a force acting in plane with the sample surface is known as the shear stress, τ. This can be related to the shear strain, γ, by the shear modulus, G,

$$G = \frac{\tau}{\gamma} \qquad 2.7$$

Additionally, pressure, Pr, and its resultant negative dilatation, Δ, are linked by the bulk modulus, K,

$$\mathrm{Pr} = K\Delta . \tag{2.8}$$

These elastic constants are not independent but are related as follows

$$E = 2G(1+\nu) \tag{2.9}$$

$$E = 3K(1-2\nu) \tag{2.10}$$

$$K = \frac{2G(1+\nu)}{3(1-2\nu)} \tag{2.11}$$

For the case of static equilibrium, the directions at which stresses and strains are acting are often defined through a tensor such that stress is represented as [Boresi et al. 1993],

$$\sigma_{ij} = \begin{bmatrix} \sigma_{11} & \sigma_{12} & \sigma_{13} \\ \sigma_{21} & \sigma_{22} & \sigma_{23} \\ \sigma_{31} & \sigma_{32} & 33 \end{bmatrix} \equiv \begin{bmatrix} \sigma_{xx} & \sigma_{xy} & \sigma_{xz} \\ \sigma_{yx} & \sigma_{yy} & \sigma_{yz} \\ \sigma_{zx} & \sigma_{zy} & \sigma_{zz} \end{bmatrix} \equiv \begin{bmatrix} \sigma_{x} & \tau_{xy} & \tau_{xz} \\ \tau_{yx} & \sigma_{y} & \tau_{yz} \\ \tau_{zx} & \tau_{zy} & \sigma_{z} \end{bmatrix} \tag{2.12}$$

and strain is represented as

$$\varepsilon_{kl} = \begin{bmatrix} \varepsilon_{11} & \varepsilon_{12} & \varepsilon_{13} \\ \varepsilon_{21} & \varepsilon_{22} & \varepsilon_{23} \\ \varepsilon_{31} & \varepsilon_{32} & \varepsilon_{33} \end{bmatrix} \equiv \begin{bmatrix} \varepsilon_{xx} & \varepsilon_{xy} & \varepsilon_{xz} \\ \varepsilon_{yx} & \varepsilon_{yy} & \varepsilon_{yz} \\ \varepsilon_{zx} & \varepsilon_{zy} & \varepsilon_{zz} \end{bmatrix} \equiv \begin{bmatrix} \varepsilon_{xx} & \gamma_{xy} & \gamma_{xz} \\ \gamma_{yx} & \varepsilon_{yy} & \gamma_{yz} \\ \gamma_{zx} & \gamma_{zy} & \varepsilon_{zz} \end{bmatrix}. \tag{2.13}$$

For an anisotropic solid, the elastic relationship between stress and strain is [Theocaris and Sokolis 1999]

$$\sigma_{ij} = C_{ijkl}\varepsilon_{kl} \tag{2.14}$$

where C_{ijkl} is the stiffness tensor whose values are characteristic of the material. The inverse of the stiffness tensor is the compliance tensor represented by S_{klij}, Equations 2.15 and 2.16.

$$\varepsilon_{kl} = S_{klij}\sigma_{ij} \tag{2.15}$$

$$C^{-1}_{ijkl} = S_{klij} \tag{2.16}$$

Figure 2.3 gives an example the directions and values of strains on a body resulting from an applied stress.

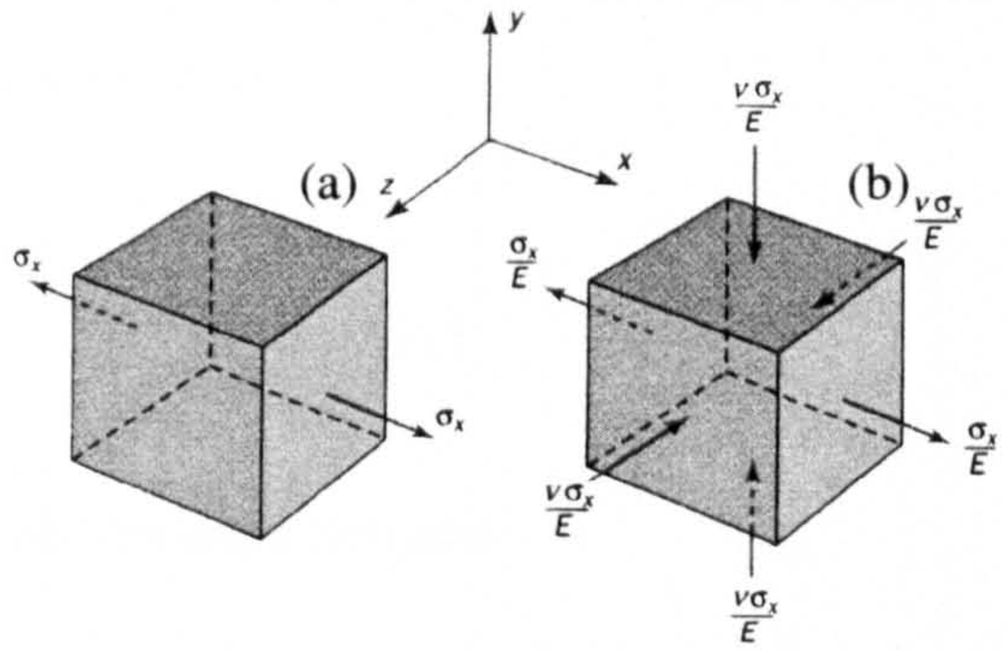

Figure 2.3. Strain (b) resulting from stress (a). The magnitude and directions of the strain and stress are shown [Benham et al. 1996].

If the stress in the z-direction is zero, then the resulting strain condition is known as plane strain and the stresses are known as plane stresses [Benham et al. 1996]. An assumption of plane stress is often made in the case of stresses in a thin cross-section body [Dieter 1961].

The plain stress tensor is

$$\sigma_{ij} = \begin{bmatrix} \sigma_{11} & \sigma_{12} & 0 \\ \sigma_{21} & \sigma_{22} & 0 \\ 0 & 0 & 0 \end{bmatrix} \qquad 2.17$$

and the corresponding strain tensor is

$$\varepsilon_{kl} = \begin{bmatrix} \varepsilon_{11} & \varepsilon_{12} & 0 \\ \varepsilon_{21} & \varepsilon_{22} & 0 \\ 0 & 0 & \varepsilon_{33} \end{bmatrix} \qquad 2.18$$

where the non-zero ε_{33} term arises from the Poisson's ratio effect.

In a body under stress, the planes at which the shear stresses, τ, are zero are known as principal planes. The normal stresses acting on these planes are known as principal stresses [Benham et al. 1996]. The principal stress tensor is shown in Equation 2.19.

$$\sigma_{ij} = \begin{bmatrix} \sigma_{11} & 0 & 0 \\ 0 & \sigma_{22} & 0 \\ 0 & 0 & \sigma_{33} \end{bmatrix} \qquad 2.19$$

Hydrostatic stress occurs when an externally applied pressure, Pr, acts equally on all planes [Benham et al. 1996]. This may occur, for example, in a body immersed in a

great depth of fluid. Hydrostatic stress results in a pressure applied on all the principal planes, Equation 2.20.

$$\sigma_{ij} = \begin{bmatrix} (\sigma_{11} - \mathrm{Pr}) & \sigma_{12} & \sigma_{13} \\ \sigma_{21} & (\sigma_{22} - \mathrm{Pr}) & \sigma_{23} \\ \sigma_{31} & \sigma_{32} & (\sigma_{33} - \mathrm{Pr}) \end{bmatrix} \qquad 2.20$$

2.2.3 Applied and Residual Stresses

Stresses can be applied (primary) or be residual (secondary) [Benning 1989, Denton 1966], depending upon the conditions the component is under. Applied or primary stresses are classified as stresses induced by a load. Residual or secondary stresses are classified as stresses that a body is under, when no external load is applied. The resulting forces and moments from the residual stresses are therefore zero. The combination of these two stress types have to be considered when addressing the overall integrity of a structure [R6 2001].

The R6 failure avoidance procedure is a method of assessing safety margins in a system and takes both primary and secondary stresses into account [R6 2001]. It is based on the premise that structures may contain flaws or cracks. Service and material parameters, namely primary and secondary stresses, affect the crack growth and thus affect the component integrity. This can be seen in the R6 failure avoidance diagram, Figure 2.4, which illustrates graphically the effect of primary and secondary stresses [McDonald et al. 2005, R6 2001].

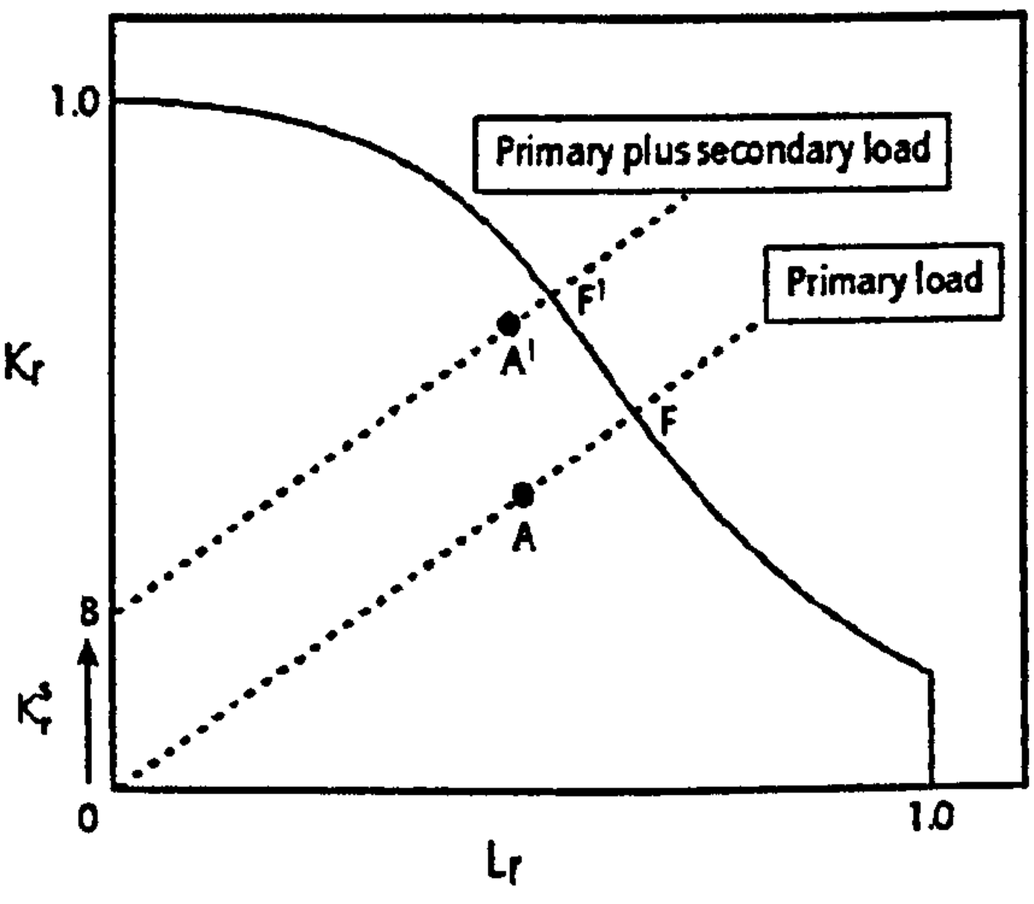

Figure 2.4. Simplified R6 failure assessment diagram [McDonald et al. 2005].

The parameters K_r and L_r define the proximity of the component to failure and the proximity of the component to ductile failure respectively [R6 2001]. K_r is defined as

$$K_r = \frac{K}{K_{IC}} \qquad 2.21$$

where K stress intensity factor and K_{IC} is the fracture toughness. L_r is defined as

$$L_r = \frac{\sigma_{ref}}{\sigma_y} \qquad 2.22$$

where σ_{ref} is a calculation of the average stress in the load bearing material due to the applied load and σ_y is the yield stress. As such, both parameters are affected by primary stresses. However, only the value of K_r is affected by secondary stresses. The contribution of secondary stresses in K_r can be seen in Equation 2.23 [R6 2001, McDonald et al. 2005].

$$K_r = K_r^p + K_r^s \qquad 2.23$$

Where K_r^p and K_r^s are the factors of K_r resulting from the applied (primary) and residual (secondary) stresses respectively. If the component conditions exceed the boundary linking K_r and L_r, failure could be conceded. Thus, as shown in Figure 2.4, the addition of residual stresses in a component could increase the value of K_r from 0 to B. This would then mean that the reserve factor would be $\frac{BA^1}{BF^1}$ rather than the original $\frac{OA}{OF}$ and as such the component would be closer to failure. It can therefore be seen that depending where A lies in the failure avoidance diagram, then the residual stresses may have a significant contribution in reducing the reserve margin.

2.2.4 Characterising Stresses

As well as being characterised by the method by which stresses are caused, they can also be characterised by the volume or length scale over which there is equilibrium [Benning 1989, Dieter 1961, (b)Withers and Bhadeshia 2001]. In a polycrystalline material, macrostresses, also known as type I stresses equilibrate over a large number of grains [Benning 1989]. Mesostresses, also called type II stresses, textural stresses or intergranular stresses equilibrate between grains. Interatomic stresses, type III stresses equilibrate over atomic scales within a grain. Another definition that is commonly used is microstress. Examples of microstresses are those caused by

dislocations or point defects [(b)Withers and Bhadeshia 2001]. Figure 2.5 illustrates the length scales over which residual stresses can act.

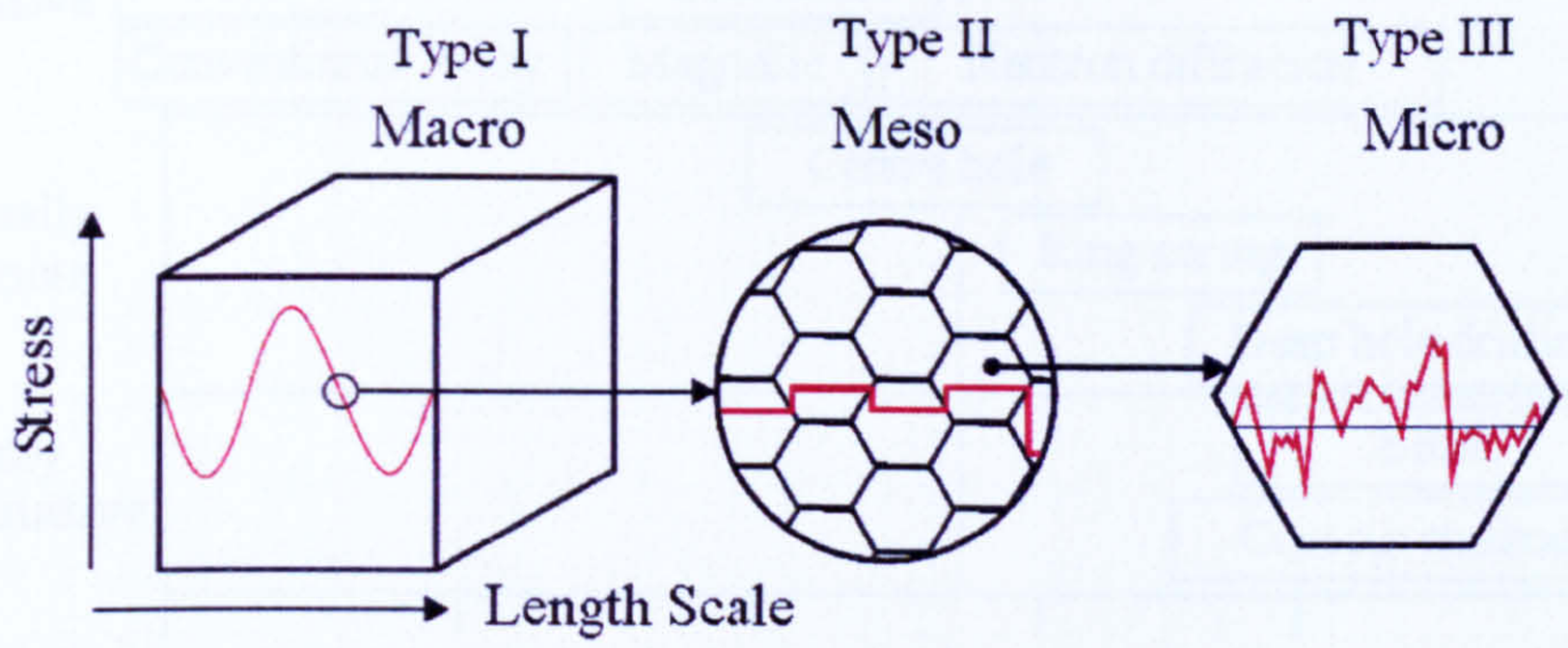

Figure 2.5. Length scales over which stresses can act. Courtesy of Profs. Peter Flewitt and David Smith, University of Bristol.

2.2.5 Stress Measurement

There are a variety of techniques, which may be employed to measure residual stress [Hilson et al. 2008, Withers 2007, Withers and Bhadeshia 2001, Withers et al. 2008]. One method of comparing these techniques is by their spatial resolution and penetration depth [Hilson et al. 2008, Withers et al. 2008]. In addition, measurement techniques can be divided according to their effect on the component whose stresses they are measuring, i.e. how invasive or destructive they are [Hilson et al. 2008, Withers et al. 2008]. Figure 2.6 shows a variety of stress measurement techniques according to their penetration depths and invasiveness. Here, photoluminescence is abbreviated by PSLS and block removal splitting and layering is abbreviated to BRSL.

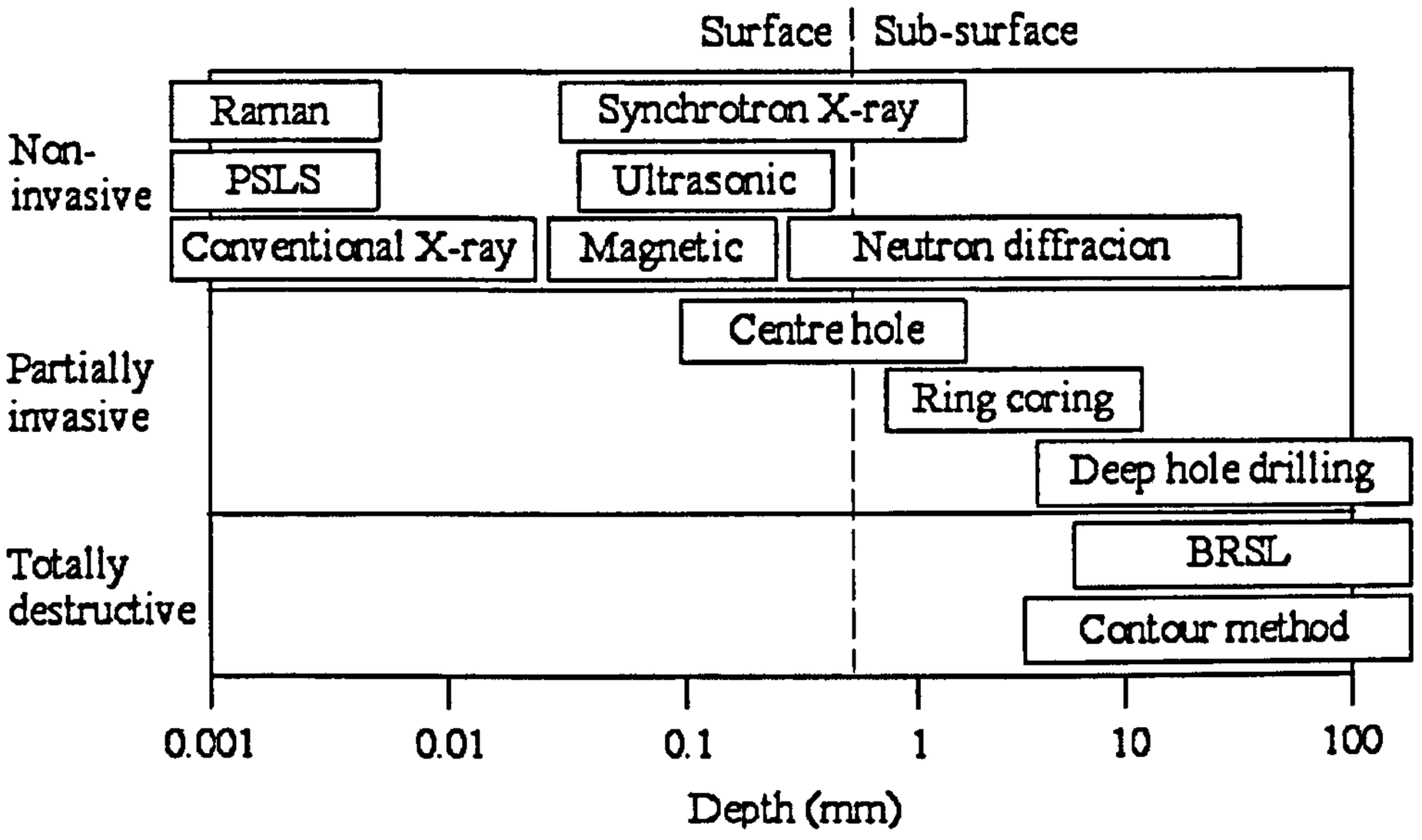

Figure 2.6. Spatial resolutions of stress measurement techniques [Hilson et al. 2008].

Although the techniques shown in Figure 2.6 are simply divided into destructive or non-destructive techniques depending on the amount of material removal required, in practice, the situation is complex. The level of invasiveness differs between the destructive techniques [Hill et al. 2005, Stefanescu et al. 2004]. Despite Raman spectroscopy being described as a non-destructive technique, the incident laser radiation has the potential to cause heating in materials [Kouteva-Arguirova et al. 2003, Shebanova and Lazor 2003]. The penetration depth of photoluminescence spectroscopy is a complex subject which has been shown to be dependent upon the specific collecting lens, laser wavelength and beam characteristics such as laser power, wavelength and spot diameter [Dassios and Galiotis 2004, Lipkin and Clarke 1995]. In addition, the material properties such as the property of the material, grain size and porosity also modify the penetration depth of the laser [Scherer et al. 1988, West 1997]. Nonetheless, despite the complexity of the calculations, an approximate measurement depth has been found to be of the order of 0.5mm in α-Al_2O_3 using a 514nm wavelength source [Dassios and Galiotis 2004]. The photoluminescence spectroscopic technique does not require the removal of material but, as with Raman spectroscopy it requires the use of a laser which has been shown to induce heating [Xu et al. 2006]. Although X-ray diffraction is described non-invasive, material is often removed from component surfaces by mechanical polishing and electropolishing

in order to create a level surface and remove machining stresses [McDonald et al. 2002]. With regards to neutron diffraction, it has been shown to be a completely non-destructive technique [Webster and Wimpory 2002, (a)Withers and Bhadeshia 2001]. However, as indicated in Figure 2.6, the technique suffers from poor spatial resolution [Webster and Wimpory 2002].

Incremental hole drilling is often referred to as partially invasive or semi destructive, as the volume of removed material is typically small and can often be tolerated in the component [Stefanescu et al. 2006]. Although deep hole drilling involves more material removal than incremental hole drilling, it is also described as partially invasive as the volume of material is again relatively small and in some applications, the hole can be removed [Stefanescu et al. 2006]. The techniques employed in this work, are discussed further in Chapter 3 - Techniques.

2.2.6 Origins of Residual Stresses

Residual stresses can arise in a variety of ways including by plastic deformation and temperature differences or misfits due to phase transformations [Callister 2000, Withers and Bhadeshia 2001]. Although they are often detrimental to the structural integrity of a component, the stresses can be engineered to improve integrity by increasing the yield strength in the surface of the material [Benning 1989, Flinn and Trojan 1986, (b)Withers and Bhadeshia 2001], or, by inducing surface compressive macrostresses which reduce the near surface tensile macrostress due to loading by an amount equal to the surface compressive stresses [Dieter 1961]. Residual stresses arising from different mechanisms can interact with each other and can strongly influence the properties of the structure or component. For example, heating a component can cause a phase transformation and can affect its subsequent volume changes [(b)Withers and Bhadeshia 2001]. Residual stresses can act on macro-, meso- and microscales and the stresses developed on these scales can extend to other scales [(b)Withers and Bhadeshia 2001]. Stresses can be superimposed to form stresses on a larger scale such as microstresses due to mixed phases resulting in long range macrostresses [(b)Withers and Bhadeshia 2001]. Furthermore, misfits on a microscale can generate stresses on a mesoscale and misfits on a mesoscale can generate stresses on a macroscale [Bouchard and Withers 2004]. A clear

understanding of the residual stresses in a structure or component is therefore necessary [Benning 1989]. The ways in which residual stresses can arise are discussed in more detail in Sections 2.2.7 to 2.2.9 and the mechanisms by which failure can occur are discussed in Section 2.3.

2.2.7 Mechanically Induced Stresses

Macrostresses can be induced mechanically such as by grinding or shot-peening [Doig and Flewitt 1978, Flinn and Trojan 1986, Lonsdale et al. 1981]. These stresses may arise as part of the manufacturing process of the component or may be induced intentionally [Menig et al. 2001]. Plastic deformation can be induced in the surface of a material together with associated compressive stresses by shot-peening [Flinn and Trojan 1986]. This increases the yield strength at the surface and therefore allows the component to undergo higher strains before yielding occurs [(b)Withers and Bhadeshia 2001]. Furthermore, as mentioned in Section 2.3, tensile surface stresses due to loading are reduced by a value equal to the mechanically induced surface compressive stresses.

Also, as mentioned previously, stresses in a component can also be induced by subjecting a component to a load or varying loads [Ashby and Jones 1996]. Sometimes these loads serve to increase the yield strength of the material [Flinn and Trojan 1986]. However, they can also reduce the lifetime of the component [Ashby and Jones 1996].

2.2.8 Thermal Effects

Temperature differentials can be the cause of residual stresses in a material [Callister 2000, Denton 1966]. When a solid body is heated or cooled, the temperature distribution throughout the body is determined by geometrical factors such as the size and shape of the body, the thermal gradient of the body and the rate of temperature change that it is experiencing for a given thermal conductivity.

Stresses can be induced by the constraint to the thermal expansion or contraction of a material [Callister 2000]. These would not occur if the material were not restrained in

some way. The magnitude of the thermal stress, σ_t, induced by a temperature change, ΔT, is related to the thermal expansion coefficient, α_t, and Young's modulus, E.

$$\sigma_{th} = \alpha_{th} E \Delta T \qquad 2.24$$

The thermal gradient itself can also be the cause of elastic/plastic strain and thereby introduce residual stresses [Callister 2000, Dieter 1961]. Although not mechanically constrained, the temperature gradient across a component can result in stresses being induced throughout as if a mechanical constraint were present. That is to say that the various parts of the component would individually behave in a particular way during the cooling process but are constrained to each other [(b)Withers and Bhadeshia 2001]. One example of thermally induced stresses is that of stresses resulting locally induced heating [Gurney 1971, Kouteva-Arguirova 2003]. The heated area may wish to expand and cool to a larger than original volume [Gurney 1971]. However, this volume is constrained by the surrounding, unheated material. This results in tensile stresses towards the centre of the heated region balanced by compressive stresses in the surrounding region.

2.2.9 Phase Transformations

Phase transformations can induce stresses in components [Callister 2000, (b)Withers and Bhadeshia 2001]. Phase transformations involve a change in microstructure. Volume changes in the component due to this change can result in stress changes in the material. They can be on a scale of different parts of a system or component to within a microstructure, i.e. acting on a macro-, meso- or microscale. The term transformation strain refers to the change in crystal structure due to phase change and is of great relevance to welding [(b)Withers and Bhadeshia 2001]. During welding of ferritic steel, austenite has been shown to form in the fusion zone upon solidification and then go on to form another phase upon cooling such as ferrite, pearlite, or martensite inducing transformation strains and stresses due to the volume changes, Figure 2.7 [Deng and Murakawa 2006, Francis et al. 2007]. It has been proposed, that if stresses in welds are to be modelled and predicted, it is necessary to take these phase transformations into account [Deng and Murakawa 2006, Yaghi et al 2007]. Another effect of importance to the understanding of structural integrity in a component is that phase transformations can also greatly affect the material properties

of the component such as strength and ductility [Callister 2000]. Figure 2.7 shows the effect of temperature on volume changes in martensitic and austenitic steel.

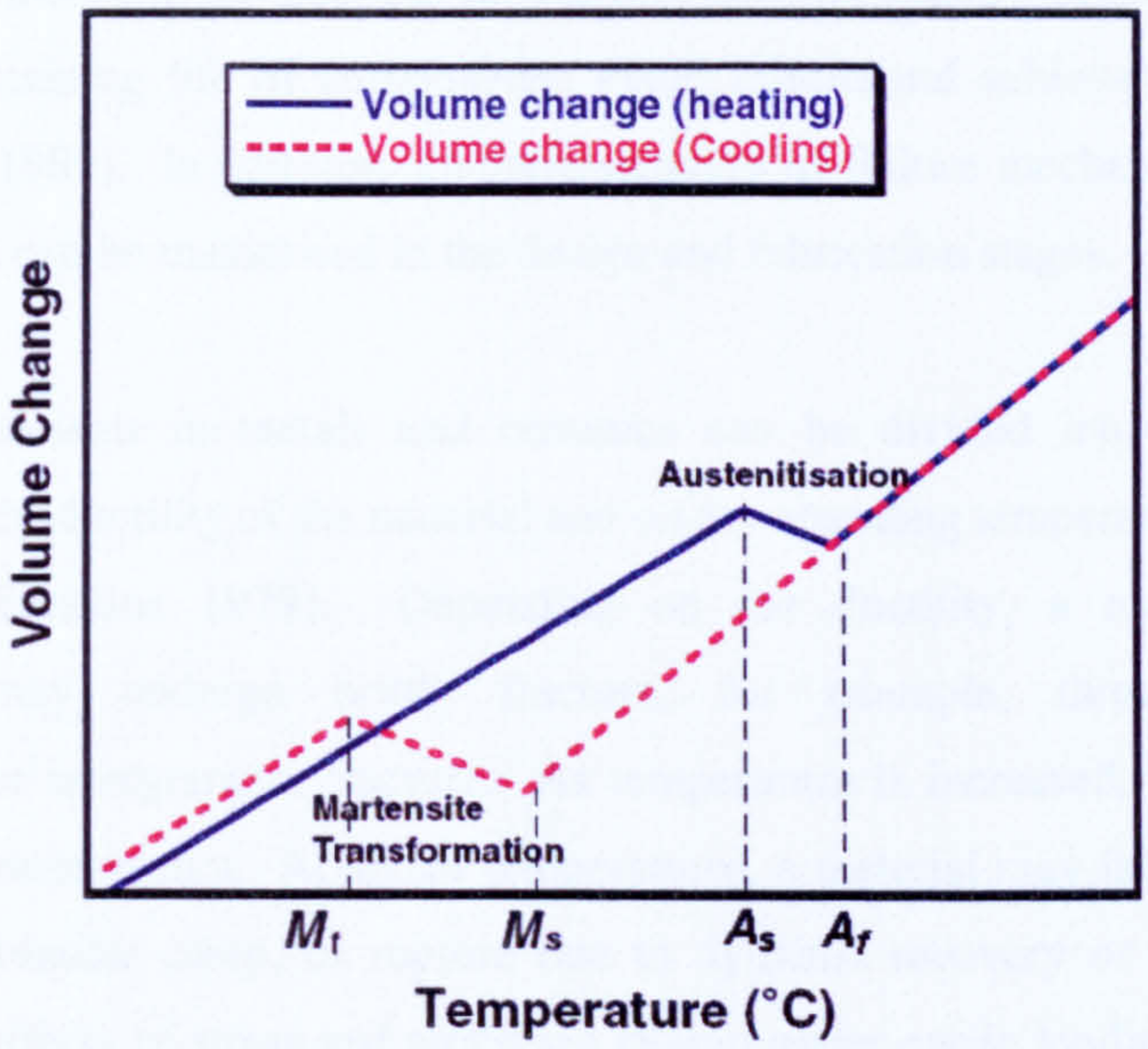

Figure 2.7. Schematic diagram of volume changes in steel due to phase transformation. M_f is the temperature at the end of the martensitic transformation, M_s is the temperature at the start of the martensitic transformation, A_s is the temperature at the start of the austenitic transformation and A_f is the temperature at the end of the austenitic transformation [Deng and Murakawa 2006].

In addition to phase transformations inducing stress, it also has been shown that the opposite effect can occur and that stress can induce phase transformations [Bhadeshia 1995]. Simultaneous stress and temperature contributions have been shown to result in phase transformations at low stresses or relatively small deviations from the equilibrium temperature. For example, austenite has been shown to transform to martensite above its normal martensite start temperature. Furthermore, the amount of martensite transformed increased with an increasing level of applied stress to the austenite sample.

2.3 Failure Mechanics

2.3.1 Background

The significance of the effects of primary and secondary stresses on a component can be seen in the mechanisms which limit lifetime can be reduced and ultimately lead to

failure [Ashby and Jones 1996]. This can occur by a variety of mechanisms [Ashby and Tomkins 1979]. With regards to conventional power plant components, it is important to understand the possible failure mechanisms which can occur in order to predict the remaining life of components, avoid failure and achieve safe operation [Viswanathan 1989]. In addition, an understanding of failure mechanics means that component life can be maximised in the design and fabrication stages.

Fracture mechanisms in metals and ceramics can be divided into broad classes depending on the ductility of the material and on the operating temperature, Figure 2.8 [Ashby and Tomkins 1979]. Depending on the ductility, a material at low temperature may undergo brittle fracture, for example, through cleavage, transgranular or intergranular fracture. As temperature is increased, slip dominates and ductile rupture occurs. At higher temperatures, a material may fail, for example, through intergranular creep, or rupture due to dynamic recovery or crystallisation. Although the effects of stress and strain are altered under cyclic loading, the fracture mechanisms of metals and ceramics remain similar.

The fracture mechanisms that can occur are summarised as a fracture-mechanism map, whereby the fracture mechanisms are shown with respect to the normalised tensile stress of the material and its homologous temperature in Figure 2.9 [Ashby and Tomkins 1979]. Five modes of fracture resulting from different stress, temperature and pre-existing flaw ranges are indicated. Cleavage 1 is the totally brittle failure by a material resulting from a pre-existing flaw. Cleavage 2 is the almost totally brittle method of failure below general yield of a material resulting from slip or twinning nucleation. Cleavage 3 is the region in which creep precedes fracture, although the failure mechanism may be by cleavage. The region representing ductile fracture and creep fracture is also shown. In ductile fracture, sample necking and the coalescing of voids results in shearing [Callister 2000]. Creep fracture also results from the coalescing of voids, however, a significant difference between creep fracture and ductile fracture is that for creep, the flow stress is controlled by strain rate [Ashby and Tomkins 1979]. B.I.F. is brittle intergranular fracture.

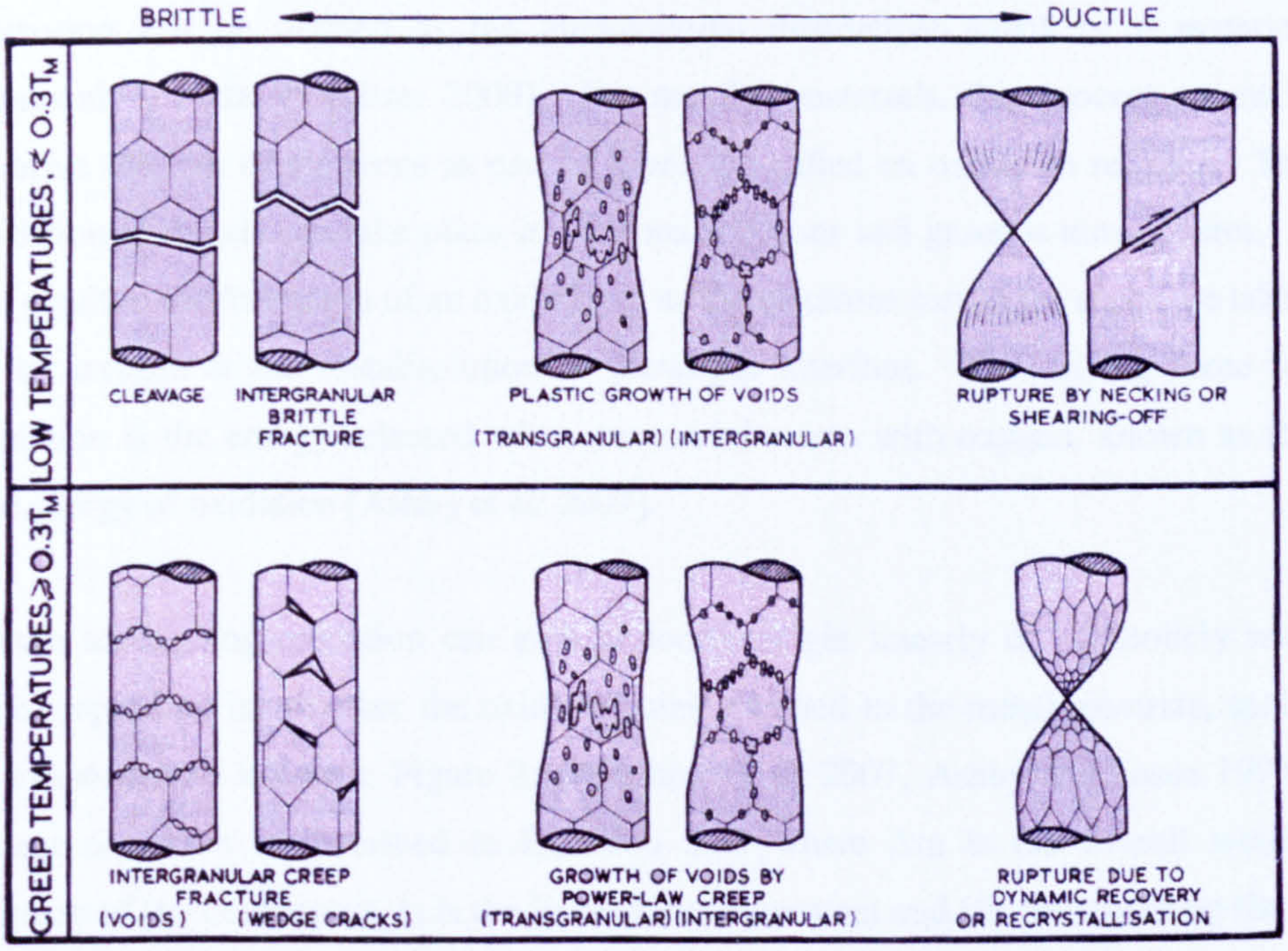

Figure 2.8. Classes of fracture mechanisms [Ashby and Tomkins 1979].

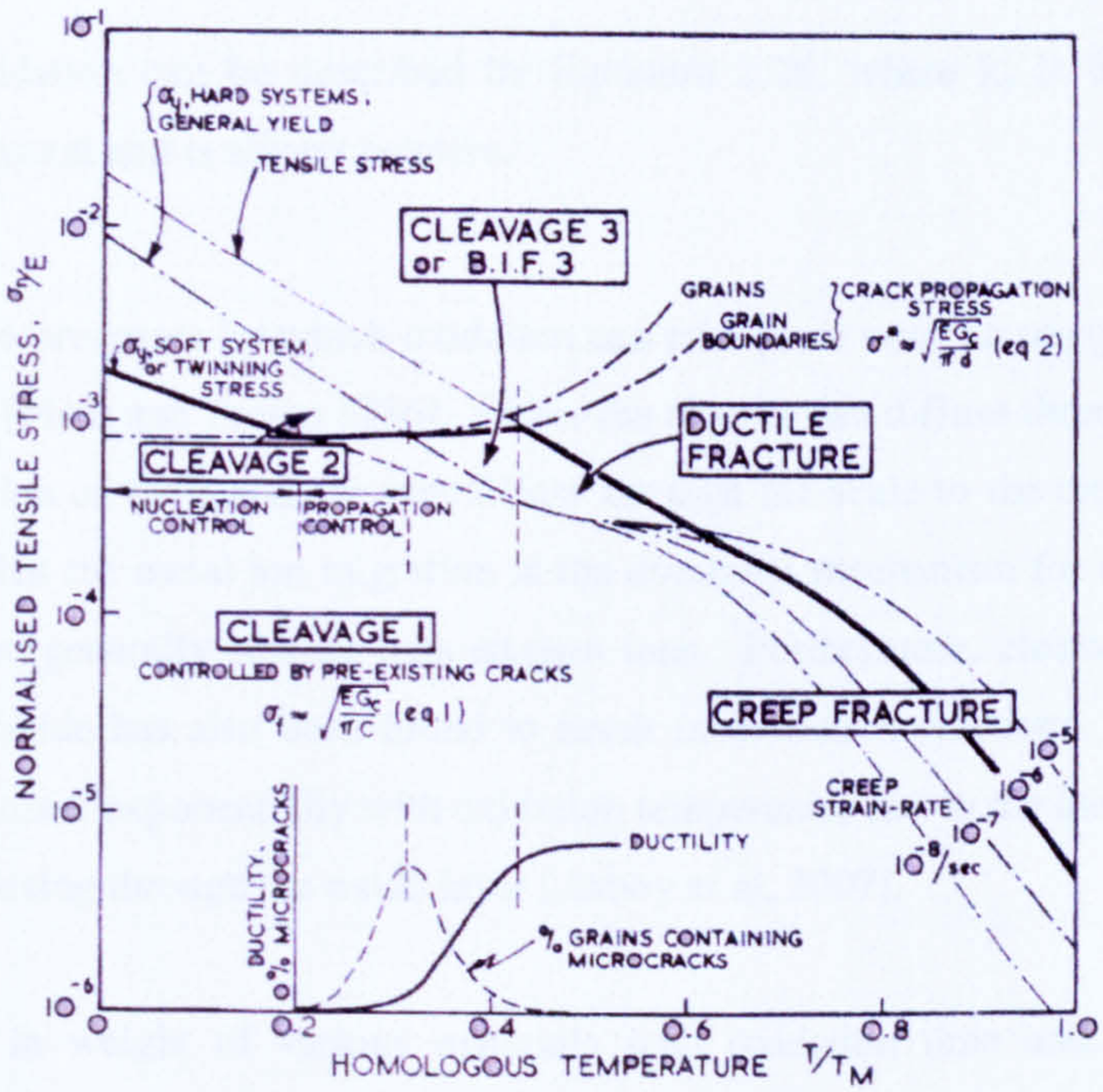

Figure 2.9. Intergranular fracture fields with respect to normalised tensile stress and homologous temperature [Ashby and Tomkins 1979].

2.4 Oxidation Kinetics

Corrosion can be defined as the unintentional destructive attack of a material, commonly a metal [Callister 2000]. For metallic materials, this process normally involves the loss of electrons as part of a process called an oxidation reaction. The oxidation of metals can take place in aqueous solutions and gaseous atmospheres. It can result in the formation of an oxide layer as the electrons lost to the metal are taken up by oxygen at the metal/solution or metal/gas interface. The driving force for oxidation is the energy released when a material reacts with oxygen, known as the free energy of oxidation [Ashby et al. 2007].

Metals undergoing oxidation can gain or loose weight linearly or parabolicly with time, depending on whether the oxide remains attached to the metal substrate, spalls or evaporates as it forms, Figure 2.10 [Ashby et al. 2007, Ashby and Jones 1996]. Linear oxidation is described in Equation 2.25 where Δm is the overall weight increase of the component, k_l is the linear kinetic constant and t is the oxidation time. The value of k_l may be positive or negative [Ashby and Jones 1996].

$$\Delta m = k_l t \qquad 2.25$$

Parabolic oxidation can be described by Equation 2.26, where k_p is the parabolic oxidation constant and is always positive.

$$(\Delta m)^2 = k_p t \qquad 2.26$$

There are two processes by which oxidation can take place once an oxygen layer has been created [Flinn and Trojan 1986]. Either the oxygen can diffuse through the scale to the metal ion or the metal ion can diffuse through the scale to the oxygen. It has been found that the metal ion migration is the dominant mechanism for oxidation, as metal ions are generally smaller than oxygen ions. Furthermore, electron migration through the oxide has also been found to result in oxidation reactions. The kinetic constants increase exponentially with oxidation temperature due to the increase in flux of atoms diffusing through the oxide layer [Ashby et al. 2007].

The change in weight of various materials with oxidation time and for a given oxidation temperature can be seen in Figure 2.10.

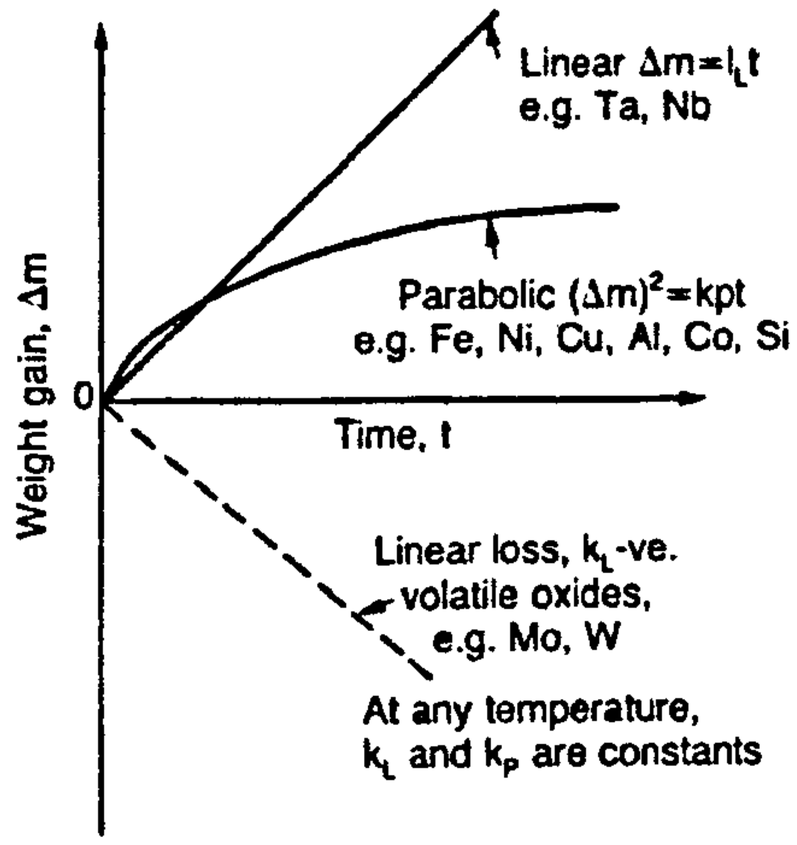

Figure 2.10. Change in weight of various materials over time for a given oxidation temperature [Ashby and Jones 1996].

The level of protection that oxide layers give to the metal substrate is dependent on their chemical properties [Flinn and Trojan 1986]. Alloys containing a sufficient amount of chromium or aluminium such as stainless steel and superalloy bond-coats can form protective Cr_2O_3 or Al_2O_3 oxide scales respectively [Evans 1995]. These scales have relatively low diffusion coefficients and high melting points [Ashby and Jones 1996]. In addition, they are electrical insulators, meaning that the diffusion of metal or oxygen ions through them occurs slowly and they also increase in thickness at a relatively slow rate. These scales therefore act as a barrier to further oxidation. However, the percentage of the alloying element in the material will reduce through the oxidation and may over time result in the oxidation of other elements [Evans 1995]. Therefore, if the oxide layer cracks or spalls due to macroscopic stress generation, it may be difficult for the layer to heal through further oxidation due to a lack of the alloying element in the metal substrate. Also, it is important to ensure that the mechanical properties of the component are not compromised by the reduced concentration of the preferentially alloying element throughout the oxidation process.

Macrostressstress can be generated in the oxide during the oxidation process such as isothermal oxidation or thermal cycling [Colombi Ciacci et al. 1999, Stott 1987]. Macrostresses can result from strains induced by differential contraction of the oxide and metal substrate produced by a decrease in temperature. However, they may also arise from volume changes within the oxide resulting from oxide growth. Furthermore, macrostresses in the oxide can also result from externally applied loads

and service stresses [Evans 1989, Evans and Lobb 1984, Stott 1987]. The macrostresses in an "as grown" oxide layer are often not distributed uniformly throughout the layer and the substrate and as a consequence comprise stress gradients [Evans 1989]. These macrostress gradients are integral to the relaxation and failure mechanisms of the oxide.

Stresses on a meso- and microscale have also been shown to be present in oxides. In aluminium oxide, mesostresses have been proposed to be caused by grain boundary mismatch due to the existence of different phases and by voids [(a)Bourne 2006, (b)Bourne 2006]. Stresses on a microscale have been suggested to have been caused by dislocations [Atkinson et al. 2000]. As the macrostresses in the oxide reach the ultimate strength of the oxide, it will stress relieve [Callister 2000]. These stresses on a meso- and microscale have been found to combine, resulting in stresses on a macroscale [Atkinson et al. 2000, (b)Bourne 2006, (b)Bourne 2006]. The four main mechanisms through which oxide relaxation on a macroscale occurs are; the plastic deformation of the oxide scale, plastic deformation of the metal substrate, elastic fracture of the scale and spallation of the scale from the metal substrate [Stott 1987].

Although there is evidence for plastic deformation of oxide scales [Stott 1987, Wang et al. 1996], it has been shown that most brittle materials such as oxides to not lend themselves to dislocation motion. Indeed, most oxides do not possess the necessary number of slip systems to deform in this way [Stott 1987]. It has, however, been shown that it is possible for grains to deform by grain boundary diffusion, a high temperature creep mechanism [Stott 1987] and by grain sliding during cooling [Wang et al. 1996]. Both of these processes occur more commonly in finer grained oxides [Stott 1987, Wang et al. 1996].

Deformation of a metal substrate can occur under the stress of an "as grown" oxide [Stott 1987]. If the stresses at the oxide/substrate interface exceed the yield strength of the substrate and the tensile strength of the oxide is not exceeded, the substrate will yield locally to accommodate the stress [Nagl and Evans 1993]. However this process is unlikely to occur in most high temperature alloys, since most possess good strength and creep properties [Stott 1987].

The conditions under which cracking and spallation of oxide occurs, depend upon the stresses in the oxide and on the relative strengths of the oxide and the oxide-metal interface [Evans 1989, Evans and Lobb 1984]. There are two mechanisms by which cracking and spallation can occur in an oxide which has compressive macrostresses as a result of cooling, Figure 2.11. For the oxide coated metal substrate shown at the top of this figure, ξ is the oxide thickness, T is the temperature of the oxide, T_o is the oxidation temperature, T_1 is the temperature of the initial oxide scale or interface failure, T_2 is the temperature at which the spalled oxide is released, σ_{ox} is the stress in the oxide, λ^2 is the lateral area of the spalled oxide particle and 2a is the diameter of the interface suffering initial decohesion.

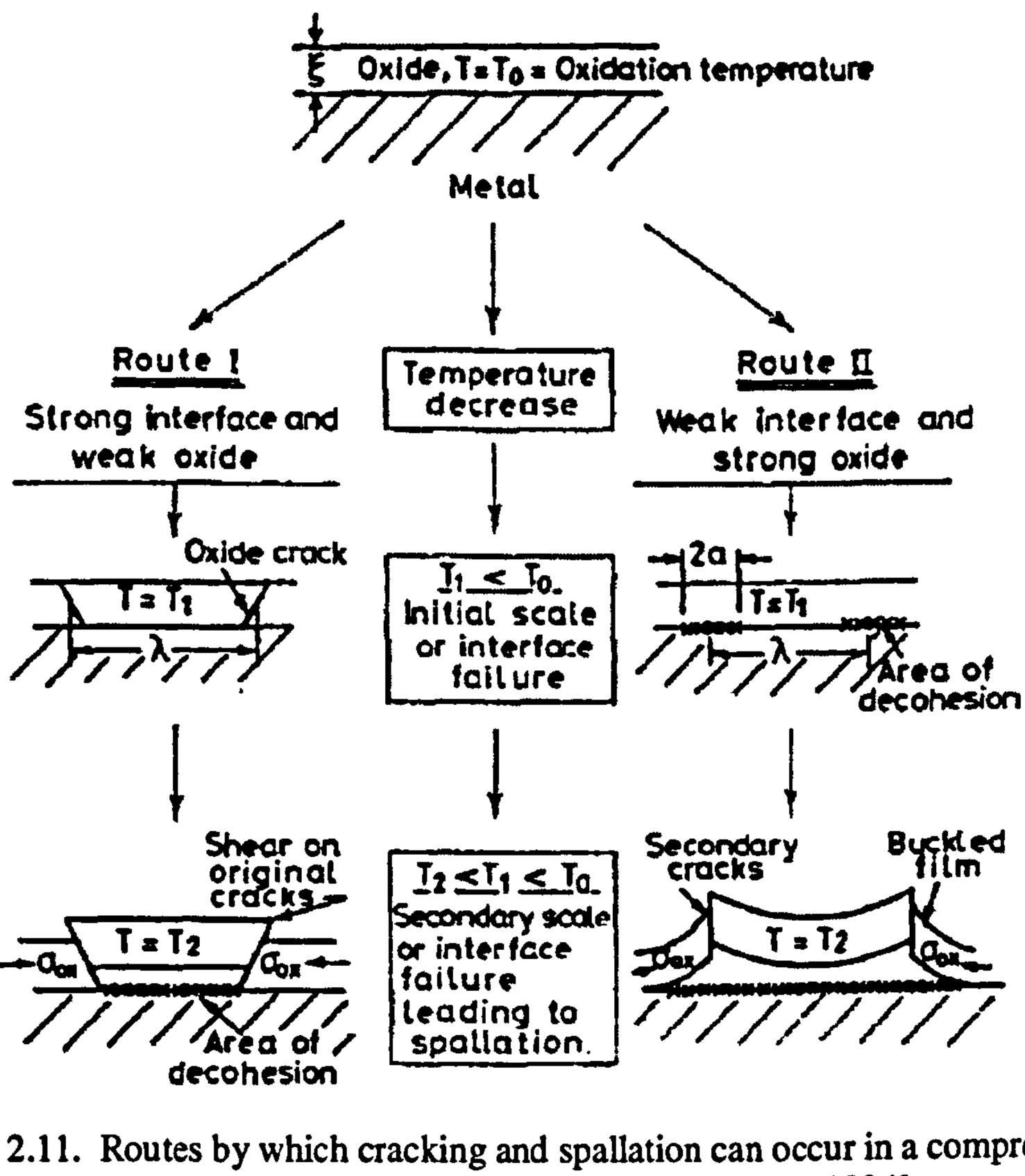

Figure 2.11. Routes by which cracking and spallation can occur in a compressively stressed oxide due to cooling [Evans and Lobb 1984].

Route I in Figure 2.11 shows how stress relieving in an oxide occurs when there is a strong oxide/metal interface [Evans and Lobb 1984]. The increase in compressive stress in the oxide cannot be stress relieved by deformation or debonding at the

interface and must occur in the form of rupture of the oxide and cracking. Compressive stresses within the oxide then force the oxide within the cracks to decohere from the substrate and spall.

By comparison, route II demonstrates how oxide delamination and spallation occur for the case of a weak oxide/substrate interface and a strong oxide. The initial oxide relaxation occurs through decohesion of the oxide layer. This results in secondary cracks in regions of high stress.

For the case of an oxide with tensile macrostresses, through-thickness cracks will develop from pre-existing defects [Evans 1989]. Interfacial fracture also occurs between the cracks due to shear. The combined effect of these two mechanisms is the spallation of oxide between cracks.

2.4.1 Thermal Cycling

Metallic-substrate deformation plays an important role in oxide scale stress relief during thermal cycling [Ambrico et al. 2001, He et al. 2000]. Cyclic yielding of the oxide and substrate can result in deformation at the oxide/substrate interface as follows. Plastic misfits introduce strains at the interface. These misfits introduce macrostresses in the oxide and substrate, which results in plastic deformation of both the oxide and substrate in and around initial interface defects [Ambrico et al. 2001]. Yielding of the oxide and substrate is increased with each thermal cycle. The continued yielding of oxide and substrate can sometimes lead to a "rumpling" effect, which can induce heat transfer due to an increased surface area [Tolpygo and Clarke 2007, (a)Tolpygo and Clarke 2004 (b)Tolpygo and Clarke 2004]. Deformation of the oxide and substrate can result in tensile stresses in some locations of the oxide, despite overall compressive stresses. It is commonly in these regions of tensile stresses that cracking of the oxide occurs [He et al. 2000].

Examples of oxide and substrate deformation resulting from thermal cycling are often found in coatings and their oxides of turbine blades used in the power generation and aerospace industries [Ambrico et al. 2001, He et al. 2000, Tolpygo and Clarke 2007]. This is of consequence, spallation of the oxide resulting from the plastic deformation

leads to further oxidation of the protective bond-coat. Furthermore, if a thermal barrier coating has been deposited on to the bond-coat, rumpling can result in a loss of adhesion of the thermal barrier coating [He et al. 2000]. An example of rumpling in a turbine blade coating and its oxide after cyclic oxidation, along with the coating and oxide after isothermal oxidation is shown in Figure 2.12.

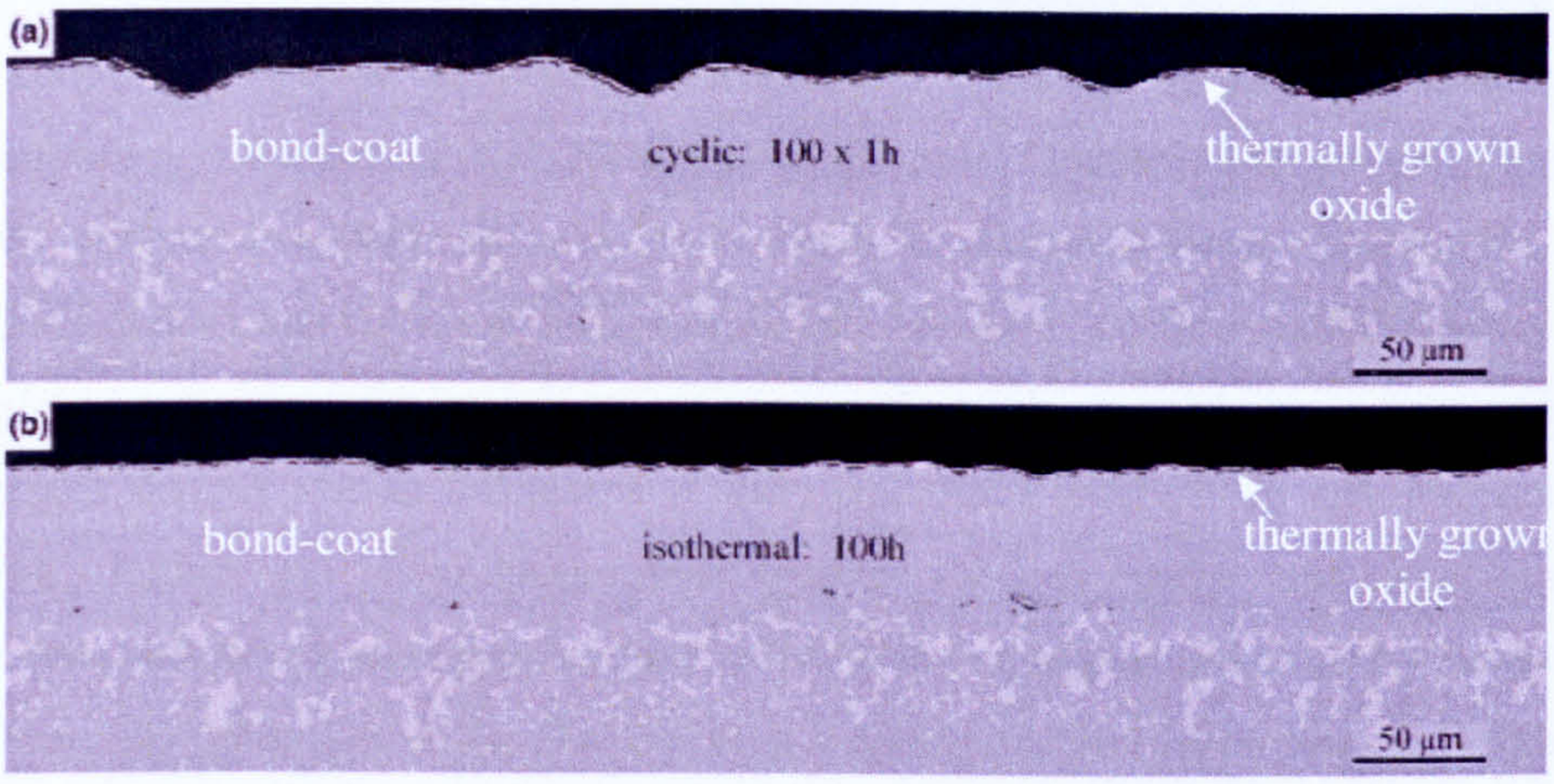

Figure 2.12. Rumpling of a thermally grown oxide and bond-coat after (a) thermal cycling and (b) isothermal oxidation [(b)Tolpygo and Clarke 2004].

2.4.2 Specimen Geometry

Specimen geometry is an important factor in the development of stress in an oxide layer [Hsueh and Evans 1983, Stott 1987]. It has been found that for an oxide formed by outward diffusion, i.e. by the outward diffusion of metal ions, the metal interface moves away from the first formed scale as the oxidation proceeds. If such an oxide is formed on a convex surface, the area of the oxide/metal interface decreases in size as the oxidation proceeds. This was found to result in the oxide becoming more compressive with oxidation time, due to the geometrical constraints of the contracting substrate area. For a concave surface with an oxide formed by outward diffusion, stresses in the oxide were found to become increasingly more tensile with oxidation time. This was due to the increasing surface area of the oxide/metal interface. Oxides formed by inward diffusion were found to behave in the opposite way to the above two examples, as the oxide grew outwards on the convex surface and further inwards on the concave surface.

2.4.3 Stress Measurement in Oxides

Much research has been carried out on the measurement of as-grown stresses in oxides. Three commonly used non-invasive methods are X-ray diffraction [(b)Mougin et al. 2001], Raman spectroscopy [Benner and Nagelberg 1981, Birnie et al. 1992, Galerie et al. 2004, Krishnan et al. 2006, (b)Mougin et al. 2001 (c)Mougin et al. 2001 (d)Mougin et al. 2001, Shim and Duffy 2002] and photoluminescence spectroscopy [Christensen et al. 1996, Gell et al. 2004, Grabner 1978, He and Clarke 1995, Krishnan et al 2006, Ma and Clarke 1993, Nychka and Clarke 2001, Nychka et al. 2003, Selcuk and Atkinson 2003, Selcuk and Atkinson 2002]. X-ray diffraction is employed to measure the interplanar spacings in the oxide crystal lattices, from which principal stresses can be calculated [Cullity and Stock 2001, Klug and Alexander 1974]. Raman and photoluminescence spectroscopy are optical laser techniques. Raman spectroscopy provides a measure of the inelastic scattering of light by phonons and uses the behaviour of the phonons as a measure of stress in the material [Smith and Dent 2006]. Photoluminescence spectroscopy uses the interaction of electrons with light as a measure of stress in the material [Colombi Ciacci et al. 1999]. The degree to which the directionality of the stresses can be ascertained in Raman and photoluminescence spectroscopy is dependent upon the level of information which can be calculated about the stress tensor of the material. Polarised laser light and an accurate prior knowledge of the directionality of the stresses are required for a complete stress tensor to be obtained [De Wolf 1996, He and Clarke 1995, Smith and Dent 2006].

These techniques are surface techniques, Figure 2.6. However, since the penetration depths of these techniques are similar to the thickness of the oxides, these surface techniques can be used to gain an understanding of stresses through substantial depths of the oxides [Mougin et al. 2002, (a)Mougin et al. 2001, (b)Mougin et al. 2001, (a)Tolpygo and Clarke 2001]. Two common areas of research have explored stresses formed in the thermally grown oxide of turbine blades [Atkinson and Selcuk 2004] and on high chromium specimens [Birnie et al. 1992, Galerie et al. 2004, (b)Mougin et al. 2001 (c)Mougin et al. 2001 (d)Mougin et al. 2001]. An understanding of the stresses in α-chromium oxide (Cr_2O_3) is important, as it is mainly this oxide type

which forms on stainless steels [Birnie et al. 1992]. Thus an appreciation of the behaviour of this oxide can aid estimations of the life of a component.

2.5 Stresses in Specific Engineering Features

2.5.1 Background

This section reviews the stresses that are developed in specific engineering features, namely weldments, oxides grown on steel substrates and turbine blades. A summary of the influences on the structural integrity of weldments is given, along with parameters that affect their residual stresses. Commonly measured stresses are also mentioned. The measurement of stresses in α-chromium oxide (Cr_2O_3) layers is considered in as-grown oxide layers as well as in deposited films. The influence of applied strain in also discussed. Stress measurements in alumina using photoluminescence spectroscopy are also considered, along with the relationship of stresses in the ceramic coating to its structural integrity. The relationship between the structural integrity of the coating to the structural integrity of the turbine blade discussed.

2.5.2 Weldments

Welding is a fabrication process that is employed in the construction, maintenance and repair of power plant components such as boilers and headers as well as the structural members of the building [Price and Alberry 1988]. The structural integrity of the weldments is therefore vital for safe and economic operation. There are several types of welding methods, which include arc, gas and laser beam welding [Callister 2000]. These all involve the joining of engineering parts through the use of molten metal.

The region adjacent to the weld is termed the heat affected zone (HAZ) and may experience changes in microstructural together with mechanical and physical properties due to diffusion and thermal effects [Callister 2000]. If the HAZ experiences recrystallisation and grain growth due to the previous cold working of the parent material, the material in the HAZ could be less strong, hard or tough than that of the parent. In addition, the thermal effects in the HAZ upon cooling can result in

residual stresses. Phase changes during the heating and cooling of the HAZ can also result in residual stresses and a change in material properties. During the welding process, some stainless steels can form chromium carbide precipitates along the grain boundaries, resulting in a chromium depleted zone adjacent to these boundaries which is therefore susceptible to corrosion. Welds commonly fail in the HAZ or surrounding regions [Ashby and Jones 1998, Price and Alberry 1988]. A schematic diagram of a weld bead showing the complex microstructure associated with the heat affected zone is shown in Figure 2.13.

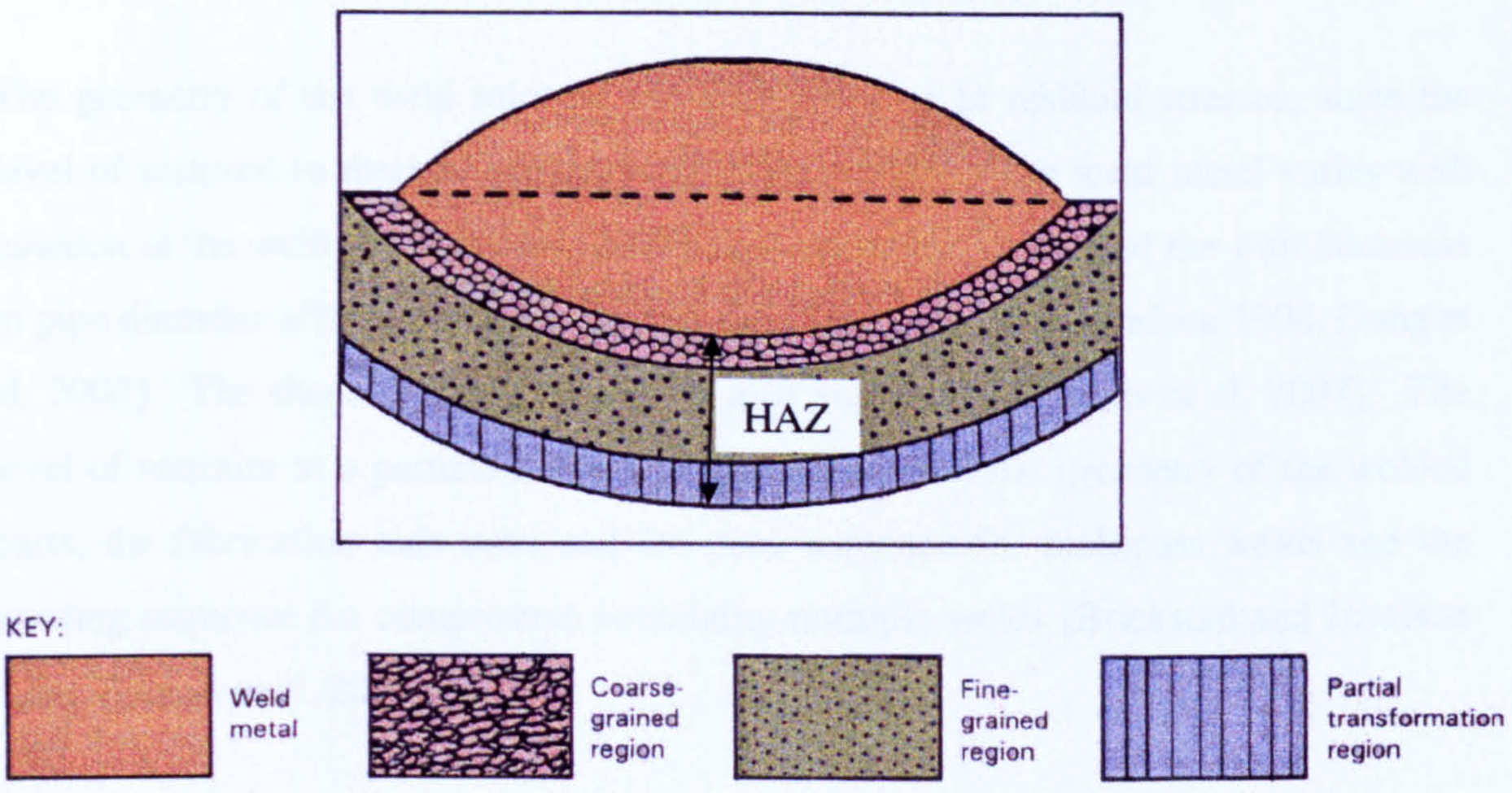

Figure 2.13. Schematic diagram of a weld bead and heat affected zone [Price and Alberry 1988].

Unlike arc and gas welding, laser beam welding does not require a filler material and instead uses a laser source to heat and melt the parts to be joined [Callister 2000]. However, it is the arc and gas welding methods that shall be discussed in this section.

Residual stresses and various defects can develop in welds depending on how the process is carried out such as the welding method and any faults that occur during the welding procedure [Brickstad and Josefson 1998, Flinn and Trojan 1986]. The defects can serve as stress concentrations [Viswanathan 1989]. Some of these defects and residual stresses are caused by flaws such as gas porosity [Flinn and Trojan 1986]. Porosity occurs due the precipitation of either the welding gas used or the gas used for the weld rod coating, as the weld metal solidifies. Slag entrapment in the

weld metal can also be problematic and can be caused by the inadequate removal of the slag between welding passes. The weld set-up and welding procedure adopted can also have an effect regardless of any flaws introduced during the welding process. An example of the stresses resulting from the weld set-up is if the parts to be welded are shifted or by the removal of fixtures [Brickstad and Josefson 1998, Flinn and Trojan 1986]. An example of the effect of the welding method is the heat distribution in the weld metal pool produced or the downward pressure in the weld pool produced by the plasma jet from arc welding [Francis et al. 2007]. Changes in these welding parameters can result in different residual stresses in the final weldment.

The geometry of the weld selected can also give rise to residual stresses, since the level of restraint to thermal expansion and contraction of the weld metal varies with position in the weld [Francis et al. 2007]. For example, the ratio of the wall thickness to pipe diameter affects the residual stress field [Brickstad and Josefson 1998, Dong et al. 2002]. The shape of the weld pool is also significant [Francis et al. 2007]. The level of restraint at a particular point is dependent upon the geometry of the welded parts, the fabrication aids used and the pass sequence for multipass welds and the welding sequence for components containing multiple welds [Brickstad and Josefson 1998, Francis et al. 2007].

The particular weld metal selected can modify the flaws and residual stresses [Callister 2000, Price and Alberry 1988]. Since the solid metal is less dense than the liquid metal, this can lead to shrinkage on cooling and can also give rise to porosity. Hot tearing occurs if the tensile stresses in the weld metal cause interdendritic rupture when the weldment is close to the solidus temperature. Consideration of the yield strength of the parent and weld metals is also integral to a weld's structural integrity [Dong and Zhang 1999, Schwalbe 1993]. Overmatching the yield strength of the weld metal may lead to lower toughness, whereas undermatching the yield strength may lead to a stress concentration in the weld metal. However, welds in power plant components are often carried out using the same composition weld metal or material with similar mechanical and physical properties to the component's parent material [Price and Alberry 1988]. Such a selection avoids problems such as those caused by yield strength mismatch or those resulting from different coefficients of thermal expansion which can lead to high stresses and potential cracking.

As shown in Figure 2.14, welds can be divided up into distinct zones, which have different microstructural and mechanical properties due to the thermal cycles they have undergone [Viswanathan 1989]. In the case of a single pass weld in ferritic steel, this results in seven distinct zones, four of which make up the heat affected zone.

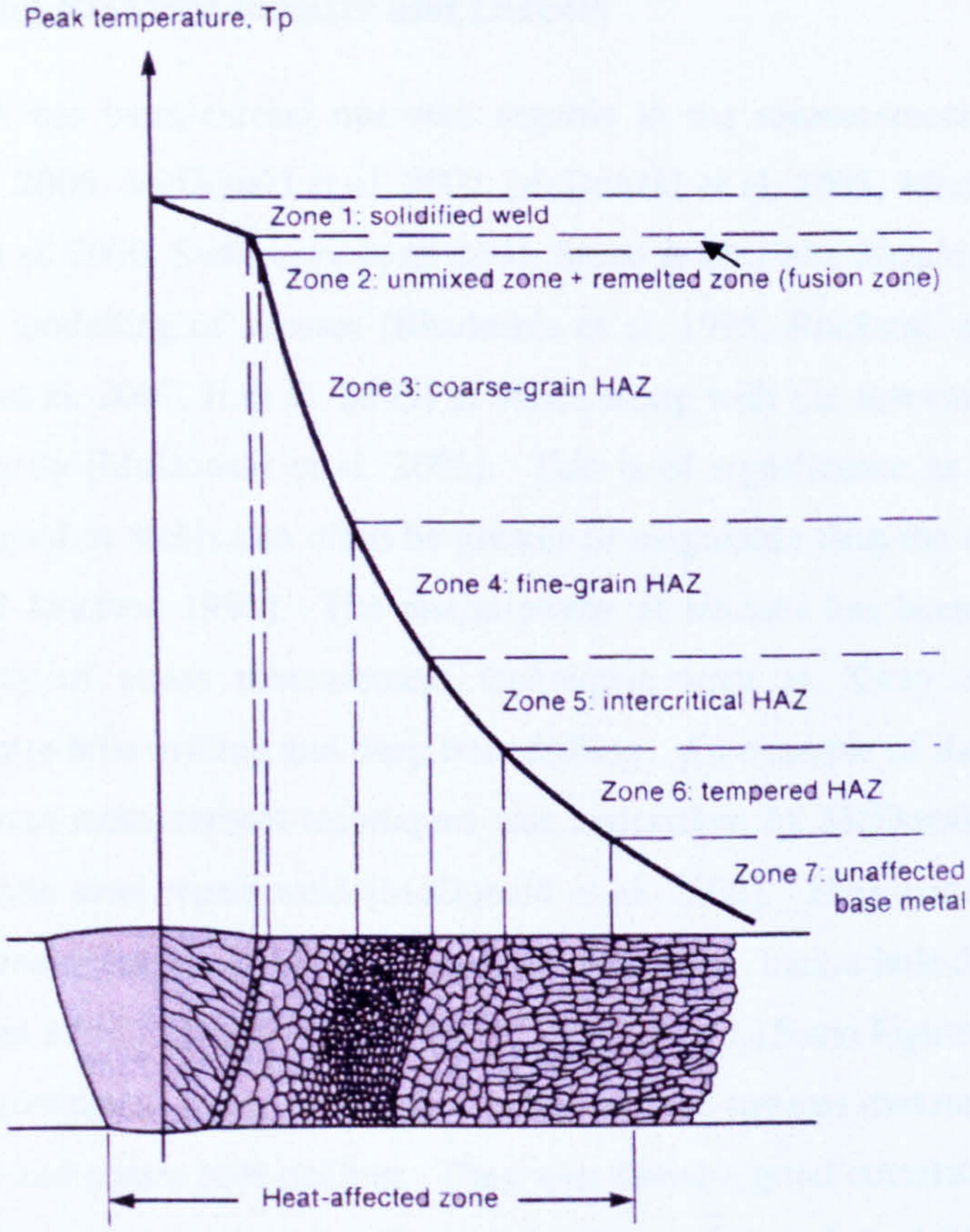

Figure 2.14. A schematic diagram showing various microstructural distributions formed in a ferritic steel weldment due to temperature distributions. These varying microstructures can be divided up into seven zones [Viswanathan 1989].

In the coarse grained region, the grain growth is the result of the high temperature austenitization of the material. The grain refined region is caused by austenitization taking place at a lower temperature. In the intercritical region, the austenite is only partially formed. The situation is more complex in a multipass weld due to weld metal bead overlaps and the multiple heat treatments the regions will have undergone. Thus weldments can be considered to be made up of the parent material parts, a complex HAZ and the weld metal.

Welds can be post weld heat treated in order to relax the stresses that have arisen due to the welding procedure [Banahan 2008]. However, although these processes do relieve the stresses, it is considered that a level of stress remains in the component and can affect its structural integrity.

2.5.3 Welding Residual Stresses and Defects

Much research has been carried out with regards to the measurement of stresses [Hossain et al. 2006, McDonald et al. 2002, McDonald et al. 2005, Mochizuki et al. 2005, Smith et al. 2000, Stefanescu et al. 2004, Stone et al. 1999, Suzuki and Holden 2006] and the modelling of stresses [Bhadeshia et al. 1995, Brickstad and Josefson 1998, Francis et al. 2007, Ji et al. 2005] in welds along with the assessment of their structural integrity [McDonald et al. 2005]. This is of significance as the residual stresses developed in welds can often be greater in magnitude than the design loads [Brickstad and Josefson 1998]. The measurement of stresses has been carried out using a variety of stress measurement techniques such as X-ray and neutron diffraction, centre hole drilling and deep hole drilling. An example of the correlation of different stress measurement techniques was undertaken by McDonald et al on a multi-pass ferritic steel repair weld [McDonald et al. 2002]. They compared X-ray diffraction measurements with measurements carried out by, centre hole drilling, deep hole drilling and a finite element model prediction, Figure 2.15 and Figure 2.16. They found a good correlation in the magnitudes of the surface stresses measured using X-ray diffraction and centre hole drilling. They also found a good correlation between through section measurements using X-ray diffraction and deep hole drilling with the finite element through-section prediction.

Although the stresses developed in welds depends on many factors such as the welding process and materials, as has been described in Section 2.5.2, investigations have been carried out in order to assess the nature of the residual stresses in particular weld types. Several weld passes are often necessary in power plant pipes due to the pipe thicknesses. This further complicates the prediction of the stresses in the weld as each bead affects the stress field as the cooling rates within beads differ through the thickness of the material [Brickstad and Josefson 1998, Ji et al. 2005]. However,

trends in stress values have arisen with regards to the prediction and measurement of residual stresses in welds.

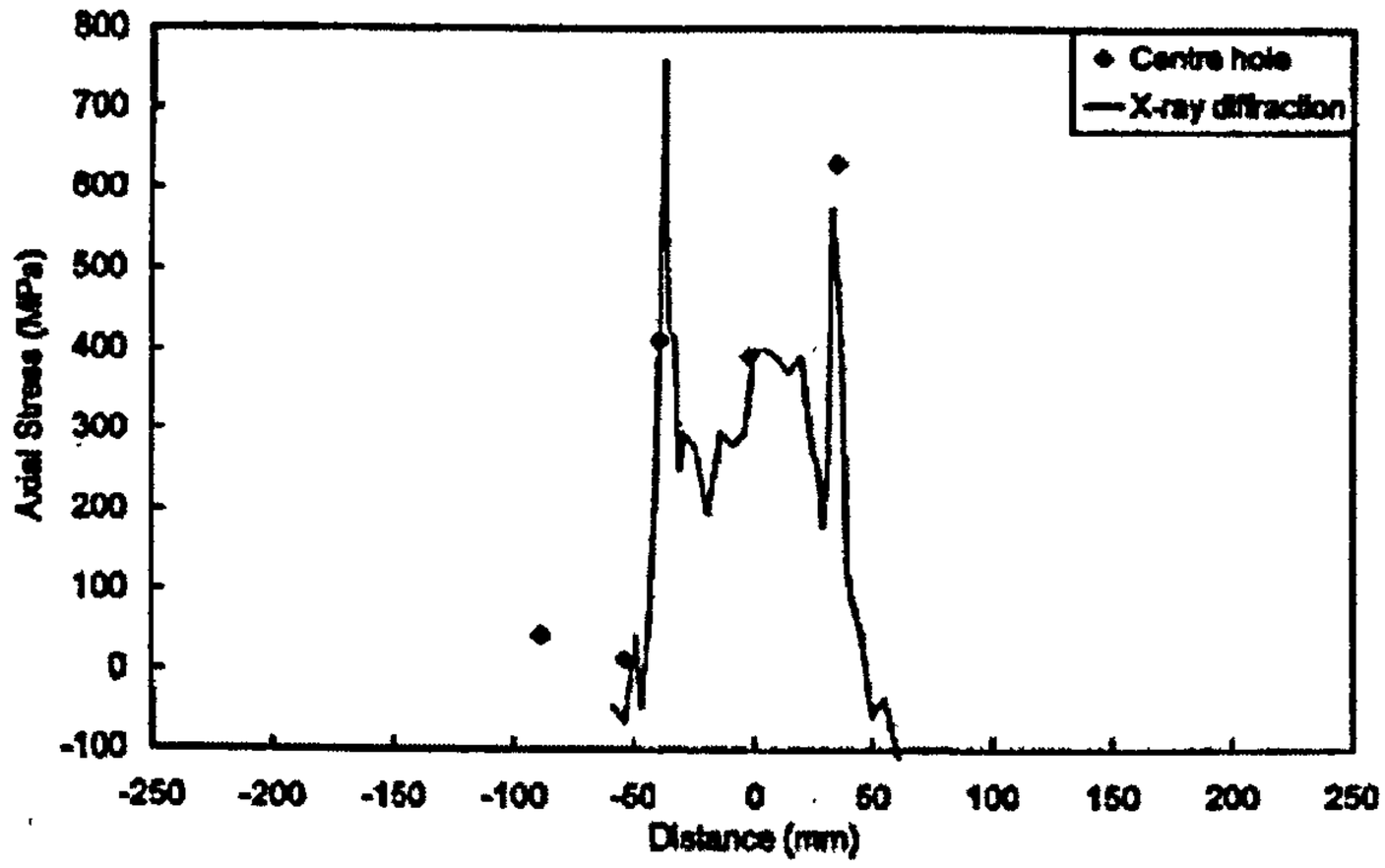

Figure 2.15. Comparison of axial stresses measured by X-ray diffraction and centre hole drilling [McDonald et al. 2002].

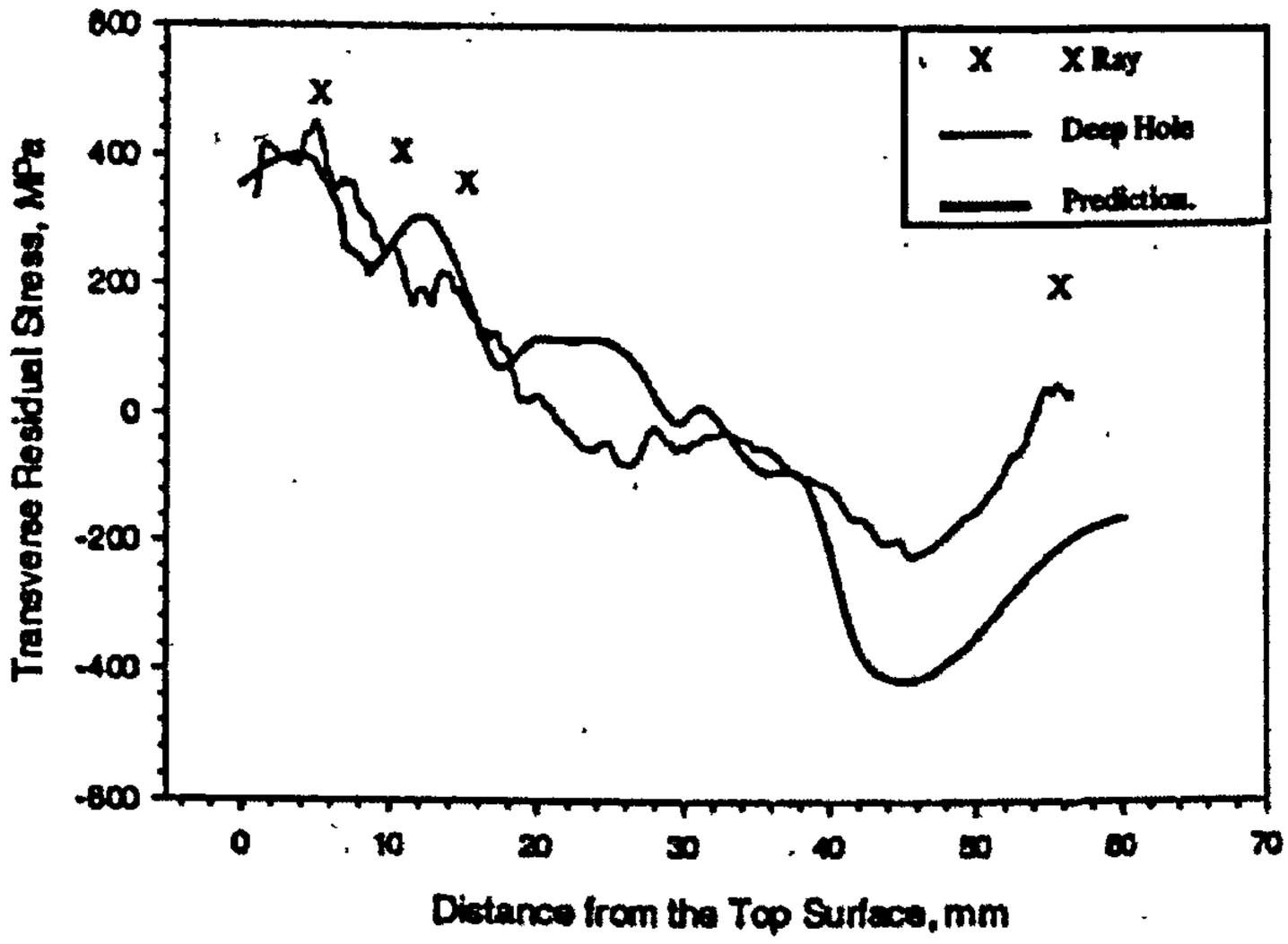

Figure 2.16. Comparison of through-section transverse residual stresses measured by X-ray diffraction and centre hole drilling and a finite element prediction [McDonald et al. 2002].

Often, particularly in butt welds, hoop tensile stresses are generated near the outer surface due to transverse shrinkage of the final weld passes [Leggatt 2008]. These are greatest near the weld arc start/stop positions due to these positions having greater constraint effects and higher cooling rates than elsewhere in the weld metal [Legatt

2008, Voutchkov 2005]. These stresses are balanced by compression within the body of the weld. High tensile stresses are often formed longitudinally throughout a weld due to strong resistance by the parts being joined [Leggatt 2008]. The resistance can be caused by geometry, physical properties of the material and external restraints. However, bending restraint can of course alter this and result in longitudinal compressive stresses rather than tensile ones. Yaghi et al. have modelled the changes that phase transformations make to the residual stresses developed in and around a P91 steel butt welded pipe using the finite element ABAQUS software [Yaghi et al. 2007]. Stresses were also predicted for the case of solid state phase transformation, austenite to martensite, which can occur in P91 steel during the cooling thermal cycle. Surface tensile stresses were predicted across the weld in both the axial and hoop directions when there was no phase transformation. However, the inclusion of a martensitic phase transformation changed the stresses so that compressive stresses would be formed towards the centreline of the weld surface.

A strategy for assessing the residual stresses introduced into welds made on plant has been proposed by McDonald et al., Figure 2.17 [McDonald et al. 2005]. Steps 1 to 3 show that a problem on plant has been identified and that a high integrity repair weld is required. As a consequence, a repair strategy and weld procedure will be prepared. In Steps 4 to 7, the surface and through-thickness residual stresses in a repair weld are measured and calculated. These measured and calculated stresses are correlated and the resulting stress profile is assessed with respect to a structural integrity assessment procedure such as R6. The residual stresses are optimised so as to have a sufficient safety reserve margin. Once the residual stresses have been optimised, the site repair is carried out, Step 8. The surface residual stresses and the quality of repair are confirmed using X-ray diffraction, Step 9. The through-section stresses are known, as the calculated profiles have previously been correlated with the experimental measurements, Steps 4 to 7. The repair weld is then returned to service, Step 10.

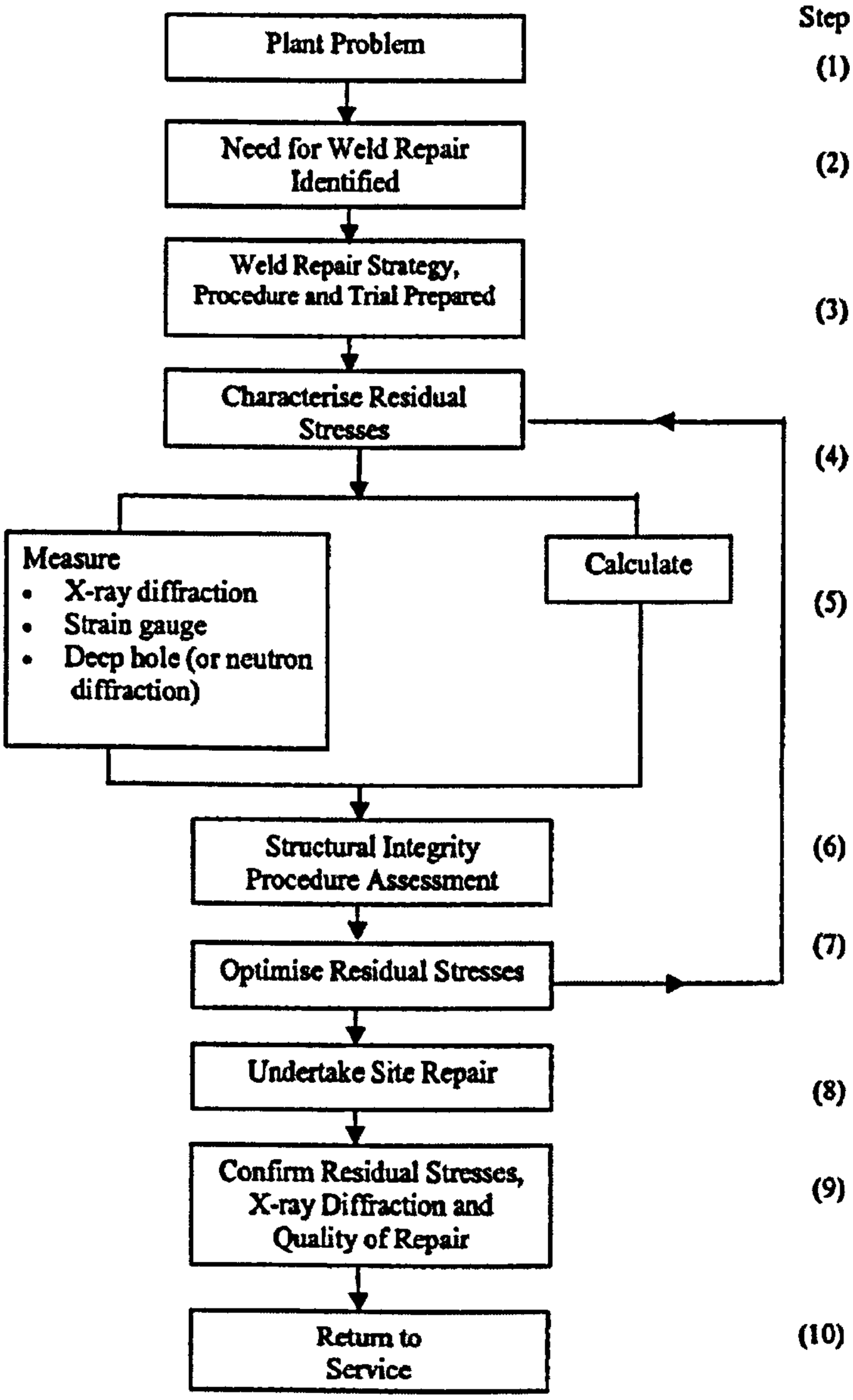

Figure 2.17. Weld repair strategy. [McDonald et al. 2005].

2.5.4 Oxide Layers

Stresses have been measured in chromia Cr_2O_3 when subjected to hydrostatic pressures in a diamond anvil cell using Raman spectroscopy and X-ray diffraction [(b)Mougin et al. 2001]. X-ray diffraction was used to measure the cell parameters of the rhombohedral oxide with pressure, Figure 2.18. These were correlated to Raman spectral peak shifts with pressure, Figure 2.19 and Figure 2.20.

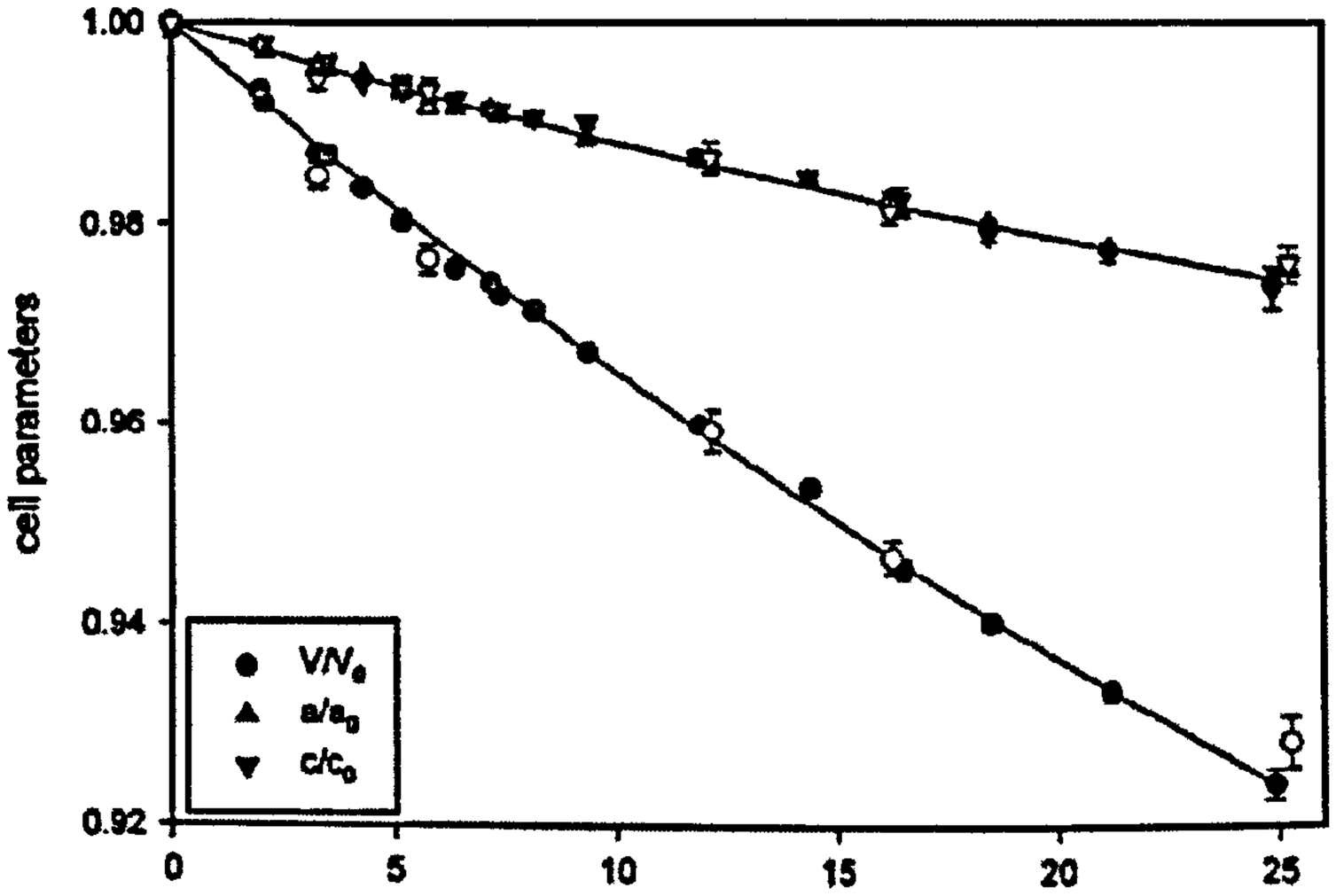

Figure 2.18. Variation of the Cr_2O_3 volume (V) and cell parameters (a) and (c) with pressure. V_o is the initial volume and a_o and c_o are the initial cell parameters. The black symbols correspond to argon as the transmitted medium. White and grey symbols correspond to silicon fluid as the transmitted medium in the diamond anvil cell with pressures of 0 to 50GPa and 2 to 30GPa respectively [(b)Mougin et al. 2001].

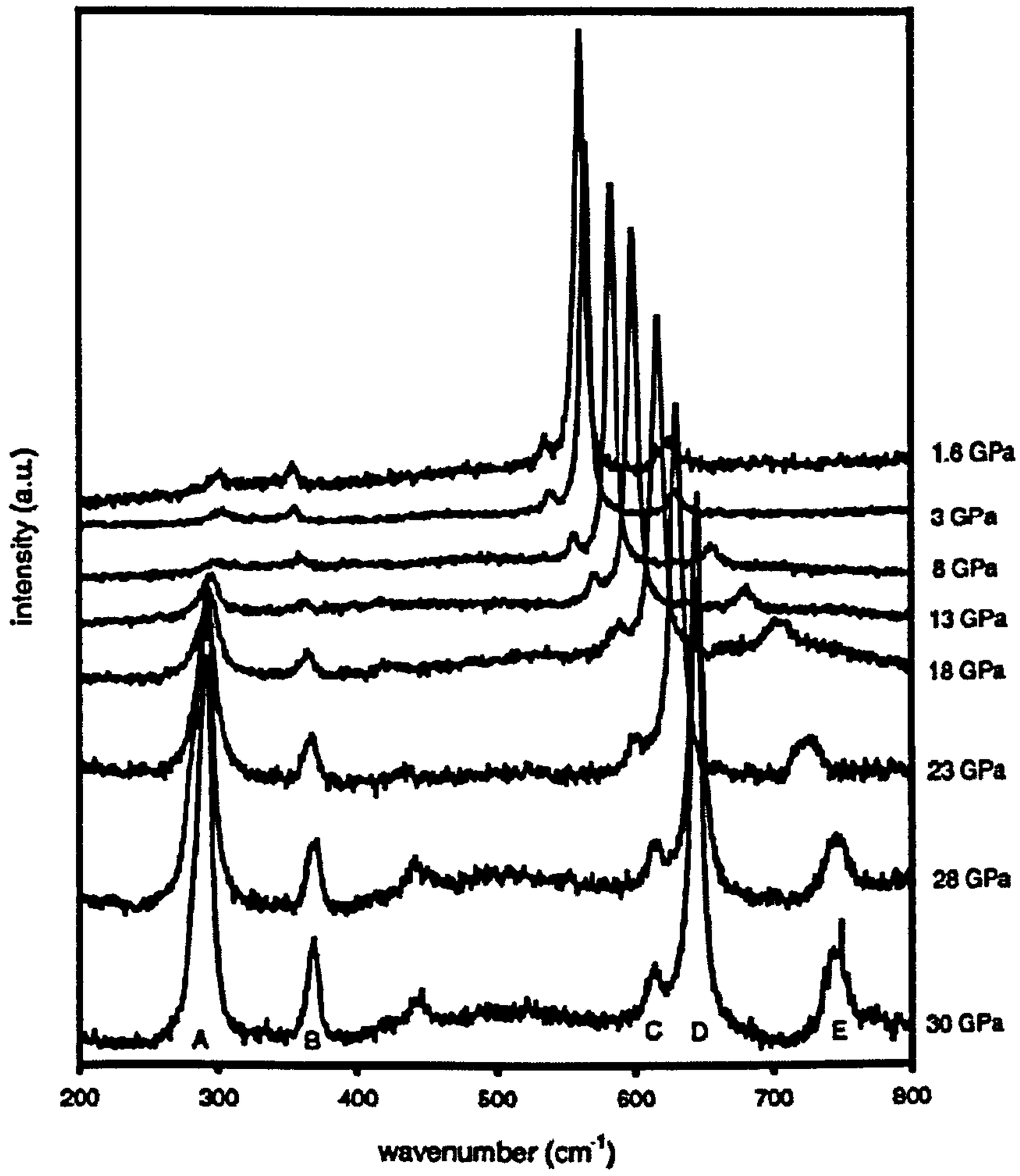

Figure 2.19. Raman spectra of Cr_2O_3 with pressure. Peaks have been marked A to E. Their wavenumber changes with applied pressure [(b)Mougin et al. 2001].

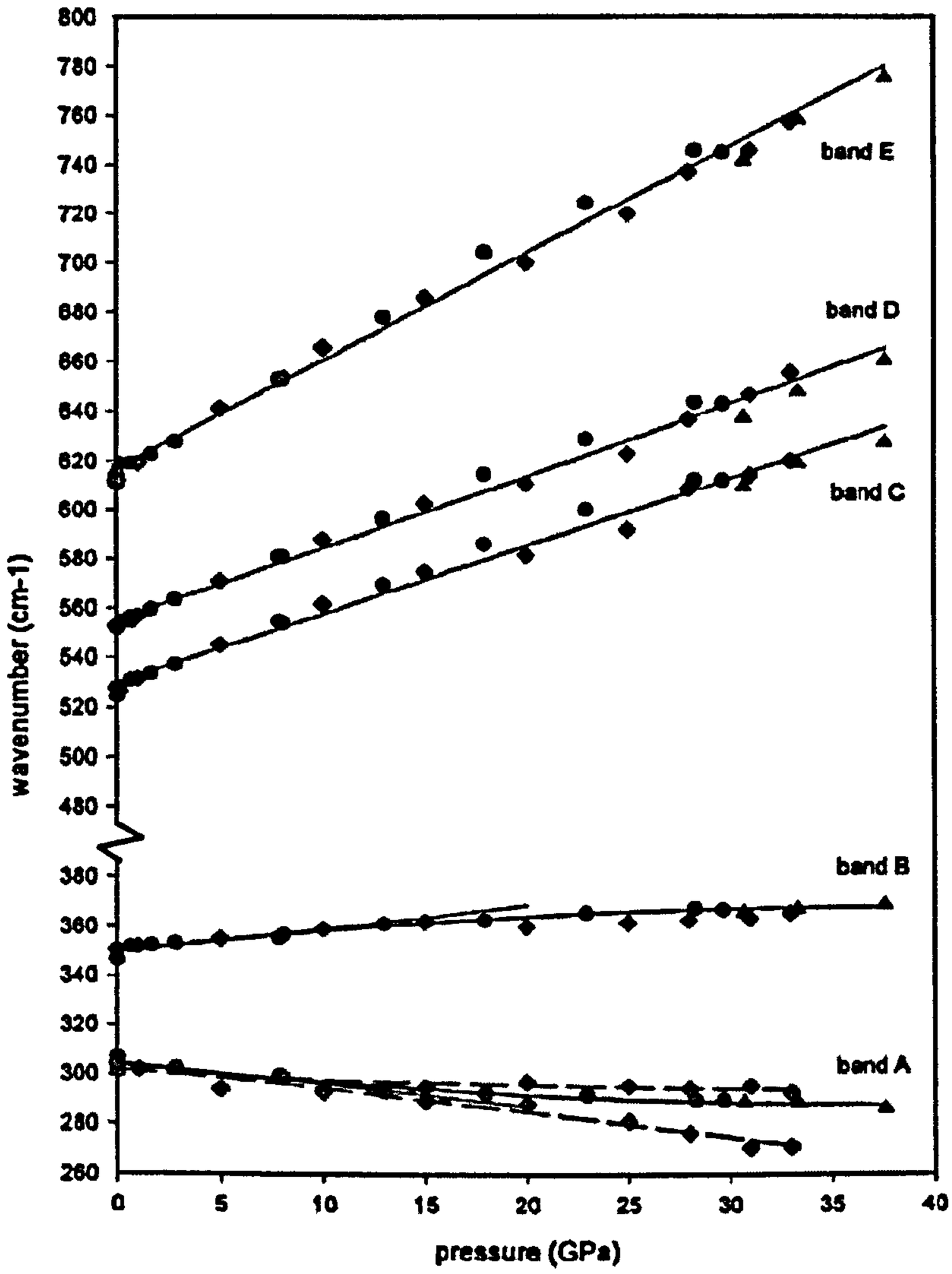

Figure 2.20. Change in Raman peak wavenumber with applied pressure. (●) Experiment with argon as transmitting medium. Experiment with silicon fluid as transmitting medium (▲) 0 to 50GPa and (◆) 2 to 30GPa after [(b)Mougin et al. 2001].

The lattice spacings and Raman peaks were found to shift linearly with pressure [(b)Mougin et al. 2001]. The Raman peak shifts could be correlated to lattice spacings and to X-ray diffraction stress measurements for stresses applied to the oxide.

The influence of cooling rate and substrate surface roughness on stresses in "as grown" oxides has been investigated by Mougin et al. [(c)Mougin et al. 2001]. Residual stresses in "as grown" oxides increased (compressively) with increased

cooling rate. This has been attributed to the stress relief of the oxide by creep of the oxide and substrate during the slower cooling process. The residual stresses formed in the oxide of the chromium specimens were found to be compressive and increased in magnitude with finer substrate surface finish. The reduction in residual stress with increasing surface roughness has been attributed to stress relief by surface cracking and oxide decohesion at the oxide crests. The cracks are attributed to tensile stresses at the surface and the increase in decohesion of the oxide layer is attributed to an increase in triaxiality of the residual stresses in the surface oxide along with the presence of tensile stresses.

The relationship between Raman shift and hydrostatic pressure in α-Fe_2O_3, haematite, has been investigated by Shim and Duffy [Shim and Duffy 2002]. This involved compressing powder samples in a diamond anvil cell. The linearity of the relationship depended upon the Raman peak analysed. There was also some discrepancy between the Raman shifts measured during the compression and decompression of the samples with a given applied pressure.

Nagl et al. have investigated crack spacings with respect to substrate tensile load [Nagl et al. 1994]. The tensile tests were carried out on mild steel and 99% nickel specimens and mean crack spacings were calculated for induced tensile loads using a four-point bend jig. The experiment was carried out in a scanning electron microscope to provide the necessary resolution to allow the crack sizes to be measured. A relationship was found between crack spacing and substrate strain, Figure 2.21. As discussed in their paper, the plots can be divided into three distinct regions. At low tensile strains, the crack spacing is infinite (Region 1). Then, once the critical tensile strain has been reached, there is the linear elastic region in which crack spacing is directly proportional to the applied strain (Region 2). Finally, oxide spallation occurs and the crack spacing remains constant (Region 3). In addition, buckling of the oxide was found to be caused by compressive stresses on the oxide acting normal to the applied stress.

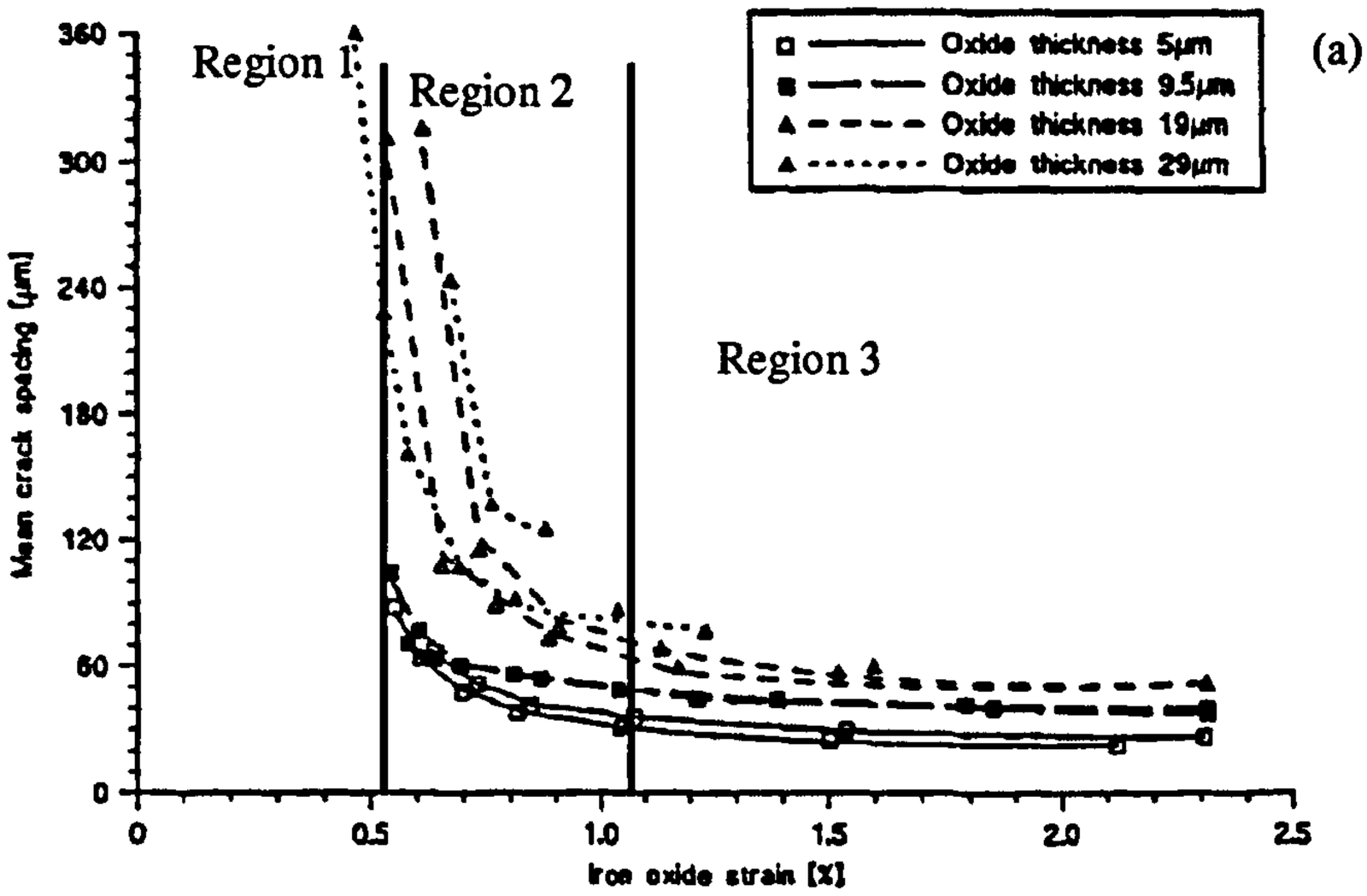

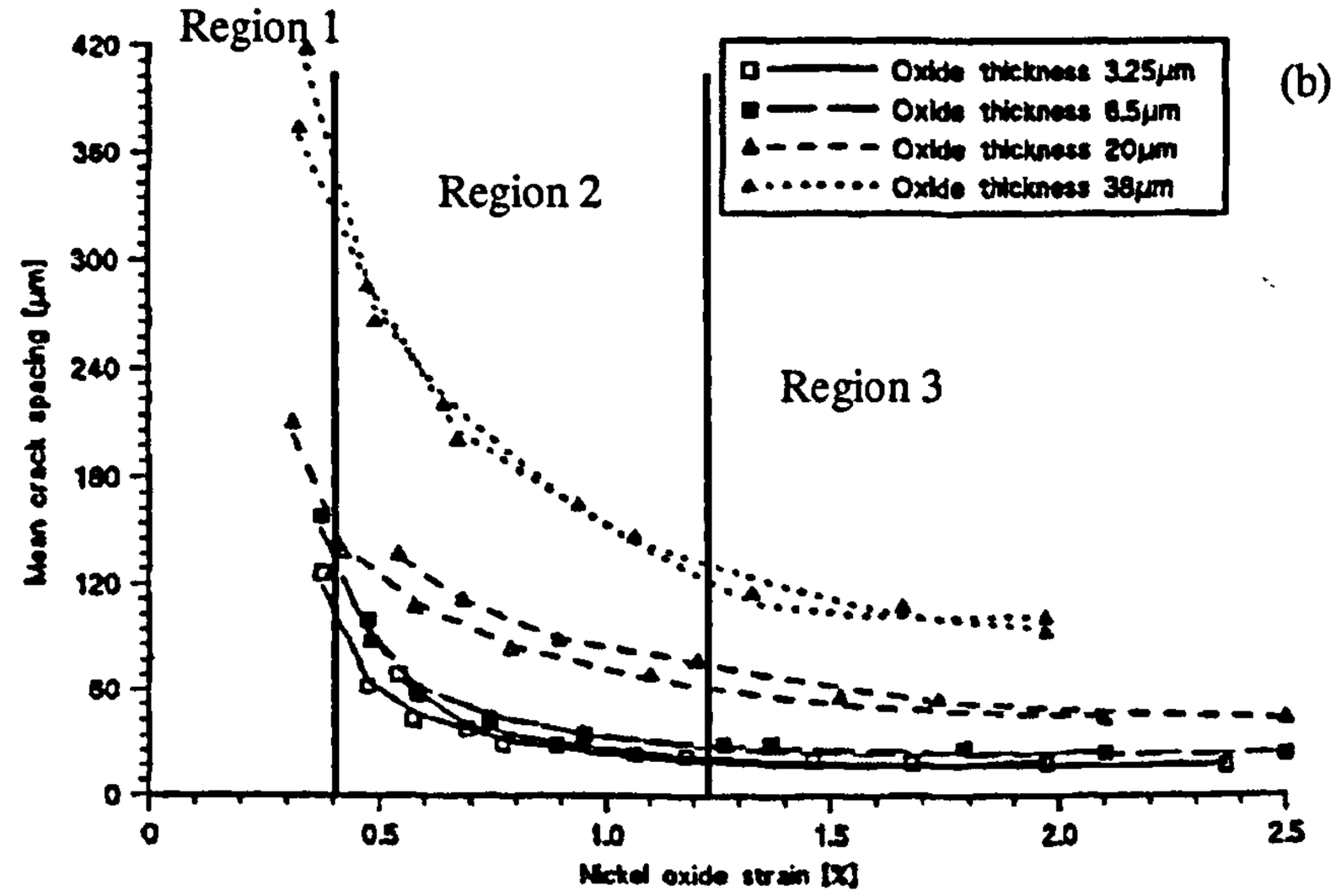

Figure 2.21. Mean crack spacing against strain for (a) iron and (b) nickel oxides of various thicknesses on a mild steel and nickel substrate respectively [Nagl et al. 1994].

2.5.5 Turbine Blades

Turbine blades provide an example of the importance of the different failure mechanisms and the need for stress measurement and life prediction [Ashby and Jones 1996]. Depending on their application (in the aerospace industry as well as in power generation), turbine blades are expected to withstand extremely high temperatures, thermal cycling and stress conditions [Padture et al. 2002, Viswanathan 1989]. A standard turbine blade used in the aerospace and power generation industry is often made of up to four layers; a superalloy substrate, a bond-coat (BC), a thermally grown oxide (TGO) and a thermal barrier coating (TBC), Figure 2.22 [Padture et al. 2002]. The coatings allow the blade to operate at higher temperatures than could be withstood by the superalloy alone.

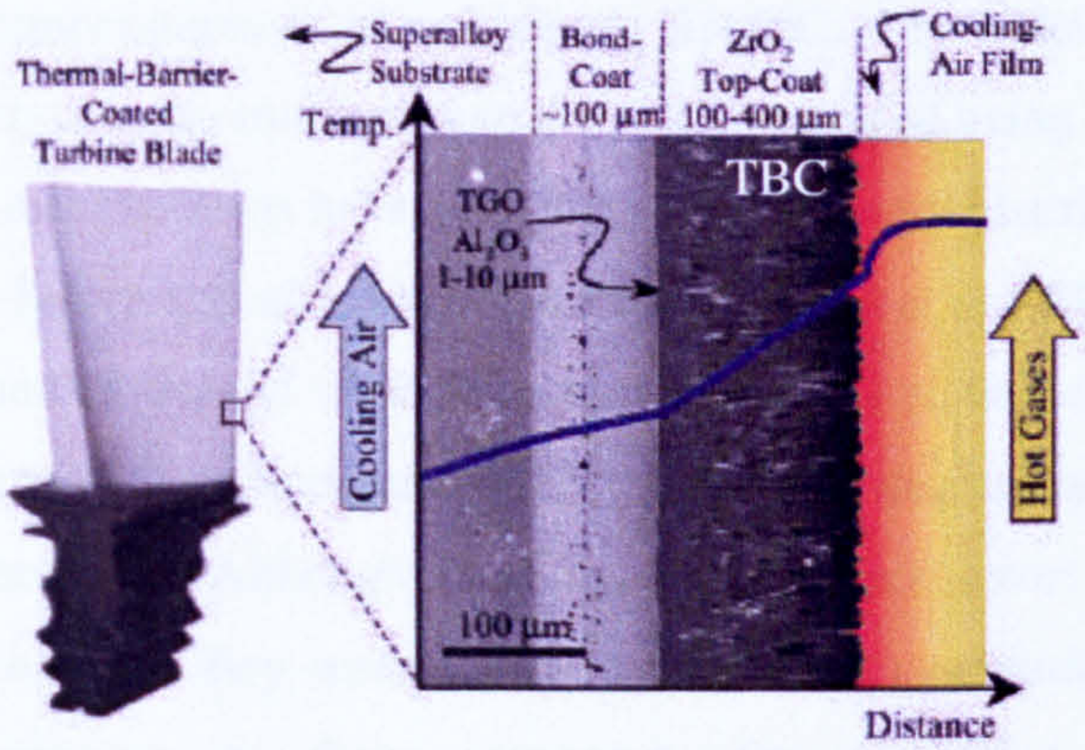

Figure 2.22. Structure of a turbine blade showing the various layers associated with the application of a thermal barrier coating and the temperature gradient through the blade [Padture et al. 2002].

The superalloy substrate is typically nickel or cobalt based. However, additional elements are often added in order to improve its mechanical and thermal properties. The superalloy is designed to form γ' precipitates, Ni_3Al, in a γ phase matrix. These ordered precipitates obstruct dislocation motion thereby making the material more creep resistant [Decker 2006, McLean et al. 1995, Nicholson 1976]. The blade is internally air cooled or cooled through internal channels in order to create a temperature gradient across the component [Padture et al. 2002]. The bond-coat is an oxidation-resistant metallic layer that is applied to the surface of the superalloy. It is typically 75 to 150µm thick and can be applied in a variety of ways such as air plasma spraying or electron-beam physical vapour deposition. Although there is variation in

the composition of bond-coats, they are typically made of a NiCrAlY or NiCoAlY alloy or platinum aluminides [Angenete and Stiller 2002, (a)Angenete and Stiller 2003, (b)Angenete and Stiller 2003, Lehnert and Meinhardt 1972]. The diffusion of elements between the superalloy and bond-coat often occurs during service. Bond-coats on turbine blades in gas turbine engines can tolerate temperatures up to about 700°C [Padture et al. 2002], approximately two thirds of the superalloy melting temperature [Ashby and Jones 1996]. Thermal barrier coatings are ceramic top-coats deposited on to the bond-coat. These can also be applied by air plasma spraying and electron-beam physical vapour deposition. They are commonly made or yttria (Y_2O_3) stabalised zirconia (ZrO_2) due to their low thermal conductivities [Padture et al. 2002]. The coatings on a turbine blade allow it to be operated at temperatures above the melting point of the superalloy substrate. As well as allowing the turbine blades to be employed at temperatures of approximately 1300°C, they make the blades more durable. However, ceramic coatings have the disadvantage of being brittle [Shin et al. 2007]. Residual macrostresses have been measured in thermal barrier coatings using X-ray diffraction before and after heat treatment [Teixeira et al. 1999]. The residual stresses were found to depend on the physical properties of the coating, deposition technique and deposition temperature, with the stresses decreasing with increasing deposition temperature. Although residual macrostresses were measured in the thermal barrier coatings, they were found to be low in magnitude (approximately 50MPa) in comparison to those measured after in-service heat treatments (approximately –230MPa).

Bond-coats are typically aluminide diffusion coatings and are either formed by the inward diffusion of Al or the outward diffusion of Ni depending on method of applying the coating and parameters used [Angenete and Stiller 2002]. Coatings that rely on the inward diffusion of Al are often referred to as either inward grown coatings or high activity coatings. After this aluminisation stage, the component is generally heat treated, causing Ni to diffuse outwards. Slow diffusing elements such as W, Re, Ta and Mo may become confined in the coating the inward alumina growth. Outward diffusing coatings, also referred to as low activity coatings, based on the outward diffusion of Ni, contain less of the previously mentioned slow diffusing elements, due to their lower rates of outward diffusion than Ni. The development of ceramic coatings has reduced the need to develop more sophisticated superalloys as

well as reducing the need for the blade material to be inherently corrosion resistant [McLean et al. 1995]. Platinum is often added to aluminide coatings [Angenete and Stiller 2002]. Although the idea was proposed by Lehnert and Meinhardt in the 1970s [Lehnert and Meinhardt 1972] and has been shown to improve the performance of the coatings, there is still much debate as to the underlying mechanisms leading to the improvement [Angenete and Stiller 2002]. An example of a high activity coating is the RT22 coating [Angenete and Stiller 2002]. This coating type has been thoroughly investigated [Angenete and Stiller 2002, (a)Angenete and Stiller 2003, (b)Angenete and Stiller 2003]. However, the CN91 coating type has been less well documented [Saint-Ramond et al. 2004].

2.5.6 Coating Integrity

The oxidation of these thermal barrier coated blades can lead to spallation of the coatings [Lacaze et al. 2006]. Moreover, degradation of the coatings leads to repeated oxidation of the metal sub-surface, in this case the turbine blade [Lacaze et al. 2006]. Furthermore, the state of the thermally grown oxide plays an important role in determining the lifetime of the thermal barrier coating [Busso et al. 2007, Padture et al. 2002, Tolpygo et al. 2001, Yanar et al. 2003]. The faster the oxide formed from the bond-coat grows, the more rapidly the thermal barrier coating will fail [Tolpygo et al. 2001]. This commonly occurs near the thermally grown oxide/thermal barrier coating interface [Busso et al. 2007]. Thus, an understanding of the degradation of the blade coatings and thermally grown oxides is key to determining the structural health of the turbine blade and assessing future service life [Busso et al. 2007].

There are various ways that have been proposed for predicting the life of a blade coating or thermal barrier coating. Empirical models of the relationship between strain and oxidation have been considered along with theoretical models centring on the cracking and delamination of the thermally grown oxide [(a)Evans et al. 2001, (b)Evans et al. 2001, Rabiei and Evans 2000]. Finite element models and measurement by photoluminescence spectroscopy have shown that stresses in thermally grown oxides initially increase due to oxide growth [Bressers et al. 2000]. Experimental observation through electron microscopy and photoluminescence stress measurement has indicated that the stresses then decrease due to relaxation caused by oxide cracking linked to local stress fields caused by defects and are surmised to grow

and coalesce to result in delamination of the thermally grown oxide followed by spallation [Busso et al. 2007, Rabiei and Evans 2000]. However, cracking and delamination has been considered by some authors to be conservative, since it is usually necessary for delamination to be quite advanced for buckling and spallation of the thermal barrier coating to occur [Busso et al. 2007]. Finite element modelling has been used to predict the failure of thermal barrier coatings based on residual stresses as a consequence of the thermal gradients, thickness of the thermally grown oxide and thermal expansion mismatch between coating layers [Busso et al. 2007, Liu et al. 2004, Martena et al. 2006]. Thermography is another method that can be used to assess turbine blade lifetime [Busso et al. 2007]. This allows maps to be created which show where damage has occurred by showing areas in which coatings have become detached. Mass change measurements have also been shown to be an effective method of predicting failure [Tolpygo et al. 2001].

Since local stress is often the cause of crack initiation, it is logical that a method of stress measurement be used in an attempt to find or predict the occurrence of this cracking. Several stress measurement techniques have been proposed to evaluate the stresses within the thermally grown oxide. These include X-ray diffraction and photoluminescence spectroscopy [Atkinson et al. 1998, Atkinson and Selcuk 2004, Christensen et al. 1996, Huntz et al. 1990, Kraus et al. 1997, Luthra and Briant 1986, Nychka et al. 2003, Selcuk and Atkinson 2003]. In the case of photoluminescence spectroscopy, spectra are obtained from the alumina in the oxidised bond-coat or thermally grown oxide. The peak shifts of the spectra can then be used to calculate stress. This will be elucidated further in Chapter 3 - Techniques. Also, since the equipment required to measure these stresses is available in portable forms [Pitt et al. 2005], it makes photoluminescence spectroscopy a practical approach to measuring stresses in-situ for blades in turbines. Another advantage to the photoluminescence method is that the zirconia in thermal barrier coatings can be penetrated by the incident laser beam due to its transparency at optical frequencies [Christensen et al. 1996], so that the alumina layer below can be interrogated.

Many investigations have been undertaken to assess the lifetimes of coated turbine blades and measure the stresses in their alumina coatings using photoluminescence spectroscopy [Busso et al. 2007, Mu et al. 2004, Nychka et al. 2003, Peng and Clarke

2000, Selcuk and Atkinson 2003, Selcuk and Atkinson 2002]. However there are complications because the common method of calculating stress from the peak position is by assuming a biaxial stress state; biaxial stress measurements do not require a polarized laser beam [He and Clarke 1995, Ma and Clarke 1994]. Since the thermally grown oxide commonly buckles prior to thermal barrier coating failure, this assumption may not be valid [Busso et al. 2007]. Also, although it is commonly the α-alumina peak positions that are used to measure the stresses in the oxide; α-alumina may not be the sole alumina phase present [Lipkin et al. 1997, Nychka and Clarke 2001, (a)Sohn et al. 2001, (b)Sohn et al. 2001, Wen et al. 2005]. The presence of θ-alumina has also been identified along with an additional luminescence contribution about which there has been much debate. Figure 2.23 shows peaks found in a photoluminescence spectrum of Al_2O_3 the peaks denoting α-Al_2O_3 are denoted R_1 and R_2, θ-Al_2O_3 is denoted θ_1 and θ_2 and the debated metastable phase is denoted M.

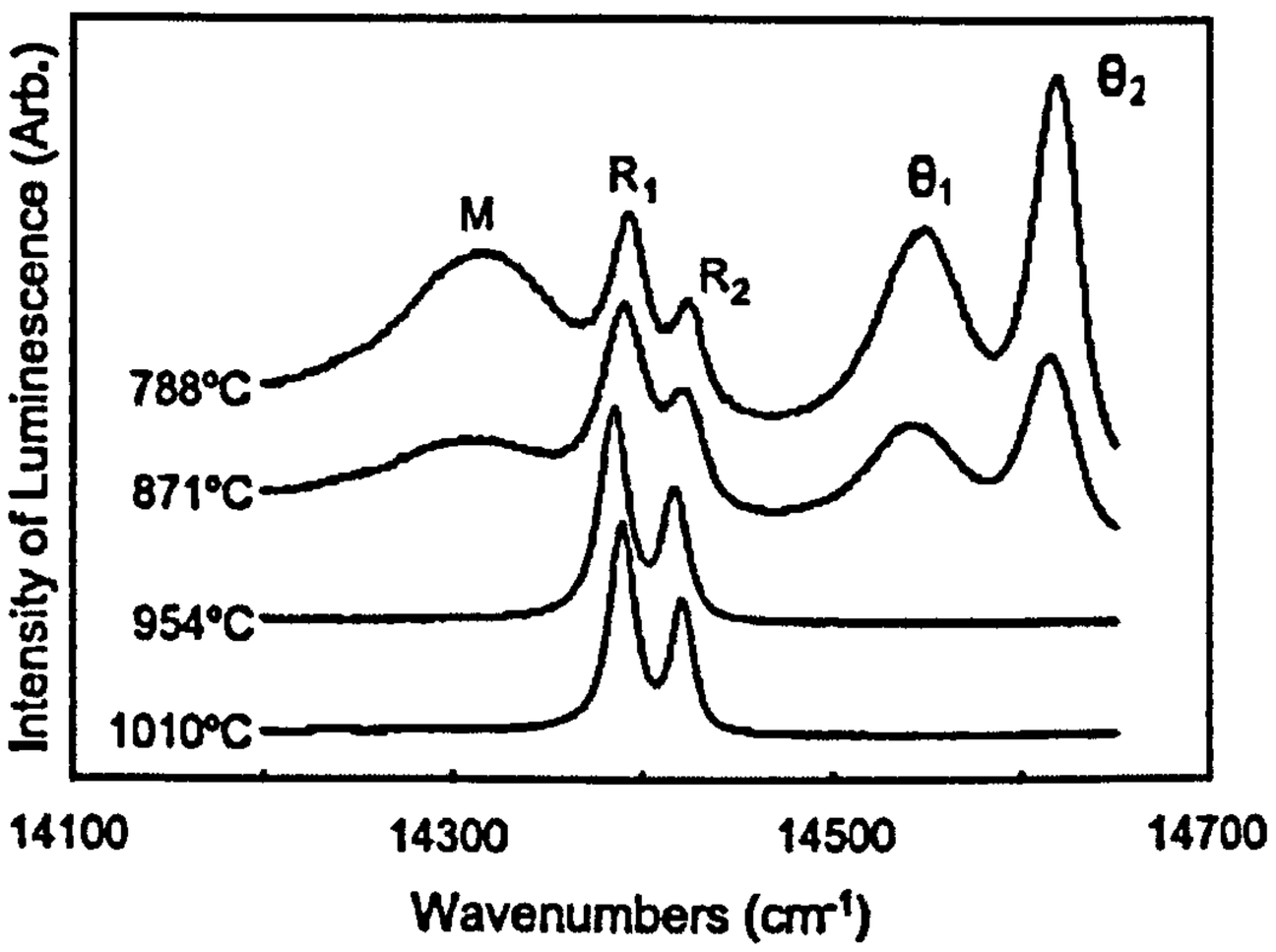

Figure 2.23. Photoluminescence spectrum from alumina at different temperatures showing the two α-Al_2O_3 peaks (marked R_1 and R_2), the two θ-Al_2O_3 peaks (marked θ_1 and θ_2) and the metastable phase (marked M) [Mu et al. 2004].

Mu et al. have attributed the peak marked M to be metastable phase [Mu et al. 2004], whilst El-Turki et al. [El-Turki et al. 2004] have attributed it to the excitation and subsequent relaxation of the electrons of the substitutional chromium (III) ions in the α-alumina lattice. The development alumina metastable phases have been linked with the early spallation of the thermally grown oxide within the base metal [Mu et al. 2004]. With regards to other alumina phases, as yet there has been no confirmation as

to the existence of γ-alumina photoluminescence peaks although there have been several apparently thorough investigations [Kadlecikova et al. 2003, Luo et al. 2006, Wen et al. 2008]. However, it has been suggested that the presence of γ-alumina photoluminescence can be observed in the photoluminescence background line in photoluminescence spectra of thermally grown oxides, Figure 2.24 [Murphy et al. 2001]. The presence of the different phases was deduced through comparison of photoluminescence spectra with transmission electron microscopy of thermally grown oxides.

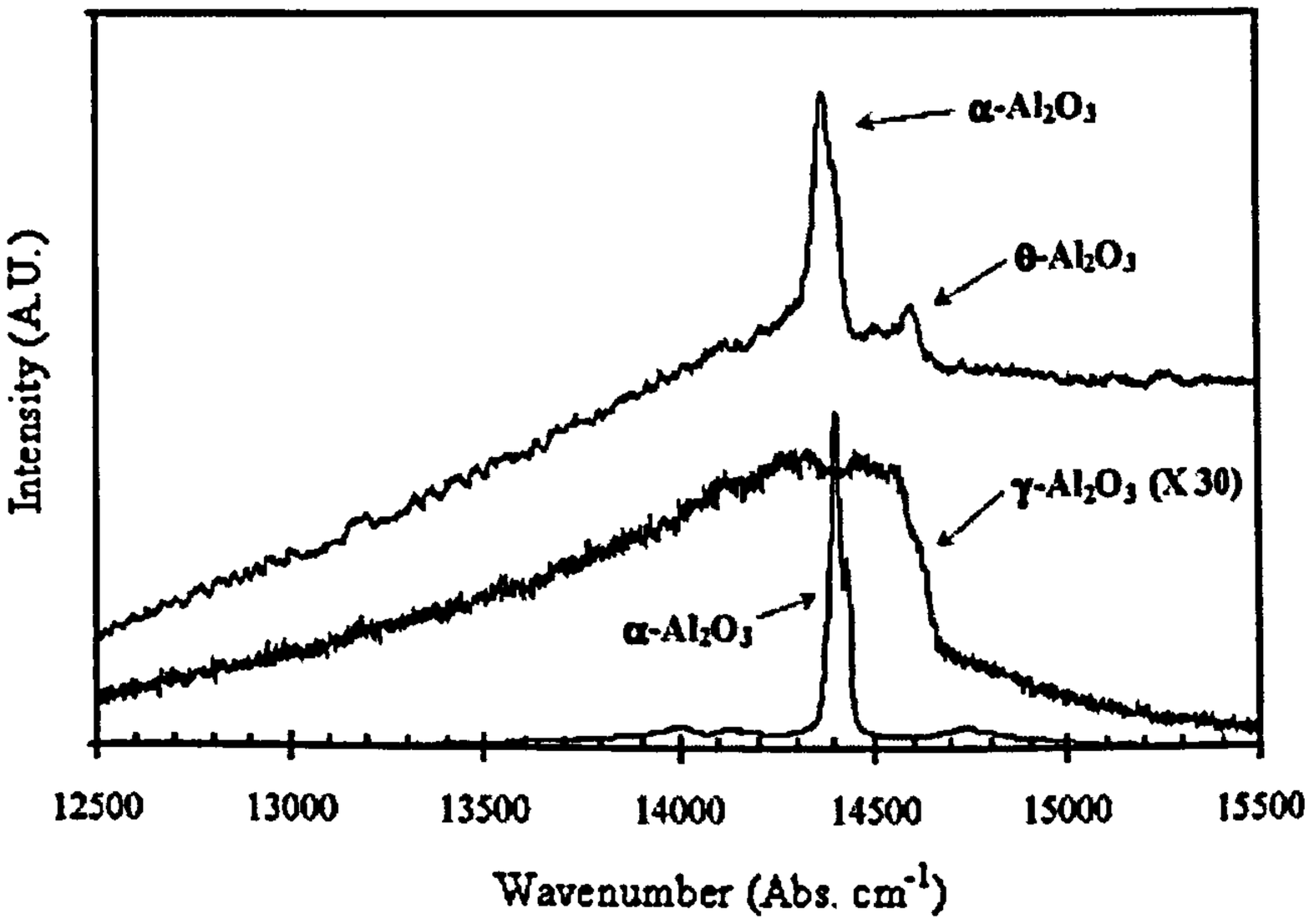

Figure 2.24. Effect of γ-alumina on photoluminescence spectrum of thermally grown oxide after [Murphy et al. 2001].

An additional issue that may arise when using photoluminescence peaks to calculate stresses in alumina, is the existence of multi-stress states [Peng and Clarke 2000, Selcuk and Atkinson 2003, Selcuk and Atkinson 2002]. Figure 2.25 shows how photoluminescence spectra taken from α-alumina with a multi-stress state cannot be fitted by a single R_1 and R_2, line but must instead be fitted by a series of R_1 and R_2 lines. The intense peak at 14355 is the argon emission line used for calibration [Peng and Clarke 2000]. Chapter 4 - Calibration and Sources of Error addresses the overlapping of alumina peaks which complicates the deconvolution and the subsequent calculation of the stress state of the alumina. It is also possible for additional information on the crystal orientation of the alumina to be found by

examining the relative heights of alumina peaks [He and Clarke 1997]. This may be of concern, as the crystal orientation of alumina can greatly affect the mechanical properties [He and Clarke 1995].

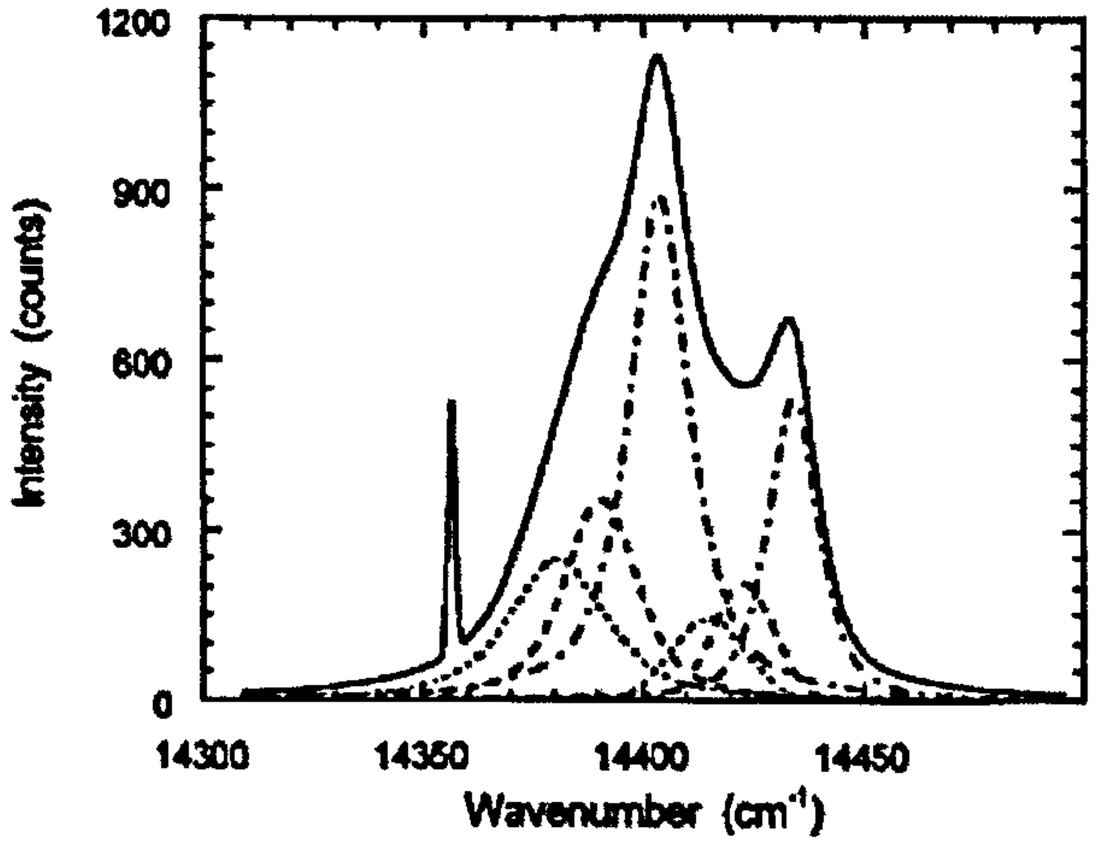

Figure 2.25. Deconvolution of a triaxial-stress state [Peng and Clarke 2000].

An issue that has plagued the field of determining the remaining life of an oxide coating using photoluminescence spectroscopy is how to link residual stress to remaining life. Some authors have found that there is a systematic trend in the average stress measured in the thermally grown oxide, with its remaining life [Wen et al. 2005]. This was found to be independent of oxidation temperature and instead related to the number of temperature cycles that the specimen had undergone. There was also a systematic change in area ratio of the R_1 and R_2 peaks with remaining coating life together with a change in peak width. Other researchers have found a change in relative intensity of the R_1-R_2 peaks with respect to the number of thermal cycles applied to a specimen and their remaining life [(b)Sohn et al. 2001]. However, some researchers propose that stress measurement is not a good indication of damage or damage quantification [Nychka and Clarke 2001, Tolpygo et al. 2001]. Instead, they considered that other peak parameters such as width and shape correlated better with coating life. For example, a bi-modal stress state whereby one doublet has narrow peaks and the other wide peaks and where there is a significant difference in stress state between the two doublets, could indicate delamination of the thermally grown oxide from the bond-coat [Nychka and Clarke 2001]. Lower stresses have been observed in regions where thermally grown oxides have become detached from a

bond-coat or thermal barrier coating interface. Higher stresses have been related to the interfaces of intact thermally grown oxides and grit blasted bond-coat interfaces. Thus the peak shape of a photoluminescence spectrum from a damaged region of a coated superalloy would be an amalgamation of the two stress states.

Microstructural analysis has been employed, in some instances, along side photoluminescence spectroscopy in order to gain a fuller understanding of the spectroscopic stress measurements [Mennicke et al. 2000, Shillington and Clarke 1999]. Shillington and Clarke showed an initial increase of compressive stress in the thermally grown oxide with oxidation time, followed by a decrease in the magnitudes of the stress, Figure 2.26 [Shillington and Clarke 1999]. A decrease in compressive stress was linked to the depletion of α-alumina and the formation of α-chromia and a (Co, Ni)(Cr, Al) spinel. The decrease in compressive stress was linked to spallation, although the kinetics of the spallation was not discussed.

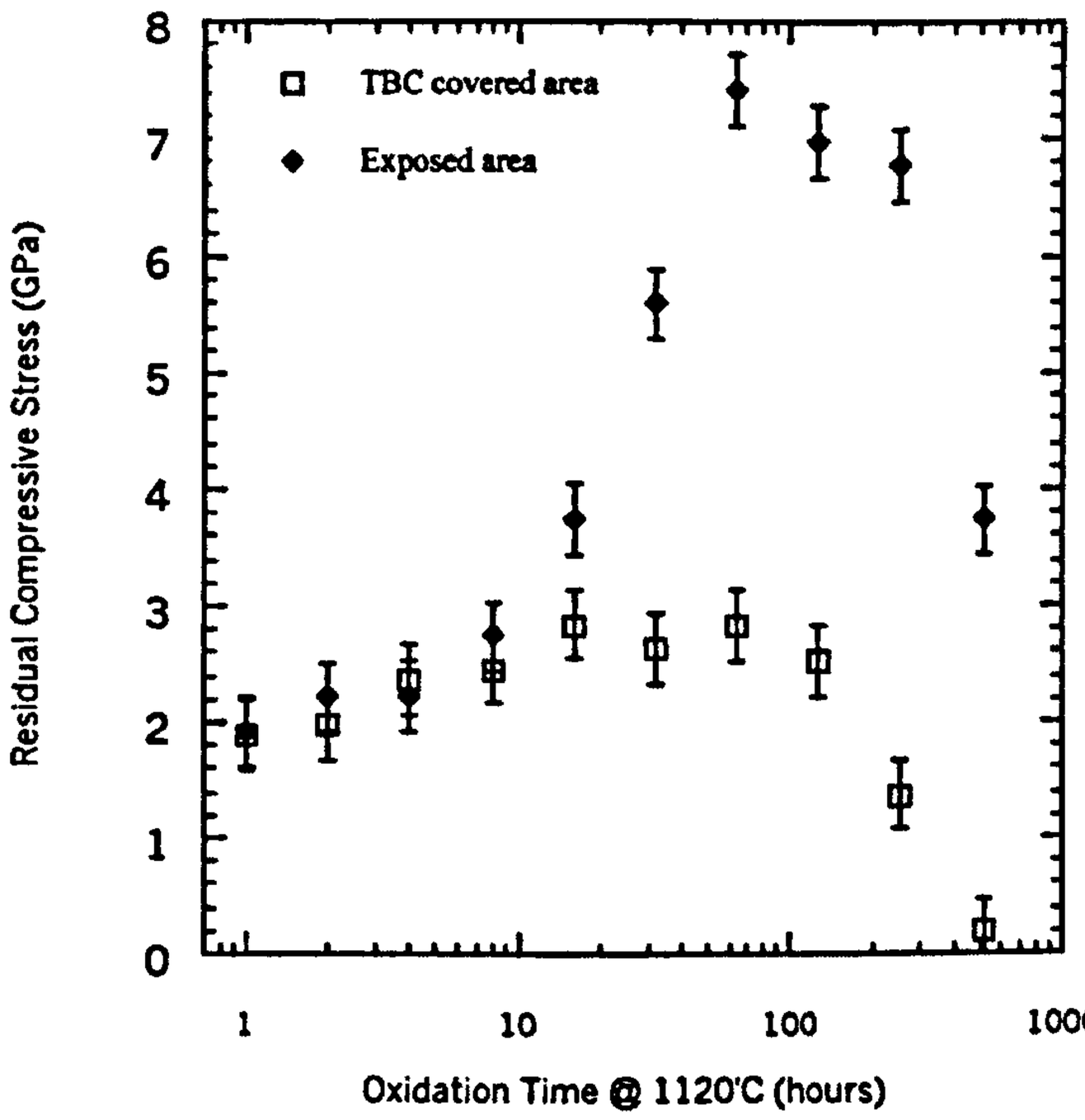

Figure 2.26. Residual compressive stress with oxidation time of a thermally grown oxide [Shillington and Clarke 1999].

Mennicke et al. have linked secondary oxide inclusions, in the form of inter-dendritic precipitates, in thermally grown oxides to an increase in fracture toughness of the

oxide [Mennicke et al. 2000]. These precipitates were found to consist of a tantalum rich oxide with an outer alumina sheath. Analysis of oxide which had spalled and which had not indicated that the presence of the dendrites reduced the probability of spallation. It was concluded that they acted as pegs to the α-alumina, thereby inhibiting spallation.

3 Techniques

This chapter discusses the methods used to measure or provide predictions of the macro- or microstresses investigated in this thesis. Where other techniques have been used, a reference is provided.

3.1 Diffraction Techniques

Diffraction techniques are based around the Bragg equation which involves the measurement of crystal lattice spacings [(a)Withers and Bhadeshia 2001]. As the strain on the crystal lattices changes, so too do the displacements between atoms and therefore the lattice spacings. A measurement of the strain in the material can therefore be gained. The Bragg equation is shown in Equation 3.1,

$$n\lambda = 2d\sin\theta \qquad 3.1$$

where n is an integer, λ is the wavelength of the incident beam typically in this case either X-rays or neutrons, d lattice spacing of the crystals and θ is the Bragg angle. The angle between the incident and diffracted beam is 2θ and is known as the diffraction angle. It is commonly this angle, which is measured experimentally [(a)Withers and Bhadeshia 2001].

3.2 X-Ray Diffraction

X-ray tubes produce characteristic X-ray emission lines by electron transition in the target metal upon the electron bombardment, thereby resulting in the characteristic spectrum of the X-ray tube target metal. More specifically, this phenomenon occurs when one of the electrons bombarding the target has sufficient kinetic energy to knock an electron out of its shell and is then replaced by an electron from another shell. These lines are referred to as K, L, M, etc. (in order of increasing wavelength), depending on the shell the replacement electron has fallen to, Figure 3.1. Since these lines can result from electrons falling from different shells, they can be described as K_α, K_β etc. A filter or monochrometer is often required to separate these α and β lines.

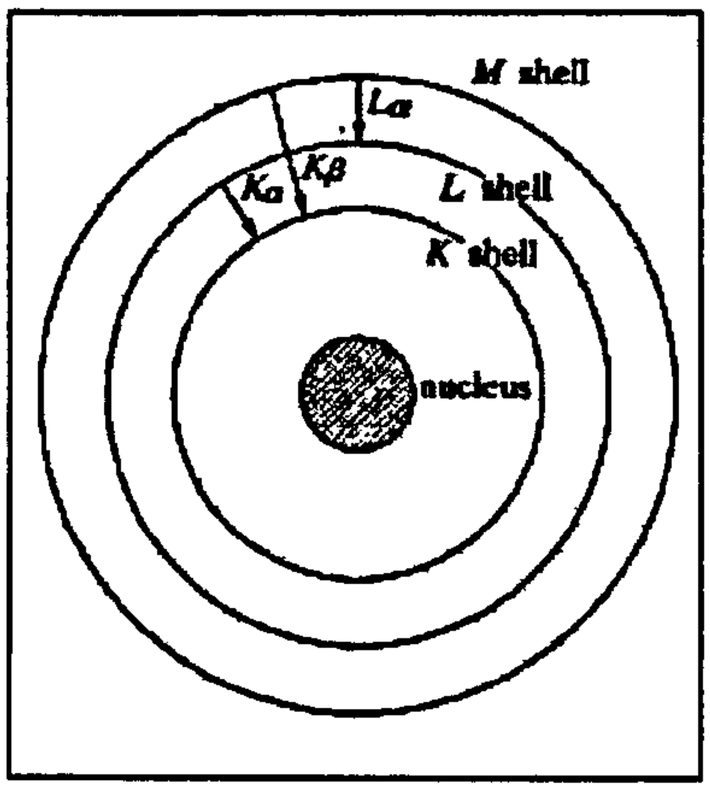

Figure 3.1. Common electronic transitions in an atom [Callister and Stock 2001].

Most X-ray diffraction or X-ray scattering exercises require some form of quantitative evaluation [Arndt 1986]. There are several types of detectors for recording the positions of the arrival of the diffracted X-rays. One common way of doing so is by using a position-sensitive detector (PSD). PSDs can be classified as one-dimensional (linear) or two-dimensional (area). One-dimensional PSDs record the detection point on a line, whereas two-dimensional PSDs locate the position on a surface. It is the one-dimensional, linear, PSD which shall be discussed further.

One common type of linear position sensitive detector is a gas filled counter. There are two compartments to a position sensitive detector, one at high pressure and one at normal pressure. The high pressure compartment uses a rare gas and has a wire anode [Wolfel 1983]. The in the case of the transportable X-ray system used, the gas was a mixture of 90% argon and 10% methane. The anode wire is commonly made from a quartz fibre coated with carbon [Arndt 1986] and has a DC current running through it [Wolfel 1983]. The wire is kept in a magnetic field. Ionisation of the gas by the X-ray photons results in the production of electrons and positive ions [Arndt 1986]. The normal pressure compartment is attached to the high pressure compartment and contains a preamplifier [Wolfel 1983]. Constant-fraction discriminators and a time-to-amplitude converter are used to monitor the X-ray signal in real time. A wire wound delay line is used to detect the position of the electrons on the wire [Wolfel 1983] and muti-channel analysers are used to store the signal [Osborn and Welberry 1990], which can then be fed into a computer. The intensity for the various channels is then calculated 2θ versus intensity data can be produced. The detector suffers from

two disadvantages. Firstly, the position resolution degrades towards the edges of the field of view. Secondly, the resistance of the wire changes with time due to damage caused by the irradiation.

3.2.1 X-Ray Diffraction Stress Measurement

X-ray diffraction is a well characterised technique which is often applied for the measurement of residual stresses [Cullity and Stock 2001, Doig and Flewitt 1978, (a)Withers and Bhadeshia 2001]. It is based on the measurement of interplanar spacings in crystals at various orientations with respect to the surface of the component. As mentioned in Section 3.2, the Bragg angle provides a measure of the lattice spacing. The measurement of the Bragg angle at various orientations to the sample surface is carried out by rotating the specimen or the diffractometer. Thus the angle between the direction of the measured strain and the normal to the specimen surface, the Psi angle, ψ, is altered. Since most of X-ray diffracted signal is derived from the near surface of the material (for chromium X-rays, the penetration depth into steel is approximately 10μm [Lonsdale et al. 1981]); the measurements are assumed to be purely surface measurements. In the simplest case, no stress component can act normal to a free surface and as a consequence, the stresses are assumed to be biaxial with the principal stresses acting in the plane of the surface.

The surface stress can be related to the measured strain can be using isotropic elasticity theory [Doig and Flewitt 1978] as can be seen in Equation 3.2.

$$\sigma = \frac{\varepsilon_{\psi} - \varepsilon_3}{\sin^2 \psi} \times \frac{E}{(1+\nu)} \qquad 3.2$$

The surface stress is denoted by σ, and the measured stress by ε. E is the elastic modulus of the diffraction plane in question, ν is Poisson's ratio and ψ is the angle between the direction of measured strain and the normal to the specimen surface. A correlation between the strain produced by a change in interplanar spacing, d, in relation to d and θ, can be found by differentiating the Bragg equation, Equation 3.3.

$$\varepsilon = \frac{\Delta d}{d} = -(\cot\theta)\Delta\theta \qquad 3.3$$

Substitution of Equation 3.3 into Equation 3.2 gives the relationship between σ and Δθ, Equation 3.4.

$$\sigma = \frac{E}{(1+\nu)} \times \frac{1}{\sin^2 \psi} \times \frac{2\Delta\theta}{2\tan\theta} \qquad 3.4$$

$2\Delta\theta$ is the angular shift of the diffracted peak and can be calculated from $2\theta_o - 2\theta_\psi$, where $2\theta_o$ is the Bragg angle of the planes parallel to the surface and θ_ψ is the Bragg angle of the inclined planes. From Equation 3.4, it can be seen that a plot of 2θ versus $\sin^2\psi$ results in a gradient of $\frac{2\sigma(1+\nu)\tan\theta}{E}$, from which the stress may be calculated.

This gradient is usually linear, as the assumptions made are normally adequate, Figure3.2(a). The assumptions being that

1) d_o is equal to $d_{(\psi=0)}$.
2) The stresses measured are biaxial or uniaxial, with no stress gradiant measured normal to the component.
3) There is little texture.

However, if these assumptions are not satisfied, the following d versus $\sin^2\psi$ plots may be obtained, Figure 3.2(b) and (c).

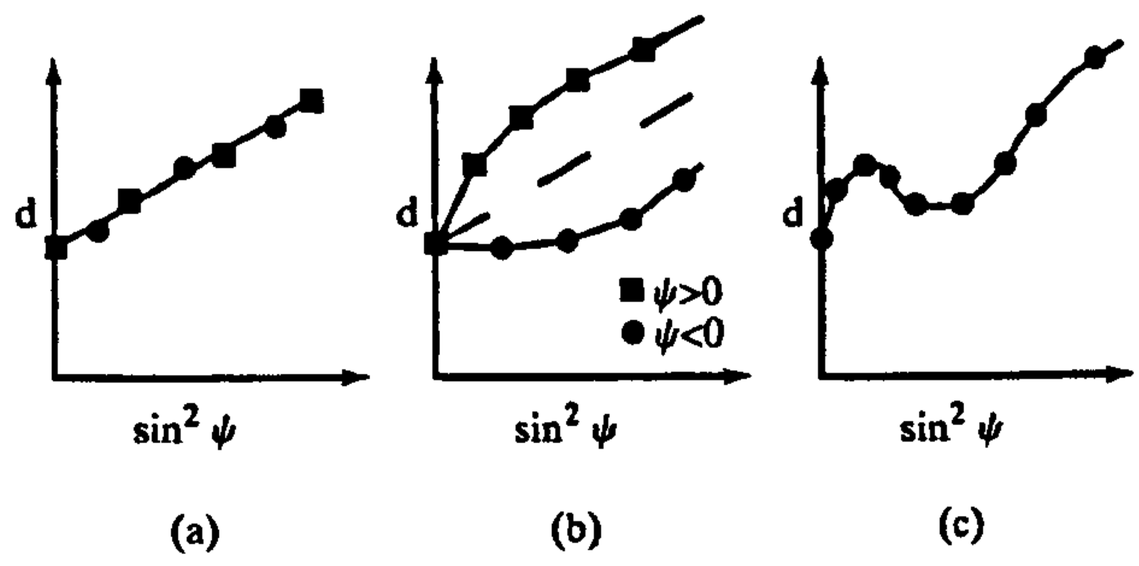

Figure 3.2. Possible d versus $\sin^2\psi$ plots [Cullity and Stock 2001].

Diagram a) shows an example of a linear plot that is obtained when all assumptions are fulfilled. Diagram b) is an example of the type of graph, said to show ψ-splitting, is obtained when the d-spacings determined for $\psi<0^\circ$ are no longer identical to those for $\psi>0^\circ$ [Brakman 1988, Cullity and Stock 2001]. Plots of this nature are characteristic of those obtained when triaxial stresses are present in the sample [Cullity and Stock 2001] and often arise after shearing-type deformations such as grinding [Brakman 1988]. Diagram c) shows the type of oscillatory graph that can be obtained if there is preferred crystal orientation, texture [Brakman 1988, Cullity and Stock 2001]. Although a moderate degree of preferred orientation causes no difficulty

in stress measurement with X-ray diffraction, a large amount of texture has two effects. First, the strength of the X-ray diffraction line used for measurement will vary greatly with ψ-angle. Second, if the material is very anisotropic, the compliance value will be dependent on specimen direction. This results in oscillation in plots of d versus $\sin^2\psi$.

3.2.2 X-Ray Diffractometer

The stress measurements were carried out using a dedicated computer-controlled transportable diffractometer system [Doig et al. 1981, Lonsdale et al. 1981, McDonald et al. 2002]. Figure 3.3 shows one type of the various options of the goniometer used). In this case, the goniometer can be held in position by four suction feet with adjustable legs or by fixing the goniometer to a steel support arm, which can be fastened to the work top. It is positioned over the component whose stress is to be measured and aligned such that the surface of the component is at the geometrical centre of the diffractometer circle. An instrument rack contains the power supplies for the X-ray tube and detector, a counter system for the detector, a stepping motor drive control unit and a computer for analysis. A recirculating water chiller supplies the X-ray tube. Once the X-ray goniometer has been connected and switched on, the measurements are automatic and remote [Lonsdale et al. 1981].

The detector used was an MBraun gas flow linear position sensitive detector in the side inclination orientation. The gas used was 90% argon, 10% methane with a pressure inside the detector of 1MPa [McDonald et al. 2002].

Chromium Kα X-rays were used with a vanadium filter which, for ferritic steel, resulted in a diffraction peak of $2\theta \sim 156^\circ$ from the {211} planes [McDonald et al. 2002]. Interchangeable collimators allowed incident beam sizes varying from 0.5mm to 5mm diameter (on the specimen at $\psi = 0$) to be chosen. However, in the following experiments a collimator of 1mm diameter was used throughout. Calibration was carried out using CeO_2 powder as the standard and the overall accuracy of the stress measurements was approximately ±10MPa [Doig et al. 1981, Lonsdale et al. 1981]. The goniometer had a linear resolution of 6μm, resulting in a 2θ angular resolution of 0.02°. The data processing accommodated peak broadening, thereby reducing any

error that this may cause. An angular range of $0^{\circ}<\psi<50^{\circ}$ was used in order to avoid a pronounced defocusing of the incident X-ray beam. The sensitivity of stress measurement increases as θ and ψ approach 90° and a practical limit of this has been shown to be when ψ is approximately 60° [Lonsdale et al. 1981]. This is caused by the spread of the X-ray beam and the rapid increase in the value of $\tan\theta$ as $\psi \rightarrow 90^{\circ}$, Equation 3.4. A linear regression procedure is used to evaluate the slope of the 2θ versus $\sin^2\psi$ plot.

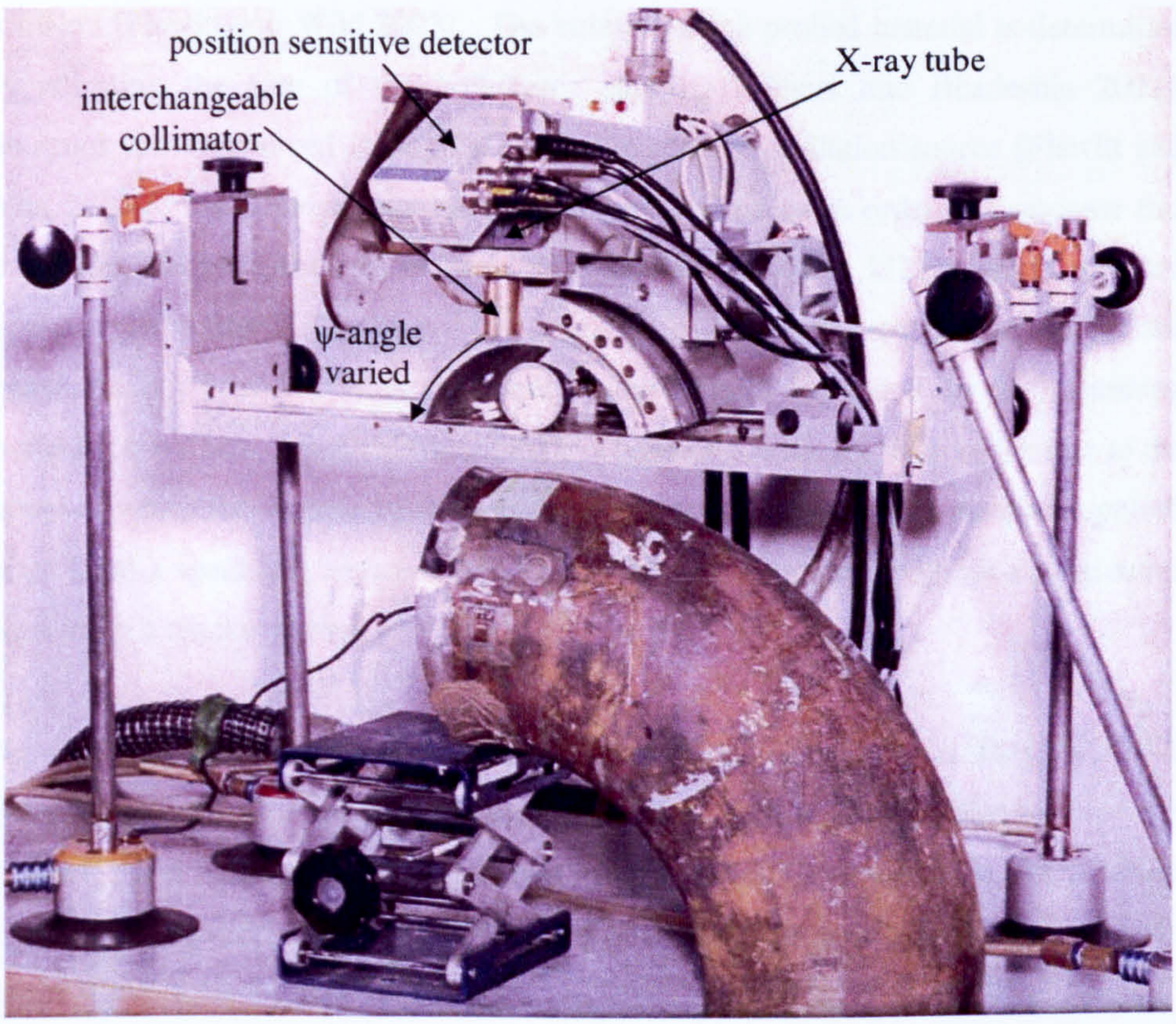

Figure 3.3. Transportable diffractometer used for stress measurement experiments. Photograph courtesy of Prof. Peter Flewitt, University of Bristol.

3.2.3 Neutron Diffraction

Whereas laboratory X-rays commonly have wavelengths between 0.1nm to 0.2nm wavelengths and react with the electrons surrounding the nucleus of an atom, neutrons have wavelengths of similar dimensions to interatomic spacings and mainly interact with the nuclei of atoms [(a)Withers and Bhadeshia 2001]. As a consequence, their penetration depths are typically of the order of many centimetres in common engineering materials. The interaction between neutrons and nuclei is a ball-type collision [Flewitt and Wild 2003]. The volume of the probed material is determined by adjusting the size of the collimator slits [(a)Withers and Bhadeshia 2001]. Neutrons can be sourced through a nuclear reactor or spallation source [Flewitt and Wild 2003]. Experimental nuclear reactors are scarce, so in order to overcome this restriction, the UK produces neutrons in a spallation source, ISIS at the Rutherford Appleton Laboratory. There are two methods of using neutron diffraction for the measurement of residual stresses, namely using time of flight and the $\theta/2\theta$ scanning method [(a)Withers and Bhadeshia 2001]. These two methods have arisen due to the nature of which the neutron beam is available. For the time of flight method, a pulsed beam from a spallation source is used. For the $\theta/2\theta$ scanning method, a continuous beam from a reactor is used.

The neutron diffraction measurements made were carried out at the ENGIN-X instrument at the Rutherford Appleton Laboratory at Oxford, UK [Mirzaee-Sisan et al. 2007]. It is based on the time of flight measurement technique and is purpose built for measuring residual stresses. A diagram of the experimental layout can be seen in Figure 3.4.

The set-up includes a sample positioning device, two position sensitive detectors placed at 90° to the incident neutron beam as well as a masking slit for the incident beam. The stresses can be evaluated after rotating the samples to different angles and measuring the lattice spacings and therefore strains at those angles [(a)Withers and Bhadeshia 2001]. Stress and strain maps can be produced by stepping the sample through the gauge volume.

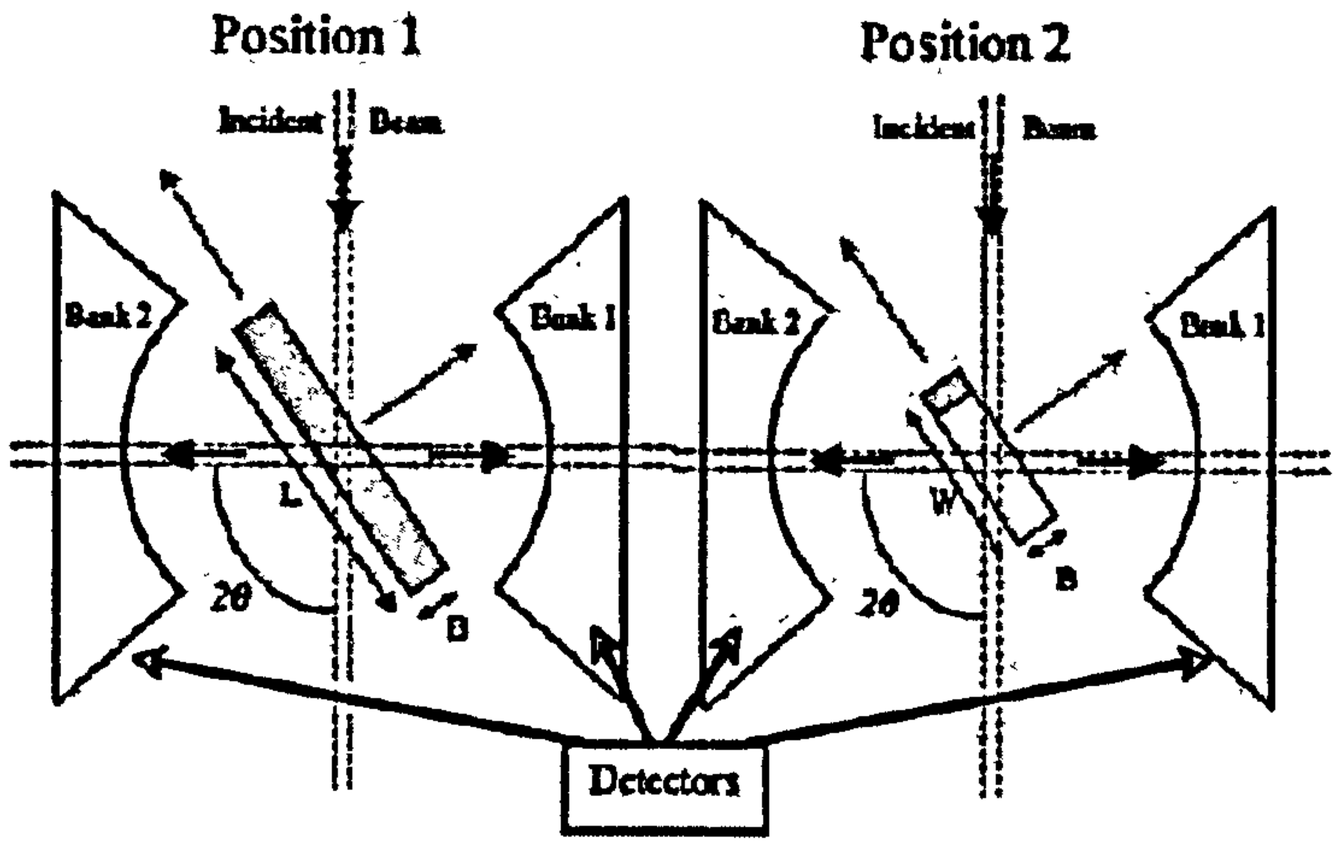

Figure 3.4. Experimental arrangement used to measure residual stresses in beam specimens by neutron diffraction using the ENGIN-X facility at the Rutherford Appleton Laboratory [Mirzaee-Sisan et al. 2007].

3.3 Raman Spectroscopy

The basis of Raman spectroscopy is the interaction of the photons with molecular nuclear motion, resulting in the inelastic scattering of the photons [Smith and Dent 2006]. In Raman spectroscopy, photons of a single frequency are used to irradiate the sample and the inelasticly scattered photons are detected [Pitt et al. 2005]. However, only one in every 10^6 to 10^8 of scattered photons are inelastically scattered to produce Raman scattering [Smith and Dent 2006].

When photons interact with the molecules of a sample, most of the photons are inelastically scattered [Smith and Dent 2006]; that is to say, only the electron clouds around the atomic nuclei are involved. This process produces a minimal frequency shift in the photons, since the electrons are relatively light and is known as Rayleigh scattering. The majority of photons are scattered in this way. However, if the electron cloud is polarised with respect to the vibrational coordinate of the molecule during the scattering process, the electron cloud can form a short-lived "virtual energy state" before the photon is re-emitted [Jones 1979]. This changes the energy of the photon. The process described is illustrated in Figure 3.5. If the molecules are in the ground vibrational energy state, m, the molecule will absorb some energy from the photon and be promoted to a higher vibrational energy state, n. This is called Stokes

scattering and results in a loss of energy from the photon [Smith and Dent 2006]. If, on the other hand, the molecule is already at the higher energy state, n, due to the addition of thermal energy for example; the photon interaction can cause the molecule to reach the virtual state and fall back to the ground state, m. This will cause the photon to gain energy and the process is called anti-Stokes scattering. The two inelastic scattering processes described above are both Raman scattering processes. Anti-Stokes scattering is relatively weak in comparison to Stokes scattering. However, the ratio of the two scattering methods will change depending on the environment. For example, the intensity of the anti-Stokes scattering relative to the Stokes scattering will increase with an increase in temperature. The ratio between the two scattering types can therefore also be used to measure temperature.

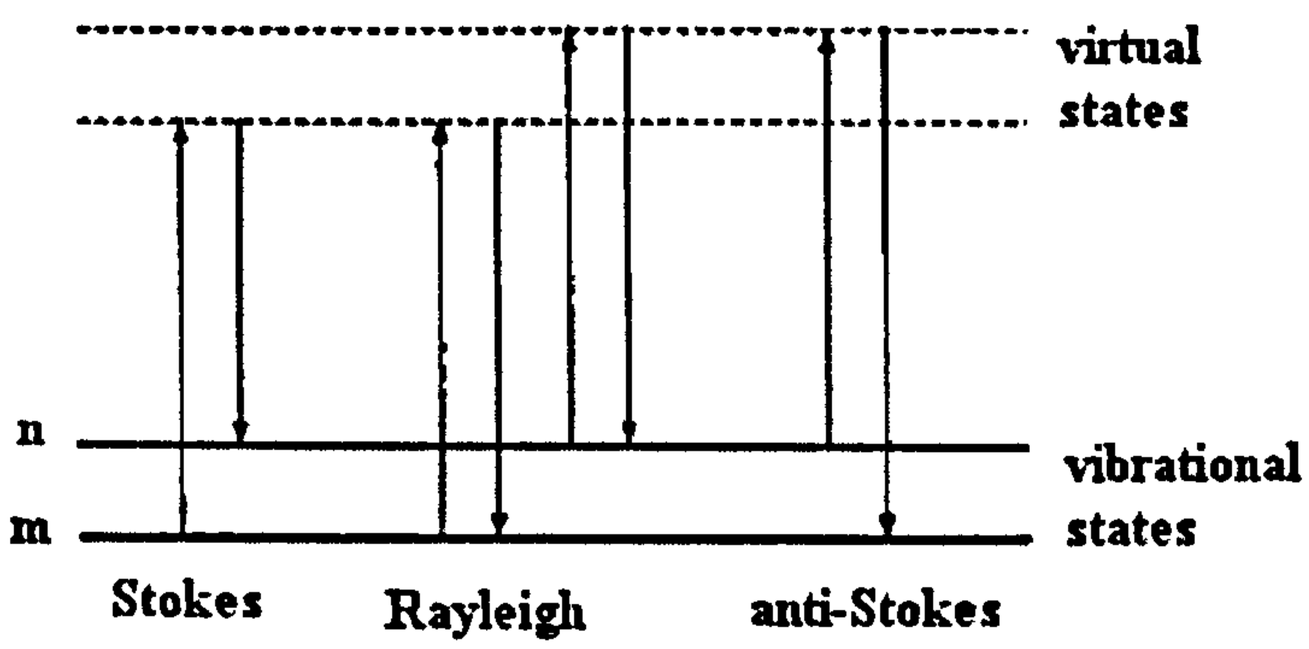

Figure 3.5. Types of photon scattering [Smith and Dent 2006].

Usually, it is the Stokes scattering that is recorded due to the relatively higher intensity involved [Smith and Dent 2006]. However, if there is a large amount of fluorescence, anti-Stokes scattering may be preferred. This is because fluorescence occurs at a lower energy than the excitation energy and since Stokes scattering is of a higher energy than the incident photons, there is no fluorescence interference. Figure 3.6 shows an example of the Stokes and anti-Stokes Raman lines for stress-free silicon.

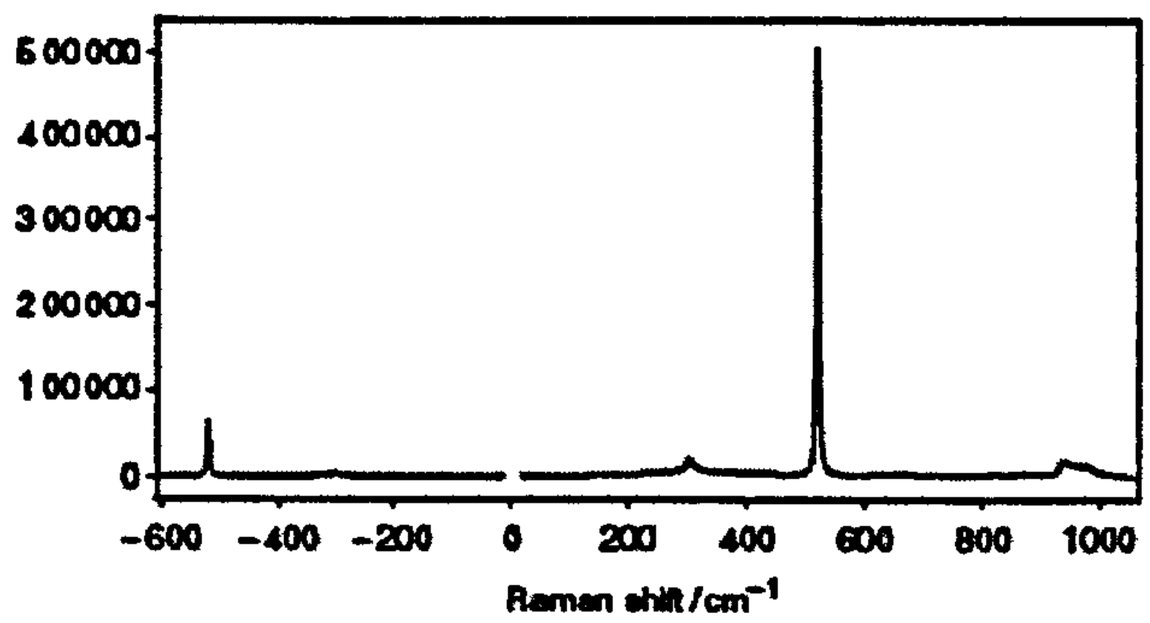

Figure 3.6. Stokes and anti-Stokes lines for stress-free silicon [Pitt et al. 2005].

Raman scattering is the shift of energy of a photon and so should be annotated as Δcm^{-1} [Smith and Dent 2006]. However, it is commonly referred to as cm^{-1}. It shall also be annotated as cm^{-1} in this work, to align with common practice. Usually, it is energy ranges of $400cm^{-1}$ to $3600cm^{-1}$ that are analysed, although it is often possible to accumulate information over a wider frequency range.

For a material to be Raman active, molecules must exhibit polarizability change with respect to the vibrational coordinate [Jones 1979]. Metals do not largely fulfil this requirement. However, oxides and carbon are common materials that do fulfil the Raman active requirements [Smith and Dent 2006]. The intensity of the Raman signal is determined by the degree of polarizability of the molecule, whereas the Raman shift is determined by the vibrational levels involved [Jones 1979].

3.4 Photoluminescence Spectroscopy

Photoluminescence is closely related to Raman spectroscopy as both are performed under similar conditions and the same laboratory equipment can be used to detect both phenomena [Flewitt and Wild 2003]. However, photoluminescence involves electronic states rather than vibrational states. Luminescence of solids occurs when the electronic states of a material are excited by an external source of energy of a particular wavelength and is released as light [Flewitt and Wild 2003, Vij 1998]. If this external source of energy is from photons of a short wavelength, the phenomenon is referred to as photoluminescence [Vij 1998]. The absorption of the photon causes an electron from the valence band to be excited to the conduction band. The photon is then re-emitted as a different wavelength (due to the conservation of energy) [Flewitt

and Wild 2003]. Photoluminescence can be divided into two categories, intrinsic and extrinsic luminescence. Most types of luminescence that have been adopted use the extrinsic form of luminescence. Extrinsic luminescence occurs when metallic impurities or defects are present in the sample [Vij 1998]. When macroscopic stresses are applied, the electronic energy levels of the electronic bands can shift [Colombi Ciacchi et al. 1999]. Therefore, electrons decaying to the ground state will emit photons of different energies, depending on the stress state of the material. One example of this phenomenon is the measurement of stresses in chromium doped alumina. However, this shall be discussed further in Section 3.12.4.

3.5 Piezospectroscopic Stress Measurement

Piezo-spectroscopy is the analysis of the shift of spectroscopic bands of a material in order to obtain information on the stress/strain under which the material has been placed [Colombi Ciacci et al. 1999]. Examples of these spectroscopic effects are Raman, InfraRed (IR) and fluorescence spectroscopies such as photoluminescence. The spectral shifts are correlated to the stresses by the following tensoral relationship, Equation 3.5, [Colombi Ciacci et al. 1999]:

$$\Delta\omega = \sum_{i,j} \Pi_{ij}\sigma_{ij} \qquad 3.5$$

Where $\Delta\omega$ is the peak frequency shift of the observed spectral band, σ_{ij} are the components of the stress tensor and Π_{ij} are the piezospectroscopic coefficients. Equation 3.6 shows that stress has a linear contribution to frequency shift. Although stress can produce higher order effects, it is seldom necessary to take these into account. Despite Raman and photoluminescence spectroscopy occuring through different phenomena (the vibrational behaviour of the system and electronic bands respectively); the tensoral relationship shown in Equation 3.5 can be applied to both.

Although radiation is often characterised by wavelength, λ, spectroscopists often describe it in terms of frequency, ν, or wavenumber, ω, [Smith and Dent 2006]. This is because the frequency and wavenumber of a photon are both linearly related to energy, as can be seen in Equations 3.6 to 3.8 where ΔE is the change in energy, h is the Planck constant and c is the speed of light.

$$\lambda = \frac{c}{\nu} \qquad 3.6$$

$$\nu = \frac{\Delta E}{h} \tag{3.7}$$

$$\omega = \frac{\nu}{c} = \frac{1}{\lambda} = \frac{\Delta E}{hc} \tag{3.8}$$

Figure 3.7 shows a schematic of a common set-up for a Raman/photoluminescence spectrometer. The laser source is directed to the sample by a series of lenses and mirrors [Pitt et al. 2005].

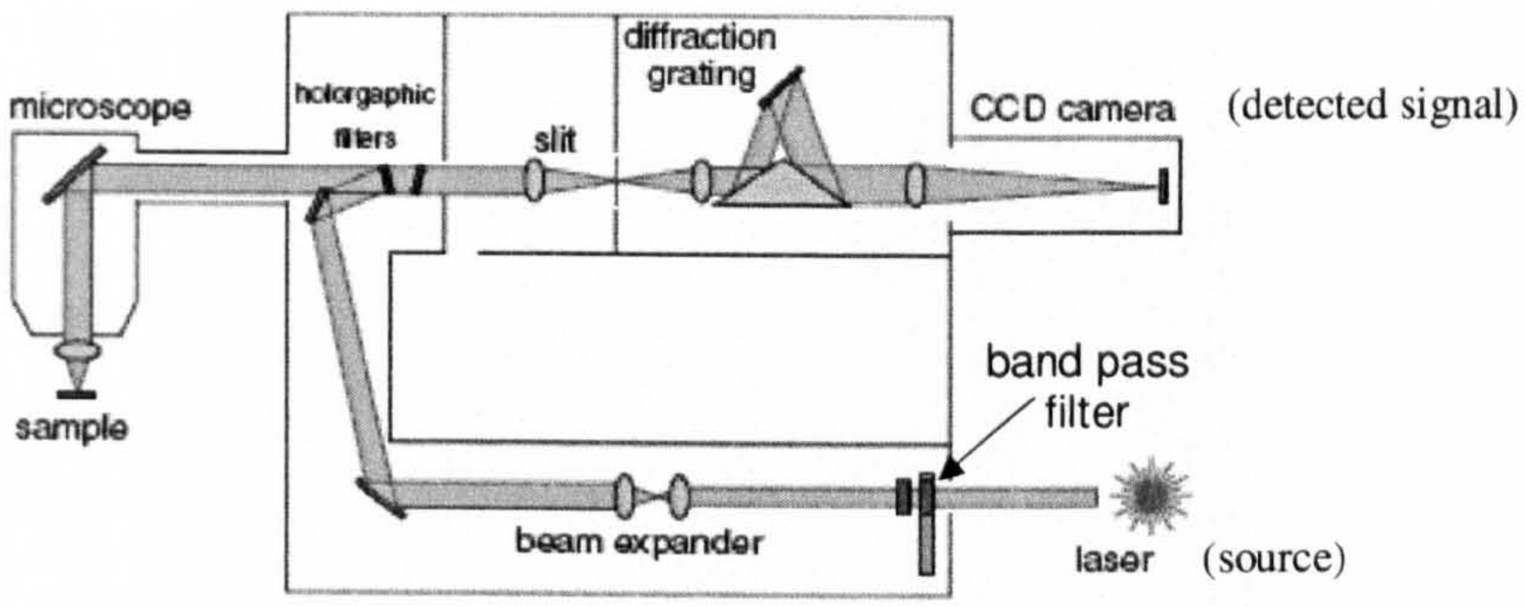

Figure 3.7. Typical Raman/photoluminescence spectrometer showing the main components [Pitt et al. 2005].

The laser beam enters the spectrometer at the at the bottom right of the equipment. In order to remove non-lasing emissions, it is passed through a narrow line band pass filter. Mirrors reflect the beam onto a holographic, notch or edge filter. A beam expander can be placed before the mirrors in order to improve the spatial properties of the laser beam. The beam expander does this by allowing for (expanding to the ratio of) the focal lengths of the microscope objectives. If the polarisation of the laser beam is required, the relevant optics can be placed before or after the beam expander. Since the light returning from the sample consist of Rayleigh scattered light as well as the required Raman scattered light and photoluminescence, it is passed through holographic filters that reject Rayleigh scattering. The beam is then passed through a slit where a linear polariser can be placed for polarisation analysis. The beam is then sent through a diffraction grating assembly, which disperses the incoming beam into the focusing lens and to the charge-coupled device (CCD) detector.

Notch and edge filters are holographic filters which are used as part of the grating assembly in order to reject Rayleigh scattering, i.e. the unwanted elastically scattered

light [Pitt et al. 2005]. They are effectively a film of gelatine sandwiched between two glass or quarz plates. The two types of filter used are edge filters and notch filters. Whereas notch filters allow transmission of both the Stokes and anti-Stokes peaks, edge filters only allow transmission of the Stokes peaks. A Raman/photoluminescence spectrometer employed for this work, a Renishaw Raman 2000 spectrometer, is shown below, Figure 3.8. The spectrometer could be fitted with a helium-neon with a wavelength of 633nm or an argon laser with a wavelength of 514nm.

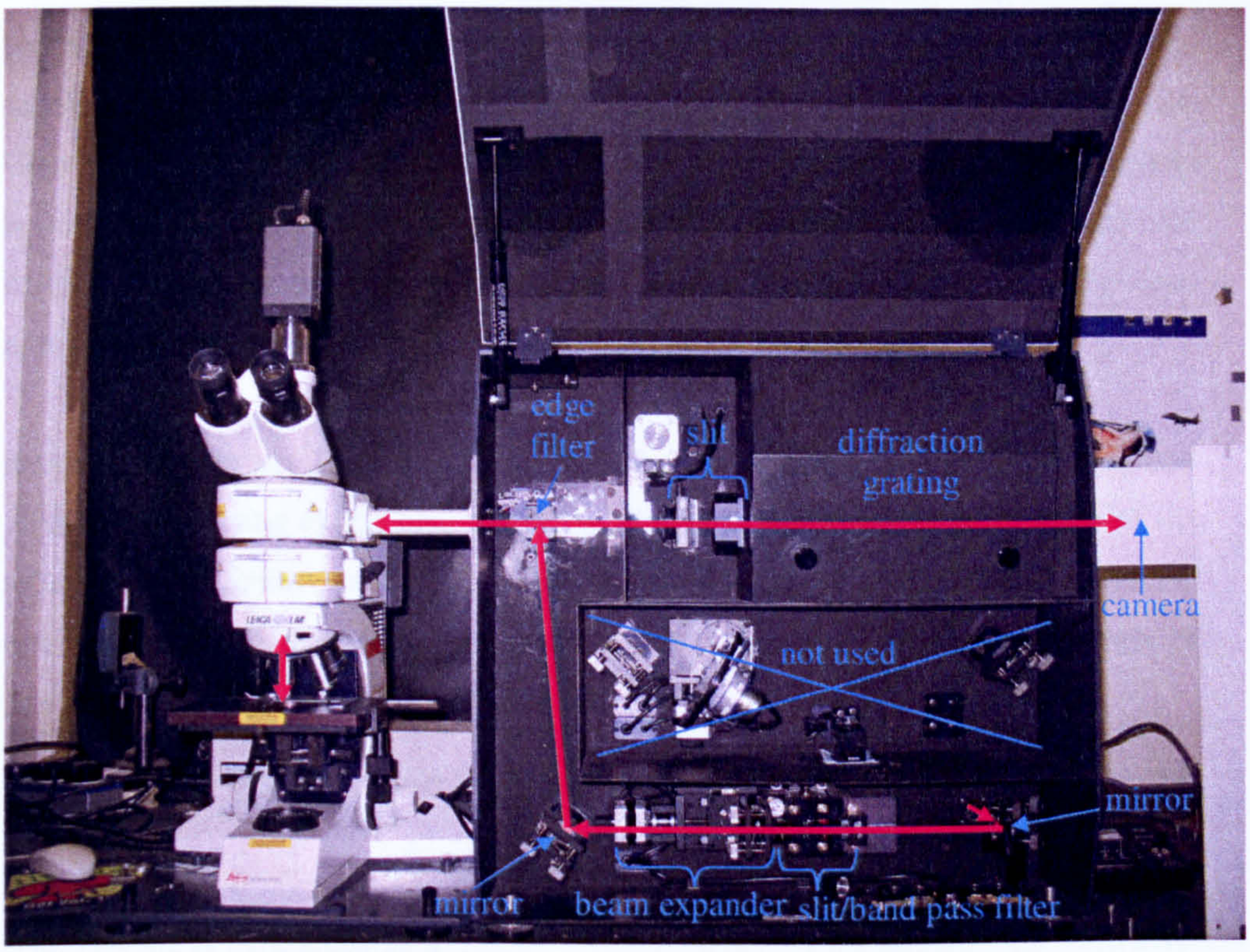

Figure 3.8. Raman spectrometer employed for measurements in present work. The red arrow shows the direction of the laser beam.

3.6 Hole Drilling

If a hole is drilled into a component of a given residual stress, the stresses around the hole will relax, causing that volume of the component to change [(a)Withers and Bhadeshia 2001]. This stress relaxation can be used to calculate the original residual stresses in that part of the component. This effect forms the basis of the deep hole drilling and incremental hole drilling techniques.

3.7 Deep Hole Drilling

Deep hole drilling involves a core being trepanned out of the component and the change in diameter of the remaining through-section hole being measured [Smith et al. 2000]. First, a block (or bush) is glued on the area of the component to provide a reference frame through which the deep hole is drilled. A reference hole is then drilled through the block and component using a gun drill. An air probe is then used to make measurements of the diameter of the reference hole at a number of angles. A core of the component with the reference hole in the centre is then trepanned free of the component. Transducers placed on the opposite wall of the component are used to monitor the changes in the shape of the core, as the trepanning is being carried out. Once the core of material has been trepanned out of the component, the reference hole is then remeasured. It is the changes in the diameter of the reference hole and the core height that are used to calculate the residual stresses. Figure 3.9 illustrates the deep hole drilling process.

Residual stresses are calculated from the measured displacements of the core and reference hole using elastic analysis of the diametral distortion, ε, at the edge of the reference hole [Smith et al. 2000]. This distortion is a function of angle θ around the reference hole and the length z of the hole. The diameter of the reference hole is denoted u. These factors are linked to stress by:

$$\varepsilon[\theta,z]=\frac{\Delta u}{u}=\frac{1}{E}\{\sigma_{xx}f[\theta,z]+\sigma_{yy}g[\theta,z]+\sigma_{xy}h[\theta,z]\} \quad 3.9$$

The functions $f[\theta,z]$, $g[\theta,z]$ and $h[\theta,z]$ are given by:

$$f[\theta,z]=A[z]\{1+B[z]2\cos(2\theta)\} \quad 3.10$$

$$g[\theta,z]=A[z]\{1-B[z]2\cos(2\theta)\} \quad 3.11$$

$$h[\theta,z]=4A[z]B[z]\sin(2\theta) \quad 3.12$$

where $A[z]$ and $B[z]$ are coefficients representing the uniform expansion and eccentricity of the reference hole respectively. In order to evaluate in-plane stress, a minimum of three measurements is needed. If measurements are made at n angles around the hole, least squares fitting of the measurements can be employed to determine the stress. At a given through thickness position, z_1, the measured distortion is given by the vector $\bar{\varepsilon}$,

$$\bar{\varepsilon} = [M]\bar{\sigma} \tag{3.13}$$

$$\bar{\varepsilon} = [\varepsilon_\theta[\theta_1, z_1], \varepsilon_\theta[\theta_2, z_1], \ldots\ldots, \varepsilon_\theta[\theta_n, z_1], \varepsilon_{zz}]^T \tag{3.14}$$

The residual stress vector $\bar{\sigma}$ is given in Equation 3.15, and $[M]$ is the compliance matrix, shown in Equation 3.16.

$$\bar{\sigma} = [\sigma_{xx}, \sigma_{yy}, \sigma_{xy}]^T \tag{3.15}$$

$$[M] = \frac{1}{E}\begin{bmatrix} f[\theta_1, z_1]\, g[\theta_1, z_1]\, h[\theta_1, z_1] \\ f[\theta_2, z_1]\, g[\theta_2, z_1]\, h[\theta_2, z_1] \\ \vdots \quad\quad \vdots \quad\quad \vdots \\ f[\theta_n, z_1]\, g[\theta_n, z_1]\, h[\theta_n, z_1] \end{bmatrix} \tag{3.16}$$

The residual stress field, $\tilde{\sigma}$, that best fits the measured distortions, $\tilde{\varepsilon}_m$, is calculated by using pseudo-inverse or Moore-Penrose inverse matrices, Equation 3.17.

$$\tilde{\sigma} = [M]^* \tilde{\varepsilon}_m \tag{3.17}$$

Where

$$[M]^* = (M^T M)^{-1} M^T \tag{3.18}$$

and

$$\tilde{\sigma} = [\tilde{\sigma}_{xx}, \tilde{\sigma}_{yy}, \tilde{\sigma}_{xy}]^T \tag{3.19}$$

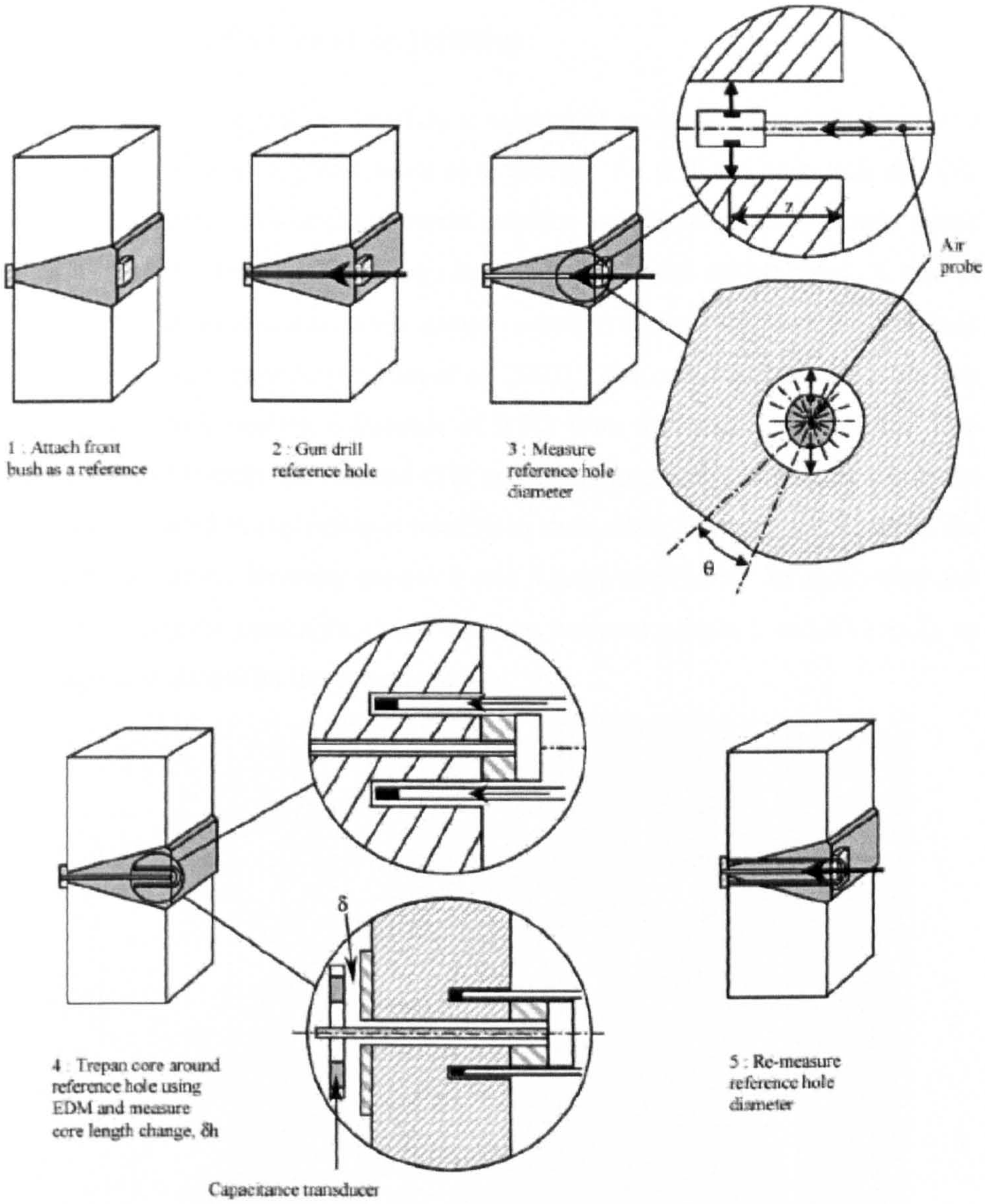

Figure 3.9. Process of deep hole drilling measurement method. The steps 1 to 5 involved are shown [Smith et al. 2000].

3.8 Incremental Centre Hole Drilling

Incremental centre hole drilling involves a volume of material being drilled out of a component in several steps [Stefanescu et al. 2004]. As with the deep hole drilling, this technique allows non-uniform stress profiles to be measured. Strain gauge rosettes are used to measure the change in strain around the drilled hole. A typical geometry for a three-element strain gauge rosette employed for incremental hole drilling is shown in Figure 3.10 [Grant et al. 2002]. The centres of the strain gauges are placed with their centres a distance of 0.5D from the centre of the hole. The gauge widths and lengths are denoted GW and GL respectively. Although the strain gauges can be placed in any position relative to each other, Figure 3.10 describes the ASTM Type A design whereby gauges 1 and 3 are placed at 90° to each other and gauge 2 lies along the centreline of the distance between gauges 1 and 3 (line 2), as this arrangement simplifies the stress analysis.

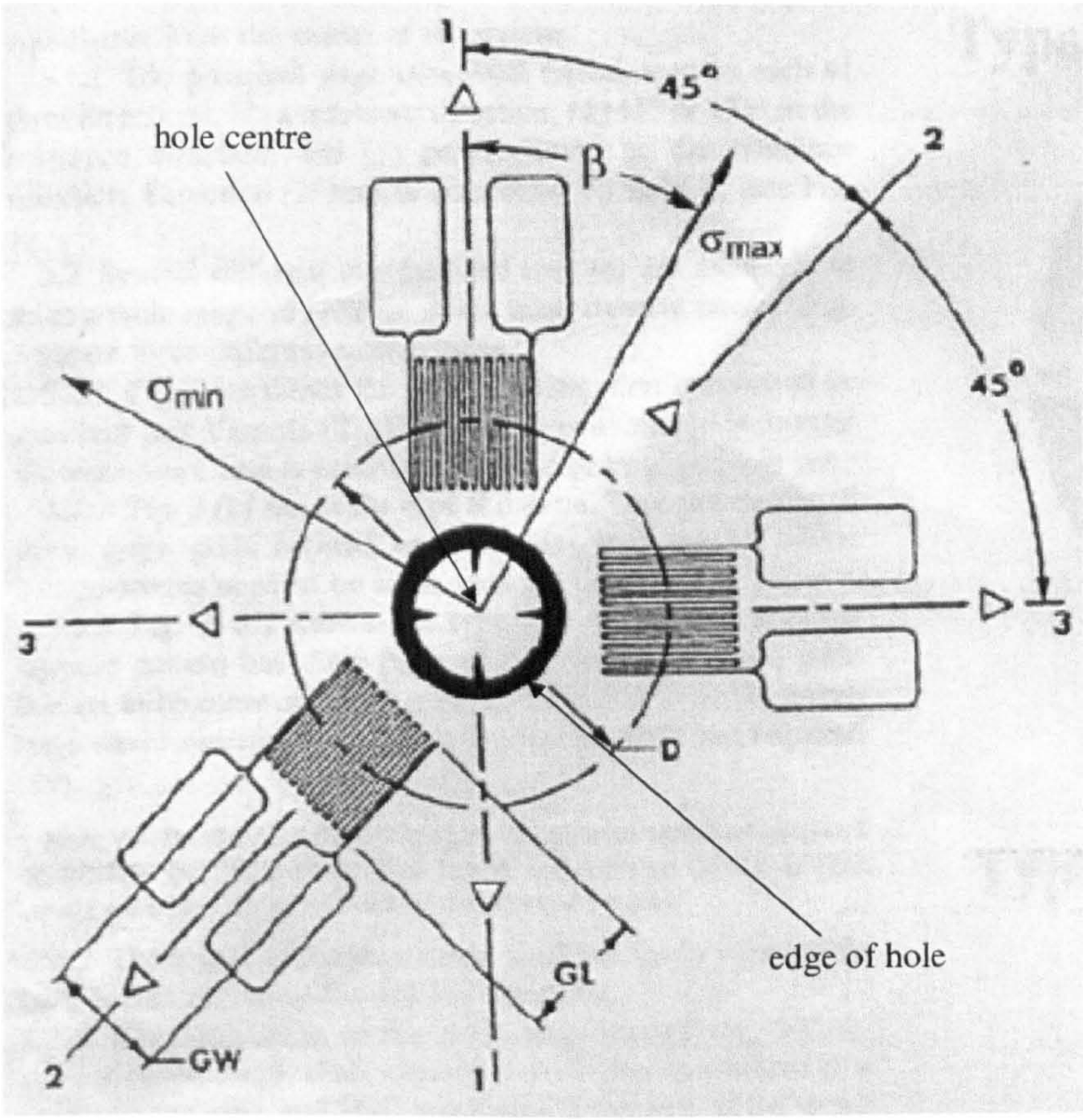

Figure 3.10. Typical geometry of strain gauge rosette used for incremental hole drilling technique [Grant et al. 2002].

The surface strain relief, ε_r, measured due to the drilling of a hole is related to the relieved principal stresses by

$$\varepsilon_r = \left(\overline{A} + \overline{B}\cos 2\beta\right)\sigma_{max} + \left(\overline{A} - \overline{B}\cos 2\beta\right)\sigma_{min} \qquad 3.20$$

where $\overline{A}$ and $\overline{B}$ are calibration constants, the values of which depend on the geometry of the strain gauges used, the elastic properties of the material and the geometrical properties of the hole. $\overline{A}$ and $\overline{B}$ can be evaluated by

$$\overline{A} = \frac{-\overline{a}(1+\nu)}{2E} \qquad 3.21$$

$$\overline{B} = \frac{-\overline{b}}{2E} \qquad 3.22$$

$\overline{a}$ and $\overline{b}$ are almost material-independent values that vary with the hole depth, ν is the Poisson ratio and E is the Young modulus of the material. Although $\overline{a}$ and $\overline{b}$ can be calculated by experimental calibration, their values can also be found as an ASTM standard [Grant et al. 2002].

For a thin specimen (<1.2D) or a through-section hole with plane stress conditions, the strain relaxations measured by the three strain gauges can be considered in terms of three combination strain variables, p,q and t; p represents the 'volumetric' strain relaxation Equation 3.23, q and t represent shear strain components of the relaxation, Equations 3.24 and 3.25 respectively [Grant et al. 2002].

$$p = \frac{\varepsilon_3 + \varepsilon_1}{2} \qquad 3.23$$

$$q = \frac{\varepsilon_3 - \varepsilon_1}{2} \qquad 3.24$$

$$t = \frac{\varepsilon_3 + \varepsilon_1 - 2\varepsilon_2}{2} \qquad 3.25$$

The angle β can be calculated using Equation 3.26.

$$\beta = \frac{1}{2}\tan^{-1}\left(\frac{t}{q}\right) \qquad 3.26$$

If $\varepsilon_3 > \varepsilon_1$, then β refers to σ_{max}. If $\varepsilon_3 < \varepsilon_1$, then β refers to σ_{min}. If $\varepsilon_3 = \varepsilon_1$, then $\beta = \pm 45^{\circ}$.

The principal stresses can be calculated by Equation 3.27.

$$\sigma_{min}, \sigma_{max} = -\left[\left(\frac{p}{\bar{a}(1+\nu)}\right) \pm \left(\frac{\sqrt{(q^2+t^2)}}{\bar{b}}\right)\right] E \qquad 3.27$$

For a thick specimen (>1.2*D*) with principal strain conditions, the combination stresses, P, Q and T, are considered, where P is the mean 'pressure' of the residual stress. Q and T are the shear stress components Equations 3.28 to 3.30.

$$P = \frac{(\sigma_3 + \sigma_1)}{2} \qquad 3.28$$

$$Q = \frac{(\sigma_3 - \sigma_1)}{2} \qquad 3.29$$

$$T = \frac{\tau_{13}}{2} \qquad 3.30$$

The angle β can be calculated from Equation 3.31 and the principal stresses can be calculated from Equation 3.32.

$$\beta = \frac{1}{2}\tan^{-1}\left(\frac{T}{Q}\right) \qquad 3.31$$

$$\sigma_{max}, \sigma_{min} = P \pm \sqrt{(Q^2 + T^2)} \qquad 3.32$$

For non-uniform through thickness stresses, an integral approach is taken, whereby small drilling increments are taken.

3.9 Finite Element Modelling

The overall basis of the finite element modelling method has been well documented [Logan 2002, Meier et al. 1991]. This method allows a structure to be described in discrete quantities, by dividing it into a mesh. Boundary conditions and input parameters are chosen, which determine the structure's behaviour to the applied forces. When the chosen forces are applied, the behaviour of the mesh allows the stresses in the various nodes of the mesh to be calculated. Finite element models can be used to analyze both structural and non-structural problems. Structural problems include stress analysis, buckling and vibration. Non-structural problems include heat transfer, fluid flow and the distribution of electric or magnetic potential. There are many commercially available finite element packages such as ABAQUS, ANSYS and SYSWELD [Logan 2002, Mirzaee-Sisan et al. 2007].

The mesh is divided into elements. These can take the form of a point mass, line, area or volume and are chosen depending on what is to be modelled. For example, a line may be used when modelling a spring or bar, whereas a volume may be used when modelling a three dimensional solid. Symmetry (where appropriate) can be used to simplify the model, so that, for example, only half the component need be modelled [Logan 2002, Yaghi et al. 2007].

When creating a finite element model, it is essential to consider the input parameters [Logan 2002]. Important input parameters for the mechanical properties are the strain/stress behaviour of the material, density, and the Poisson ratio [Mirzaee-Sisan 2007]. Thermal properties include thermal conductivity, specific heat capacity and the coefficient of expansion.

The finite element work described in this thesis has involved thermal stresses and therefore mechanical properties as well as thermal properties have been considered [Mirzaee-Sisan et al. 2007, Yaghi et al. 2008]. As well as the previously mentioned thermal properties, solid-state phase transformation has in some instances also been taken into account [Yaghi et al. 2008].

3.10 Focused Ion Beam Milling

A focused ion beam (FIB) instrument relies on a focused ion beam to create an image of or to mill the specimen investigated [Giannuzzi and Stevie 1999, Utke et al. 2008]. A tungsten needle is placed near a gallium reservoir. A high extraction field is used to pull the gallium into a cone whose tip is approximately 5 to 10nm. Ions are emitted as a consequence of field ionization and post ionization and are accelerated down the FIB column. Probe current can be adjusted through the use of lenses and by adjusting the effective aperture sizes. Stigmatism of the ion beam can be reduced through the use of octupoles, which are also used to deflect the beam during scanning. During the milling process, gallium ions are accelerated towards the specimen. Contact with the sample can result in the ejection of a particle as well as the generation of secondary electrons. The particle can be an ion or neutral. The intensity of the secondary electrons produced allows an image of the specimen to be constructed. Specimen milling speed and finish is adjusted through the probe current; increasing the probe current increases the sputtering rate of the material investigated. A platinum layer can

be deposited on to the sample in order to protect the specimen surface during the milling of a cross-section. Figure 3.11 is a schematic diagram of liquid metal ion source and lenses of a focused ion beam instrument.

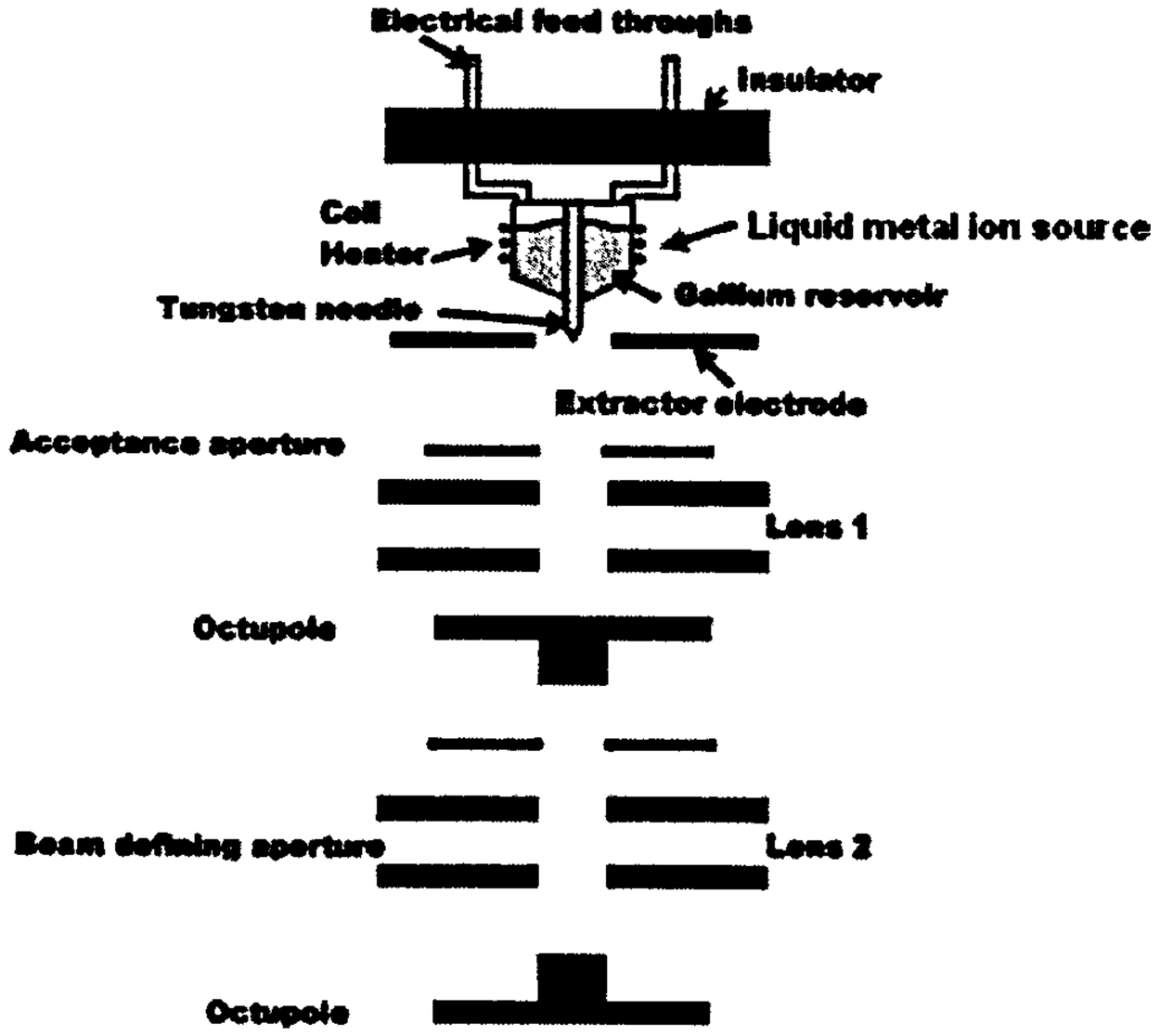

Figure 3.11. A schematic diagram of the liquid metal ion source and lens system of a focused ion beam system [Giannuzzi and Stevie 1999].

3.11 Transmission Electron Microscopy

Transmission electron microscopy (TEM) is a technique used to investigate the microstructure of materials [Flewitt and Wild 2003]. It involves the emitting of a high voltage electron beam by an electron source such as a tungsten filament or LaB_6 crystal. The beam is accelerated by an anode with respect to the cathode (electron source). The beam is then focused and transmitted through the specimen to be examined. After emerging from the specimen, the beam is magnified by the objective lens system of the microscope. A viewing screen allows an image of the magnified transmitted beam to be seen. This screen often comprises a metal plate coated with a zinc phosphor which scintillates with electron interaction. The image is recorded by using a camera or digital recording system.

Scanning transmission electron microscopy (STEM) is a modification of transmission electron microscopy, which allows the electron beam to raster across the sample, to

form an image over a larger area [Chescoe et al. 1990]. Information can be gained on size, shape and arrangement of particles over the transmitted area of the specimen such as dislocations [Flewitt and Wild 2003]. Electron dispersive X-ray analysis can be combined with scanning transmission electron microscopy to give elemental information of the scanned area. Although transmission electron microscopy has many advantages, it suffers the disadvantage that thin samples are required [Kawasaki et al. 1999]. The maximum transmittable thickness of a specimen depends on the density of the material [Kubel et al. 2005]. However, the thickness limit typically of the order of 100nm [James et al. 2007, Kubel et al. 2005]. The sample preparation can be therefore time consuming [Kawasaki et al. 1999].

High-angle annular detector dark-field microscopy (HAADF) allows an image to be formed by electrons scattered incoherently at high angles (approximately 5°) in a scanning transmission electron microscope [Kubel et al. 2005]. A finely focused electron beam of approximately 2Å diameter is scanned across the specimen. The intensity of the incoherently scattered electrons is varies with atomic number and as a consequence can be employed to assess the composition of the material. This phenomenon is known as Z-contrast.

3.12 Accuracy of Measurements

When analysing data and more specifically comparing data acquired from different techniques, it is important to consider the errors inherent in the different measurements. This section reviews possible sources of error in the various techniques that have been used for the present work. Theoretical calculations and experimental measurements carried out as part of this work to confirm confidence in employed stress measurement techniques are described in Chapter 4 - Calibration and Sources of Error.

3.12.1 X-Ray Diffraction

It can be shown that a height displacement, Δh, from the Rowland circle results in a measured angular shift $\Delta 2\theta$ [Klug and Alexander 1974]. This is discussed in more detail in Section 7.4. With regards to the transportable diffractometer used throughout the stress measurement experiments [Doig et al. 1981], the dial gauge employed to

adjust the height had a sensitivity of ±0.01mm resulting in an accuracy of approximately ±5MPa for austenitic steels and ±1MPa for ferritic steels.

The recorded diffraction intensity from a sample increases rapidly as 2θ increases over the range of 90° to 180° [Doig et al. 1981]. This has a similar effect to the diffraction peak having a non-linear background and results in the peak position moving towards higher values of 2θ. Since the non-linear sensitivity is also a function of ψ, this will result in an error in the gradient of 2θ versus $\sin^2\psi$.

Broadening of the incident X-ray beam area can increase as ψ increases. This in turn can cause measurement errors [Doig et al. 1981]. The ψ-angle is not used above 50° in order to minimise broadening effects.

The X-ray emission from an X-ray tube consists predominantly of two spectral lines, $K\alpha_1$ and $K\alpha_2$ [Doig et al. 1981]. The angular separation of the two resulting superimposed diffraction peaks from these lines increases as 2θ increases. The resulting intensity of the measured diffraction peak from the $K\alpha_1$ line is approximately twice that of the $K\alpha_2$ line. The total intensity $I_{2\theta}$ of the superimposed peaks can be approximated by the following equation for two superimposed Gaussian curves, Equation 3.33, which can then be used to separate the two spectral peaks

$$I_{2\theta} = I_o\left[e^{\frac{-(2\theta)^2}{W}} + 0.5e^{\frac{-(2\theta-\varphi)^2}{W}}\right] \qquad 3.33$$

where I_o is a constant, θ is the diffraction angle, φ is the angular separation of the two spectral components at that particular diffraction angle, and W is the width of the individual spectral peaks. Once the peaks have been deconvoluted, they can be peak fitted such as with the centre of gravity or peak turning point procedures.

As X-ray diffraction is a near surface measurement technique, it has been recommended that unless the stresses to be measured are at the surface of the component such as machining stresses, that the surface be prepared before examination [Cullity and Stock 2001, Lonsdale et al. 1981]. Authors have suggested that mechanical polishing methods be followed by electropolishing, since electropolishing removes material without inducing stress [McDonald et al. 2002]. It

has also been calculated that surface profile has an effect on the measured stress [Doig and Flewitt 1981]. Rough surface profiles such as those generated by machining processes can cause the diffracted beam to broaden and shift due to differential absorption and surface orientation effects.

The area of the incident and diffracted beam is also of importance. It is this parameter, that determines the sample volume and it is necessary to have an adequate sample volume in order to have statistical confidence in the measurements taken [Lonsdale 1986, McDonald et al. 2002]. Also, since the X-ray diffraction technique relies on a random distribution of grain orientations, it is necessary for the sampled area to be large enough for this to be the case. The grain size of the specimen must therefore also be considered when deciding which collimator and as such X-ray beam size to employ. As mentioned previously, the overall measurement errors in using the transportable X-ray diffractometer have been calculated to be approximately ±10MPa on ferritic steels [Lonsdale et al. 1981].

3.12.2 Neutron Diffraction

Three significant sources of error in neutron diffraction can arise due to;

1) Material uncertainties

Knowledge of stress-free lattice parameters and crystallographic elastic constants are required in order to calculate strain and convert strain to stress [Goudar et al. 2008]. However, the determination of stress-free lattice parameters can be problematic [Winholtz 2003]. Errors can arise if there is a shift in lattice spacing due to the changing microstructure of the sample [Holden et al. 2006]. The changing microstructure might not induce Type I stresses but could bias the diffraction measurements and therefore be measured as such. This can be overcome with the use of stress-free reference blocks of the material to be investigated. Although stress-free powders can be used, care must be taken to ensure that the powder used has undergone the same thermo-mechanical treatment as the specimen position investigated [Winholtz 2003]. Elastic constants can be calculated or determined experimentally [Lodini 2003]. Nonetheless, it is often necessary to measure the diffraction elastic constants in order to verify the calculated values.

2) The computation of the diffraction spectra

Variation of the measured lattice parameters can be defined by fitting the diffraction spectra, such as by a least squares refinement method [Goudar et al. 2008]. The error in the fitting of the spectra adds to uncertainties in the measured lattice parameters.

3) Near surface stress measurements

Errors can arise when undertaking near-surface stress measurements due to geometric effects [Edwards 2003]. If the diffracting gauge volume is only partially filled, its centroid is moved relative to the detector system. If the detector system is a multi-detector one, such as a position sensitive detector, the displacement of the centroid causes a change in diffraction angle, resulting in a shift of the peak on the detector.

3.12.3 Raman Spectroscopy

The main sources of potential error in Raman spectroscopy involve the calibration of the instrumentation, data handling and specimen laser heating effects [De Wolf 1996, Kouteva-Arguirova 2003, Smith and Dent 2006]. The wavenumber position can be calibrated using lamps or standards [Smith and Dent 2006]. Both of these methods have drawbacks. To calibrate intensity, response corrections can be used from standards. The intensity of the spectrum produced by a calibration lamp depends upon its distance relative to the microscope. However, the peak profiles are very sensitive to changes in the position of the diffraction grating and this must be taken into account when calibrating and analysing peak properties.

The wavenumber position of the spectrum produced by the calibration lamp is dependent upon the lamp's energy and therefore temperature [Smith and Dent 2006]. Since the temperature of the lamp decreases throughout its lifetime, the wavenumber position cannot be considered to be constant. A common standard material for measuring wavenumber position is silicon. However, since a material's stress affects its peak properties, it is necessary to ensure that the stress state is minimal or, preferably is known, when using the material as a calibration standard. The Raman shift of stress-free silicon is approximately $520cm^{-1}$ [De Wolf 1996]. If the instrument is stable and sensitive, it should be possible to measure changes in Raman shifts of up to $0.05cm^{-1}$, thereby producing an accuracy of approximately 25MPa in silicon. Nevertheless, as has already been indicated, this is an ideal situation.

It has been shown that the laser used to produce the Raman effects can induce thermal stresses in materials such as silicon [Duong et al. 2000, Khoi et al. 1999, Kouteva-Arguirova et al. 2003]. It is well documented, that tensile stresses in silicon result in peak shifts (due to a softening of the phonon frequency) and line broadening (due to a reduction in phonon decay time); whereas compressive stresses also result in peak shifts (due to a stiffening of the phonon frequency) but do not produce line broadening [Kouteva-Arguirova et al. 2003]. The consequence of a focused laser on a silicon sample has been shown to be a result of a combination of temperature and pressure effects. The laser heats a local area, which is put under compressive stress by the surrounding area. Since the heating effects alone would result in shifts to lower frequencies and the compressive stresses would result in shifts to higher frequencies, it was concluded that these effects could, to a certain extent, cancel each other out and result in almost negligible Raman shifts in some cases. It was also discussed that the temperature gradient across the laser heated area could result in asymmetric peaks. An experiment was reported in which the power of the laser focused on a silicon wafer was increased stepwise and the Raman shifts recorded, Figure 3.12. The temperature was calculated from the measured beam profile and from the relevant material properties such as thermal diffusion and reflectivity. This was followed by a stepwise reduction in the laser power. The recording time was kept constant (15s) throughout the experiment. It was shown that a maximum frequency shift was under $2cm^{-1}$ and it was suggested that it might be possible to use peak width and position to calculate thermally induced stresses, due to the suggested negligible effect of hydrostatic pressure on peak width. Nevertheless, it can be seen that a thermally induced Raman shift of $2cm^{-1}$ is significant if one is expecting to measure peak positions to an accuracy of $0.05cm^{-1}$ [De Wolf 1996], even if the frequency shift has been reduced by the resulting compressive stresses produced by the surrounding material. Another significant result of laser induced heating has been reported by [Shebanova and Lazor 2003]. It was found that increasing the laser power could transform magnetite into other forms of ion oxides such as maghemite and hematite. Such an effect could lead to errors in the assignment of a material and it was concluded that it had occurred in some previous studies [Dunnwald and Otto 1989, Verble 1974].

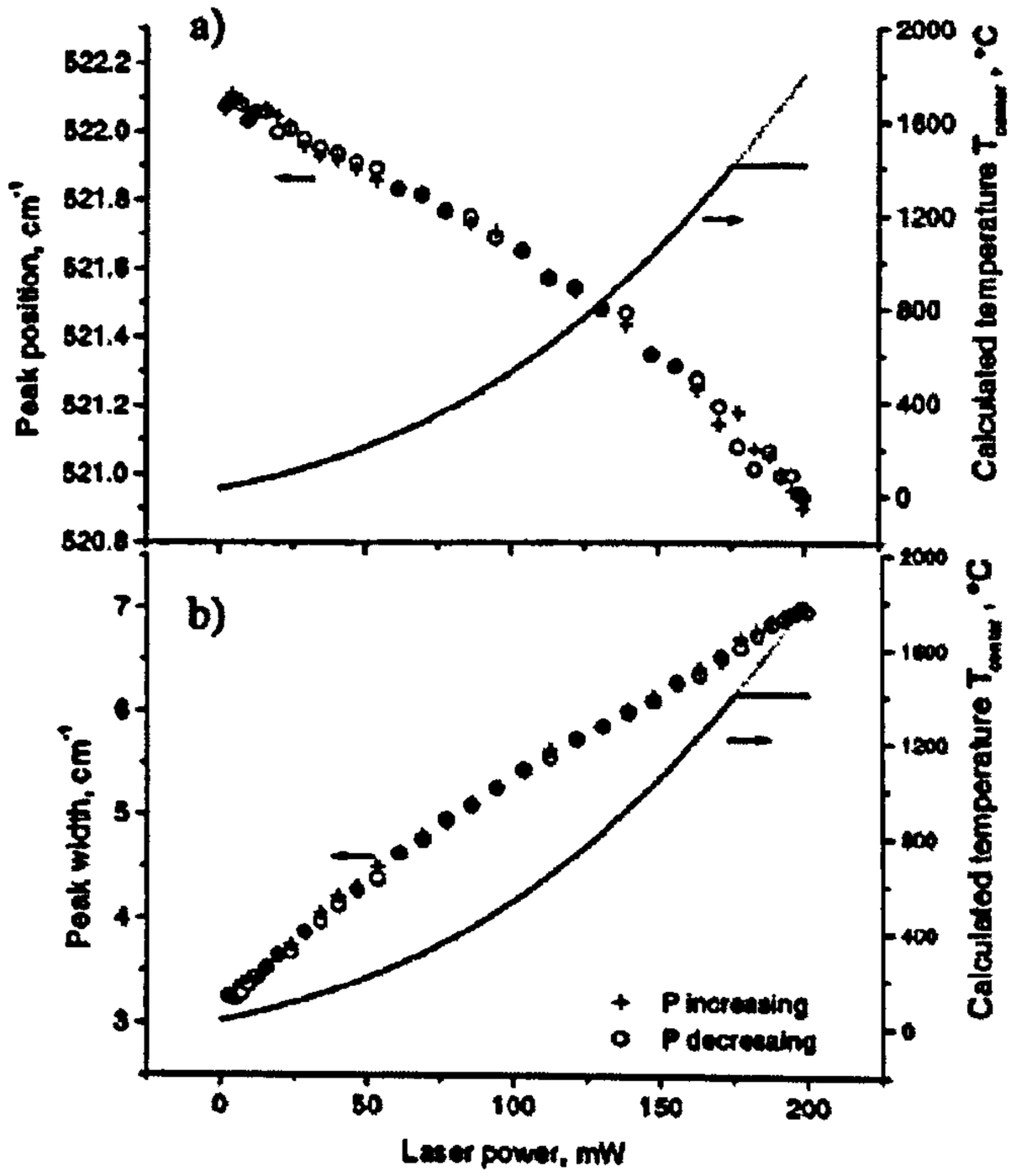

Figure 3.12. Changes in (a) peak position and (b) width of a silicon substrate under a varying laser power [Kouteva-Arguirova et al. 2003]. The circles give the decreasing laser power steps and the crosses give the calculated temperature at the centre of the spot.

The manipulation and deconvolution of spectra is also significant to achieve a true measure of peak position [Smith and Dent 2006]. There are a variety of ways in which this can be done, such as using smoothing, baseline flattening, peak fitting and other software manipulation methods. The effects of peak fitting and which fitting procedure to use, have been discussed by many researchers [Allen and McMeeking 1978, Baruya and Maddams 1978, Bradley 2004, Di Rocco et al. 2001, Meier 2005, Perram 1968, Vickers et al. 2001]. Common methods of fitting peaks are by Gaussian, Equation 3.34, Lorentzian, Equation 3.36, mixed Gaussian-Lorentzian, Equation 3.38 and Voigt profiles, Equation 3.39 [Di Rocco 2001, Meier 2005]. There are two conflicting views on the method in which the Raman spectra of solids should be fitted, as a consequence of whether the molecular vibrations or the effective lifetime of the signal is considered to be the predominant influence in defining the peak profile shape. The optimum method of peak fitting has also been considered in

relation to the deconvolution overlapping peaks and whether some peak curve fitting procedures might disguise side bands.

In his paper on the curve fitting of vibrational spectra, Meier [Meier 2005] discussed the various peak fitting procedures along with how backgrounds should be dealt with. The focus point for his examples was overlapping bands, as it was stated, that for well isolated bands, traditional measurement of peak widths, with a ruler, would be sufficiently accurate for most purposes. The Gaussian profile, G(x), was considered to be as follows [Di Rocco et al. 2001, Meier 2005]

$$G(x) = G_o \exp\left[-\left(\frac{(x-x_o)^2}{\omega_G}\right)\right] \qquad 3.34$$

where x denotes frequency or wavenumber, ω_G is related to the Gaussian half width half maximum, γ_G, through

$$\omega_G = \frac{\gamma_G}{\sqrt{\ln 2}} \text{ and } G_o = \frac{1}{\omega_G\sqrt{\pi}} \qquad 3.35$$

The Lorentzian profile was considered to be

$$L(x) = L_o \frac{\omega_L^2}{(\omega-\omega_o)+\omega_L^2} \qquad 3.36$$

where ω_L is related to the Lorentzian half width half maxima, γ_L by

$$\omega_L = \gamma_L \text{ and } L = \frac{1}{\pi\omega_L} \qquad 3.37$$

The mixed Gaussian-Lorentzian profile was considered to be Equation 3.38 where α was the fraction of the Gaussian contribution to the line profile.

$$S(x) = \alpha G(x) + (1-\alpha)L(x) \qquad 3.38$$

The Voigt profile considered by Meier and Di Rocco is shown in Figure 3.39.

$$V(x)\alpha \int_{-\infty}^{\infty} L_o \frac{\omega_L^2}{x-x^{'}+\omega_L^2} G_o \exp\left[-\left(\frac{x^{'}}{\omega G}\right)^2\right] dx^{'} \qquad 3.39$$

It was argued that vibrational spectra such as Raman spectra are Lorentzian in nature [Meier 2005]. This could either be shown by hydrodynamic theory or by considering the vibrations as a sinusoidally oscillating force and solving the equations of simple harmonic motion. However, it was also stated, that the spectrometer could cause

Gaussian line broadening due to the rectangular entry and exit slits of the spectrometer and as a consequence the Voigt profile might me the most appropriate.

The theory behind curve fitting has been viewed another way by Bradley [Bradley 2004] who considered the effective lifetime τ of the signal to be a central issue when deciding which peak fitting procedure should be used. The relaxation lifetime or amplitude correlation time, τ_a was considered to be the time taken for the laser excited molecules to return to the ground state. The coherence lifetime τ_c was considered to be the time taken for the initially coherent vibrational frequencies of the laser excited molecules to randomise. In the case of solids, the excited molecules would relax before severe incoherence set in i.e. $\tau_c >> \tau_a$ and that this effect would result in a Gaussian profile.

In their paper on the deconvolution of spectra by least squares fitting, Allen and McMeeking [Allen and McMeeking 1978] fitted a series of spectra using both Gaussian and Lorentzian fitting procedures. The computer program used was one created for general spectral data. It was found that Gaussian fits tended to smooth data whereas Lorentzian fits did not, thereby preserving potentially important features. This effect was found to be particularly significant in strongly overlying doublets. This is in agreement with the work of other authors [Baruya and Maddams 1978, Perram 1968].

Background noise is also an important consideration when analysing spectra [Bradley 2004, Meier 2005, Pitt et al. 2005, Smith and Dent 2006], with the effect of fluorescence being very common. The fluorescence bands detected in an experiment conducted at room temperature may be relatively broad in comparison to the Raman peaks, due to the combination of several ground states [Pitt et al. 2005]. This can result in the Raman bands being swamped by the fluorescence. An example of this can be seen in Figure 3.13. As a consequence of some of the above contradicting views, it was decided to further investigate the effects of peak fitting in Raman spectra, Section 4.3.3.

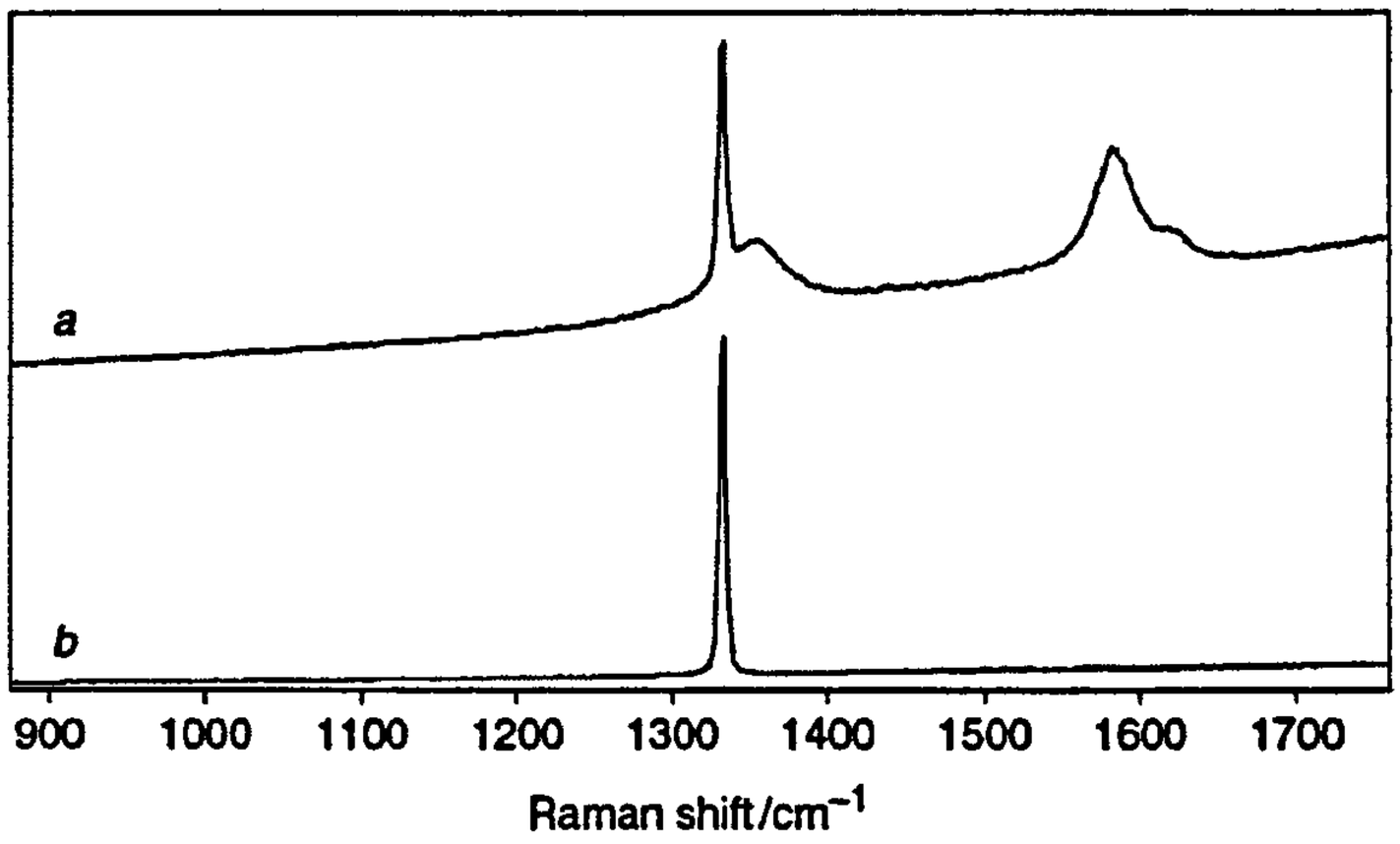

Figure 3.13. Raman spectra of diamond films. The spectrum marked (a) has a higher carbon content than the pure diamond film marked (b). It can also be seen that in spectrum (a), there is a sloping background and the peak at 1332cm^{-1} has a reduced intensity due to the effects of fluorescence [Pitt et al. 2005].

3.12.4 Photoluminescence Spectroscopy

Issues affecting the calibration and analysis of photoluminescence spectroscopy are very similar to those associated with Raman spectroscopy. As with Raman spectroscopy, peak position (in this case the absolute wavenumber) and intensity can be calibrated with standards [El-Turki 2004, Selcuk and Atkinson 2003, Wen et al. 2005] and lamps [Lipkin and Clarke 1996, Ma and Clarke 1993, Wunder and Schoen 1981]. The same issues concerning the reliability of the lamp and the standards can be applied to photoluminescence spectroscopy. Indeed, there have been many studies discussing the effects of temperature on a commonly used standard, chromium-doped sapphire or ruby.

The variation in the ruby R_1 and R_2 line parameters with temperature have been documented [Forman et al. 1972, Grabner 1978, He and Clarke 1995, Ma and Clarke 1993, Munro et al. 1985, Nychka et al. 2003, Ragan et al. 1992, Silvera and Wijngaarden 1985, Wunder and Schoen 1981, Yen and Nicol 1992]. A comprehensive study on the effect of temperature on the R_1 and R_2 lines has been carried out by Ragan et al. [Ragan et al. 1992]. Measurements were carried out on a ruby specimen containing an unknown amount of Cr_2O_3 as well as oriented samples of 0.5 wt% Cr_2O_3. The samples were held in an adapted Merill-Bassett diamond anvil cell. For the experiment at ambient temperature and above, the diamond anvil cell

was placed in a vacuum oven. In order to acquire the low temperature data, the diamond anvil cell was placed in a Displex refrigerator. The temperatures acquired were measured using thermocouples. The shifts in line position induced by temperature change can be seen in Figure 3.14 and the dependence of the R-line full width half maxima with temperature can be seen in Figure 3.15.

It has also been found, that the intensity of the peaks as well as their relative intensity varies with temperature [Munro et al. 1985]. However, it should perhaps be noted, that intensities and relative intensities of the R_1 and R_2 lines of a single crystal are also dependent on the orientation of the sample with respect to a polarised laser beam [He and Clarke 1997]. The dependence of R-line position with temperature is discussed further in Chapter 4 - Calibration and Sources of Error.

As with Raman spectroscopy, there is some debate about the use of peak fitting in photoluminescence spectroscopy. Equally, calculations have shown that unperturbed photoluminescence spectroscopic lineshapes are Lorentzian [Lipkin and Clarke 1995]. Line broadening has been shown to be caused by sample probe interaction [Lipkin and Clarke 1996], stress [El-Turki et al. 2004] and as mentioned previously, temperature. A detailed analysis can be carried out to include the probe shape and the spatial variation in the perturbation of the stress field [Lipkin and Clarke 1996]. However, some authors have found that fitting peaks using a mixed Gaussian-Lorentzian procedure with a quadratic baseline can also provide an adequate deconvolution of the peaks in some instances [Atkinson et al. 2000]. As discussed in Chapter 4 - Calibration and Sources of Error, a mixed Gaussian-Lorentzian profile was used for the deconvolution of alumina photoluminescence spectra as a convenient method of adapting to and monitoring varying line profiles.

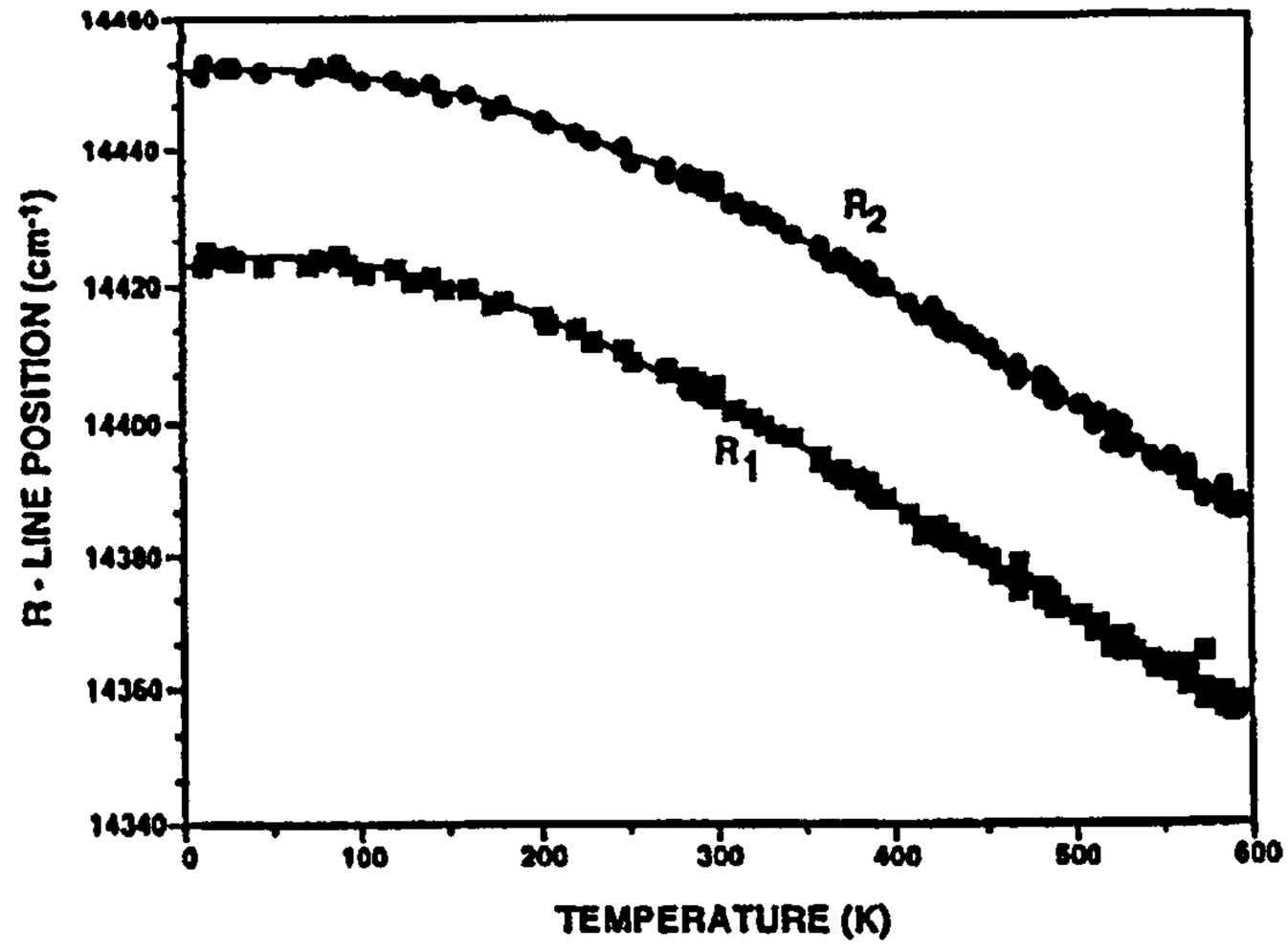

Figure 3.14. R-line position of Ruby versus temperature. The data shown is for ruby samples of two orientations and one ruby sample of an unknown origin [Ragan et al. 1992].

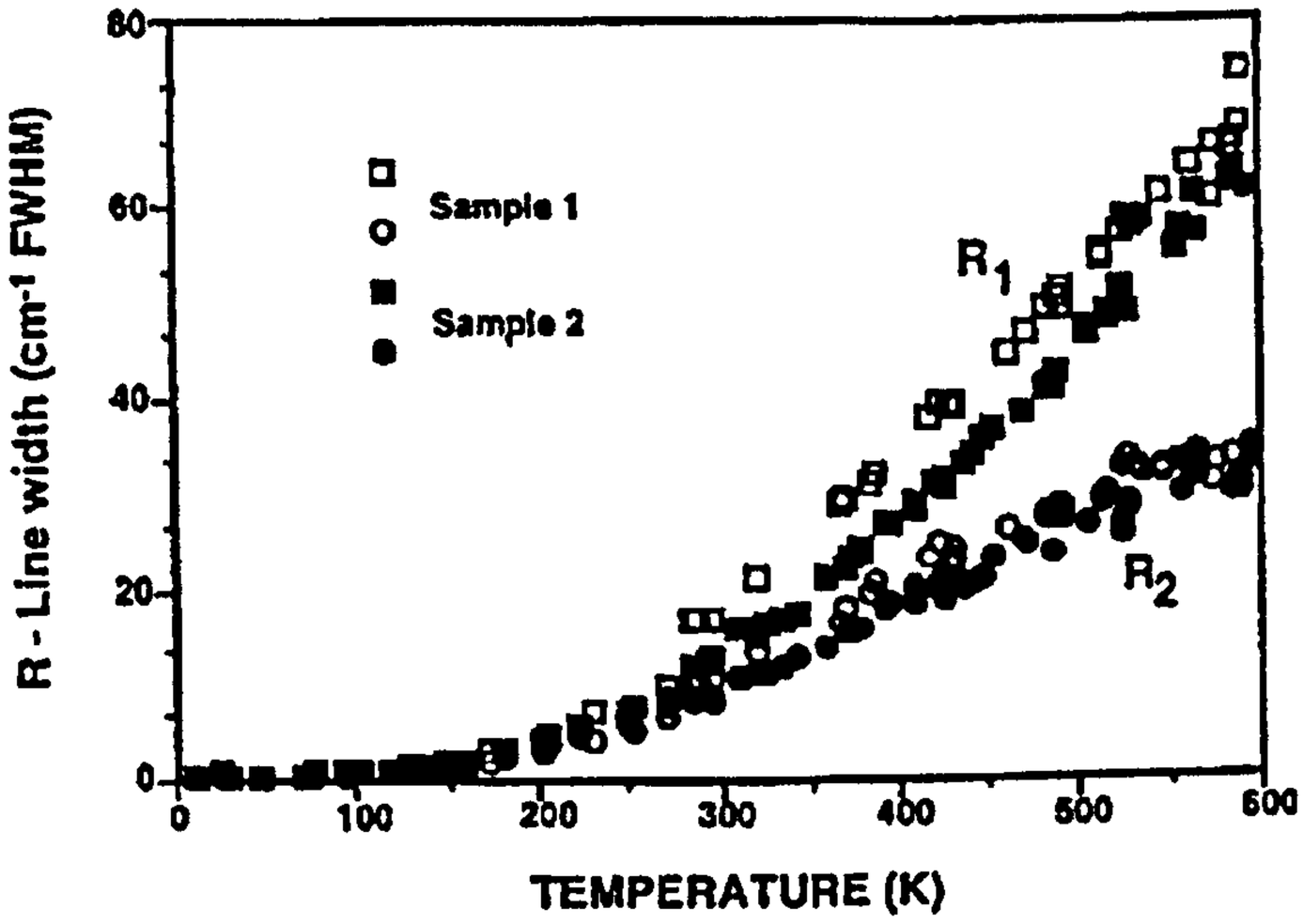

Figure 3.15. R-line width versus temperature. The open symbols are for the ruby of unknown origin and the closed symbols are for the ruby samples with known orientation [Ragan et al. 1992].

3.13 Stress Relaxation Methods

3.13.1 Deep Hole Drilling

As described in Section 3.7, deep hole drilling stress measurements are carried out through the following steps [Goudar et al. 2008];

1) Drilling a reference hole through the component.
2) Measuring the reference hole using an air probe system at known depths and at several angles at each depth.
3) Removing a core of material by trepanning using electric discharge machining.
4) The reference hole is remeasured using the air probe system at similar positions to those in the reference hole.

Calibration of the air probe system is therefore essential to ensuring accurate measurements [Goudar et al. 2008]. Goudar et al. have considered the accuracy of the air probe system by making repeated measurements of air probe calibration rings [Goudar et al. 2008]. The standard deviation of calibration ring measurements was calculated. This was followed by fitting a polynomial curve to the standard deviation measurements and the errors in the measured diameters were calculated from the polynomial function. The errors were then converted from stress to strain. The largest principal stress error resulting from the accuracy of the air probe was calculated to be ±21MPa and approximately ±12MPa in the shear direction.

Trepanning of the core is carried out by electrodischarge machining. This process can introduce thermal stresses [Yadav et al. 2002]. It is therefore necessary to remove any thermal effects from the raw data before the out of plane residual stresses can be calculated [Stefanescu et al. 2004]. A further potential source of error is the calculation of elastic moduli, these are necessary to convert strains to stresses [Goudar et al. 2008].

There is a debate as to the accuracy of the deep hole drilling technique on the surface of components [Stefanescu et al. 2004]. This is due to the stress relaxation near the surface of the component whilst the hole is being introduced. This effect does not occur in the bulk of the component due to its geometrical constraints.

Overall, errors in stress measurement using the deep hole drilling technique have been found to be of the order ±30MPa with an accuracy of measurement 0.5μm and a Young's modulus 200GPa [Stefanescu et al. 2004].

3.13.2 Incremental Centre Hole Drilling

The factors which affect the accuracy of the centre hole drilling method are mostly associated with the introduction of the hole and there are strain sensitivity limitations [Stefanescu et al. 2006]. The errors associated with the introduction and drilling of the hole are [Stefanescu et al. 2006];

1) Strain measurement errors

These errors comprise those associated with instrumentation and thermally induced strains from the drilling process. Stresses induced by the surface preparation and addition of the strain gauges can induce strain into the component [Vishay Micro-Measurements 2007]. The drilling process itself must also be considered. Unlike the following sources of error, these sources are independent of the magnitude of the residual stresses present in the component. They can therefore exist even if the component is stress free. It is considered to be the dominant uncertainty in the incremental centre hole drilling technique.

2) Hole depth measurement errors

These errors include those associated with measuring the hole depth and the fact that bottom surface of the hole may not be perfectly flat.

3) Material constants

Errors may be introduced to the analyses by uncertainties associated with the material constants required.

4) Hole eccentricity errors

Any eccentricity of the hole from the strain gauge rosettes provides a source of error.

5) Data analysis

Another important factor in the accuracy of the technique is the data analysis method used since some procedures rely on the accuracy of the finite element models which are used as calibration or on experimental calibration.

Total stress errors have been calculated to be approximately ±30MPa for an assumed strain uncertainty of approximately ±2μm/m [Stefanescu et al. 2006].

3.13.3 Finite Element Modelling

The mesh chosen plays an important factor in determining the accuracy of a finite element model, since the boundary conditions and geometry affect the outcome [Logan 2002, Meier et al. 1991]. The design, involving the place of the nodes and the size of the mesh, must take into account the load to be applied and the results required from the model. Therefore a certain degree of prior knowledge is necessary, when generating the structure of the mesh.

Input parameters properties, such as Young's modulus and the coefficient of thermal expansion, also play a decisive role in determining the accuracy of the model as they determine how the mesh behaves under given conditions [Logan et al. 2002, Meier et al. 1991]. These properties have often been obtained from experiment and difficulties (and errors) arise when the data required is not known or unavailable.

4 Calibration and Sources of Error

4.1 Introduction

When undertaking stress measurements with a particular technique, it is important to ensure appropriate confidence in the measurements. This can be achieved through an understanding of calibration requirements and potential sources of error. X-ray diffraction, Raman spectroscopy and photoluminescence spectroscopy were the predominant techniques used in this work. As a consequence, various aspects of calibration and sources of error were reviewed and investigated as necessary.

Peak fitting parameters were explored by varying some of the input options of the two available peak fitting programs. It was then possible to see whether the programs and parameters resulted in similar peak profiles.

4.2 X-Ray Diffraction

4.2.1 Background

Five major contributing factors are influential to the calibration and reliability of X-ray diffraction measurements of macrostrain and stress.

1) Calibration [Cullity and Stock 2001, Klug and Alexander 1974].
2) The effect of surface profile [Cullity and Stock 2001, Doig and Flewitt 1981].
3) The effect of counting statistics [Lonsdale 1986, Lonsdale and Flewitt 1985].
4) The consequences of temperature on stress measurement [Cullity and Stock 2001, Klug and Alexander 1974].
5) X-ray elastic constants used to calculate stress [Cullity and Stock 2001, Klug and Alexander 1974, Lonsdale et al. 1981, Macherauch 1966].

The effect of specimen height and specimen profile, Factors 1 and 2, has been discussed in Chapter 3 - Techniques, as these factors have traditionally played an integral part in the fundamental X-ray diffraction experimental set-up process. The research by other workers has been reviewed in more detail in the present chapter and, as a consequence of perceived gaps in the knowledge of the effects of specimen height and surface profile; these subjects have been investigated in more detail in

Chapter 7 - Ferritic Steel Edge Quenched Plateand Chapter 8 - Spatial Resolution and Length Scale Investigations of Techniques on a Ferritic Steel Butt Welded Pipe. Factors 3 to 5 have been researched by other workers. Their research has been in order to gain an understanding of the confidence levels that could be achieved in the present X-ray diffraction stress measurements. The effects of peak fitting, though important, have been adequately addressed [Fitzpatrick et al. 2005, Lonsdale 1986].

4.2.2 Calibration

The importance of specimen height has already been discussed in Section 4.2.1, as a displacement of the specimen surface from the diffractometer axis causes a shift in Bragg angle, even in stress free specimens [Cullity and Stock 2001, Klug and Alexander 1974]. A method of ensuring the correct specimen distance from the diffractiometer axis is by using a calibration sample with a known stress [James and Cohen 1979]. The specimen height is thus adjusted so that the correct stress is recorded for the calibration specimen. Stress free powders can be used as calibration specimens [Fitzpatrick et al. 2005, Hawkes 1957, Moore 1960] and, as mentioned in Section 4.2.1, cerium oxide, CeO_2, was used as the calibration specimen in this work. Additionally, the calibration specimen peak profiles, such as peak intensities and peak widths, can be used to monitor equipment performance. For example, in an X-ray tube, some tungsten from the filament can evaporate and then become deposited on the target [Cullity and Stock 2001]. This then results in an increase in background noise as the tungsten emits radiation alongside the characteristic radiation of the target.

4.2.3 Specimen Surface Profile

As discussed in Chapter 3 - Techniques, differential absorption and surface orientation effects due to irregular surface profiles have been shown to broaden and shift diffracted X-ray beams [Doig and Flewitt 1981]. This has been shown to introduce errors into measurements. Furthermore, the high points in a rough material do not necessarily have the same stresses as the bulk and therefore are not necessarily representative of the stresses to be measured [Cullity and Stock 2001]. As a consequence, it is generally recommended that X-ray diffraction measurements should be made on smooth clean surfaces [Cullity and Stock 2001] and that surfaces should be prepared for the measurements if necessary [McDonald et al. 2002].

However, although errors due to surface profile were calculated theoretically [Doig and Flewitt 1981], experimental confirmation of these errors could not be found in the literature. It was therefore decided to experimentally investigate the feasibility of carrying out X-ray diffraction measurements on rough surfaces on a component with a known stress profile and then on an engineering component.

4.2.4 Counting Statistics

The uncertainty in peak location due to counting statistics has been shown by Lonsdale to be a potential source of error in stress measurement [Lonsdale 1986]. Here, the results of various X-ray diffraction investigations were analysed and assessed to establish contributing errors. Lonsdale used theoretical models of X-ray peaks resulting from a Monte Carlo computer program which was used to create two Gaussian overlapping profiles to represent the predicted profile of X-ray diffraction Kα doublets which would be obtained from diffraction of {211} planes of ferritic steel with chromium Kα radiation. The peaks were then deconvoluted and fitted using a parabolic fit as if they had been experimental data. These theoretical models were combined with errors achieved from repeated X-ray diffraction stress measurements on a ferritic steel specimen. As a consequence, Lonsdale was able to calculate optimum peak intensities for different peak widths and sample orientations to obtain an adequate confidence of the resulting stress measurement see Figure 4.1 and Figure 4.2.

Figure 4.2 shows that for a given peak width, the standard deviation of measured stresses decreases with increasing peak counts. This implies increasing confidence in the measurements due to increasing peak area as a consequence of increasing counts, a supposition which has been confirmed by other authors [Cullity and Stock 2001, Klug and Alexander 1974]. The standard deviations decrease with an increasing number of sample orientations or ψ-angles [Lonsdale 1986]. Figure 4.2 shows that for a 95% confidence limit in a measurement to be achieved with a given peak height, fewer sample orientations are needed for an increasing peak width. This can again be attributed to the need for a sufficient number of peak counts to have statistical confidence in the peak and if this confidence is not achieved, it must to be obtained by making an increasing number of measurements. In addition, Figure 4.2 shows that for

a lower magnitude confidence limit, a higher peak width and more sample orientations are required to achieve a 95% confidence limit [Lonsdale 1986].

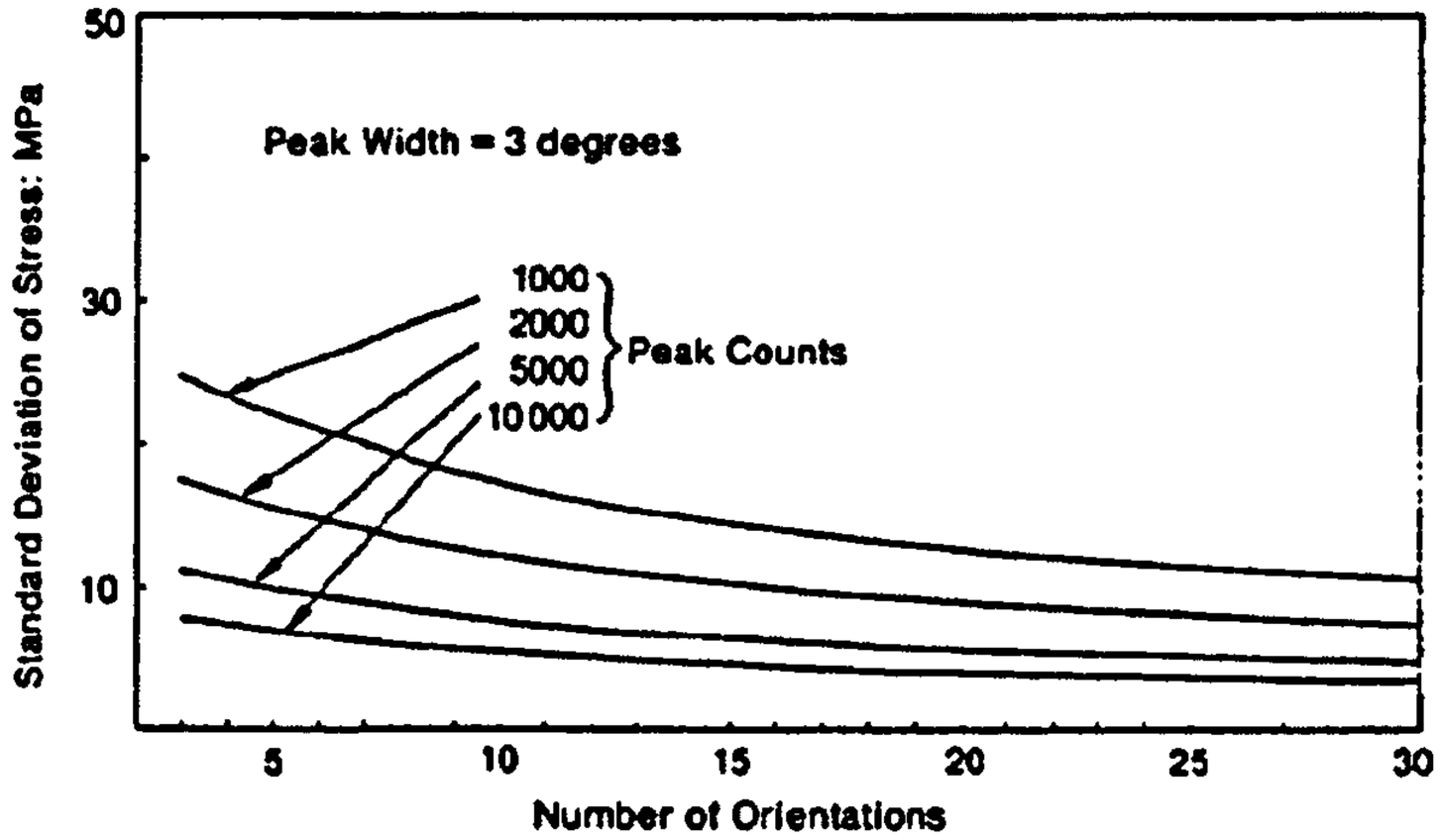

Figure 4.1. Standard deviation of stress for varying numbers of ψ orientations and peak counts for a given peak width [Lonsdale 1986].

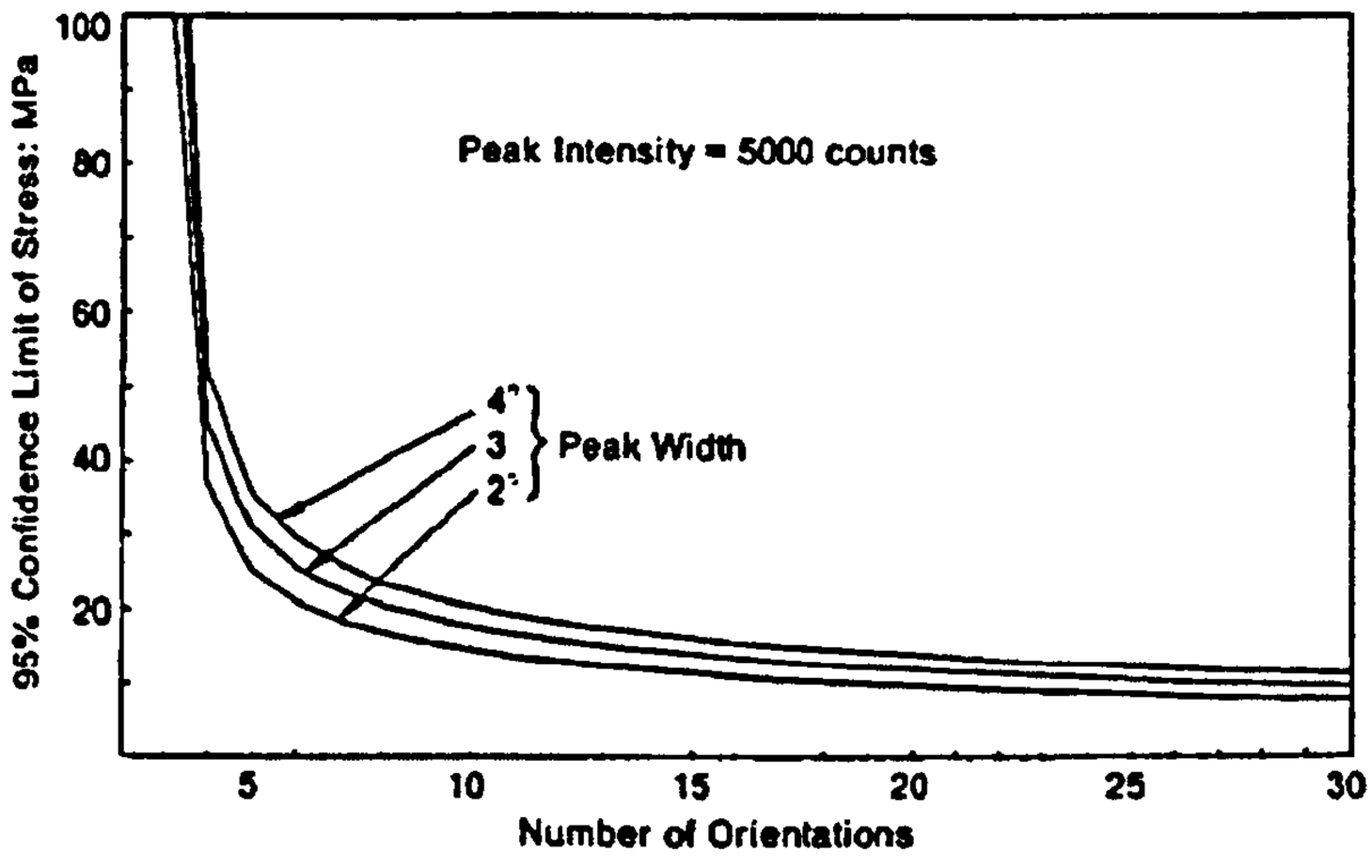

Figure 4.2. 95% confidence limits of stresses for varying peak widths and sample orientations for a given peak intensity [Lonsdale 1986].

The investigation undertaken by Lonsdale therefore emphasises the need for a sufficient number of peak counts and ψ-angles to be measured in order to have confidence in calculations of peak position. In addition, it has been shown that lower magnitude confidence limits can be obtained with higher peak widths and more sample orientations emphasising the requirement for good statistical confidence in data through peak counts and number of measurements taken.

In this work, 15 ψ-angle positions were used in each X-ray diffraction stress measurement as the standard deviations of measured stress and confidence limits plateau in value with the use of 15 ψ-angles or above. Further, acquisition times were increased when necessary in order to achieve sufficient peak to background ratios for accurate peak deconvolution.

As mentioned in Section 4.2.1, one method of locating peak position in X-ray diffraction is the centre of gravity method. It is this method, which has been used throughout the X-ray diffraction stress measurement investigations. It is commonly used due to the relatively small effect from background noise on the final result [Lonsdale 1986]. Although it requires that the peak is well defined [Fitzpatrick et al. 2005], this has not been an issue in the measurements discussed as the peak chosen for analysis was selected for this reason.

4.2.5 Temperature

The effect of temperature on X-ray diffraction measurements is well documented [Cullity and Stock 2001, Klug and Alexander 1974]. It has been shown that diffraction intensities decrease with increasing temperature due to the increasing vibration of atoms around their equilibrium positions in the crystal lattice. In addition, lattice parameters have been shown to be dependent on temperature [Klug and Alexander 1974, Misture 2003]. It has been found that the lattice parameters increase with increasing temperature due to thermal expansion. It can be concluded therefore that measurements of 2θ are dependent on the temperature of the material and that this, in turn, would affect the stress measurements [Cullity and Stock 2001, Klug and Alexander 1974]. As a consequence, knowledge of the temperature of the specimen investigated is of great importance. It must also be ensured that the technique used to measure the stress does not itself cause any sample heating.

With regards to heating effects of X-ray beams and therefore from the experimental set-up itself, there is information on heating effects due to synchrotron X-ray sources [Bourne et al. 1994]. These systems are capable of producing kilowatts of total power over areas of millimetres in diameter. However, the power used for the diffractometer was approximately 9W over an area of 1mm diameter and therefore it was concluded that heating effects were insignificant and need not be considered.

The effect of room temperature changes on stresses in MgF_2 type ceramics and in iron was calculated. MgF_2 ceramics were chosen as one such ceramic, cerium oxide (CeO_2) was employed in a powder form as the calibration standard. Iron was also chosen, as it had similar properties to materials investigated experimentally in this work. The linear coefficients of expansion were found in the literature to be 9 to 11 × 10^{-6} °C^{-1} for MgF_2 type ceramics and 14 × 10^{-6} °C^{-1} for iron [Flinn and Trojan 1986]. The linear coefficients of expansion were related to a change in nominal strain by Equation 4.1,

$$\Delta\varepsilon_n = \Delta T \times \alpha \qquad 4.1$$

where $\Delta\varepsilon_n$ is the change in nominal strain, ΔT is the change in temperature and α is the linear coefficient of expansion [Flinn and Trojan 1986]. The nominal stress, equal to the maximum principal stress was calculated using Equation 4.2,

$$\Delta\sigma_n = E \times \Delta\varepsilon_n \qquad 4.2$$

where σ_n is the nominal stress and E is Young's modulus. The values of Young's modulus were found in the literature to be approximately 200GPa for iron based alloys [Ashby and Jones 1996]. No value could be found in the literature for the Young's modulus of cerium oxide. It was therefore decided to use a Young's modulus value of 200GPa as this value encompassed a wide range of ceramics and their different manufacturing processes [Ashby and Jones 1996, Ashby and Jones 1998, Flinn and Trojan 1986]. Using Equations 4.1 and 4.2, it was calculated that for a temperature change of ±5°C, the maximum change in principal stresses in iron would be 14MPa and in cerium oxide (using a 11 × 10^{-6} °C^{-1} linear coefficient of expansion) [Flinn and Trojan 1986] would be 11MPa, with stresses becoming more tensile with increasing temperature. However, Young's moduli of steels have been found to decrease with increasing temperature [Hopkins and Rogers 1905, Kagawa et al. 1987, Kimball and Lovell 1925]. Although the Young modulus of mild steel was not found to be linearly dependent on temperature [Kimball and Lovell 1925], it was found to be sufficiently linear in the range of 20°C to 40°C for this work. Indeed, the Young modulus was found to vary by 0.025% (of its value at 20°C) per °C. This implies that for a given strain, the stress also varies by 0.025%°C^{-1}. For a mild steel sample of stress 100MPa at 20°C, the stress would change by 12.5MPa with a temperature change of ±5°C thereby resulting in an overall stress increase of 1.5MPa due to an increase in d-spacing (if the behaviour of d-spacings in mild steel is

considered to be equal to that for iron in this exercise). Little information on the variation of Young's modulus of cerium oxide with temperature could be found. A direct measurement of the effect of temperature on iron and cerium oxide is therefore complex with two at times opposing factors, namely d-spacings and Young's modulus.

4.2.6 X-Ray Elastic Constants and Compliance Values

The X-ray elastic constants for the specific diffraction planes allow the lattice strain to be converted to stress [Klug and Alexander 1974, Lonsdale et al. 1981, Macherauch 1966]. A distinction between X-ray elastic constants and bulk elastic constants should be made as there can be differences between the constants for the specific crystal planes sampled and the bulk properties [Lonsdale et al. 1981].

The compliance value, k, is a material constant and is a function of the elastic constants. It is this value that is used to correlate the information obtained from the $\sin^2\psi$ plots to the desired stress measurements as follows. The relationship between uniaxial stress, σ, and the Bragg angle, θ, can be given by Equation 4.3 where m is the gradient of the $\sin^2\psi$ plot and k is the previously discussed compliance value [Lonsdale et al. 1981].

$$\sigma = \frac{m \cot\theta}{k} \qquad 4.3$$

Compliance values and elastic constants can be theoretically and experimentally derived. As a consequence of their significance to X-ray diffraction stress measurements, they have been investigated in depth by other researchers. They have been calculated using theoretical methods [Lonsdale et al. 1981, Macherauch 1966] and compared to experimental measurements of steel [Garrod and Hawkes 1963, Klug and Alexander 1974, Lonsdale et al. 1981, Macherauch 1966]. Indeed, Macherauch compared measured elastic constants available in the literature to theoretically calculated values [Macherauch 1966]. He found that experimental measurements of elastic constants and therefore the corresponding compliance values, varied with the carbon content of mild steel. Three theoretical methods of calculating X-ray elastic constants were considered. The Voigt approximation assumes that the crystallites in a polycrystal undergo equal deformation when strained. This has been shown to rarely be the case. The Reuss approximation assumes equal stresses in the crystals of a

polycrystalline material but then takes into account the measured lattice planes. The third, the Neerfeld rule, which uses both the Voigt and Reuss approximations, has been shown to be the most appropriate approximation of X-ray elastic constants. However, the derived values still did not always agree with experimental data.

Lonsdale et al. measured compliance values for the {211} lattice planes of ferritic steels commonly used in power plant components using a four-point bend jig [Lonsdale et al. 1981]. The values they measured are given in Table 4.1. It was found that although there were differences between the measured constants, these differences were not dependent on carbon content for this range of alloy steels. In addition, the differences lay within the errors associated with the X-ray diffraction technique and the equipment employed for the measurements.

Table 4.1. X-ray constants measured for a range of ferritic steels [Lonsdale et al. 1981].

Nominal Specification of Steel	Percentage Carbon Content (%)	X-Ray Constant: kx10^6 (MPa)
Carbon Manganese (normalised)	0.22	5.05 ± 0.30
2¼%Chromium 1%Molybdenum (quenched and tempered)	0.07	4.72 ± 0.31
9%Chromium 1%Molybdenum (quenched and tempered)	0.14	4.67 ± 0.27
14%Chromium (quenched and tempered)	0.17	5.18 ± 0.32

Further, it has been shown, that X-ray elastic constants and compliance values can vary with the thermo mechanical history of the steel, for example with plastic deformation [Lonsdale et al. 1981, Macherauch 1966]. Thus it may be concluded, that it is advantageous to use experimentally measured rather than theoretically calculated compliance and elastic constant values when undertaking X-ray diffraction measurements. The following investigations using the X-ray diffraction method use an experimentally obtained compliance value, which was obtained using four-point bend tests carried out by Lonsdale and co-workers [Lonsdale et al. 1981]. The compliance value of steel used for the present investigations was obtained from 21/4%chromium 1%molybdenum quenched and tempered steel as shown in Table

4.1, [Lonsdale et al. 1981]. This value was chosen as the material, from which it was derived, had undergone significant plastic strain and it was assumed that many materials measured would have also undergone significant levels of plastic strain, such as across a weldment. Moreover, the chromium content of the steels was found to have little effect on the compliance values. Although there may be an error associated with this compliance value on measurements made on materials which had not undergone plastic strain, this error would be within the error of the compliance value measurement.

4.3 Spectroscopic Techniques

4.3.1 Background

Some main areas of uncertainty and error in the spectroscopic techniques were found to relate to calibration, statistical confidence, sampling size, peak fitting and temperature effects. It was decided that it was necessary to investigate the statistical confidence in the peak position by analysing the peak intensity as well as analysing the number of data points necessary to have confidence that the parameter being measured was representative of the sample. This emphasized the need to explore the effects of sampling size. Background noise and background subtraction were also explored with a view to improving the quality of the peak profiles.

4.3.2 Calibration

Calibration of spectroscopic techniques often employs the use of calibration standards (such as silicon or alumina) or using a lamp with a known wavelength [Singha et al. 2005]. Standards facilitate the calibration of the spectroscopic peak profiles as well as their positions, since calibration standards can readily be placed in a given position relative to the microscope. Mirrors and gratings in the spectrometer can be adjusted in order to achieve constant peak profiles for the standards. However standards can be heated by the focused laser beam resulting, in calibration errors. Laser heating effects are discussed in more detail in Section 4.3.8. The spectroscopic lines of lamps can be used to calibrate Raman and photoluminescence spectrometers. This calibration process has the advantage that no laser heating can occur [Kouteva-Arguirova et al. 2003]. It was found in this study that using lamps had the disadvantage of being less readily fixed to a particular position relative to the

microscope. It was therefore harder to monitor peak profiles and achieve consistency in this respect.

4.3.3 Peak Fitting

The peak fitting procedures available were an "in house" computer program called Pisces written by Day [Day 2006] and a program called GRAMS produced by Thermo Fisher Scientific Inc. [Thermo Fisher Scientific 2000]. These programs have different optional fitting parameters, some of which are highlighted in Table 4.2. The Pisces fitting program allowed peaks to be fitted without the use of background removal or using a linear background removal procedure. In addition to these, the GRAMS fitting program allowed the use of a quadratic background removal procedure. Both the Pisces and GRAMS programs allowed peaks to be fitted with Lorentzian, Gaussian and mixed Gaussian-Lorentzian curves. In addition, the Grams program enabled the peaks to be fitted with a Voigt curve.

Table 4.2. Peak fitting options for Pisces and GRAMS programs.

Fitting Parameters		Pisces	GRAMS
Background Subtraction			
	None	Yes	Yes
	Linear	Yes	Yes
	Quadratic	No	Yes
Line Shape			
	Lorentzian	Yes	Yes
	Gaussian	Yes	Yes
	Mixed Lorentzian-Gaussian	Yes	Yes
	Voigt	No	Yes

In order to investigate these parameters and whether fitting with different input options would produce consistent Raman shifts and hence consistent measurements of strain/stress, a series of tests were undertaken. The first was carried out on a silicon sample under strain, as it resulted in only one peak to analyse. Since the silicon Raman peak shift linearly under strain [De Wolf 1996], it was be possible to analyse these shifts with the various fitting parameters. This was therefore a method of assessing the coherency of the chosen peak fitting procedures in the simplest case.

The second test was to analyse the peak fitting procedures for an oxide specimen under strain. The specimen comprised a Type 316 stainless steel strip of dimensions 45mm × 5mm × 0.4mm, which was oxidised for one hour at 950°C. This resulted in a complex surface oxide. As with the silicon sample, the applied strain resulted in peak shifts from the oxide. Thus it was possible to analyse what effect fitting parameters had on the measured peak shifts from a more complex spectrum. The analysis of oxides produced on Type 316 stainless steel and stresses developed in those oxides is discussed in more detail in Chapter 5 – Stresses within Surface Oxides Grown on Austenitic Steel.

4.3.4 Silicon under Strain

The single crystal silicon sample of dimensions 45mm × 10mm × 0.7mm, was strained in a three-point bend jig and Raman spectra were recorded at positions along the thickness of the specimen starting from the contact point of the bend jig, i.e. moving from compressive to tensile stresses [Parsley 2005]. The spectrometer employed was a Renishaw Raman 2000 model fitted with a helium-neon laser of wavelength 633nm. An example of a Raman spectrum obtained from silicon can be seen in Figure 4.3. The spectra were then fitted with the GRAMS and Pisces software using Gaussian, Lorentzian and mixed profiles with linear and quadratic background subtraction in order to investigate the effect of peak profile on a simple spectrum. The peak positions calculated by using the three peak profiles with the different background subtractions can be seen in Figure 4.4 – Pisces program, Figure 4.5 – GRAMS program with linear background subtraction, Figure 4.6 – Grams program with quadratic background subtraction.

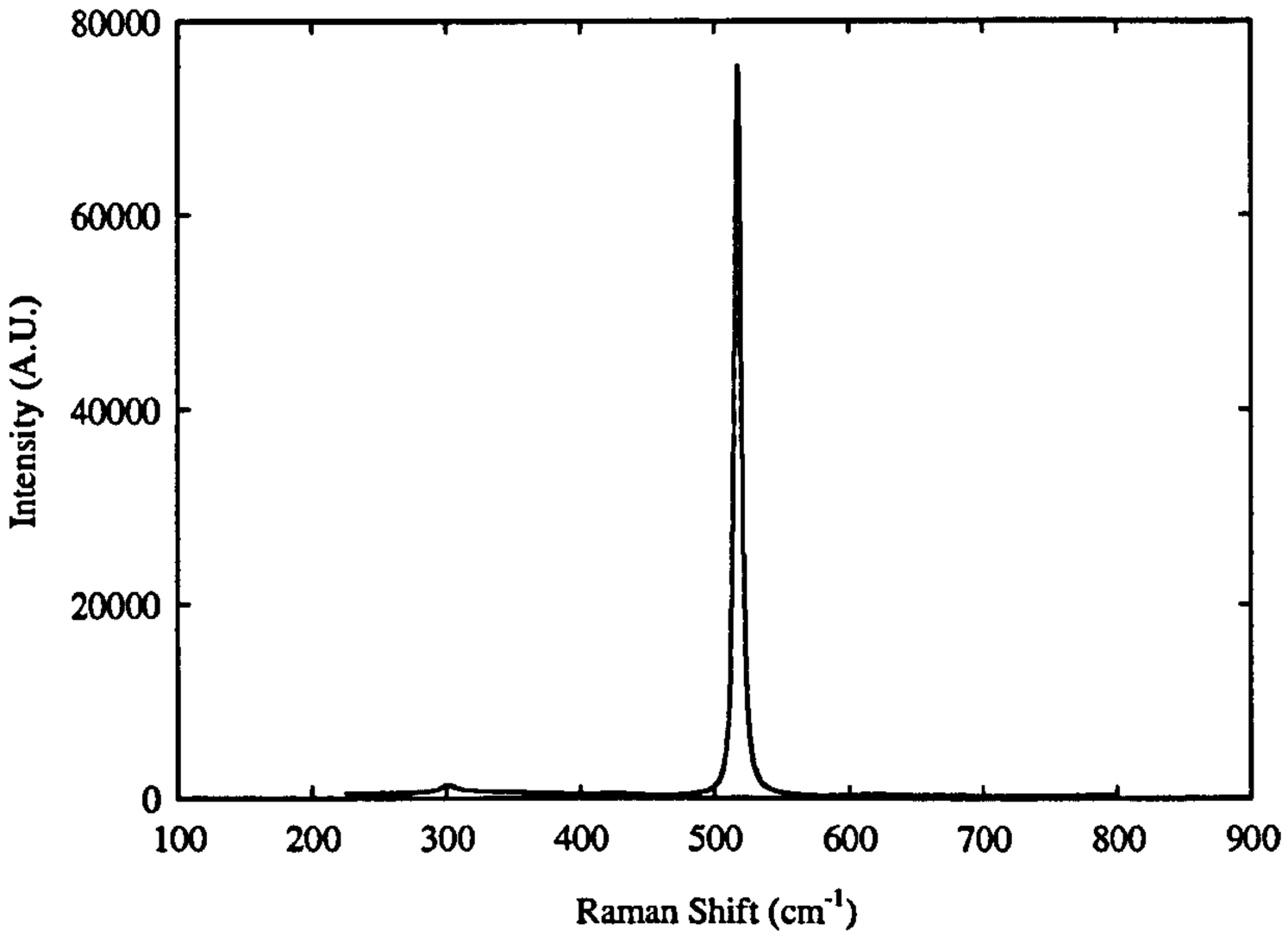

Figure 4.3. Raman spectrum of silicon.

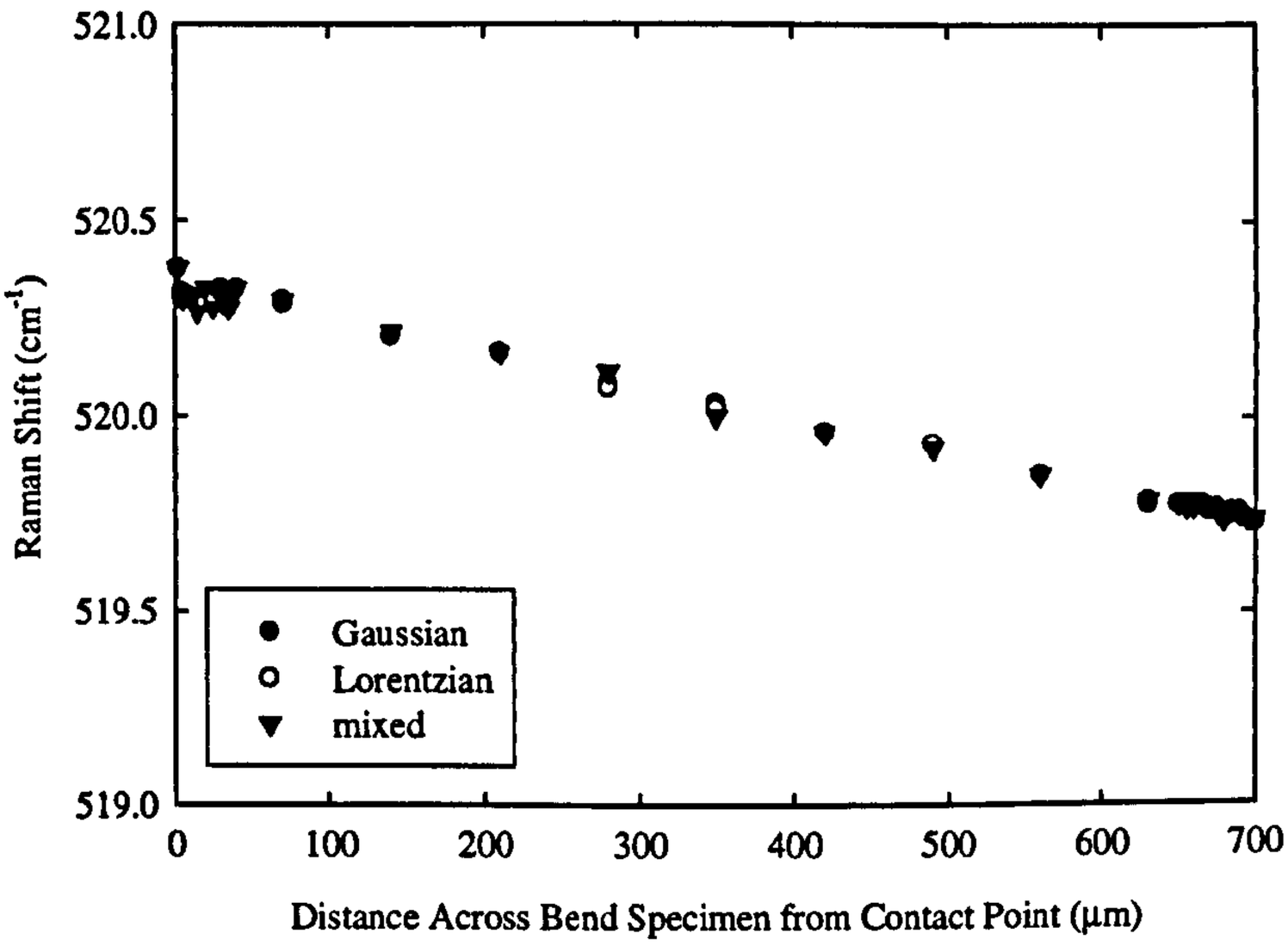

Figure 4.4. Comparison of fitted Gaussian, Lorentzian and mixed peak positions using the Pisces peak fitting program with linear background subtraction.

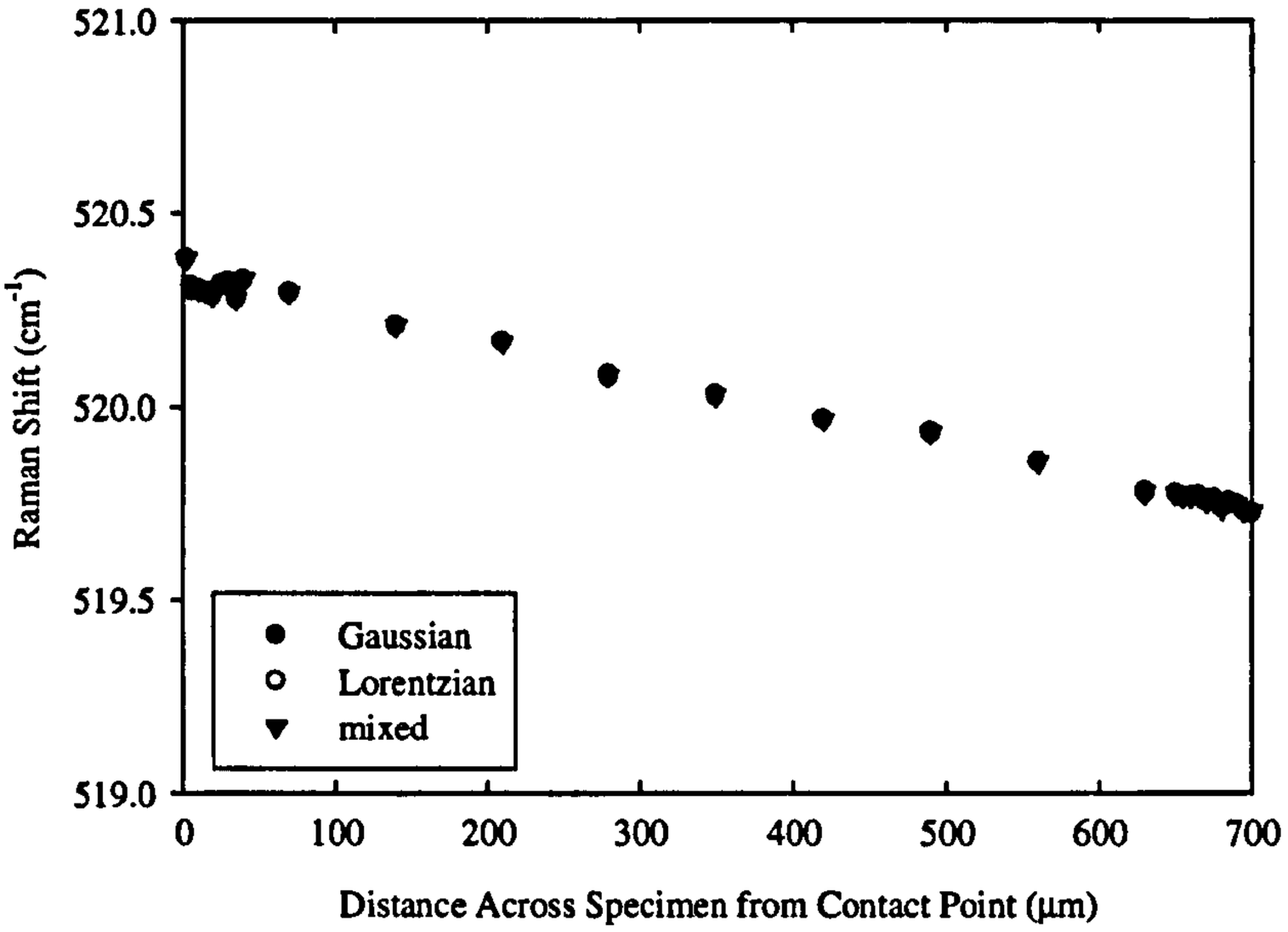

Figure 4.5. Comparison of fitted Gaussian, Lorentzian and mixed peak positions using the GRAMS peak fitting program with linear background subtraction.

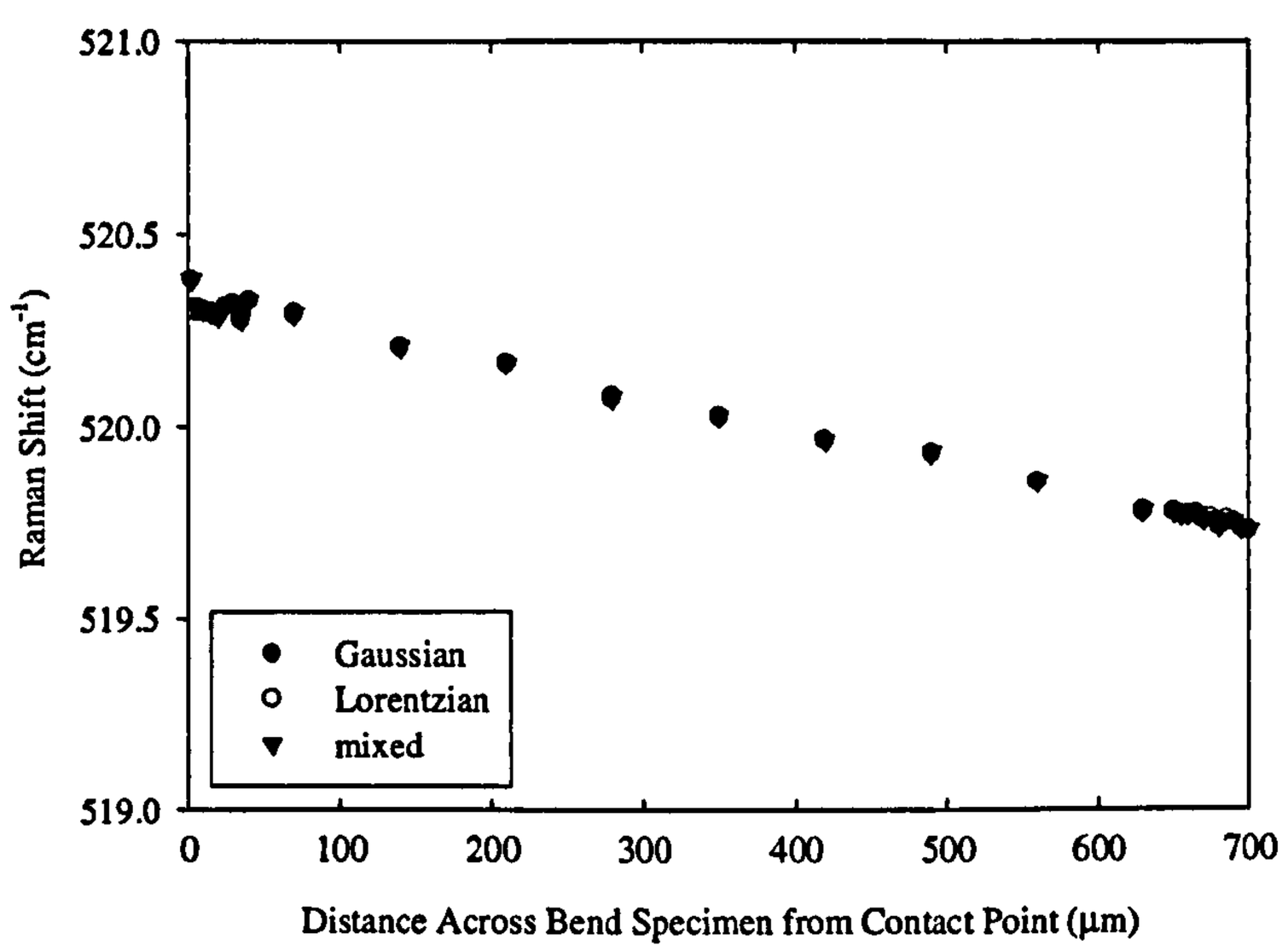

Figure 4.6. Comparison of fitted Gaussian, Lorentzian and mixed peak positions using the GRAMS peak fitting program with quadratic background subtraction.

It can be seen that there is good agreement in peak position between the three fitting procedures in the programs used. The scatter between data points fitted by the different procedures was less than a Raman shift of 0.05cm^{-1}. A Raman shift of

$0.05cm^{-1}$ is commonly quoted as being the minimum detectable stress in silicon and is equivalent to approximately 25GPa [De Wolf 1996]. Since all of the investigated peak fitting procedures lie within the calibration error of each other, it can be concluded that any of the previously mentioned fitting procedures can be used when fitting single crystal silicon. The investigation also indicates that for spectra with well defined peaks and a relatively linear background, the fitting procedure used, amongst the previously mentioned procedures, would not have a significant effect on the measured stress. This agrees with investigations undertaken by other authors which have been discussed in Section 3.12.3. Line profiles from photoluminescence spectroscopy have been discussed in Section 3.12.4. Due to the complex and varying shapes of photoluminescence peaks and the elaborate nature of some of the suggested fitting procedures, the peaks were fitted with mixed Lorentzian-Gaussian profiles and quadratic background subtraction. This procedure has been found by others to be sufficiently accurate in similar investigations [Atkinson et al. 2000].

4.3.5 Oxide under Strain

A Type 316 austenitic stainless steel specimen of dimensions 45mm × 10mm × 0.4mm was oxidised for one hour at 950°C in order to produce a complex oxide and therefore result in complex overlapping Raman peaks [(a)Hilson et al. 2006] (see Figure 4.7 for the oxide Raman spectrum). Raman spectra were acquired using a Renishaw Raman 2000 spectrometer fitted with a helium-neon laser of wavelength 633nm. Spectra were acquired for 60 seconds with a 50x magnification lens and the system was calibrated using a silicon standard. The Raman spectra were acquired on the top face of the oxidised specimen and a strain gauge was attached to the back face in order to monitor the applied strain. The Raman spectra were fitted using a Pisces Lorentzian, Gaussian and mixed fitting procedure with a linear background subtraction. This was to understand the effect of line shape on fitted peak positions. The spectra were fitted with nine peaks, as this proved to be the most suitable arrangement to fit the original spectrum. Figure 4.8 shows the way in which the, in this case Lorentzian, peaks interact to form the spectra. The measured peak shifts were compared for the three procedures. Raman peak shifts and stresses in oxides grown on Type 316 stainless steel are discussed in more detail in Section 5.3.

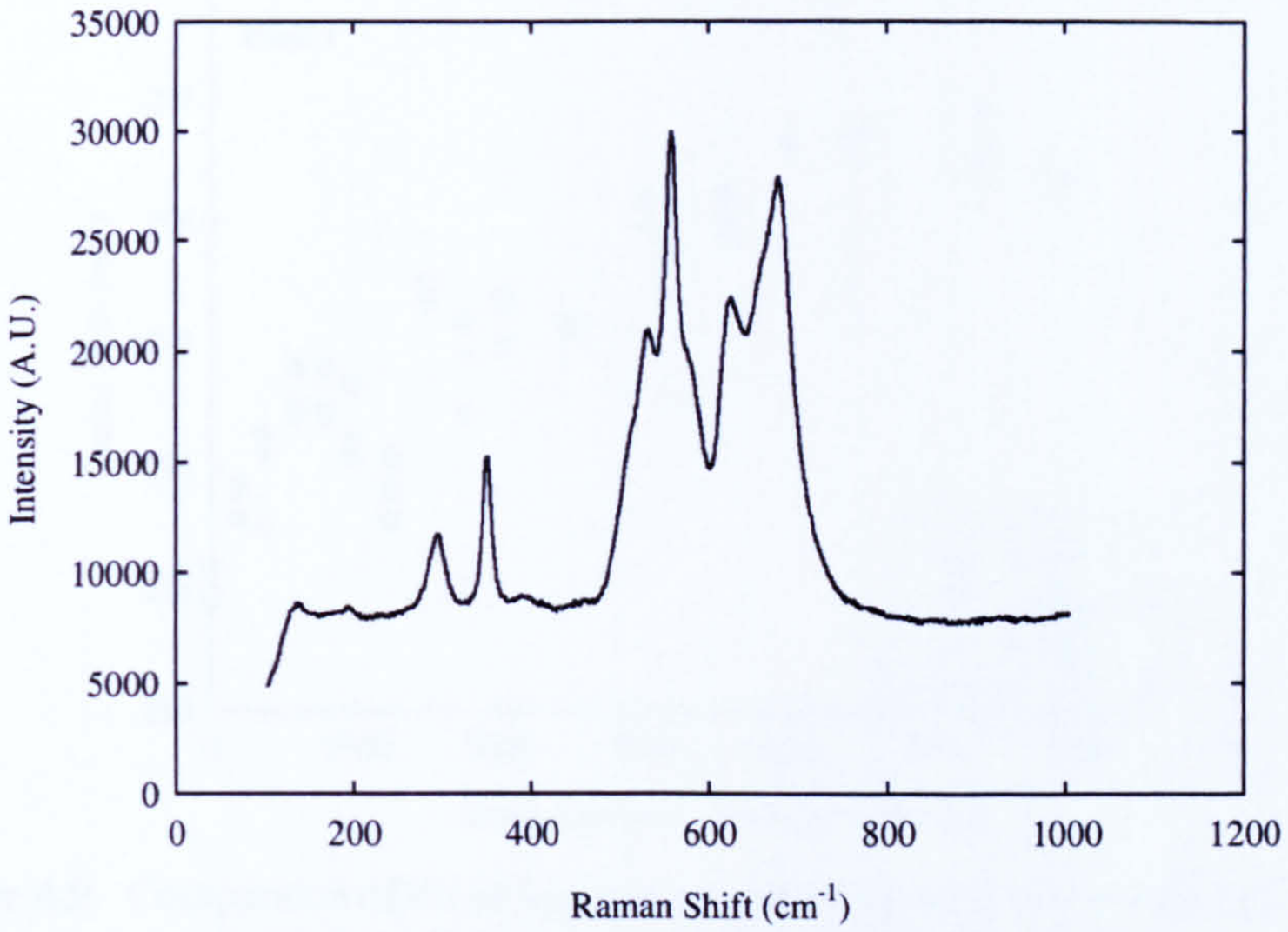

Figure 4.7. Raman spectrum obtained from oxide formed on Type 316 austenitic stainless steel oxidised for one hour at 950°C.

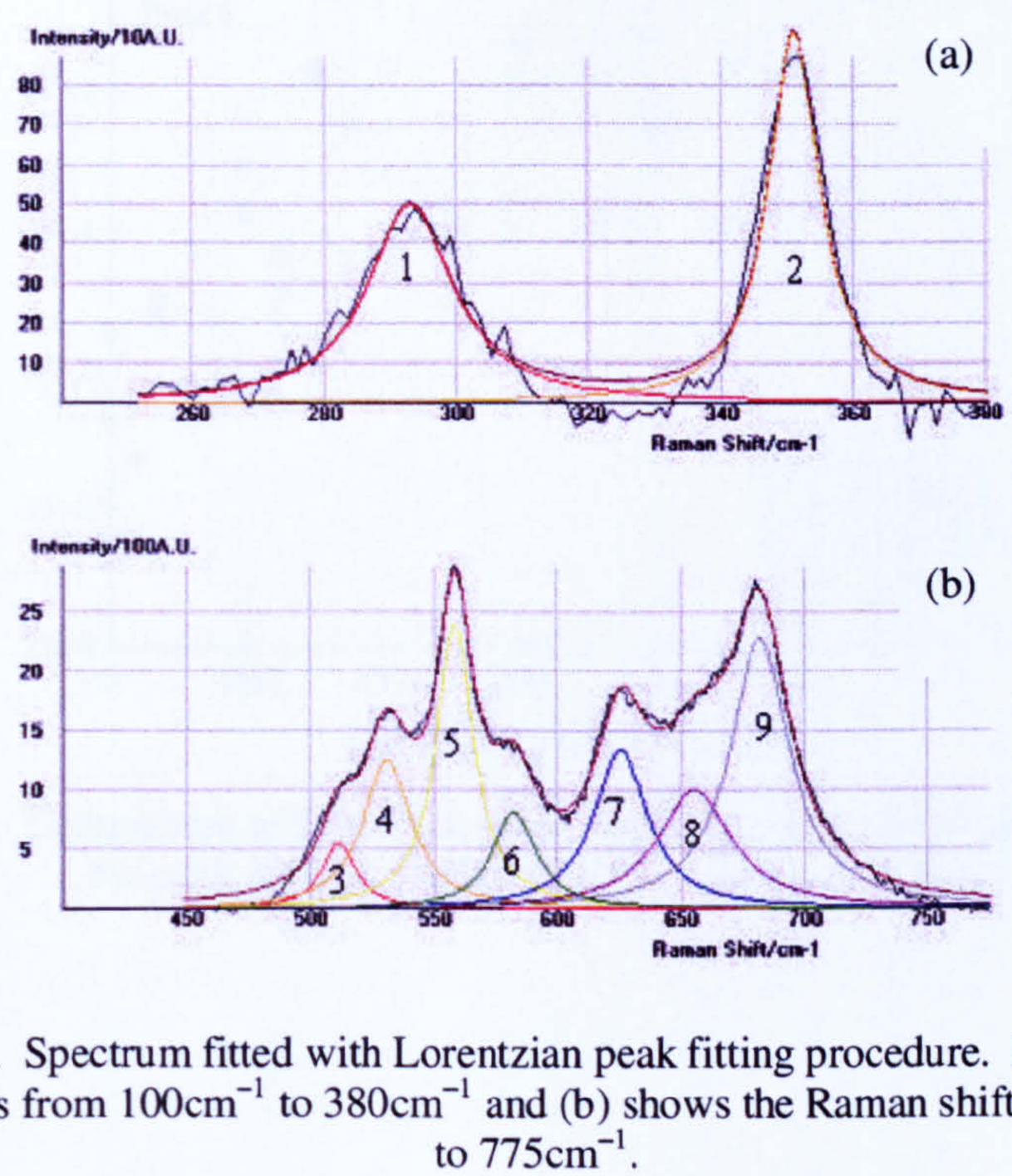

Figure 4.8. Spectrum fitted with Lorentzian peak fitting procedure. Part (a) shows Raman shifts from 100cm^{-1} to 380cm^{-1} and (b) shows the Raman shifts from 380cm^{-1} to 775cm^{-1}.

The calculated Raman shifts for the peaks labelled 1 to 9, Figure 4.8, with respect to applied strain in the oxide can be seen in Figures 4.9 to 4.17.

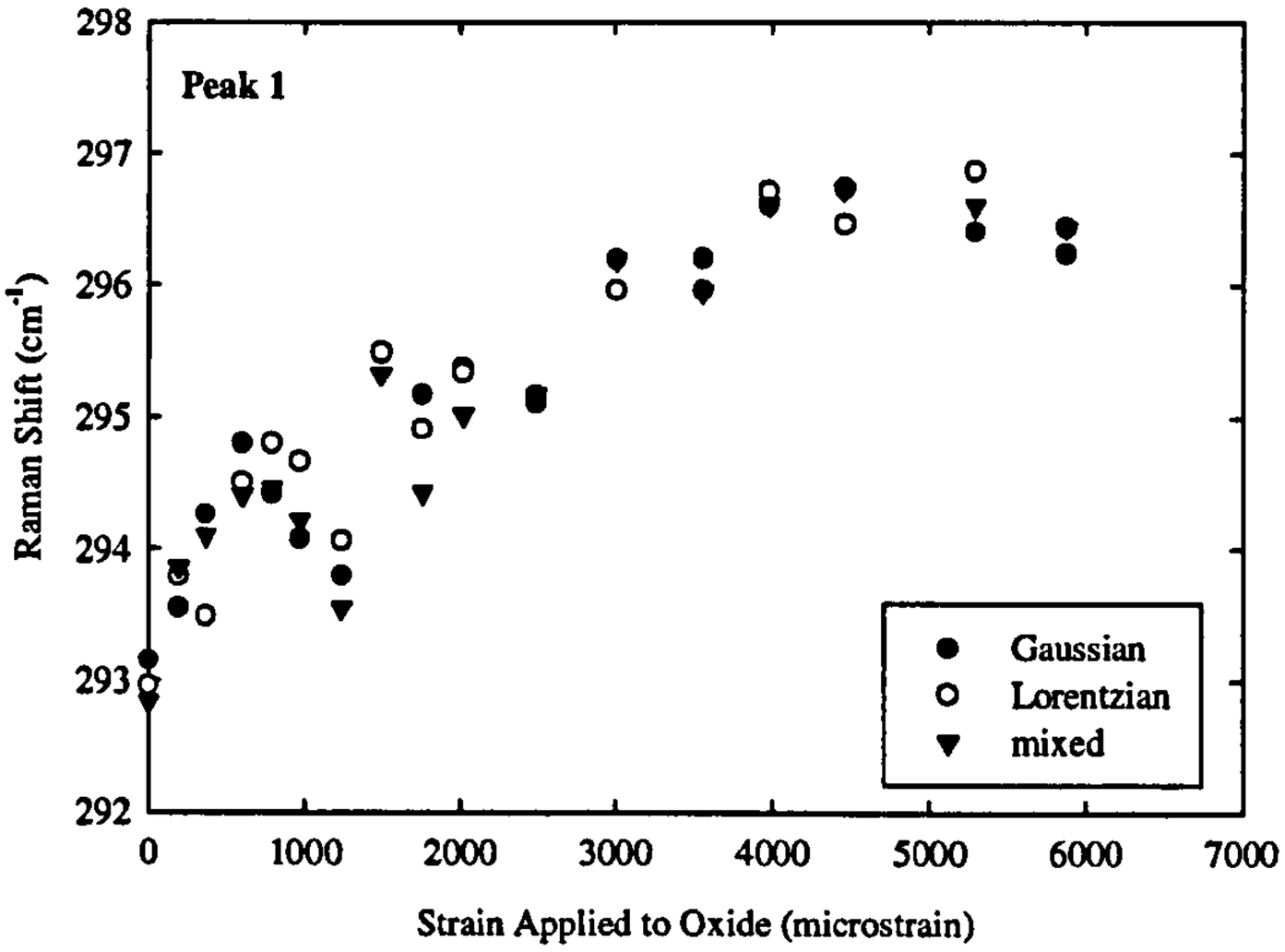

Figure 4.9. Comparison of fitted Gaussian, Lorentzian and mixed peak positions for the peak marked 1 using the Pisces fitting program.

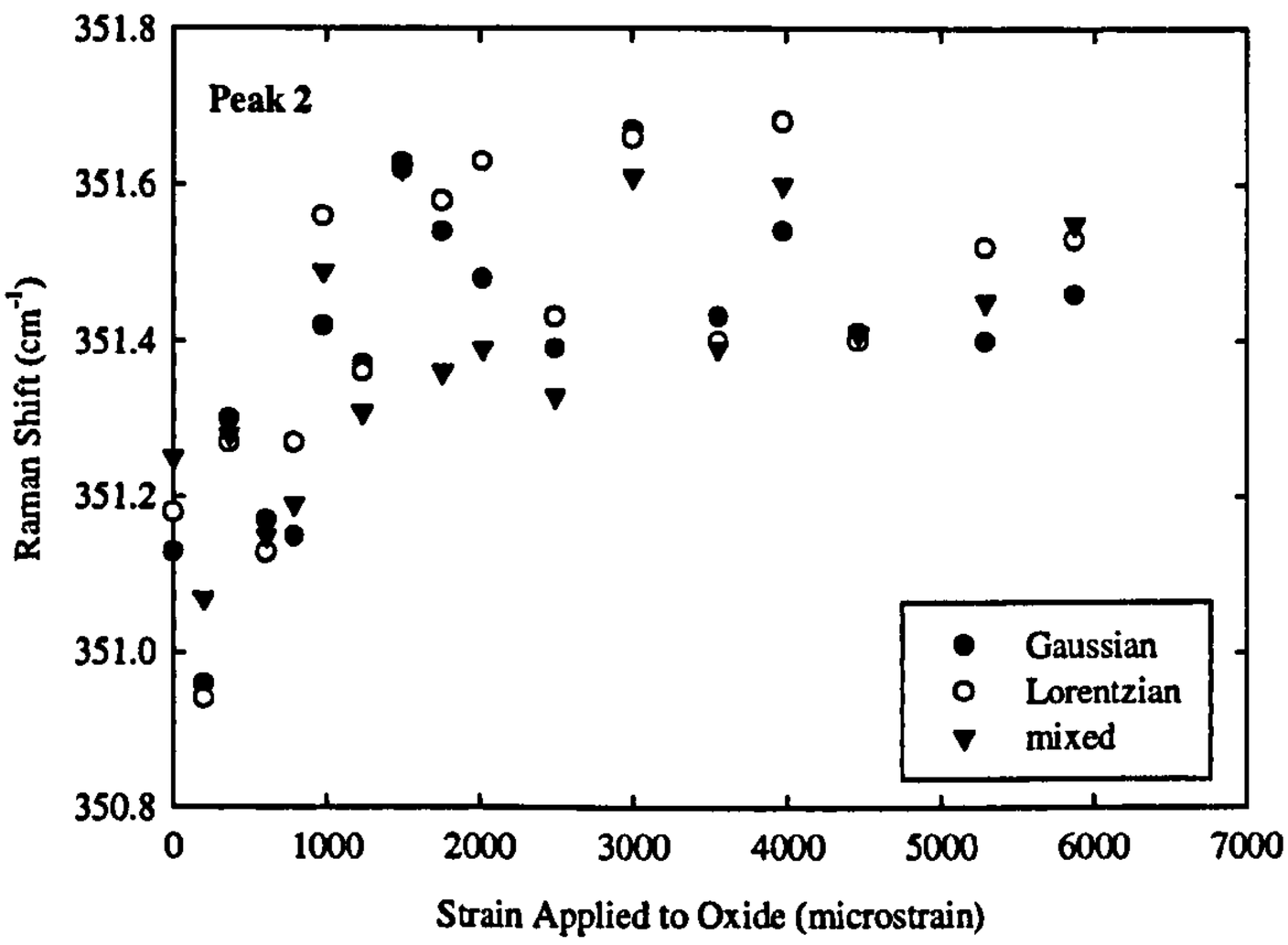

Figure 4.10. Comparison of fitted Gaussian, Lorentzian and mixed peak positions for the peak marked 2 using the Pisces fitting program.

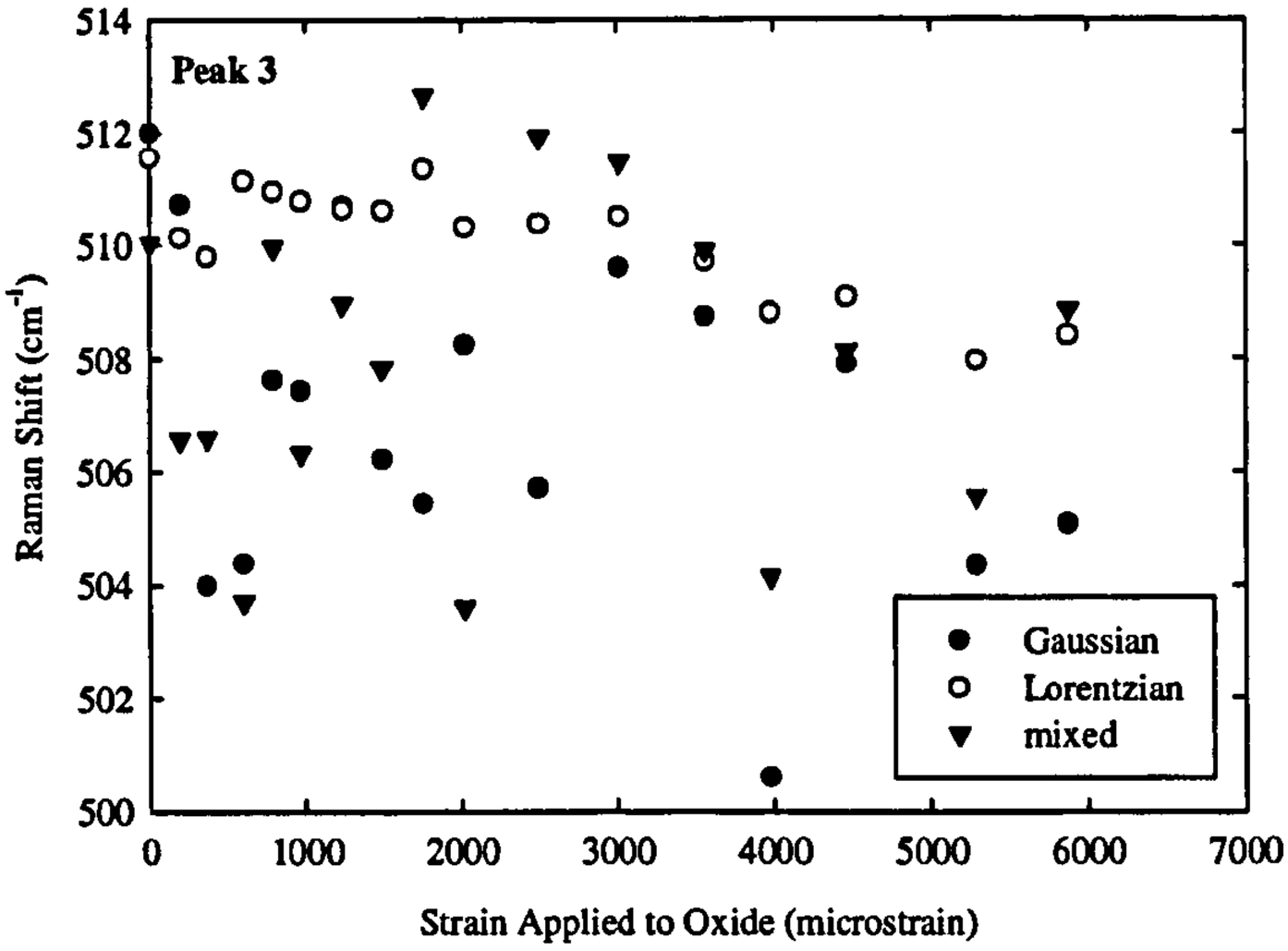

Figure 4.11. Comparison of fitted Gaussian, Lorentzian and mixed peak positions for the peak marked 3 using the Pisces fitting program.

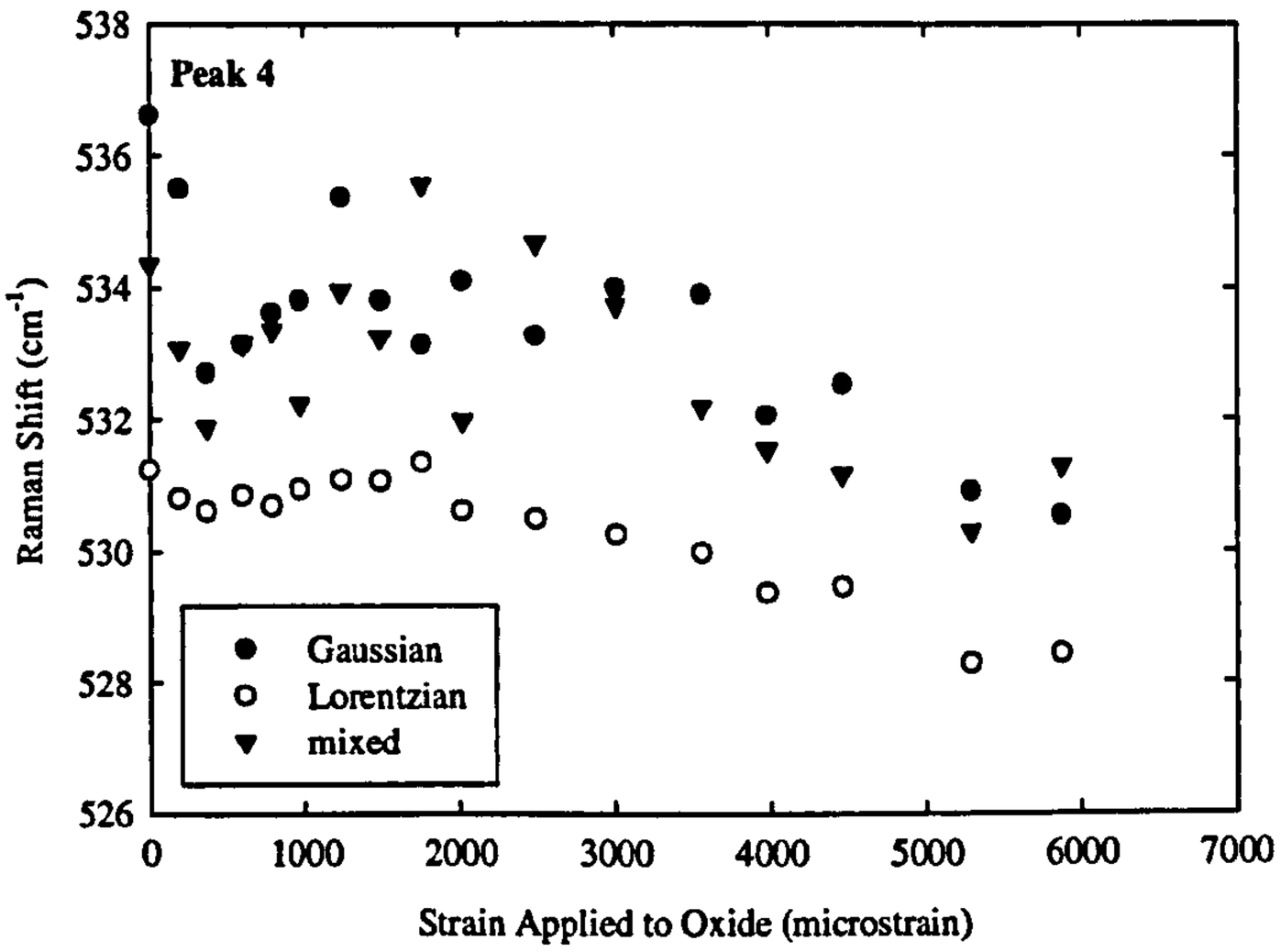

Figure 4.12. Comparison of fitted Gaussian, Lorentzian and mixed peak positions for the peak marked 4 using the Pisces fitting program.

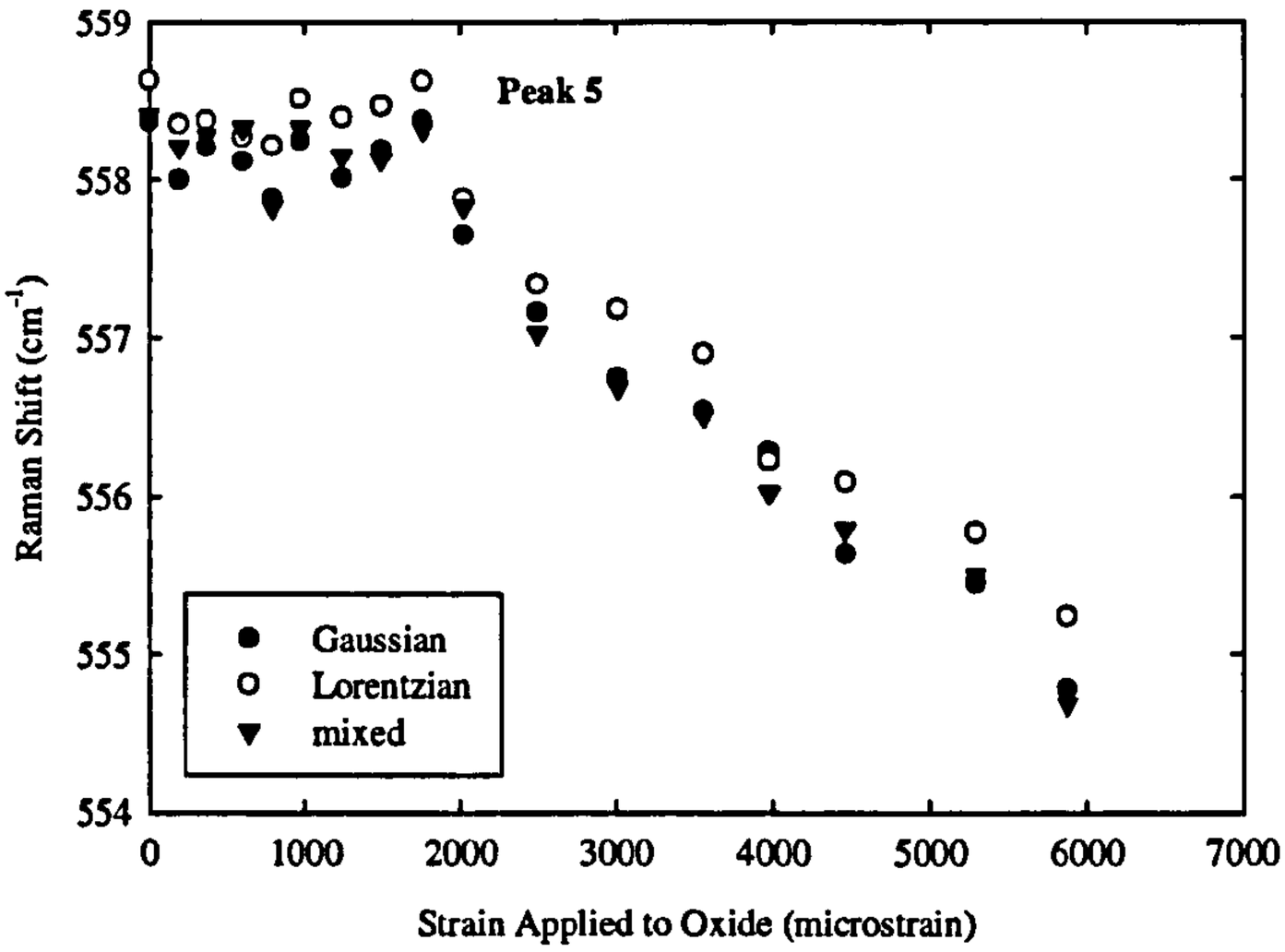

Figure 4.13. Comparison of fitted Gaussian, Lorentzian and mixed peak positions for the peak marked 5 using the Pisces fitting program.

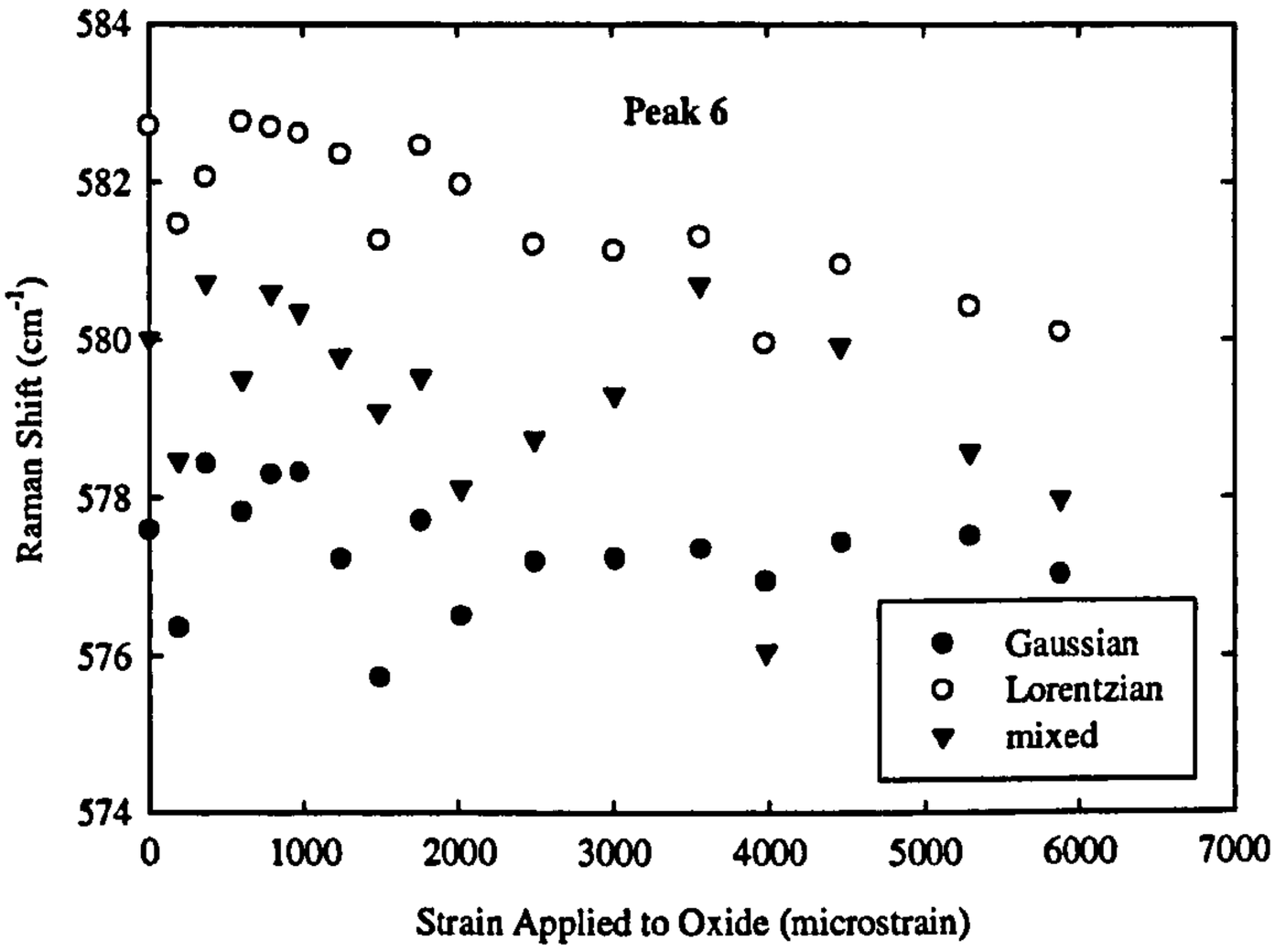

Figure 4.14. Comparison of fitted Gaussian, Lorentzian and mixed peak positions for the peak marked 6 using the Pisces fitting program.

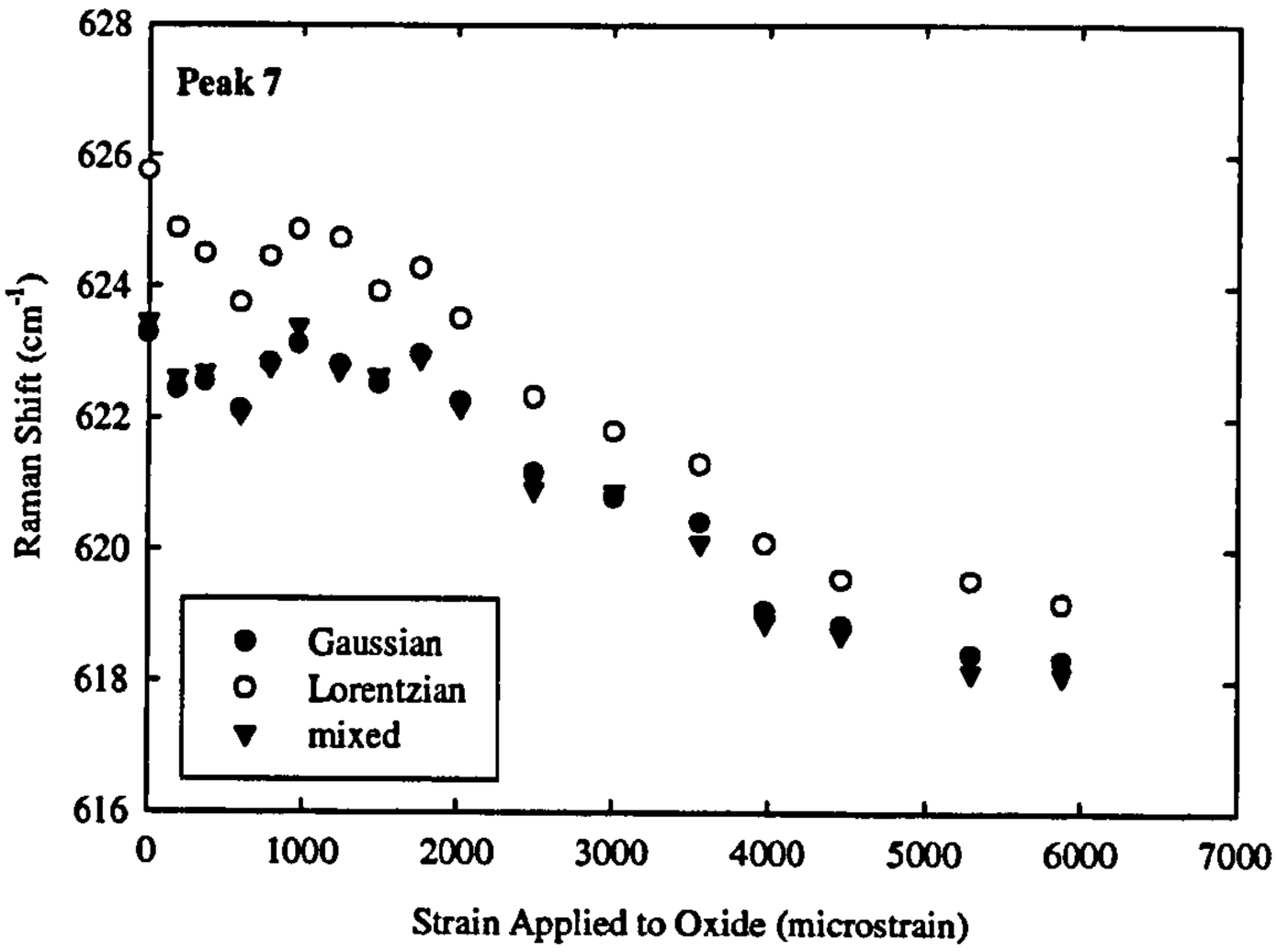

Figure 4.15. Comparison of fitted Gaussian, Lorentzian and mixed peak positions for the peak marked 7 using the Pisces fitting program.

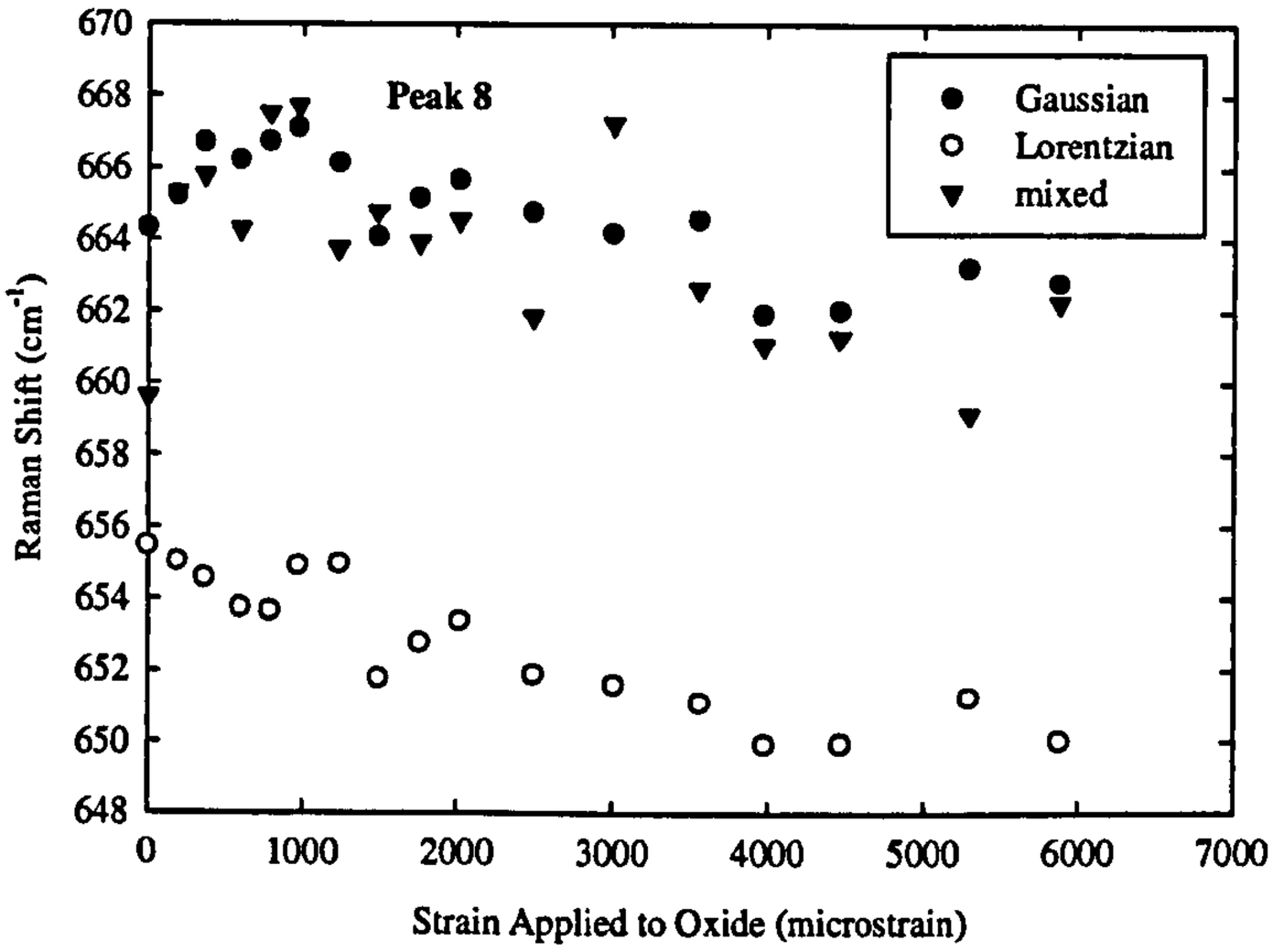

Figure 4.16. Comparison of fitted Gaussian, Lorentzian and mixed peak positions for the peak marked 8 using the Pisces fitting program.

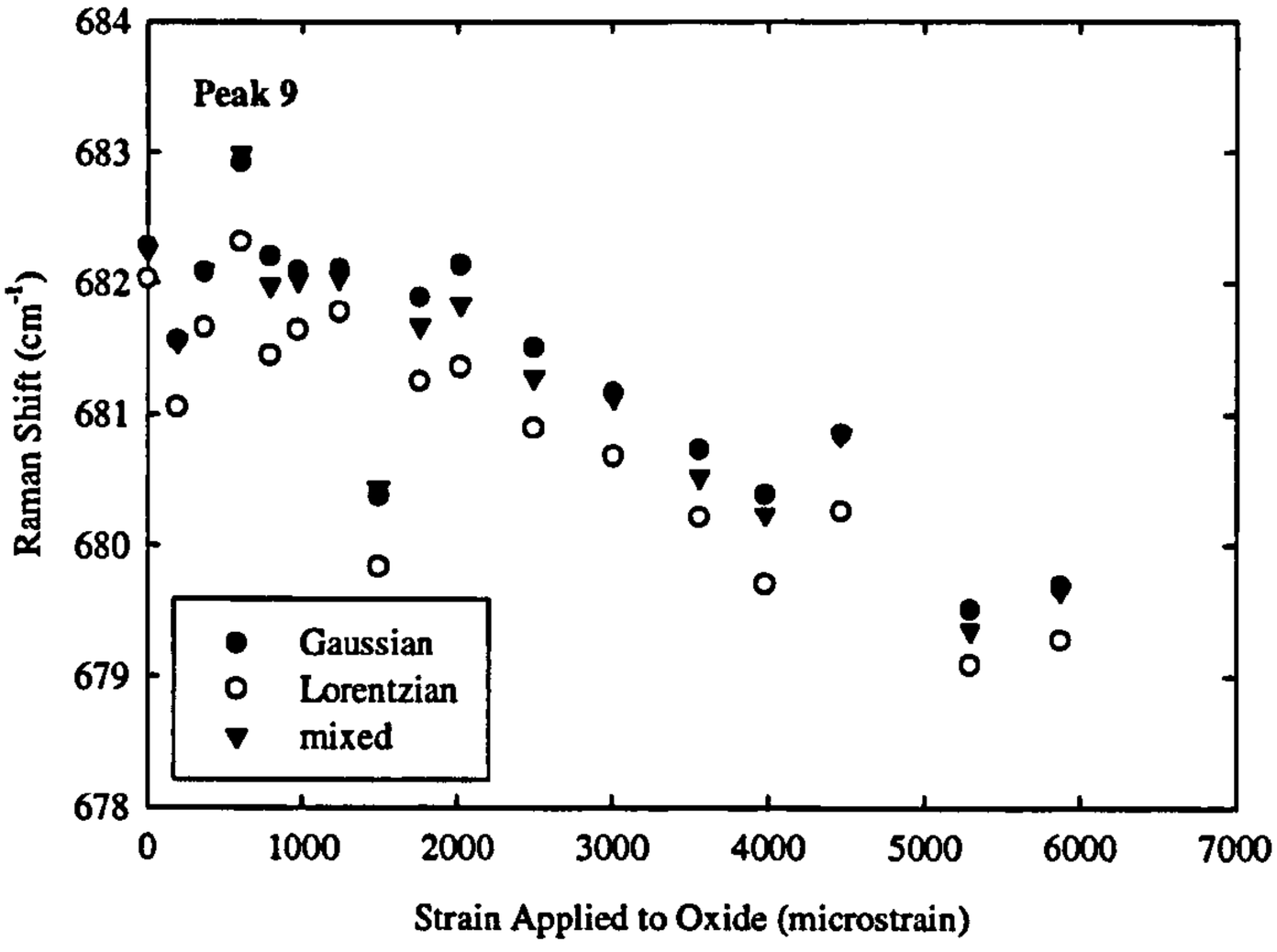

Figure 4.17. Comparison of fitted Gaussian, Lorentzian and mixed peak positions for the peak marked 9 using the Pisces fitting program.

The Raman shifts of some peaks, such as Peak 5, shifted systematically with applied strain whereas others did not, such as Peak 2. This agrees with investigations by other workers, who found that there was a variation in the behaviour of Raman peaks with applied stress [(b)Mougin et al. 2002, Shim and Duffy 2002]. The differences in frequency shifts with applied stress/strain have been attributed to the differences in phonon frequency shifts of atomic bonds with applied changes in volume [Birnie et al. 1992].

There was good agreement in the trends of Raman shifts with strain for the well defined peaks such as the peak labelled 5, which shifted systematically with applied strain for all the fitting procedures. Whereas the less well defined peaks did not shift systematically for all fitting procedures and there was sometimes poor agreement between them. For example, it can be seen that for peak 4, Figure 4.12, there is a systematic change in peak position with applied strain when the spectrum in fitted with a Lorentzian profile. However, this is not the case for the Gaussian and mixed profiles where there is far more scatter in the Raman shift. The fitting of Peak 8, Figure 4.16, resulted in a systematic trend with applied strain with a Lorentzian or Gaussian profile, whereas there was far more scatter when the peak was fitted with a

mixed profile. However, there is poor agreement between the calculated Lorentzian and Gaussian Raman shifts.

The above discussed results confirm that the fitting procedure would not have a significant effect on the measured stress on well defined peaks. Since, as with the previously described experiment on single crystal silicon, there was good correlation between the fitting procedures carried out on the well defined peaks. However, the results show uncertainties that can arise when fitting complex peaks, particularly when using a mixed fitting procedure, as this produced the greatest scatter. Although it is not possible to tell from this experiment what the absolute Raman peak position of the analysed peaks, the Lorentzian fitting procedure resulted in the least scatter in the fitting of the more overlapping peaks. It can therefore be concluded that if consistency of measurements is desired, it is be preferable to use a Lorentzian fitting procedure for complex peaks. This has been concluded by other authors as discussed in Section 3.12.3.

4.3.6 Laser Spot Size

When analysing a specimen using Raman or photoluminescence spectroscopy, it is important to consider the magnitude of the surface area and hence volume to be analysed [Flewitt and Wild 2003]. For example, in the case of laser techniques, if a small feature is to be analysed, it is prudent to use a small laser spot size. However, if one wishes to obtain average material properties over a larger area, a larger spot size should be used.

Moreover, because of the differences in count rate when a higher magnification lens, with a smaller laser spot size is used on the spectrometer, less time is required to reach a certain number of counts than with a lower magnification lens with a larger laser spot size, Figure 4.18. However, a larger laser spot size samples over a larger area, thereby giving greater statistical confidence over the analysed sample. Thus a series of tests were carried out on a calibration standard, single crystal silicon, in order to assess the importance of the sampled area.

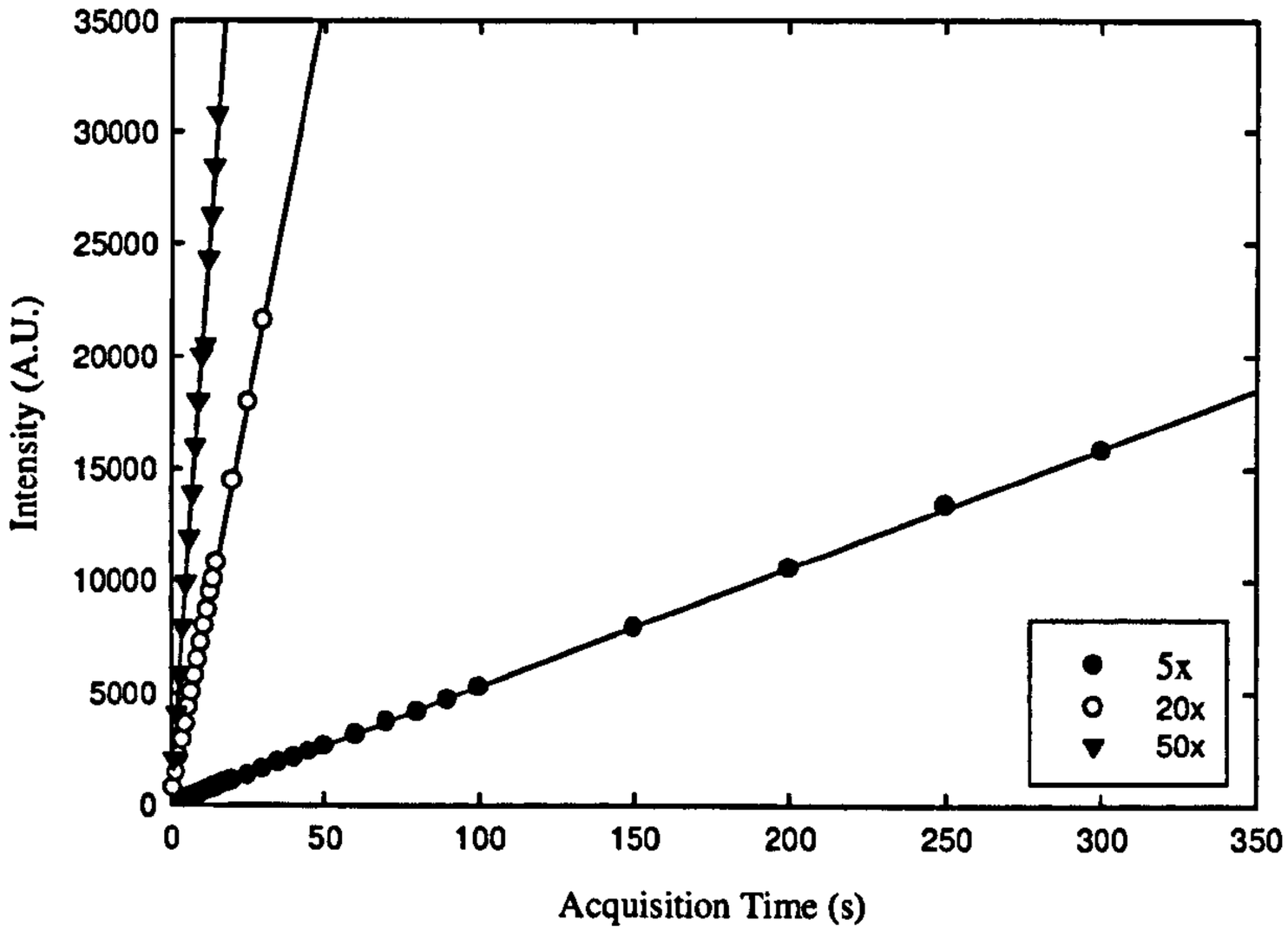

Figure 4.18. Silicon Raman peak intensity against acquisition time for various lens magnifications.

Laser spot sizes were calculated by focusing the laser on a piece of silicon and then using an in-house program written by Day to calculate the light intensity across the spot [Day 2000]. The full width half maximum of this peak was then calculated using a Gaussian peak fitting procedure in order to gain a measurement of the spot diameter. The calculated spot size diameters can be seen in Table 4.3. The error in each case was equivalent to one pixel on either side of the laser spot image. The error in measuring the spot diameter was calculated by converting the pixels into micrometres. This therefore gives an indication of the laser beam full width half maxima corresponding to some lenses commonly used and as such is an indication of the lenses' relative spot sizes.

Table 4.3. Laser spot size diameters for different microscope lenses used.

Lens Magnification	Spot Diameter (μm)	Error (μm)
5	6.25	2.08
20	1.43	0.52
50	1.02	0.20

4.3.7 Statistical Confidence

Statistical confidence in a result is dependent upon the number of tests carried out and data points sampled [Lonsdale and Flewitt 1985]. One method of analysing the

statistical confidence in a series of measurements is by calculating the variance [Lonsdale and Flewitt 1985]. The variance in a series of data points is inversely proportional to the number of data points. Thus the trend in variance (rather than the absolute variance) with respect to the number of data points is shown in Figure 4.19.

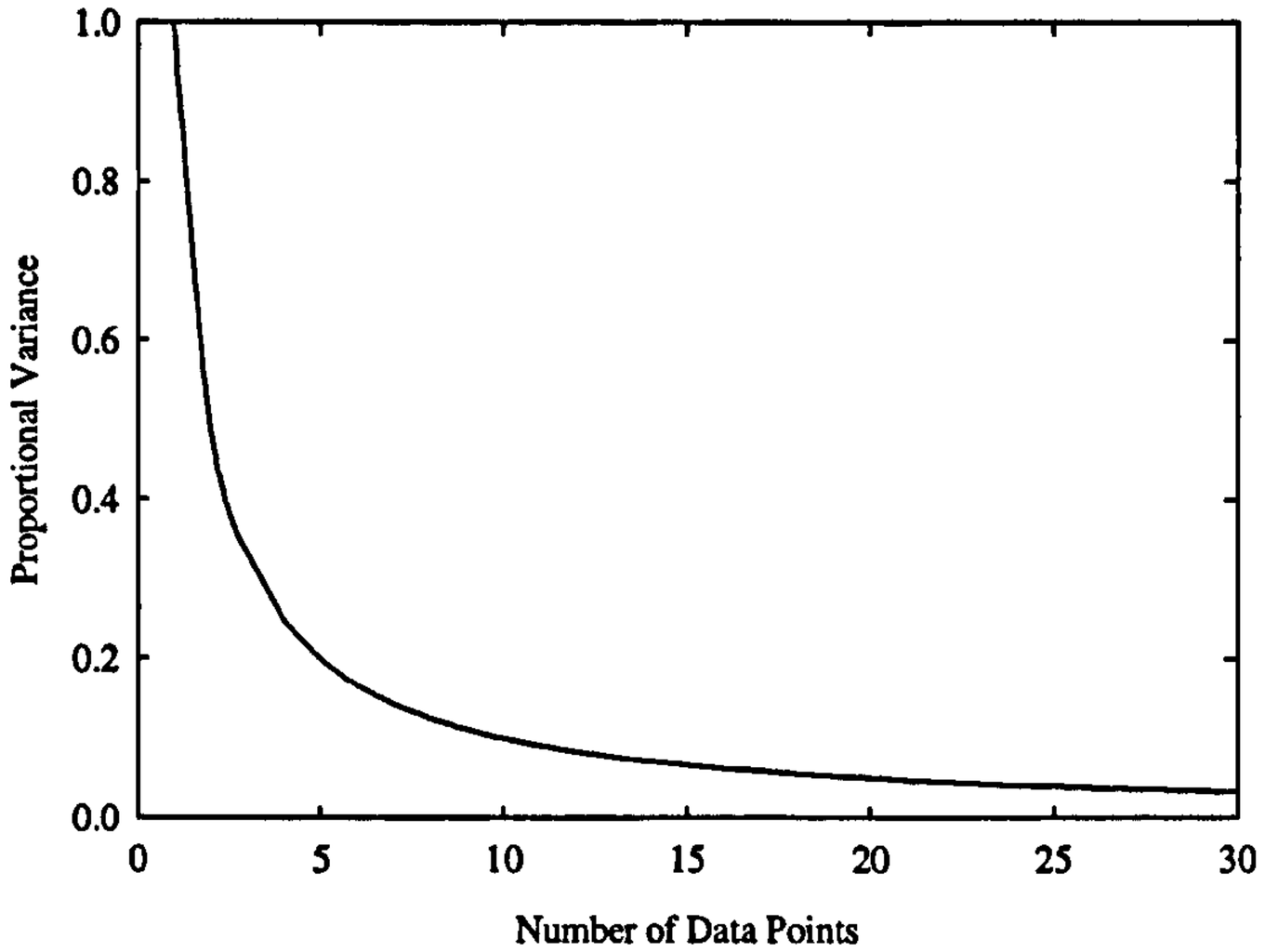

Figure 4.19. Trend of variance with respect to number of data points.

It can be seen that the variance decreases rapidly between 5 to 15 data points. It was decided that twenty data points on each specimen should be used for investigations in which a statistical confidence was required to allow for any outliers.

In order to investigate the difference in peak position scatter obtained when different lens magnifications and therefore spot sizes were used, experiments were carried out on a calibration specimen, single crystal silicon. Twenty spectra were obtained using the 5x, 20x and 50x microscope lenses from a single crystal silicon specimen. The investigation was conducted using a fixed power laser of 12mW and 633nm wavelength with an accumulation time of 100s. Average peak positions, standard deviations and 5^{th} and 95^{th} percentiles were then calculated for the acquired spectra. The Raman spectra obtained from the silicon specimen were fitted with a Lorentzian fitting and a linear background subtraction using the GRAMS software. Preliminary tests showed that this experiment was not possible with alumina powder, as a signal

could not be obtained from the three lenses with the same laser power and accumulation time without saturating the detector.

Table 4.4 shows the average Raman shifts obtained from the silicon specimen with different lens magnifications along with the standard deviations and 5th and 95th percentiles of the Raman shifts. Table 4.5 shows the equivalent biaxial stresses different lens magnifications along with the standard deviations and 5th and 95th percentiles of the stresses.

Table 4.4. Average Raman shifts from silicon and their variations obtained for three lens magnifications.

Lens Magnification	Average Raman Shift (cm^{-1})	Standard Deviation	5th Percentile Raman Shift (cm^{-1})	95th Percentile Raman Shift (cm^{-1})
5x	519.375	0.063	519.276	519.454
20x	519.703	0.107	519.512	519.806
50x	519.728	0.060	519.631	519.795

Table 4.5. Average biaxial stress from silicon and their variations obtained for three lens magnifications.

Lens Magnification	Average Biaxial Stress (GPa)	Standard Deviation	5th Percentile Biaxial Stress (GPa)	95th Percentile Biaxial Stress (GPa)
5x	0.272	0.027	0.315	0.237
20x	0.129	0.047	0.212	0.084
50x	0.118	0.026	0.161	0.089

The average Raman shift decreases with decreasing magnification and therefore increasing laser spot size. The 5th and 95th percentiles also show this trend in decreasing shift with decreasing lens magnification. The difference in average Raman shift between the 5x magnification lens and 50x magnification lens is 0.35cm^{-1}, which is greater than the minimum detectable Raman peak shift of 0.05cm^{-1} described by De Wolf [De Wolf 1996]. An increasing Raman shift in silicon corresponds to an increasing compressive stress [De Wolf 1996, Kouteva-Arguirova etc. 2003] (see also Section 4.3.4). Therefore, if the average Raman shifts for the different lens magnifications were to be converted into stress, the measurements in Table 4.4 would correspond to an increasing measured compressive stress with increasing lens

magnification, Table 4.5, and therefore an increasing measured compressive stress with decreasing laser spot size. The standard deviation in peak position of the spectra recorded with the 20x magnification lens is greater than that of the measurements made with the other lenses. This can be explained by the presence of an outlier with a Raman shift of 519.433cm^{-1}. The outlier could be due to an anomaly on the specimen surface.

Two possible explanations for the change in peak positions with lens magnifications are the experimental arrangements or the techniques employed. With regards to experimental arrangement, differences in measured peak positions could arise due to differences in the areas sampled. However, as twenty data points were analysed per lens magnification on the calibration sample, the trend towards increasingly compressive stresses with decreasing laser spot size is unlikely to have been caused by variations in the surface stresses within the probed volumes of the sample. The techniques employed could also be a factor in the peak shifts with varying lens magnification and laser spot size. Laser heating effects have been observed in Raman spectroscopy and have been shown to result in compressive stresses [Kouteva-Arguirova et al. 2003]. Heating effects are discussed further in Section 4.3.8.

4.3.8 Heating Effects

In Section 4.3.7, it was shown that varying the lens magnification and therefore spot size resulted in a difference in average Raman shift in a silicon standard. This can be explained through heating effects. As the laser spot size decreased, the average Raman shift or photoluminescence peak position resulted in a corresponding to a greater compressive stress [Atkinson and Selcuk 2004, De Wolf 1996, Kouteva-Arguirova et al. 2003, Ma and Clarke 1993, McCumber and Sturge 1963]. The mechanism of laser heating effects in silicon samples has already been considered by Kouteva-Arguirova et al. [Kouteva-Arguirova et al. 2003] and has been discussed in Chapter 3 - Techniques.

The dependence of spectroscopic shifts of two calibration standards, namely single crystal silicon and alumina, on temperature has been investigated by other researchers and has been found to result in Raman shifts of approximately $-0.032 cm^{-1} {}^{o}C^{-1}$ [(a)Wu et al. 2007, (b)Wu et al. 2007] for single crystal silicon and

photoluminescence frequency shifts of approximately 0.15cm^{-1}°C for α-alumina, Section 3.12.3 and Section 3.12.4. However, although the phenomenon of laser heating in silicon has been researched, Section 3.12.3, laser heating of alumina has only been alluded to in publications [He and Clarke 1995, Ma and Clarke 1994].

In order to establish how to minimize heating effects during experimental measurements, particularly on the thermally grown oxides of turbine blades, a series of tests were undertaken on another calibration standard, α-alumina powder, and coated superalloys from which stress measurement data were to be obtained. Tests were carried out on α-alumina powder in order to better understand any heating effects caused by the laser. These tests were carried out at the National Physical Laboratory in collaboration with Dr. John Nunn. The spectrometer used was a Dilor system equipped with a 532nm wavelength laser. A long distance lens of 10x magnification was used and the spectrometer had a maximum power of 250mW. First, the laser power was increased by increasing the percentage current in the incident laser and the photoluminescence spectra were recorded, Figure 4.20.

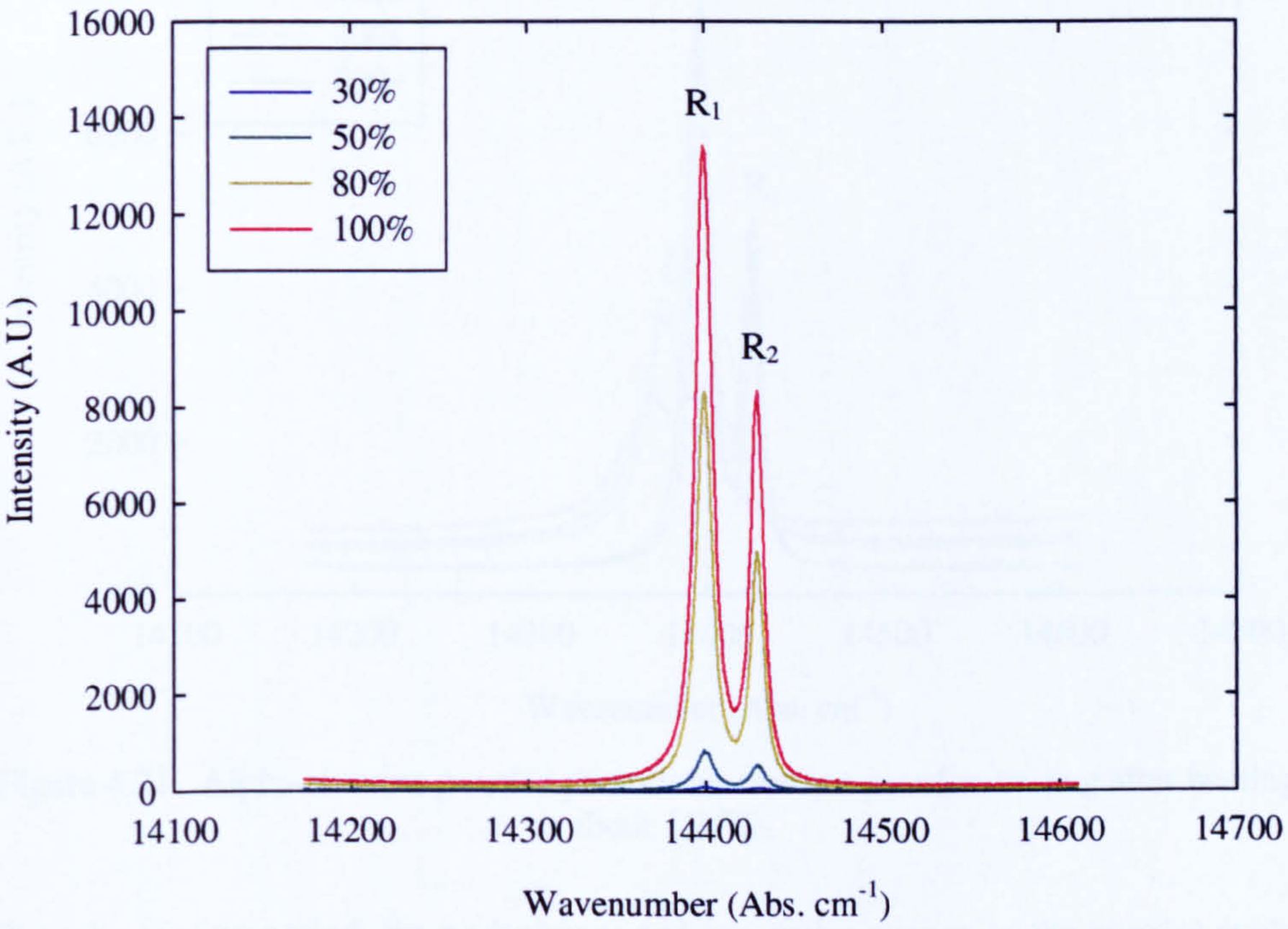

Figure 4.20. Alpha-alumina powder photoluminescence with increasing percentage current.

The key in Figure 4.20 shows the percentage laser current for the accumulation of each spectrum. The intensity of the spectra increases with increasing percentage current and that increasing the laser current and therefore power has little effect on peak position.

Next, fresh alumina powder was heated on a hot plate to approximately 150°C. Photoluminescence spectra were recorded until there was little difference in the spectral shapes and positions, thereby indicating that the powder had cooled to room temperature, approximately 20°C. The photoluminescence spectra were recorded for 20 seconds with 60 between acquisitions. Thus the total time between acquisitions was 80 seconds. The percentage current used when acquiring the spectra was 75 percent, Figure 4.21. The key shows the times at which the spectra were recorded from the start of the experiment.

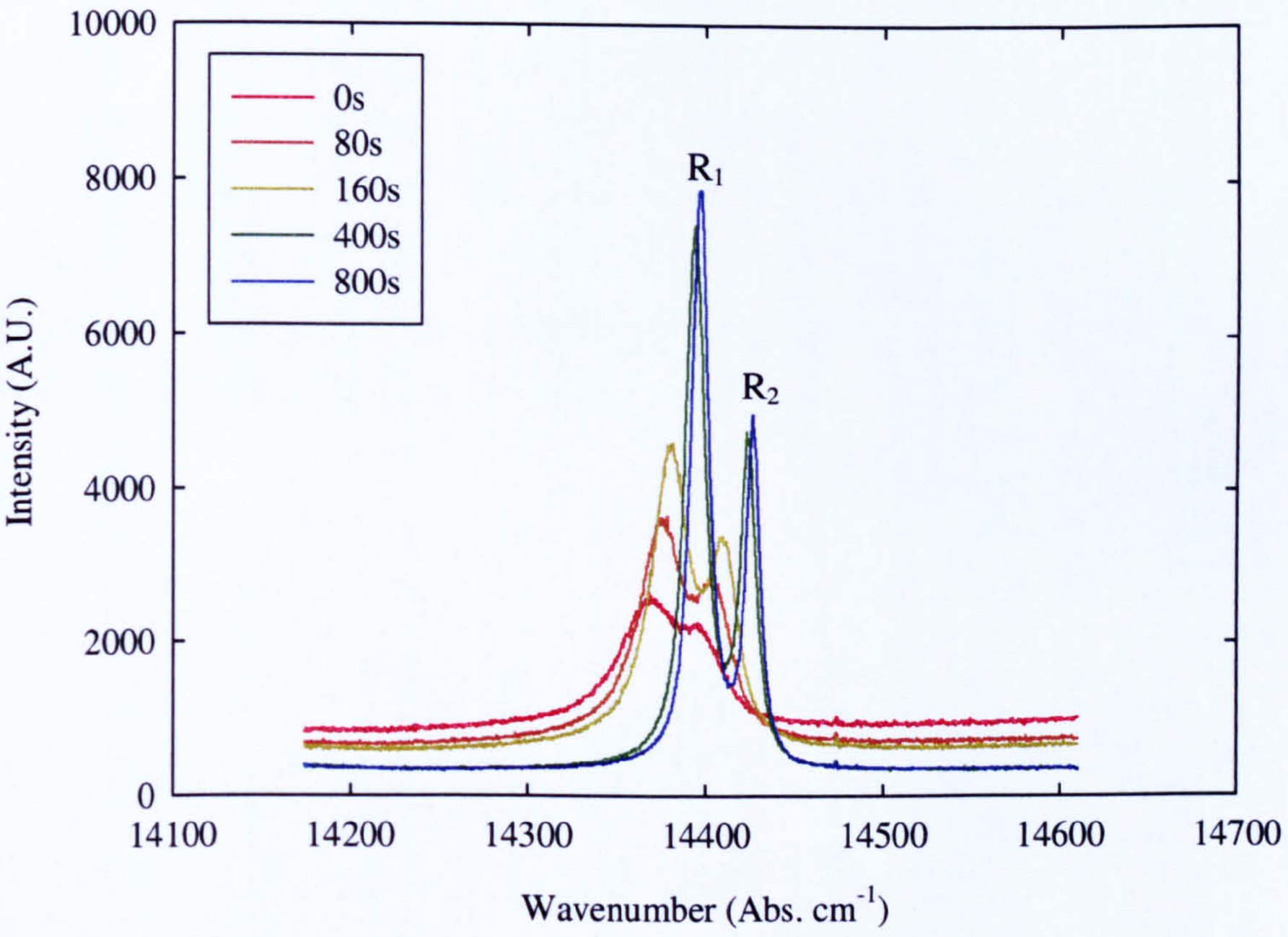

Figure 4.21. Alpha-alumina powder photoluminescence powder cooling after heating to about 150°C.

Over the cooling period, the peak shapes and intensities change as the powder cools. Initially, when the powder has just been heated, the peaks are broad and their position

is indicative of a compressive stress in the sample. However, as the powder cools, the peaks become narrower and move to a less stressed position.

The effect of laser current on coated superalloys oxidised for 1000 hours at temperatures ranging from 950°C to 1050°C was conducted in order to ensure confidence in the technique. This was to determine whether the acquired spectra were altered by incident laser power and, if this were the case, whether a threshold could be found below which the acquired spectra were consistent. The laser current was increased steadily at a point on a series of superalloys with two types of bond-coat, RT22 and CN91, oxidised for 1000 hours at temperatures of 950°C, 1000°C and 1050°C. The RT22 coated sample, which was oxidised at 1050°C contained areas of higher stress and lower stress. One corresponding to each was selected. Both these areas were analysed over a range of laser currents. Photoluminescence peaks from the high stress and low stress areas in the RT22 coated superalloy oxidised at 1050°C can be seen in Figure 4.22 and Figure 4.23, the percentage laser currents used are shown in the key. Photoluminescence peak positions and corresponding biaxial stress of the RT22 and CN91 coated superalloys with increasing laser current can be seen in Figure 4.24 and Figure 4.25. The test was also conducted on α-alumina powder for comparison. The peaks were fitted using the GRAMS software with a mixed Gaussian Lorentzian fit and a quadratic background in order to best allow for the varying peak shapes with laser current and stress, Figure 4.26.

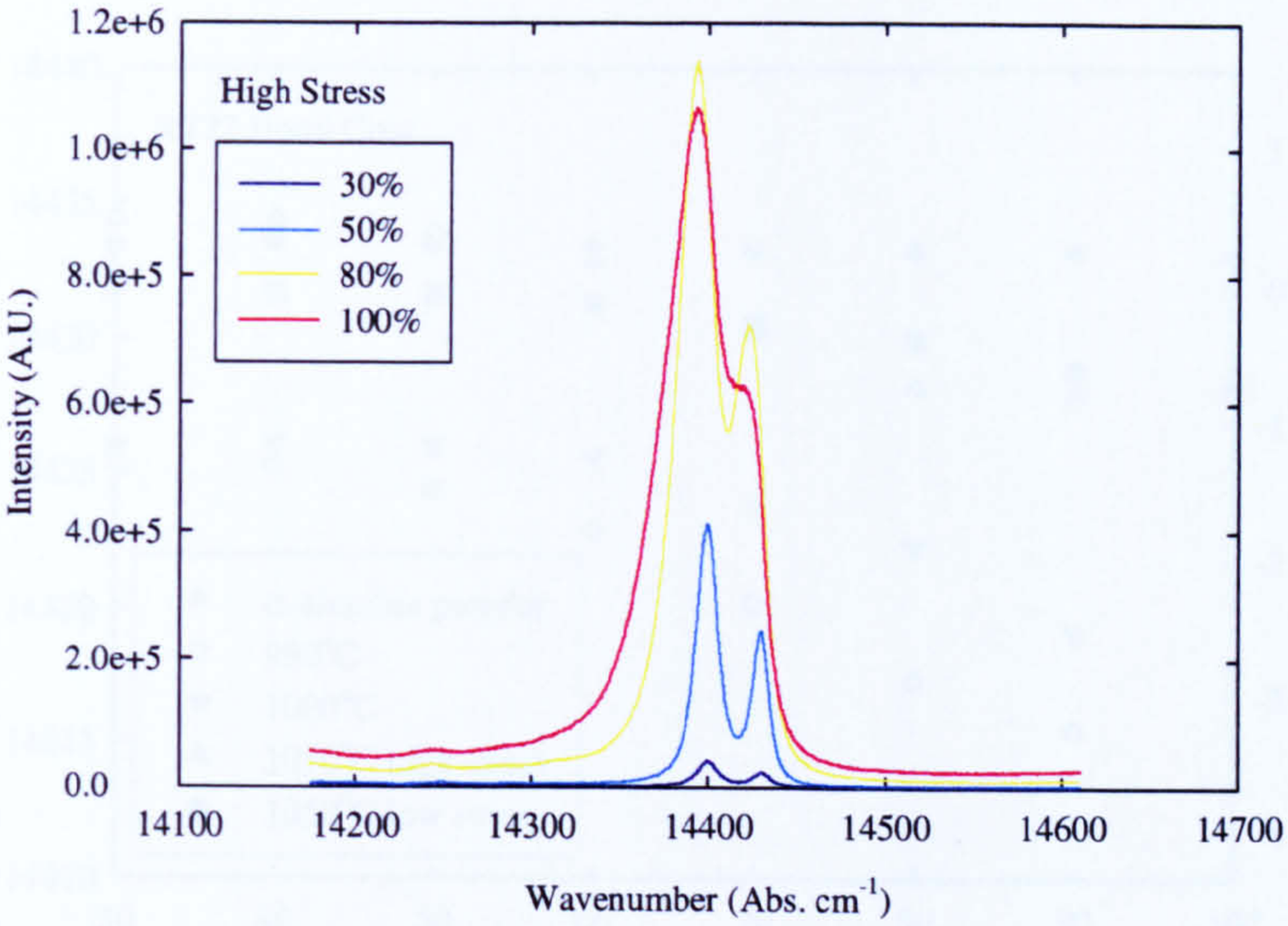

Figure 4.22. Photoluminescence peaks of a high stress region in an RT22 coated superalloy oxidised for 1000 hours at 1050°C with increasing laser current.

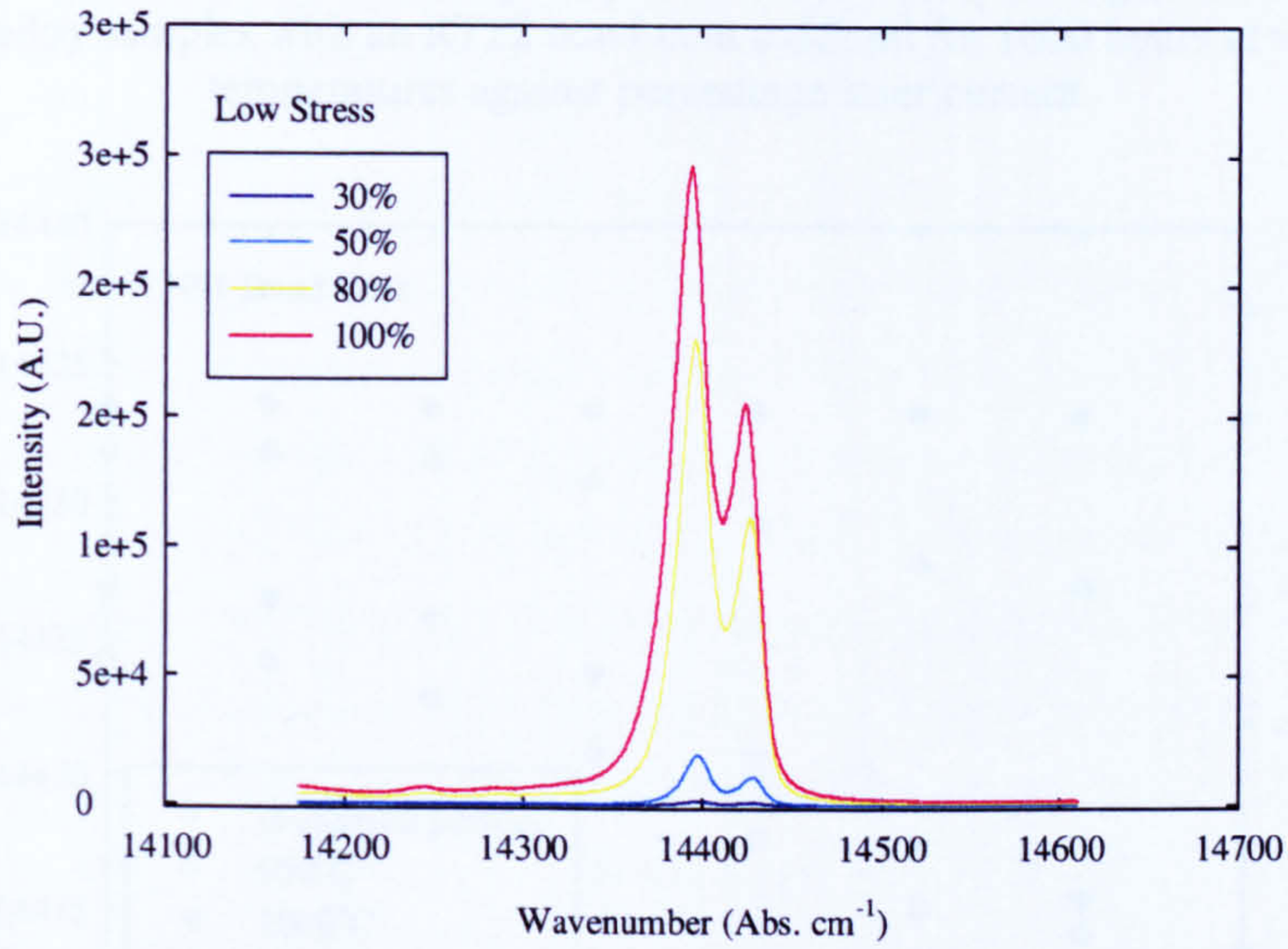

Figure 4.23. Photoluminescence peaks of a low stress region in an RT22 coated superalloy oxidised for 1000 hours at 1050°C with increasing laser current.

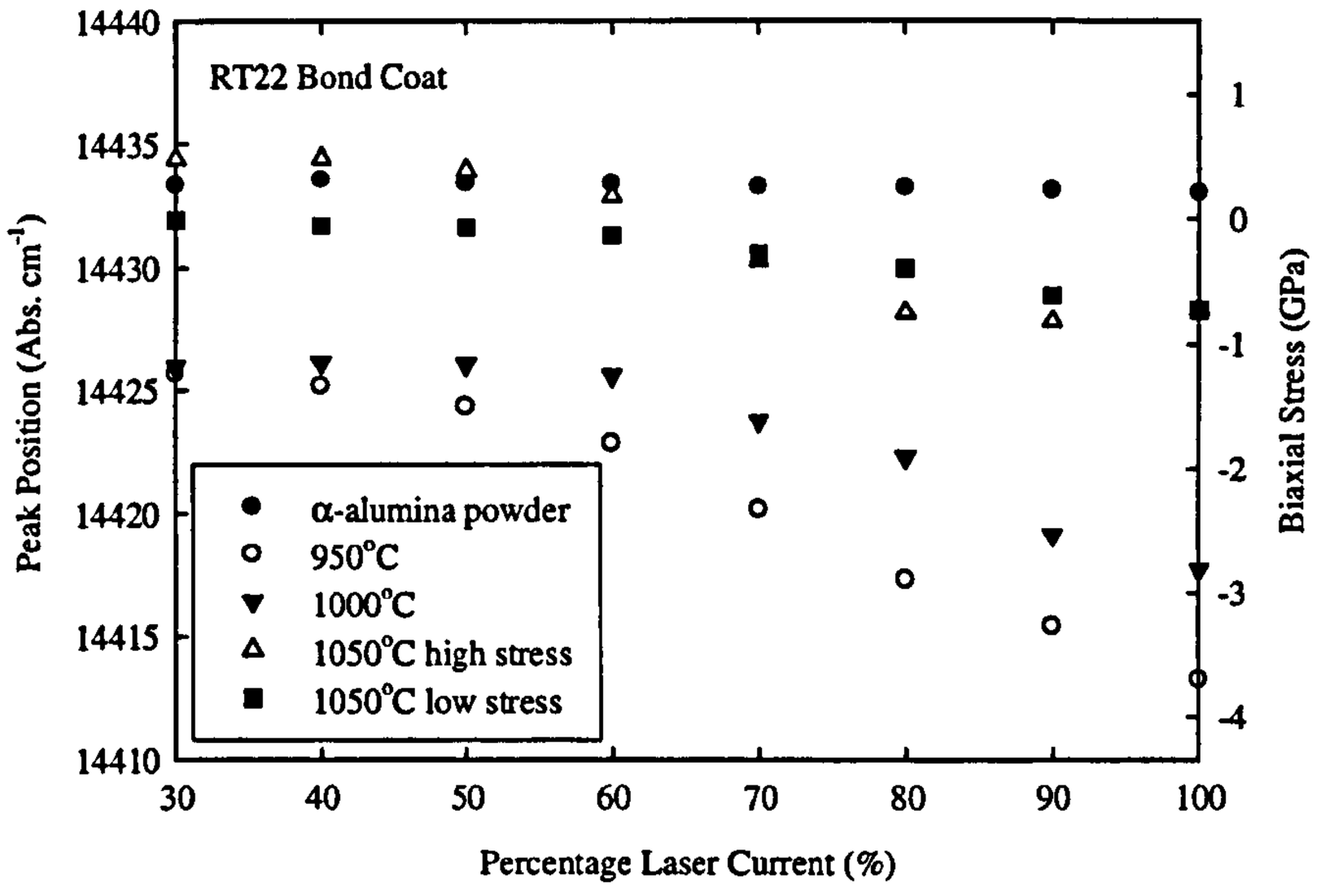

Figure 4.24. Photoluminescence peak position and corresponding biaxial stress of superalloy samples with an RT22 bond-coat oxidised for 1000 hours at various temperatures against percentage laser current.

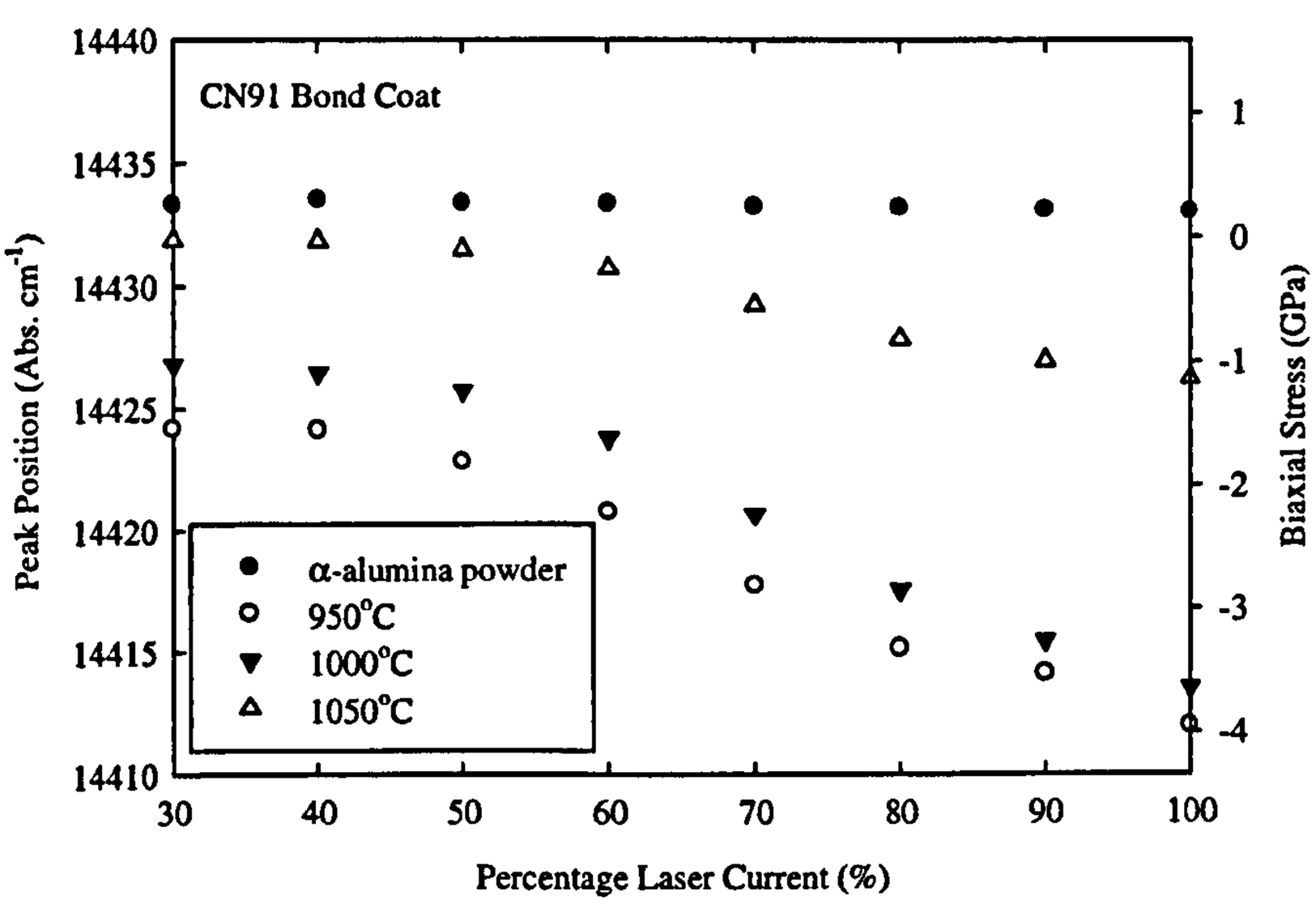

Figure 4.25. Photoluminescence peak position and corresponding biaxial stress of superalloy samples with a CN91 bondcoat oxidised for 1000 hours at various temperatures against percentage laser current.

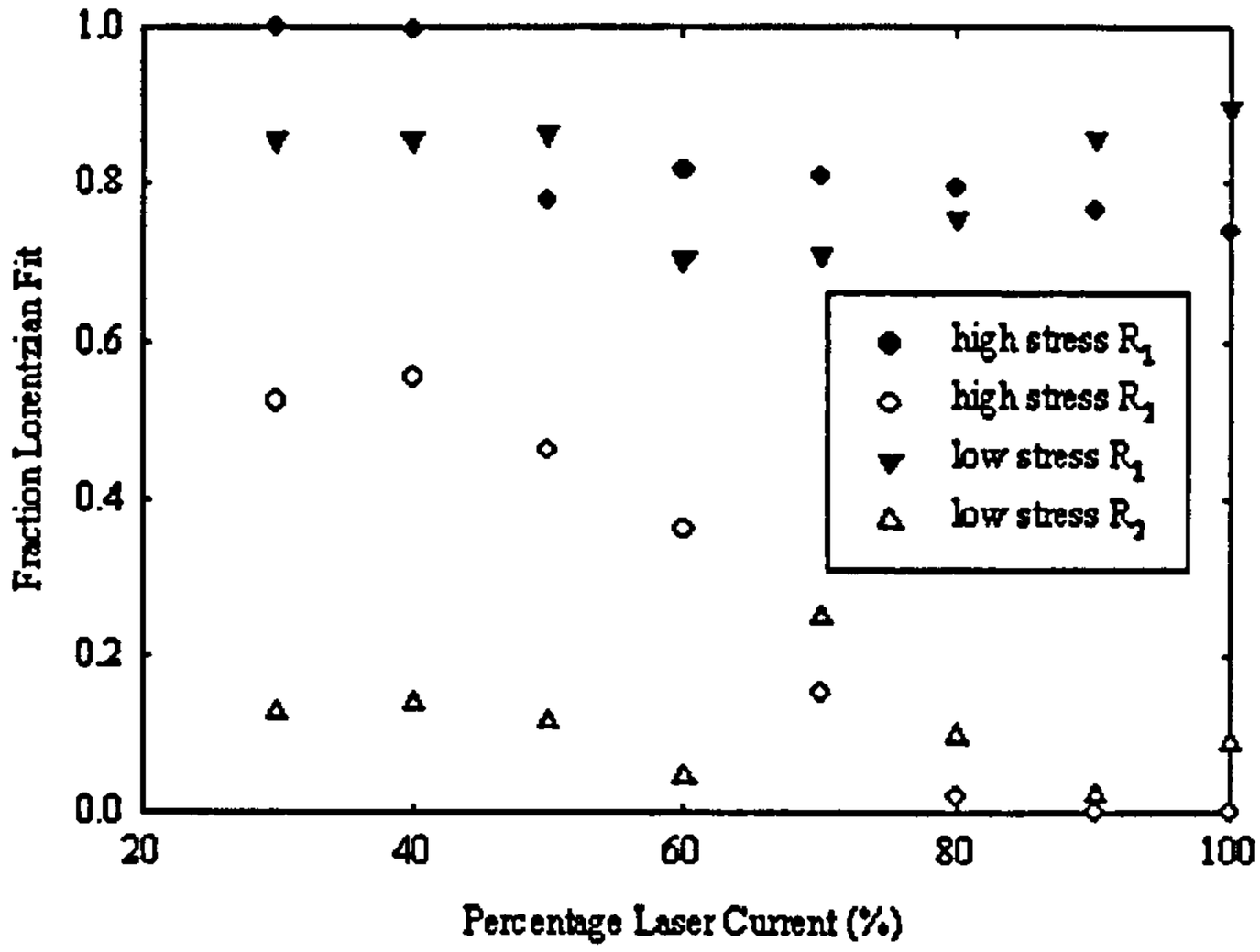

Figure 4.26. Fraction of Lorentzian peak fit with laser current for α-Al_2O_3 spectra acquired from an RT22 coated sample oxidised at 1050°C for 1000 hours. Spectra obtained from positions of high and low stress.

Figure 4.22, Figure 4.23, Figure 4.24 and Figure 4.25 show that the variation of photoluminescence peak position and corresponding biaxial stress with respect to laser current is dependent upon the initial level of stress in the thermally grown oxide. The change in peak position with increasing laser current is less if the initial stress state is low. This is reflected in the behaviour of the alumina powder with increasing laser current, Figure 4.24 and Figure 4.25. Although the peak position of the powder changes with increasing current, it only changes by 0.52cm^{-1}. In Figure 4.24, the peak position of the thermally grown oxide on the higher stress RT22 coated sample oxidised at 1050°C corresponds to a biaxial stress of 0.48GPa at a laser current of 30%. As the laser current increases, the peaks broaden and shift. At a laser current of 100%, the peaks have shifted to a position corresponding to a biaxial stress of –0.73GPa, a change of 1.21GPa. However, in the lower stress state, Figure 4.23, the initial peak position corresponds to a stress of –0.02GPa and although the peaks broaden and shift with increasing laser current, the broadening is less than in the high stress state and the peak position at 100% laser current has moved to a position corresponding to a biaxial stress of –0.74GPa, which is a change of 0.72GPa. A similar trend occurs on the CN91 coated sample, whereby the stresses in oxides, which are initially at a higher stress state, show a greater increase in stress with

increasing laser current than those which are initially at a lower stress state. The photoluminescence acquisitions with increasing laser current reveal that, for all the specimens tested, there was little change in peak position and biaxial stress when using laser currents of less than 50%. After this, the photoluminescence peak positions rapidly increased and their corresponding biaxial stresses rapidly increased in magnitude. As a consequence, stress measurements made in this work using this spectrometer employed laser currents of 50%.

4.3.9 Background Noise

In general, when acquiring data in the form of peaks it is necessary for them to be sufficiently distinct and intense from the background counts [Lonsdale 1986]. Difficulties can arise in when endeavouring to achieve this with spectroscopic techniques such as Raman spectroscopy and photoluminescence spectroscopy [Bell et al. 1998, Walton and Fairley 2005]. It is often necessary to use a relatively low laser power to reduce errors due to laser heating effects, Section 4.3.8. Longer acquisition times are therefore required in order to obtain suitable peak intensity. However, this can result in a high level of background noise which can obscure much of the data,

Figure 4.27. The spectrum shown was obtained from an RT22 coated CMSX4 superalloy sample after oxidation at 850°C for 1000 hours. A Renishaw Raman 2000 spectrometer equipped with a helium-argon laser of wavelength 514nm was used to acquire the spectrum.

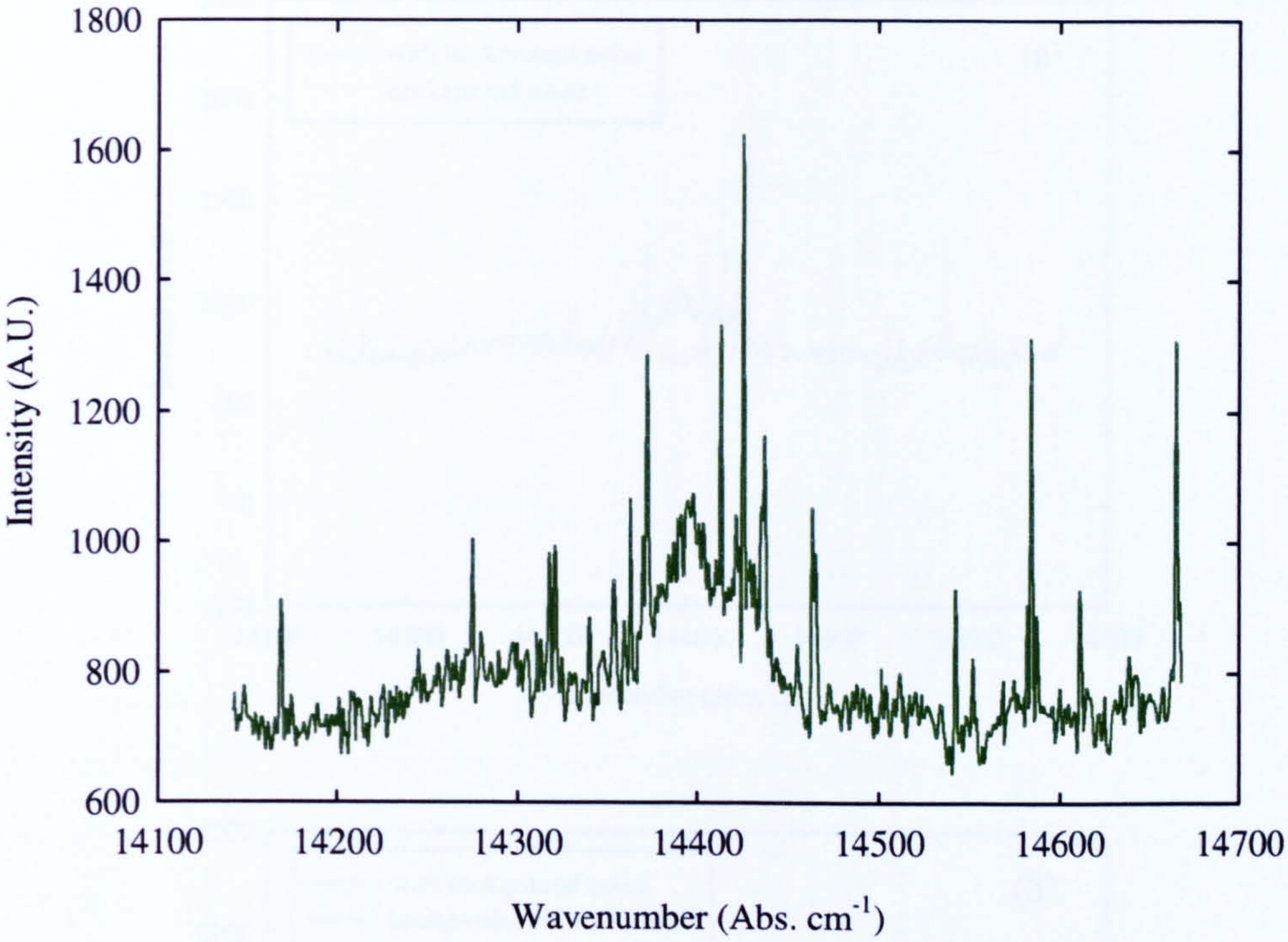

Figure 4.27. Photoluminescence spectrum acquired from an RT22 coated superalloy after oxidation at 850°C for 1000 hours.

One method of dealing with spectra containing high levels of background noise is to carry out a background scan and then subtract the background from the acquired spectra [Watkins and Brierley 1996], Figure 4.28.

A macro was written with Jones in order facilitate the background removal of spectra using the previously described method, Appendix [Jones 2008].

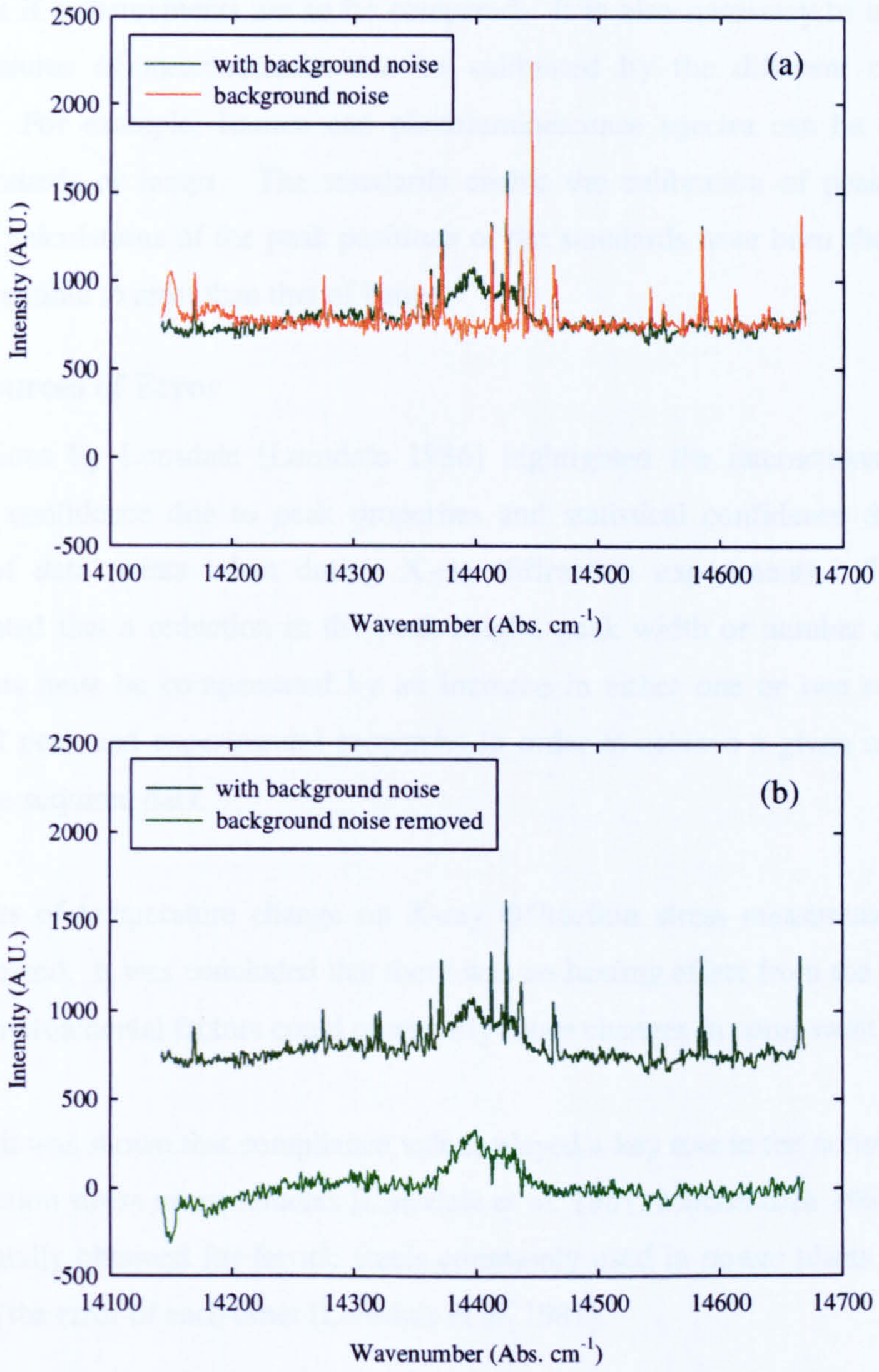

Figure 4.28. Example of background noise removal of a spectrum acquired from an RT22 coated superalloy oxidised at 850°C for 1000 hours. (a) shows the effect of background noise and (b) shows the effect of noise removal.

4.4 Summary

4.4.1 Calibration

The importance of calibration to X-ray diffraction and Raman and photoluminescence spectroscopy has been established with respect to confidence in data obtained and errors introduced by experimental technique. The limitations of calibration have been

highlighted. For example, it is necessary to understand signal degradation due to equipment if measurements are to be compared. It is also necessary to understand which features of measurements can be calibrated by the different calibration methods. For example, Raman and photoluminescence spectra can be calibrated using standards or lamps. The standards enable the calibration of peak profiles. However, calculations of the peak positions of the standards have been shown to be more susceptible to error than that of lamps.

4.4.2 Sources of Error

Investigations by Lonsdale [Lonsdale 1986] highlighted the interactions between statistical confidence due to peak properties and statistical confidence due to the number of data points taken during X-ray diffraction experiments. This work demonstrated that a reduction in the peak height, peak width or number of sample orientations must be compensated by an increase in either one or two of the just mentioned peak and experimental properties in order to achieve a given confidence level in the acquired data.

The effects of temperature change on X-ray diffraction stress measurements have been discussed. It was concluded that there was no heating effect from the technique but that environmental factors could potentially cause changes in component stresses.

Although it was shown that compliance values played a key role in the accuracy of X-ray diffraction stress measurements [Lonsdale et al. 1981, Macherauch 1966], values experimentally obtained for ferritic steels commonly used in power plants generally lay within the error of each other [Lonsdale et al. 1981].

A single silicon Raman peak was fitted with a variety of peak fitting procedures. The stress measurement data points obtained were within the minimum error of each other as quoted by De Wolf [De Wolf 1996]. This leads to the conclusion that any of the tested peak fitting procedures may be used for a single peak with a relatively linear background. This is consistent with conclusions reached by other researchers, Section 3.12.3. However, in more complex overlapping peaks, the Lorentzian fitting procedure resulted in less scatter than the Gaussian and mixed Lorentzian-Gaussian fitting procedures, with the mixed fitting procedure resulting in the most scatter.

Although it was not possible to know from the experiment undertaken, which peak fitting profile was resulted in the most correct Raman peak positions, the results indicate, that for continuity between measurements on complex peaks, the Lorentzian fitting procedure is to be preferred. This is also in agreement with conclusions reached by other researchers such as Allen and McMeeking [Allen and McMeeking 1978].

Statistical confidence in the number of measurements taken was considered for investigations in which an indication of average material properties over an area is required. It was decided that twenty data points would be sufficient to allow for outliers in measurements.

Laser spot size was investigated and it was found that the largest spot size resulted in the least scatter in stress measurements on a single crystal silicon calibration specimen and is therefore the most appropriate if the aim of an experiment is to average over an area. However, as demonstrated on a single crystal silicon standard, Figure 4.18, a longer acquisition time may have to be used to obtain a sufficient peak height. In addition, a discrepancy was found between the average stress measurements obtained with the three laser spot sizes employed. These discrepancies were attributed to local heating effects and emphasised the need for caution when selecting experimental conditions. Further, changes in photoluminescence peak positions and properties were obtained in samples containing α-alumina. These were also attributed to laser heating effects and again emphasised the need for caution with regards to experiment conditions that could introduce systematic errors through the heating the specimen or through the heating of the calibration specimen. The behaviour of materials when locally heated through an increase in laser power was found to dependent upon the stress in the materials. Removal of the background counts of the photoluminescence specimens could reduce the need for higher powers and longer acquisition times to allow sufficient peak to noise ratio for peak fitting

5 Stresses within Surface Oxides Grown on Austenitic Steel

5.1 Introduction

Components in high temperature environments such as steam pipes and headers in power plants develop an oxide scale over time [Ashby et al. 2007, Ashby and Jones 1996, Hurst et al. 1975, Viswanathan 1989]. In general, these oxides act as a protective barrier to further oxidation [Ashby et al. 2007, Ashby and Jones 1996, Hurst et al. 1975, Viswanathan 1989]. Any failure of the oxide layer can lead to enhanced oxidation of the component [Hurst et al. 1975]. Therefore, surface oxides should perhaps be considered integral to the structural integrity of such components [Hurst et al. 1975]. The stresses within oxide layers can determine their failure mechanism [Evans 1989]. These stresses can develop within the oxide as it forms. In addition, the total strain accumulated within a component can affect the oxide and it is known that the oxides are susceptible to cracking under the stress operating on the component [Schutze 1985].

The present work seeks to understand the stresses developed within growing oxides, what stresses can be accommodated and the stress redistribution within the oxide when subjected to an external load. The latter offers the potential to establish whether it is possible to use the measured strain in the oxide to interpret the strain within the substrate material. Raman spectroscopy was used to measure the stresses in the oxides, as the instrumentation can be portable and therefore be used in-situ. It was decided that two experiments should be carried out. The first experiment involved the oxidation of stainless steel samples and straining them in a bend jig. The oxide Raman peak shifts could then be correlated with strain in the substrate. The second experiment involved oxidising stainless steel samples to the same times and temperatures as the previous ones and cutting taper sections. Raman shifts were recorded along the length of the taper sections. These shifts were once again related to hydrostatic stress. This experiment was carried out in order to simulate the effects of spallation and to therefore verify, whether the measurement of stresses in oxide layers of plant components could be correlated with substrate strain and so offer a measure of the latter.

5.2 Substrate under Tension

Four Type 316 austenitic stainless steel samples were oxidised for times of one hour to four hours and strained in a three point bend jig. Raman spectra were recorded as the samples were strained and the peak shifts analysed. The oxide peak shifts were related to oxide stress. These shifts and stresses were then related to the tensile strain applied to the substrate.

5.2.1 Experimental Procedure

Four specimens of Type 316 stainless steel (dimensions: 45mm×10mm×0.4mm, nominal compositions, Table 5.1, were polished on one face to 1μm grit finish The specimens were oxidised in a tube furnace in air at 950°C for 1, 2, 3, and 4 hours and then removed and left to cool in air. Although the oxidation temperature was higher than that which the material would normally experience in plant, it was chosen in order to accelerate oxidation. The specimens were then polished on one face and a strain gauge attached. They were placed in a three point bend jig with the strain gauged on the compressive face. A strain was applied to the specimens and the strain gauge used to measure the magnitude of the strain on the top-face of the specimens. Thus the strain applied to the metal could be correlated with a Raman oxide peak shift.

Table 5.1. Nominal composition of Type 316 stainless steel (wt. %).

C	Si	Mn	P	Cr	Mo	Ni	Al	B	Sn	Ti	S	N	Fe
<0.15	<1.00	<2.00	<0.045	17-19	-	8-10	-	-	-	-	<0.03	-	Bal.

The characteristics of the oxides and the associated stresses were recorded using a Renishaw System 2000 Raman spectrometer equipped with a helium neon laser (λ = 633nm). A 50x magnification lens was used. The power was measured to be approximately 2.4mW with a power meter. All Raman spectra were calibrated using silicon and the peaks were analysed using a Lorenzian peak fitting procedure as described in Section 3.12.3 [Allen and McMeeking 1978, De Wolf 1996]. Spectra were acquired for a total of 1000 seconds.

In addition, to characterise the oxides, slots of 20μm×10μm×5μm were milled into the oxide/substrate using an FEI FIB 201 focused ion beam work station operating using a

gallium liquid metal ion source accelerated to 30keV. The work station was also used to provide secondary electron images.

The type of oxide was characterisation using secondary ion mass spectroscopy (SIMS) [Flewitt and Wild 2003]. The spectra were recorded using an in-house magnetic sector SIMS fitted with an FEI gallium ion source.

5.2.2 Calibration Verification

In order to correlate the magnitude of the compressive strain applied to the back-face strain gauge to the tensile strain applied to the oxide, a strain gauge was fixed to both faces of a Type 316 stainless steel sample and incremental loads were applied. A graph of the two sets of measured strains with applied load can be seen in Figure 5.1.

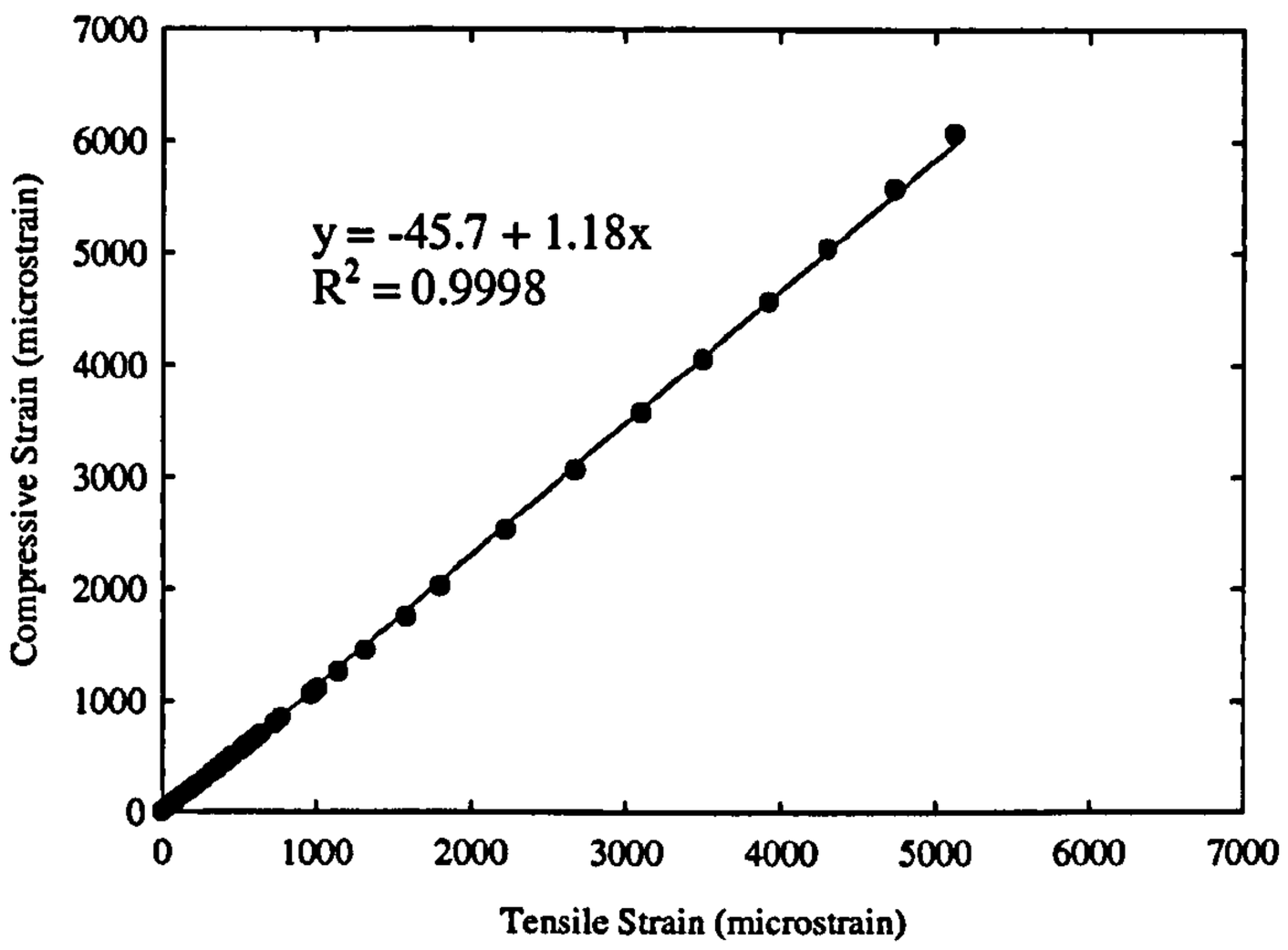

Figure 5.1. Measured strains for top and back face strain gauges against applied load. R^2 is the correlation coefficient [Boas 1983].

The relationship between strain gauges was used to calibrate the back-face strain gauge to take compression effects from the bend jig's third point into account. The quoted accuracy for the manufacturers was up to 4000 microstrain [RS Catalogue 2005]. It was therefore not possible to assess whether discrepancies after 4000 microstrain were due to compression on the back face strain gauge or due to inaccuracies in both strain gauges.

5.2.3 Results

A typical Raman spectrum obtained from the oxide of a Type 316 stainless steel specimen can be seen in Figure 5.2.

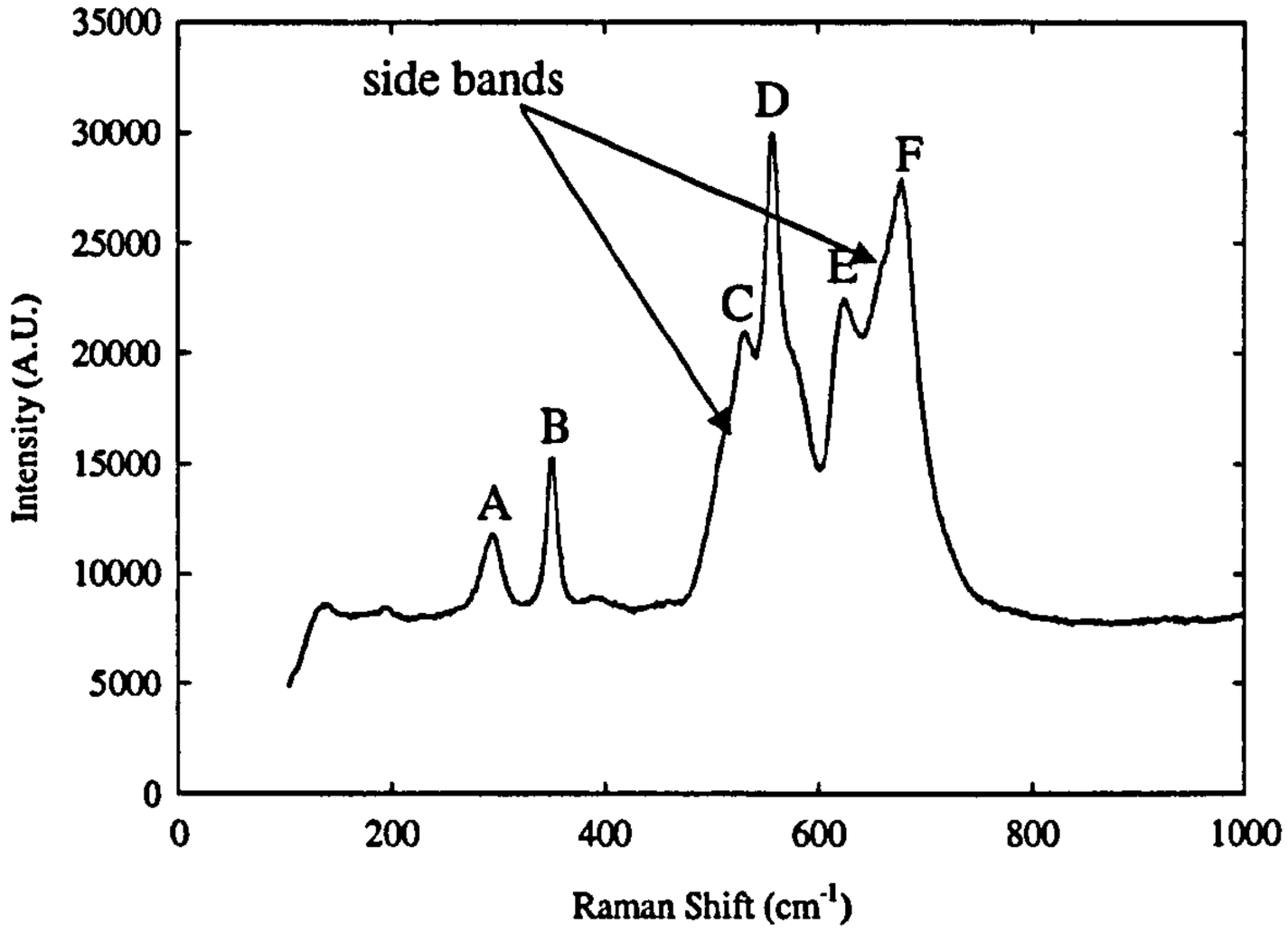

Figure 5.2. Raman spectrum of Type 316 stainless steel taken after oxidation of three hours at 950°C.

Peaks A, B, C, D, and E have been identified by Mougin et al. as being Cr_2O_3 [(b)Mougin et al. 2001]. Peak F and the remaining side bands can be attributed to a complex spinel being present [Pickard 2000]. A spinel is defined as an oxide whose structure is $A^{2+}B_2^{3+}O_4$ where A and B are metal ions [Flinn and Trojan 1986]. Due to a range of spinels having peaks between $650cm^{-1}$ and $800cm^{-1}$ [Pickard 2000], it is difficult to derive an exact composition. However, possible spinels are a combination of iron nickel and chromium such as $NiFe_{0.5}Cr_{1.5}O_4$ or $MnFe_2O_4$ [Pickard 2000].

SIMS spectra were acquired whilst the oxide was being etched with gallium ions at 25keV and 2nA in collaboration with Dr. Tom Scott, University of Bristol. This allowed a depth profile to be produced. A SIMS depth profile revealed a high percentage of chromium in the oxide, Figure 5.3. Contributions from the oxide layer and base metal can be separated by analysing the intensity of the oxygen signal with depth. A cross-section of oxide and substrate was produced using focused ion beam milling and an image of SIMS intensities across the oxide revealed the composition to

be as follows, Figure 5.4. Figure 5.3 and Figure 5.4 both indicate a layer of magnesium at the surface of the oxide with chromium below. Iron is present throughout the thickness. The SIMS results therefore indicate that Peak F is more likely to result from $MnFe_2O_4$ than $NiFe_{0.5}Cr_{1..5}O_4$.

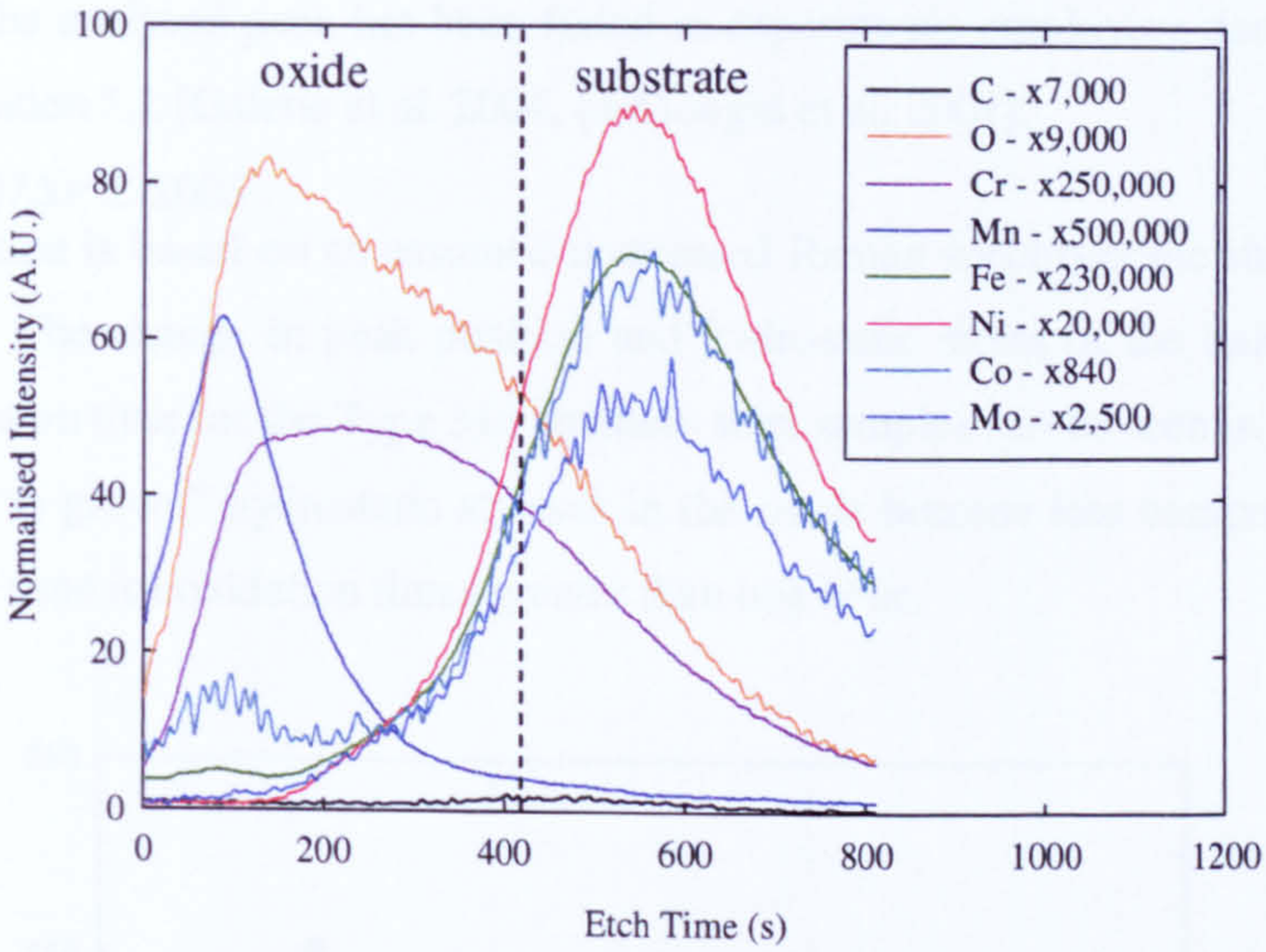

Figure 5.3. The composition of the surface oxide with etch time (depth) on a Type 316 stainless steel specimen after one hour oxidation at 950°C using secondary ion mass spectroscopy.

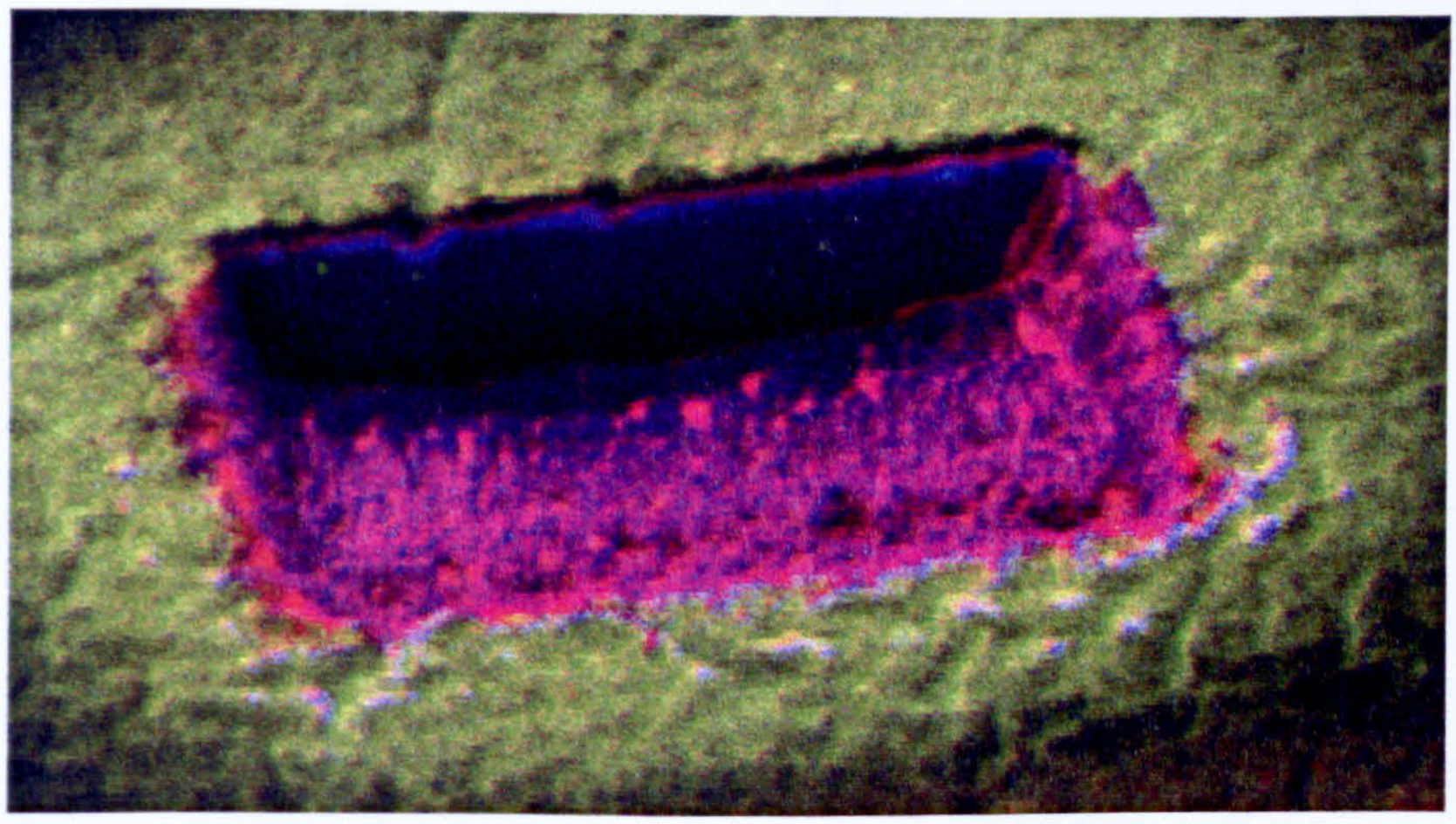

Figure 5.4. Intensity image of compositional intensities obtained from a FIB milled section through the oxide of Type 316 stainless steel oxidised for three hours at 950°C. Chromium is indicated with red, magnesium with green and iron with blue.

The Cr_2O_3 peak at approximately 549cm^{-1}, Figure 5.2, was selected for stress analysis, as it was the most documented [Birnie et al. 1992, Galerie et al. 2004, (d)Mougin et al. 2001] and the has the most linear relationship of Raman shift with applied strain (Section 4.3.5) and stress of the chromia peaks [Galerie et al. 2004, (d)Mougin et al. 2001]. The correlation between Raman peak shift and hydrostatic stress in Cr_2O_3 for the peak the analysed peak has been found in experiments employing diamond anvil cells, Equation 5.1 [Galerie et al. 2004, (d)Mougin et al. 2001].

$$\sigma = -0.307\Delta\nu \pm 0.005 \qquad 5.1$$

This equation is based on an assumed unstressed Raman spectroscopic shift value of 549cm^{-1}. The change in peak position and hydrostatic stress of the analysed peak with oxidation time for the Type 316 stainless steel samples can be seen in Figure 5.5. Here the "as grown" hydrostatic stresses in the oxide become less compressive with increasing time for oxidation times greater than one hour.

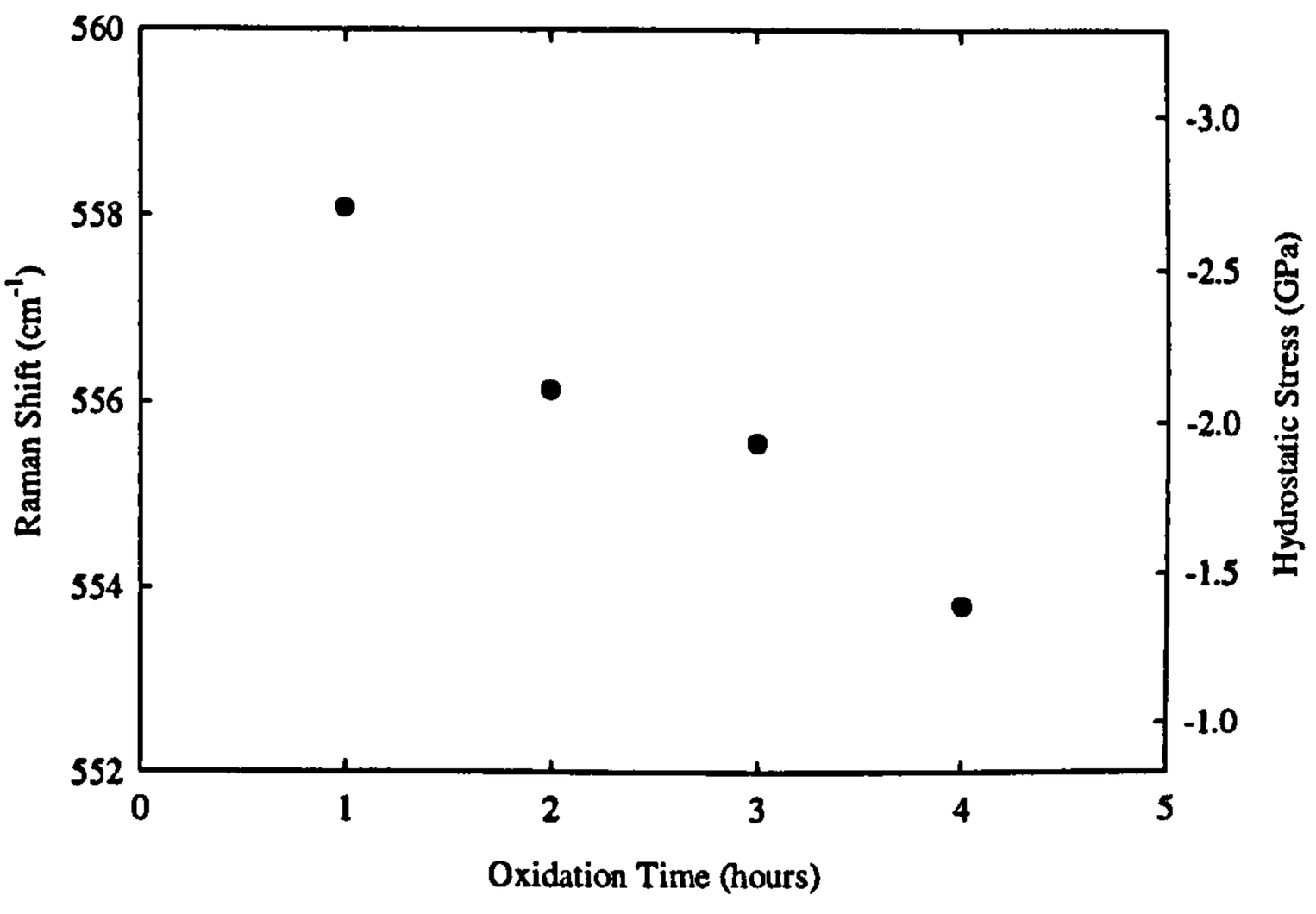

Figure 5.5. Change in Cr_2O_3 hydrostatic stress and Raman shift with oxidation time.

The change in Cr_2O_3 hydrostatic stress and Raman peak shifts with applied strain in the stainless steel samples can be seen in Figure 5.6. The Raman shifts and values of the hydrostatic stresses show little or no variation for the first applied 1000 microstrain, with the exception of the specimen which had been oxidised for 1 hour. However, at greater applied microstrains, the Raman shifts progressively decrease and their corresponding hydrostatic stresses become steadily less compressive. All the samples tend to a similar value of approximately –0.8GPa at approximately

6500microstrain. The plots of Raman shift against applied strain to the oxide do not result in a convergence at a hydrostatic stress of 0GPa at a corresponding Raman shift of 549cm^{-1} as might have been expected for an oxide stress relieving. There are several possibilities why this could be the case. First, there may be inaccuracies in the calibration for zero stress in chromia. Second, there may be laser heating effects inducing a stress in the oxide. Third, the oxide may not be stress free after the applied strain. Cracks in the oxide may result in the oxide only partially stress relieving. Spallation of oxide islands may still leave other oxide islands which contain stresses.

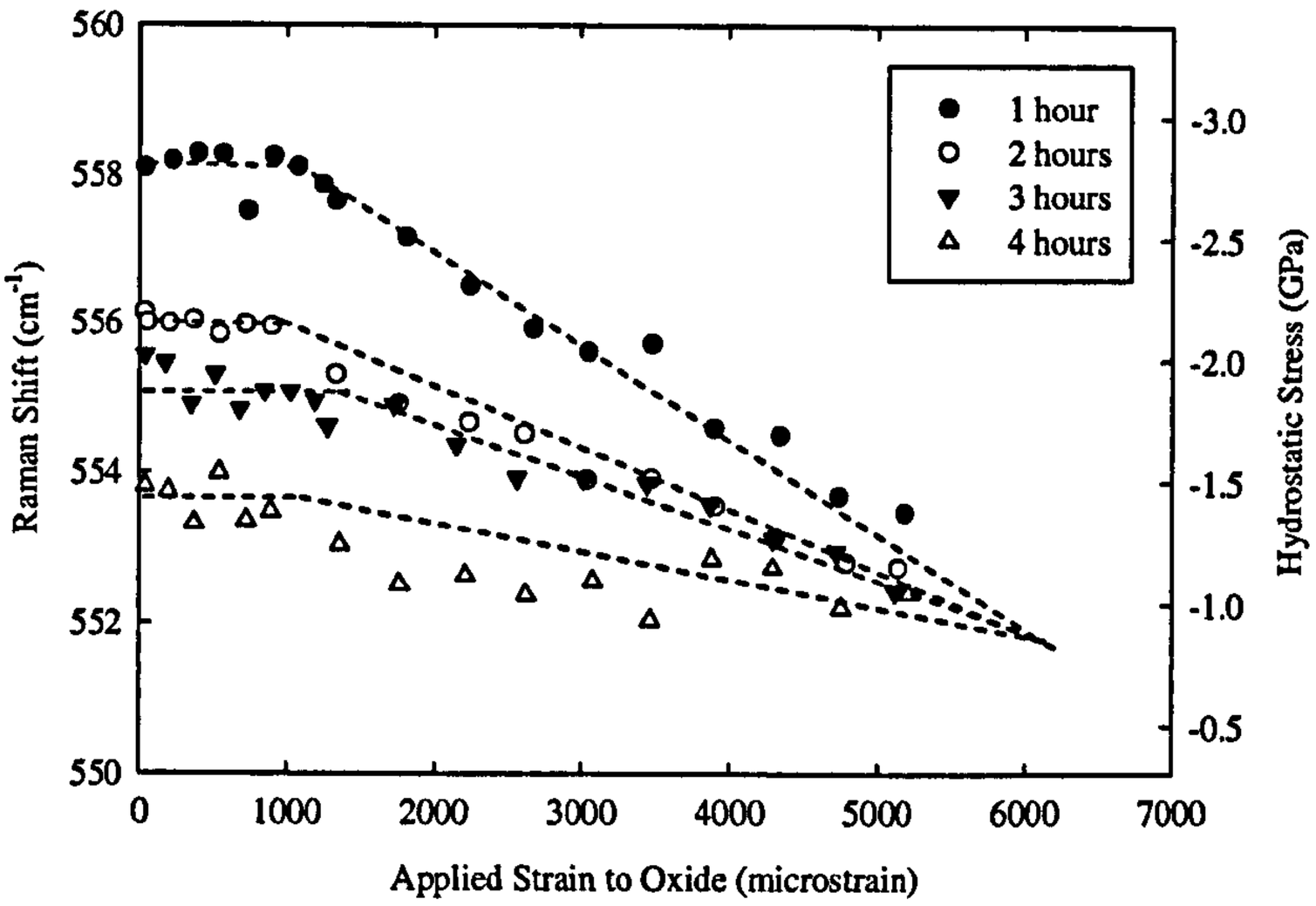

Figure 5.6. Raman peak shifts and hydrostatic stress with applied strain in Cr_2O_3 produced by oxidation times of 1, 2, 3 and 4 hours.

5.3 Oxide Taper Sections

To investigate the effects of spallation on stresses in oxide layers, taper sections were made through oxide layers on four heat treated Type 316 austenitic stainless steel specimens. Raman spectra were recorded along their length and the Raman shifts were then related to stress.

5.3.1 Experimental Procedure

Four Type 316 stainless steel specimens were polished to 1μm using silicon carbide paper and heat treated for 1 to 4 hours at 950°C. The composition of the steel and oxide is the same as described in Section 5.2.1. The specimens were then tilted to 5° and a section was tapered by focused ion beam milling using a FEI Strata FIB201

system, Figure 5.7. The dimension of the taper removed was 20μm across, 40μm long and 3μm deep. A secondary electron image of one of the sections can be seen in Figure 5.8.

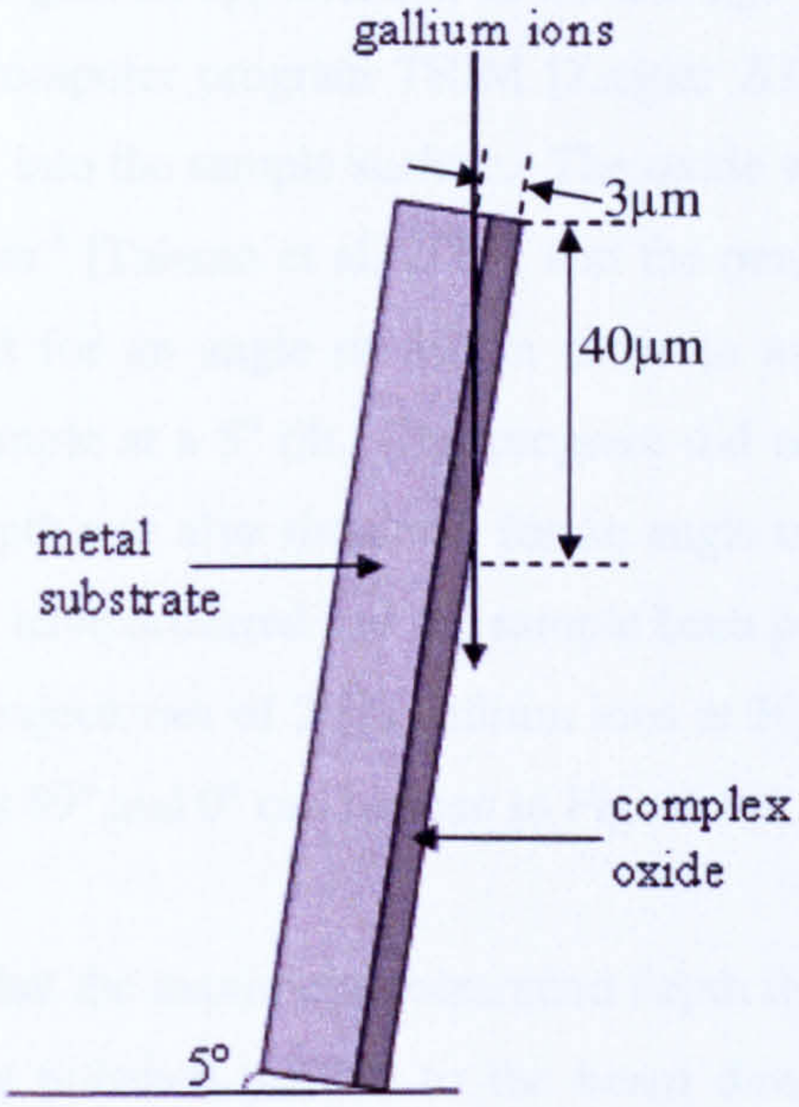

Figure 5.7. Creating a taper section through the substrate and oxide using focused ion beam milling.

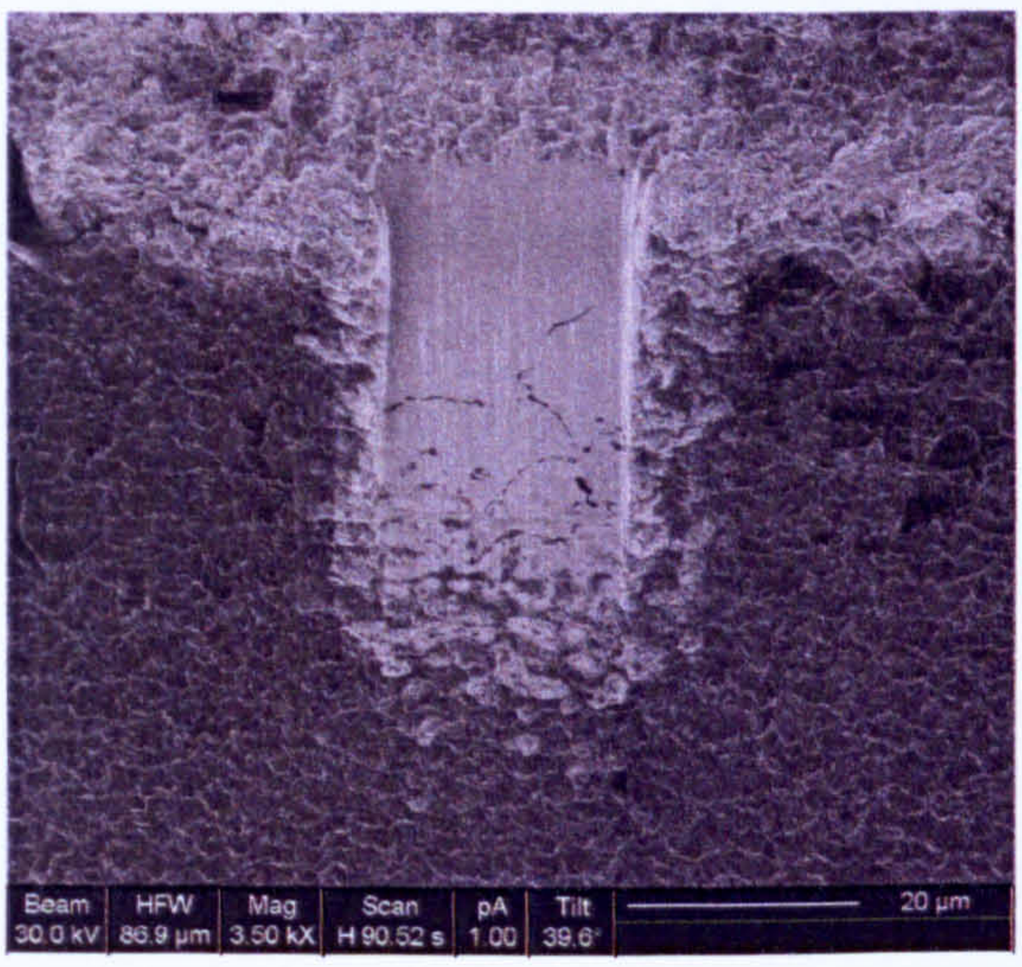

Figure 5.8. Focused ion beam image of a tapered section of oxidised sample. Sample is at a 40° tilt whilst taper section is at a tilt of 45° to the incident ion beam.

This method was chosen so as to avoid any induced surface damage and stress effects from the gallium ions such as ion channelling [Matteson et al. 2002, Phillips et al. 2000] and to obtain a surface area of sufficient size from which stress measurements could be made. To gain an appreciation of the damage induced in the sample by the gallium ions, the computer program TRIM [Ziegler 2003] was used to simulate the damage introduced into the sample surface. The oxide was modelled as Cr_2O_3 with a density of 5,210kgm^{-3} [Takano et al. 2001] and the penetration depth of the gallium ions was simulated for an angle of 89° in order to as this best approximated the polishing of the sample at a 5° tilt. The program did not allow for an angle of 90°. The penetration depth was also simulated for an angle of 0°, in order to compare the damage that would have occurred had the sample been perpendicular to the ion beam. In both cases, the trajectories of 2000 gallium ions at 30keV were modelled. Images of the trajectories at 89° and 0° can be seen in Figure 5.9.

The models show that the maximum penetration depth the of gallium ions in chromia, for a sample being polished parallel to the beam direction is approximately 50Å. However, for a sample being polished perpendicular to the beam direction, the penetration depth of the gallium ions is over 250Å. This shows that less damage is created when polishing parallel to the beam direction.

As with the investigation described in section 5.2.1, a Renishaw System 2000 Raman spectrometer equipped with a helium neon laser (λ = 633nm) was used. The laser was focused on a spot of approximately 1μm diameter using a lens of 50x magnification. As with section 5.2.1, the power was measured to be approximately 2.4mW with a power meter. Scans of 30 seconds were used and the system was calibrated with a silicon standard prior to each sample.

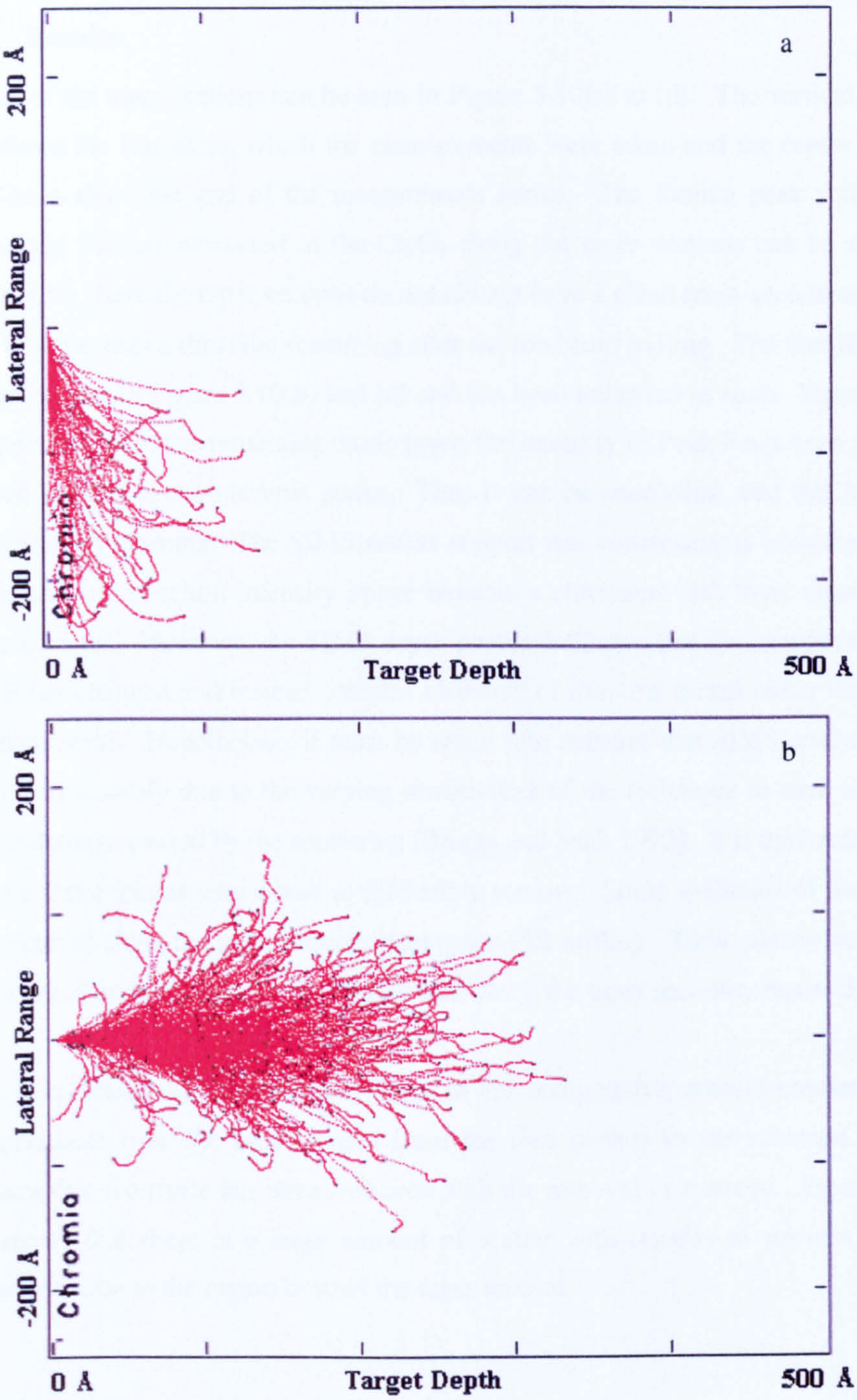

Figure 5.9. Trajectories of gallium ions into Cr_2O_3 at a sample angle of (a) 89° and (b) 0° to the incident beam.

5.3.2 Results

Images of the taper sections can be seen in Figure 5.10(a) to (d). The vertical cross-hair shows the line along which the measurements were taken and the centre of the cross-hairs show the end of the measurement series. The Raman peak shifts and hydrostatic stresses measured in the Cr_2O_3 along the taper sections can be seen in Figure 5.11. Here the taper sections do not always have a clean cross-section and that there is sometimes a thin film remaining after the ion beam milling. The thin film can clearly be seen in Figure 5.10(b) and (d) and has been indicated as such. Figure 5.12 is a spectrum from this remaining oxide layer; the intensity of Peak F has been greatly reduced relative to the chromia peaks. Thus it can be concluded, that this layer is predominantly chromia. The SIMS results support this conclusion as both the depth profile and cross-section intensity image indicate a chromium rich layer adjacent to the base metal. However, the SIMS depth profile indicates that the composition of Peak F has changed and instead contains elements of iron and nickel rather than iron and manganese. Nonetheless, it must be taken into account that SIMS analyses are difficult to quantify due to the varying sensitivities of the technique to each element and the damage caused by the sputtering [Briggs and Seah 1992]. It is the hardness of chromia that explains why it was so difficult to remove. Some spallation of the oxide also occurred along the taper sections during the FIB milling. These places have also been marked on the graphs of the Raman shift along the taper sections, Figure 5.10.

It has been established that the magnitude of the compressive stress decreases in all the specimens over the tapered area from the free surface to the substrate. This indicates that the oxide has stress-relieved with the removal of material. Figure 5.11 also shows that there is a large amount of scatter with regards to stresses in the untapered oxide in the region beyond the taper section.

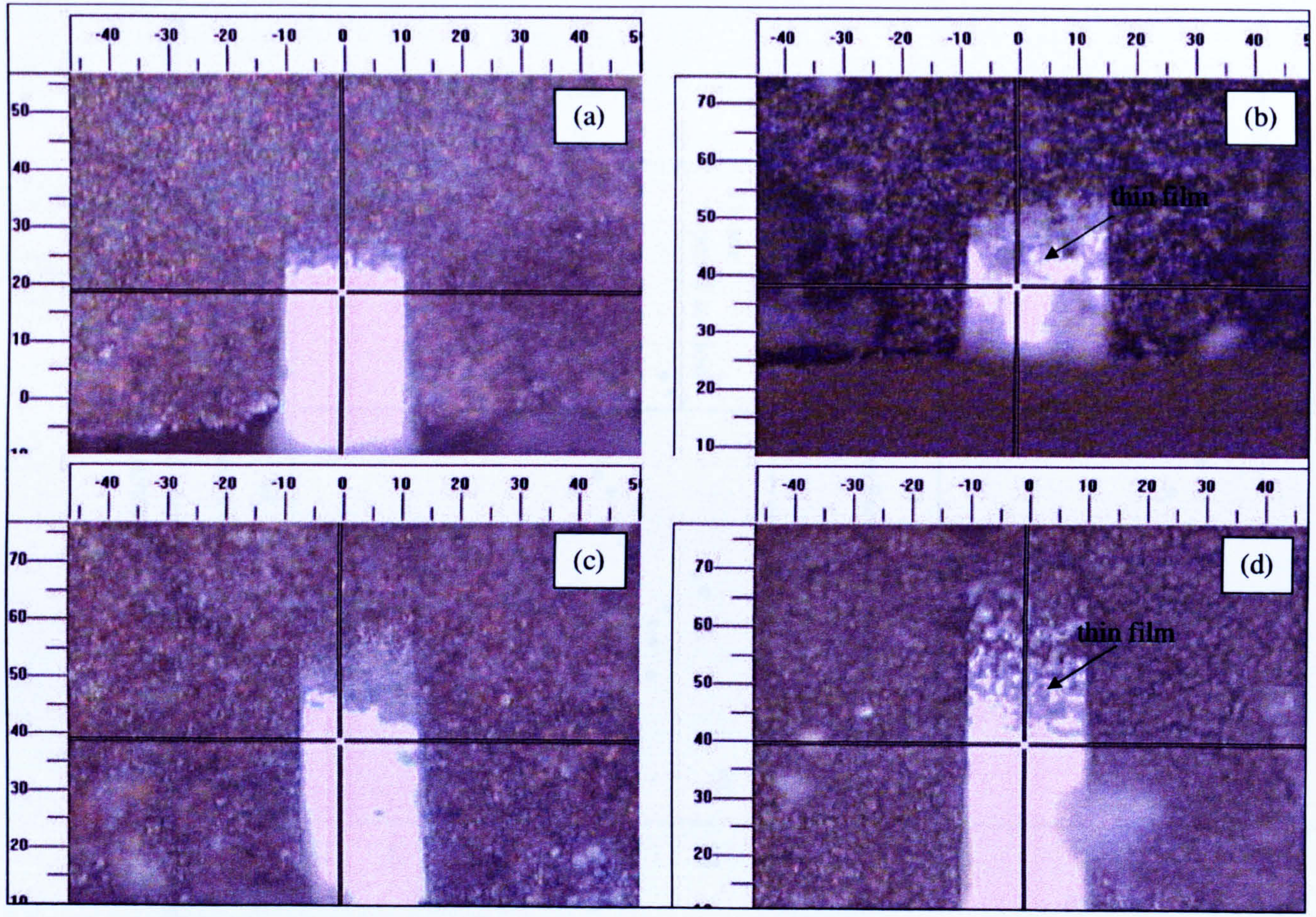

Figure 5.10. Taper sections for specimen oxidation times of (a) 1 hour, (b) 2 hours, (c) 3 hours and (d) 4 hours.

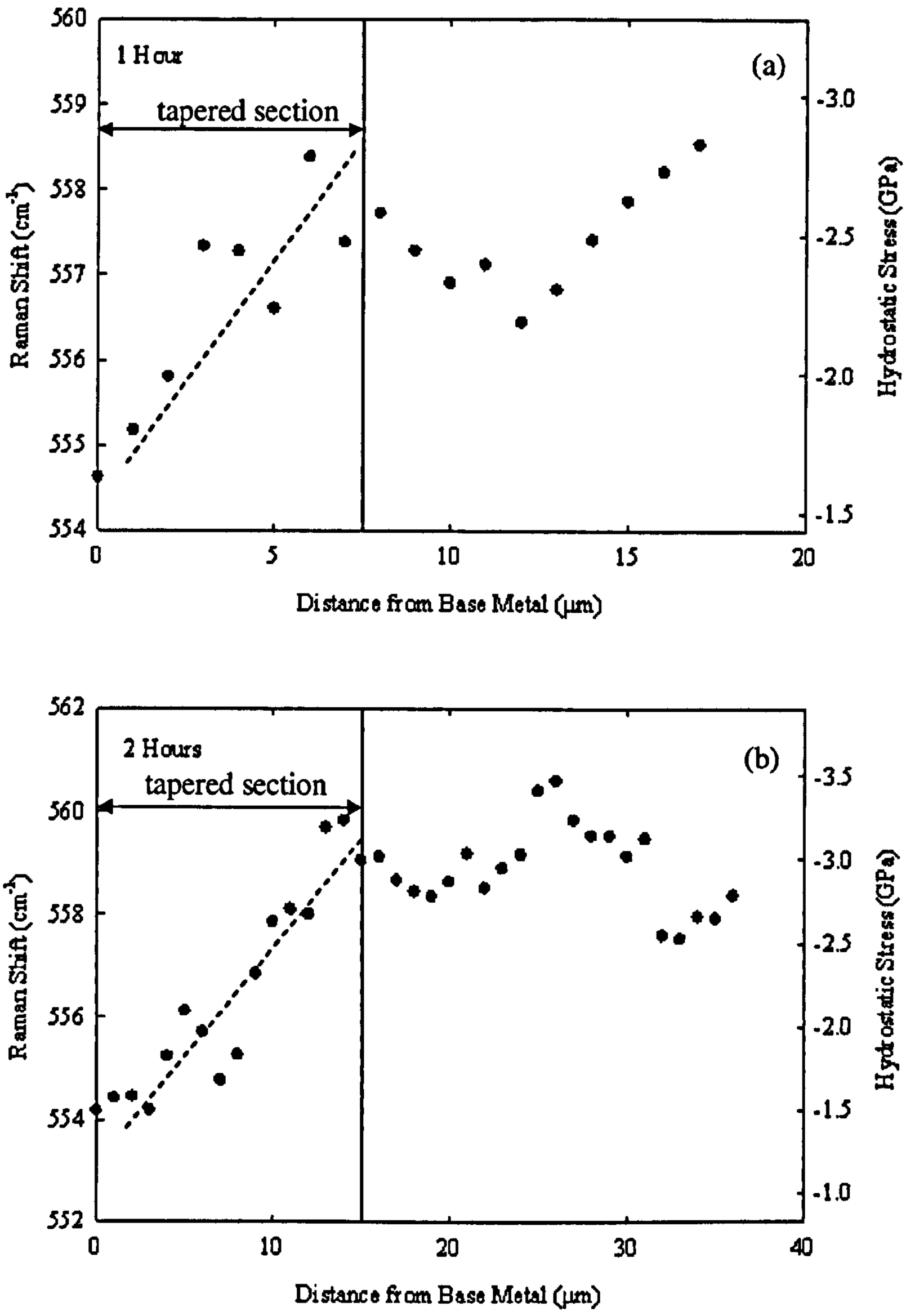

Figure 5.11(a) and (b). Raman shift and corresponding hydrostatic stress in oxide of tapered specimens with oxidation times of one hour (a) and two hours (b).

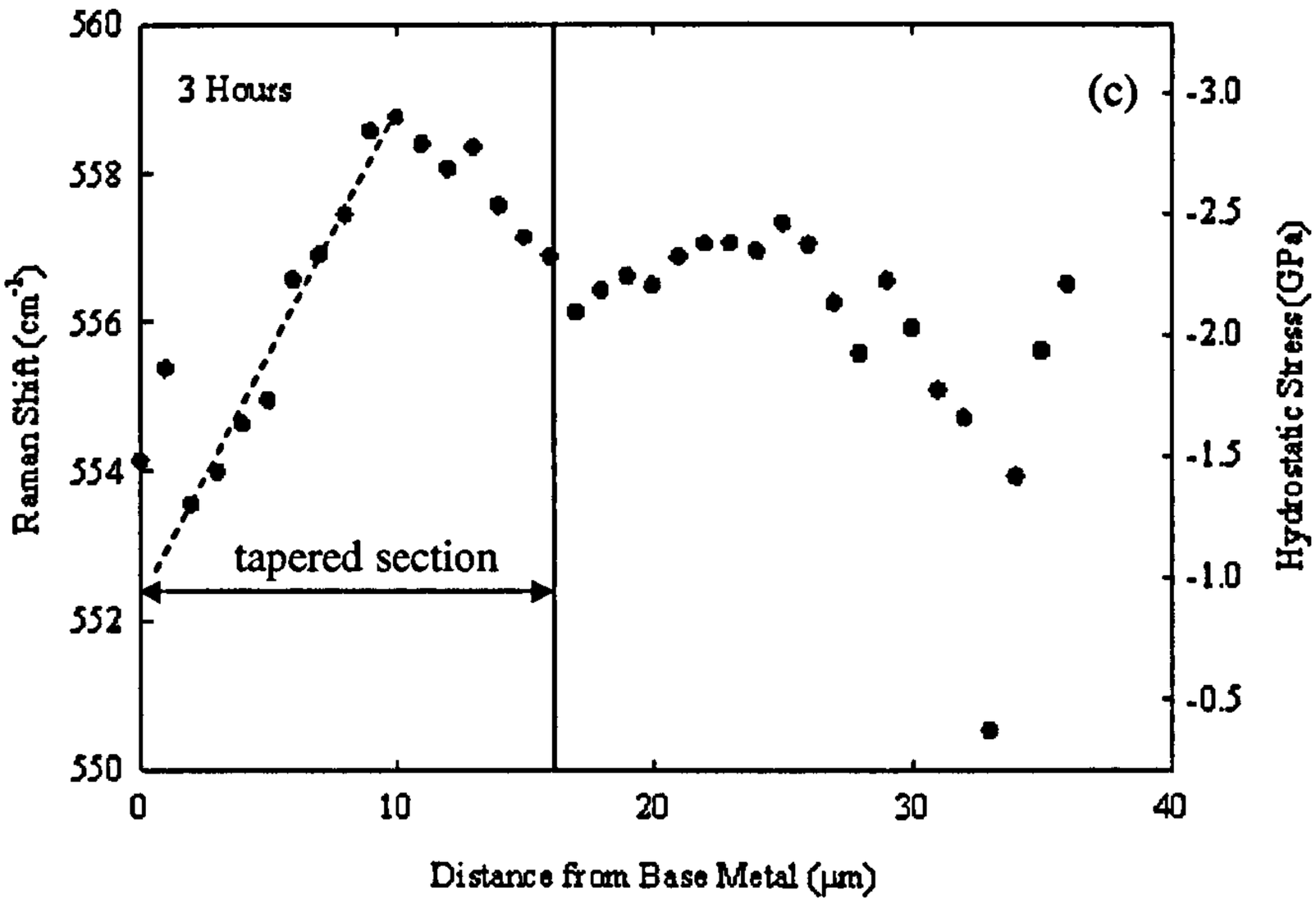

Figure 5.11(c) and (d). Raman shift and corresponding hydrostatic stress in oxide of tapered specimens with oxidation times of three hours and four hours.

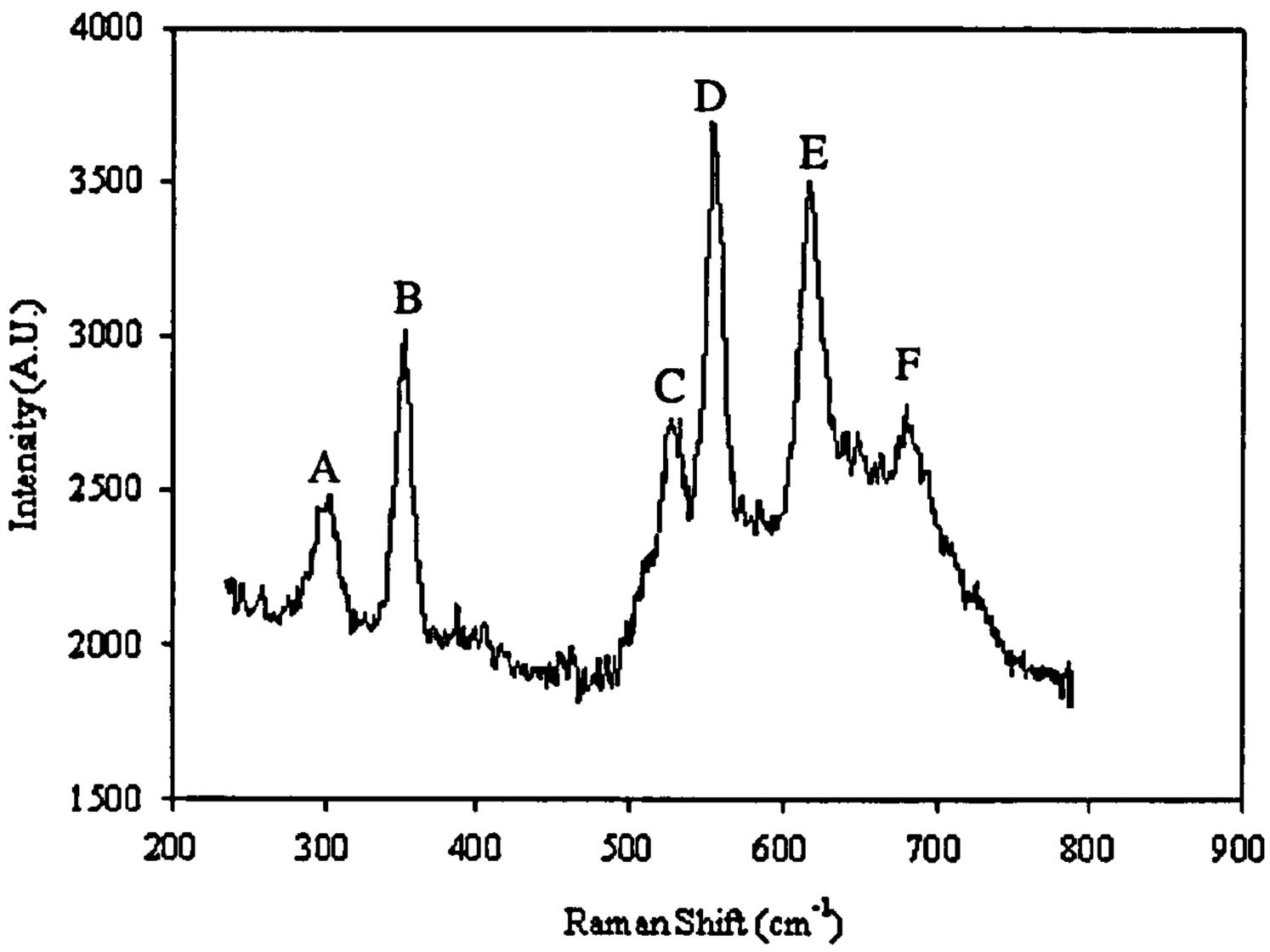

Figure 5.12. Raman spectrum of Cr_2O_3 acquired at 3μm from the base metal.

5.4 Summary

It has been possible to measure residual strains and stresses in oxides grown on a polycrystalline, austenitic steel. Hydrostatic stresses have been measured for "as grown" oxides; grown for different times and then strained. It has been observed that the stresses are dependent upon oxidation time, thickness and the level of strain in the substrate. Hydrostatic stresses have been measured in tapered oxide sections. The removal of material was found to result in stress relieving of the remaining oxide. The effect of spallation on the measured stresses has been observed in the areas of the taper sections where spallation has occurred. Scatter in the stress measurements of the "as grown" oxide has also been observed. Thus, when seeking to use the measurement of residual stresses in oxide layers as a means of understanding the stresses and strains in the substrate, the characteristics of the oxide must also be considered.

6 Stresses within Surface Oxide Grown on Ferritic Steel

The Raman shifts of an oxide formed on a ferritic steel substrate were measured with applied strain in order to investigate whether Raman spectroscopy could be used to monitor the strain or stress in the substrate. The Raman shifts obtained from the oxide were then converted to hydrostatic stress.

6.1 Experimental Procedure

An iron 3% silicon specimen was oxidised at a temperature of 650°C for 2 minutes and air cooled, Table 6.1. This formed a coherent oxide of the order 0.5μm in thickness. As with the Type 316 stainless steel specimens described in Chapter 5 - Stresses within Surface Oxides Grown on Austenitic Steel, the specimen was then polished on one face and a strain gauge attached. Next, it was placed in a three point bend jig (with the strain gauged side facing down) so that the strain applied to the metal could be correlated with a Raman oxide peak shift.

Table 6.1. Composition of iron 3% silicon steel, wt.% [Bodycoat 2004].

C	Si	Mn	P	Cr	Mo	Ni
0.05	3.39	0.08	0.013	0.04	<0.01	0.02
Al	B	Sn	Ti	S	N	Fe
0.02	<0.005	0.09	<0.005	0.026	0.009	Bal.

A Renishaw Raman 2000 spectrometer with a helium neon laser of wavelength 633nm was used to acquire the spectra. The lens magnification was 50x and the laser power, measured with a power meter, was approximately 2.4mW. All spectra were calibrated with a silicon standard. Peak fitting of the spectra was carried out using a Lorentzian fit with linear background subtraction with the Pisces program.

6.2 Oxide Formed

A spectrum of the oxide formed on the iron 3% silicon, Figure 6.1. This is consistent with that for haematite, Fe_2O_3 [Massey et al. 1990, Shebanova and Lazor 2003, Shim and Duffy 2002].

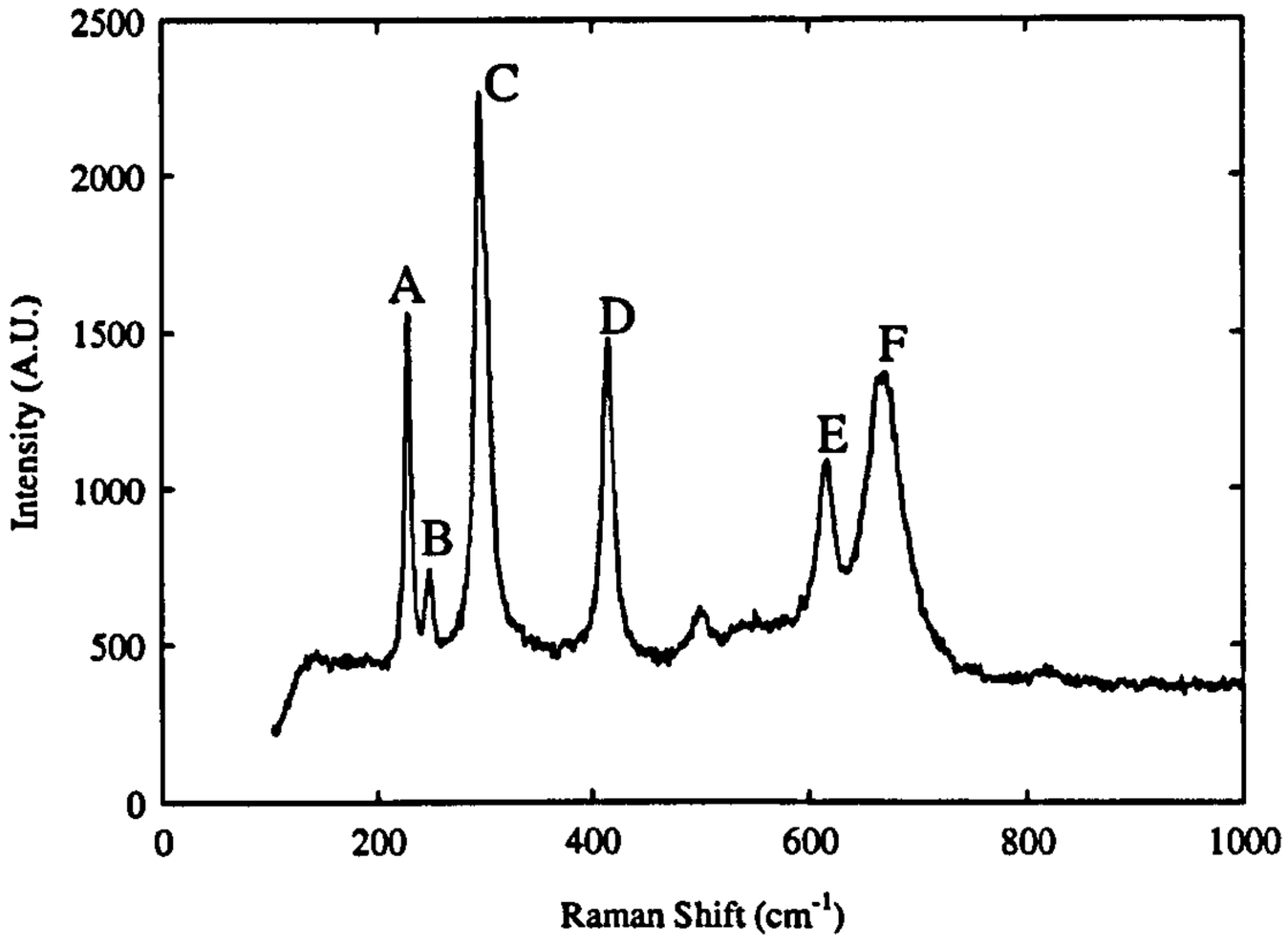

Figure 6.1. Spectrum of oxide formed on iron 3% silicon steel.

6.3 Stress in Haematite

It was decided to concentrate on the peak marked D, Figure 6.1, for the stress measurement, as it did not overlap with any other peak in this spectrum. In this work, the correlation between hydrostatic stress and Raman shift in haematite has been found to be as follows, Equation 6.1.

$$\sigma(GPa) = -0.31\Delta\nu(cm^{-1}) \pm 0.006 \qquad 6.1$$

The equation was derived from the relationship between the Raman shift of haematite powder under hydrostatic pressure in an experiment performed by Shim and Duffy with the stress-free value of haematite having a Raman shift of 408cm^{-1} [Shim and Duffy 2002]. The error was derived from the scatter in the measurements. The gradient was calculated for the first 10GPa of applied pressure. As the relationship between Raman shift and applied pressure is not linear, it was considered prudent for this work to calculate the approximately linear relationship for the window of stress values that might have been achieved. The centre of the data points were used to calculate the gradient and the error.

6.4 Results

The correlation between Raman shift and hydrostatic stress with respect to the strain applied to the oxide can be seen in Figure 6.2. The back-face strain gauge was calibrated using the relationship found in Section 5.2.2.

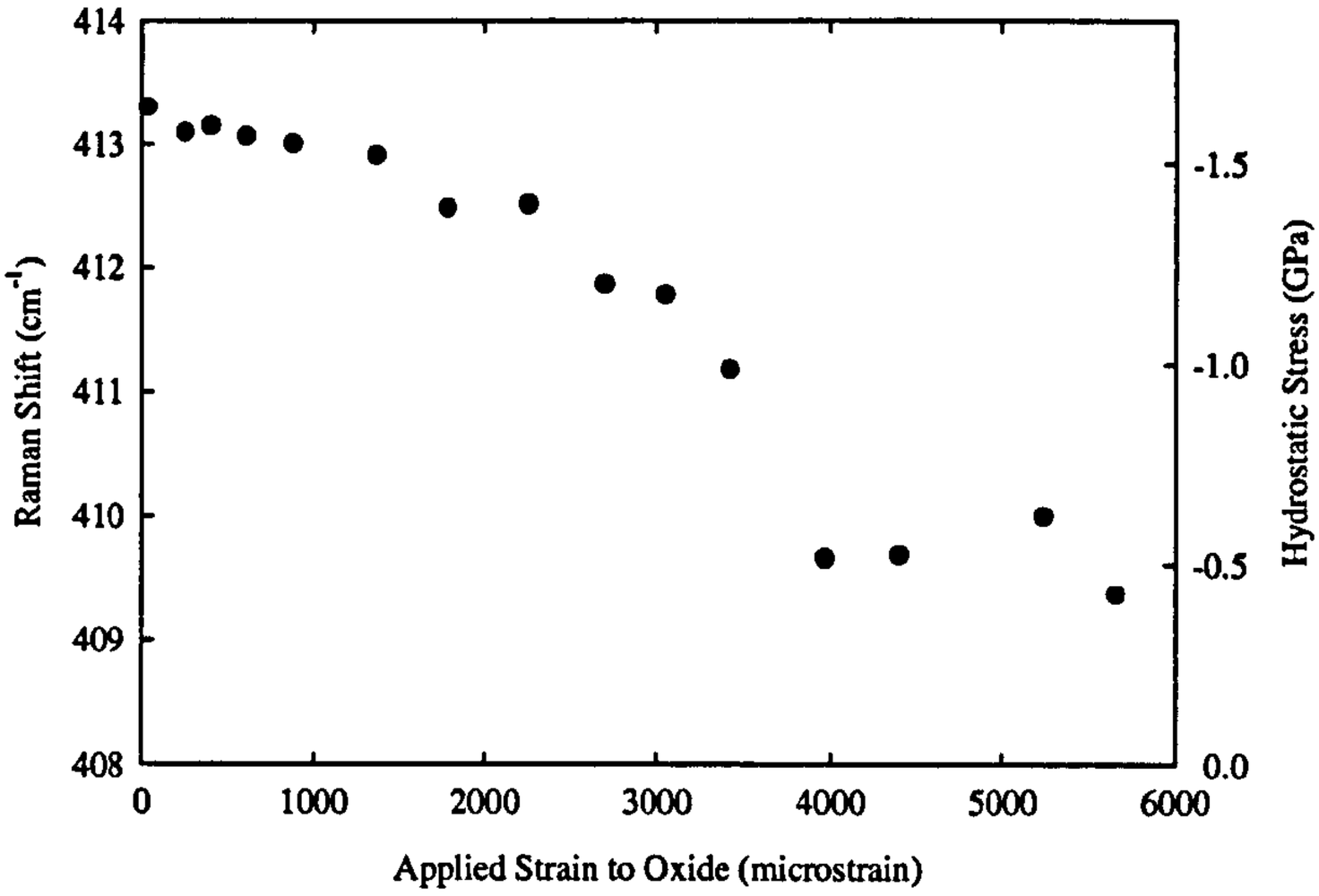

Figure 6.2. Raman shift and hydrostatic stress against strain applied to the oxide grown on the iron 3% silicon steel sample.

Figure 6.2 shows that the stresses in the "as grown" oxide are compressive. There is a progressive decrease in the Raman spectral shift up to approximately 3000 microstrain corresponding to a decrease in compressive stress. However, in the range of 3000 to 4700 microstrain, the decrease in Raman shift and corresponding hydrostatic stress becomes rapid until a constant value of approximately 409cm^{-1} to 410cm^{-1} or –0.4GPa to –0.6GPa is obtained. The hydrostatic stresses measured in the haematite were lower in magnitude to those measured in the chromia. The hydrostatic stresses measured in the chromia of the oxide grown on the Type 316 stainless steel showed displayed a linear relationship with applied strain at applied strains greater than approximately 1000microstrain. This was not the case with the hydrostatic stresses measured in the haematite, which did not display any linear behaviour of hydrostatic stress with applied strain.

6.5 Summary

Stresses have been measured in an oxide formed on a ferritic steel substrate. It has been shown that changes in Raman shift can be measured with applied strain to the substrate and therefore oxide. Corresponding hydrostatic stresses have also been calculated for the Raman shifts. There was no linear relationship between the strain applied to the substrate and Raman shift/hydrostatic stress of the oxide.

7 Ferritic Steel Edge Quenched Plate

7.1 Introduction

In general, it is necessary to have an understanding of the through-section stress distribution in a component to be able to assess the structural integrity [R6 2001, McDonald et al. 2005]. This includes both primary and secondary stresses. For example, in the case of weldments, complex stress profiles develop both with position on the surface and through the cross-section of the material, Chapter 8 - Spatial Resolution and Length Scale Investigations of Techniques on a Ferritic Steel Butt Welded Pipe. An example is the assessment of repair welds [McDonald et al. 2005] which is described in Section 2.5.3. A strategy to underwrite high integrity repair welds made on plant is proposed based upon knowledge of the surface and through-section stresses. Indeed, the strategy is only viable if surface stresses can be related to through-section stresses. As a consequence, the inter-relationship between near surface and through-section stresses developed in a ferritic A533B plate with a known induced residual stress profile was considered. The geometry and preparation procedure selected provides an experimental model to address these aspects. Stresses measured with different length scales have been compared with prediction made by finite element modelling. Additionally, investigations were undertaken to assess whether the stress measurement in the surface oxide of the plate could be used as an indication of the magnitude or variations of the stresses in the surface metal.

The surface stress measurements were carried out using X-ray diffraction. Neutron diffraction was employed for the through-section measurements. Raman spectroscopy was used for stress analysis of the surface oxide. Finite element analysis was used to predict the stress variations through the plate and support the interpretation of the measured stresses.

7.2 Preparation of Edge Quenched Plate

The A533B ferritic steel plate had dimensions 250mm x 50mm x 10mm thick with a machined finish. It was heat treated in a furnace at 600°C for one hour in order to stress relieve it and then edge quenched in water at 17°C [Mirzaee-Sisan et al. 2007], Figure 7.1. The plate was heat treated to produce a bainitic microstructure with a

prior austenitic grain size of ~80μm (mean linear intercept) [(b)Hilson et al 2006]. A specially designed rig was used to carry out the quenching and allowed the plate to be quenched to a depth of 15mm. The furnace temperature was chosen so as not to result in a phase transformation upon cooling. This provided a well defined thermally induced stress distribution for comparing the surface and through-section measured stresses. A diagram of the plate is shown in Figure 7.2.

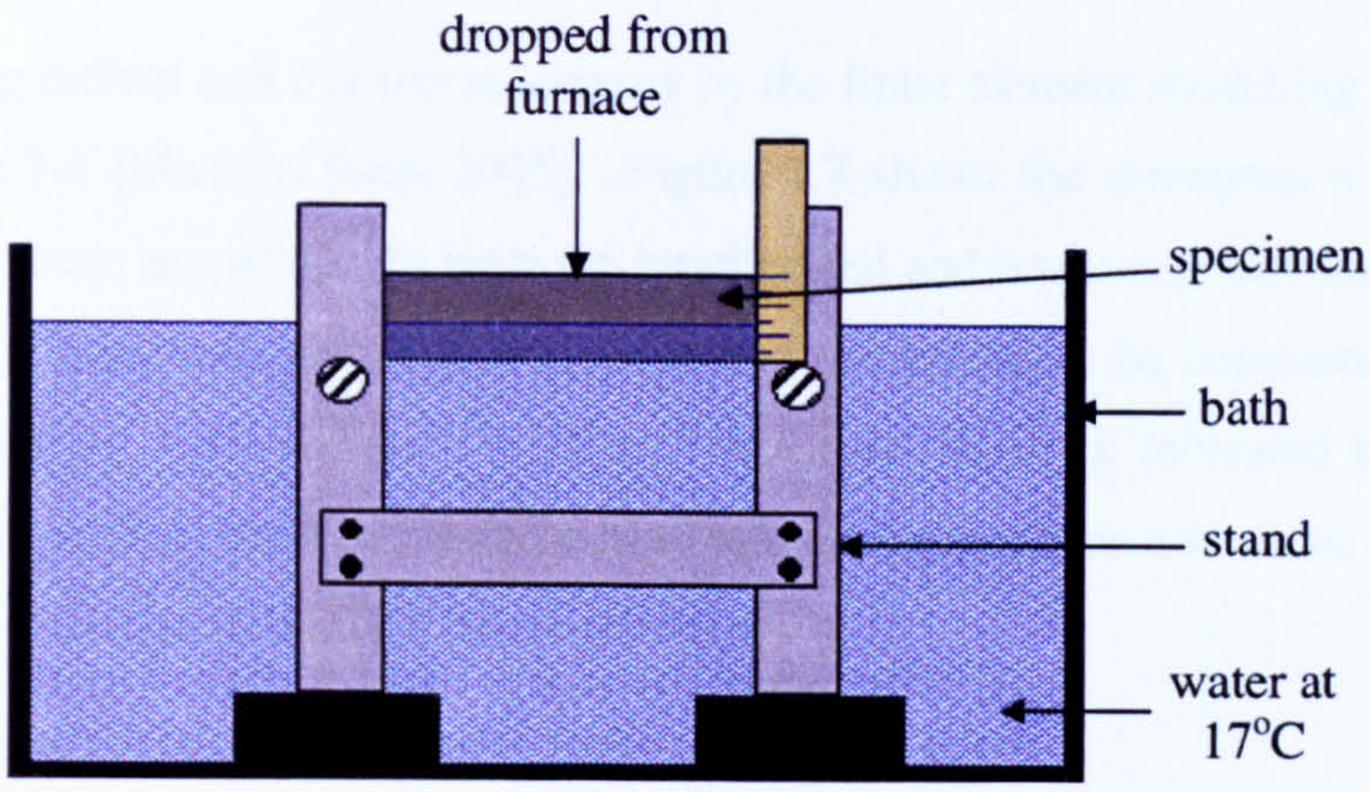

Figure 7.1. Schematic of quench jig used. Courtesy of A. Mirzaee-Sisan, Department of Mechanical Engineering, University of Bristol.

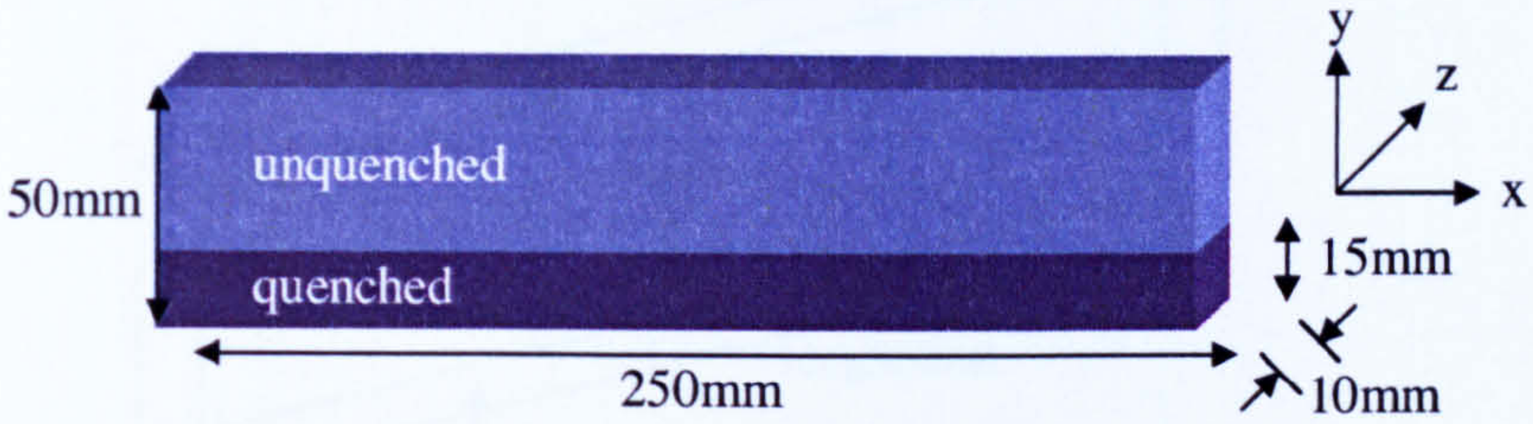

Figure 7.2. Diagram of quenched plate.

7.3 Finite Element Modelling

Finite element modelling was carried out using the ABAQUS – CAE6.4 code [Mirzaee-Sisan 2005]. The material properties physical and mechanical properties employed for the simulation have been shown [Mirzaee-Sisan et al. 2007]. The Poisson ratio used was 0.294 [Mirzaee-Sisan et al. 2007]. The quenching process was simulated with an uncoupled heat transfer analysis and a sequential non-linear thermal stress analysis. One half of the plate was modelled, with the symmetry plane half way across the width. A displacement constraint was imposed in the z-direction. Two

points of constraint were placed on the quenched face of the plate along the y-axis. One of the constraints was fixed, whereas the other was a rolling constraint. The outer surface of the plate was assigned a convective heat transfer of 16,700 W/m^2K. An adiabatic condition was imposed on the symmetry plane of the plate. Since there was no phase transformation involved when quenching the steel from 600°C, only thermally induced stresses were calculated.

The predicted longitudinal and transverse stresses by the finite element modelling can be seen in Figure 7.4 [Mirzaee-Sisan 2005]. Figure 7.3 shows the directions along which the stresses were modelled. In both the longitudinal and transverse directions, the thick black line represents the surface stresses and can therefore be compared to measurements made by X-ray diffraction. The centre measurements, indicated by a red line for the longitudinal predictions and a blue line for the transverse stresses, can be compared to the neutron diffraction measurements.

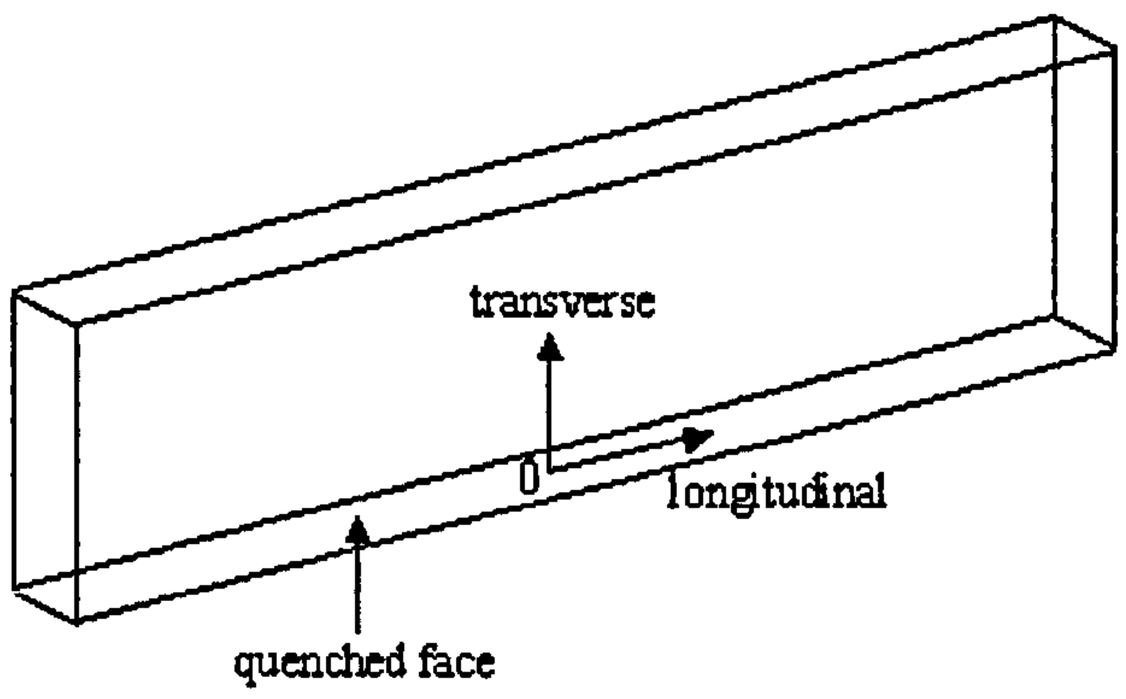

Figure 7.3. Directions along which stresses were modelled.

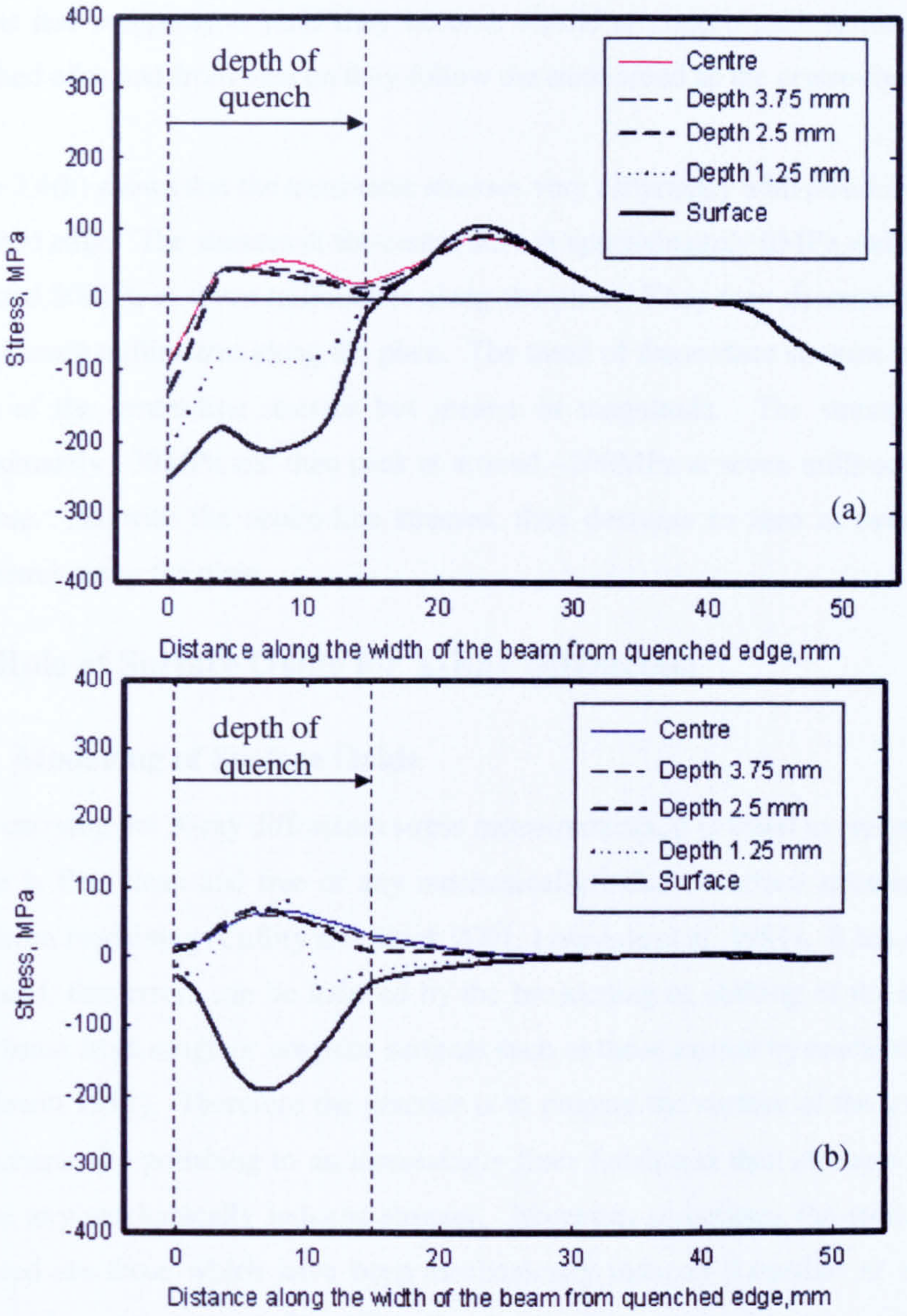

Figure 7.4. Calculated stress distributions. (a) Longitudinal and (b) transverse stresses along the A533B plate. Figure courtesy of A. Mirzaee-Sisan, Department of Mechanical Engineering, University of Bristol.

Figure 7.4(a) shows that the centre-line longitudinal stresses start in the compressive region at −90MPa but become tensile at four millimetres into the quenched region. They then remain tensile, peaking at approximately 100MPa at twenty-three millimetres along the plate. However, at forty-one millimetres along the plate they become compressive again. The surface stresses start at −250MPa. They gradually

become less compressive until they become tensile at sixteen millimetres from the quenched edge and from then on they follow the same trend as the centre-line stresses.

Figure 7.4(b) shows that the transverse stresses vary differently with position from the quenched edge. The stresses at the centre start at approximately 0MPa and then peak at around 80MPa at seven millimetres along the plate. They then decrease to zero at twenty-seven millimetres along the plate. The trend of the surface stresses is a mirror image of the centre-line stresses but greater in magnitude. The stresses start at approximately –30MPa and then peak at around –200MPa at seven millimetres along the plate. As with the centre-line stresses, they decrease to zero at twenty-seven millimetres along the plate.

7.4 Role of Surface Oxide for X-Ray Diffraction

7.4.1 Modelling of Surface Oxide

When carrying out X-ray diffraction stress measurements, it is usual to ensure that the surface is flat, clean and free of any mechanically induced surface stresses such as those from machining [Cullity and Stock 2001, Lonsdale et al. 1981]. It has also been calculated, that errors can be induced by the broadening or shifting of the diffracted X-ray beam from rough or irregular surfaces such as those caused by machining [Doig and Flewitt 1981]. Therefore the practice is to prepare the surface of the component by mechanically polishing to an increasingly finer finish and then electropolished to remove any mechanically induced stresses. However, sometimes the stresses to be measured are those which have been mechanically induced [Lonsdale et al. 1981]. These surface stresses can often affect the structural integrity of a component [Dolby et al. 2008].

As in-situ measurements are ideally carried out with as little additional component preparation as possible, it was considered important to revisit the role of surface oxide and specimen preparation. As a consequence, X-ray stress measurements were carried out on the "as oxidised" unprepared surface as well as using the more conventional surface preparation. This way, the measurements on the two surface types could be compared and the level of preparation required before measurement could be better assessed.

The thickness of a surface oxide affects the analysed penetration depth of X-rays into a substrate and therefore the stresses measured in the substrate [Delhez et al. 1988]. This is due to the X-rays having to penetrate the oxide before the substrate can be reached. Penetration depths into an α-iron substrate were therefore calculated for various oxide thicknesses at ψ-angles from 0° to 60°. Consequently it was possible to assess the depth of measurement that would be made in the substrate if it were covered by a given thickness of surface oxide. This assists with the definition and interpretation of the measured data for the conditions selected.

It is known that even without the presence of oxides the ψ-angle is a contributing factor to the penetration depth of X-rays into a sample [Delhez et al. 1988]. Further, Delhez et al. [Delhez et al. 1988] have considered the effect of surface layers on the the substrate examined by X-ray diffraction. If stresses occur in the layer, these must be balanced within the substrate in order to achieve equilibrium. However, as the resultant stresses in a substrate from a surface layer have many contributing parameters and are only partially understood, it was decided to verify these effects experimentally rather than theoretically.

As it is known that a displacement of the sample from the reflecting-plane normal causes a shift in the measured peak position and as a consequence the measured stress [Cullity and Stock 2001, Klug and Alexander 1974], it was prudent to investigate these influences since the oxide layer would be used as the reference position rather than the metal substrate. The change in θ caused by a change in measurement height due to the presence of an oxide layer was also considered as depicted in Figure 7.5.

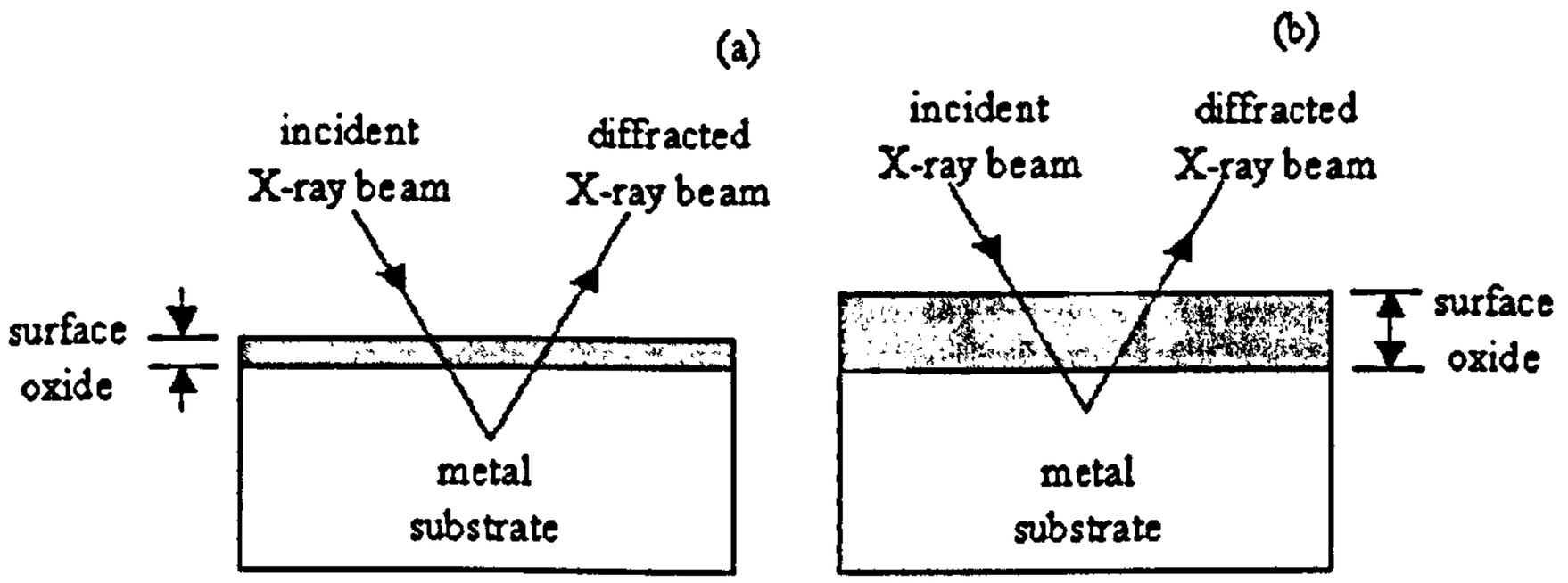

Figure 7.5. Schematic of penetration depths with (a) a thin surface oxide layer and (b) a thick surface oxide layer.

The machining stresses measured with a surface oxide present were calculated for different oxide thicknesses. This was to understand what difference the measurement depth would make to the resulting stress measurement. It was also considered important to understand how changes in ψ-angle would affect the stress measurements.

The line broadening was examined with respect to ψ-angle for the "as oxidised" and electropolished surfaces of the A533B plate by measuring the full width half maxima of the peaks. Since line broadening is related to the presence of microstresses, this would allow effects due to the plastic deformation to be examined.

Penetration depths into an iron substrate for various oxide thicknesses at ψ-angles from 0° to 60° are given in Figure 7.6. The angle between the incident and diffracted X-ray beams, 2θ, was considered to be approximately 156° for diffraction of the {211} peak in α -iron using CrKα radiation. The specific geometry of the incident and diffracted beams was modelled as that for diffractometer employed for the stress measurements [McDonald et al. 2002].

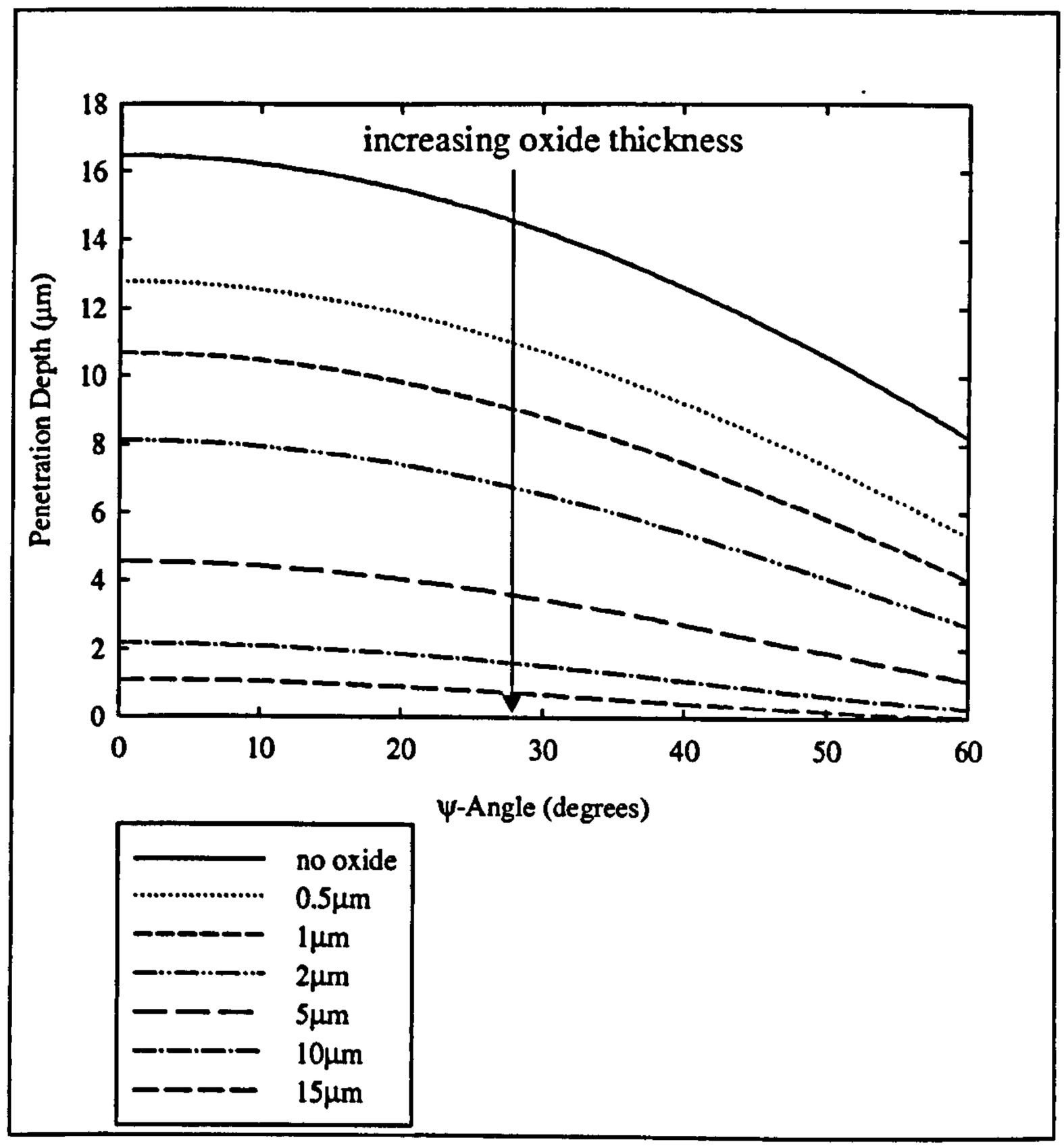

Figure 7.6. Penetration depth into α-iron substrate against ψ-angle for various oxide thicknesses up to 15μm.

The intensity, I, of an X-ray beam transmitted through a material is given by Equation 7.1 [Cullity and Stock 2001],

$$I = I_0 e^{-\mu x} \qquad 7.1$$

where I_0 is the intensity of the incident beam, μ is the linear absorption coefficient of the material and x is the thickness of the material through which the beam is transmitted. The substrate material was modelled as α-iron and the oxide as haematite. The linear absorption coefficient, μ, was 890cm^{-1} for α-iron [Cullity and Stock 2001] and calculated to be 479cm^{-1} for haematite from Equation 7.2

$$\mu = \rho\left\{w_1\left(\frac{\mu_1}{\rho_1}\right) + w_2\left(\frac{\mu_2}{\rho_2}\right) + ...\right\} \qquad 7.2$$

where ρ is the density of the material, w_1, w_2 etc. are the weighted fractions of the constituent elements and $\left(\frac{\mu_1}{\rho_1}\right)$, $\left(\frac{\mu_2}{\rho_2}\right)$ etc. their mass absorption coefficients. The fraction of the total diffracted intensity (G_x) contributed by an oxide layer of thickness x_o was calculated from equation 8.3; where μ_o is the linear absorption coefficient of the oxide, in this case haematite [Cullity and Stock 2001].

$$G_x = \left[1 - e^{\frac{-2\mu_o x_o}{\cos\psi \sin\theta}}\right] \qquad 7.3$$

The penetration depth into the α-iron substrate was calculated by assuming that only a fraction of the total diffracted beam intensity contributes to X-ray diffraction stress measurement, Equation 8.4; where F is the fraction of the contributing diffracted beam intensity, μ_s is the linear absorption coefficient of the substrate, in this case iron and d is the resulting effective penetration depth into the substrate.

$$F - G_x = \left[1 - e^{\frac{-2\mu_s d}{\cos\psi \sin\theta}}\right] \qquad 7.4$$

Rearranging Equation 8.4 results in an expression for the effective penetration depth, Equation 8.5.

$$d = \frac{\cos\psi \sin\theta \ln[1 - (F_x - G_x)]}{-2\mu_s} \qquad 7.5$$

A value of 0.95 was given to F for the calculation of the effective penetration depth, d, Equation 8.5, as it was assumed that any contribution from surface layers below this could be ignored [Cullity and Stock 2001].

The change in the Bragg angle by setting the goniometer height with reference to the surface oxide layer can be seen in Figure 7.7. This is calculated using Equation 7.6 [Klug and Alexander 1974], where Δh is the displacement of the sample from the reflecting-plane normal, π is in radians and h is the distance between the focused diffractiometer and sample.

$$\Delta 2\theta = (\pi - \theta)\frac{\Delta h}{h} \qquad 7.6$$

For varying ψ-angles Equation 7.6 becomes as shown in Equation 7.7.

$$\Delta 2\theta = (\pi - 2\theta)\left(\frac{\Delta h}{h\cos\psi}\right) \qquad 7.7$$

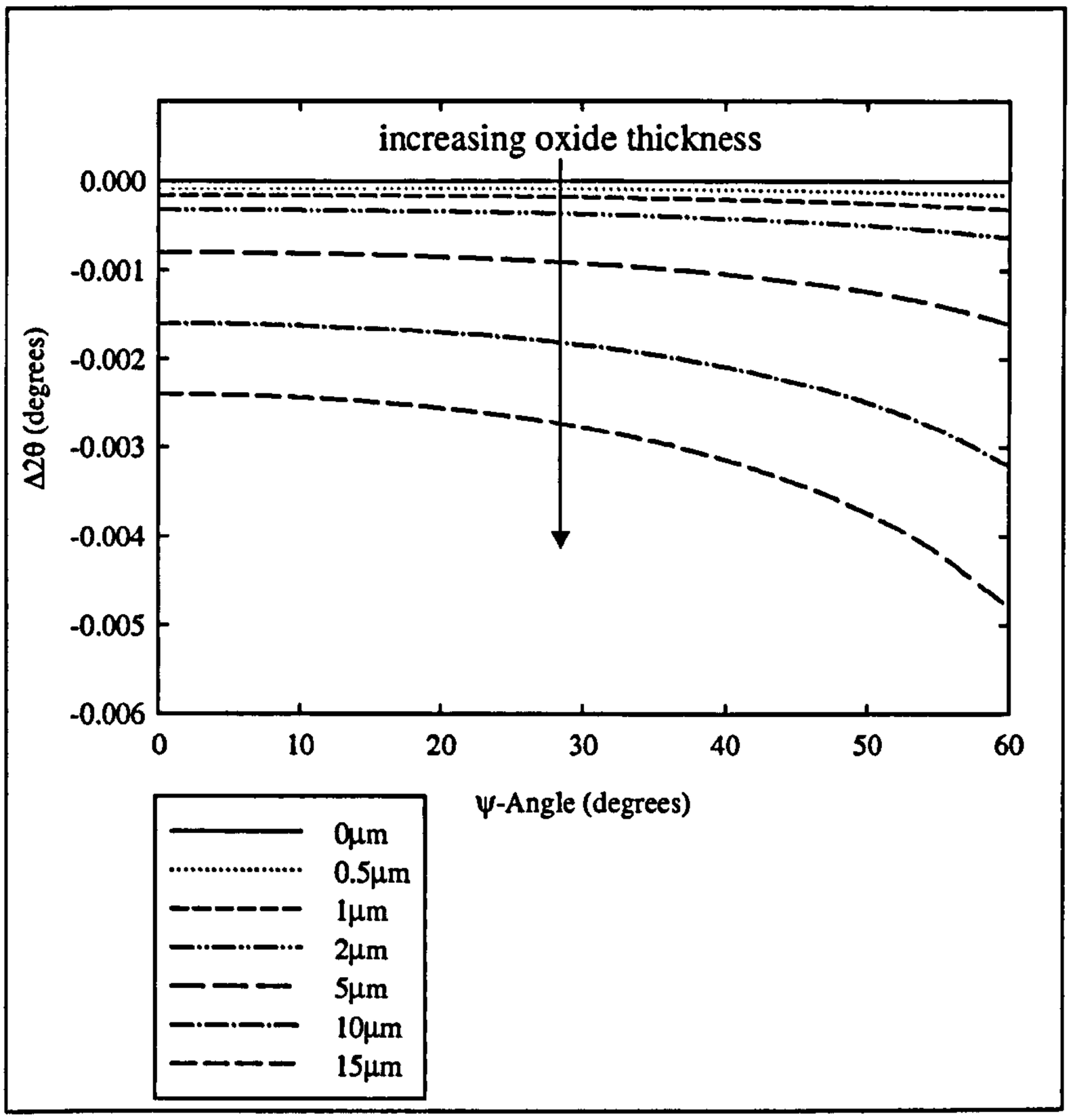

Figure 7.7. $\Delta 2\theta$ against ψ-angle resulting from the height displacement caused by surface oxide layers of various thicknesses.

The value of 2θ decreases as both the thickness of the oxide layer and the ψ-angle increase. The greatest difference to the initial value of 2θ is less than 0.005° and occurs with an oxide layer of $15\mu m$ at a ψ-angle approaching 60°. This is less than half the level of resolution available from the diffractometer used for the measurement of 2θ [McDonald et al. 2002].

The effect of surface oxide on the measurement of a typical machining stress profile was investigated. This was done by calculating the effect of a reduced penetration depth into a machined α-iron substrate due to X-ray beam intensity being lost by penetration through a haematite surface oxide. A measured stress profile obtained by Lonsdale et al. [Lonsdale et al. 1981] into a ferritic steel specimen with a machined surface is shown in Figure 7.8.

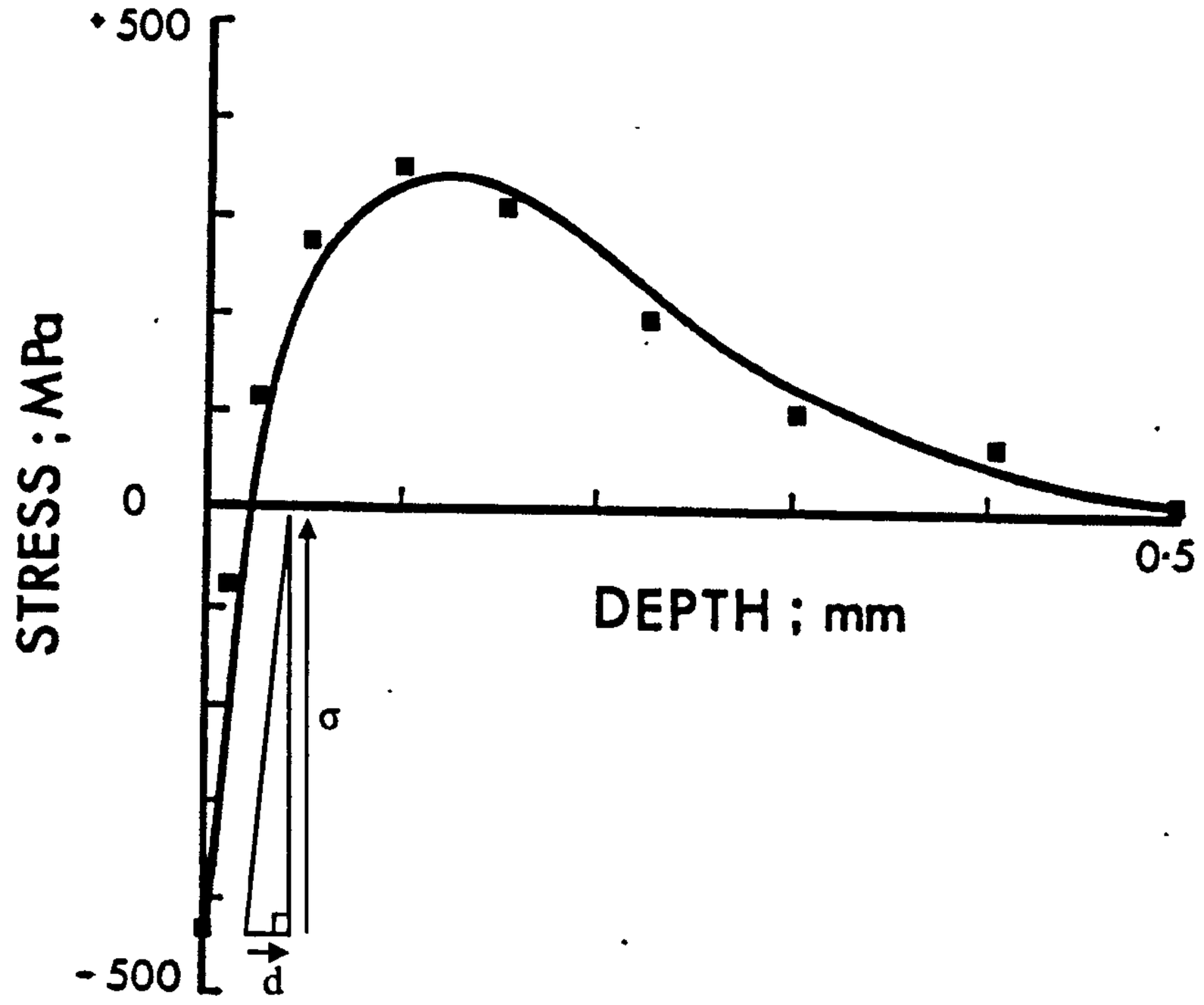

Figure 7.8. Stress profile through a machined surface [Lonsdale et al. 1981].

The sampled stress versus depth into the specimen was approximated to a linear relationship for the first 0.02mm, Equation 7.8, where σ is the measured stress in MPa and d is the depth into the specimen in μm.

$$\sigma = 19d - 430 \qquad 7.8$$

Substituting Equation 7.5 into Equation 7.8 results in a method of calculating stress in a substrate for different oxide thicknesses, where varying the oxide thicknesses result in varying values of G_x.

$$\sigma = \frac{19\cos\psi \sin\theta \ln\left|1-\left(F - G_x\right)\right|}{-2\mu_s} - 430 \qquad 7.9$$

The calculated result of varying penetration depth on the measured stress due to surface oxide layers is shown in Figure 7.9. The calculations show that the measured stress increases in magnitude as the oxide thickness increases and as the ψ-angle increases.

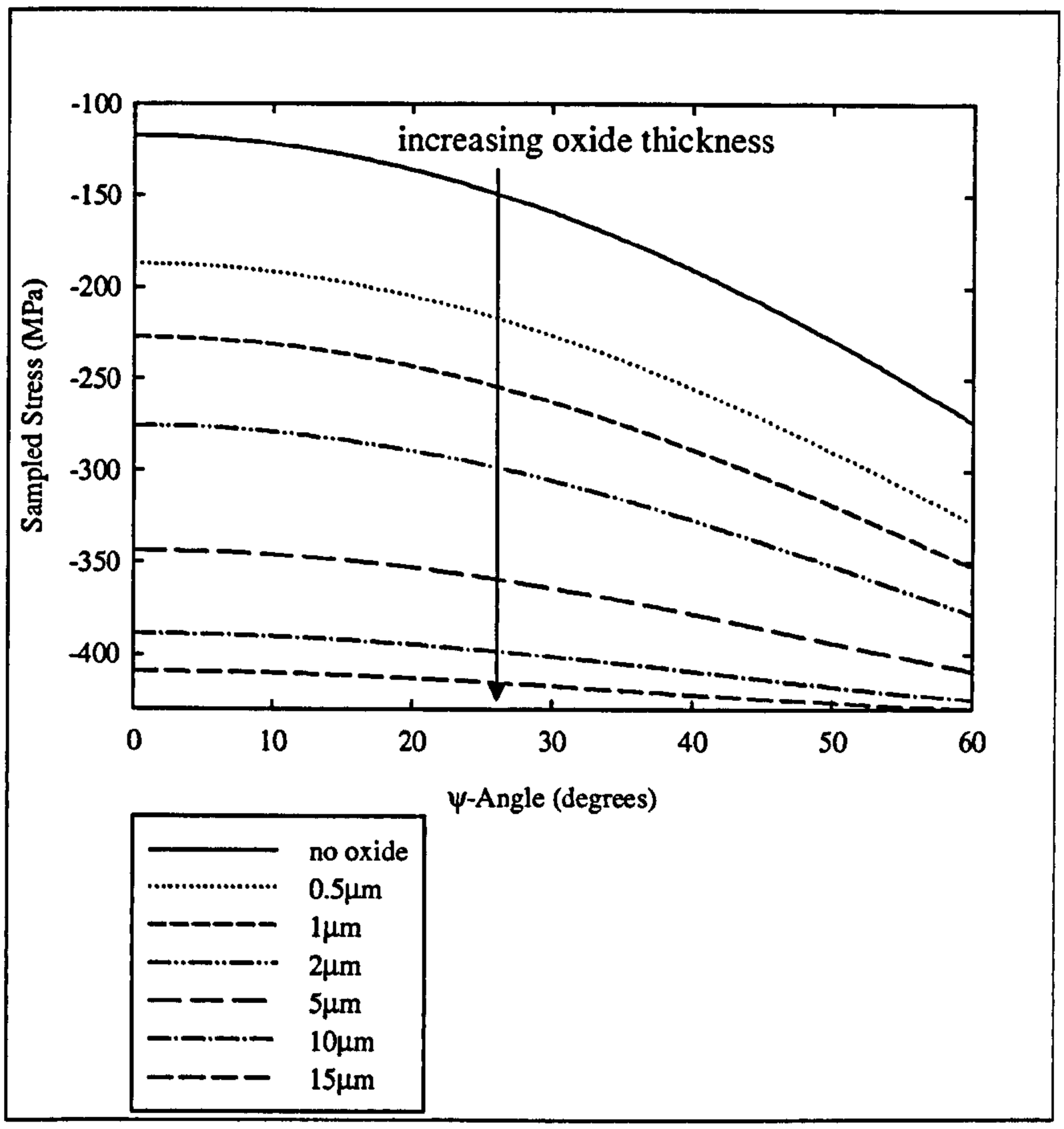

Figure 7.9. Sampled stresses in a machined surface against ψ-angle for various surface oxide thicknesses.

7.4.2 Hardness

A sample of dimensions 10mm×10mm×40mm was removed from the side of the plate. The inner surface was polished to a 1μm finish and then electropolished, Figure 7.10. Vickers hardness, HV_{30}, measurements [Ashby and Jones 1996] were then made along the centre of the inner surface, Figure 7.11.

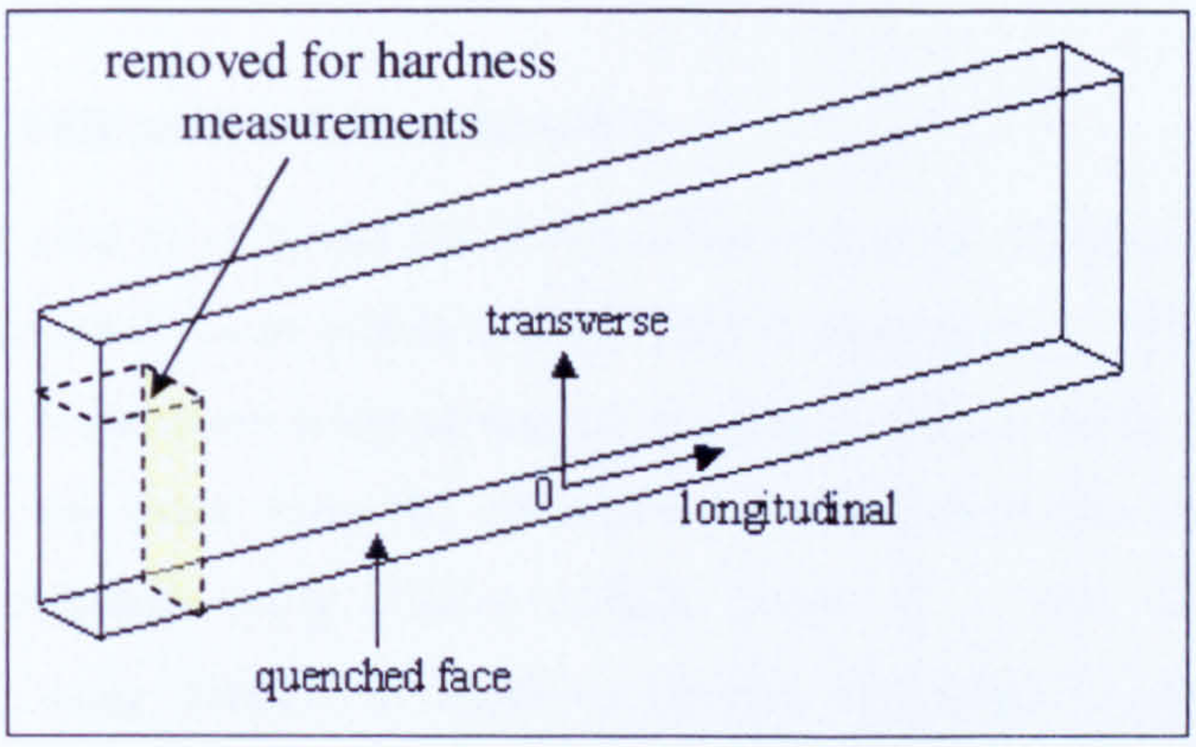

Figure 7.10. Sample removed for hardness measurements. The surface on which measurements were made is shaded.

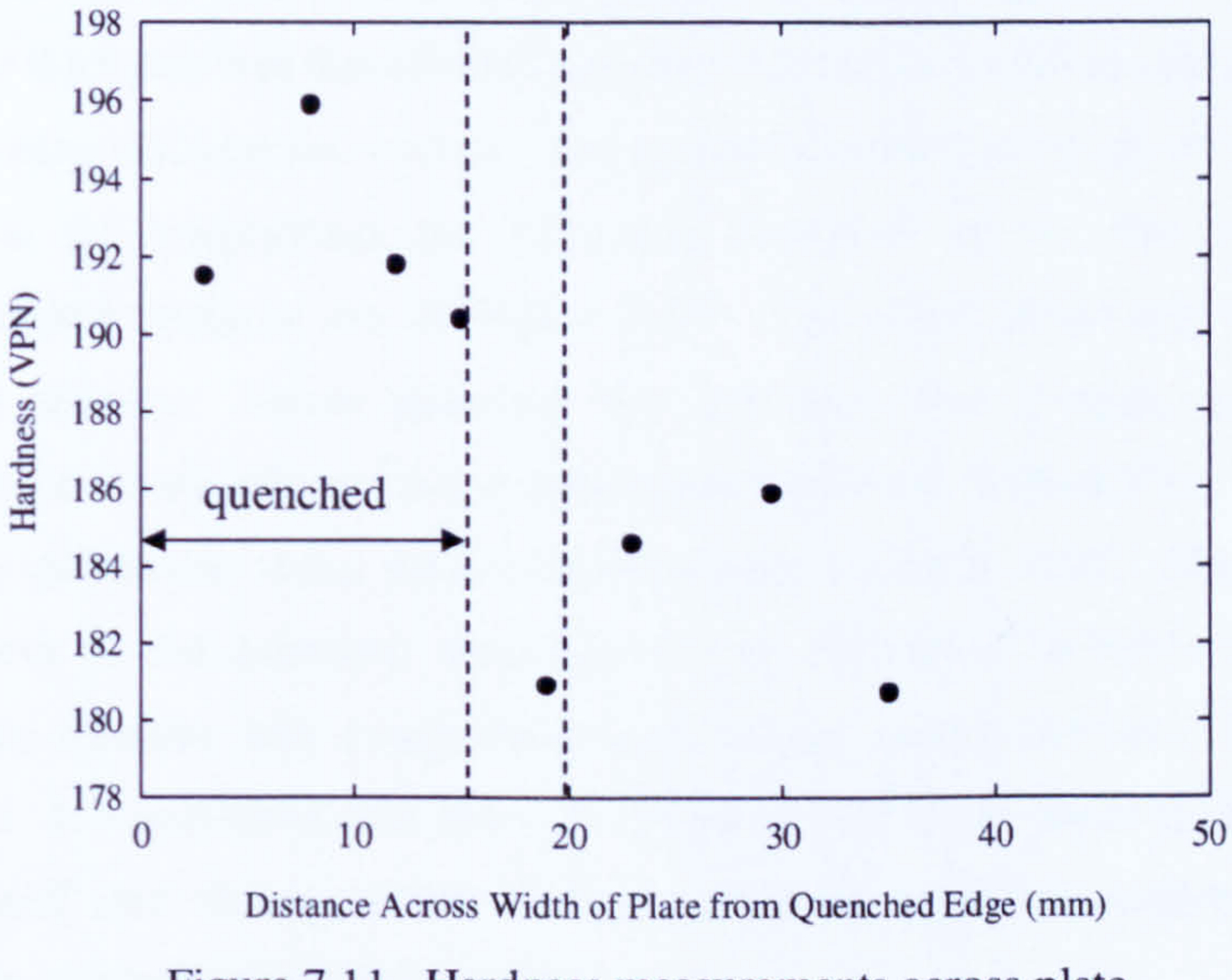

Figure 7.11. Hardness measurements across plate.

The hardness is greatest across the quenched volume. This could be due to an increase in dislocations in the quenched volume. The hardness measurements define the depth into the plate affected by the quenching. The measurements suggest that a depth of approximately 15mm to 18mm was affected. The definition of the quenched region could be refined by further hardness measurements of increased proximity at a distance of 15 to 18mm across the width of the plate.

7.4.3 X-Ray Diffraction Measurements

The equipment used to carry out the X-ray diffraction stress measurements has been discussed in Section 3.2.2 as well as in references [Lonsdale et al. 1981, McDonald et al. 2005]. The X-radiation selected was Cr Kα and a 1mm diameter collimator was used to direct the beam onto the specimen. A section across the sample was mechanically polished using silicon carbide paper to a 1μm finish and then electropolished using 5%HCl in water to remove any stresses induced from the mechanical polishing. This removed approximately 10μm to 20μm of material. X-ray diffraction measurements were taken over the electropolished area as well as an "as oxidised" area. This corresponds to positions X and Y respectively in Figure 7.12. The oxide thickness was measured to vary between 0.5μm to 2.5μm using a Hitachi S-2300 scanning electron microscope. The stresses measured using the centre of gravity method in the longitudinal and transverse directions on the "as oxidised" and electropolished surfaces are in Figure 7.13. The errors given are those for the evaluated stresses. Oxide thickness was not taken into account, as it was not considered to be significant for the thicknesses measured, Section 7.4.1. In all cases, the X-ray diffraction stress measurements follow a similar trend. The stresses are compressive in the quenched area, between approximately 400MPa and 500MPa. They then become less compressive and remain mostly between 100MPa and −100MPa. It is noticeable, that there is a closer correlation between the stresses in the "as oxidised" and electropolished surfaces across the quenched regions of the plate than across the remaining plate surface.

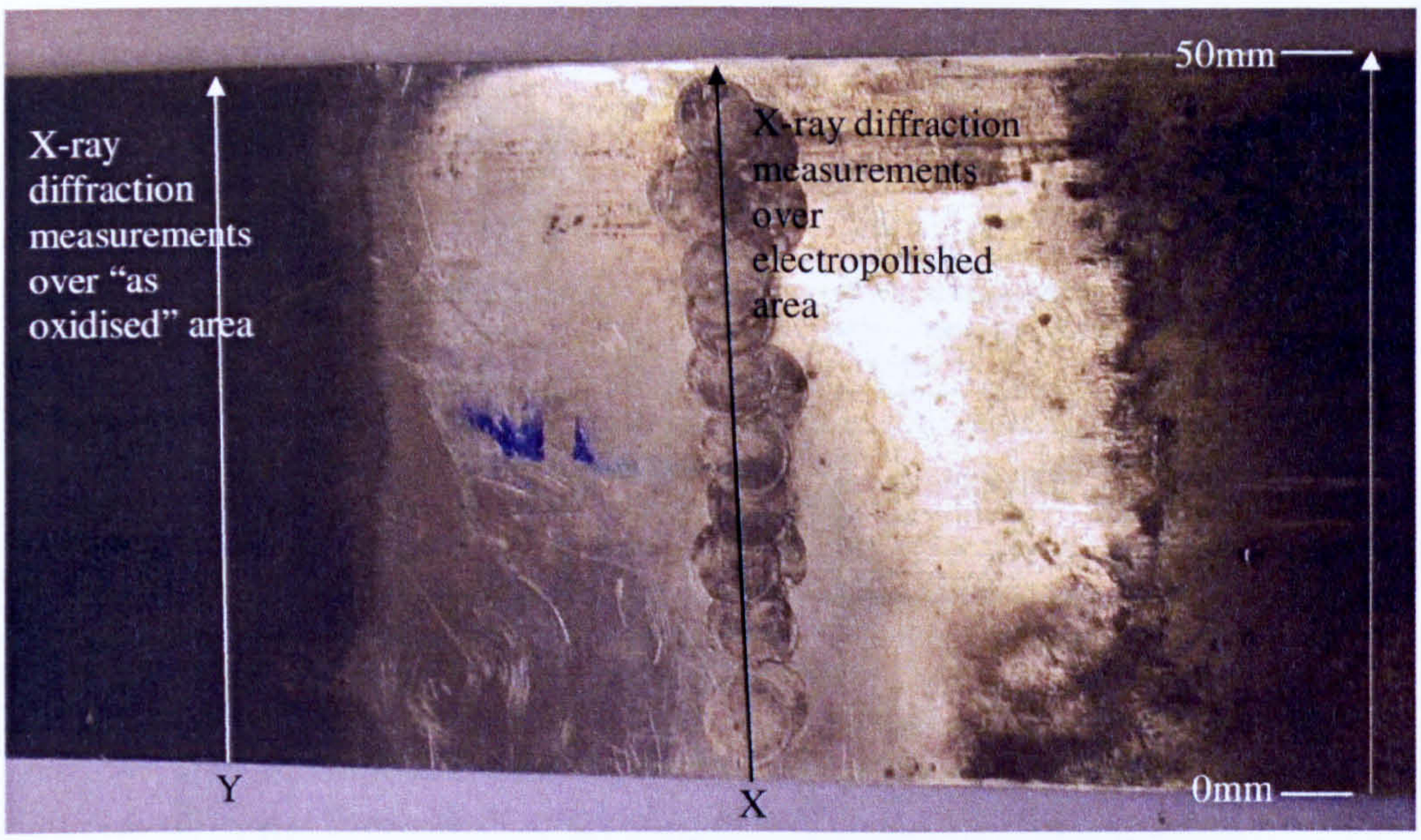

Figure 7.12. Areas over which X-ray diffraction measurements were made. Position X is electropolished and position Y is "as oxidised".

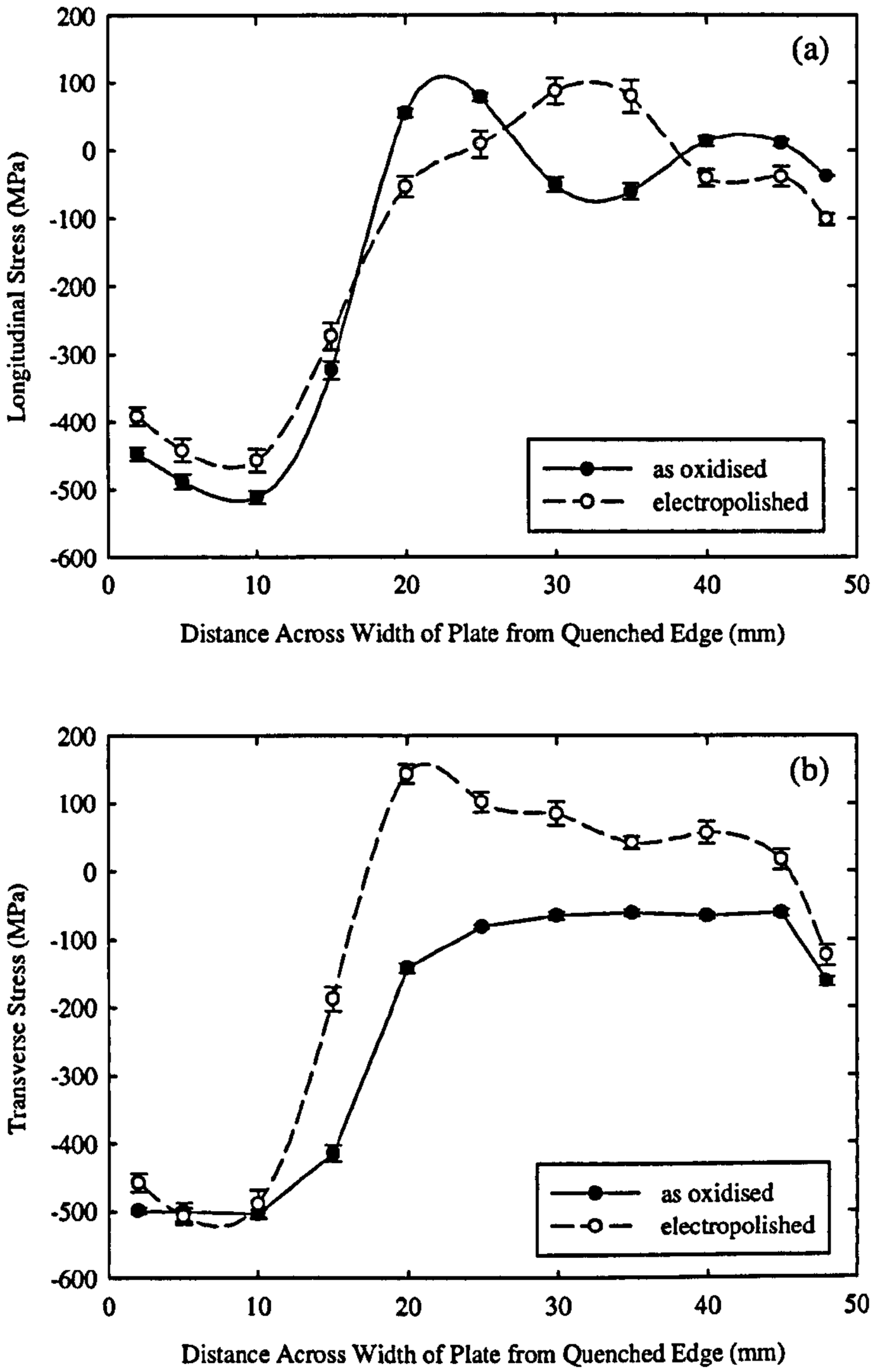

Figure 7.13. (a) Longitudinal and (b) transverse stresses on the "as oxidised" and electropolished surfaces.

7.5 Oxide Stresses Measurements

7.5.1 Introduction

The measurement and analysis of residual stresses in oxides using Raman spectroscopy has been well documented (Chapter 2 – Literature Review) [Galerie et al. 2004, Mougin et al. 2002, (b)Mougin et al. 2001, (b)Mougin et al. 2001, Shim and Duffy 2002]. However, these investigations involve either the measurement of the

stresses in the oxide due to its formation [Galerie et al. 2004, Mougin et al. 2002, (c)Mougin et al. 2001] or due to applied loads (Chapter 6 - Stresses within Surface Oxide Grown on Ferritic Steel) or pressure [(b)Mougin et al. 2001, Shim and Duffy 2002]. Although the effects of substrate surface roughness have been taken into account [(c)Mougin et al. 2001], there appears to limited information concerning the correlation between stresses in the substrate and oxide [Park et al. 2004].

7.5.2 Raman Spectroscopy

Raman spectra of the "as grown" oxide on the plate revealed the oxide to be haematite, Figure 7.14 [Shebanova and Lazor 2003, Shim and Duffy 2002]. Raman spectroscopy was carried out with a Renishaw Raman 2000 spectrometer and a 633nm helium neon laser equipped with a 5x magnification lens. The spectra were recorded for 600 seconds. The laser power, 29μW, was the lowest available and was measured with a power meter. The spectrometer was calibrated using a silicon standard. Changes in the peak position and their corresponding hydrostatic stress values, Figure 7.15, show that the magnitude of the hydrostatic stress in the oxide is greater in the quenched area of the plate than in the unquenched area. The outlier at 17.5mm across the width of the plate (with a Raman shift of 428.12cm^{-1} and a corresponding hydrostatic stress of –6.24GPa) is shown in Figure 7.15(a). However, it is not shown in Figure 7.15(b) in order to increase the clarity of the trend in Raman shift and hydrostatic stress across the width of the plate. The hydrostatic stresses across the oxide are most compressive between 0mm and 25mm across the plate.

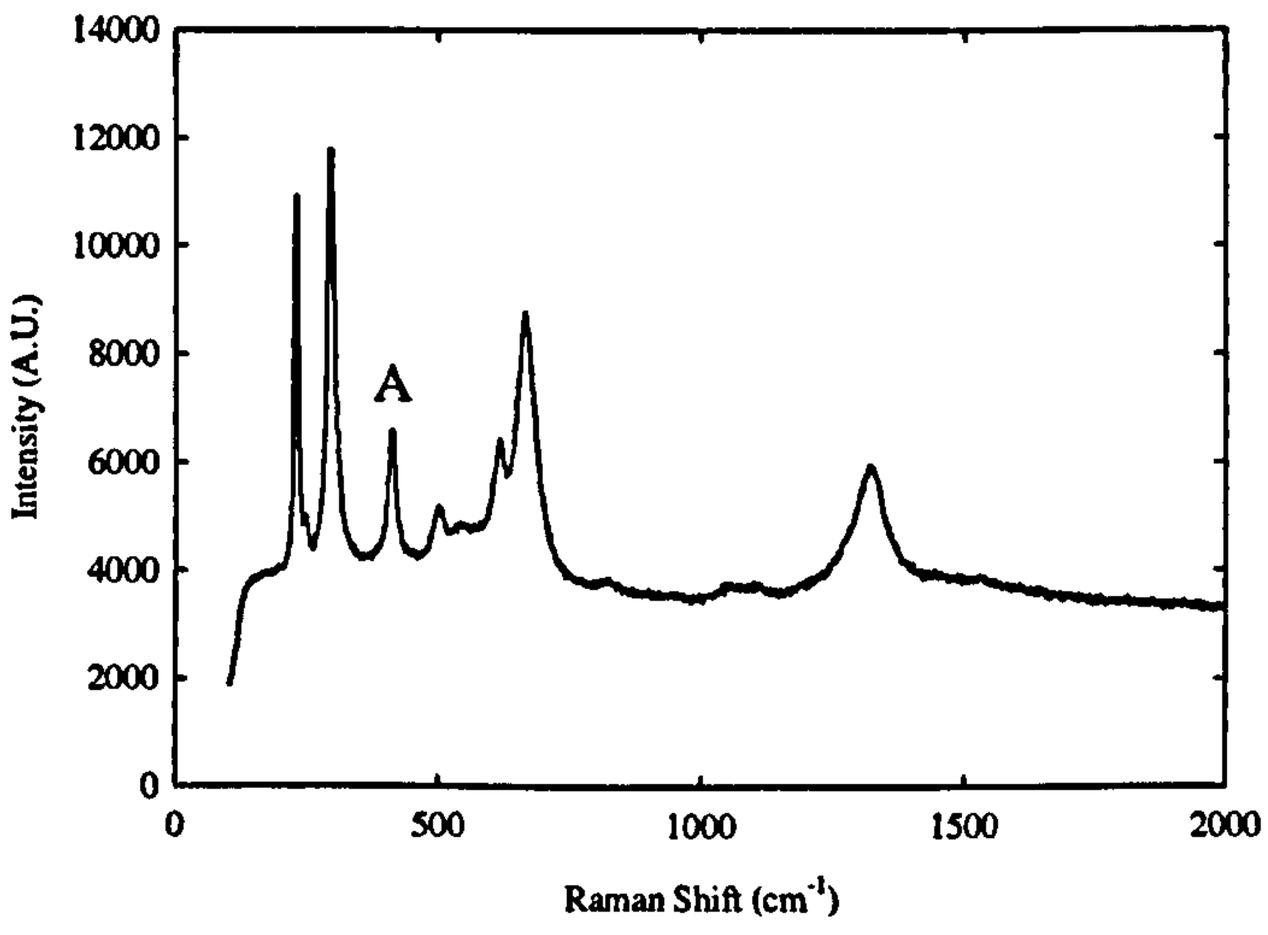

Figure 7.14. Typical Raman spectrum from surface oxide.

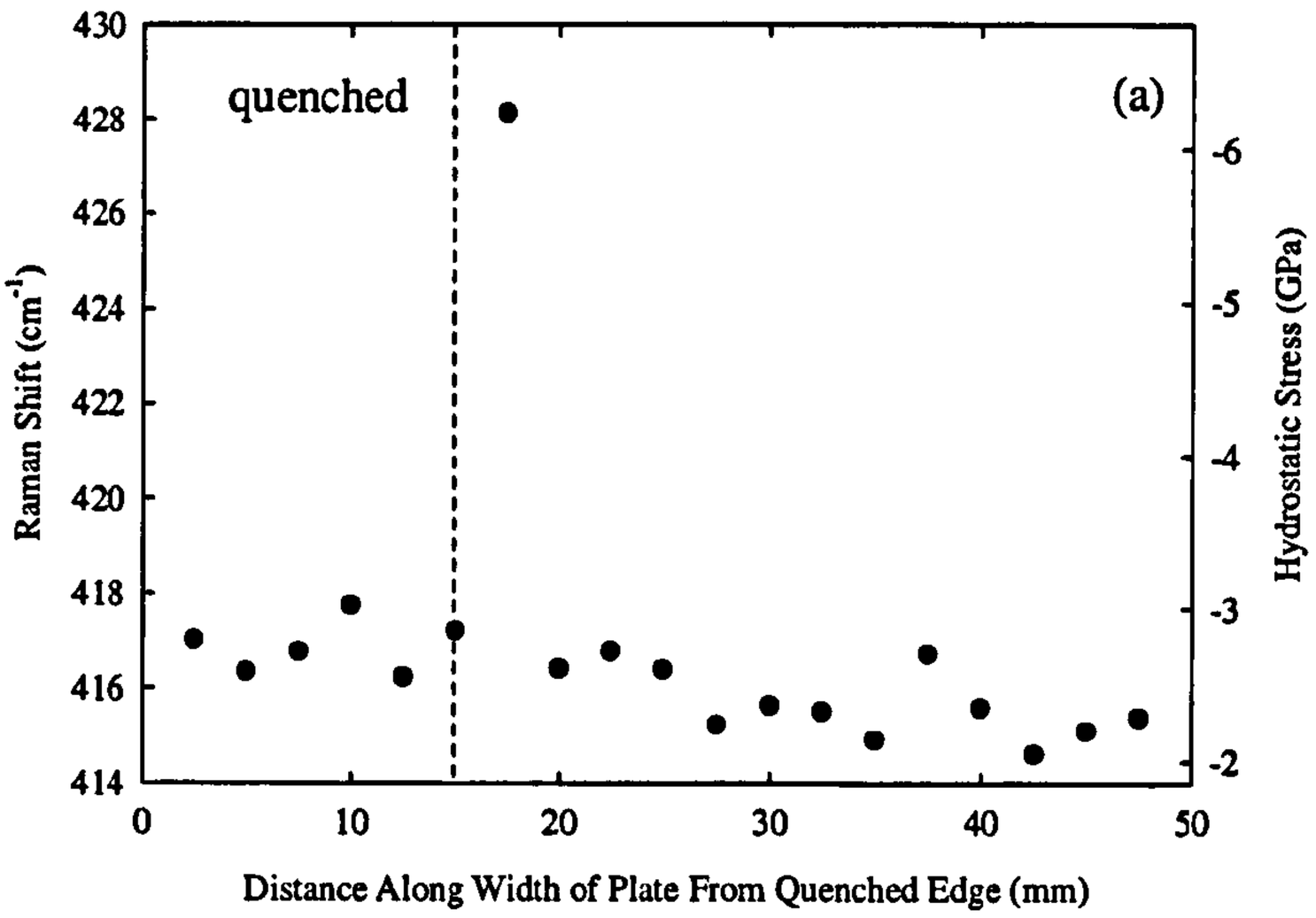

Figure 7.15. Raman shift and corresponding hydrostatic stress for peak marked A along the width of the plate. (a) is with outlier and (b) is without outlier.

7.6 Through Section Stress Measurements

Neutron diffraction was carried out at the ENGIN-X facility at the Rutherford Appleton Laboratory. A $10mm^3$ corner was removed from the unquenched part of the plate and was prepared to provide as stress-free sample to determine the stress-free lattice parameter d_0 [Mirzaee-Sisan 2005]. This provided a valid measure of d_0 throughout the volume of the plate as the material did not undergo a phase change

during quenching. A gauge volume of 1mm^3 was used for stress measurements and care was taken to ensure that this was contained within the specimen. The diffraction peaks were analysed using the Rietveld refinement technique. The longitudinal and transverse stress measurements through the centre of the width of the plate are shown in Figure 7.16.

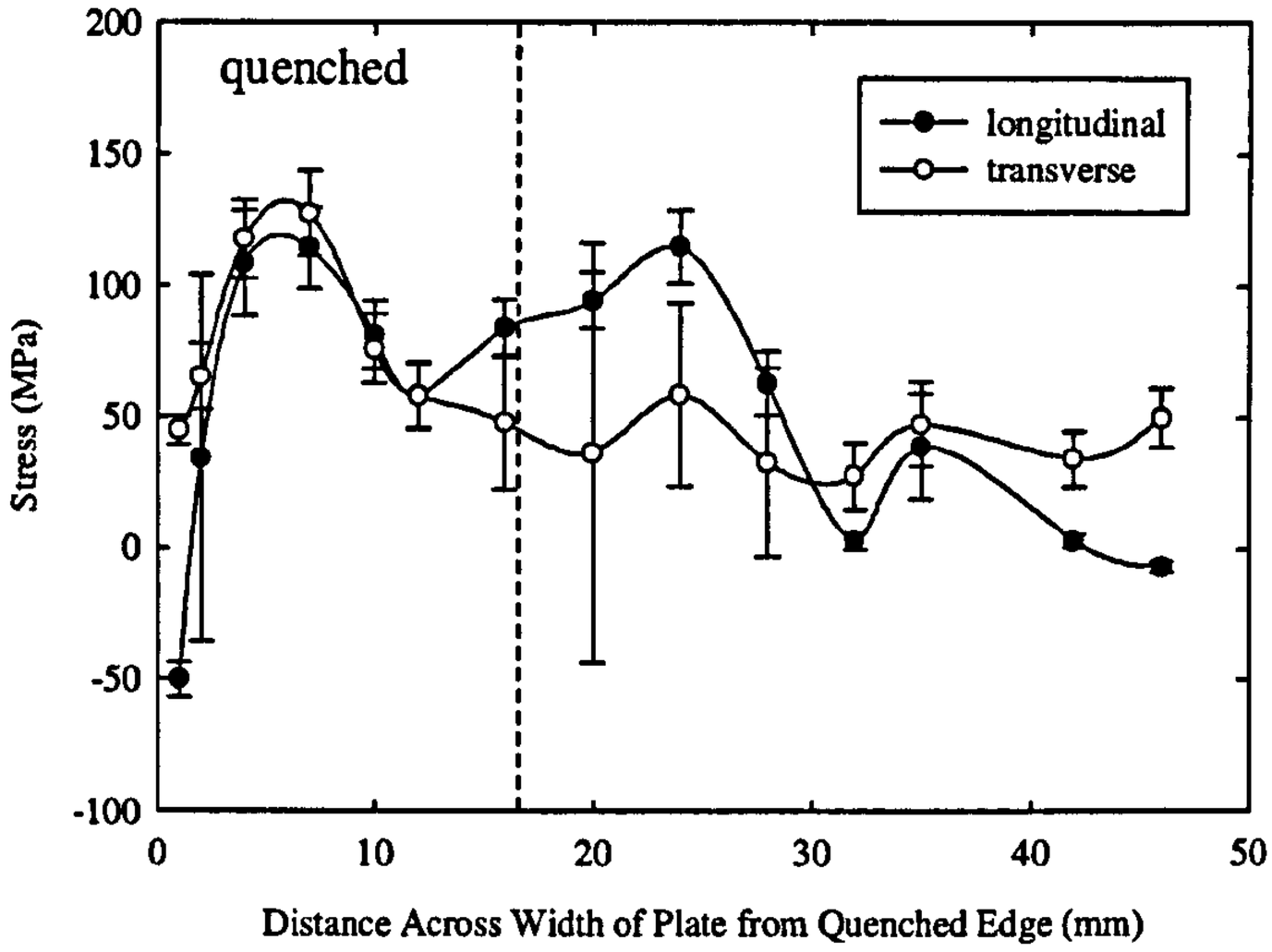

Figure 7.16. Neutron diffraction longitudinal and transverse stress measurements across the edge of the quenched plate.

The neutron diffraction measurements show that there is an initial increase in the magnitudes of the stresses in the quenched region, after which the trend in the stress measurements tends towards zero stress. The errors in stress measurements in the transverse direction are often greater than the differences in stress values in the unquenched region. It is therefore not always possible to distinguish whether the differences in stress measurement through the unquenched region in the transverse direction is due to variation in the stress through the plate in this direction or due to measurement error.

7.7 Comparison of Predicted and Measured Stresses

7.7.1 Macrostresses

There is now measured stress data across different length scales to allow comparison between surface (X-ray) and centre line (neutron) stress measurements. In addition,

these measured values can be compared with the predictions of the finite element ABAQUS through-thickness model. Graphs of the measured and predicted longitudinal and transverse stresses across the plate can be seen in Figure 7.17 and Figure 7.18.

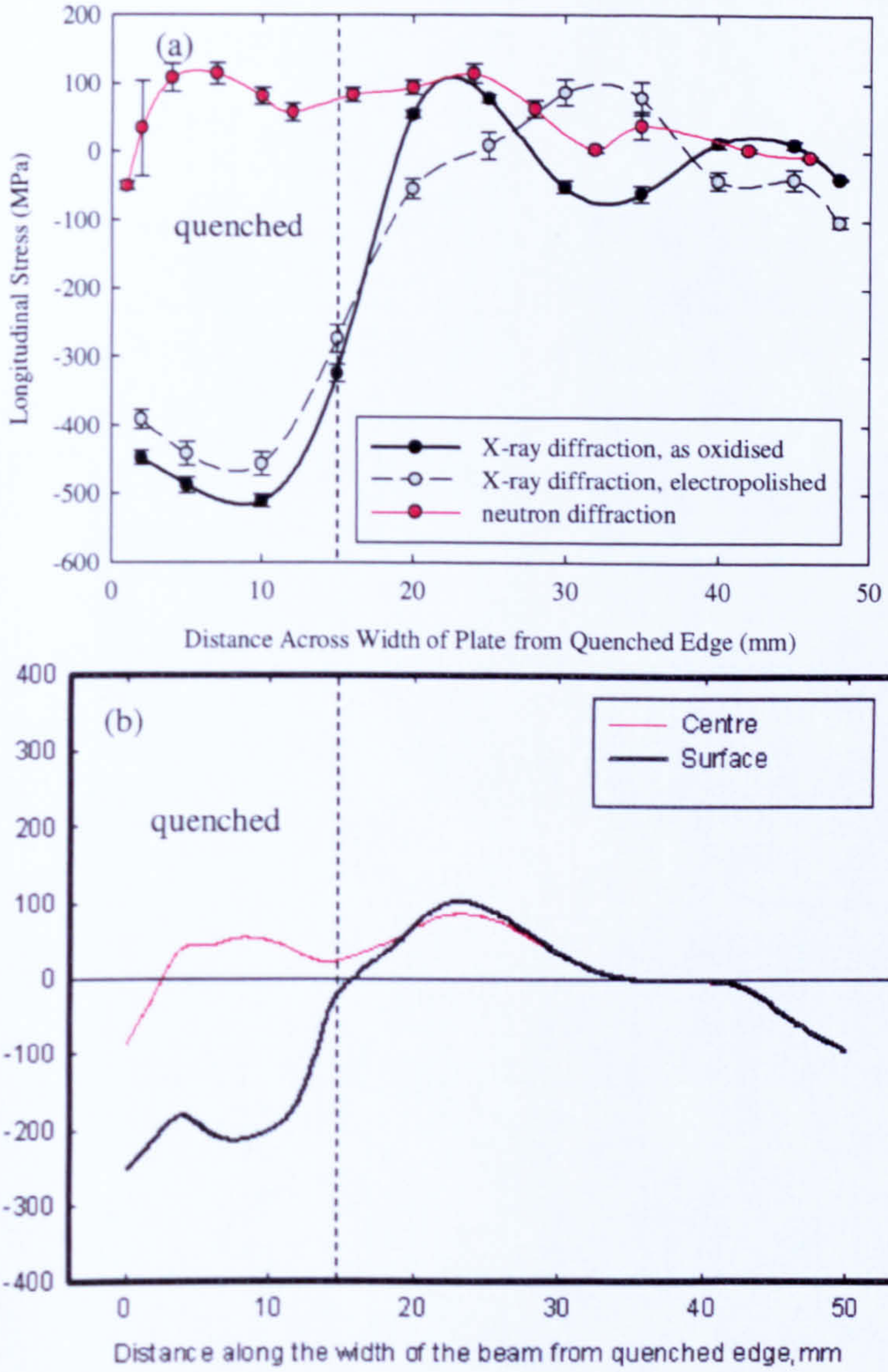

Figure 7.17. (a) Measured and (b) predicted stresses in the longitudinal direction.

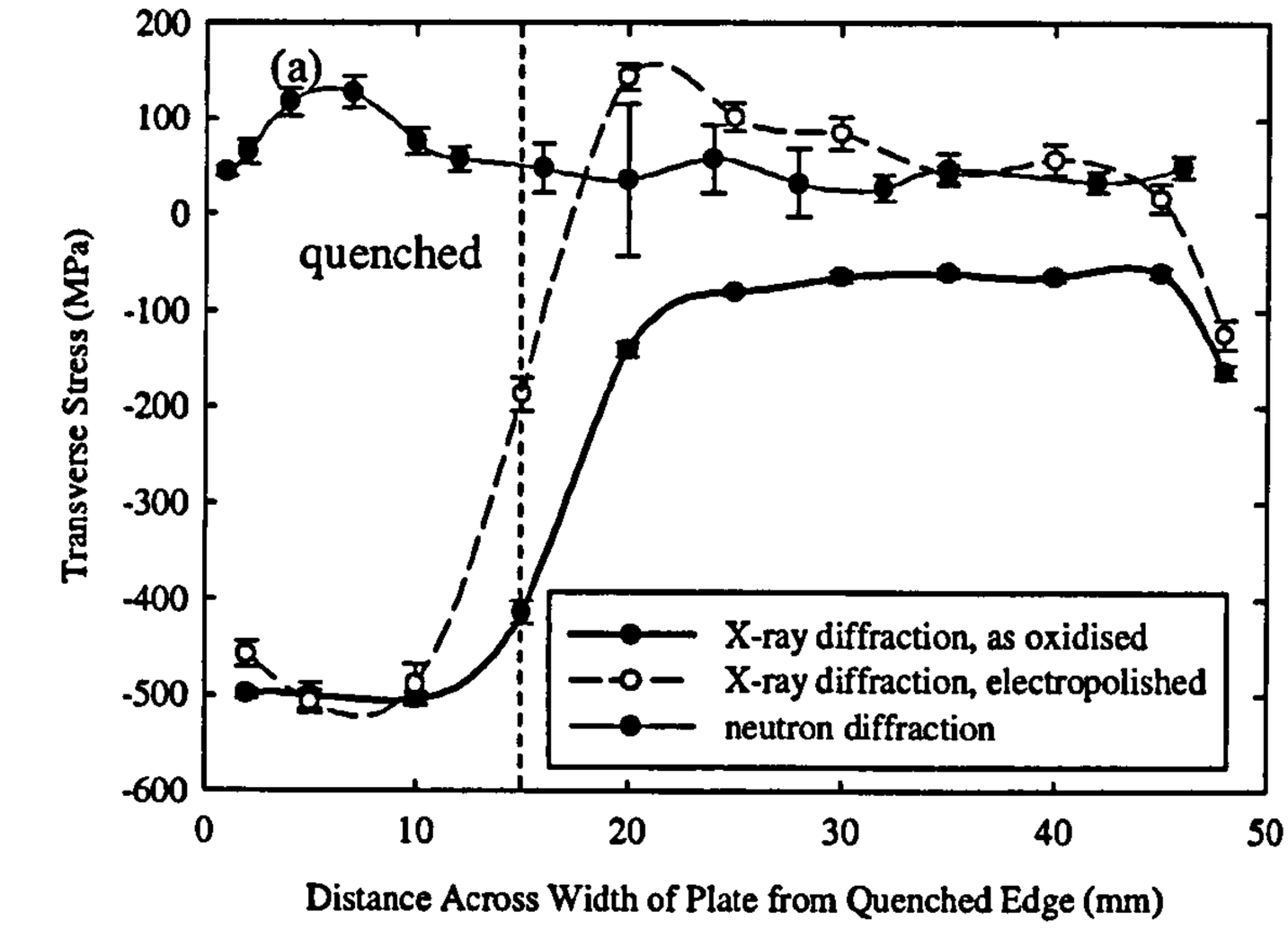

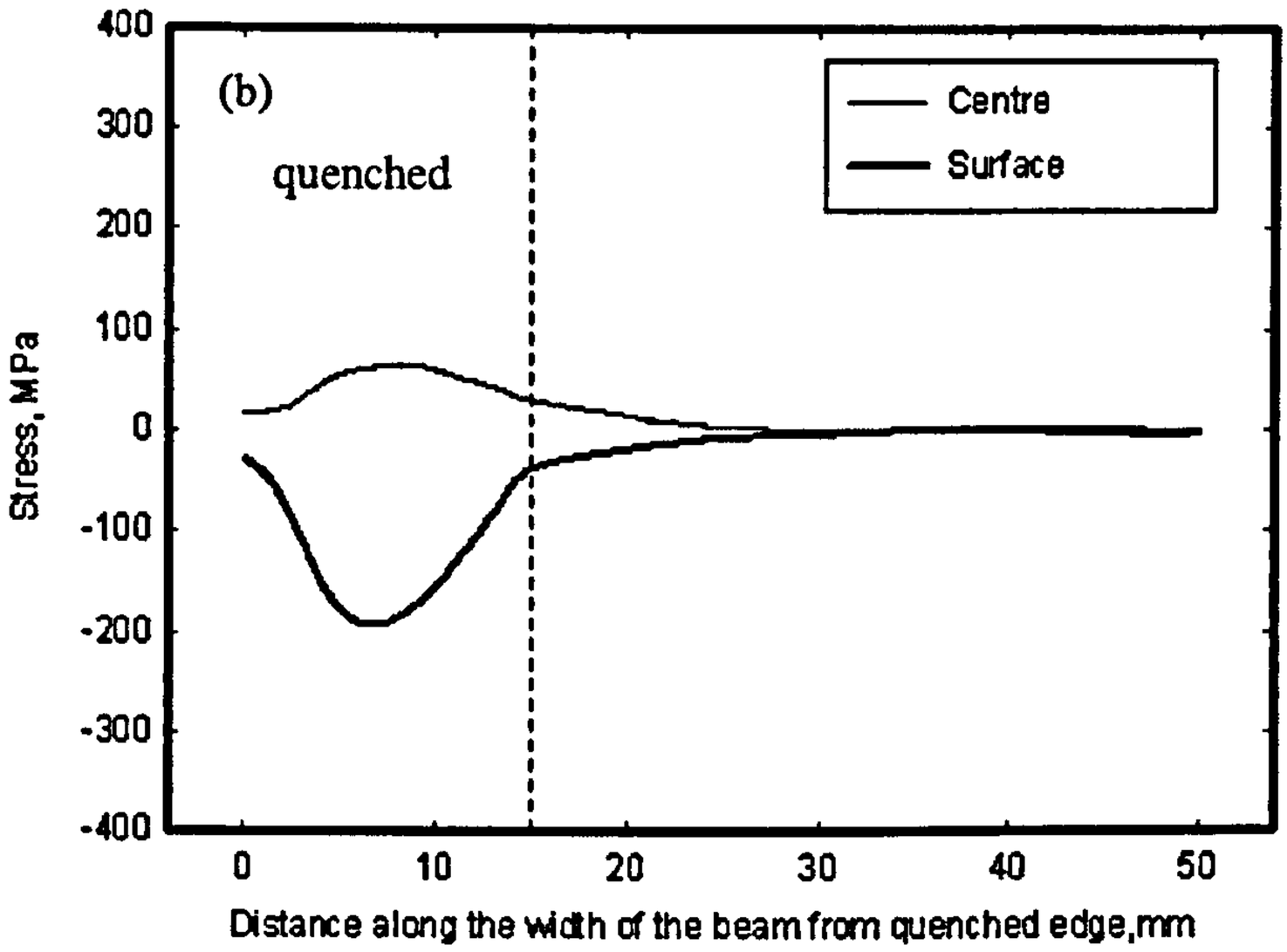

Figure 7.18. (a) Measured and (b) predicted stresses in the transverse direction.

The centre line finite element predictions have the same general variation with depth to the through-section neutron diffraction measurements and the surface X-ray diffraction measurements. Although the magnitudes of the measured stresses are greater than those of the predicted stresses, the trends in the stresses are, in general, similar. In the longitudinal direction, the X-ray diffraction surface measurements on the electropolished area follow a similar trend to the predicted surface stresses.

However, there is a difference between the trend of the X-ray diffraction measurements made on the "as oxidised" surface to the predicted surface stresses in the unquenched part of the plate. This could be due to any residual machining stresses on the "as oxidised" surface having a greater influence on the stress magnitudes in the unquenched part to the quenched part. The case is similar for the longitudinal measurements and predictions in the transverse directions. The measurements follow the same trend as the predicted stresses but there is a distinct discrepancy between the X-ray diffraction measurements on the "as oxidised" surface and the predicted stresses. Unlike the predicted stresses in the unquenched part of the plate, which tend to and then remain at zero stress, the X-ray diffraction measurements on the "as oxidised" surface tend to approximately −100MPa. This could again be due to remnant machining stresses. Although the plate was heat treated to stress-relieve these, they may not have been completely removed. There is indication of this in the difference between the measured and predicted stresses in the transverse direction. Unlike the predicted stresses, which are largely zero across the unquenched area of the plate, the X-ray and neutron diffraction measure stresses in this region. An additional difference between measured and predicted stresses is that both sets of X-ray diffraction measurements in the transverse direction show edge effects by showing more compressive stresses at 5mm away from the unquenched edge which are not reflected in the neutron diffraction measurements or the predictions.

7.7.2 Microstresses

The full width of X-ray diffraction peaks can be used as a measure of microstresses in the analysed material. As discussed in Section 7.4, the greater the ψ-angle, the shallower the detected penetration depth of the X-ray beam. Thus, by analysing the full width half maxima at different ψ-angles, it is possible to gain an understanding of microstresses at different depths in a material.

The full width half maxima across the plate were measured at a ψ-angle of 3° to consider the behaviour of the microstresses over a depth of approximately 10μm, the greatest penetration depth achievable with CrKα radiation on the electropolished and "as oxidised" surfaces, Figure 7.19 [Lonsdale et al. 2001]. Unfortunately, there was

no direct means of calculating the error in the fitted full width half maxima of the peaks.

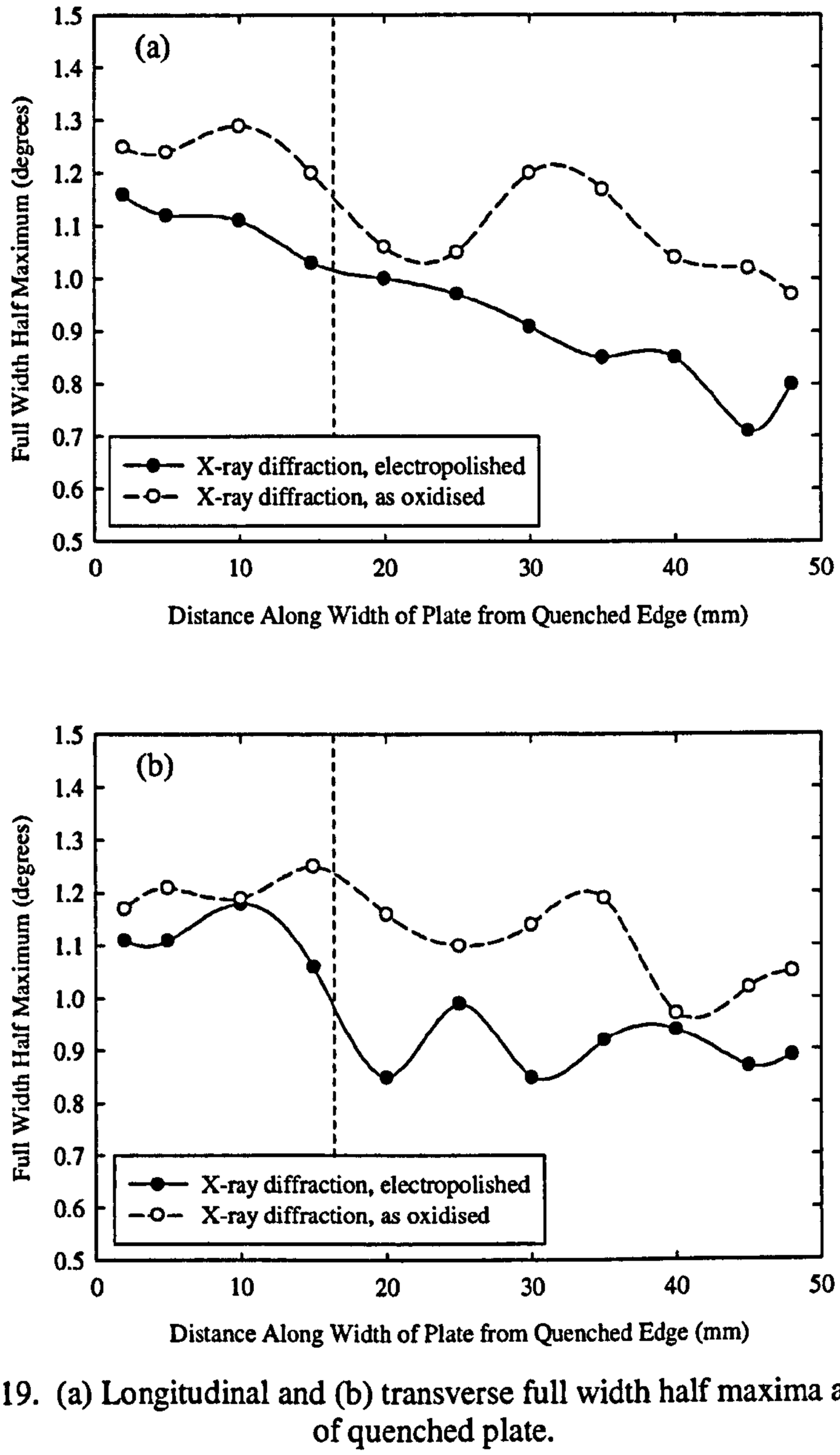

Figure 7.19. (a) Longitudinal and (b) transverse full width half maxima along width of quenched plate.

Figure 7.19(a) and (b) shows that the microstrains measured along the electropolished area of the plate are lower than those measured along the "as oxidised" surface. In all cases, the full width half maxima indicate that the microstrains are greatest in magnitude over the quenched section of the plate.

The effect of ψ-angle on the measured full width half maximum for the can be seen in Figure 7.20, Figure 7.21, Figure 7.22 and Figure 7.23 for the longitudinal and transverse cases; both the electropolished and "as oxidised" surfaces. They are also shown for areas 5mm and 45mm along the plate, in order to assess variations between the quenched and unquenched areas of the plate.

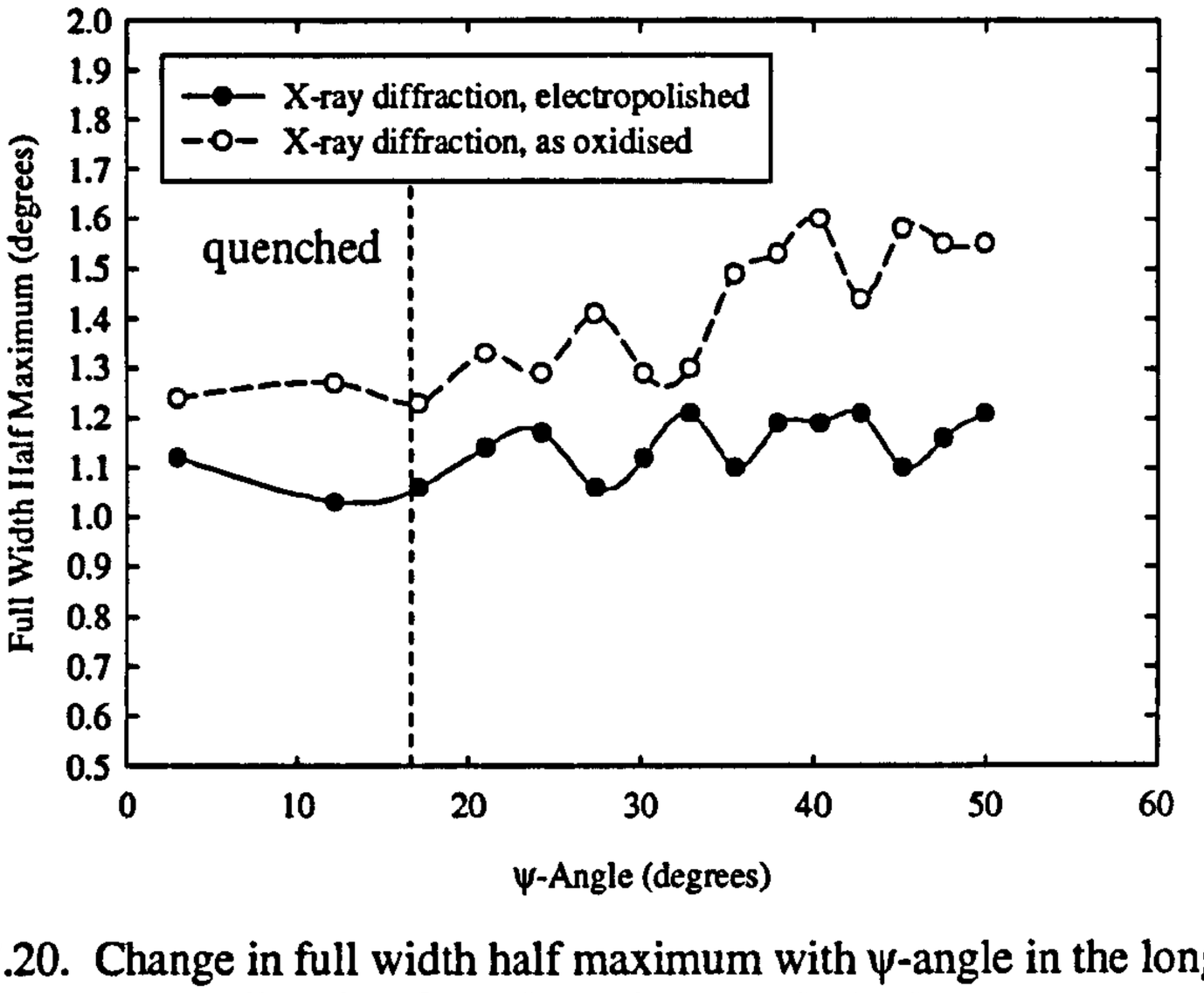

Figure 7.20. Change in full width half maximum with ψ-angle in the longitudinal direction 5mm from the quenched edge.

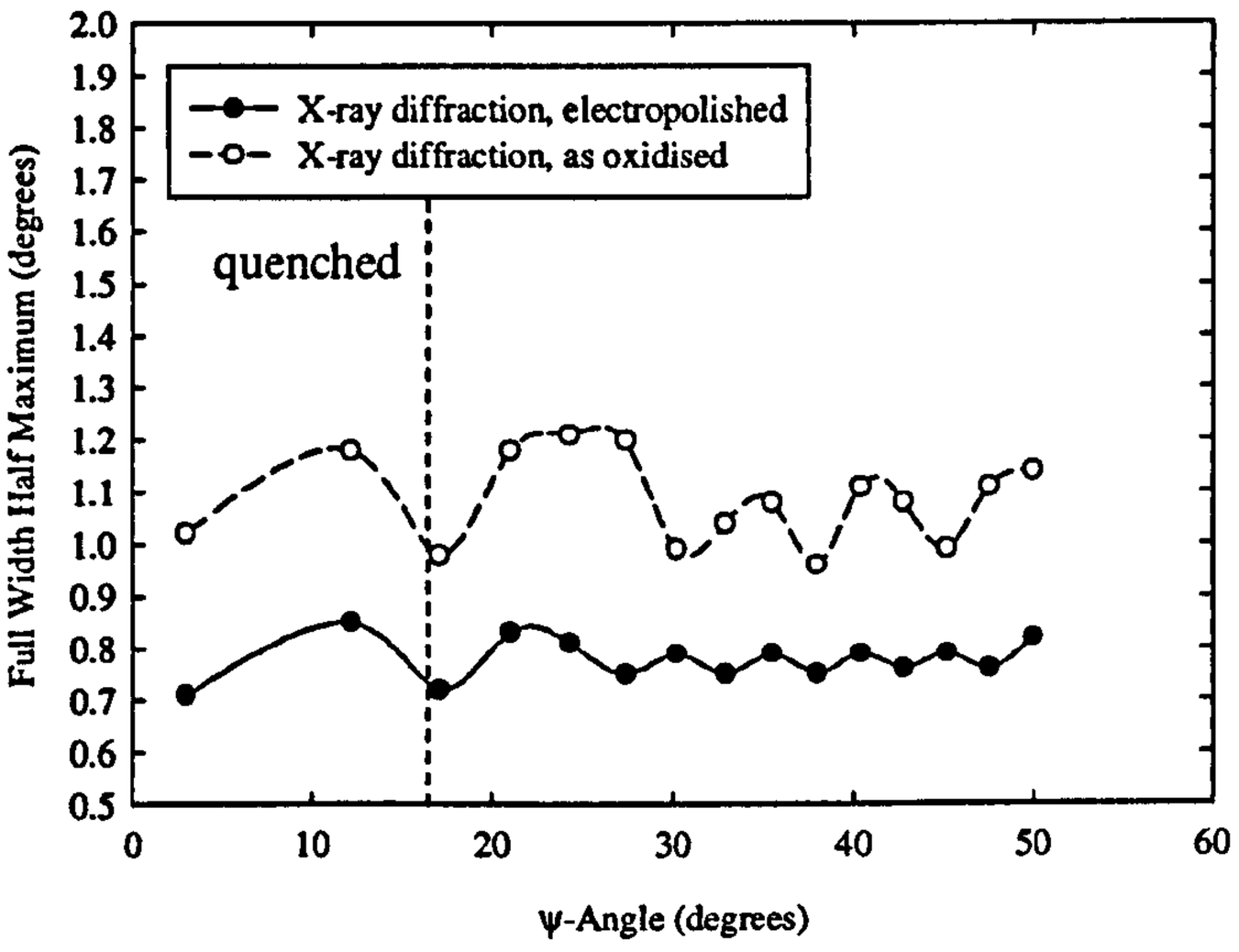

Figure 7.21. Change in full width half maximum with ψ-angle in the longitudinal direction 45mm from the quenched edge.

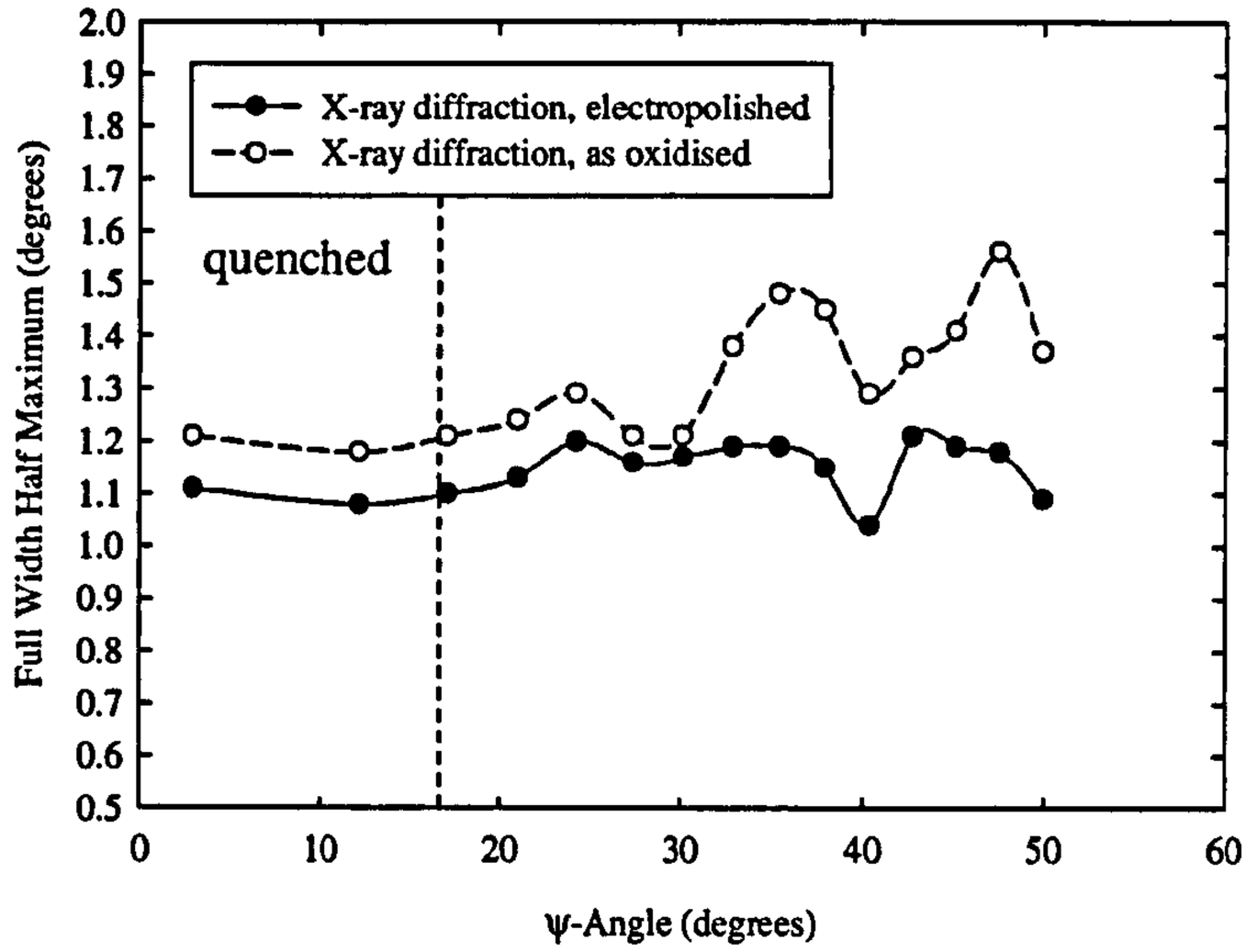

Figure 7.22. Change in full width half maximum with ψ-angle in the transverse direction 5mm from the quenched edge.

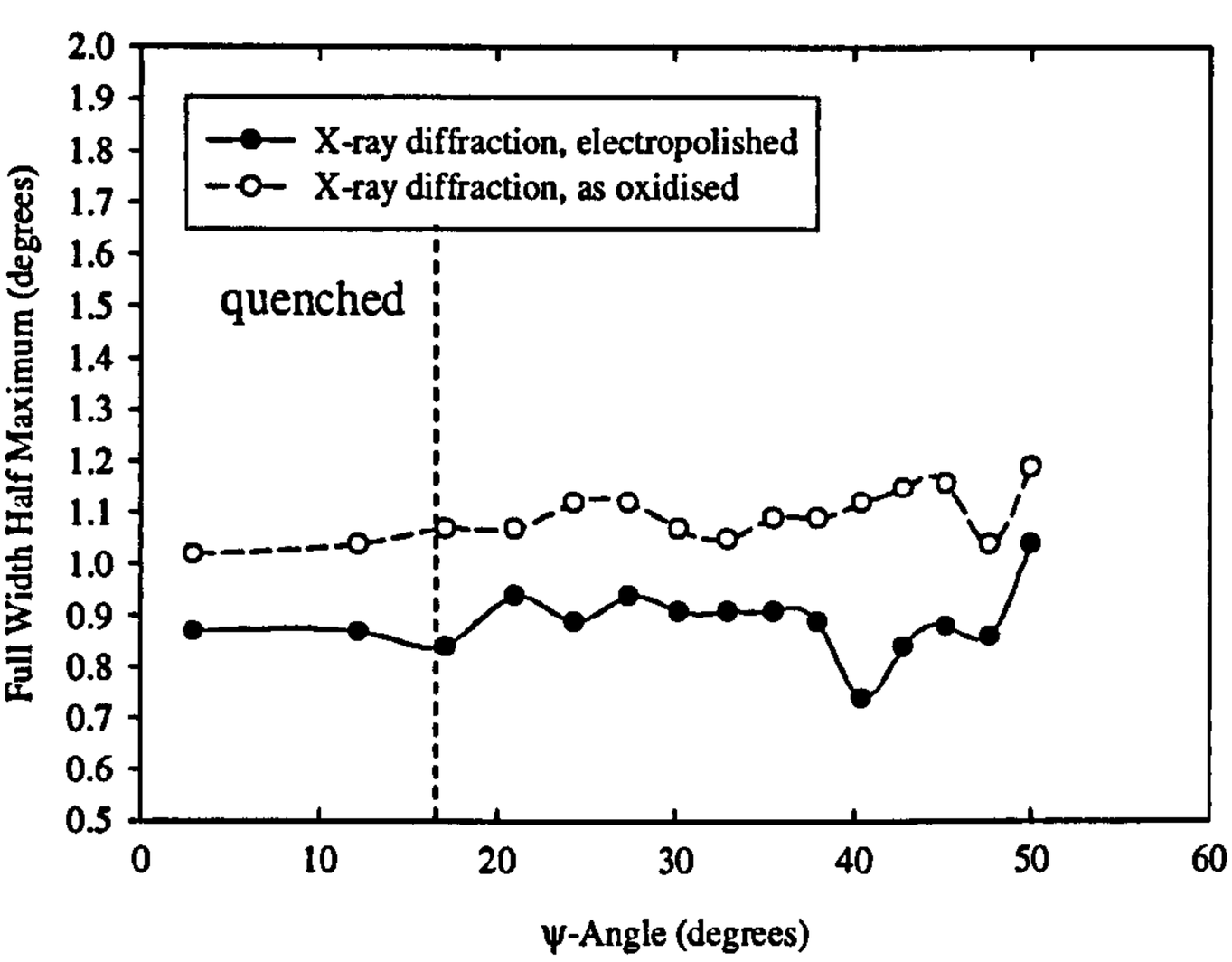

Figure 7.23. Change in full width half maximum with ψ-angle in the longitudinal direction 45mm from the quenched edge.

In all cases, magnitude of the full width half maxima measurements is greater for the "as oxidised" surface than the electropolished surface. The full width half maxima are also greater in the quenched area than the unquenched area. There is little variation in the full width half maxima with ψ-angle in the electropolished areas, or the relatively stress-free areas at 45mm from the quenched edge of the plate.

However, the full width half maxima markedly increase with ψ-angle in the as-received surfaces in the quenched region, particularly for ψ-angles of 35° and over. Thus the microstresses are greater in the quenched area than the unquenched area. These stresses are also greatest on the surface of the "as oxidised" plate than on the electropolished area. Additionally, for the "as oxidised" surface, the magnitude of the measured microstresses increases with ψ-angle for angles of 35.5° and above.

7.8 Summary

Stresses have been predicted and measured in an edge-quenched plate with a well characterised stress distribution. To address length scale aspects, the stresses were predicted using finite element modelling and they were measured using neutron and X-ray diffraction. Additionally, the hydrostatic stresses in the "as-grown" oxide have been measured using Raman spectroscopy. There is a good correlation between the distributions of the residual macrostresses, although the magnitude of the predicted stresses is lower than the measured stresses. As with the macrostresses, the microstresses were greatest in the quenched volume of the plate and towards the surface of the plate. With regards to the Raman spectroscopic measurements, there is a distinct difference between the magnitudes of the measured stresses in the quenched and unquenched areas of the plate. Although the oxide is compressive along the entire width of the plate, the stresses are greater in magnitude in the quenched area than the unquenched area.

8 Spatial Resolution and Length Scale Investigations of Techniques on a Ferritic Steel Butt Welded Pipe

8.1 Introduction

A method for assessing high integrity repair weldments has been proposed by McDonald et al. [McDonald et al 2005]. As discussed in Section 2.5, this method relies on surface and through-section stress measurements being made on a trial weldment along with a surface and through-section finite element model prediction. This is followed by surface measurements across the repair weldment to be used in service in order to confirm the quality of the repair. In this investigation on a ferritic steel butt welded pipe, the proposed method of assessing repair welds is explored with particular emphasis on the extent to which surface stress measurements using X-ray diffraction and through-section stress measurements, using techniques with different spatial resolutions and length scales, can be compared. In addition, the importance of surface preparation of engineering components prior to X-ray diffraction measurements is explored.

Residual stresses in a multipass butt welded P91 ferritic steel pipe with a martensitic microstructure weld were measured using X-ray diffraction on the "as oxidised" surface and after the surface had been electropolished. These measurements were carried out when the pipe was in the "as welded" condition and after post weld heat treatment. The X-ray diffraction measurements (with a penetration depth of $\leq 10\mu m$) are compared to sub-surface and through-section measurements in the form of incremental hole drilling (with a depth penetration of $\leq 1mm$) and deep hole drilling measurements (through-section) carried out by the Department of Mechanical Engineering at the University of Bristol. In addition, these experimental measurements are compared to finite element modelling predictions carried out by the Department of Mechanical Engineering at the University of Nottingham of a similar welded pipe.

8.2 Fabrication of Weldment

Typical composition of P91 ferritic steel pipe and the mechanical properties are given in Table 8.1 and Table 8.2 [Courtesy of Doosan Babcock].

Table 8.1. Typical composition of P91 steel (wt.%).

C	Si	Mn	Cr	Mo	V	Nb	Ni	P	S	N	Fe
0.104	0.27	0.46	8.17	0.90	0.194	0.064	0.16	0.014	0.003	0.055	Bal.

Table 8.2. Typical mechanical properties of P91 steel at ambient temperature.

Yield Strength, σ_y (MPa)	Tensile strength, UTS (MPa)	Young's Modulus, E (GPa)
450	666	214

The welding process was carried out courtesy of Doosan Babcock. First the pipe was preheated to between 200°C and 250°C. The pipe was maintained at this temperature throughout the welding process. The process of manual metal arc welding was used. The heat input per unit length was 1.5kJ/mm and a 4mm diameter Babcock Type M welding rod with composition as shown in Table 8.3 was used.

Table 8.3. Chemical composition of the Type M weld rod metal (wt%).

C	Si	Mn	Cr	Mo	P	Al	Ni	V	Cu	Fe
0.098	0.45	1.11	8.61	1.02	0.015	<0.01	0.22	0.21	0.05	Bal.

The weld consisted of 73 passes, which were carried out by welding in one direction from the bottom of the weld preparation to the outer surface of the pipe. The final layer of the weld consisted of six capping runs which extended over the original weld prepared surface by approximately 5mm on each side and extended above the pipe surface by up to 4mm. The pipe was cooled to room temperature on completion. Diagrams of the weld runs and weld dimensions can be seen in Figure 8.1 and Figure 8.2 respectively. The post weld heat treatment of the pipe was carried out at a temperature of 760°C for 3 hours with a heating rate of 100°C/hour and a cooling rate of 46°C/hour.

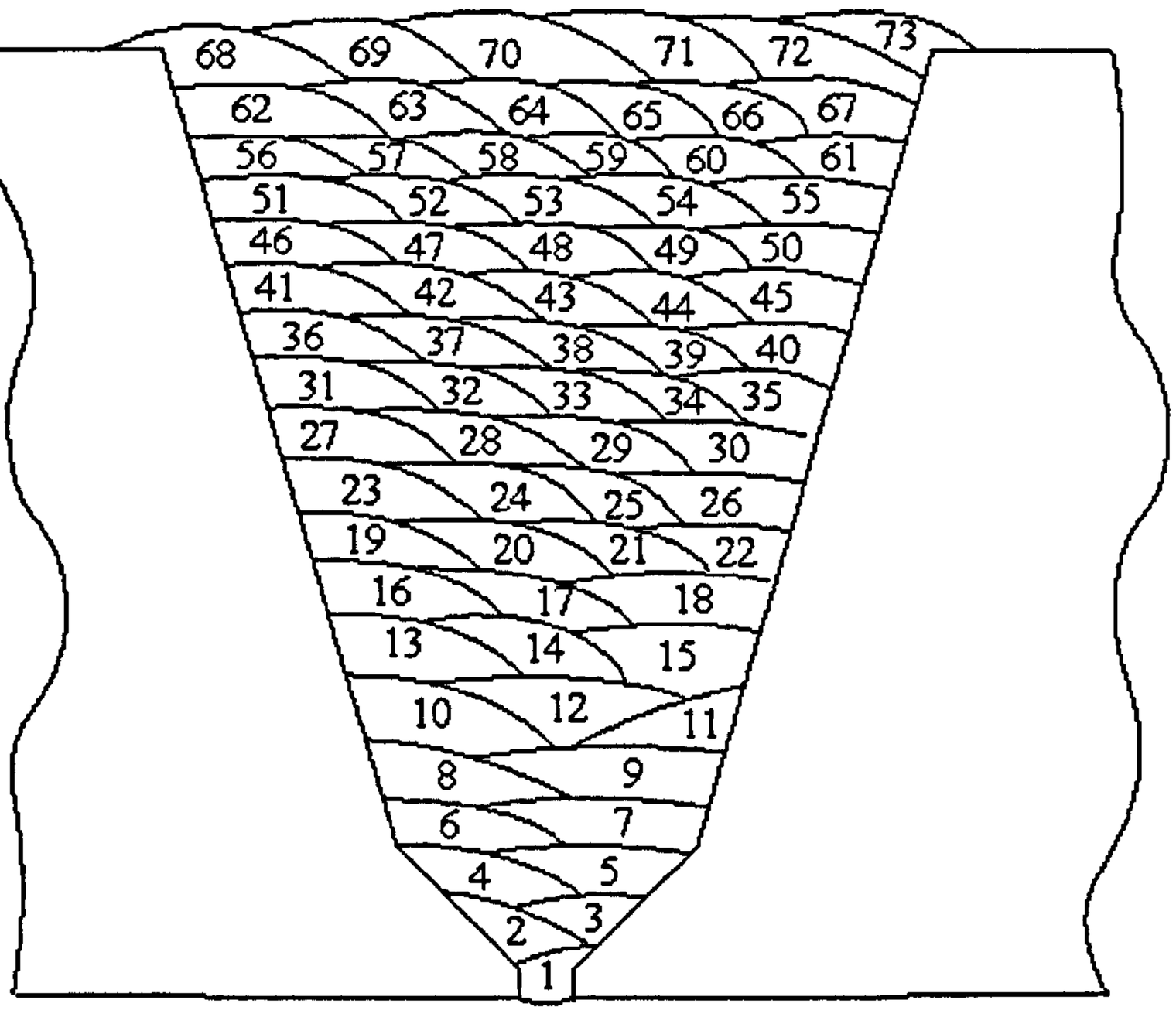

Figure 8.1. Sequence of runs in multipass butt weld.

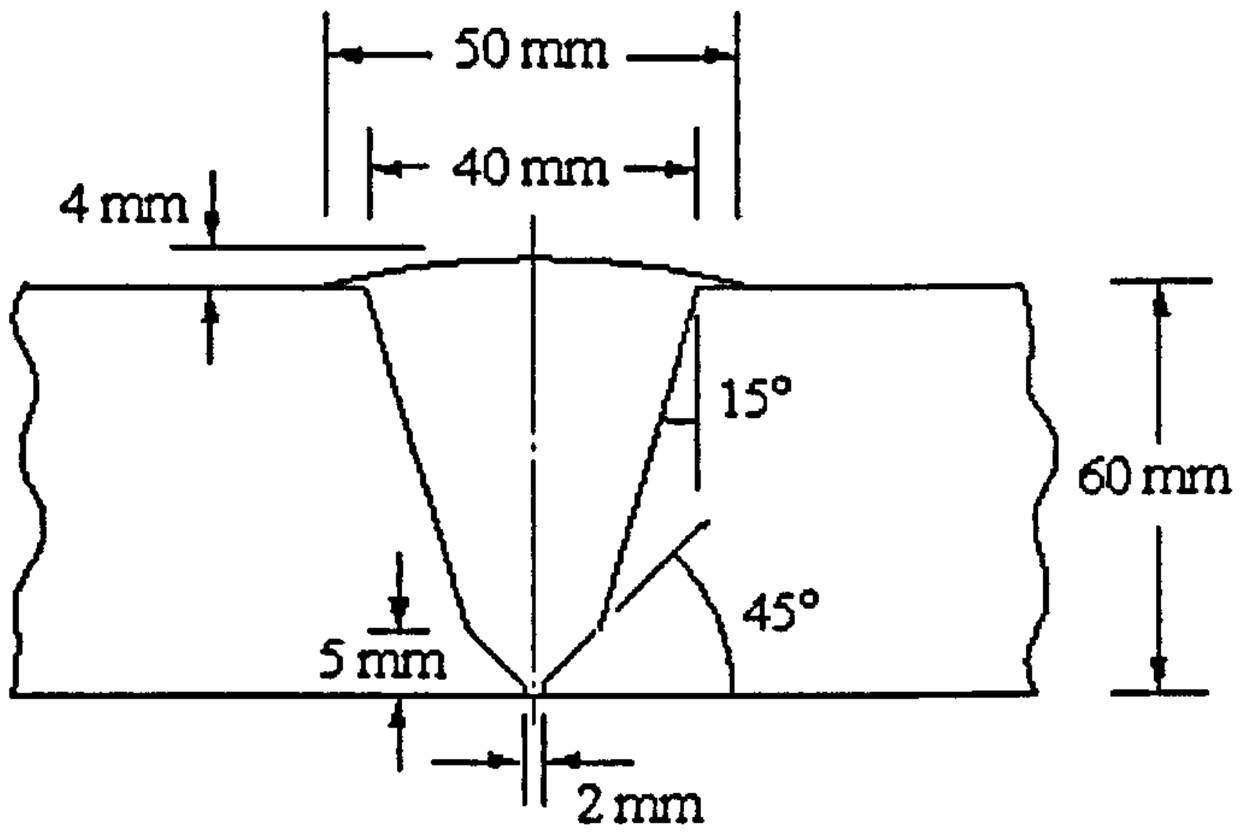

Figure 8.2. Butt weld dimensions.

The parent material had a tempered martensitic microstructure with a prior austenite grain size of approximately 20μm diameter (calculated using the mean linear intercept method). The weld beads consisted of "as cast" columnar grains and grain refined regions which arose from the heat treatment caused by the laying-down consecutive beads. The microstructure within these grain refined regions was tempered martensite

with a small proportion of delta ferrite. The heat affected zone (HAZ) extended visually over a distance of approximately 4mm from the adjacent weld bead, Figure 8.3. There were two main microstructural regions within the HAZ. There was a coarse grained tempered martensite region adjacent to the fusion boundary with a prior austenite grain size of approximately 40μm. Adjacent to this was a region of varying microstructure with a prior austenite grain size of approximately 10μm.

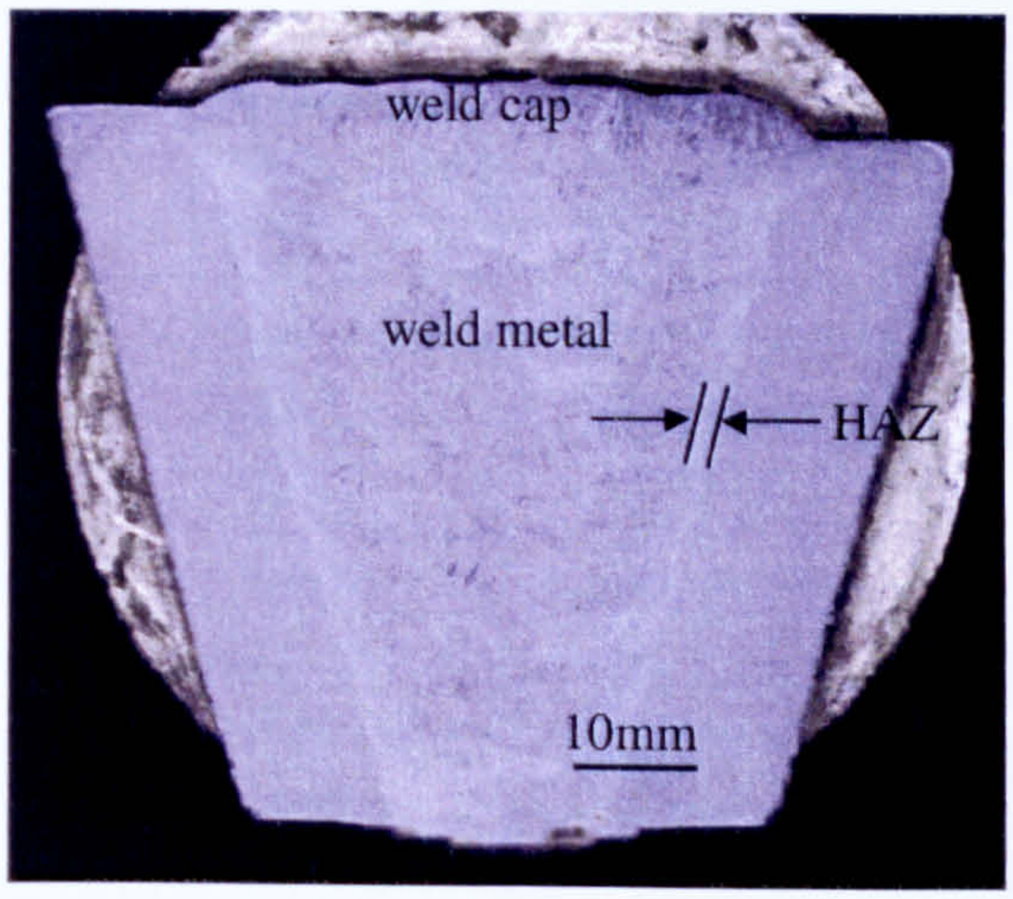

Figure 8.3. Macro-section of weld showing the heat affected zone and the height of the weld cap. Courtesy of Dr. Wei Sun, University of Nottingham.

8.3 Measurements

The locations at which the measurements were carried out can be seen as a third angle projection in Figure 8.4. The lines across which X-ray diffraction (referred to as XRD) measurements were made are shown along with positions at which incremental hole drilling (ICHD) and deep hole drilling (DHD) measurements were made. The incremental hole drilling measurements (ICHD1 and ICHD2) were made prior to heat treatment. The deep hole drilling measurements labelled DHD1, DHD2 and DHD3 were made prior to heat treatment. DHD4 and DHD5 were made post heat treatment. The measurement procedures at these locations are discussed in more detail in Sections 8.3.1, 8.3.2 and 8.3.3.

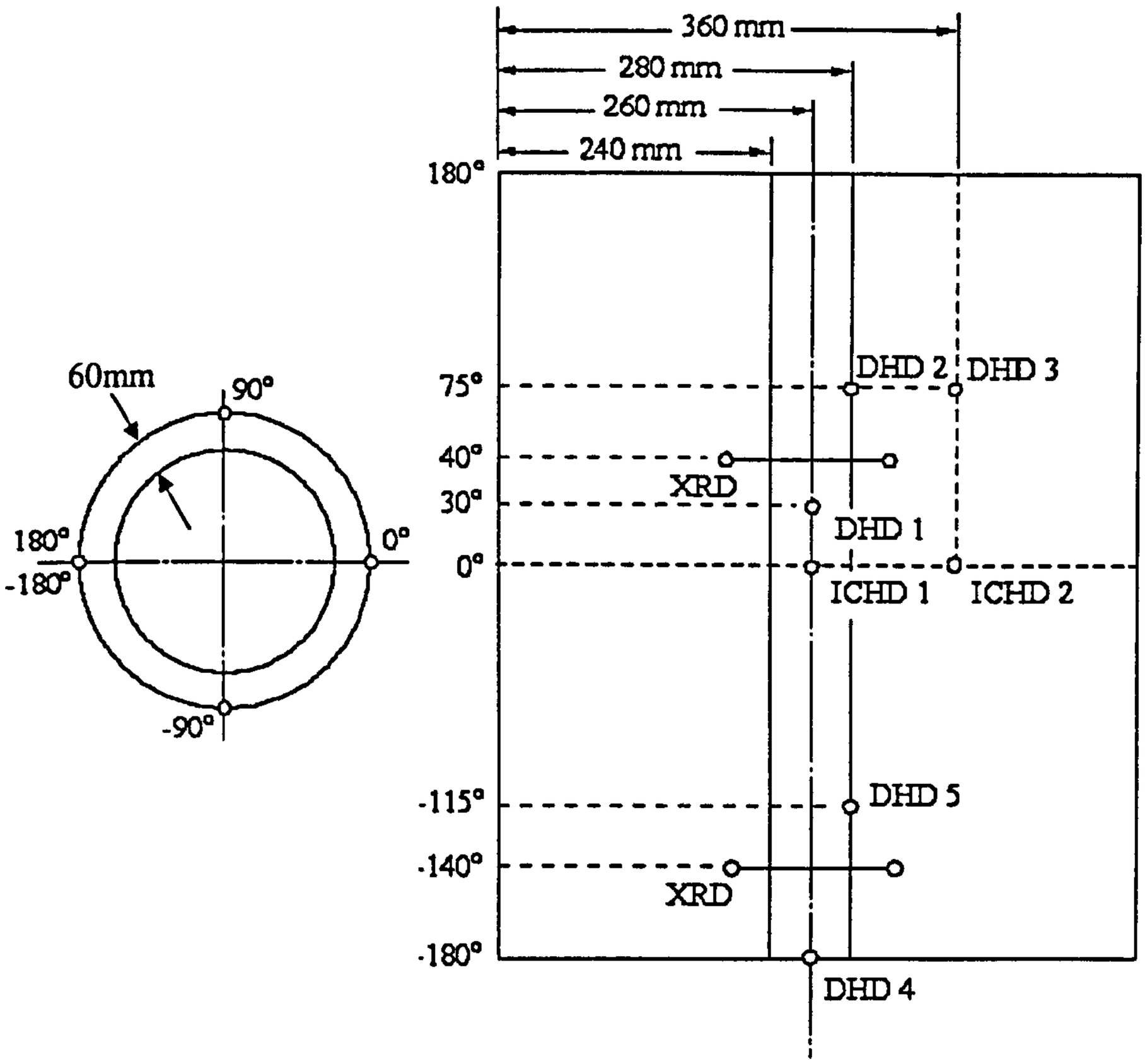

Figure 8.4. Measurement locations on weld and parent pipe.

8.3.1 X-Ray Diffraction

The X-ray diffraction technique and the transportable goniometer used have been discussed in Chapter 3 - Techniques. A collimator with a 1mm diameter aperture was selected. The X-radiation was provided by a CrKα X-ray tube which resulted in the analysed {211} diffraction peak being at approximately 156°. The voltage across the X-ray tube was approximately 30kV and the current approximately 25mA. All measurements were calibrated with a cerium oxide powder.

X-ray measurements were taken across the weld in the hoop and axial directions. The diffracted X-ray peak positions were used to measure macrostresses and the peak widths were used to give an indication of the microstresses present. Prior to the post weld heat treatment, this was done on the "as oxidised" surface and after surfaces had been prepared by mechanical polishing and electropolishing using 5%HCl in water.

Measurements on the "as oxidised" surface were made across two lengths of the pipe at a circumferential displacement of 100° in order to establish whether bending stresses were present. Following measurements on the "as oxidised" surface, measurements on the prepared, electropolished pipe were repeated along the 40° axis as shown in Figure 8.4. Figure 8.5, a photograph of the welded P91 pipe investigated, shows the surfaces along which X-ray diffraction measurements were made and demonstrates the surface preparation which was undertaken. Prior to the electropolishing, 2 to 2.5mm of material was ground from the weld metal cap on the previously described 40° axis in order to produce a flat, level surface. However, as little parent material as possible was removed from the parent pipe. The ground length was then mechanically polished and electropolished. Only measurements taken on the "as oxidised" surface were made after the post weld heat treatment. These were taken adjacent to the previously electropolished region. The post weld heat treatment of the pipe is described in Section 8.2.

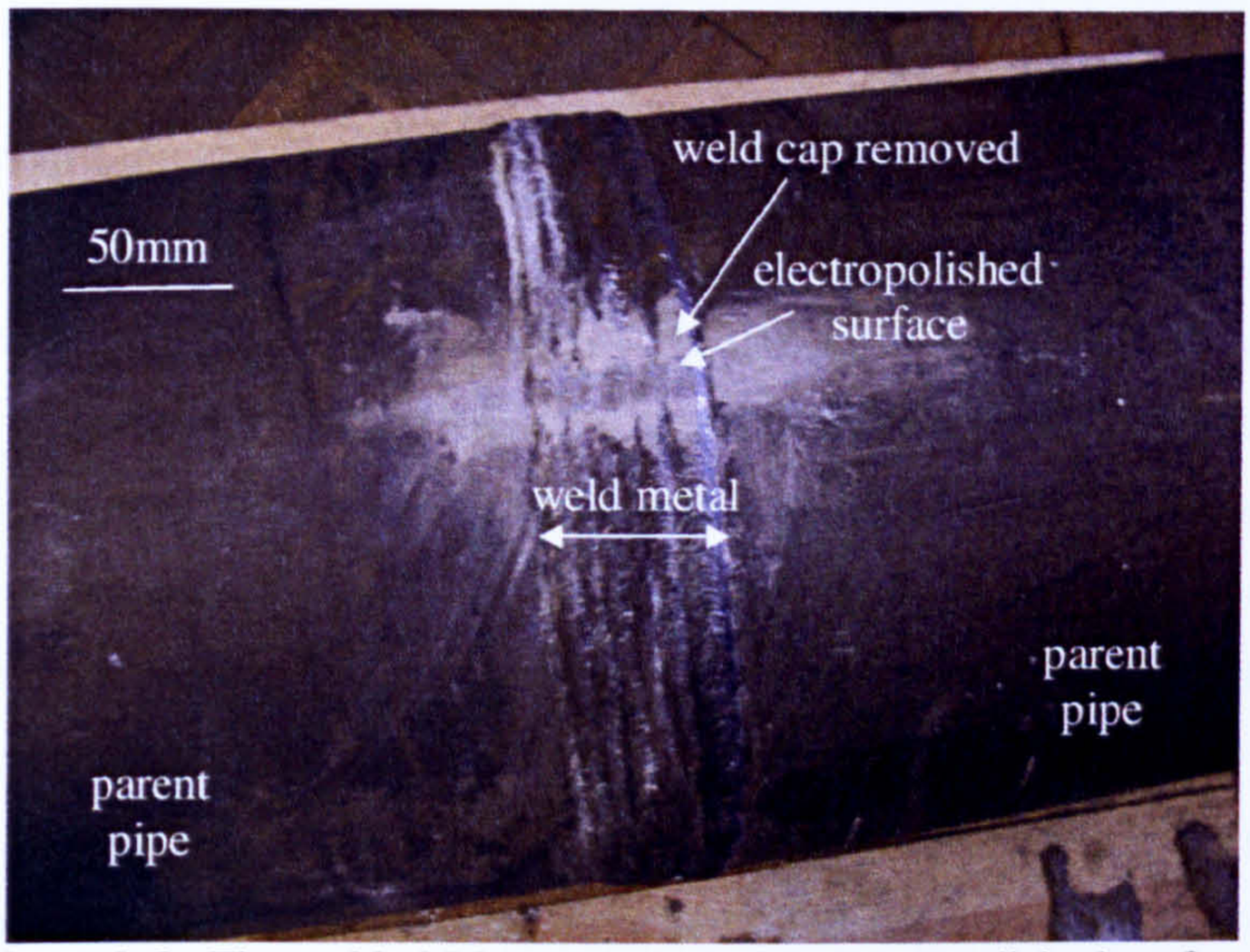

Figure 8.5. The welded P91 steel pipe with electropolished surface.

8.3.2 Incremental Hole Drilling

Incremental hole drilling measurements were made on the weldment prior to the post weld heat treatment [Hilson et al. 2008]. No measurements were made after the post weld heat treatment. The strain gauges used were three element strain gauge rosettes with a mean radius of 2.57mm. The surface near the centre of weld metal was machined to remove approximately 2mm from the top of the weld beads to create a flat surface for the strain gauge rosettes. This was done by electro-discharge

machining with a copper electrode of 25mm in diameter and energy of approximately 0.8J. The surface was polished with 800µm silicon carbide paper before the strain gauge rosette was applied. The electro-discharge machined surface was carried out so as to span weld beads 69 to 71 and the centre of the rosette was positioned to be approximately over the 70th weld bead. A drill size of 1.6mm was chosen which resulted in a hole of approximately 1.7mm in diameter. Measurements were made starting from a depth of 16µm up to a depth of 1mm into the pipe wall.

8.3.3 Deep Hole Drilling

Prior to the post weld heat treatment, measurement locations were selected for deep hole drilling (i) at the centre of the weld, (ii) at the edge of the weld, and (iii) remote from the weld in parent metal. After the post weld heat treatment had been carried out, measurements were taken (i) through the centre of the weld and (ii) the parent material, remote from the weld. The diameter of the drilled hole was measured every 0.2mm through the thickness of the pipe in all cases.

8.3.4 Finite Element Prediction

As part of the integrated Supergen project, finite element modelling was carried out using ABAQUS software based using the solid mechanics approach, consisting of the modelling of the thermal process followed by a sequentially coupled thermal analysis [Yaghi et al. 2008]. Models were made with and without including solid state phase transformation, which allows for the effect of volumetric changes due to austenitic-martensitic phase transformations. The root bead (the first bead) was modelled so as to protrude below the inner bore by 1.5mm and the weld crown (last layer) protruded 1.55mm above the outer surface. Each bead was considered to be a pass in the finite element mesh, so that the number of passes in the finite element model was equal to the number of beads. The element birth technique was used to model the laying of the weld beads [Brickstad and Josefson 1998]. This technique avoids displacement or strain mismatch at nodes connecting weld elements to the parent material. The thermal analysis was simulated by applying a distributed heat flux (DFLUX) to the weld elements [Yaghi et al. 2008]. The thermal boundary conditions allowed for heat transfer by convection and radiation. A time gap was allowed between each pass for the weld beads to cool to ambient temperature.

8.4 Results

8.4.1 X-Ray Diffraction

The linearity of the 2θ versus $\sin^2\psi$ plots in the weld metal were shown to be sufficiently linear for measurement without the need for surface preparation, Figure 8.6.

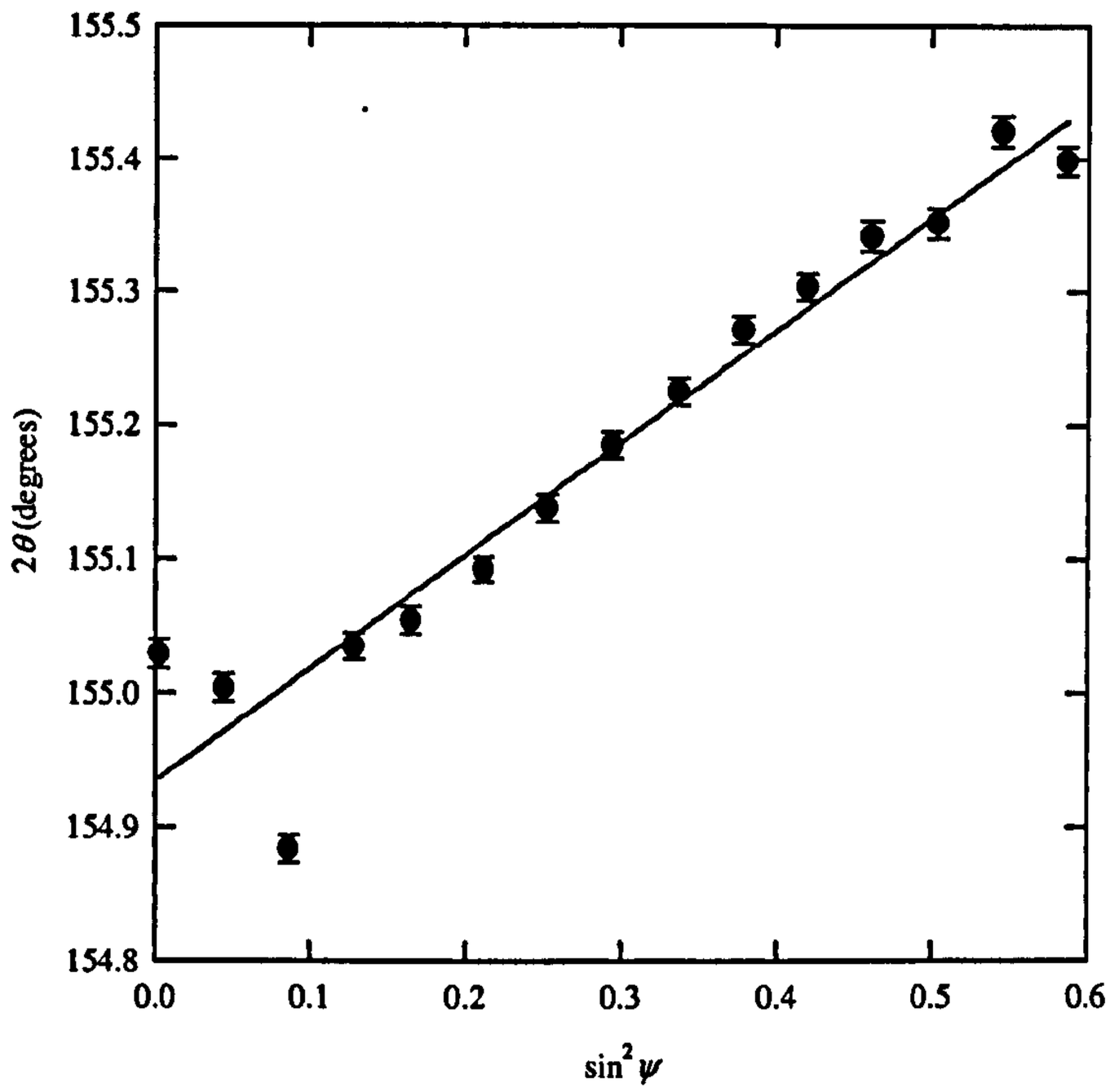

Figure 8.6. Linear relationship of 2θ versus $\sin^2\psi$ for weld metal.

The X-ray diffraction distribution of hoop and axial stresses measured by the centre of gravity method, can be seen for the weld region at the 40° axis along the pipe, Figure 8.7(a) and (b) respectively. They can be seen for the "as oxidised" and electropolished surfaces.

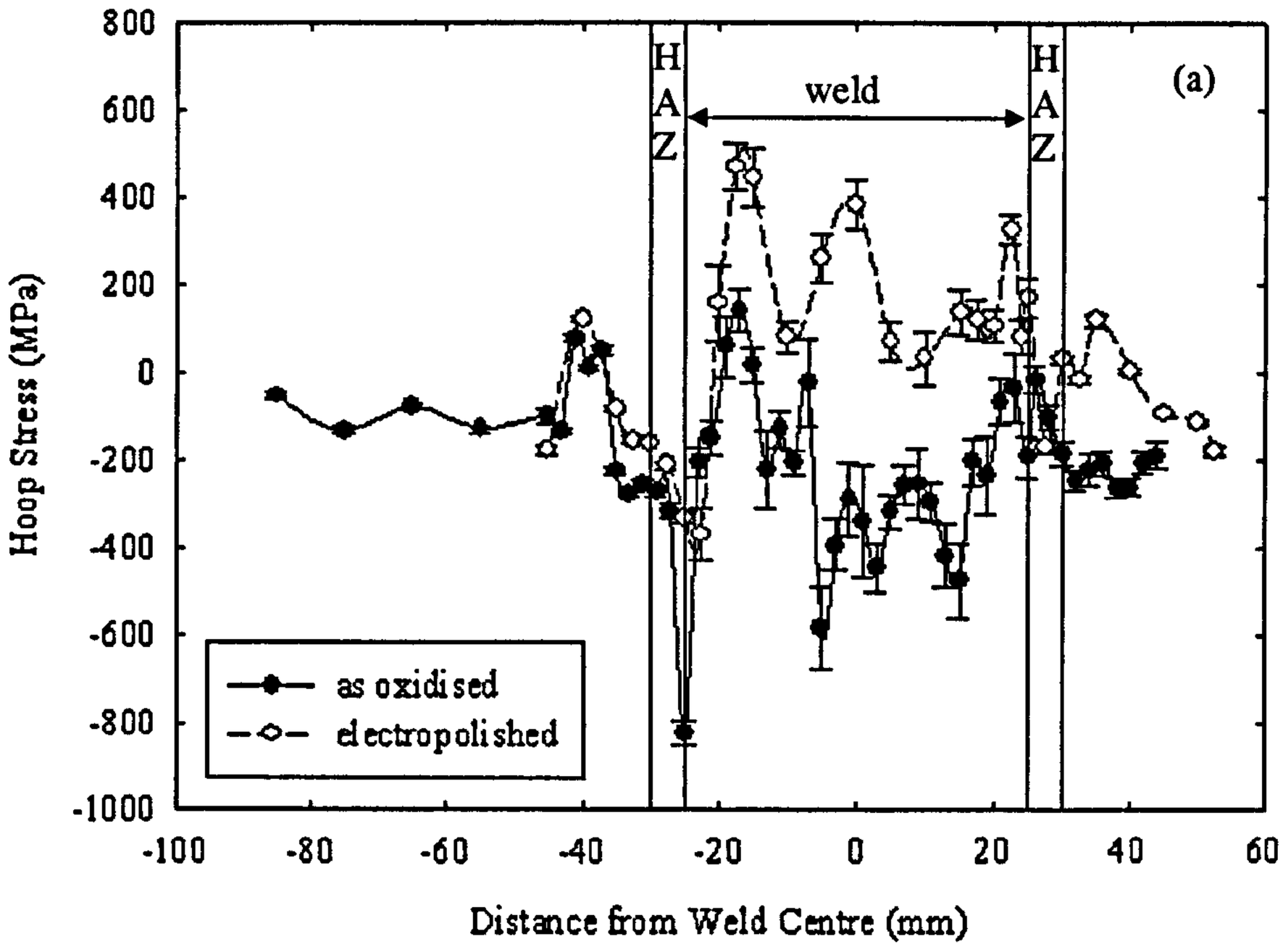

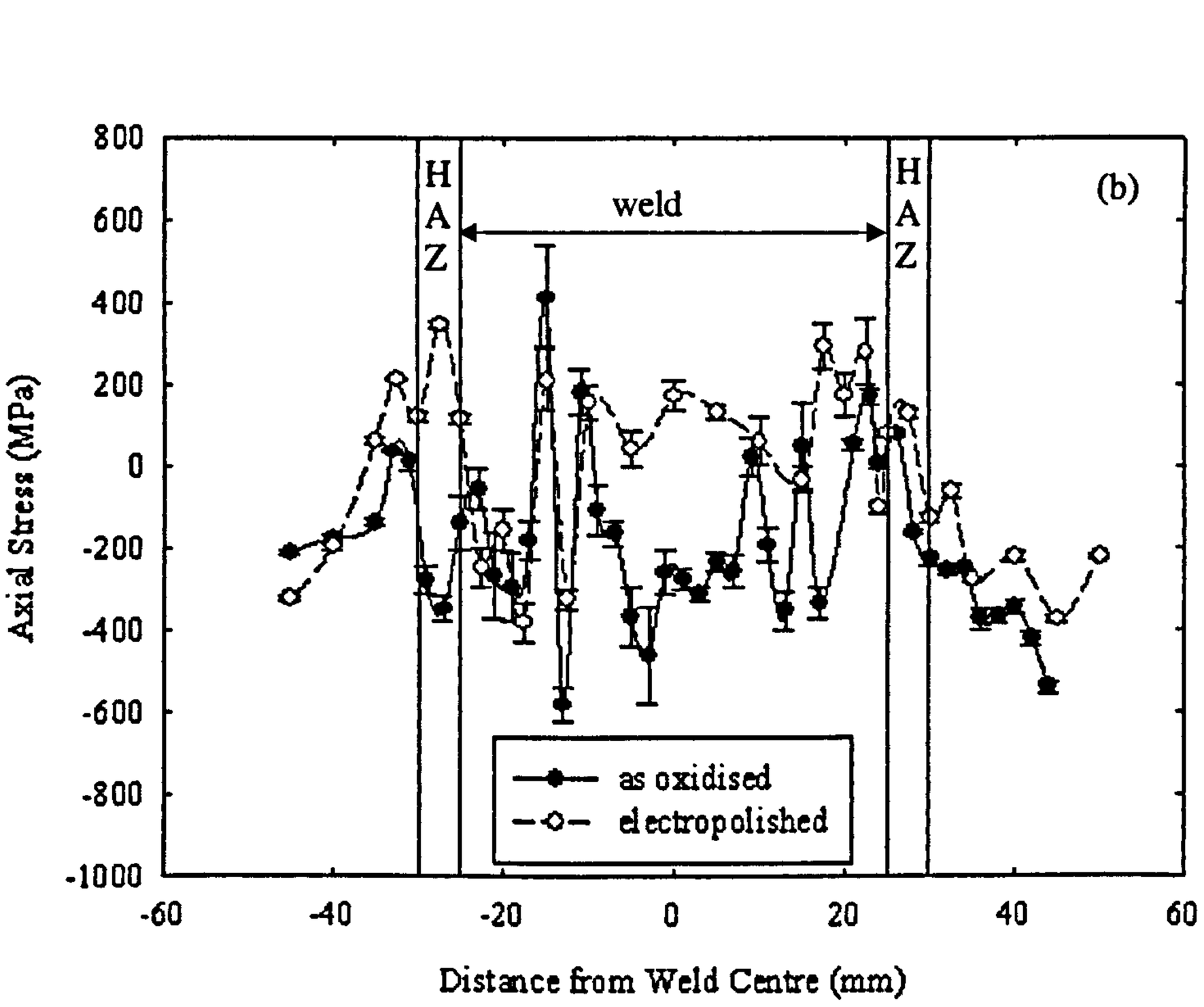

Figure 8.7. Stresses at 40° along the pipe for the as oxidised and electropolished surfaces. The hoop stresses are shown in (a), the axial stresses are shown in (b).

Hoop stress measurements made in the weld metal on the "as oxidised" surface are predominantly compressive and fluctuate between –800MPa and 200MPa. However, the measurements made on the electropolished surface are predominantly tensile in the weld region and fluctuate between –400MPa and 450MPa. There is little correspondence in the trends of the stresses measured along the two surfaces. On either side of the weld metal, the stresses measured are lower in magnitude, aside from one measurement made in the heat affected zone. The magnitudes and trends of the stress measurements on the "as oxidised" and electropolished surfaces in the parent pipe and heat affected zone are comparable on one side of the weld metal but not the other. Between –25mm to –50mm i.e. on one side of parent pipe and heat affected zone there is good correlation between the measurements made on the "as oxidised" and electropolished surfaces. The measurements lie close to the error of each other and follow the same stress trend with distance. Between 25mm and 55mm, i.e. across the heat affected zone and parent pipe to the other side of the weld, the measurements made on the "as oxidised" surface show predominantly compressive stresses and the measurements made on the electropolished surface show a combination of compressive and tensile stresses. There is therefore poor correlation between the measurements made on the "as oxidised" and electropolished surfaces in this region of the parent pipe and heat affected zone.

Axial stresses measured within the weld region reveal predominantly compressive stresses along the "as oxidised" surface and predominantly tensile stresses along the electropolished surface, as is the case with the hoop stresses. Again, on either side of the weld, the stresses measured are smaller in magnitude than those measured in the weld metal. Between –25mm to –30mm, there is little correlation between the stresses measured on the "as oxidised" and electropolished surfaces. The stresses measured on the "as oxidised" surface are compressive and those on the electropolished surface are tensile. They also do not follow the same trend. However, between approximately –30mm and –50mm, i.e. in the parent pipe away from the heat affected zone, the stresses measured along both surfaces are more coherent. The magnitudes of the stresses measured on "as oxidised" and electropolished surfaces are close in value, within 100MPa of each other, and follow the same trend. On the other side of the weld, there is a good correlation between the

stresses measured on the two surfaces in the heat affected zone and the parent pipe with the measurements largely within 100MPa of each other.

Hoop and axial stresses across the "as oxidised" surface of the weld on the 140° axis in Figure 8.8(a) and (b) respectively, are of similar magnitudes to those across the weld on the 40° axis. The hoop stresses measured across the weld are predominantly compressive and reach a maximum compressive stress of approximately –500MPa. On either side of the weld i.e. in the heat affected zone and parent material, the stresses measured are also compressive, although smaller in magnitude. As with the, the axial stresses measured in the weld metal are also predominantly compressive and reach a maximum compressive stress of approximately –600MPa. However, the stresses in the heat affected zones become tensile and then fluctuate between being tensile and compressive in the parent material. Similarities between the measurements across the two axes suggest that the welding process did not induce bending stresses.

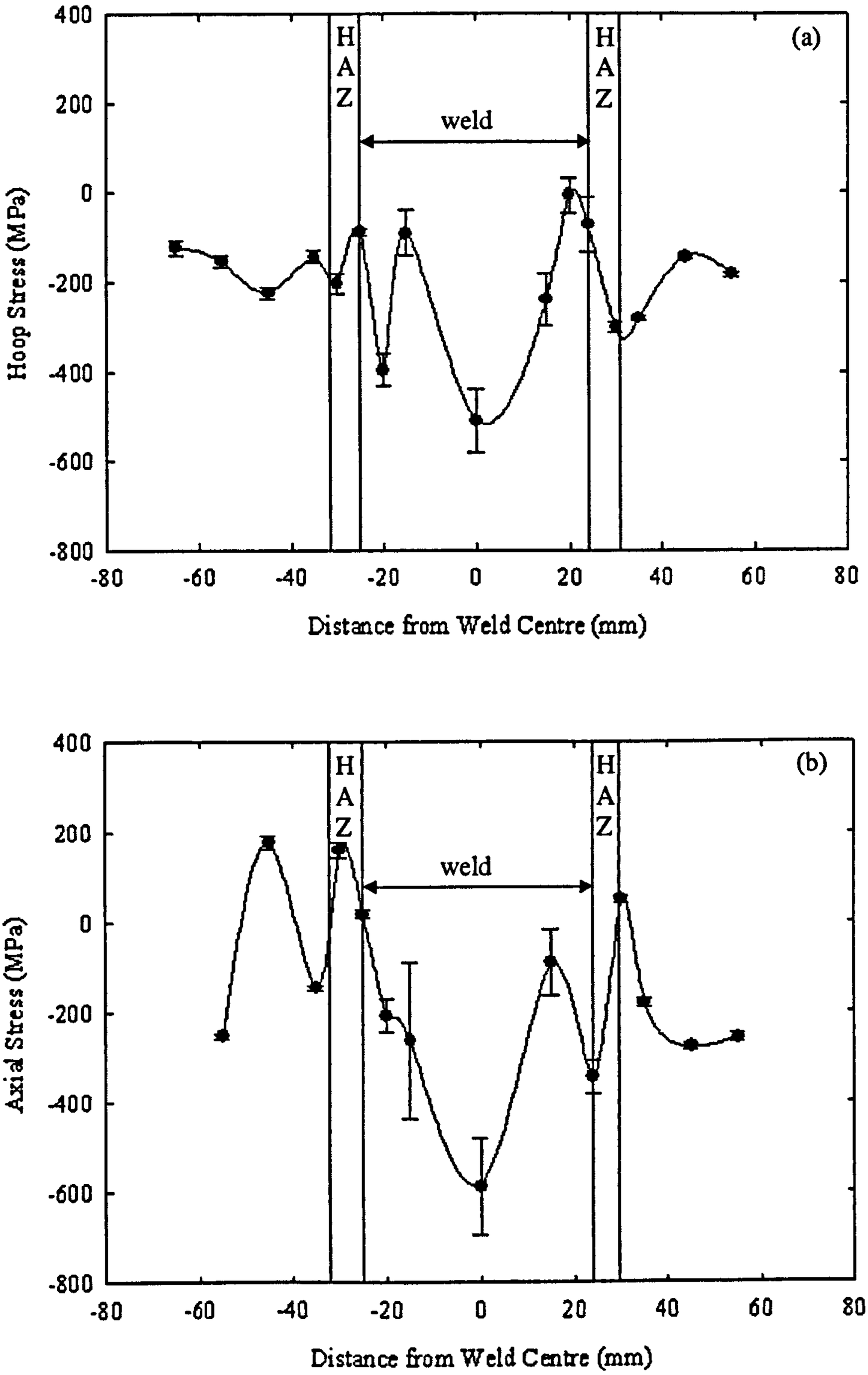

Figure 8.8. Stresses at 140° along the pipe on the as oxidised surface. Hoop stresses are shown in (a) and axial stresses are shown in (b).

Hoop and axial stresses on the post weld heat treated pipe across the weld at the 40° region on the as oxidised surface are compared in Figure 8.9.

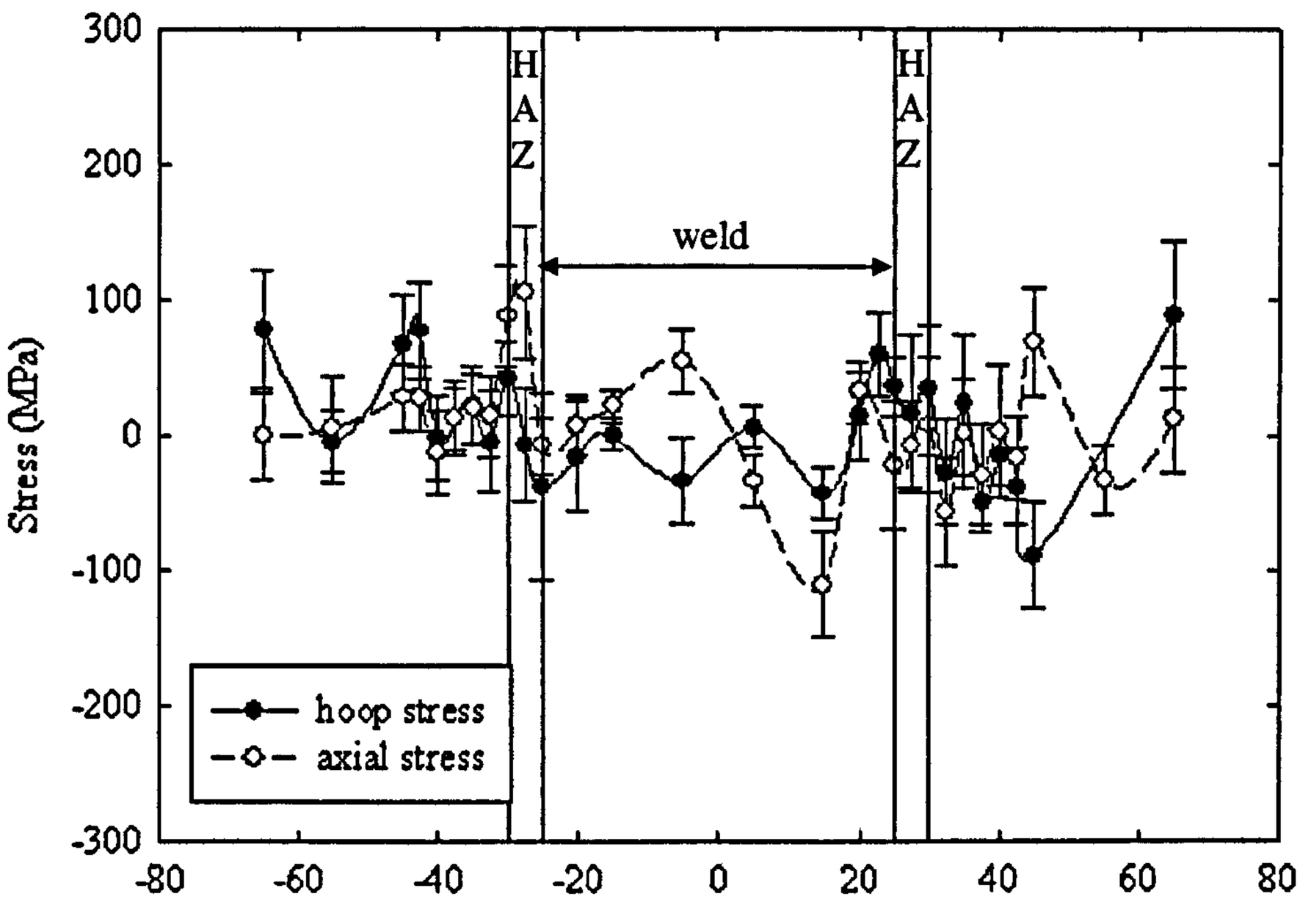

Figure 8.9. Post weld heat treated hoop and axial stresses across weld.

There is a good correlation between the hoop and axial stresses after the post weld heat treatment, with the data points often lying within the error of each other. The hoop and axial stress measurements were made on the "as oxidised" surface and the measured stresses predominantly fluctuate between −100MPa and 100MPa.

Full width half maxima at a ψ-angle of 3° were recorded across the weld, in order to establish whether information could be gained on the level of microstresses across the weld metal, heat affected zones and parent pipe. The ψ-angle was chosen, as it would result in the sample surface being approximately normal to the direction of the incident X-ray beam and the greatest available penetration depth would therefore be analysed. Figure 8.10 is the full width half maxima against distance from weld centre along the 40° axis for the hoop and axial conditions.

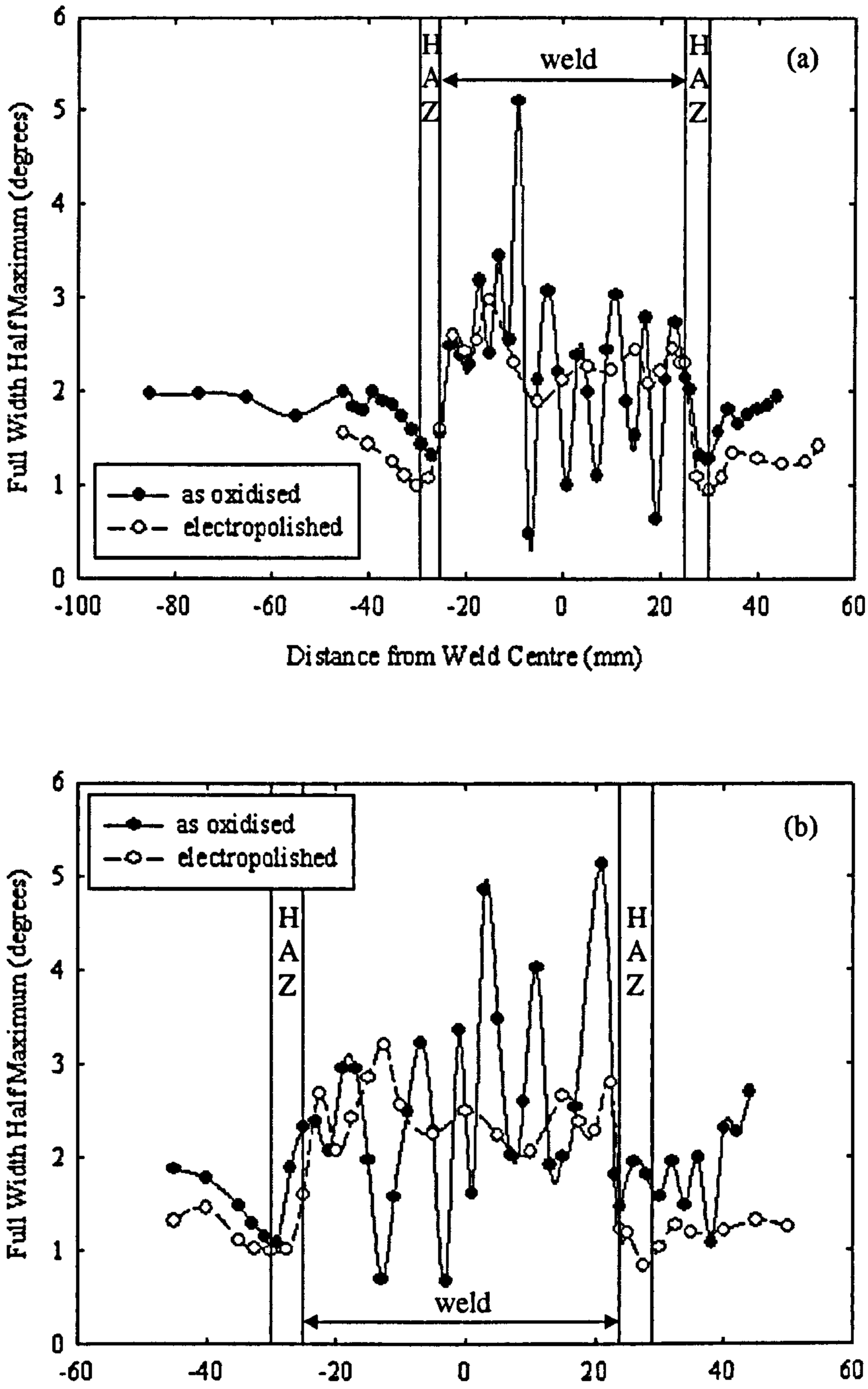

Figure 8.10. Full width half maxima against distance from weld centre along the 40° axis. Full width half maxima in the hoop direction are shown in (a) and in the axial direction are shown in (b).

In the hoop direction along the 40° axis (Figure 8.10(a)), the full width half maxima along the "as oxidised" surface in the parent metal and heat affected zone are greater in magnitude than those on the electropolished surface, indicating microstresses of greater magnitude on the "as oxidised" surface. However, there is a similar trend for both surfaces, with a dip in full width half maximum on either side of the weld coinciding with the heat affected zone and indicating a reduction in the level of microstress in that area. There is more fluctuation in the full width half maxima on the "as oxidised" surface in the weld region than on the electropolished surface in that region. The full width half maxima measured on the electropolished surface in the weld region are relatively stable in magnitude, between approximately 2° and 3°. The full width half maxima of the as oxidised surface, on the other hand, vary between approximately 0.5° and 5°.

In the axial direction along the 40° axis (Figure 8.10(b)) there is a good correlation between the trends of the full width half maxima on the "as oxidised" and electropolished surfaces in the heat affected zone and parent material to one side of the weld (at distances below –25mm), with both sets of data forming a dip immediately after the weld. However, on the other side of the weld, at distances above 25mm, there is poor correlation between measurements taken on the two surfaces. The measurements taken from the electropolished surface show a dip in magnitude of full width half maximum after the weld but the measurements from the "as oxidised" surface fluctuate and there is no clear trend. On either side of the weld, the full width half maxima on the "as oxidised" surface are greater then on the electropolished surface, indicating higher microstresses on the "as oxidised" surface. In the weld region, the measurements from the electropolished surface are relatively stable in magnitude, as with the full width half maxima in the hoop direction, and are of similar values as those in the hoop direction. Also, as per the measurements made in the hoop direction, the measurements taken on the "as oxidised" surface in the weld region fluctuate between approximately 0.5° and 5°.

Figure 8.11 shows the full width half maxima across the weld in the axial and hoop directions along the 140° axis. The measurements were made along the "as oxidised" surface.

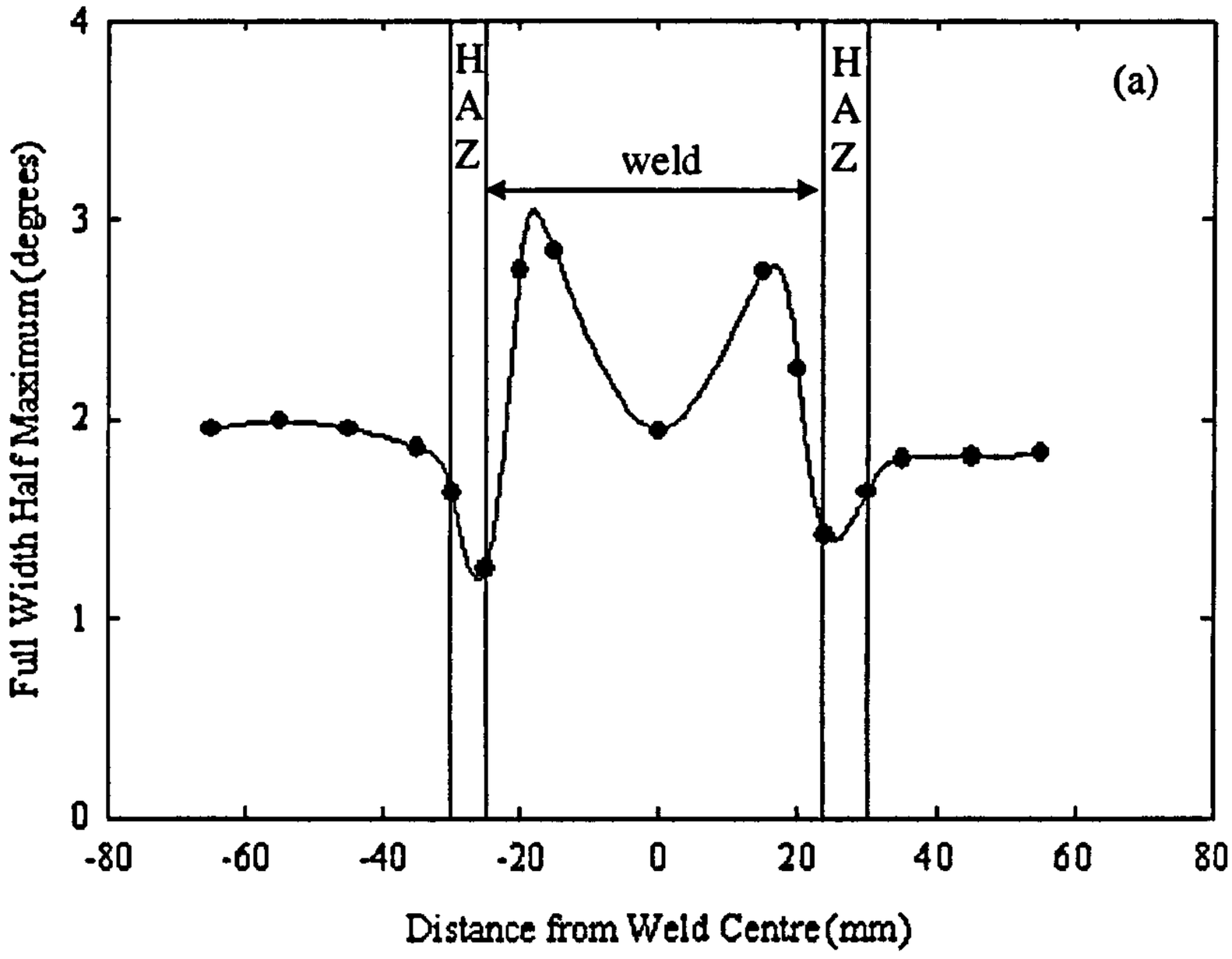

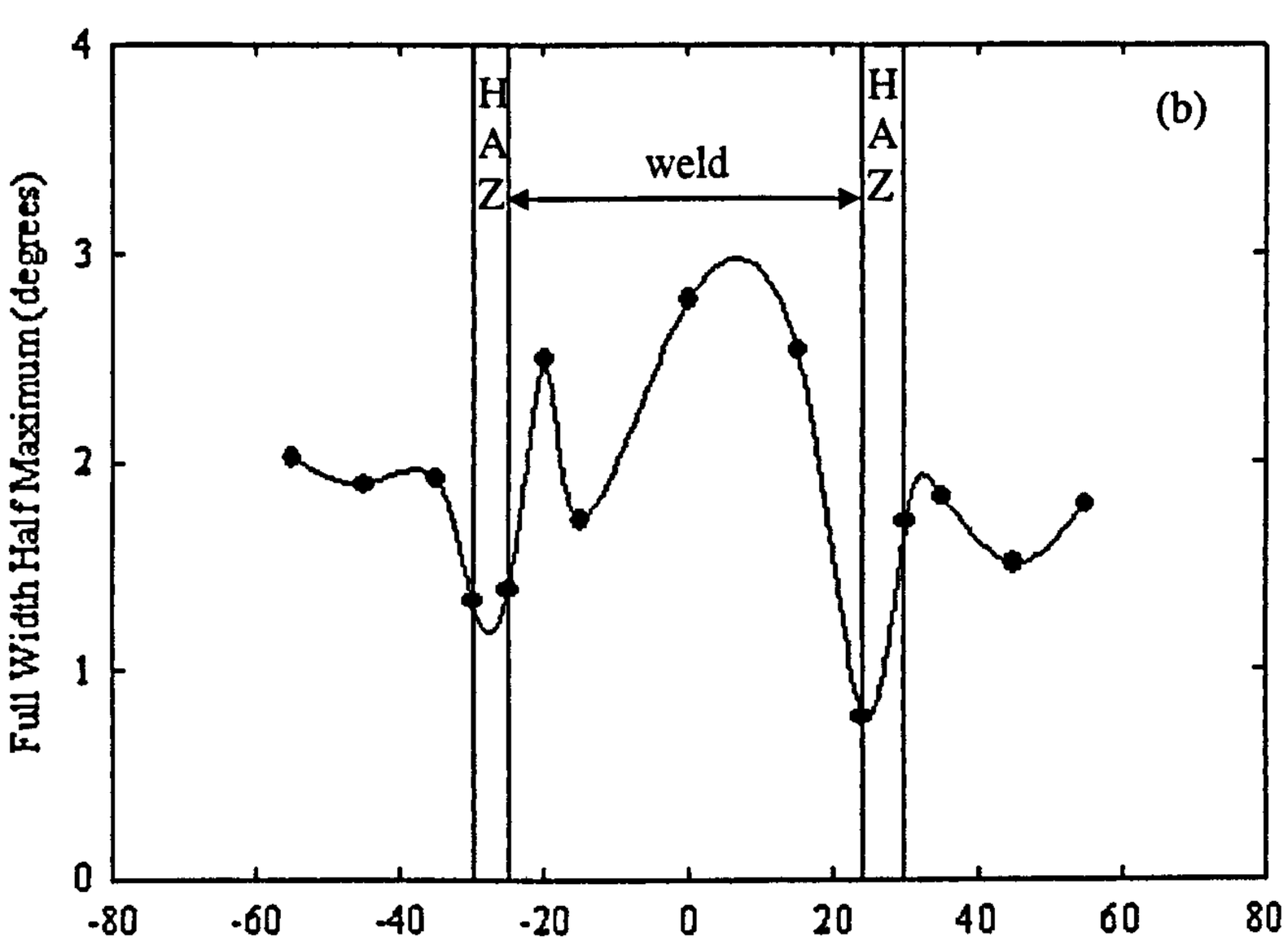

Figure 8.11. Full width half maximum on the "as oxidised" surface in the (a) hoop and (b) axial directions against distance from weld centre along the 140° axis.

The full width half maxima in both the axial and hoop directions have the greatest magnitudes in the weld metal. The full width half maxima then decrease in the heat affected zones. The full width half maxima increase on either side of the heat affected zones and plateau between approximately 1.5° to 2°.

Figure 8.12 shows the full width half maxima along the 40° axis after post weld heat treatment. The measurements were made along the "as oxidised" surface.

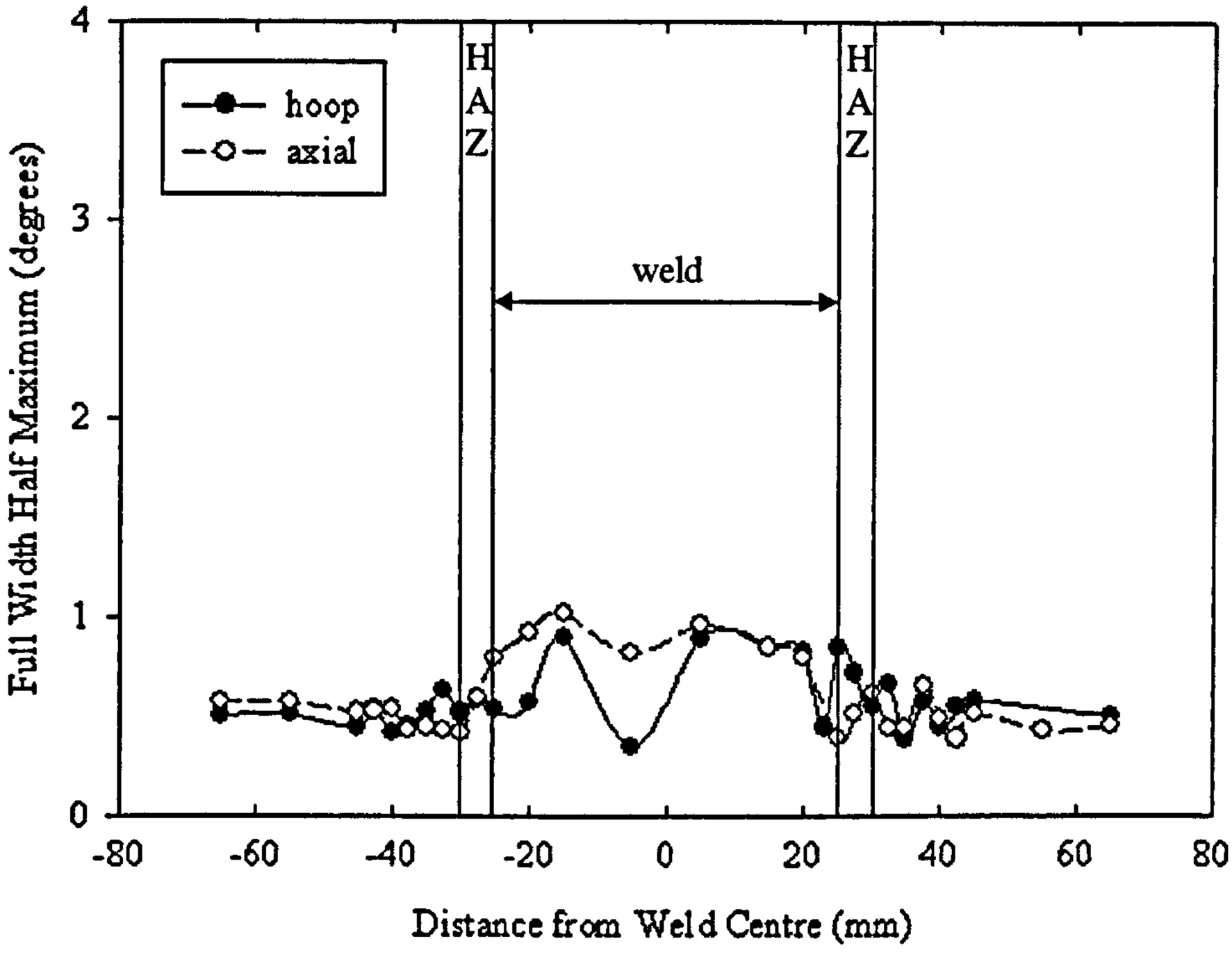

Figure 8.12. Full width half maximum on the "as oxidised" surface in the hoop and axial directions against distance from weld centre along the 40° axis.

The full width half maxima in the after the heat treatment are lower in magnitude in both the hoop and axial directions than prior to the heat treatment. This indicates that the microstresses have been reduced by the heat treatment. However, the magnitude of the full width half maxima remains greater in the weld region than in the parent pipe. This therefore indicates that magnitude of the microstresses in the weld region is greater in the weld material than the parent pipe and suggests that although the

macrostresses in the weld have been relieved by the post weld heat treatment (Figure 8.9), the microstresses have not.

8.4.2 Incremental Hole Drilling

Stress measurements using incremental hole drilling, Figure 8.13, show the hoop and axial stresses through the centre of the weld and parent metal to a depth of 1mm. There is little similarity between the trends of the hoop and axial stresses with depth. The hoop stresses in the centre of the weld, Figure 9.13(a) are approximately –5MPa at the surface of the weld. They then become more compressive over the following 0.5mm to approximately –100MPa and remain close to this value for the remaining 0.5mm. The axial stresses in the centre of the weld, Figure 9.13(b) are approximately 50MPa at the surface of the weld. However, they become increasingly compressive and reach approximately –30MPa at a depth of 1mm. The hoop stresses through the parent metal are compressive at the surface, approximately –25MPa, but rapidly become more tensile and remain at approximately 25MPa from a depth of 0.1mm onwards. The axial stresses through the parent metal fluctuate throughout the measurement depth. Tensile stresses are measured at the surface. They then become compressive reaching a maximum compressive stress of –50MPa at a depth of 0.08mm. The measured axial stress then becomes more tensile and is approximately 10MPa at a 1mm depth.

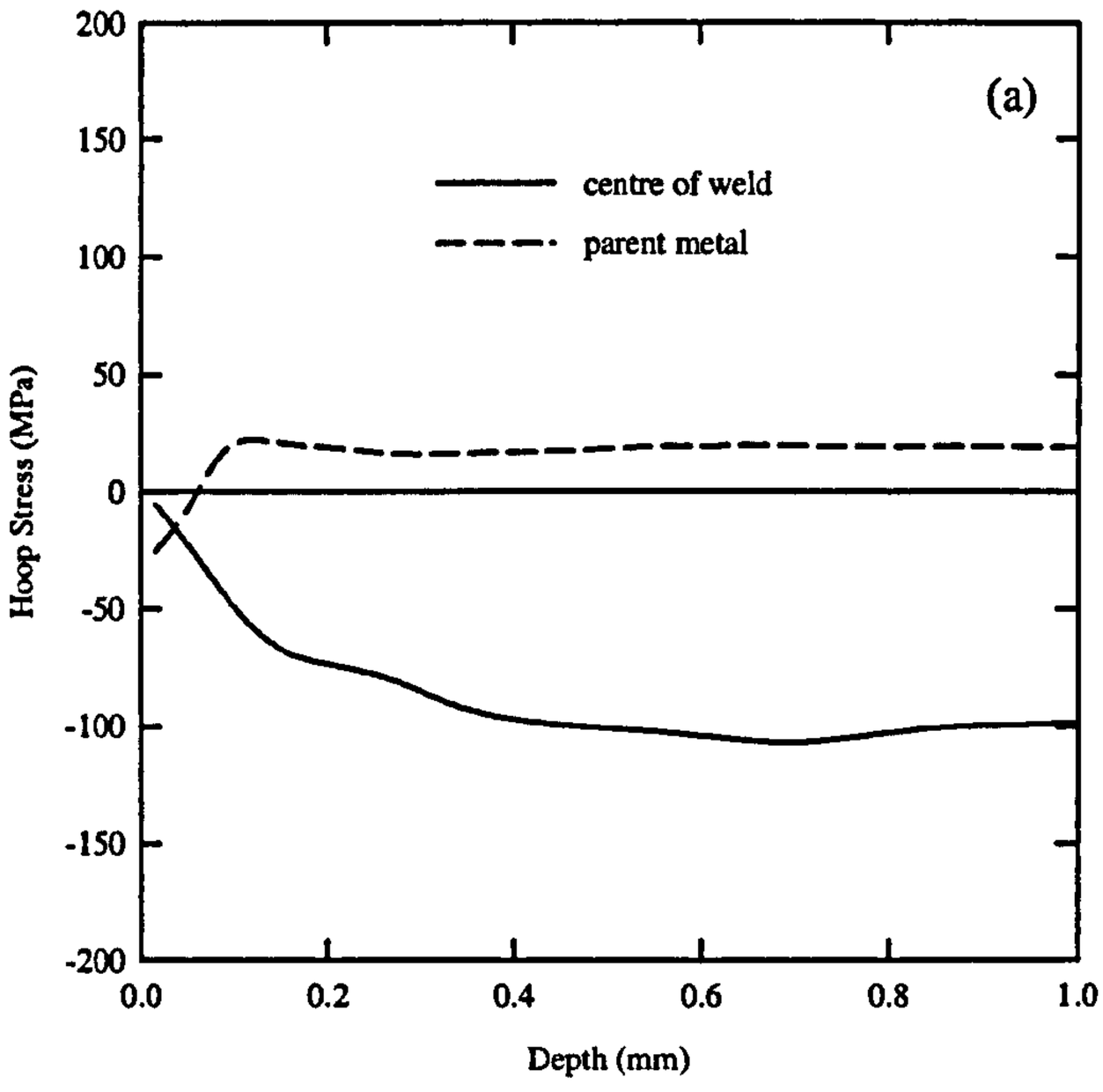

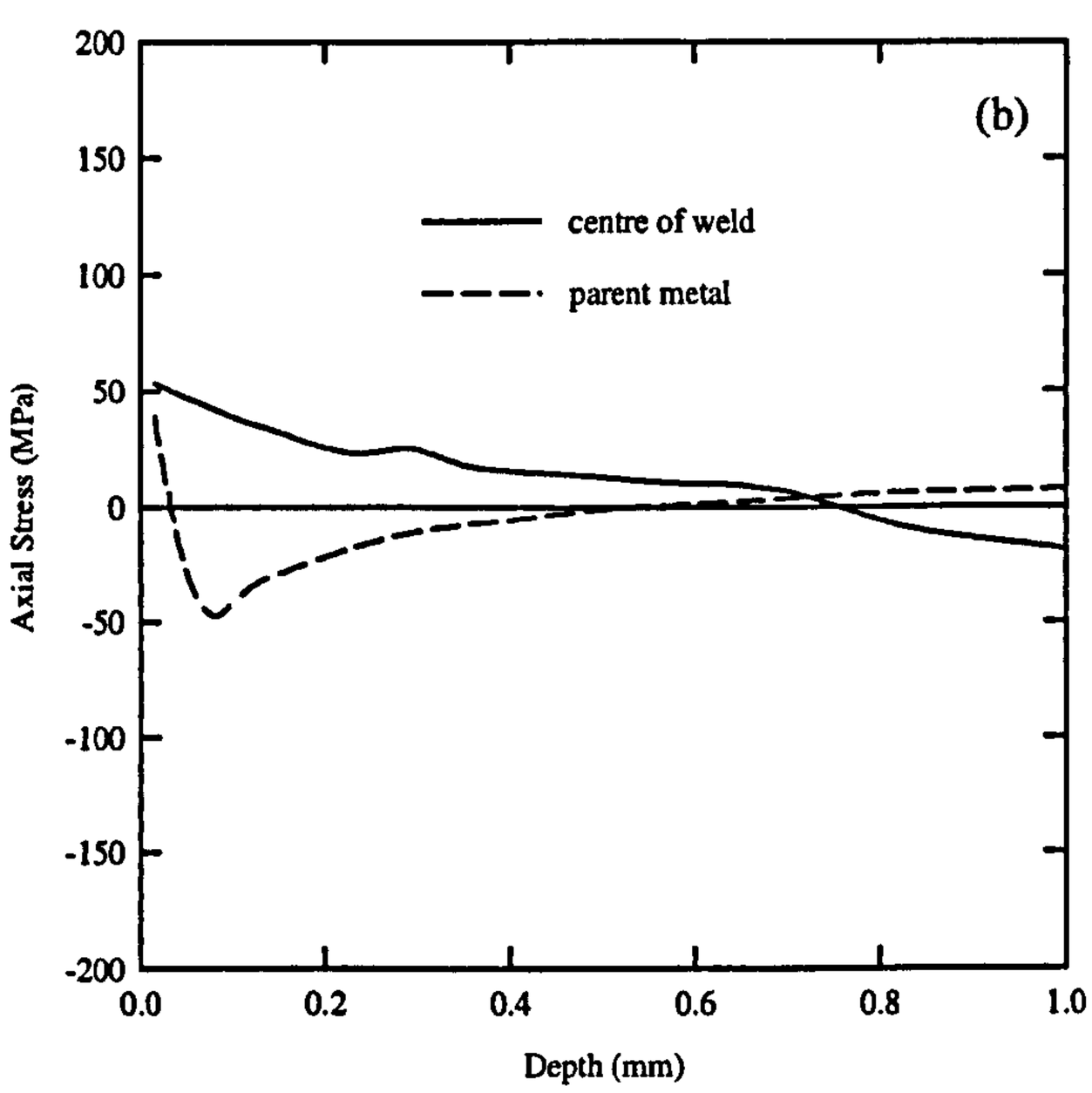

Figure 8.13. Stress measurements through the centre of the weld and parent metal using incremental hole drilling in the (a) hoop and (b) axial directions. Courtesy of Dr. Sarinova Simunjuntak, University of Bristol.

8.4.3 Deep Hole Drilling

The deep hole stress drilling stress measurements are shown in Figure 8.14 and Figure 8.15, for the hoop and axial directions respectively. These were obtained before and after the post weld heat treatment. Prior to the heat treatment, the measured stresses in the hoop and axial directions through the weld centre are compressive at the weld surface. They then become more tensile reaching a maximum tensile stress at a depth of approximately 15mm, after which the stresses become more compressive. The hoop and axial stresses reach compressive stresses greater than –150MPa at the inner surface of the weld.

At the edge of the weld, both the measured hoop and axial stresses are similar to those in the centre of the weld, aside from an initial increase in compressive stress at a depth of <5mm, reaching between –250MPa and –300MPa before becoming more tensile.

The magnitudes of the hoop and axial stresses measured on the parent pipe with depth are generally lower than those measured in the centre of the pipe and the edge of the weld. On the surface of the parent metal, both the hoop and axial stresses are compressive, between –20MPa and –50MPa. They then become more tensile over the following 5mm. From a depth of 5mm, the hoop stresses remain in the region of 50MPa until the value drops to zero at a depth of 50mm. The axial stresses change gradually from tensile to compressive over the depth of the parent pipe. However, the values of the measured stresses remain between 50MPa and 75MPa.

After post weld heat treatment, Figure 8.15, the hoop and axial stresses measured through the centre and at the edge of the pipe using deep hole drilling have reduced in magnitude. The values of the measured stresses do not exceed a magnitude of 50MPa. No measurements were made on the parent pipe.

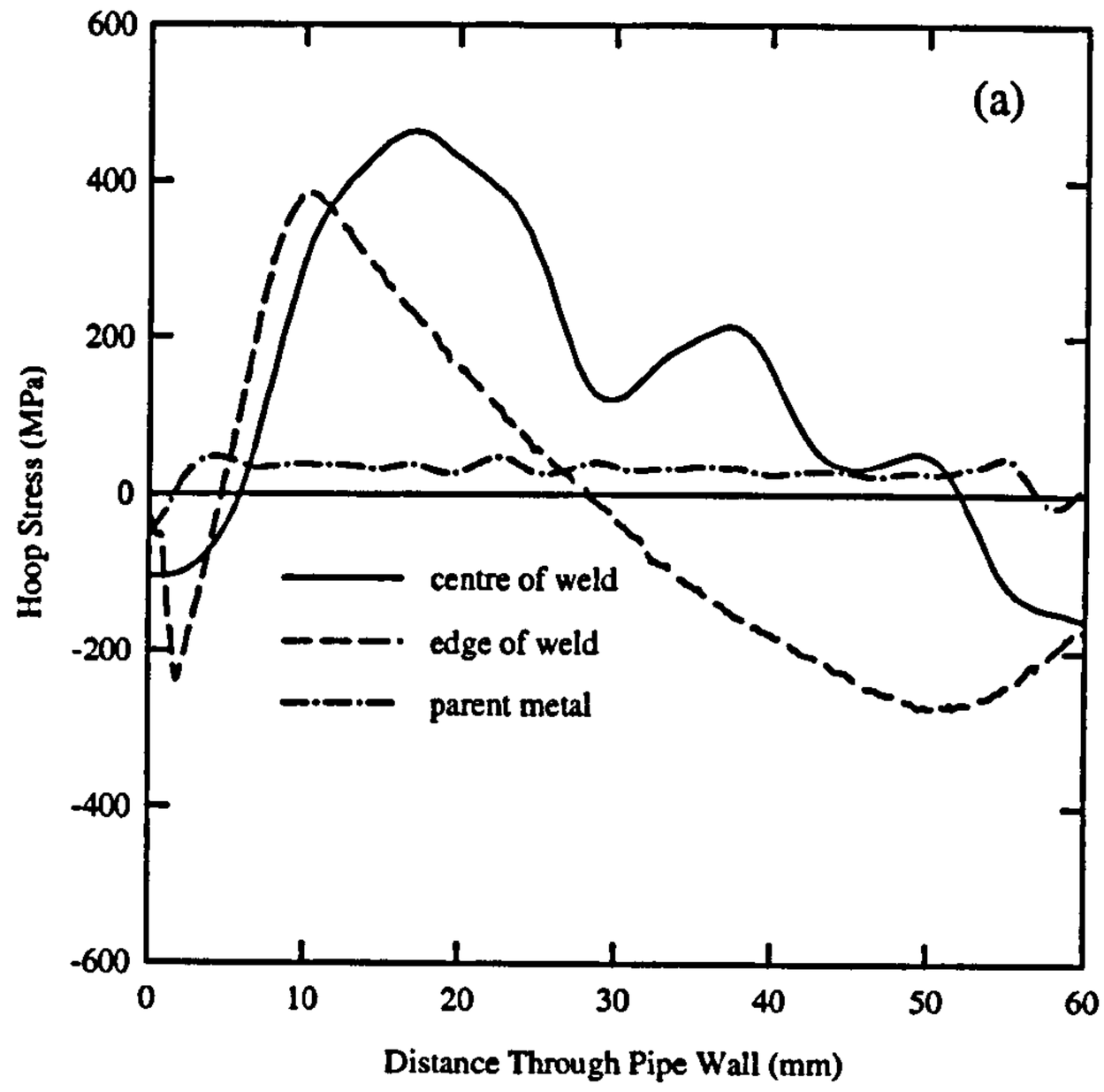

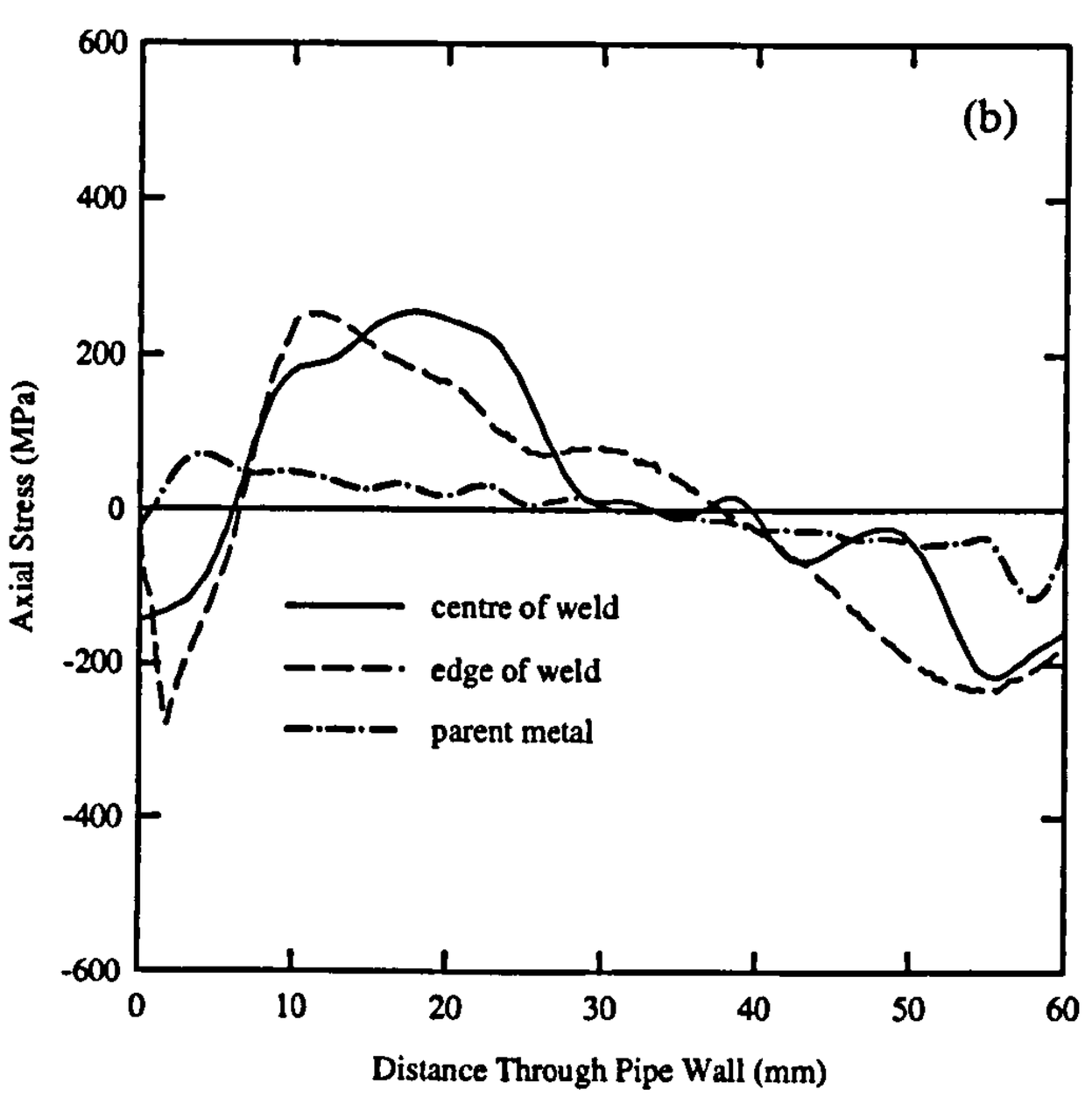

Figure 8.14. Stress measurements through the centre of the weld, edge of the weld and parent metal using incremental hole drilling in the (a) hoop and (b) axial directions. Courtesy of Dr. Sarinova Simunjuntak, University of Bristol.

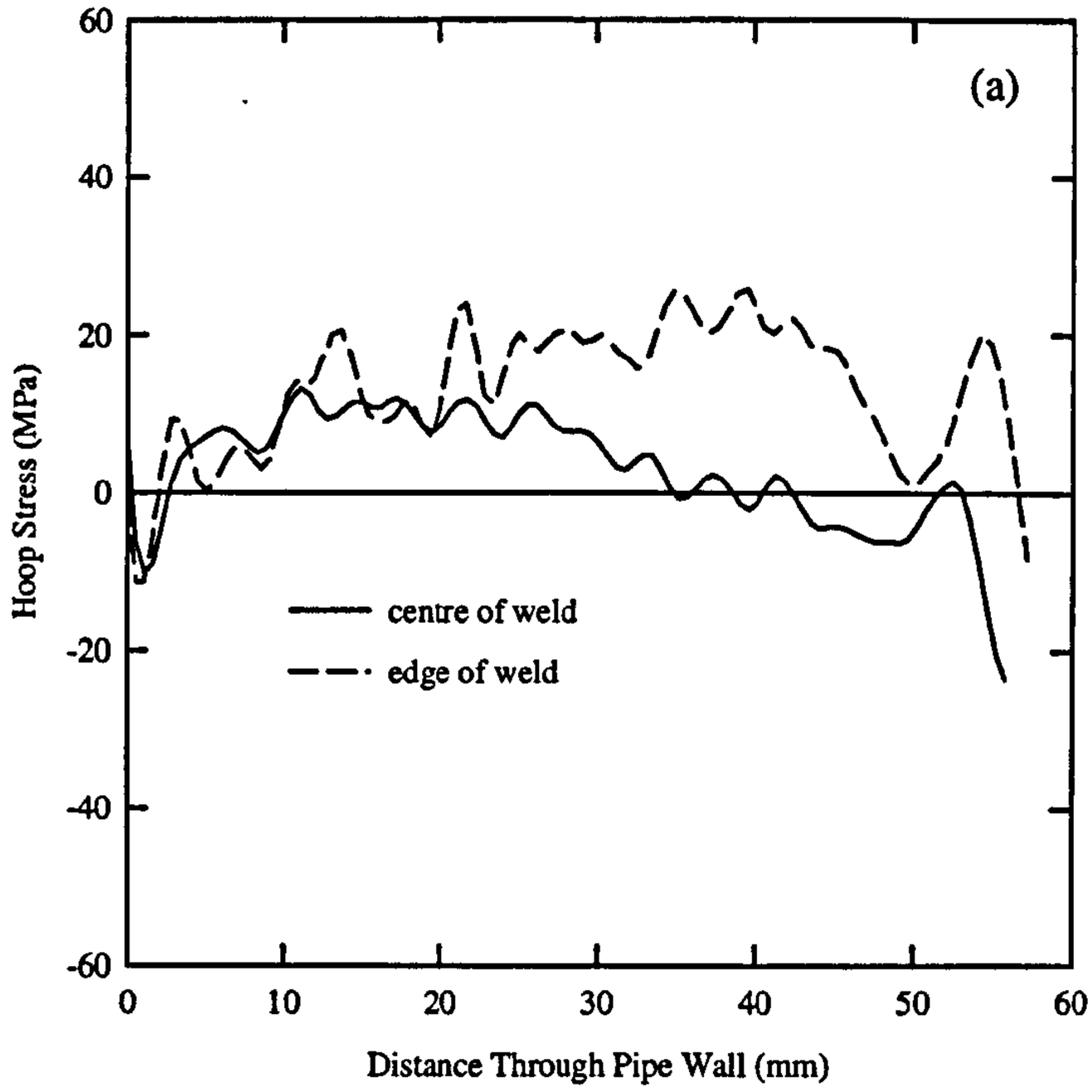

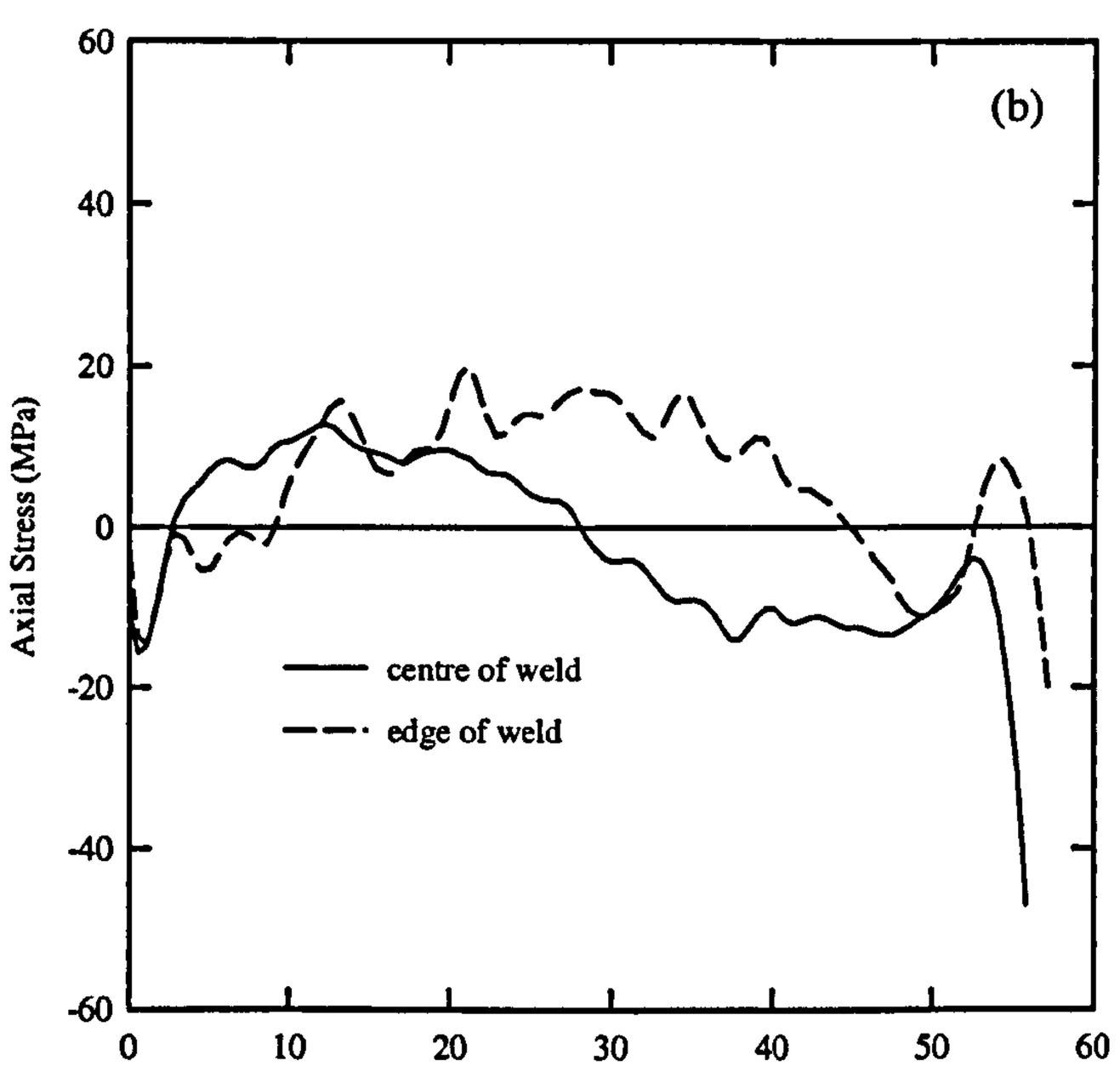

Figure 8.15. Stress measurements after post weld heat treatment through the centre of the weld and parent metal using incremental hole drilling in the (a) hoop and (b) axial directions. Courtesy of Dr. Sarinova Simunjuntak, University of Bristol.

8.4.4 Finite Element Modelling

The weldment stresses were calculated before and after the removal of the weld crown, Figure 8.16 and Figure 8.17 respectively. In all cases, there is a variation in the magnitude of the stresses as the weld beads are traversed and the highest compressive stresses are in the region of the final bead. A comparison of Figure 8.16 and Figure 8.17 reveals that the removal of the weld crown results in only a small effect on the surface residual stresses.

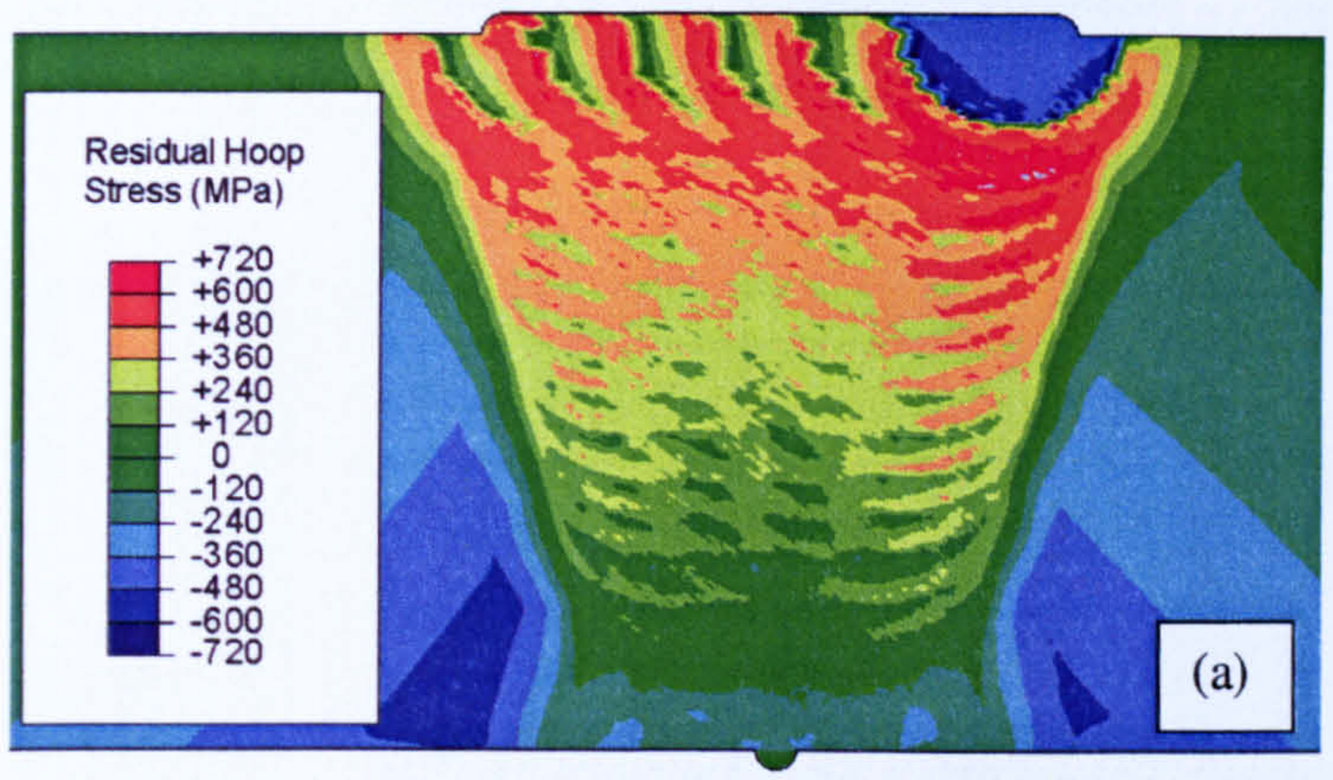

Figure 8.16. (a) Hoop and (b) axial stress before the removal of the weld crown [Yaghi et al. 2008].

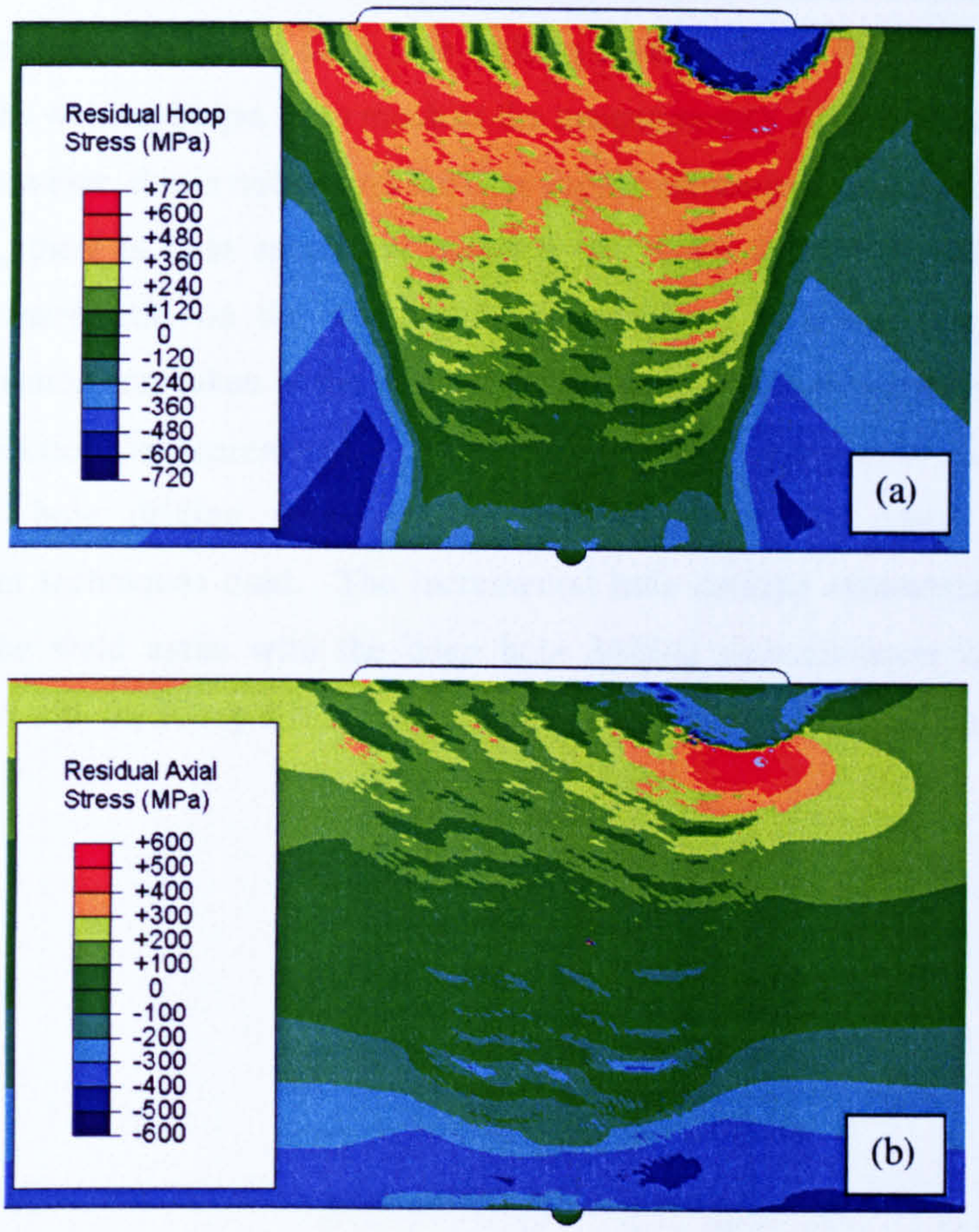

Figure 8.17. (a) Hoop and (b) axial stress after the removal of the weld crown [Yaghi et al. 2008].

8.4.5 Comparison of Experimental Methods

As described in Section 8.1, the experimentally obtained stress measurements have been acquired over different length scales and spatial resolutions. Thus the extent to which the measurements can be correlated defines the extent to which surface measurements can be used as an indication of subsurface and through section stresses in a component. Comparisons of the hoop and axial residual stresses measured through the centre of weld prior to the post weld heat treatment are shown in Figure Figure 8.18(a) and (b) respectively. A comparison of hoop and axial measurements taken at the edge of the weld can be seen in Figure 8.19(a) and (b) respectively. The X-ray results show the stress distribution over the weld for the "as oxidised" and electropolished surfaces.

Although there is much scatter in the X-ray diffraction stress measurements, the X-ray measurements agree with the deep hole drilling measurements on the "as oxidised" surface of the weld and pipe, in as much as the measurements all indicate compressive stresses. However, this is not always the case for the electropolilshed surfaces. In the weld metal, there is little agreement between the X-ray diffraction and deep hole drilling measurements on the electropolished surface. Although, the deep hole drilling measurements taken at the edge of the weld lie within the distribution of the X-ray diffraction measurements. There is no clear agreement between the incremental hole drilling measurements and either of the other two stress measurement techniques used. The incremental hole drilling measurements in the centre of the weld agree with the deep hole drilling measurements in the hoop direction but with the X-ray diffraction measurements in the axial direction.

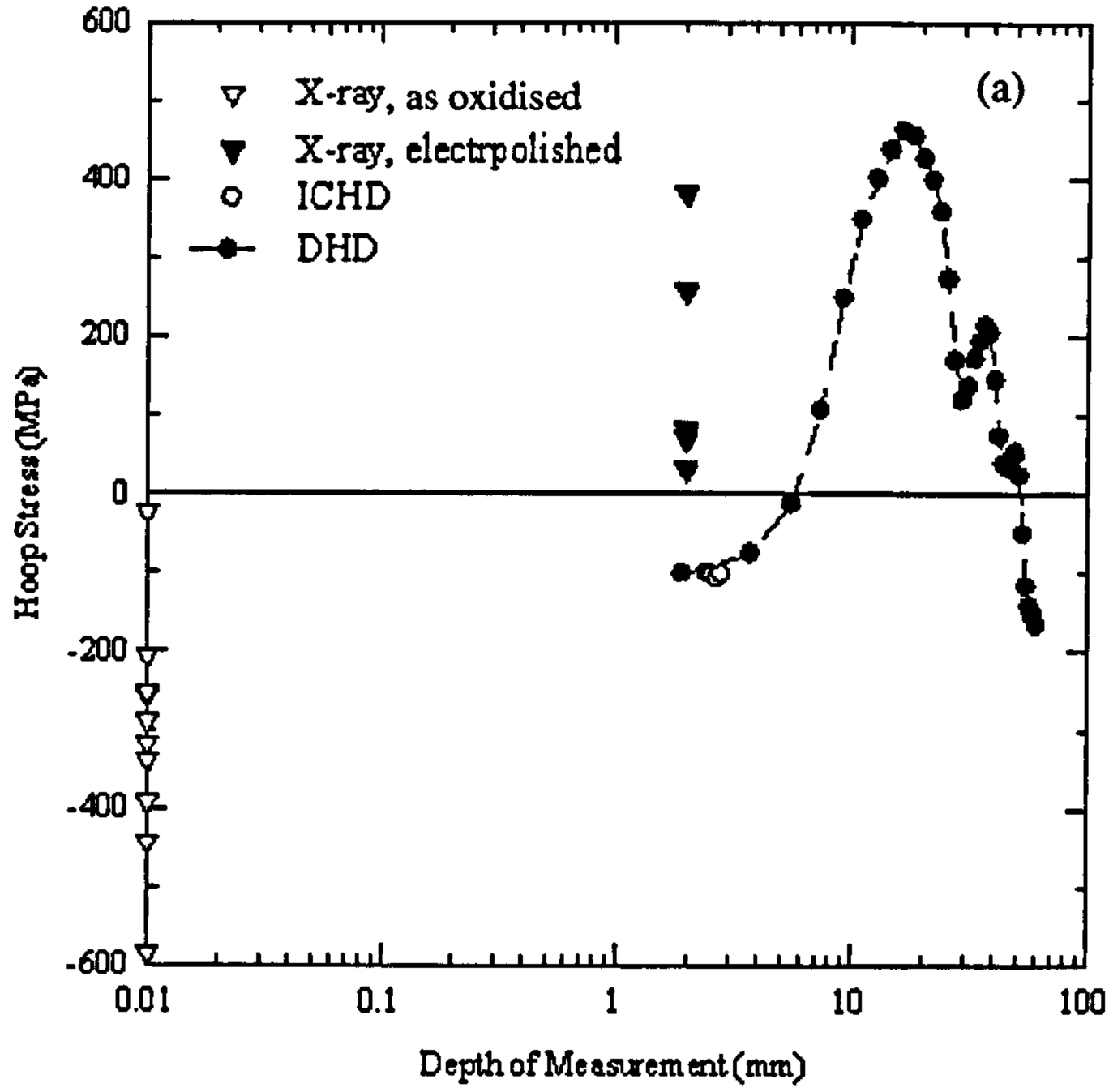

Figure 8.18. Measured (a) hoop and (b) axial stresses through the centre of the weld [Hilson et al. 2008].

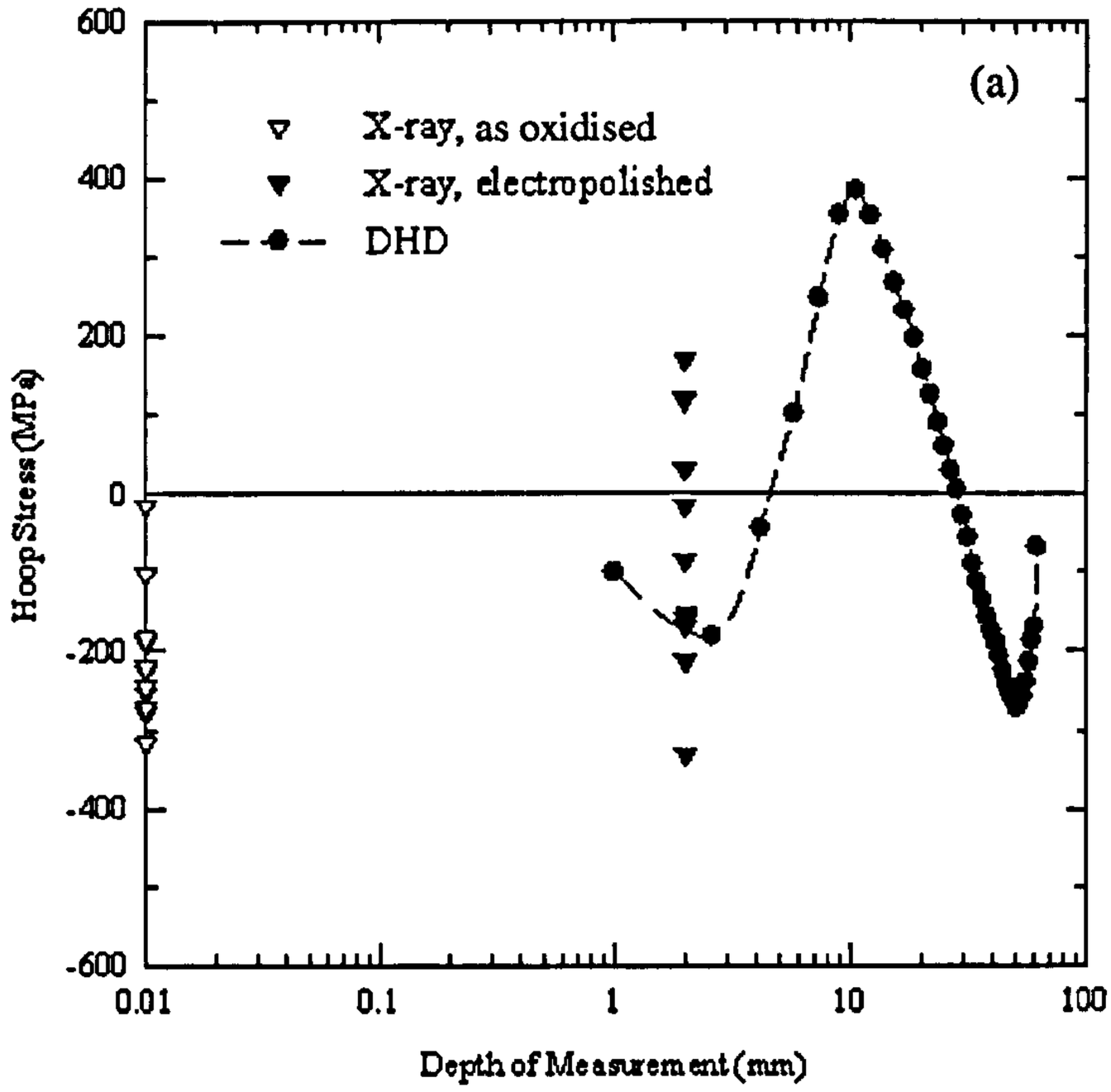

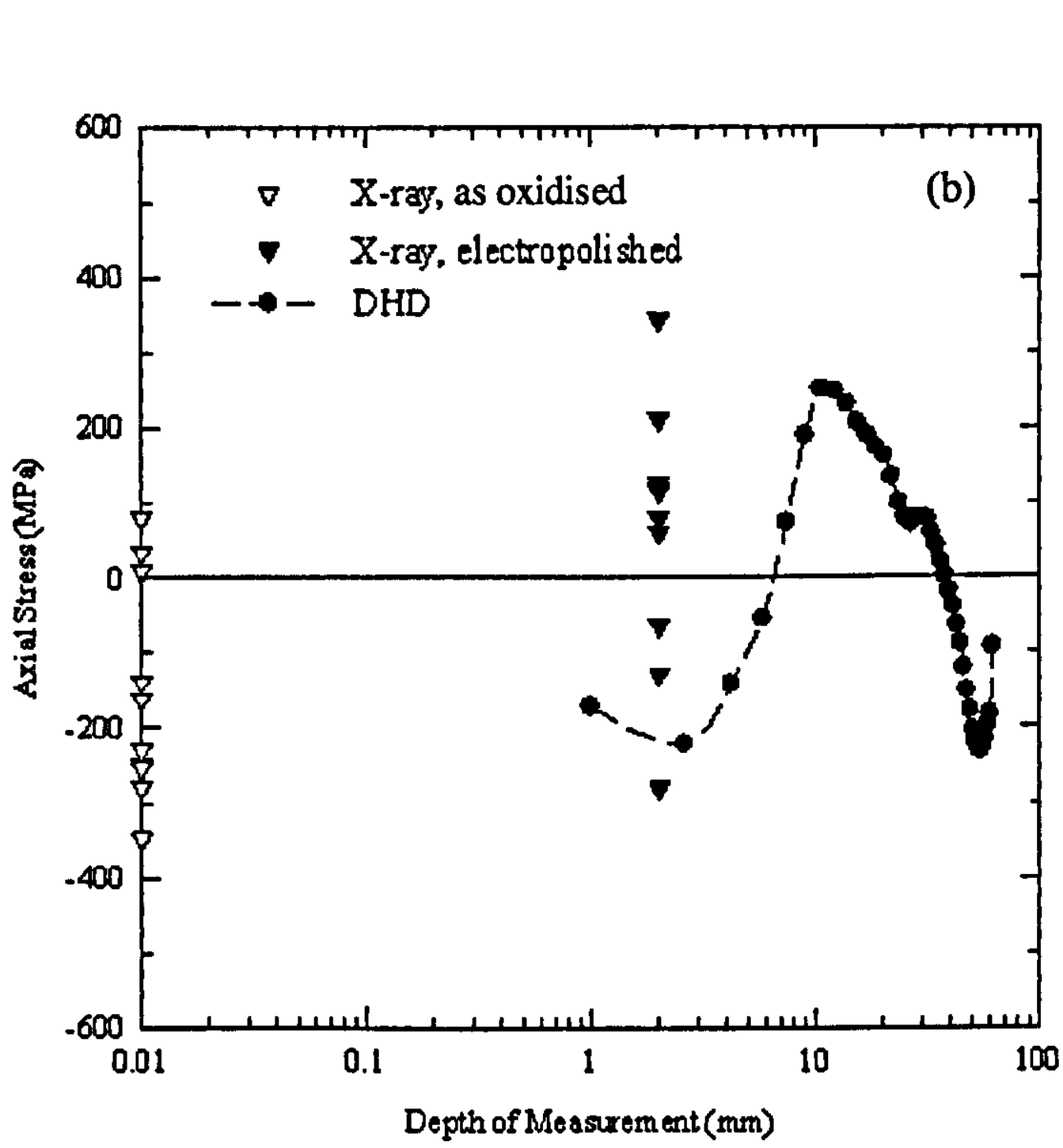

Figure 8.19. Measured (a) hoop and (b) axial stresses through the edge of the weld [Hilson et al. 2008].

8.4.6 Comparison of Experimental Methods with Finite Element Modelling

Comparisons of the experimental methods with the theoretical prediction enable an understanding as to the extent to which the strategy to accommodate residual stresses in repair weldments, as proposed by McDonald et al. [McDonald et al. 2005], can be used. A comparison of the X-ray diffraction (XRD) measurements and finite element (FE) predictions along the weld after the removal of the weld cap can be seen in Figure 8.20. The heat affected zones are denoted HAZ. The negative x-axis is the side of the last weld bead.

In general, there is a good correlation between the X-ray diffraction measurements and finite element predictions, as there is much overlap between them. However, there are discrepancies, particularly in the axial stress measurements and predictions. This could be due to the difference in the amount of material removed in the X-ray diffraction measurements and finite element predictions. Furthermore, there is some discrepancy between the size of the weld beads in the prediction and the actual pipe.

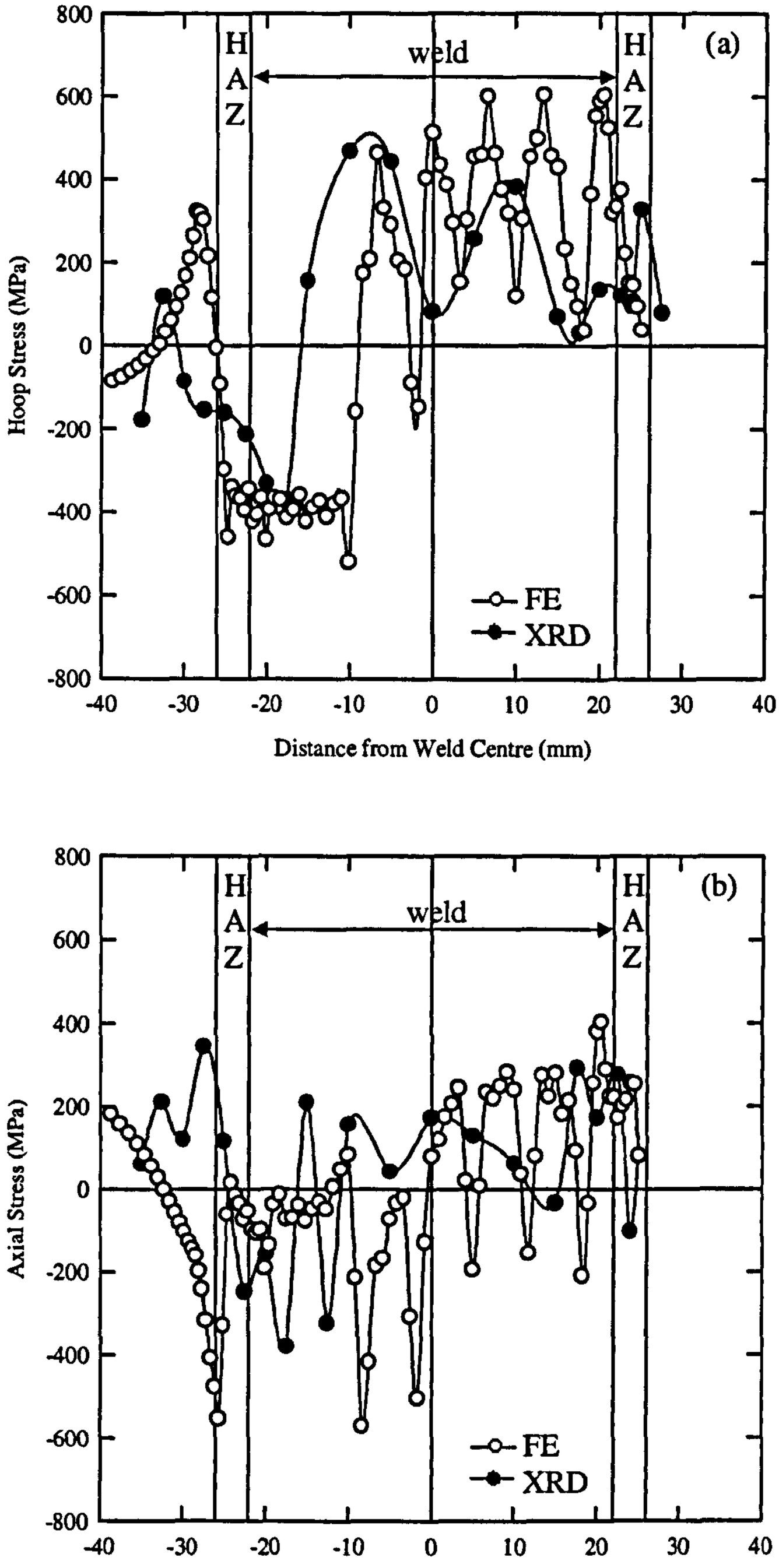

Figure 8.20. Comparison of (a) hoop and (b) axial residual stresses measured by X-ray diffraction and predicted by finite element modelling after the removal of the weld cap [Yaghi et al. 2008].

A comparison between through section deep hole drilling (DHD) measurements and through-section finite element predictions can be seen in Figure 8.22. Figure 8.21 illustrates the where the measurements and predictions were taken. The edges of the deep hole drilling measurements are shown. The finite element predictions run along the weld centre line (WCL) and the lines marked L1, L2 and L3. The weld metal (WM) and parent metal (PM), fusion zone (FZ) heat affected zone (HAZ) are also shown.

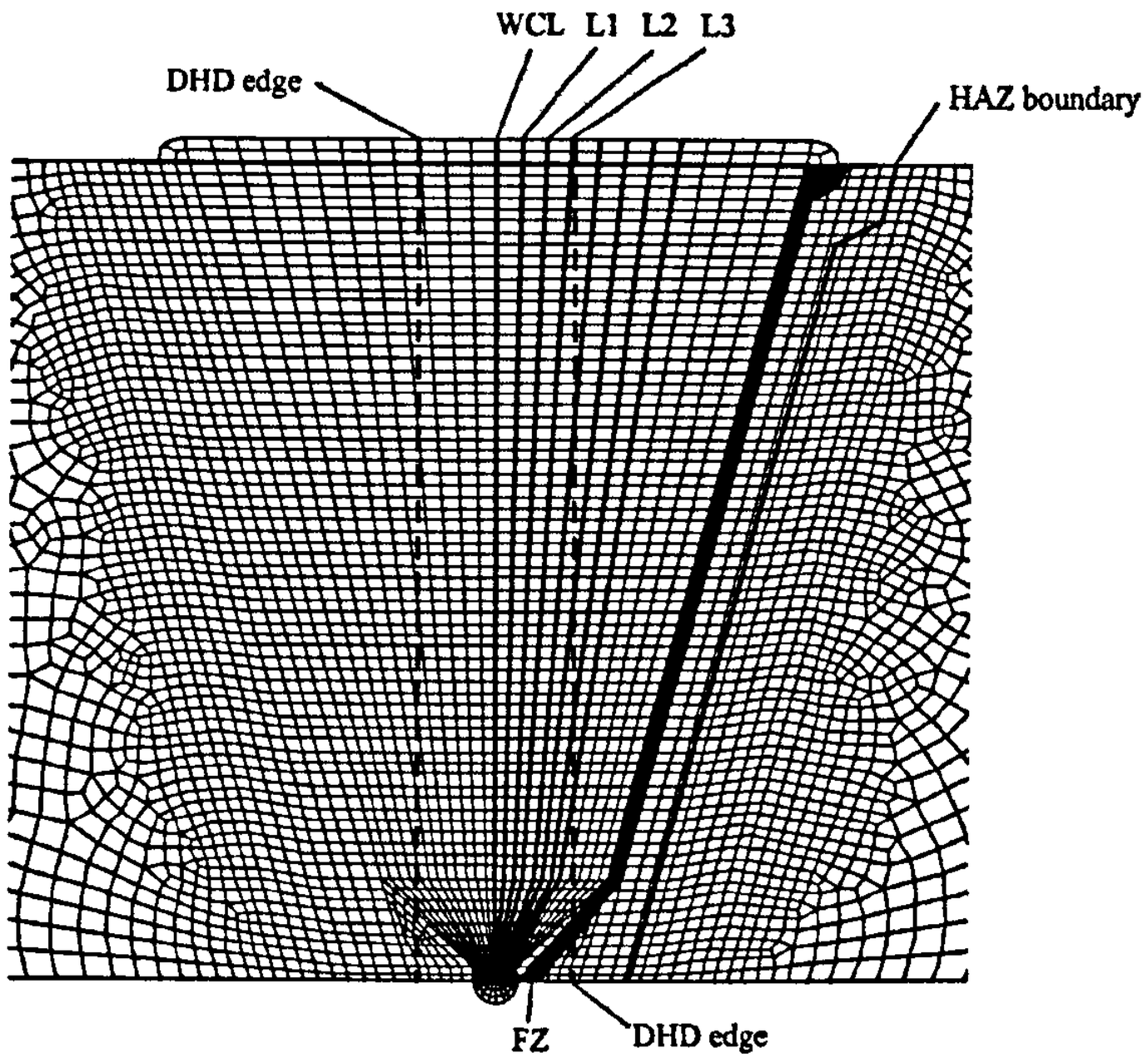

Figure 8.21. Structure of the finite element model [Yaghi et al. 2008].

There is much overlap between the deep hole drilling measurements and the finite element predictions. The discrepancies at the surface could be due to the positions over which measurements and predictions were made. The deep hole drilling measurements were averaged over a 10mm diameter where as the predictions were taken from particular nodes in the finite element model. This would be exaggerated at the surface as it is at the surface that there is the greatest fluctuation in stress magnitudes across the weld. Discrepancies could also be due to surface errors in the deep hole drilling technique [Stefanescu et al. 2008].

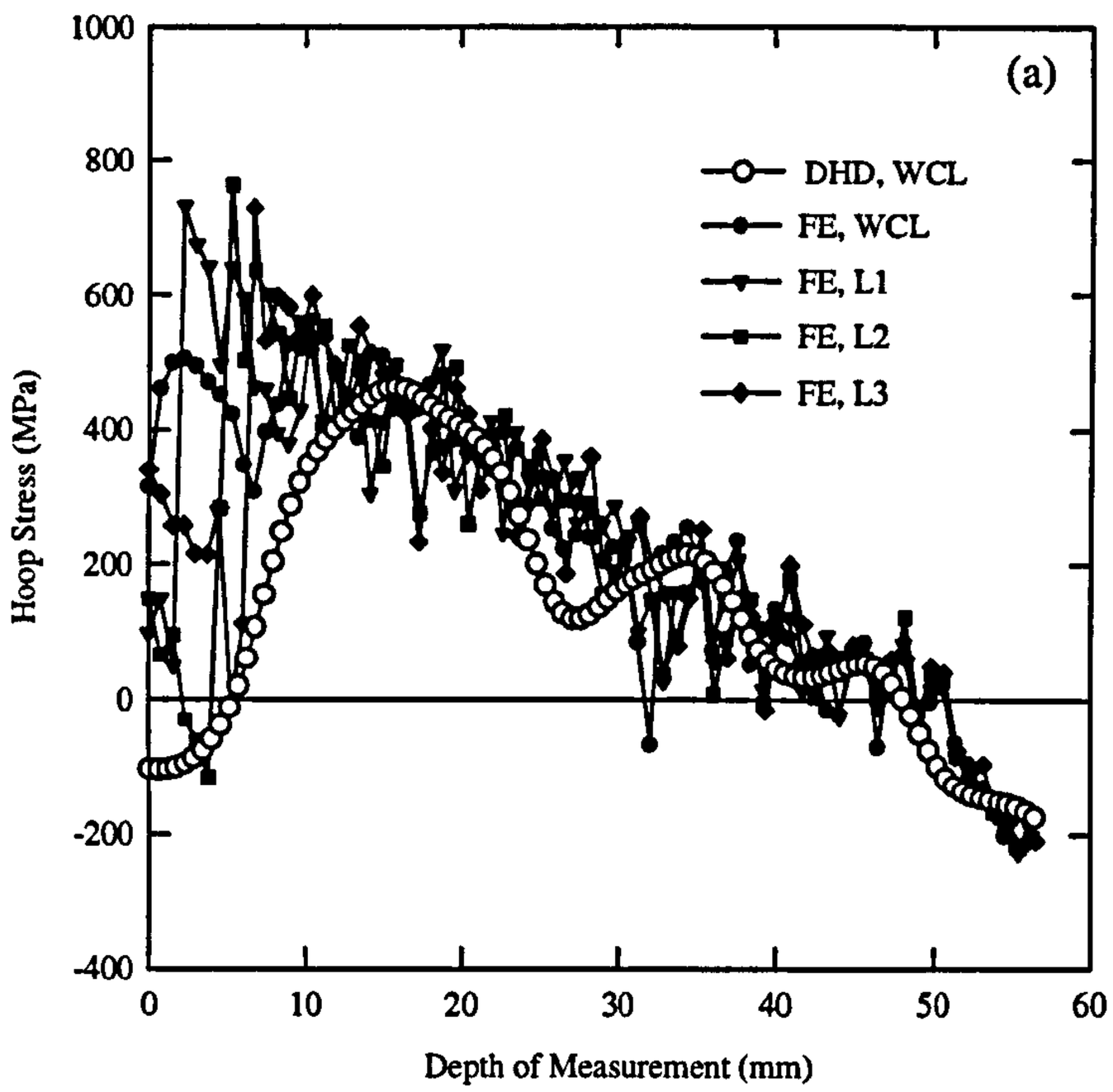

Figure 8.22. Deep hole drilling (DHD) and finite element (FE) (a) hoop and (b) axial stresses through the wall thickness at the centre of the weld, starting from the outside surface [Yaghi et al. 2008].

8.5 Summary

The measurements taken on the "as oxidised" surface reveal compressive stresses at the surface of the weld cap tensile stresses increasing with depth in the vicinity of the capping run. This emphasises the importance of the capping run, as compressive surface stresses are largely beneficial to structural integrity [Callister 2000]. The X-ray diffraction measurements taken along the 40° and 140° axes are in good agreement and as such there do not appear to be bending stresses in the pipe which could contribute to the bending stresses.

Although there are discrepancies between experimental residual stress measurements, there is a good correlation between the experimental measurements and finite element model predictions. Differences between measurement and prediction could be due to the structure of the weld varying from that of the finite element model and differences in measurement position from prediction position in the weld.

Indications of the relative magnitudes of microstresses across the weld have been given by analysing the full width half maxima of the X-ray diffraction peaks. The microstresses have been shown to be greater in the weld than in the parent pipe. They have also been shown to be greatest in the surface of the weld and the pipe. The measurements on the electropolished surface have also given a clear indication as to the effect of the weld and correspond to the visual identification of the heat affected zone. The X-ray diffraction stress measurements and full width half maxima measurements show that although the post weld heat treatment relieved the macrostresses in the weld metal, microstresses clearly remain, thereby indicating the presence of dislocations, inclusions or point defects [(b)Withers and Bhadeshia 2001].

9 Platinum Aluminide Coated Superalloy

9.1 Introduction

Cotton reel samples of a nickel based superalloy, CMSX-4, were coated with platinum aluminide bond-coats, courtesy of Chromalloy Ltd, and oxidised for a variety of times at different temperatures, at Cranfield University. The superalloy selected, CMSX-4 is a common superalloy used for turbine blades [McLean et al. 1995]. One of the bond-coats, RT22, is an inward grown bond-coat and is a well documented blade coating [Angenete and Stiller 2002, (a)Angenete and Stiller 2003 (b)Angenete and Stiller 2003]. The other bond-coat investigated, CN91, is less well documented and is an outward grown type [Ogden 2007]. No thermal barrier was present on the samples, so as not to complicate investigations into the behaviour of the bond-coats. Both the RT22 and CN91 coatings have been discussed in more detail in Chapter 2 – Literature Review. The times and temperatures were chosen to simulate possible service conditions of turbine blades. The oxidised bond coats were investigated using Raman and photoluminescence spectroscopy to understand the behaviour of the coatings with the oxidation conditions. This was directed to understanding the behaviour of coated turbine blades over their service life. However, the service conditions investigated did not include service loads, both static and cyclic, which have been shown to have an effect on turbine blade behaviour [Viswanathan 1989]. A cross-section of the substrate and oxidised bond-coat can be seen in Figure 9.1 [Ogden 2007]. The thermally grown oxide, as well as the other sections of the sample, has been marked out.

9.2 Results

9.2.1 Background

Photoluminescence spectra were taken from the surface of the specimens to measure the strains and calculate the stresses which had developed in the thermally grown oxides. Spectra were also recorded using Raman spectroscopy to ascertain the composition of the thermally grown surface oxides. The heat treatments for the RT22 and CN91 coated samples can be seen in Table 9.1, where Y indicates that the sample was analysed.

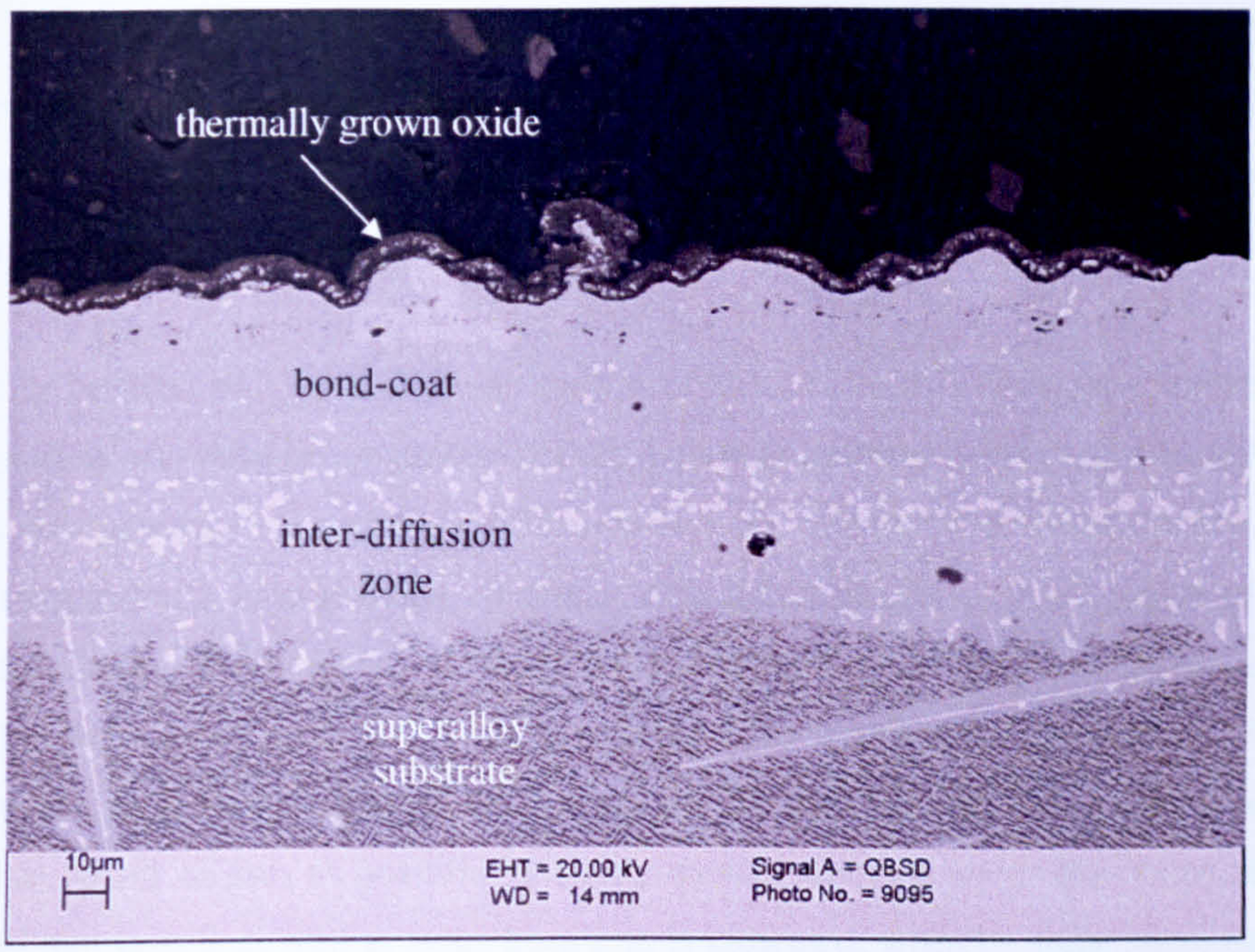

Figure 9.1. Scanning electron micrograph (secondary electron image) of an RT22 coated CMSX4 sample oxidised for 1000 hours at 1000°C. Courtesy of Dr. Sarah Ogden, Loughborough University.

Table 9.1. Heat treatments used to oxidise coated samples.

RT22	Oxidation Temperature (°C)				
Oxidation Time (hours)	850	900	950	1000	1050
1000	Y	Y	Y	Y	Y
2000	Y	Y	Y	Y	Y
4000	Y	Y	Y	Y	Y
CN91	Oxidation Temperature (°C)				
Oxidation Time (hours)	850	900	950	1000	1050
1000	Y	Y	Y	Y	Y

The photoluminescence spectra were obtained using a Renishaw Raman 2000 spectrometer fitted with a 514nm and a 633nm wavelength laser. In addition, some measurements were made using a Dilor spectrometer fitted with a 532nm wavelength laser at the National Physical Laboratory in collaboration with Dr. John Nunn.

As can be seen in Figure 9.1, the surface of the oxide layer was very uneven in topography and thickness with undulations typically between 10μm and 15μm thick. Photoluminescence spectroscopic measurements were acquired at twenty points over the sample surface to provide statistical confidence in the average value of the measurements. The positions of the points from which to take the photoluminescence spectra were chosen so as to mitigate any effects caused by sample preparation. Some of the samples were the end of the cotton reels, Figure 9.2 and data were collected over as varied an area as possible by taking measurements towards the centre of the cotton reel sample as well as away from it as is indicated, whereby some approximate points at which data was acquired are shown. The same system of randomly acquiring some spectra throughout the breadth of the sample was used across all such samples.

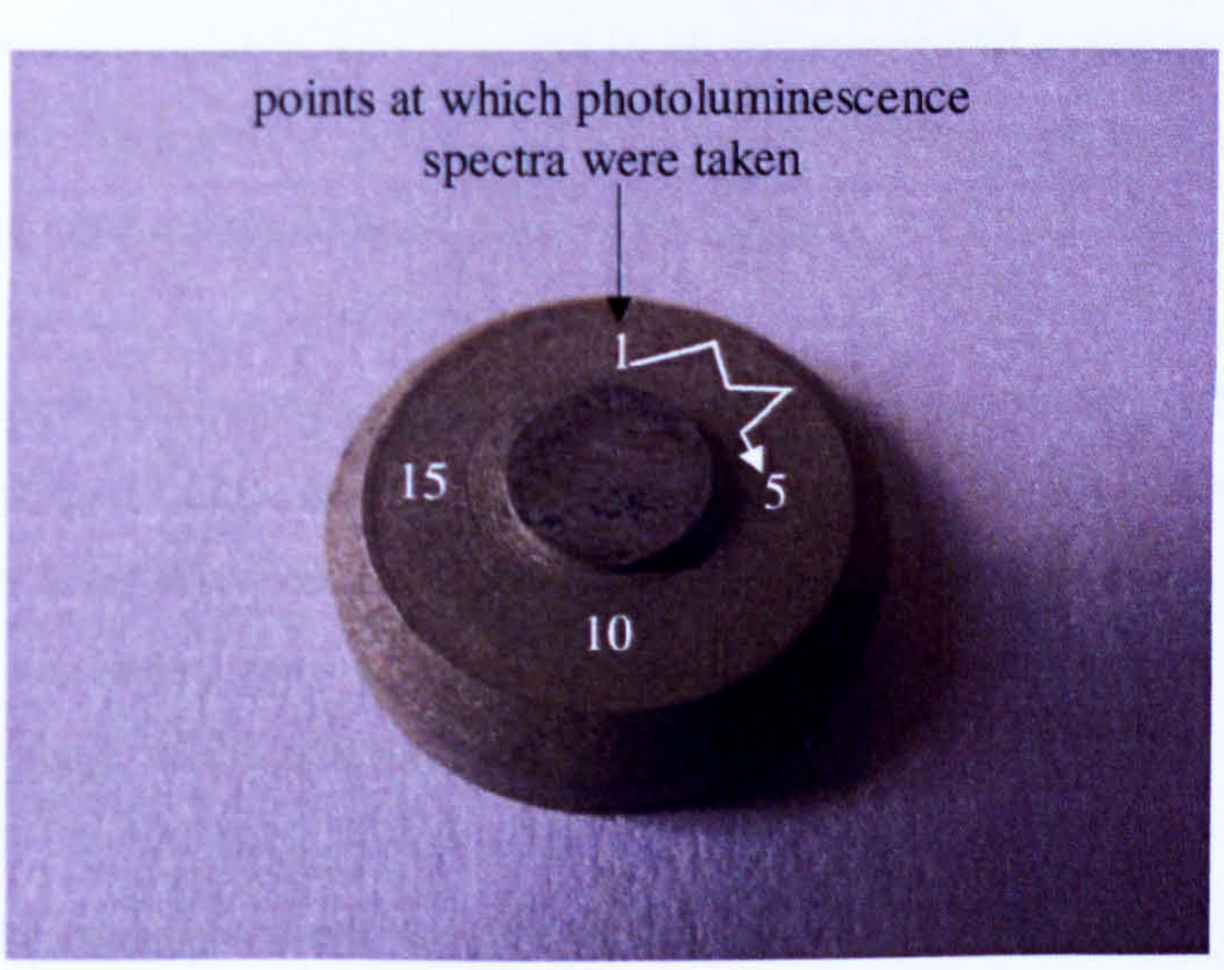

Figure 9.2. Image of an oxidised superalloy sample with a platinum aluminide bond-coat. The approximate points at which measurements were made are marked.

In other cases Figure 9.3, the samples were removed from the centre of the cotton reels and, as with the edge samples, data points were taken over as varied an area as possible. This was done by taking measurements from across the total circumference and randomly varying the acquisition position across the width of the sample.

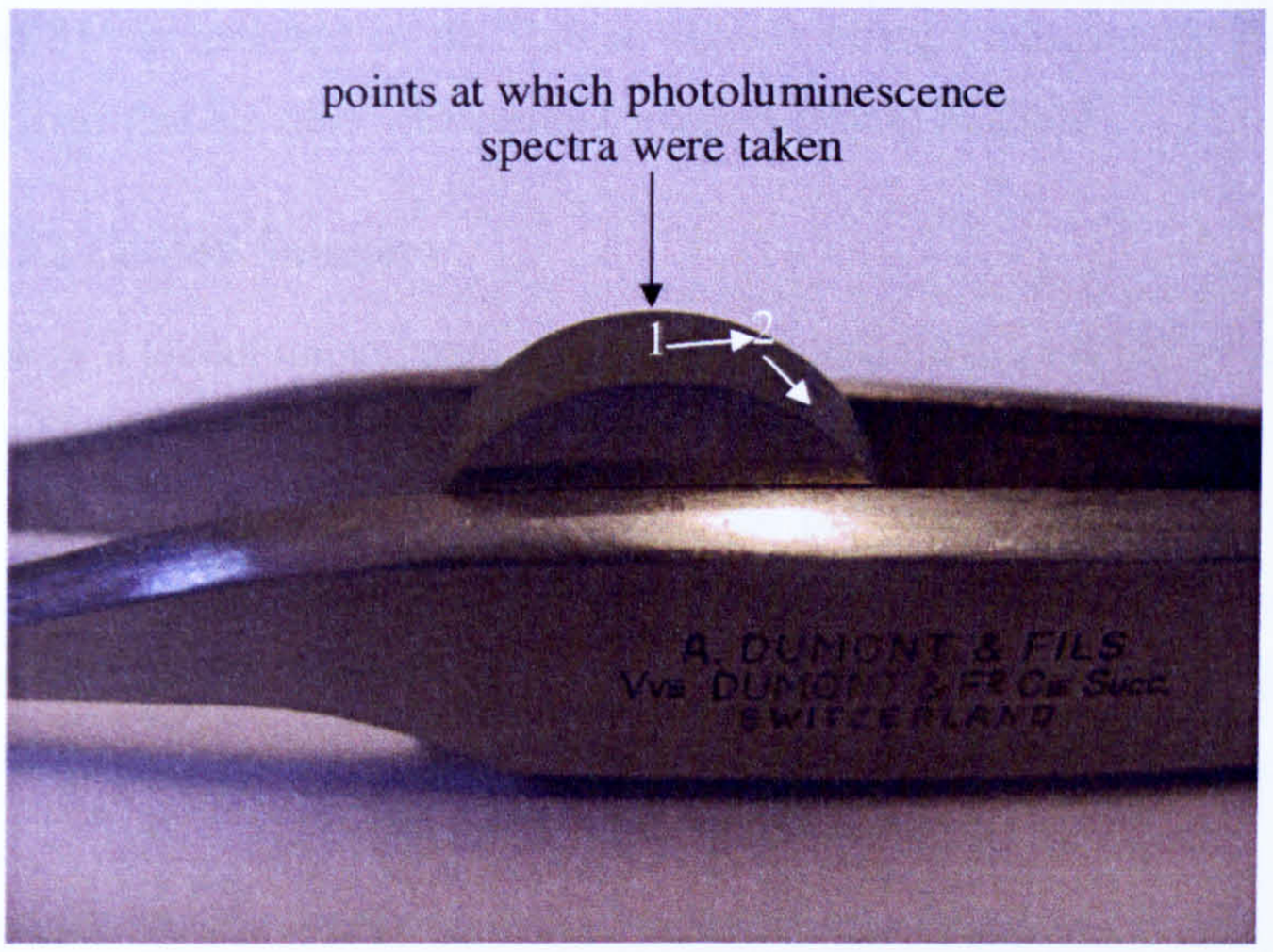

Figure 9.3. Image of an oxidised superalloy sample with a platinum aluminide bond-coat taken from the centre of a cotton reel specimen. The approximate points at which measurements were made are marked.

A lens magnification of 5x for the Renishaw Raman spectrometer was used throughout as it provided the largest spot size available. A power of approximately 29μW, the lowest available, was selected in all occasions and a computer macro was used to remove background noise. All spectra were fitted with a mixed Gaussian-Lorentzian fit and a quadratic background subtraction.

In addition, photoluminescence spectra were recorded across the thermally grown oxide width of an RT22 coated specimen oxidised at 950°C for 4000 hours using a 5x magnification long distance working lens. This was done so as to establish any variation in the stress profile across the oxide which could not be observed by analysing the shape of the spectral peaks.

Raman spectra were acquired for two RT22 coated samples and a CN91 coated sample in order to ascertain whether any information could be gained about the composition and crystal structure of the thermally grown oxides. The measurements were recorded using an inVia Raman Spectrometer at the University of Bristol. A 50x magnification long distance working lens was used with an argon-ion laser of wavelength 488nm. This laser wavelength was chosen as use of laser wavelengths

633nm and 514nm resulted in the Raman signals being swamped by fluorescence signals, an issue that has also been found by others [Pitt et al. 2005].

9.2.2 RT22 Coated Samples

An example of a photoluminescence spectrum acquired from an RT22 coated sample is shown in Figure 9.4. The α-alumina R_1 and R_2 lines were each fitted with a single curve. In this case, there is also evidence of the presence of a possible metastable phase as well as peaks resulting from background noise. Although there is some debate as to the origins of these peaks, it shall be annotated as a metastable phase in this work, as this is a predominant description in the literature, Section 2.5.6.

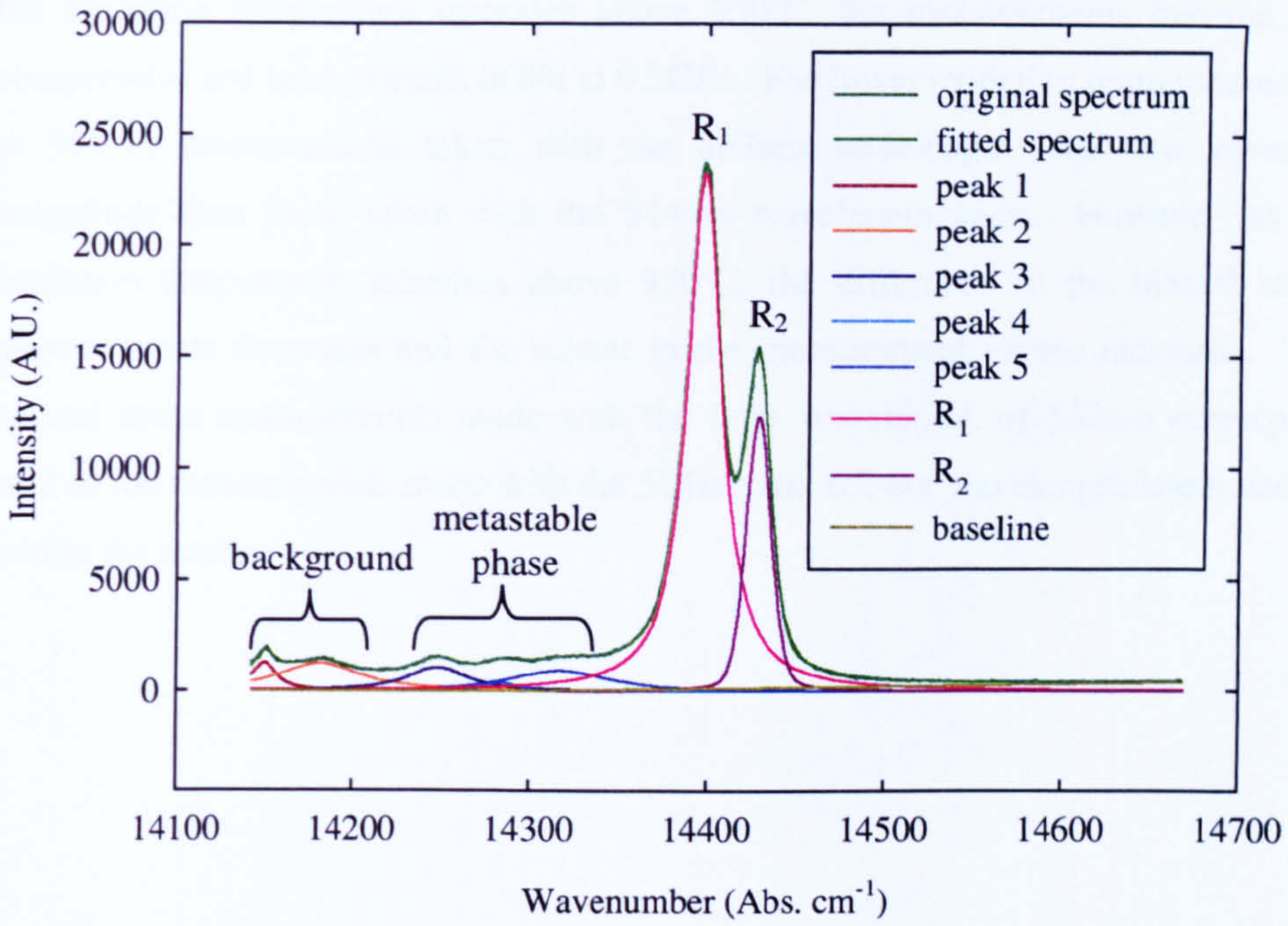

Figure 9.4. Original and peak fitted spectrum obtained from an RT22 coated sample oxidised for 4000 hours at 950°C. Peaks 1 and 2 are background noise. Peaks 3 to 5 have been fitted to a metastable phase.

Biaxial stress measurements against oxidation temperature using photoluminescence spectroscopy, made on the RT22 coated samples after various oxidation times and for temperatures between 850°C and 1050°C can be seen in Figure 9.5. Figure 9.5(a) shows the biaxial stress measurements against temperature after an oxidation time of 1000 hours; Figure 9.5(b) shows the biaxial stress measurements after an oxidation

time of 2000 hours and Figure 9.5(c) shows the biaxial stress measurements after an oxidation time of 4000 hours. The average measurement values are indicated and the error bars are the lowest 5th and highest 95th percentile measurements. These values were calculated to take distributions in measurements into account. In all sections of Figure 9.5, the measurements are shown for spectra acquired with laser wavelengths of 514nm and 633nm. In addition, measurements made with a laser wavelength of 532nm can be seen in Figure 9.5(a) for oxidation temperatures of 950°C, 1000°C and 1050°C.

The biaxial stress measurements for the 514nm and 633nm wavelengths become more compressive with increasing temperature, reaching a maximum value at 950°C. As the oxidation temperature increases above 950°C, the measurements become less compressive and tend towards 0GPa to 0.5GPa. For lower oxidation temperatures, up to 950°C, measurements taken with the 633nm wavelength laser are lower in magnitude than those taken with the 514nm wavelength laser. However, as the oxidation temperature increases above 950°C, the difference in the biaxial stress measurements decreases and the scatter in the measurement values increases. The biaxial stress measurements made with the laser wavelength of 532nm correspond well to the measurements made with the 514nm and 633nm wavelength lasers and lie within the scatter.

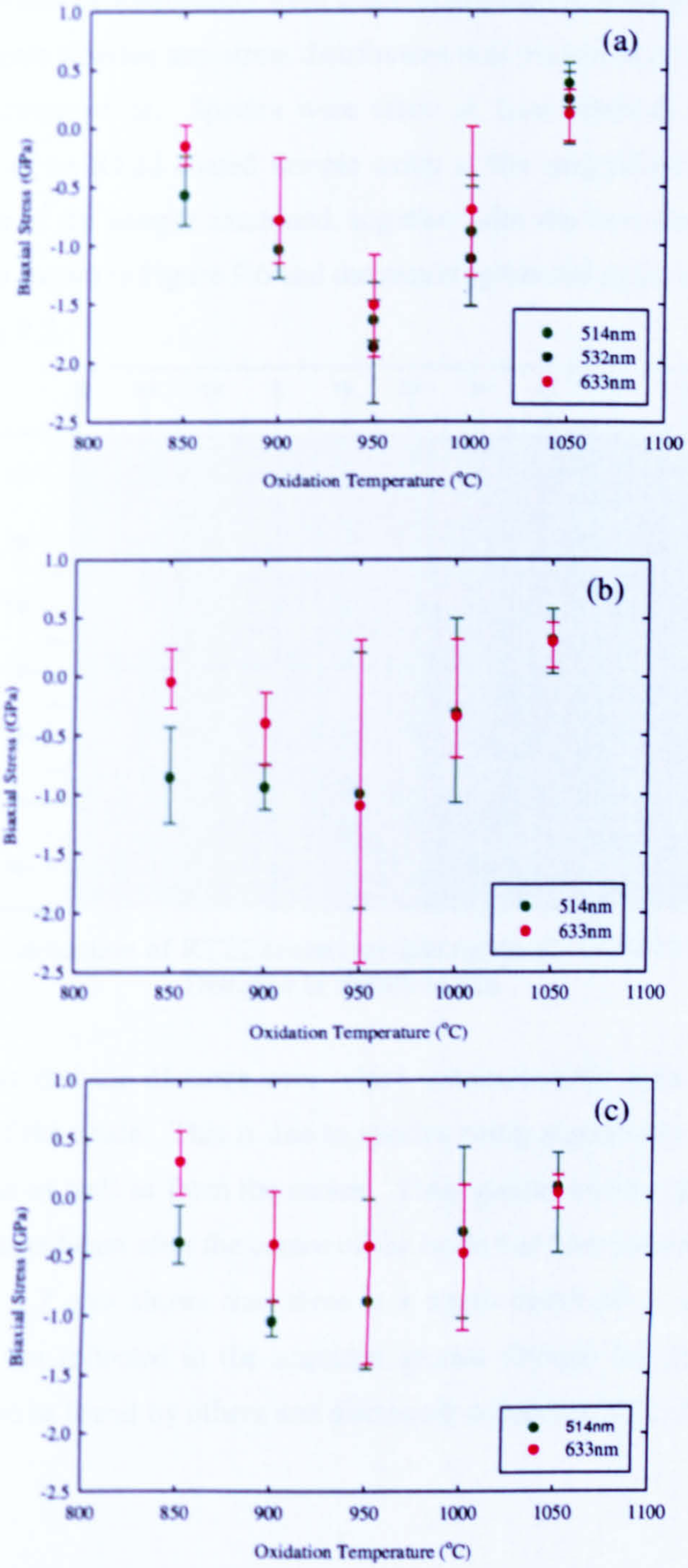

Figure 9.5. Biaxial stress against oxidation temperature for samples oxidised for (a) 1000 hours, (b) 2000 hours[1].and (c) 4000 hours. The wavelengths used for measurements are indicated.

[1] There is a question as to the origin of the sample oxidised for 2000 hours at 950°C, as the form of the acquired spectra did not resemble that of the other RT22 coated samples.

The following stress measurements were made along the cross-section of a sample in order to investigate whether any stress distribution was present across the thickness of the thermally grown oxide. Spectra were taken at 1μm intervals across the cross-section surface of an RT22 coated sample using a 50x magnification long distance lens. An image of the sample examined, together with the line along which spectra were acquired is shown in Figure 9.6 and the resulting biaxial stress measurements are shown in Figure 9.7.

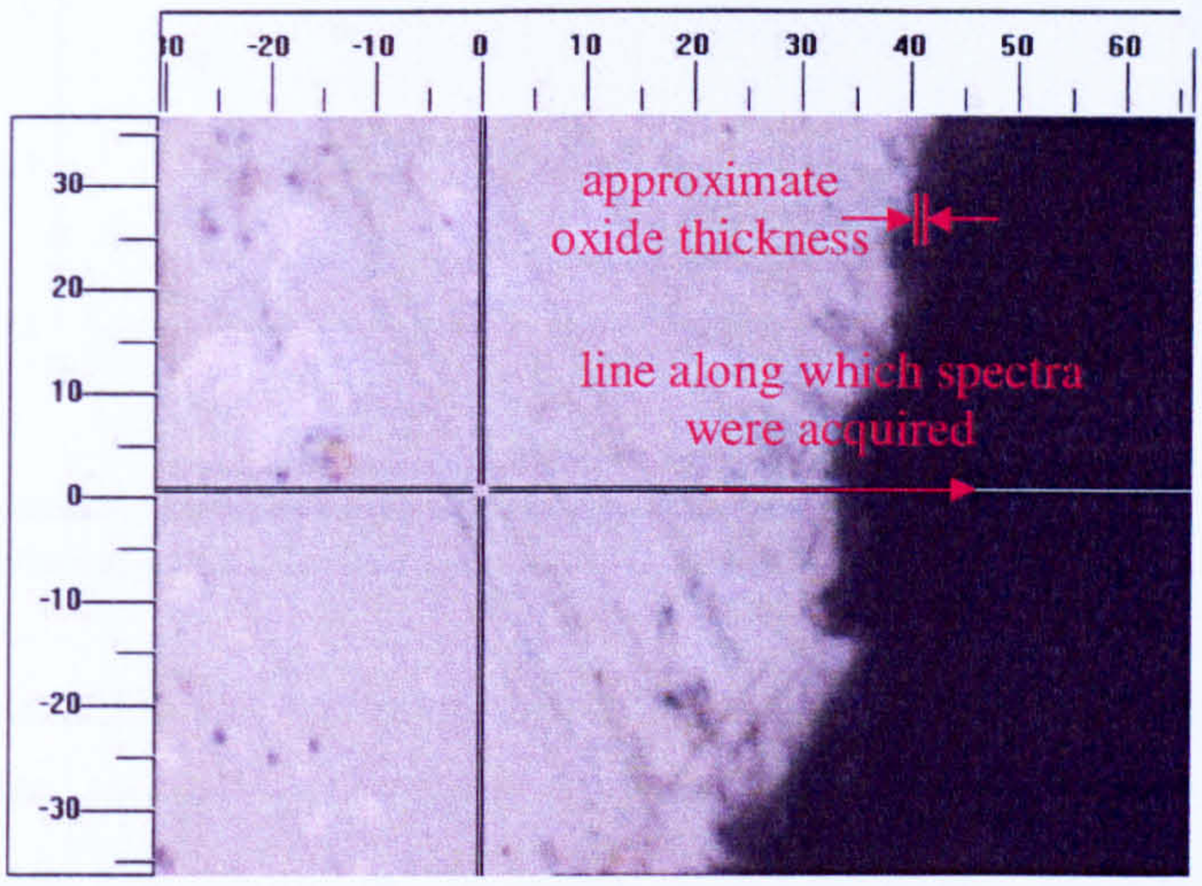

Figure 9.6. Cross-section of RT22 coated sample oxidised for 4000 hours at 950°C. Distance is shown in μm.

Figure 9.6 shows that the distance over which measurements were taken is greater than the width of the oxide. This is due to spectra being acquired from the periphery of the laser beam as well as from the centre. Thus spectra can be acquired from the edges from the laser beam after the centre of the beam has been moved away from the sample. Figure 9.7 also shows that there is a stress distribution across the oxide, although this is not reflected in the acquired spectra through the oxide by a multi-modal distribution as found by others and discussed in Section 2.5.6, Figure 2.25.

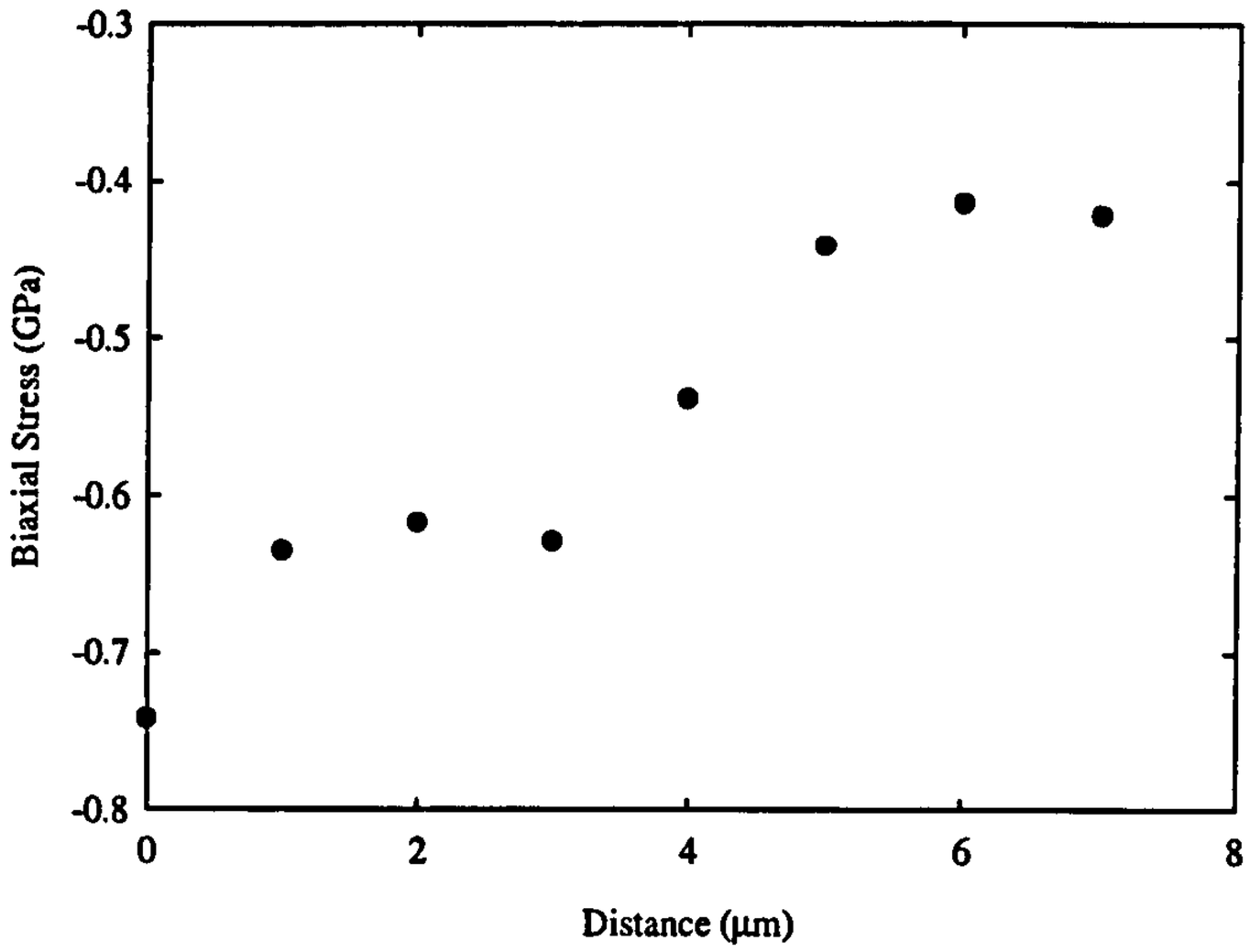

Figure 9.7. Biaxial stress against distance across RT22 coated sample, starting from the oxide/bond-coat interface, position 0, oxidised for 4000 hours at 950°C.

Scanning transmission electron microscope (STEM) images, high-angle annular dark field (HAADF) images and energy dispersive X-ray maps were obtained in conjunction with Loughborough University of RT22 coated samples oxidised for 1000 hours at 850°C, 950°C and 1050°C. The samples were prepared by focused ion beam milling, Section 3.10. The STEM system used was a Philips Tecnai F20 and the HAADF detector used was a Fischione.

A scanning transmission electron microscope image and a high-angle annular dark field image of the RT22 coated sample oxidised for 1000 hours at 850°C are shown in Figure 9.8 and Figure 9.9. Energy dispersive X-ray composition maps corresponding to the scanning transmission electron image are shown in Figure 9.10.

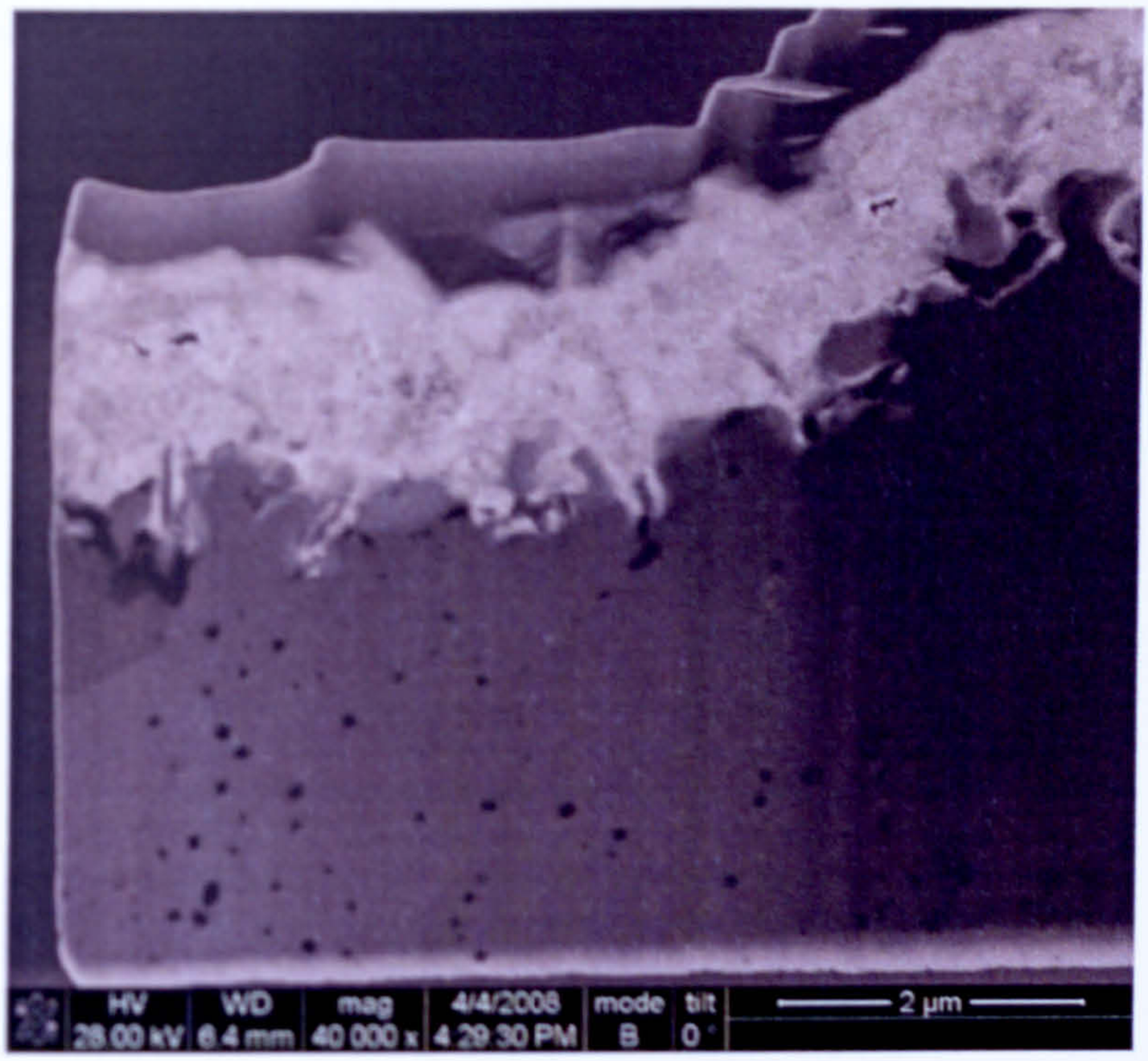

Figure 9.8. Scanning transmission electron image of RT22 coated sample oxidised for 1000 hours at 850°C. Courtesy of Dr. Geoff West, Loughbourough University.

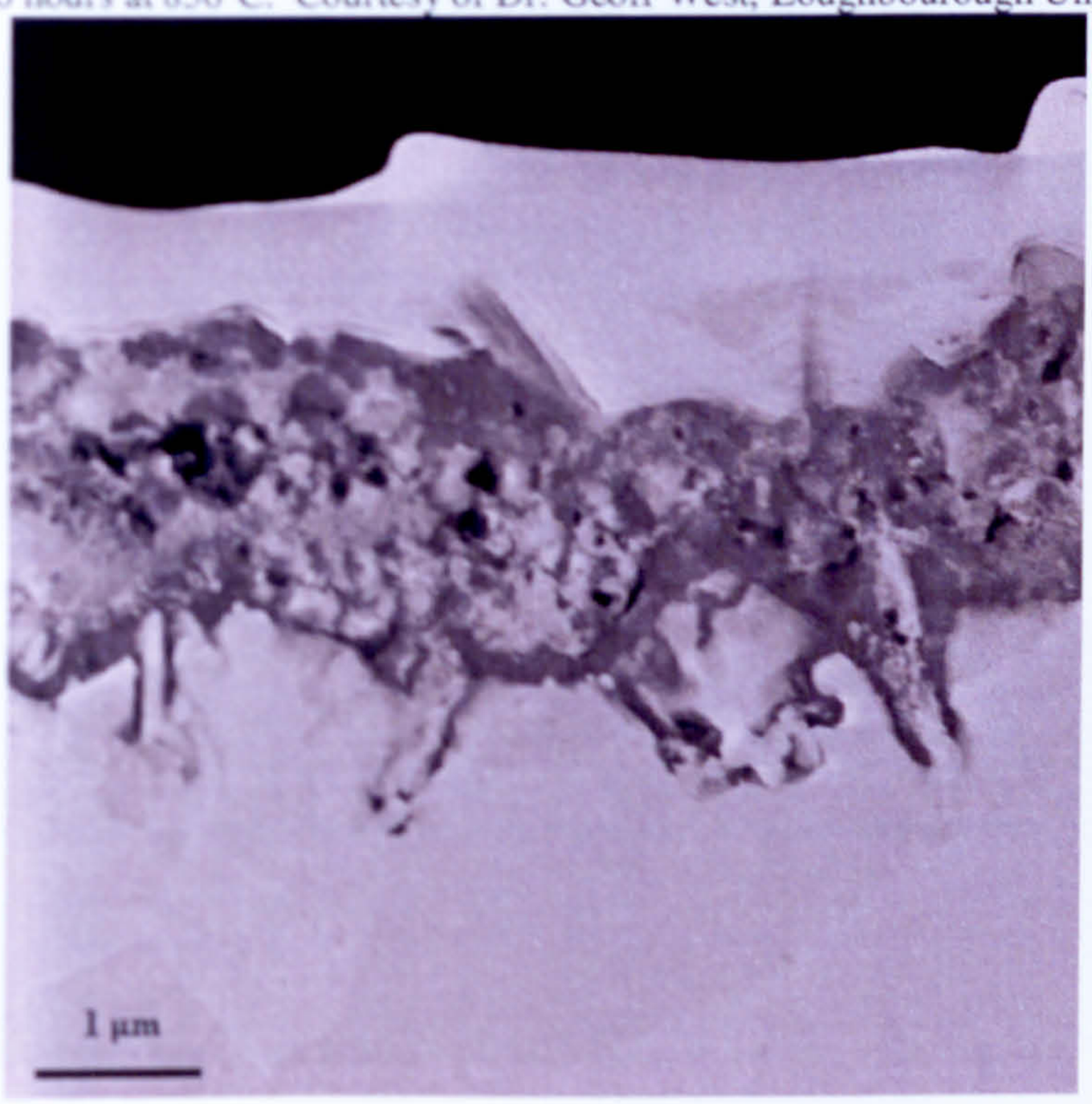

Figure 9.9. HAADF diffraction contrast image of RT22 coated sample oxidised for 1000 hours at 850°C. Courtesy of Dr. Geoff West, Loughbourough University.

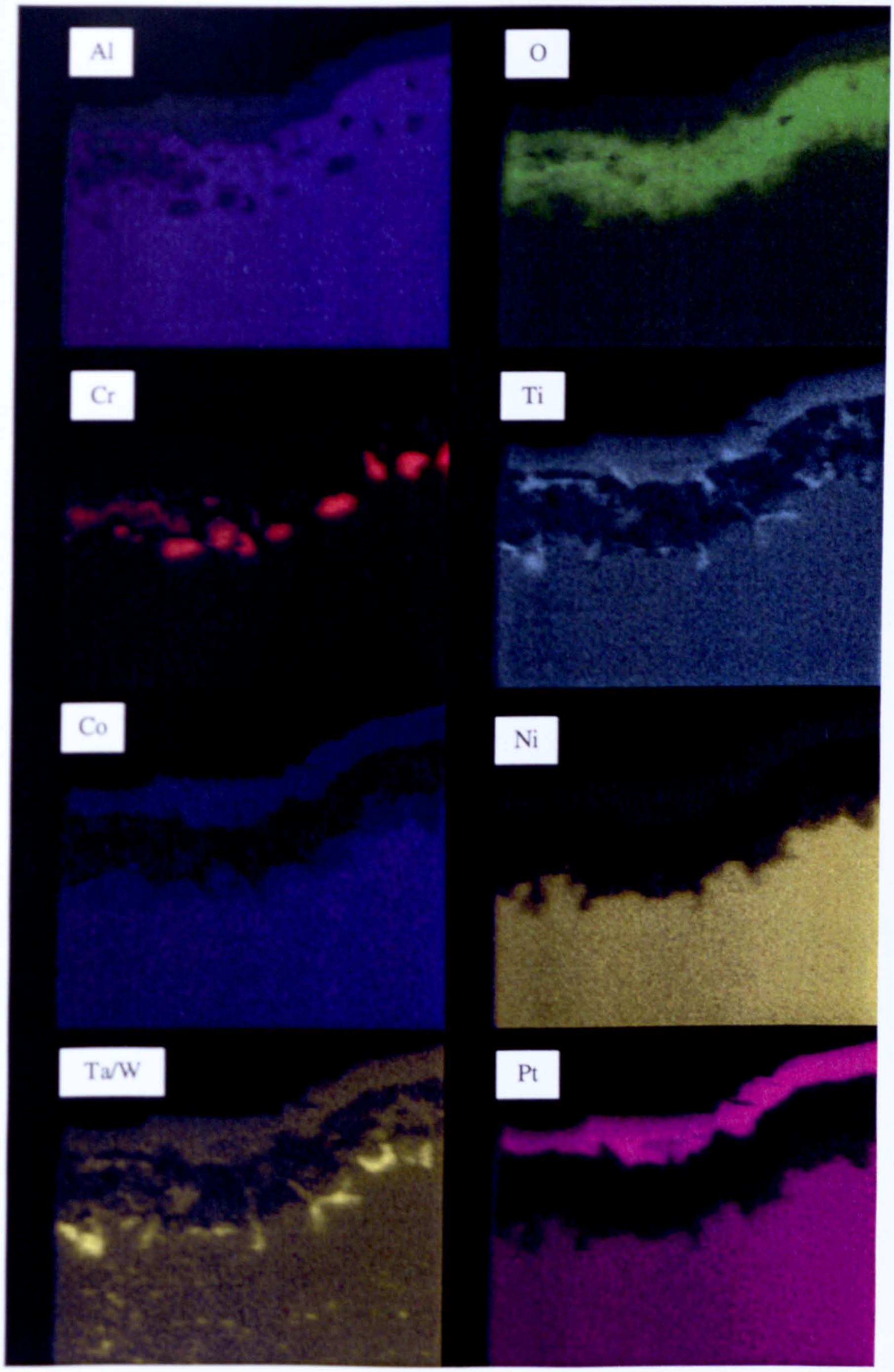

Figure 9.10. Energy dispersive X-ray maps of RT22 coated sample oxidised for 1000 hours at 850°C. Courtesy of Dr. Geoff West, Loughbourough University.

The STEM and HAADF images show that the oxide consists of a mixed fine scale microstructure, with grains typically under 0.3μm diameter. The EDX composition distribution maps reveal that the oxide consists primarily of aluminium oxide with a discontinuous chromium oxide layer contained within it. There are fine needles of titanium/tantalum/tungsten oxide at the thermally grown oxide/bond-coat interface. The platinum in the EDX composition maps results from the platinum placed on the sample for the focused ion beam milling during the TEM sample preparation.

STEM and HAADF images of an RT22 coated superalloy sample oxidised for 1000 hours at 950°C can be seen in Figure 9.11 and Figure 9.12. Corresponding composition maps can be seen in Figure 9.13.

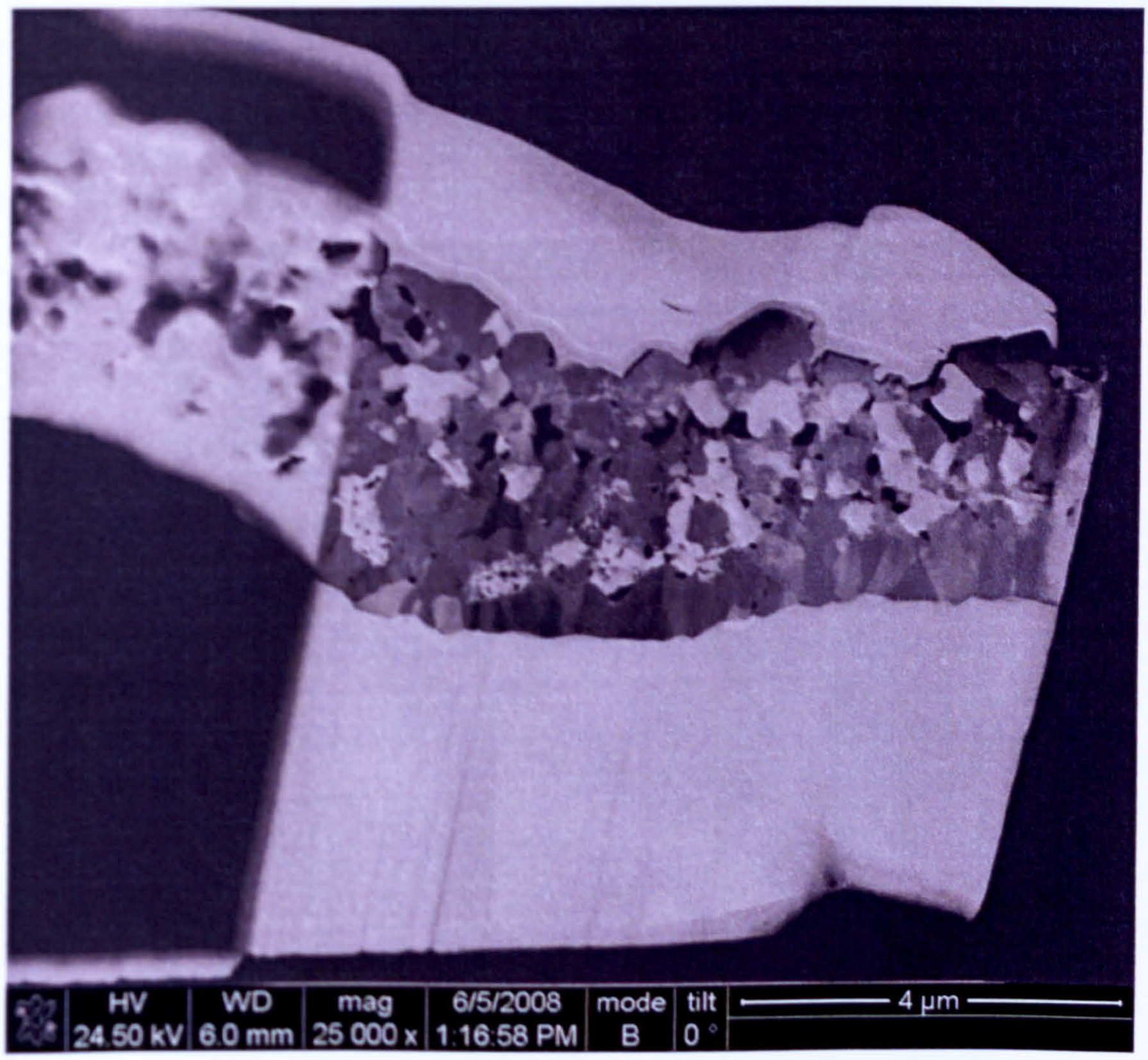

Figure 9.11. Scanning transmission electron image of RT22 coated sample oxidised for 1000 hours at 950°C. Courtesy of Dr. Geoff West, Loughbourough University.

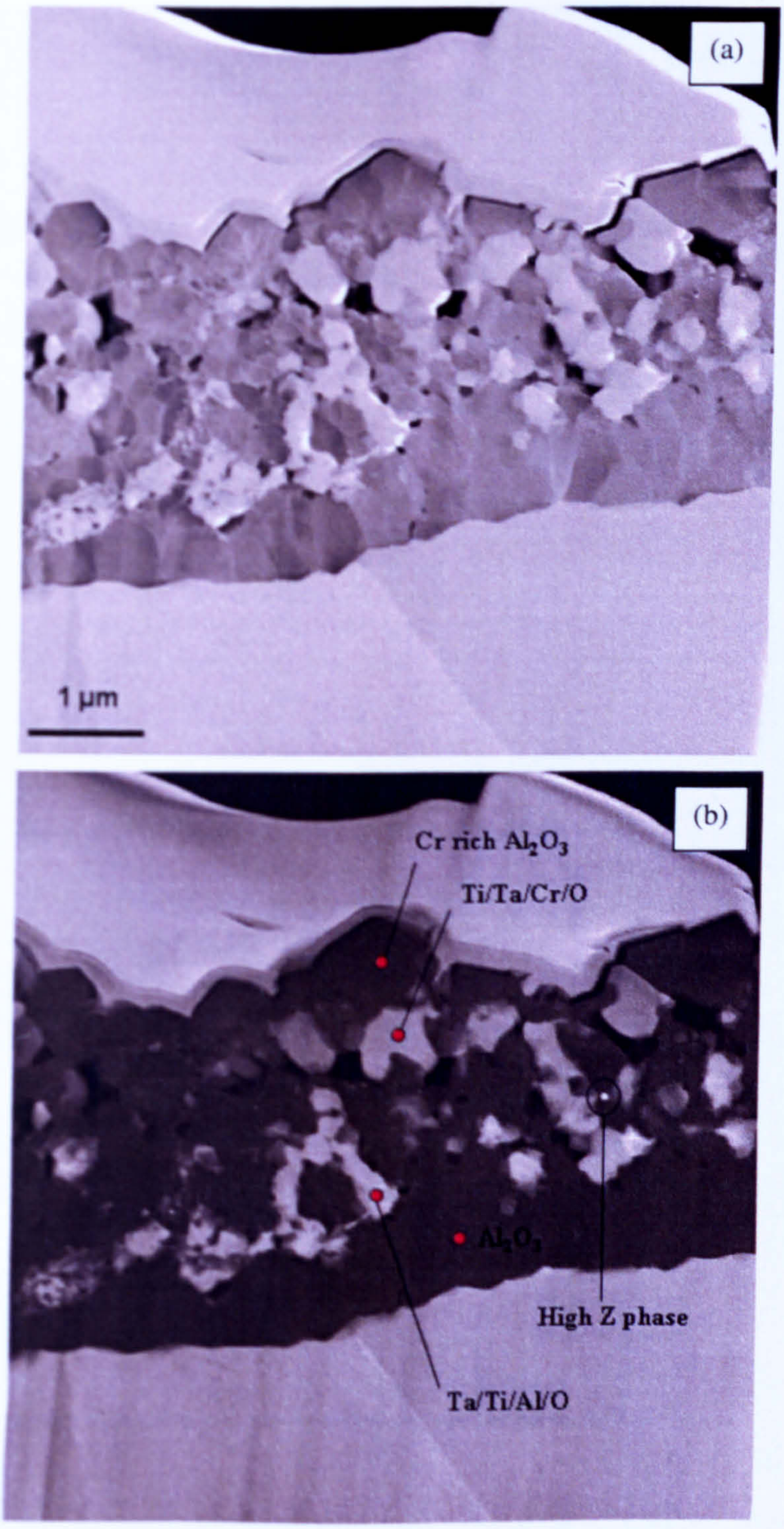

Figure 9.12. HAADF images of RT22 coated sample oxidised for 1000 hours at 950°C; (a) is a diffraction contrast image and (b) is a Z contrast image. Courtesy of Dr. Geoff West, Loughbourough University.

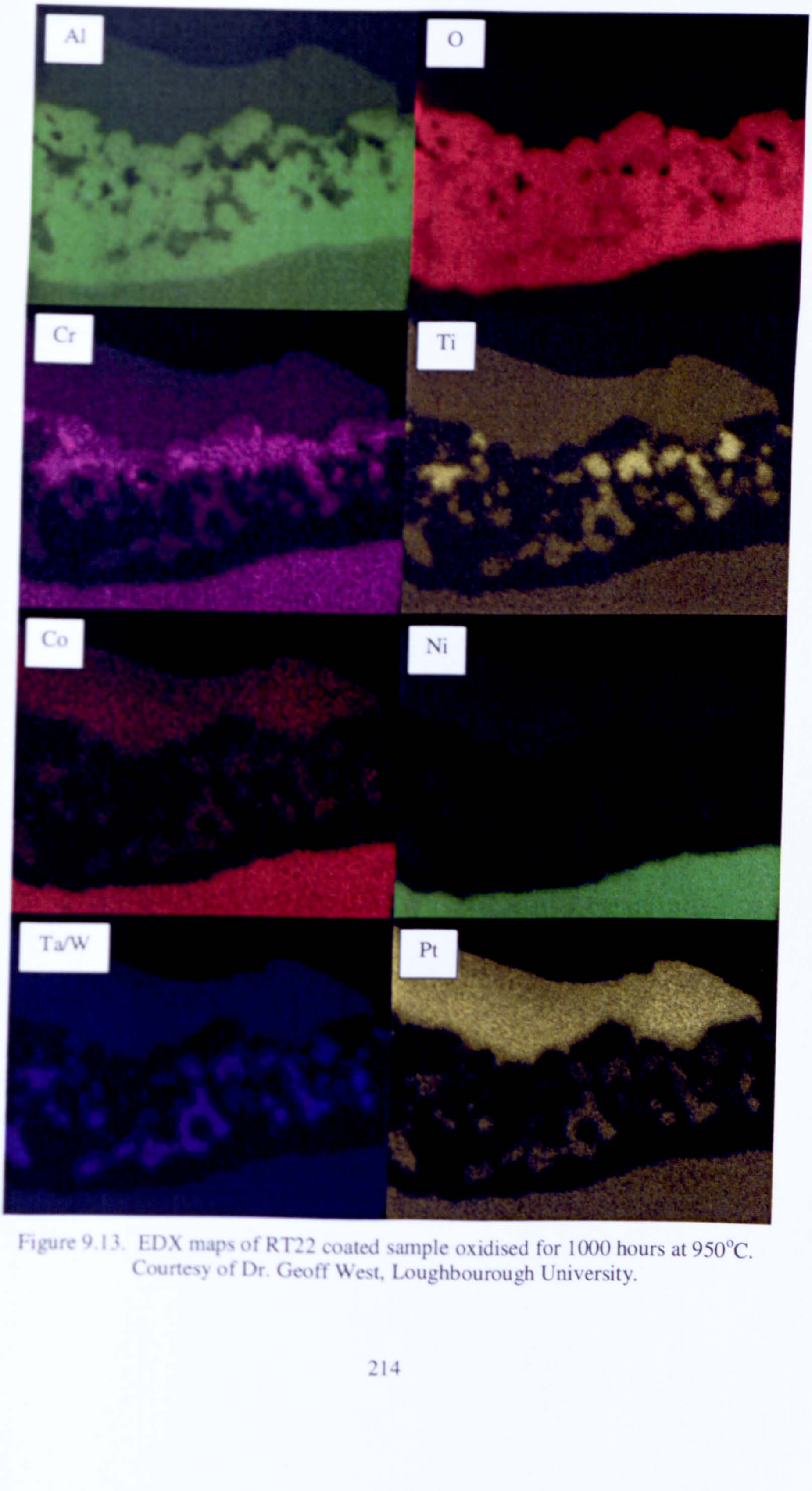

Figure 9.13. EDX maps of RT22 coated sample oxidised for 1000 hours at 950°C. Courtesy of Dr. Geoff West, Loughbourough University.

The thermally grown oxide grains are coarser at an oxidation temperature of 950°C than 850°C. There is a distribution of grain size throughout the oxide, with predominantly coarser grains at the thermally grown oxide/bond-coat interface, approximately 0.8μm thick, and finer grains towards the outer surface of the oxide, typically under 0.3μm diameter. The EDX composition maps reveal that the thermally grown oxide still predominantly consists of alumina. However, the layer of chromium oxide is no longer present. Instead, there is a chromium rich layer of aluminium oxide towards the outer surface of the thermally grown oxide. The titanium/tantalum/tungsten needles are also no longer present. The titanium/tantalum/tungsten oxide instead forms clusters within the alumina. The information gained from the EDX composition maps is confirmed by the Z contrast image.

A STEM image of a thermally grown oxide grown on an RT22 coated superalloy sample oxidised for 1000 hours at 1050°C can be seen in Figure 9.14. EDX images for the area can be seen in Figure 9.15.

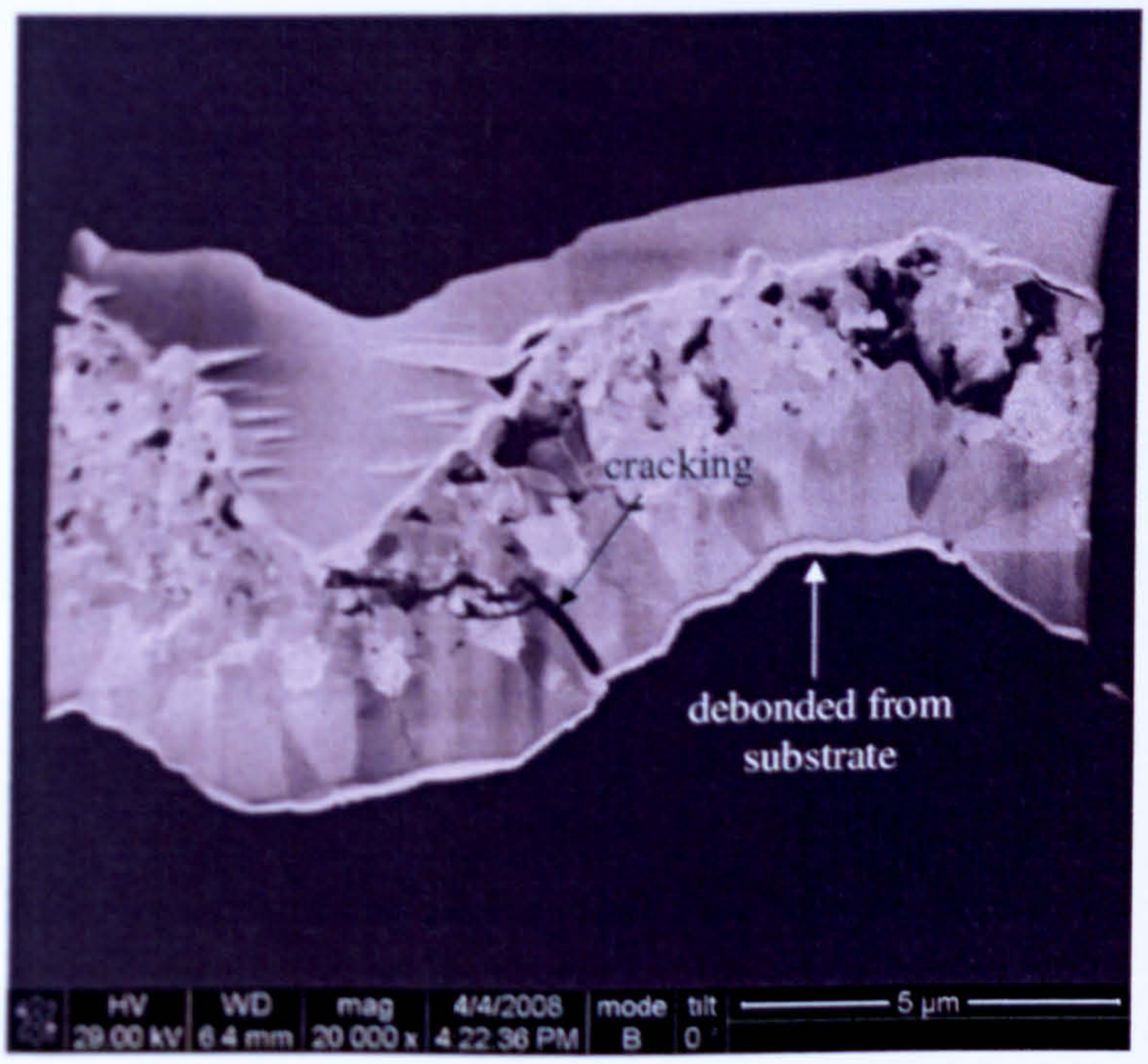

Figure 9.14. Scanning transmission electron image of RT22 coated sample oxidised for 1000 hours at 1050°C. Courtesy of Dr. Geoff West, Loughbourough University.

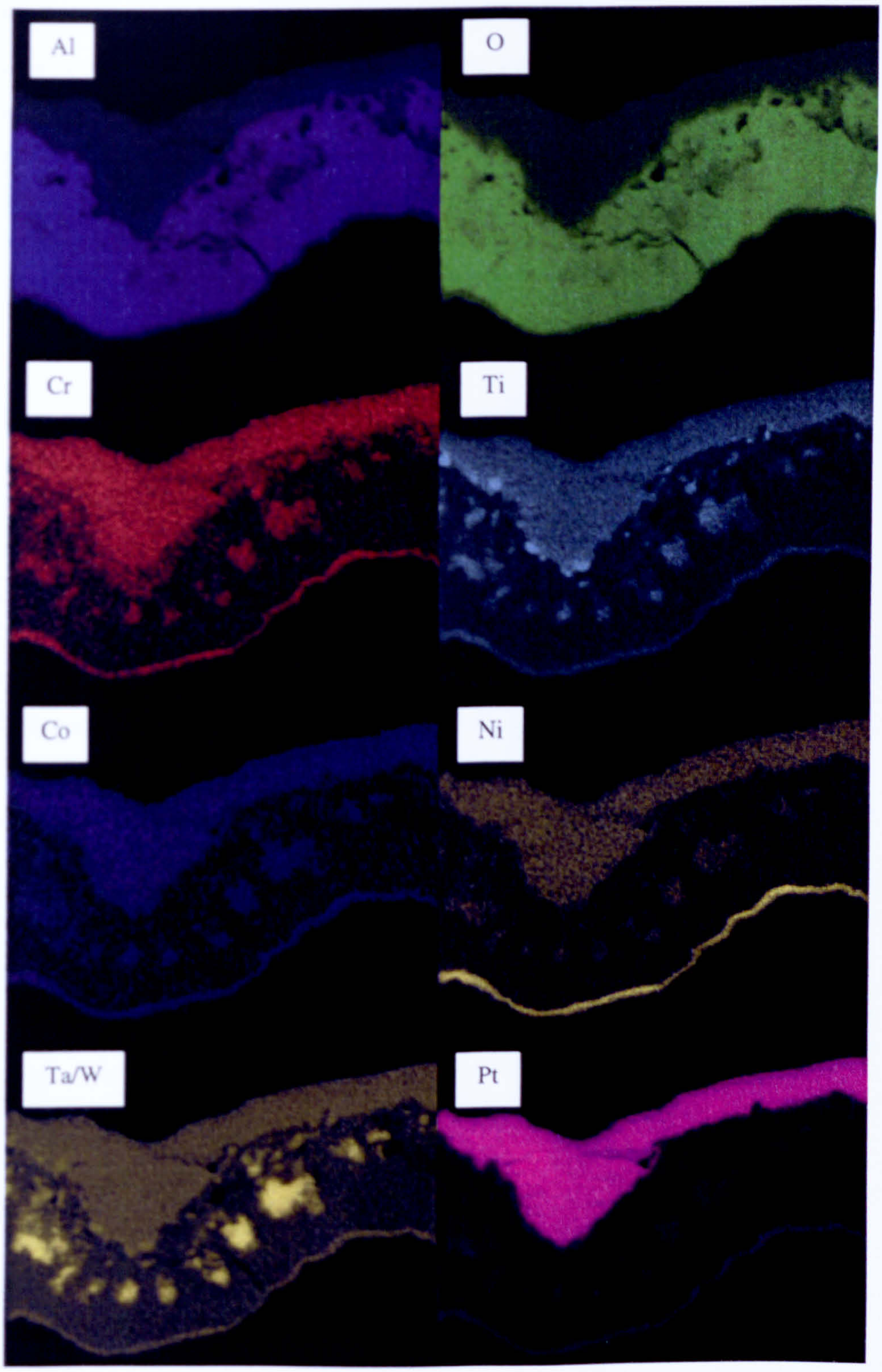

Figure 9.15. Energy dispersive X-ray maps of RT22 coated sample oxidised for 1000 hours at 1050°C. Courtesy of Dr. Geoff West, Loughbourough University.

The STEM image, Figure 9.14, reveals that the oxide has debonded from the bond-coat or substrate. There is also cracking at what would have been the oxide/bond-coat or substrate interface. The distribution of grain sizes has become more pronounced, with the larger grains towards what would have been the oxide/bond-coat or substrate interface, sometimes over 1μm thick, and finer grains towards the outer surface of the oxide, with diameters varying between approximately 0.5μm and 0.1μm diameter. The EDX composition maps, Figure 9.15, reveal chromium rich clusters within the alumina. These clusters are also rich in titanium/tantalum/tungsten.

Raman spectra were acquired from the thermally grown oxide of RT22 coated superalloy samples oxidised for 1000 hours at 1050°C and 1000°C. These can be seen in Figure 9.16. The Raman spectra were acquired using a Renishaw inVia spectrometer equipped with a 488nm wavelength laser.

Peaks belonging to the Raman spectrum of α-Al_2O_3 can clearly be seen in Figure 9.16 [Aminzadeh 1997, Gouadec et al. 2005]. However, these are overlaid by a series of additional peaks. These peaks can be attributed to TiO_2, rutile [Mazza et al. 2007]. There are additional peaks between 700cm^{-1} and 800cm^{-1}. Unfortunately, it was not possible in this work to correlate these peaks to any compounds.

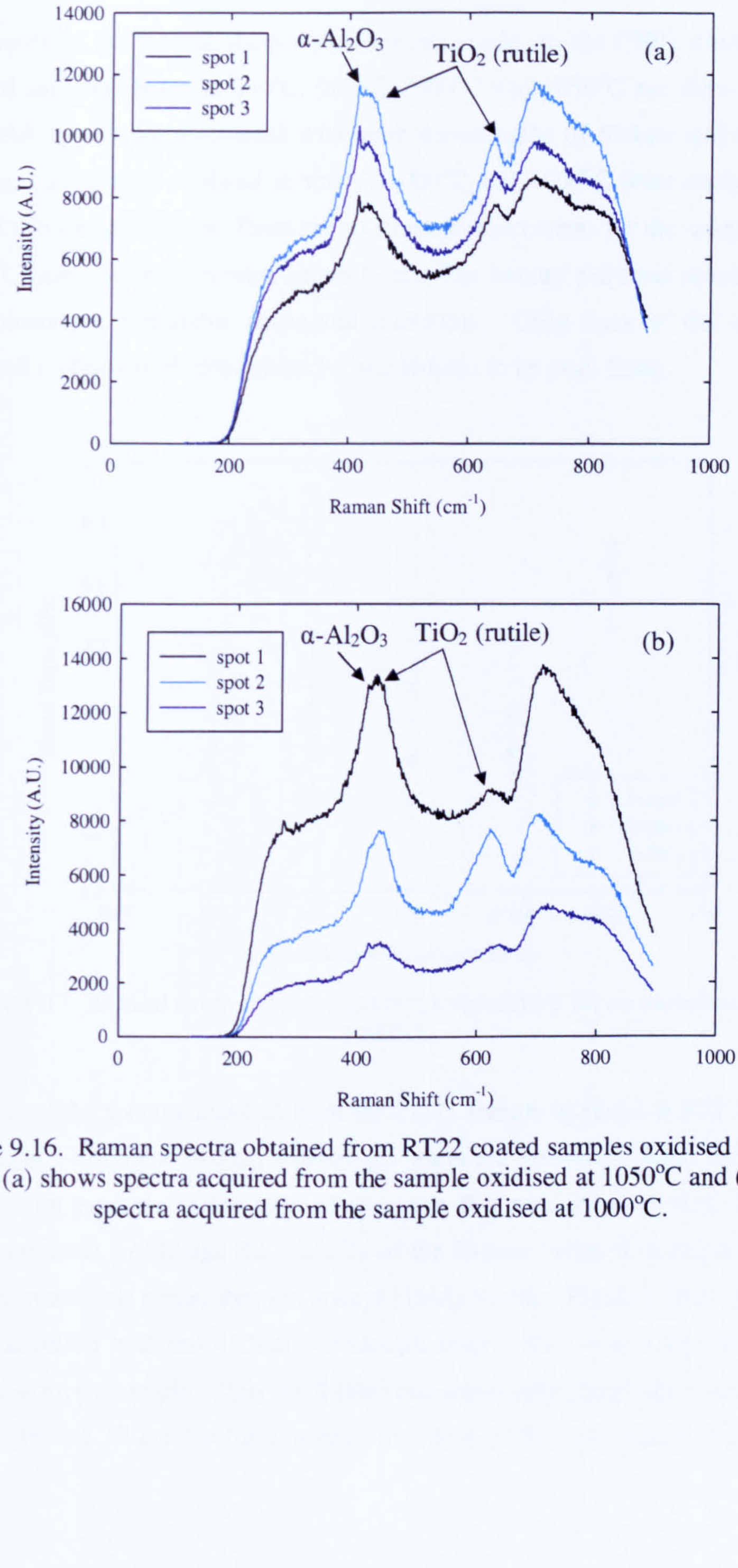

Figure 9.16. Raman spectra obtained from RT22 coated samples oxidised for 1000 hours. (a) shows spectra acquired from the sample oxidised at 1050°C and (b) shows spectra acquired from the sample oxidised at 1000°C.

9.2.3 CN91 Coated Sample

The results of the biaxial stress measurements made on the CN91 coated samples oxidised for 1000 hours at 850°C, 900°C, 1000°C and 1050°C are shown in Figure 9.17. All spectra were obtained with laser wavelengths of 514nm and 633nm. In addition, the samples oxidised at 950°C, 1000°C and 1050°C were analysed with a laser of wavelength 532nm. There are no stress measurements for the sample oxidised at 850°C using the 633nm wavelength laser. The twenty acquired spectra revealed predominantly a metastable phase and θ-alumina. Only three of the spectra had sufficiently intense α-alumina characteristic R-lines to be peak fitted.

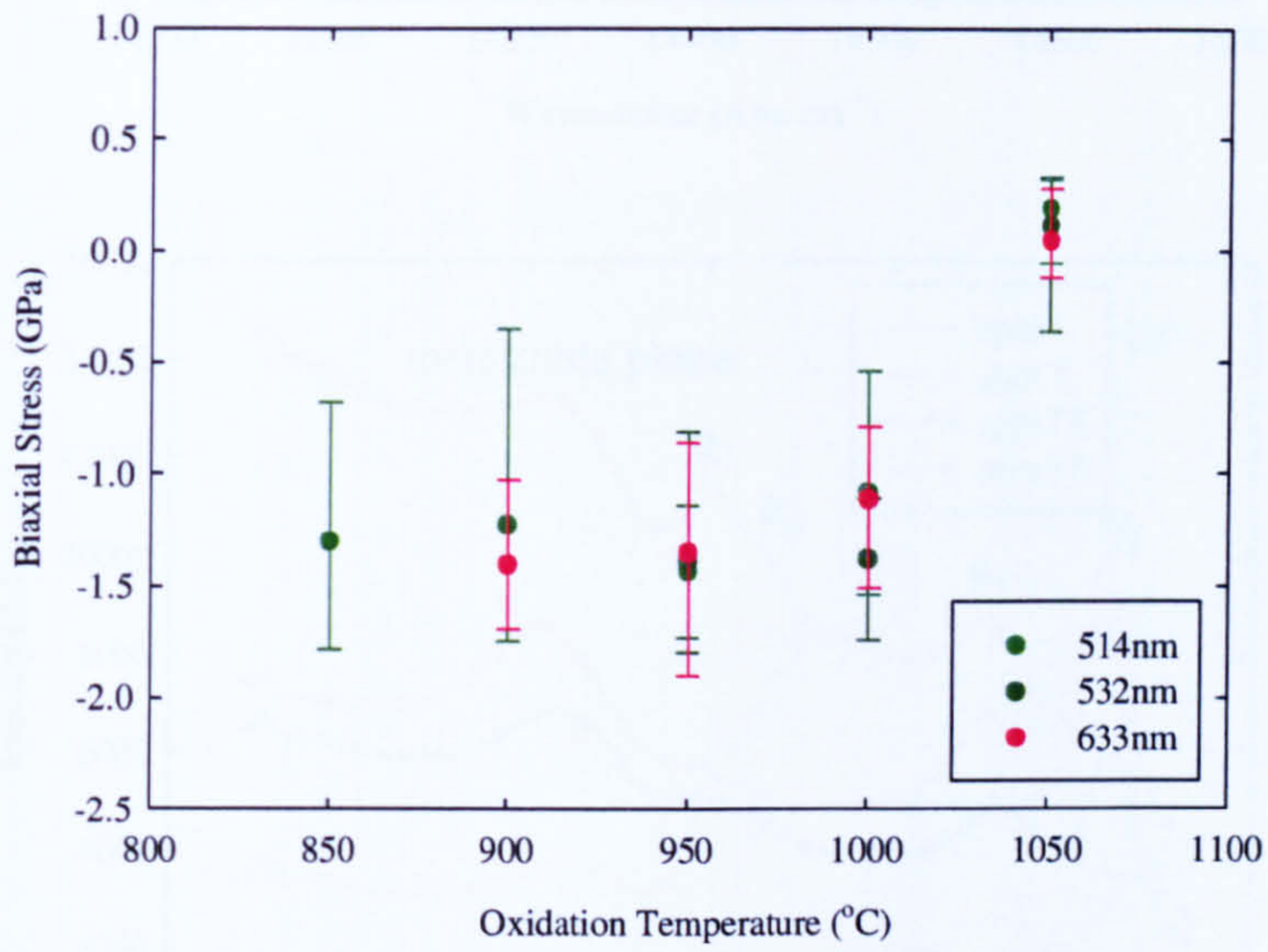

Figure 9.17. Biaxial stress against oxidation temperature for an oxidation time of 1000°C.

Examples of the spectra acquired from the CN91 sample oxidised at 850°C for 1000 hours using 514nm and 633nm wavelength lasers are shown in Figure 9.18. Figure 9.18(a) is an example of the type of spectrum that was acquired with the 514nm wavelength laser. Although the intensity of the R-lines varies with respect to the θ-lines and metastable phase, they are always clearly visible. Figure 9.18(b) shows four spectra acquired with the 633nm wavelength laser. Spot 1 is a typical spectrum obtained from the sample. Only the θ-lines and metastable phase can clearly be seen. Spots 7, 16 and 17 are the three spectra in which sufficiently distinct R-lines were present.

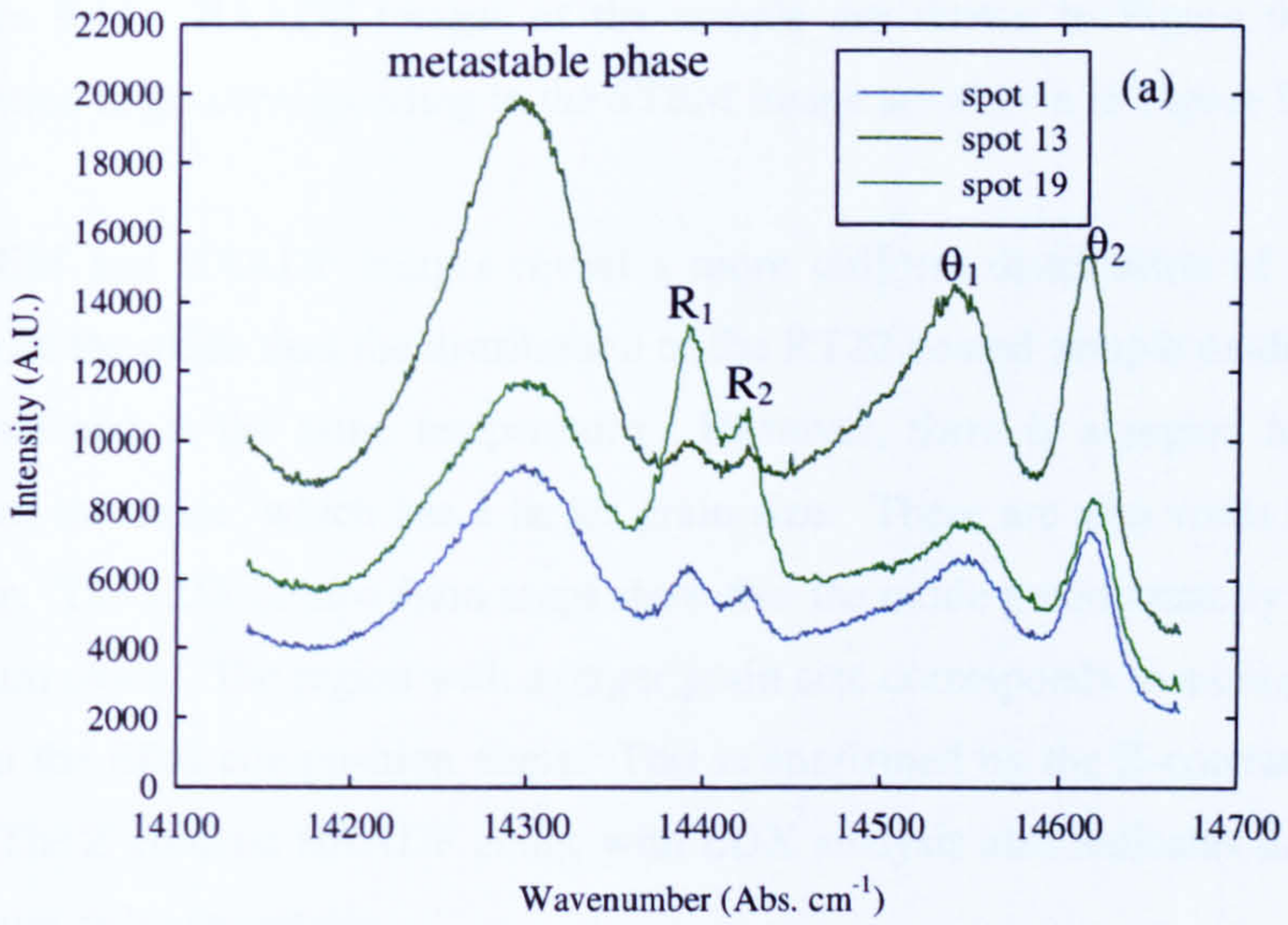

Figure 9.18. Photoluminescence spectra taken from the CN91 coated sample oxidised at 850°C for 1000 hours. The section marked (a) shows examples of spectra acquired using the 514nm wavelength laser and the section marked (b) using the 633nm wavelength laser where spots 7, 16 and 17 revealed sufficiently intense α-alumina peaks.

A STEM image of a CN91 coated sample oxidised at 950°C for 1000 hours is shown in Figure 9.19. HAADF images of the sample are shown in Figure 9.20. EDX composition maps corresponding to the STEM image are shown in Figure 9.21.

The STEM and HAADF images reveal a more uniform distribution of grain sizes throughout the oxide than the distribution of the RT22 coated sample oxidised for the same time and at the same temperature. However, there is a region towards the surface of the oxide, which has a larger grain size. There are also voids throughout the oxide. The EDX composition maps show that the oxide predominantly consists of aluminium oxide. The region with a larger grain size corresponds to a chromium rich region in the EDX composition maps. This is confirmed by the Z-contrast HAADF image. The Z-contrast HAADF image with EDX analysis also indicates the presence of platinum rich precipitates.

Figure 9.19. Scanning transmission electron image of CN91 coated sample oxidised for 1000 hours at 950°C. Courtesy of Dr. Geoff West, Loughbourough University.

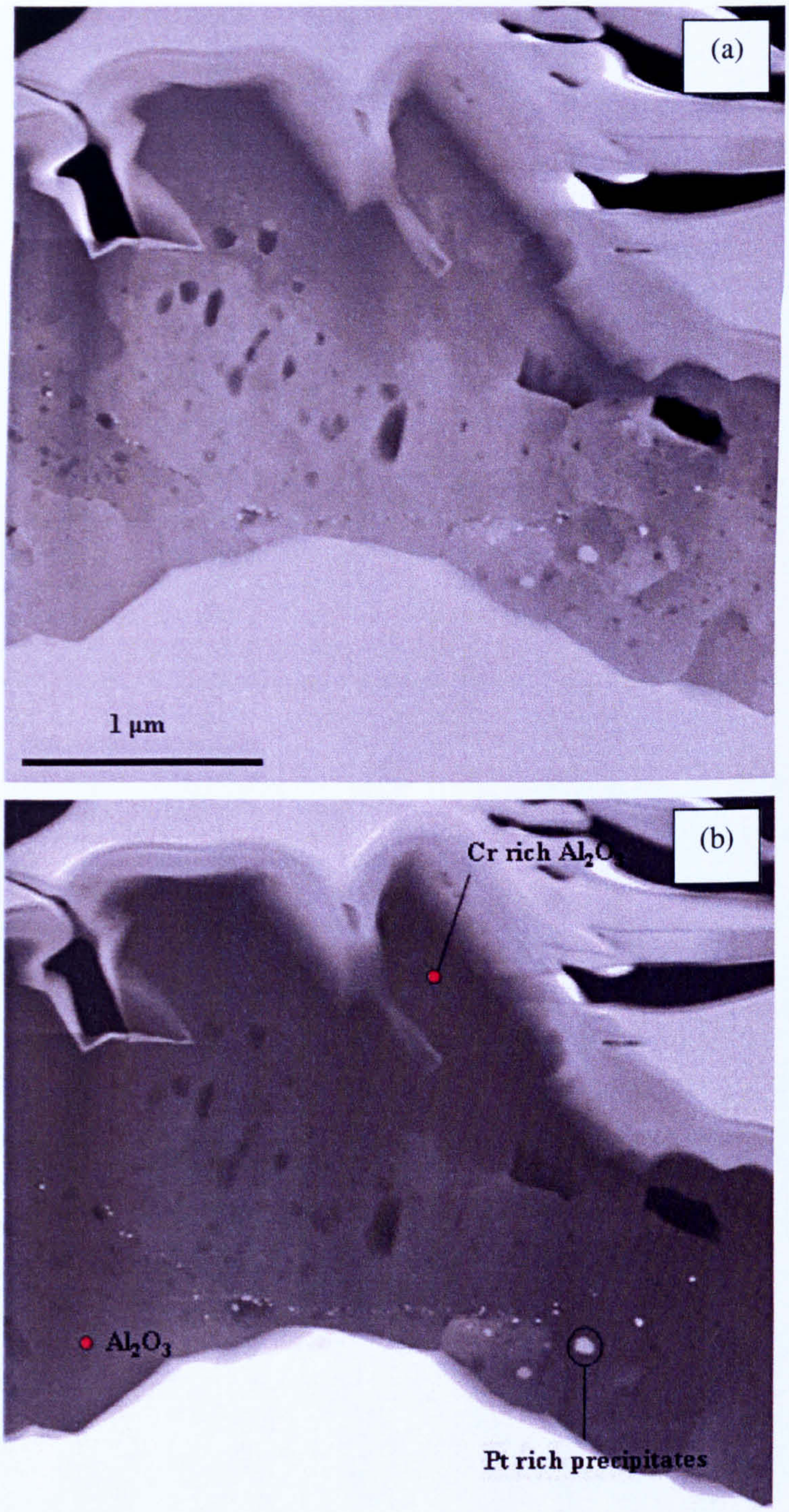

Figure 9.20. HAADF images of CN91 coated sample oxidised for 1000 hours at 950°C; (a) is a diffraction contrast image and (b) is a Z contrast image. Courtesy of Dr. Geoff West, Loughbourough University.

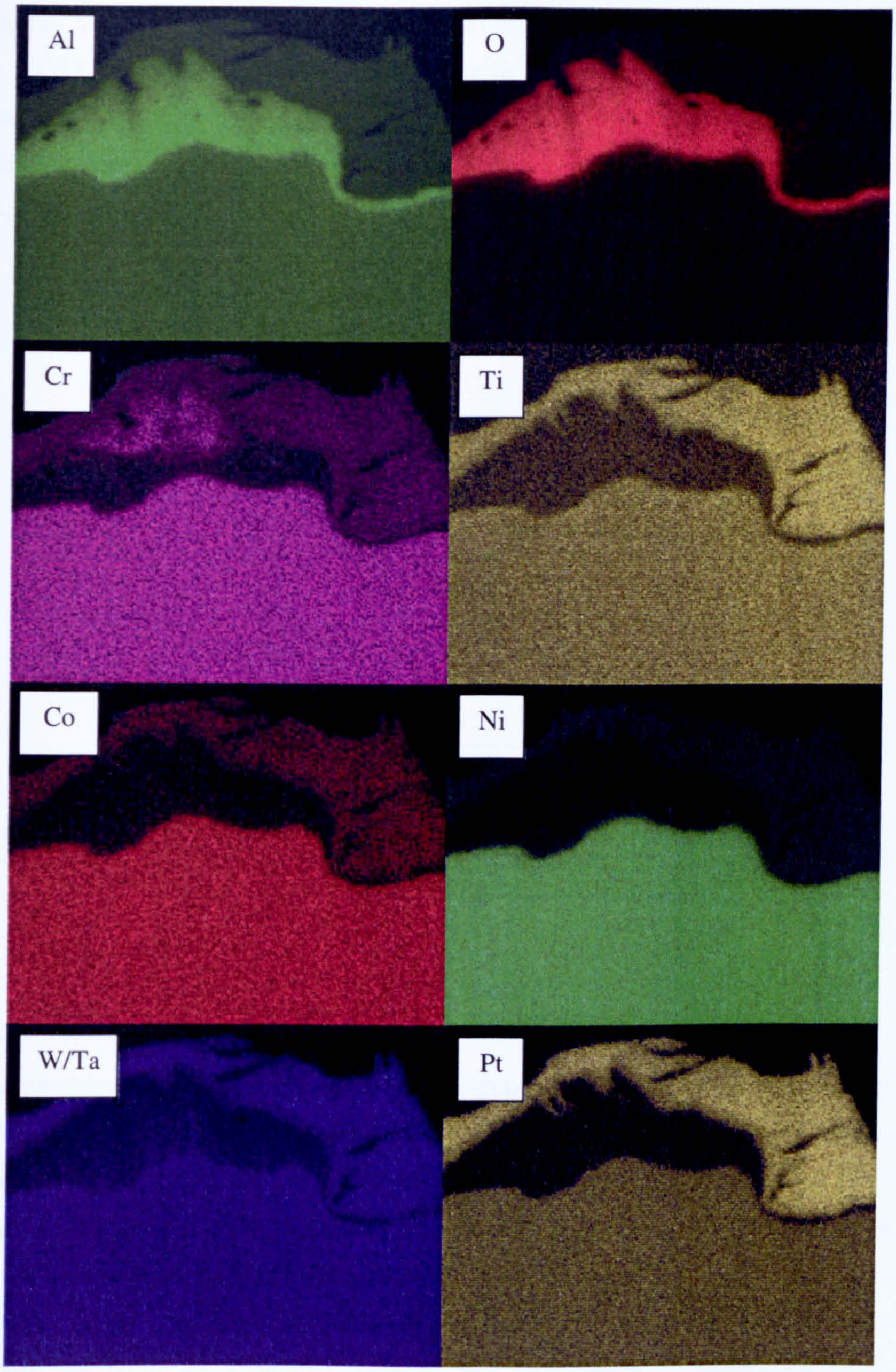

Figure 9.21. Energy dispersive X-ray maps of CN91 coated sample oxidised for 1000 hours at 950°C. Courtesy of Dr. Geoff West, Loughbourough University.

Raman spectra were acquired from the CN91 coated sample oxidised for 1000 hours at 1000°C, an example of which can be seen in Figure 9.22. The spectrometer used was again the Renishaw inVia spectrometer fitted with a 488nm wavelength laser. This spectrum agrees with spectra obtained by others to be that of α-Al_2O_3 [Aminzadeh 1997. Gouadec et al. 2005].

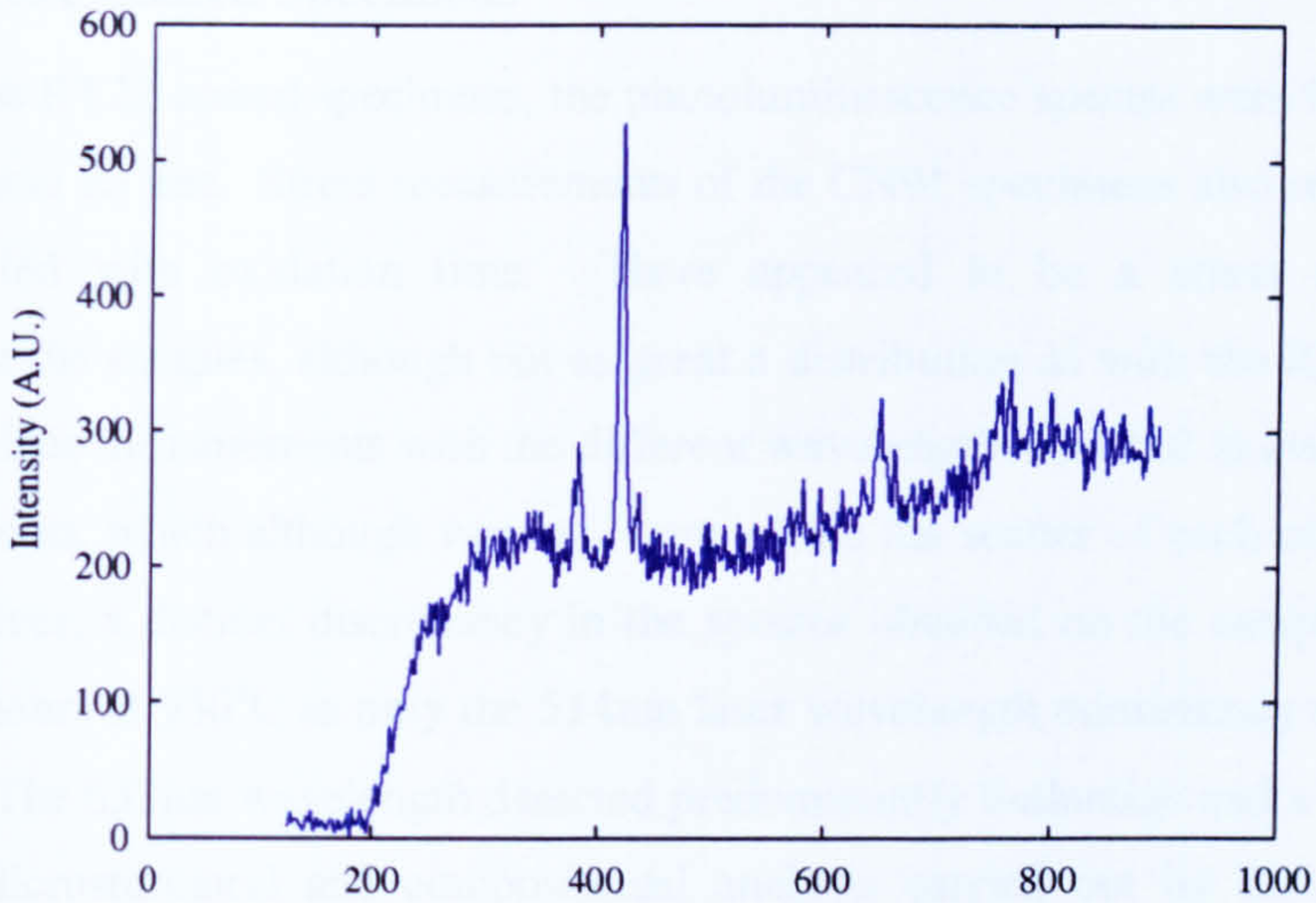

Figure 9.22. Raman spectrum acquired from CN91 coated sample oxidised for 1000 hours at 1000°C showing α-Al_2O_3.

9.3 Summary

9.3.1 RT22 Coated Specimens

The photoluminescence spectra were fitted with a single R_1 and R_2 line. However, the stress measurements with the different wavelengths indicate that there is a stress distribution throughout the samples; since the stress measurements with the different laser wavelengths resulted in different measurements of average stresses which were not always within the distribution of each other. This distribution decreased with oxidation time. A stress distribution is confirmed by the measurement of stresses across the width of a sample oxidised for 4000 hours at 950°C, Figure 9.7. Microstructural analysis, carried out by Loughborough University, of RT22 coated samples oxidised for 1000 hours at 850°C, 950°C and 1050°C reveals a complex microstructure of varying grain sizes throughout the individual oxides and varying grain sizes with oxidation temperature. Analysis of the composition, carried out by

Loughborough University showed that the oxide is not purely alumina. It also contained varying levels of chromium and other metal oxides. Raman spectra of two thermally grown oxides revealed the presence of TiO_2 (rutile) as well as α-alumina, which corresponds well to the EDX composition maps and HAADF analysis carried out by Loughborough University.

9.3.2 CN91 Coated Specimens

As with the RT22 coated specimens, the photoluminescence spectra were fitted with a single R_1 and R_2 line. Stress measurements of the CN91 specimens also revealed that stress varied with oxidation time. There appeared to be a stress distribution throughout the samples, although not as great a distribution as with the RT22 coated samples; since measurements with the different wavelengths resulted in average stress measurements, which although varying, were within the scatter of each other. There was, however, a distinct discrepancy in the spectra obtained on the sample oxidised for 1000 hours at 950°C as only the 514nm laser wavelength consistently detected α-alumina. The 633nm wavelength detected predominantly θ-alumina and a metastable phase. Microsturctural and compositional analysis carried out by Loughborough University revealed a more uniform oxide made up predominantly of relatively uniform aluminium oxide grains with larger chromium rich grains towards the surface. This agrees with the Raman spectrum of an oxide, Figure 9.22, which was that of α-alumina.

10 Discussion

10.1 Overview

The overall Supergen programme provided packages of work, which were interlinked in several topic areas. In the present thesis, emphasis has been placed on the role of oxides and associated residual stresses. The inter-relationship between the experiments undertaken and the surface stress measurement techniques employed is shown in Figure 10.1. The investigations were undertaken in order to assess what information could be gained from measuring the near surface stresses of components. However, links were established with other measurements of stress to different length scales. These included neutron diffraction, deep hole drilling and incremental hole drilling. In addition, the measurements were used to ascertain whether stress measurements at different penetration depths with different length scales could be correlated to give an understanding of the stress profiles within samples and hence within components. The measured stress profiles were compared to finite element model predictions. These measured and predicted stress profiles were again related to understanding the structural integrity of components and to a weld repair strategy [McDonald et al. 2005].

10.2 Calibration and Sources of Error

Critical factors affecting confidence in stress measurement were reviewed for the surface stress measurements employed for this work.

10.2.1 X-Ray Diffraction

Instrumental calibration was conducted using a stress-free cerium oxide powder, CeO_2. Counting statistics were reviewed and as a consequence 15 ψ-angles were made for each stress measurement. Further, acquisition times were at times increased to ensure an adequate peak to background ratio for peak fitting.

Little experimental confirmation could be found that "as grown" surface oxides should be removed prior to X-ray diffraction stress measurement. As a consequence, X-ray diffraction stress measurements were carried out on an engineering specimen

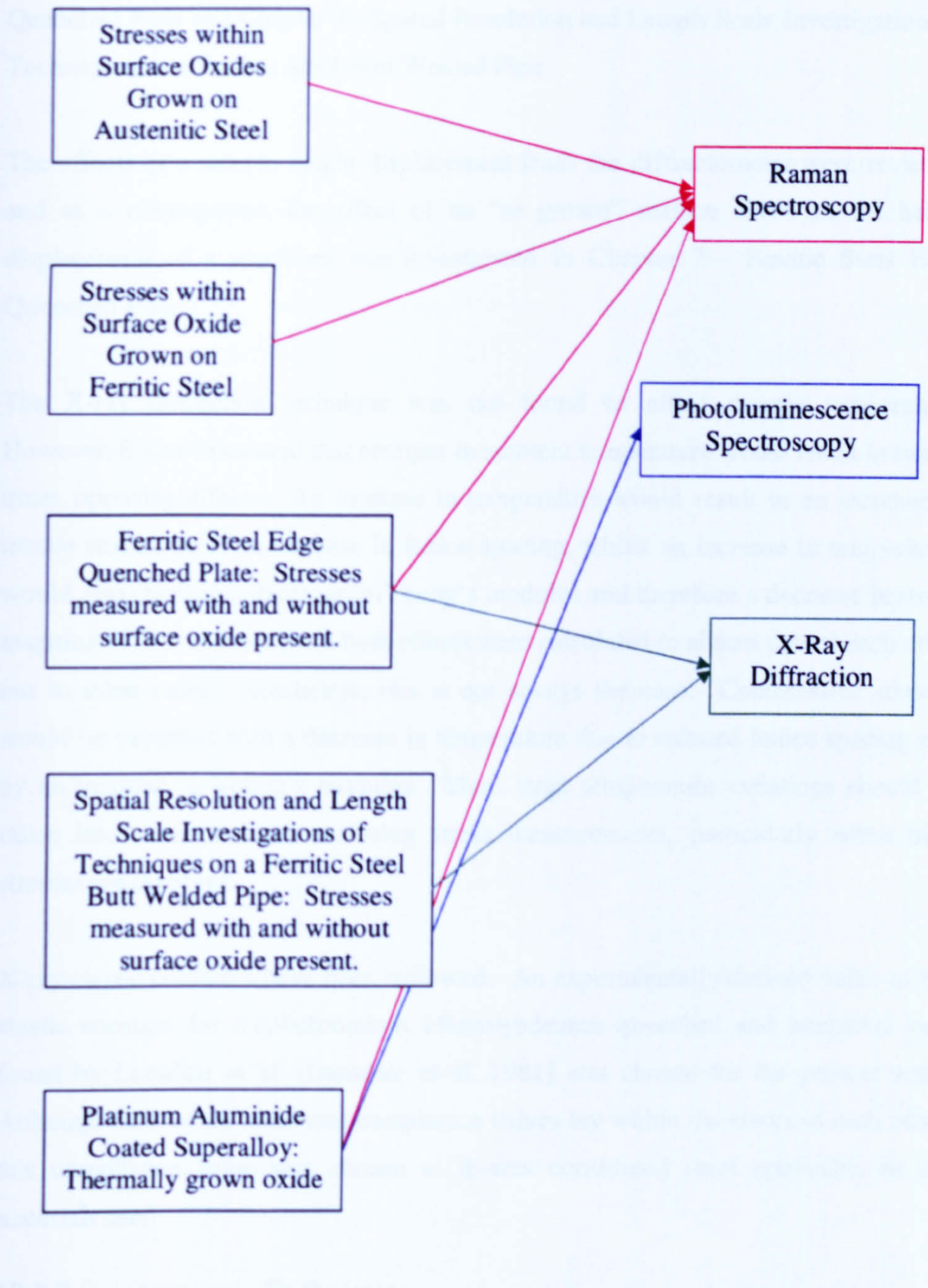

Figure 10.1. Interrelationship between the experimental measurements made for the range of specimens considered in this programme of work and the measurement techniques employed.

with a known stress profile and a welded P91 pipe, Chapter 7 - Ferritic Steel Edge Quenched Plate and Chapter 8 - Spatial Resolution and Length Scale Investigations of Techniques on a Ferritic Steel Butt Welded Pipe.

The effects of a sample height displacement from the diffractometer were reviewed and as a consequence, the effect of an "as grown" surface oxide on the height displacement of a specimen was investigated in Chapter 7 - Ferritic Steel Edge Quenched Plate.

The X-ray diffraction technique was not found to affect sample temperature. However, it was calculated that changes in ambient temperature would result in two at times opposing effects. An increase in temperature would result in an increase in tensile stress due to an increase in lattice spacing, whilst an increase in temperature would also result in a decrease in Young's modulus and therefore a decrease in stress magnitude. The stresses from both effects were calculated to almost cancel each other out in some cases. Nontheless, this is not always the case. Compressive stresses would be increased with a decrease in temperature due to reduced lattice spacing and by an increase in Young's modulus. Thus, large temperature variations should be taken into account when analysing stress measurements, particularly when high stresses are involved.

X-ray elastic constants have been reviewed. An experimentally derived value of the elastic constant for $2^{1}/_{4}$%chromium 1%molybdenum quenched and tempered steel found by Lonsdale et al. [Lonsdale et al. 1981] was chosen for the present work. Although most of the measured compliance values lay within the errors of each other, this compliance value was chosen as it was considered most applicable to the materials used.

10.2.2 Spectroscopic Techniques

Calibration lamps and standards can be used to monitor peak positions and profiles of Raman and photoluminescence spectroscopic peaks. The distance of calibration standards from the microscope can readily be adjusted using the microscope stage and a constant microscope distance can be ensured. Any change in spectroscopic peak profile of the standards can therefore be assumed to result from the spectrometer.

However, calibration standards can suffer the disadvantage of laser heating effects and achieving a uniform near-surface stress distribution across the standards. Calibration lamps do not have this disadvantage, although the spectral lines do shift over time as the temperature of the lamps decrease. In the case of the spectrometers used, achieving a constant lamp to microscope distance proved more complex than with the calibration samples, primarily due to difficulties fixing the calibration lamp in position and focusing the microscope on it. So, although the calibration lamp did not suffer from heating effects or non-uniform stress distributions, it was not possible to monitor the spectrometer mirrors or grating via the stress profile as simply.

It was found fitting a single Raman peak with a Lorentzian, Gaussian or mixed Lorentzian-Gaussian profile resulted in less scatter than the commonly quoted error for well-calibrated Raman spectroscopic stress measurements, Section 4.3.4. Fitting of more complex overlapping peaks resulted in Lorentzian profiles producing the least scatter, Section 4.3.5. These results corresponded to the work of others Section 3.12.3 and can be attributed to lower full width half maxima of Lorentzian peaks in comparison to Gaussian peaks of the same intensity and area, leading to reduced overlap of the peaks [Allen and McMeeking 1978, Baruya and Maddams 1978]. Raman peaks were therefore fitted with a Lorentzian profile throughout this work. There was found to be much discussion about the most appropriate way to fit photoluminescence peaks, Section 3.12.4. Following a brief review of the suggested methods, it was decided to fit photoluminescence peaks with a mixed Gaussian-Lorentzian profile as this was the most direct method of accommodating the varying peak profiles with stress and temperature.

Decreasing the laser spot size was found to induce heating whilst acquiring Raman spectra in silicon for a given laser power, Section 4.3.6. Heating effects were also found to be induced by increasing the laser current whilst acquiring photoluminescence spectra in alumina, with a given laser spot size, Section 4.3.8. However, it was found that when less than 50% of the available laser current was used, there was little change in the measured stresses. The experiments undertaken in Sections 4.3.4 and 4.3.5 along with Chapter 5 - Stresses within Surface Oxides Grown on Austenitic Steel and Chapter 6 - Stresses within Surface Oxide Grown on Ferritic Steel used a microscope lens of 50x and a laser power of 2.4mW to increase peak

intensity and peak to background ratio. The Raman spectra acquired in Chapter 7 - Ferritic Steel Edge Quenched Plate were done with a lens magnification and a laser power of approximately 29μW. However, acquisition times were increased to 600s so as to improve peak intensity, which would have been reduced by a reduction in laser power. Chapter 9 - Platinum Aluminide Coated Superalloy employed a lens magnification of 5x and a laser power of 29μW. A macro was written to remove background noise in order to reduce acquisition times

10.3 Stresses within Surface Oxides Grown on Austenitic Steel

10.3.1 Introduction

As discussed in Chapter 2 – Literature Review, components employed for use at high temperatures, such as in electrical power plants, can develop a surface oxide over time [Ashby et al. 2007, Ashby and Jones 1996, Hurst et al. 1975, Viswanathan 1989]. This oxide layer can be critical to the components integrity. Oxide layers can provide a protective barrier to further oxidation and therefore be integral to the structure integrity of the component [Evans 1989, Hurst et al. 1975]. As such, an understanding of the levels of stress that can be accommodated in the oxide of a component is of beneficial when assessing the structural integrity for safe and economic operation.

In order to understand further the role of such oxides, stresses in oxides grown on the surface of a Type 316 austenitic stainless steel were measured using Raman spectroscopy. The steel substrates were then strained and the Raman shifts relating to the oxide layers were recorded and the associated stresses derived. This therefore provided a measure of the stresses developed in "as grown" oxides and the level of strain that could be accommodated in the oxides when subjected to loading. It also enabled the relationship between strain in oxides and their substrates to be investigated. Taper sections made in "as grown" oxide gave a better understanding of the relationship between stress and oxide thickness on and the effects of spallation on the stresses in the remaining oxides.

10.3.2 Stress Measurements

Specimens made from Type 316 austenitic stainless steel were oxidised at 950°C for times of one to four hours. The composition of the as grown specimen oxides was analysed using Raman spectroscopy and secondary ion mass spectroscopy and was found to be predominantly chromia (Cr_2O_3) with a high level of manganese at the surface, Figure 5.2 and Figure 5.3. A chromia Raman peak was used to convert Raman shifts to hydrostatic stress.

It was found that the stresses in the "as grown" oxides were compressive but became less compressive with oxidation time. This indicates that the oxides were stress relieving with increasing oxidation time and therefore oxide thickness. There was little variation in the Raman peak position for the first 1000 microstrain applied to the oxide. There was then a progressive decrease in Raman shift, thereby indicating a decrease in compressive stress. All the samples reach a similar Raman shift value of $552cm^{-1}$, –0.8GPa at approximately 6500 microstrain. An explanation for the lack of variation in the Raman peak positions for the first 1000 microstrain is the onset of cracking as discussed in Section 2.4.3. A critical tensile failure strain is required for the onset of cracking and once this occurs, cracks form at the oxide/metal interface [Nagl et al. 1994]. In this case, it is apparent from Figure 5.5 that the tensile failure strain for cracking to occur in the present oxide is 1000 microstrain. In addition, initial applied tensile stresses could have induced buckling in the oxide [Nagl et al. 1994]. These two phenomena combined could indeed account for the initial scatter in the measured Raman shifts and corresponding stresses in the oxides. The cracks then grow with an increase in strain and the crack spacing is directly proportional to the applied strain. This would cause continuous stress relieving of the oxide and explain the reduction in the magnitude of the compressive stresses in the oxide leading to total stress-relieving of the oxide.

The information obtained was limited by the laser spot size. Throughout the above described experiment, a 50x magnification lens with a calculated laser spot size of 1.02μm ±0.20 was employed. It is not known, from the experiment undertaken, the extent to which cracking and oxide spallation would have affected the area of oxide under observation. Cracking and spallation may have occurred in the region

surrounding the oxide area under investigation, but may not have affected the experiment.

The linearity of Raman shift with applied strain decreased with increasing oxidation time. This can be explained by the fact that the oxides grown over lower oxidation times were thinner and therefore underwent less microcracking than in the thicker oxides [Nagl et al. 1994]. Another factor could be the reduced adhesion energy of the oxide with increasing oxide thickness [Mougin et al. 2003].

The stresses measured in the taper sections were found to decrease in magnitude, become less compressive, over the length of the taper (i.e. as the thickness of the oxide decreased), Figure 5.11. The hydrostatic stresses measured in the thickest parts of the oxide, i.e. before the taper section, were between approximately –3.5GPa and –2.5 depending upon the sample. The hydrostatic stresses measured in the thinnest part of the oxide i.e. at the end of the taper were between –1.75 and –0.5GPa. This reduction in stress can be explained by the oxide stress relieving, as the compressive oxide is able to expand through surface layer removal. The greater the thickness of the oxide removed, the less constraint there is on the remaining oxide and the more it is able to expand.

The effect of oxide spallation was also observed. The Raman shifts decreased, corresponding to a decrease in compressive hydrostatic stress, in areas in which oxide had spalled. There was also scatter in Raman shifts and corresponding stresses across the untapered oxide surfaces, corresponded to approximately 1.5GPa in all cases.

10.3.3 Summary

Raman shifts in oxide layers grown on an austenitic stainless steel were measured when the substrate was put under tension. It was found that Raman peak shifts varied with applied strain when the strain was over 1000 microstrain. Furthermore, it was found, through different oxidation times, that oxide Raman shift is dependent upon the oxide thickness. This is consistent with the experimental and theoretical findings of other authors such as [Galerie et al. 2004, Mougin et al. 2002, (c)Mougin et al. 2001]. The tapering of oxide layers resulted in the stress relieving of the oxides layers. In each taper section, the greatest stress relieving occurred in the regions from

which the greatest volume of oxide had been removed. Scatter was found in the magnitudes of the measured stresses in the "as grown" oxides. This scatter is greater than that recorded when measuring stresses in a calibration material, Section 4.3.4, and can therefore be attributed to variations in stress across the oxide.

10.3.4 Implications for Structural Health Monitoring

The residual stress in the oxide grown on a Type 316 austenitic stainless steel has been investigated. The stress in the complex but predominantly chromia has been shown to be dependent on a variety of factors such as the strain in the steel substrate, although only after the substrate has undergone a substantial level of strain. In addition, the level of stress in the oxide has been shown to be affected by oxide thickness, oxide removal and spallation. It would only be possible to use oxide as a measure of strain and stress in substrate if thickness of oxide and oxide history (to take account of spallation) were known. Further, it was found that oxide stresses measured by Raman spectroscopy did not vary when the strain in the substrate was below a threshold level. It would therefore be very difficult to use the measurement of stresses in oxides grown on an austenitic steel using Raman spectroscopy as an indication of the strains in the substrate.

10.4 Stresses within Surface Oxide Grown on Ferritic Steel

10.4.1 Introduction

The previously described experiment in Section 10.3 established the behaviour of an oxide grown on an austenitic strainless steel. However, as many components in an electrical power plant are manufactured from ferritic steels [Viswanathan 1989], it was decided to investigate the behaviour of an oxide grown on a ferritic steel using Raman spectroscopy. This was done with a view to assessing the residual stresses in the oxide, the level of stress/strain accommodation in the oxide and to what extent the strains in the substrate could be evaluated.

10.4.2 Stress Measurements

A ferritic steel sample, iron 3% silicon steel, was oxidised for 2 minutes. Raman shifts from the "as grown" oxide, haematite, were measured with as increasing levels of strain were applied to the substrate, Figure 6.2. As with the Type 316 austenitic

stainless steel specimens described in Chapter 5 - Stresses within Surface Oxides Grown on Austenitic Steel, the stresses in the "as grown" oxide on the iron 3% silicon steel specimen were also found to be compressive. However, unlike the oxide grown on the Type 316 stainless steel, the relationship between Raman shift and applied strain was found to be non-linear. This could be due to differences in the distribution of of cracking, interfacial and transcracking, between the haematite and substrate to the relationship described in Section 2.4.3 and Section 10.3. In this work, the relationship between hydrostatic stress and Raman shift was calculated by deriving an approximate linear relationship between Raman shift and applied strain in the work by Shim and Duffy for 0GPa to 10GPa. If Raman shifts of haematite were to be used to calculate hydrostatic stresses in haematite to a higher degree of accuracy, it might be necessary to fit the relationship between Raman shift and hydrostatic pressure by using a more complex equation such as a polynomial equation.

10.4.3 Summary

Raman peak shifts were observed in the grown oxide with applied strain to the substrate. However, unlike the peak shifts obtained from the oxide grown on the austenitic steel as described in Section 5.2, the relationship of Raman shift and strain applied to the substrate was not linear.

10.4.4 Implications for Structural Health Monitoring

Although it is possible to relate the Raman shifts and their corresponding stresses from the oxide grown on the ferritic steel to the strains applied to the substrate, the relationship is non-linear. It would, therefore, be very complicated to use the Raman shifts obtained from the oxides and their corresponding stresses as a measure of strains in components.

10.5 Ferritic Steel Edge Quenched Plate

10.5.1 Introduction

The macrostresses across an edge quenched plate with a well characterised stress profile were measured. The measurements were acquired using X-ray and neutron diffraction in order to obtain and compare surface and through-section stress values. The X-ray diffraction measurements were made across the "as oxidised" surface as

well as an electropolished surface. These measurements were also compared to finite element model predictions. In addition, stresses across the surface oxide were measured using Raman spectroscopy. These measurements were undertaken in order to investigate two themes of importance to structural integrity assessment, the level of surface preparation required for X-ray diffraction and the correlation of the techniques to finite element models whilst considering the effects of the techniques having different spatial resolutions. As discussed in Section 2.5.2, the correlation of the measurements using surface and through-section techniques has implications for a proposed weld repair strategy [McDonald et al. 2005]. If surface and through-section techniques can be correlated, only non-destructive surface measurements using X-ray diffraction need be made on plant to underwrite the repair weld integrity. The novel approach to X-ray diffraction stress measurements with the surface oxide remaining also has important implications for structural integrity assessment. The lack of any surface preparation means that the technique is completely non-invasive and as a consequence can be used on plant more readily. The role of the surface oxide was examined with respect to its influence on the X-ray diffraction measurements and whether information on the stress profile of the plate could be obtained using Raman spectroscopy. The X-ray diffraction measurements were also used to obtain information on the microstresses across the plate using the full width half maxima of the X-ray peaks.

10.5.2 Theoretical calculations

The maximum change in distance (height) of the sample with respect to the goniometer arising from the presence of a surface oxide results in a change in Bragg angle of under 0.005° for an oxide thickness of 15μm, Figure 7.7. Since the degree of accuracy to which the Bragg angle can be measured is 0.01° equivalent to approximately 10MPa, the effect of the change in distance can be considered as negligible as it corresponds to a stress error of under 5MPa in ferritic steel.

Theoretical calculations have predicted the depth into an α-iron substrate with a surface layer of haematite of varying thicknesses, arising from X-ray absorption in the oxide. These penetration depth calculations also took into account the range of ψ-angles typically used to obtain stress measurement, Figure 7.6. The penetration depth of the X-rays into the substrate has been quantified and found to decrease as both

oxide thickness and ψ-angle increase. The calculated penetration depth change caused by a surface oxide on the measured stress in a typical machined surface emphasises the importance of understanding this contribution to the stresses measured. A thicker oxide layer resulted in a greater predicted measured compressive stress due to the decreased measurement depth into the iron substrate. Therefore it is necessary to quantify the oxide thickness through which measurements are being taken in order to understand the depth over which the information is being accumulated.

10.5.3 Comparison of Macrostress Measurements with Finite Element Model

There is a good agreement between the surface (X-ray diffraction) and through-section (neutron diffraction) measurements with the finite element predictions. Although there is some difference between the magnitude of the measurements made and the stress predictions, these can be accounted for by uncertainties in the input parameters of the finite element model such as the heat transfer coefficient employed when modelling quenching or changes in local yield stresses as demonstrated by the hardness measurements, Figure 7.11.

10.5.4 Full Width Half Maxima

X-ray diffraction peak widths can provide a measure of microstresses present in a material, as the peak widths are dependent on the causes of microstress such as dislocation density and precipitates [Benning 1989, Cullity and Stock 2001, Klug and Alexander 1974]. As there has been no phase transformation, it can be assumed that the full width half maxima recorded in these measurements have been affected by dislocation density. The full width half maxima across the width of the plate at a ψ-angle of 3° show a decrease in magnitude across the width of the plate for the "as oxidised" and electropolished surfaces in the longitudinal and transverse directions, Figure 7.19. In particular, there is a sudden decrease at 15mm to 20mm along the width of the plate. The one exception is in the case of the full width half maxima along electropolished surface in the longitudinal direction, whereby the full with half maxima decrease monotonically along the width of the plate; there is no sudden decrease in the proximity of the quenched region. This indicates that the microstresses are greatest in the quenched region than in the unquenched region of the

plate. The fact that the full width half maxima are greater across the plate on the as-received surface than the electropolished surface indicates that the microstresses are greater in the surface of the "as oxidised" material. There is also more fluctuation in the peak width across the plate along the as-received surface than the electropolished surface. This could be due to machining stresses along with surface roughness effects [Cullity and Stock 2001, Doig and Flewitt 1981].

The variation of peak width with ψ-angle at positions of 5mm and 45mm across the plate indicate magnitude of microstresses with measurement depth, Figure 7.20, Figure 7.21, Figure 7.22 and Figure 7.23. These measurements have been carried out on the "as oxidised" surface as well as on the electropolished surface, both in the longitudinal and transverse directions. As with the previously described measurements, the microstresses are greater on the "as oxidised" surface than the electropolished surface. The measurements made on the electropolished surface at 5mm across the width of the plate show a gradual increase with ψ-angle, indicating an increase in the magnitude of the microstresses towards the electropolished surface of the plate. However, there is much more fluctuation of these measurements with ψ-angle on the "as oxidised" surface at a position 5mm across the width of the plate, indicating a greater fluctuation of microstresses. Nontheless, in general the peak widths increase gradually with ψ-angle up to an angle of 35° after which they increase more rapidly. This could arise from two of contributions. First, surface roughness effects are more pronounced, the shallower the depth sampled. Second, the magnitude of the microstresses could have increased towards the surface of the plate due to an increase in dislocation density. At 45mm across the plate, the magnitudes of the peak widths measured are lower for the electropolished and "as oxidised" at 5mm across the plate respectively. This can be explained by the material being relatively stress free at 45mm as opposed to having been quenched at 5mm across the plate and therefore having lower dislocation densities. Lower microstresses would thus be expected at 45mm across the plate than at 5mm. The full width half maxima measured on the "as oxidised" surface are greater than those measured on the electropolished surface. This can be explained by higher stresses at the sample surface caused by the plate not being completely stress relieved or by the effects of surface roughness on diffraction peaks.

10.5.5 Raman Spectroscopy

The Raman shifts of the analysed haematite peak produced on the ferritic steel plate correspond to compressive hydrostatic stresses of between approximately –3GPa and –2GPa across the quenched edge of the plate. The Raman shifts are reduced in the unquenched area with the Raman shifts corresponding to compressive hydrostatic stresses of between –2.5GPa and –1.5GPa. These measurements are consistent with the surface residual stress measurements taken by X-ray diffraction, which show the stresses in the quenched region of the plate, are more compressive than in the remainder of the plate. The correlation between oxide and substrate stress could result from two factors. First, the stresses in the oxide could be affected by stress changes in the substrate as discussed in Section 2.5.4, Chapter 5 - Stresses within Surface Oxides Grown on Austenitic Steel and Chapter 6 - Stresses within Surface Oxide Grown on Ferritic Steel. Second, the stresses in the oxide could be due to the quenching of the oxide rather than the quenching of the substrate [Chen et al. 2003]. It can be seen that the magnitude of the compressive hydrostatic stresses does not decrease immediately in the quenched region of the plate but instead decreases at just over 20mm along the width. This can be explained by any splashing or bubbling of the water, which would have occurred during the quenching process. The outlier discussed in Section 7.5 and the scatter in the data emphasises the need for a sufficient number of data points in order to have sufficient confidence in measurements.

10.5.6 Summary

Predictions of X-ray diffraction depth into a substrate with a covering surface oxide have shown that the analysed depth decreases as the oxide thickness increases. This needs to be taken into account when carrying out stress measurements through an oxide layer. There is therefore a need to know the thickness of surface oxides when making through-oxide X-ray stress measurements.

There is a good correlation between the measured macrostresses across the plate by neutron and X-ray diffraction with the finite element model predicted trend. Discrepancies between measured and predicted values can be explained by uncertainties of finite element input parameters such as the heat transfer coefficient as well as the sampled volumes in the measurement techniques and the stress accommodated in the predicted model.

Peak widths indicate that the magnitude of the microstresses is greatest along the quenched edge. The microstresses also increase towards the surface of the "as oxidised" plate.

The Raman shifts measured in the analysed haematite peak indicate a change in oxide stress with position across the plate. The magnitude of the stresses measured in the quenched area was greater than those in the remainder of the plate. This corresponds to surface stresses measured by X-ray diffraction and indicates that stresses in the oxide can be correlated to stresses in the substrate.

10.5.7 Implications for Structural Health Monitoring

X-ray diffraction stress measurements can reliably be made through oxide covering a specimen or component. This is practical for in-situ stress measurement, as the surface oxide need not be removed and no surface preparation needs to be undertaken.

Since the surface and through-section stress measurements correlate well to the finite element predictions, it thereby provides confidence that the repair weld strategy described in Section 2.5.2 and by McDonald et al. [McDonald et al. 2005] can be used for measurements on engineering components.

The trend in the magnitude of microstresses across the plate, as indicated by the full width half maxima of the X-ray peaks, correlates with macrostress measurements. This shows that the stresses vary within the grains across the plate as well as between them. The magnitudes of the microstresses were also found to increase towards the surface of the plate. These measurements of the microstresses therefore allow a fuller understanding of component surface stresses. The measurement of the peak width with ψ-angle could also be used to indicate the variation of machining stresses with depth into a component. Although increases in peak widths could also be caused by surface roughness effects, the fact that they are greater in the quenched region than in the unquenched region indicates that surface roughness is not the sole cause of peak broadening.

Raman peak shifts across the plate oxide correlate to the stress distribution across plate. This implies that it is possible to relate stresses in oxide to substrate stresses in

an engineering component. Although Raman spectroscopy could be practical for in-situ measurements, it would be difficult to obtain suitable accuracy in the measurements due to scatter. Issues raised in Section 10.3.4 such as the dependence of Raman shifts on oxide thickness, spallation and complications in relating the measured oxide stress to strain in the substrate make it impractical as a tool for measuring the substrate strain. Further, since the stresses in the oxide could result from environmental influences, in this case the quenching of the oxide, as well as the behaviour of the substrate, oxide stress would in this case be an unreliable method of monitoring the stresses in the substrate.

10.6 Spatial Resolution and Length Scale Investigations of Techniques on a Ferritic Steel Butt Welded Pipe

10.6.1 Introduction

Surface stress measurements, using X-ray diffraction, as well as through-surface measurements, using incremental hole drilling and deep hole drilling, were made across the weld of a ferritic steel butt welded pipe, Figure 8.4. The spacial resolution of the techniques was investigated with a particular emphasis on the effect on the mapping of component macrostresses. The effect of surface preparation on X-ray diffraction measurements was assessed experimentally. It has been calculated that surface roughness can lead to errors in X-ray diffraction stress measurements due to differential absorption and surface orientation effects, Section 4.2.3. Further, surface oxides have been shown to reduce X-ray penetration depths. As welds can have very uneven surface profiles and can have surface oxides, it was deemed necessary to investigate whether it would be feasible to carry out X-ray diffraction stress measurements across a welded component in the "as received"/"as oxidised" condition. Information on the microstresses across the weld was also obtained from the full width half maxima of the diffraction peaks.

10.6.2 X-Ray Diffraction

The X-ray diffraction measurements prior to the heat treatment revealed compressive stresses on the "as oxidised" surface and tensile stresses on the electropolished surface in the weld metal. There was generally a good agreement between the values of the macrostresses measured on the two surface positions across the parent pipe, Figure

8.7. The correlation of the stresses measured on the two surfaces in the heat affected zones was variable. There was a good correlation between the measurements made along the 40° and 140° axes, Figure 8.8. This is therefore an indication that the welding procedure did not cause bending stresses in the parent pipe or the weld metal.

10.6.3 X-Ray Diffraction Full Width Half Maxima

The full width half maxima, peak width, across the weld and parent pipe revealed that the width magnitudes and therefore microstresses were greater in the weld than the pipe. Comparisons of the peak widths on the "as oxidised" surface and the electropolished surface showed that the microstresses were greater on the "as oxidised" surface than the electropolished surface. This corresponds to the finite element models of the weld, which show that the magnitude of the residual stresses decrease through the depth of the weld cap, Figure 8.16 and Figure 8.17. However, the broader diffraction peaks on the "as oxidised" surface could also be due to the irregularity of the surface, as calculations have shown that irregular surfaces induce peak broadening, Section 4.2.3. There was also more fluctuation in these values across the "as oxidised" weld metal surface than across the electropolished weld surface. This implies that there is greater variability in the values of the microstresses in the "as oxidised" weld surface than once the surface has been electropolished. This could be due to increased stress variability across the surface of the weld beads induced during the cooling of the uneven surface [Sosa et al. 2007], due to the the uneven surface causing increased variability of diffraction peak width or a combination of these effects. However, the reduced difference in peak width between that obtained for the weld and parent pipe after heat treatment means that surface roughness could not have been the sole contributing factor.

10.6.4 Post Heat Treatment

The X-ray diffraction macrostress measurements across the weld show that the stresses were reduced in magnitude and fluctuated across the weld and pipe between values of −100MPa and 100MPa, with the majority of values between −30MPa and 30MPa. The peak full width half maxima were also reduced in magnitude. However, widths across the welded region remained greater than across the parent pipe. This shows that although the macrostresses were so greatly reduced in the weld and the parent pipe, so as not to have a noticeable trend, this was not the case for the

microstresses. The magnitude of the microstresses was greatly reduced but was still significant enough to result in a distinctive difference across the weld and pipe. These microstresses could be due to a cumulative effect of strain fields from precipitates and dislocations remaining after the post weld heat treatment as well as a surface roughness effect, Section 2.2.6. The reduction of the full width half maxima on the weld metal after heat treatment suggests that the greater peak widths across the weld metal did not result from surface roughness alone.

10.6.5 Comparison of Experimental Measurements with Finite Element Modelling

Finite element models including solid state martensitic phase transformation predicted compressive stresses in areas along the width of the weld surface. These measurements show compressive stresses along the width of the weld surface, as do the X-ray diffraction stress measurements. This is in contrast with finite element models that exclude solid state phase transformations, which predict largely tensile stresses across the weld surface [Yaghi et al. 2007]. The measurements on the electropolished surface revealed tensile stresses and correspond well to the predictions that there are tensile stresses below the surface.

The deep hole drilling measurements showed compressive stresses at the start of the measurements, i.e. towards the surface of the weld and the pipe. This corresponds well to the X-ray diffraction measurements taken on the "as oxidised" surface. However, the deep hole drilling measurements did not correspond well to the measurements made on the electropolished surface and the incremental hole drilling measurements only corresponded on one occasion to the measurements made by X-ray diffraction. In general, there is no obvious correlation between the stress measurements at the different length scales. This is due to the measurements having different spatial resolutions and being made over varying length scales. The areas over which the measurements are acquired, and therefore averaged, are different. The depths over which the measurements are made vary according to technique from approximately 10μm for X-ray diffraction to approximately 60mm for deep hole drilling. Further, the methods by which the stresses are averaged over these depths also vary. Nontheless, they can all be correlated to the finite element models. This is because the finite element model provided a comprehensive map of the stresses

throughout the weldment and could therefore be compared and related to each technique. For example, the model showed the stress variation across the weld beads, as had been measured by the X-ray diffraction (with an aperture size of 1mm) but which the deep hole drilling was not able to demonstrate. The modelled through section stresses could be compared at the depths of the experimental measurements and differences in through-section resolutions could be shown to average out relative to each other. Although there is good correlation between the stress measurements and finite element predictions, there are some discrepancies. This could be due to the finite element input parameters. The temperatures required for solid state transformation are composition dependent [Callister 2000]. There may therefore be disparities between the temperatures modelled and those of the weld and as a consequence, errors in the predicted stresses. Further, the model took no account of the bead shape, which again could have been a source of error.

10.6.6 Summary

The X-ray diffraction stress measurements did not show any indication of bending stresses across the pipe. Compressive stresses were measured along the "as oxidised" surface of the weld metal. These were confirmed by deep hole drilling stress measurements and the finite element models carried out by Yaghi et al. [Yaghi et al. 2007]. The compressive stresses were attributed the solid state austenitic-martensitic phase transformation. Stresses at weld surfaces are often reported to be tensile [Leggatt 2008, McDonald et al. 2005, (a)Withers and Bhadeshia 2001]. However, in some cases, this could be due to surface measurements using X-ray diffraction often involving prior weld preparation [McDonald et al. 2002, McDonald et al. 2005] and as a consequence, removal of material from the surface to depths of the order of millimetres. As surface compressive stresses are often beneficial to the structural integrity of components [(a)Withers and Bhadeshia 2001], the surface compressive stresses measured in this study demonstrate the importance of the capping run on the structural integrity of weldments.

There was good correlation between the experimentally derived stress measurements with the finite element model. This indicates that the proposed repair weld strategy by McDonald et al. [McDonald et al. 2005] can successfully be used on a welded pipe.

Post weld heat treatment was found to relieve the macrostresses in the pipe to within the accuracy of the stress measurement methods. However, analysis of the X-ray diffraction peak widths shows the existence of microstresses across the weld metal.

10.6.7 Implications for Structural Health Monitoring

The experimental stress measurement methods have been correlated to finite element models of the weld produced by the University of Nottingham [Yaghi et al. 2007], thereby confirming that the weld repair strategy proposed by McDonald et al. [McDonald et al. 2005] can be used on a welded pipe. Although there was no obvious correlation between the experimentally derived stresses, this is not essential in order to employ the weld repair strategy. The fundamentally important factor is the ability to relate the experimental measurements to the finite element model. The X-ray diffraction through oxide stress measurements produced sufficiently accurate data for the technique to be used on plant without surface preparation. The X-ray diffraction stress measurements also showed compressive stresses in the weld capping run, which is beneficial for the weld's structural integrity [(b)Withers and Bhadeshia 2001].

Analysis of the macrostresses after post weld heat treatment indicated that the macroresidual stresses had been reduced significantly. However, X-ray peak widths showed that there were still greater magnitudes of microstresses in the weld metal than in the parent pipe and therefore that the weld metal had not completely stress relieved.

10.7 Platinum Aluminide Coated Superalloy

10.7.1 Introduction

Superalloy cotton reel samples were coated with two platinum aluminide bond-coats, RT22 and CN91. The stresses in the thermally grown oxides were measured using photoluminescence spectroscopy. The structure of the thermally grown oxides was observed using scanning transmission electron microscopy (STEM) and high angle annular dark field scanning transmission electron microscopy (HAADF). Energy dispersive X-ray maps were created of the sample surface cross-sections and Raman spectroscopy was employed to further investigate the composition of the oxide.

10.7.2 Analysis

Background peak removal improved the background to noise ratios of the alumina photoluminescence peaks. This enabled lower laser powers and acquisition times, than would have otherwise been necessary, to be used whilst maintaining confidence in the accuracy of the fitted peaks, Section 4.3.9.

The stresses in the thermally grown oxides of the RT22 coated samples with oxidation temperature and time are shown in Figure 9.5. The stress behaviour in the oxides can be explained by the the thickness of the oxide increasing [(c) Mougin et al. 2001] and developing more compressive stresses with oxidation temperature until a critical value of oxide thickness and compressive stress is reached with an oxidation temperature of 950°C. After this oxidation temperature, cracking occurs at the interface of the oxide and bond-coat/substrate interface due to the stress mismatch and the oxide starts to stress relieve until it has almost completely stress relieved at an oxidation temperature of 1050°C. Figure 9.14 shows that substrate debonding has occurred at an oxide temperature of 1050°C after an oxidation time of 1000 hours. The increase in stress distribution between oxidation temperatures of 850°C and 950°C can be explained by the onset of cracking in the oxide; some areas of the oxide begin to stress relieve whilst other areas remain firmly bonded to the substrate and hence remain at a higher stress magnitude [Bressers et al. 2000, Evans and Lobb 1984]. However, as larger areas of the oxide layer begin to stress relieve, after an oxidation temperature of 950°C, the distribution of the stresses decreases. Overall, the stress magnitudes in the oxides decrease with an increasing oxidation time. This could be caused by cracking at the oxide surface crests due to increased oxide thickness as described by Mougin et al. [(c) Mougin et al. 2001], microcracking [Nagl et al. 1994] or due to local debonding at the oxide/substrate interface [Bressers et al. 2000, Evans and Lobb 1984]. Although the stresses in the oxides oxidised at 1050°C have almost completely stress relieved, the average stresses and distributions show stresses varying between 0GPa and 0.5GPa. These tensile stresses can be explained by the surface of the oxides having developed tensile stresses due to buckling [Evans 1989], which have not completely relieved with the debonding at the substrate oxide interface.

The microstructure and composition of the oxide grown on the RT22 coated samples was found to be complex consisting of a microstructure that varied with oxide depth

and oxidation temperature. As a result, no direct correlation could be found between any particular features of the microstructure or oxide composition and stress in this work. Raman spectra acquired from the RT22 coated samples revealed complex overlapping peaks consisting of α-Al_2O_3, TiO_2 (rutile), Figure 9.16. This correlates with EDX composition maps of the RT22 samples, Figure 9.10, Figure 9.13 and Figure 9.15. The Raman spectra contained two additional peaks that could not be assessed in this work. The complexity of the oxides, which include compounds other than α-Al_2O_3, indicates that assessing the stresses in α-Al_2O_3 may not be the most appropriate method of analysing the stresses in the thermally grown oxides formed on RT22 bond-coats, although the measurements indicate the onset of the substrate debonding.

The average stresses in the CN91 coated samples were found to remain between approximately –1GPa and –1.5GPa for oxidation temperatures of 850°C to 1000°C. The magnitudes of the stresses decreased to between 0GPa and 0.5GPa at an oxidation time of 1050°C. This could be due to a non-linear oxide growth with oxidation temperature as found in chromia scales by Mougin et al. [Mougin et al. 2002], a non-linear relationship between stress and oxide thickness [Ambrico et al. 2001] or a combination of these. Raman spectra acquired from the CN91 coated sample revealed solely α-Al_2O_3, Figure 9.22. This corresponds to the EDX composition maps, which revealed that the thermally grown oxide predominantly consisted of alumina, Figure 9.21. However, the Raman spectra did not reveal chromia, as shown in the EDX composition maps. The predominance of α-Al_2O_3 in the oxide shows that the measurement of stress in α-Al_2O_3 using the photoluminescence spectroscopic technique is a more appropriate method of measuring stress in the thermally grown oxides formed on CN91 bond-coats to those grown on RT22 bond-coats.

Differences were found in the stress measurements in the thermally grown oxides, which had been oxidised at the lower temperatures, with two laser wavelengths (633nm and 514nm). This could be due to the different penetration depths of the lasers. These different stress values at different penetration depths in the samples indicate multiple stress states in the samples. Stress measurements across a cross-section of an RT22 sample also revealed a varying stress distribution throughout the

oxide. Since laser penetration depths depend on microstructure and material composition [West 1997], it was not possible in this work to calculate the laser penetration depths into the oxides due to the complex microstructure and compositions of the oxides, which have been shown to vary with oxidation temperature. However, correlating the cross-section stress measurements with the through-section measurements indicates that the laser of wavelength 514nm has a greater penetration depth in the thermally grown oxide of the RT22 coated sample oxidised for 4000 hours at 950°C than that of wavelength 633nm.

Multi-mode stress states have been found in thermally grown oxides by other researchers [Peng and Clarke 2000, Selcuk and Atkinson 2003, Selcuk and Atkinson 2002, (b)Sohn et al 2001], who observed that some peak profiles could not be fitted with a single R_1 and R_2 lines but had to be fitted with two or more. As a consequence, it was concluded that the number of stress states corresponded to the number of peaks required to fit each R_1 or R_2 peak, Section 2.5.6. However, in this study the spectroscopic peak profiles did not indicate a multi-mode stress state, as the R_1 and R_2 peaks could be fitted by single profile per peak. This demonstrates that multi-modal stress states cannot necessarily be seen in the peak profile and as a consequence the peak profile is not a reliable method of assessing the stress state modes in thermally grown oxides.

In addition to α-Al_2O_3, θ-Al_2O_3 and a metastable phase were observed in the photoluminescence spectra, Figure 9.18. The ratio of the phases observed was dependent upon the laser wavelength employed. This indicates that the ratio of these phases varies with depth in the thermally grown oxide.

10.7.3 Summary

There were systematic trends of oxide stress with oxidation time and temperature in the RT22 coated samples. A possible explanation was given for the variation of oxide stress with oxidation temperature in the CN91 coated sample. The measurement of stresses in α-Al_2O_3 using the photoluminescence spectroscopic technique is more appropriate to the thermally grown oxides formed on CN91 bond-coats to RT22 bond-coats. The method of analysing stresses in thermally grown oxides using photoluminescence spectroscopy was reviewed. There was good correlation between

Raman spectra obtained from the thermally grown oxides and energy dispersive X-ray analysis of the oxides.

10.7.4 Implications for Structural Health Monitoring

Background noise removal has been shown to improve the peak to noise ratios of the photoluminescence signals. As a consequence, lower laser powers and acquisition times can be used, thereby reducing any laser heating to the investigated material and improving the accuracy of the stress measurements.

The number of peaks required to fit R_1 and R_2 photoluminescence peaks is not an accurate measure of the stress distribution through thermally grown oxides.

The RT22 coated samples revealed systematic trends in stress with oxidation time and temperature. However, more investigations are required before stress can be used as a measure of quantifying residual life. The behaviour of the stresses in the thermally grown oxides formed on the CN91 coated samples was monitored. As with the thermally grown oxides formed on the RT22 coated samples, more investigations are required before stress can be used as a measure of quantifying residual life.

Raman spectroscopy could be used to investigate the compositions of thermally grown oxides in order to decide whether photoluminescence spectroscopy is an appropriate method of measuring stresses in the oxides. If Raman spectra reveal that the composition is predominantly α-Al_2O_3, the technique is appropriate. However, if the spectra revieal that the oxide has a more complex composition, consideration should be taken as to whether another technique may be more appropriate or should be used in conjunction with photoluminescence spectroscopy.

11 Conclusions

The objectives of the programme of work have been discussed in Chapter 1 – Introduction. The first objective, the exploration of calibration is discussed in Section 11.1. The second objective, the feasibility of using oxides as an "in-built" strain gauge, is discussed in Section 11.2. In addition, the key conclusions from X-ray diffraction through-oxide stress measurements are drawn. The third objective, the assessment of the correlation of surface X-ray stress measurements with through-section stress measurements, comparison these measurements to finite element models and the relation of the stress values to a proposed weld procedure is discussed in Section 11.3.1. Conclusions are also drawn on the importance of a weld cap and the effect of a post weld heat treatment. The fourth objective, the measurement of stresses in thermally grown oxides of superalloy bond-coats and the relation of these stress measurements to lifetime prediction is discussed in Section 11.3.2.

11.1 Techniques

- When undertaking stress measurements it is necessary to understand the sources of error in the experiment, monitor measurement conditions and to calibrate equipment so that systematic errors can be understood and avoided.
- When undertaking stress measurements using Raman or photoluminescence spectroscopy, it is necessary to understand the power of the laser and its effect on the sample material so as not to induce stresses via material heating.
- Investigations in this work revealed a laser current (laser power) threshold below which measurements could be made without inducing laser heating.
- The scatter in the photoluminescence spectroscopic stress measurements due to the inherent variability of the thermally grown oxides of the turbine blade bond-coats highlights the need for statistical confidence in oxide stress measurements.

11.2 Role of Oxide

- It is possible to carry out X-ray diffraction stress measurements on components with a surface oxide and surface roughness: an unprepared surface. X-ray diffraction measurements can therefore be taken in-situ without the need for surface preparation.

- Calculations showed that the maximum thickness of an oxide covering a substrate, through which X-ray diffraction stress measurements could be made on the substrate, were small enough for a height correction not to be necessary. However, the presence of the oxide would decrease the penetration depth of the X-rays into the substrate. If knowledge of the measurement depth into the substrate is required, it is necessary to know the thickness of the oxide. This is important if seeking to address stress profiles.
- It is recommended not to use stresses in surface oxides as an "in-built" strain gauge. Although it has been shown that stresses in surface oxides are affected by applied and residual stresses in the substrate, and can be measured with Raman spectroscopy, it has been found that stresses in oxides are also dependent on oxide thickness and oxide history such as spallation. Further, the stresses in oxides can be related to environmental factors as well as substrate behaviour. It would therefore be very complex and impractical to correlate stresses in oxides on engineering components with stresses within the components without being able to account for these contributions.

11.3 Stress Measurements

11.3.1 Edge Quenched Plate and P91 Pipe

- Measured surface and through-section stresses have been correlated to finite element predictions on a steel plate with a known stress profile (Chapter 7 - Ferritic Steel Edge Quenched Plate) and an engineering component, a pipe with a circumferential butt weld (Chapter 8 - Spatial Resolution and Length Scale Investigations of Techniques on a Ferritic Steel Butt Welded Pipe). This confirms the weld repair strategy proposed by McDonald et al. [McDonald et al. 2005]. In both the edge quenched plate and the P91 pipe, unprepared surface stresses compared well to prepared surface stresses.
- In order to employ the weld repair strategy, it is not necessary for measurements with different spatial resolutions and length scales to have an obvious correlation with each other, as they may be measuring different stresses. However, a finite element model provides a basis for assisting such correlations.

- Post weld heat treatment relieved the macrostresses across the weldment. However, full width half maxima of X-ray peaks indicated that microstresses were still present in the weld metal.
- Variation of X-ray full width half maxima with ψ-angle can be used to assess the variation of microstress with depth into the component by using ψ-angle as a measure of penetration depth and peak widths as a measure of microstress.

11.3.2 Platinum Aluminide Coated Superalloy

- The oxides grown on superalloy bond-coats revealed systematic trends in stress with oxidation temperature and time and indeed a point at which the stresses became less compressive due most probably to the onset of cracking within the oxide. However, more investiagations need to be done before residual stress measurement can be used as a quantitative measure of residual life of turbine blades.
- When considering whether to use photoluminescence spectroscopy to measure stresses in thermally grown oxides on turbine blades, it is recommended to also record Raman spectra of the oxides. This would confirm that if the Raman spectra indicate that the oxides consist of α-alumina, the photoluminescence spectroscopic α-alumina stress measurements would be representative of the stresses in the oxides. However, if the Raman spectra indicate that the oxides have a more complex composition, photoluminescence spectroscopic α-alumina stress measurements may not be representative of the stresses in the oxides and therefore another stress measurement technique may be more suitable.
- The thermally grown oxides formed on CN91 coated samples were found to be more applicable to the photoluminescence spectroscopic technique than those formed on RT22 coated samples.

12 Future Work

The following suggestions for future work have arisen from the investigations undertaken in this thesis:

- The weld repair strategy proposed by McDonald et al. [McDonald et al. 2005] should be investigated for different engineering components over service life. If measured and predicted surface and through-section stresses in components are correlated for in-service conditions, regular measurements of surface stresses could be used as an indication of the through-section stresses in the engineering components.
- Instead of using stresses in oxides to indicate the stresses in substrates, other coatings could be investigated as a method of measuring the change in component surface stresses and strains using Raman spectroscopy. By using coating materials that are more resilient to oxidation or spallation, changes in coating stresses can be attributed to changes in substrate strain. These coatings could be placed on areas of components that are known to be prone to failure such as the on the heat affected zones of welds and regions of complex geometry.
- Further investigations should be carried out to correlate stresses in thermally grown oxides of bond-coats and remnant life.
- The photoluminescence stress measurements of the thermally grown oxides investigated should be repeated with the presence of a thermal barrier coating to investigate the effect of thermal barrier coatings on thermally grown oxide stresses.
- Although it was found that thermally grown oxides formed on RT22 coated oxides contained a mix of compounds, α-Al_2O_3 could still provide a measure of the oxide stresses depending on how closely linked the stresses in the α-Al_2O_3 are to the other oxide components. However, the stresses in the oxidised components would first have to be monitored simultaneously for this to be confirmed. Alternative techniques could be invoked such as X-ray diffraction.
- Other non-destructive techniques should be investigated as an alternative to photoluminescence spectroscopy to determine thermally grown oxide remnant

life. For example, thermography is one possible method of investigating the defects in turbine blade coatings [Busso et al. 2007]. Another possible method of flaw detection is eddy current sensors and inspection [Goldfine et al. 2002].

13 References

Akhurst, K.A., Materials facts: One side of the structural integrity equation. CEGB Research – Structural Integrity. Central Electricity Generating Board 1988. pp. 5-14.

Allen, G.C. and McMeeking, Deconvolution of spectra by least squares fitting. Analytica Chimica Acta, 1978. Vol. 2(1): pp. 73-108.

Ambrico, J.M., M.R. Begley and E.H. Jordan, Stress and shape evolution of irregularities in oxide films on elastic-plastic substrates due to thermal cycling and film growth. Acta Materialia, 2001. Vol. 49(9): pp. 1577-1588.

Ananthakrishna, G., Current theoretical approaches to collective behavior of dislocations. Physics Reports-Review Section of Physics Letters, 2007. Vol. 440(4-6): pp. 113-259.

Angenete, J. and K. Stiller, Comparison of inward and outward grown Pt modified aluminide diffusion coatings on a Ni based single crystal superalloy. Surface & Coatings Technology, 2002. Vol. 150(2-3): pp. 107-118.

(a)Angenete, J., K. Stiller and V. Langer, Oxidation of simple and Pt-modified aluminide diffusion coatings on Ni-base superalloys I. Oxide scale microstructure. Oxidation of Metals, 2003. Vol. 60(1-2): pp. 47-82.

(b)Angenete, J. and K. Stiller, Oxidation of simple and Pt-modified aluminide diffusion coatings on Ni-base superalloys II. Oxide scale failure. Oxidation of Metals, 2003. Vol. 60(1-2): pp. 83-101.

Arndt, U.W., X-ray position sensitive detectors. Journal of Applied Crystallography, 1986. Vol. 19: pp. 145-163.

Ashby, M., H. Shercliff and D. Cebon, Materials: Engineering, science, processing and design. 2007, Elsevier Butterworth-Heinemann.

Ashby, M.F. and D.R.H. Jones, Engineering materials 1: An introduction to their properties and applications. Second Edition 1996, Butterworth-Heinemann.

Ashby, M.F. and D.R.H. Jones, Engineering materials 2: An introduction to microstructures, processing and design. Second Edition. 1998, Butterworth-Heinemann.

Ashby, M.F. and B. Tomkins. Micromechanisms of fracture and elevated fracture mechanics. Third International Conference on Mechanical Behaviour of Materials 1979, Pergamon Press, pp. 47-93.

Atkinson, A., D.R. Clarke and S.J. Webb, Mapping residual stress using optical microprobe in alumina films formed by thermal oxidation of NiAl. Materials Science and Technology, 1998. Vol. 14(6): pp. 531-534.

Atkinson, A. and A. Selcuk, Piezo-spectroscopy studies of stress and damage evolution in the thermally grown oxide in TBCs. High Temperature Corrosion and Protection of Materials, 2004. Vol. 6(461-464): pp. 655-661.

Atkinson, A., A. Selcuk and S.J. Webb, Variability of stress in alumina corrosion layers formed in thermal-barrier coatings. Oxidation of Metals, 2000. Vol. 54(5-6): pp. 371-384.

Banahan, B.D., Application of secondary and residual stresses to the assessment of the structural integrity of nuclear power-generating plant. International Journal of Pressure Vessels and Piping, 2008. Vol. 85(3): pp. 191-197.

Baruya, A. and W.F. Maddams, Examination of uniqueness of Gaussian and Lorentzian profiles. Applied Spectroscopy, 1978. Vol. 32(6): pp. 553-566.

Bell, S.E.J., E.S.O. Bourguignon and A. Dennis, Analysis of luminescent samples using subtracted shifted Raman spectroscopy. Analyst, 1998. Vol. 123(8): pp. 1729-1734.
Benham, P.P., R.J. Crawford and C.G. Armstrong, Mechanics of engineering materials. Second Edition. 1996, Harlow Longman.
Benner, R.E. and A.S. Nagelberg, Characterization of ZrO_2 - Y_2O_3 thermal barrier coatings by Raman spectroscopy. Thin Solid Films, 1981. Vol. 84: pp. 89-94.
Benning, O., Non-destructive determination of load and residual stresses by the X-ray stress method. The Rigaku Journal, 1989. Vol. 6(2): pp. 15-21.
Bhadeshia, H.K.D.H., Possible effects of stress on steel weld microstructures. Mathematical Modelling of Weld Phenomena, 1995, Institute of Materials, pp. 71-118.
Bhadeshia, H.K.D.H., D.J.C. MacKay and L.E. Svensson, Impact toughness of C-Mn steel arc welds - Bayesian neural network analysis. Materials Science and Technology, 1995. Vol. 11(10): pp. 1046-1051.
Birnie, J., C. Craggs, D.J. Gardiner and P.R. Graves, Ex-situ and in-situ determination of stress distributions in chromium-oxide films by Raman microscopy. Corrosion Science, 1992. Vol. 33(1): pp. 1-12.
Boas, M., Mathematical methods in the physical sciences. Second Edition 1983, John Wiley and Sons.
Boresi, A.P., R.J. Schmidt and O.M. Sidebottom, Advanced mechanics of materials. Fifth Edition 1993, John Wiley and Sons.
Bouchard, P.J. and P.J. Withers, The appropriateness of residual stress length scales in structural integrity. Journal of Neutron Research, 2004. Vol. 12(1): pp. 81-91.
(a)Bourne, N.K., Impact on alumina I: Response at the mesoscale. Proceedings of the Royal Society A, 2006. Vol. 462(2074): pp. 3061-3080.
(b)Bourne, N.K., Impact on alumina II: Linking the mesoscale to the continuum. Proceedings of the Royal Society A, 2006. Vol. 462(2075): pp. 3213-3231.
Bradley, M., Curve fitting in Raman and IR spectroscopy: Basic theory and applications. 2004, Thermo Electron Corporation: Madison, USA.
Brakman, C.M., On the interpretation of diffraction line-shift measurements on textured cubic materials. 1988, Technical University of Delft.
Bressers, J., S. Peteves and M. Steen, Coatings for hot secton gas turbine applications. Fracture Mechanics: Applications and Challenges, 2000. Vol. 26: pp. 115-134.
Brickstad, B. and B.L. Josefson, A parametric study of residual stresses in multi-pass butt-welded stainless steel pipes. International Journal of Pressure Vessels and Piping, 1998. Vol. 75(1): pp. 11-25.
Budden, P.J., Structural integrity of power plant components: The R5 and R6 procedures. Life Management of Power Plants, 1994: pp. 128-136.
Busso, E.P., L. Wright, H.E. Evans, L.N. McCartney, S.R.J. Saunders, S. Osgerby and J. Nunn, A physics-based life prediction methodology for thermal barrier coating systems. Acta Materialia, 2007. Vol. 55(5): pp. 1491-1503.
Callister, W.D.Jr., Materials science and engineering: An introduction. Fifth Edition 2000, John Wiley and Sons, Inc.
Çengel, Y.A. and M.A. Boles, Thermodynamics: An engineering approach. Third Edition 1998, McGraw-Hill.

Chen, K-S., X. Zhang and S-Y. Lin, Intrinsic stress generation and relaxation of plasma-enhanced chemical vapour deposited oxide during deposition and subsequent thermal cycling. Thin Solid Films, 2003. Vol. 434: pp. 190-202.
Chescoe, D. and P.J. Goodhew, The operation of transmission and scanning electron microscopes. 1990, Oxford University Press.
(a)Christensen, R.J., D.M. Lipkin, and D.R. Clarke, The stress and spalling behavior of the oxide scale formed on polycrystalline Ni_3Al. Acta Materialia, 1996. Vol. 44(9): pp. 3813-3821.
(b)Christensen, R.J., D.M. Lipkin, D.R. Clarke and K. Murphy, Nondestructive evaluation of the oxidation stresses through thermal barrier coatings using Cr^{3+} piezospectroscopy. Applied Physics Letters, 1996. 69(24): p. 3754-3756.
Coffey, J.M., Non-destructive testing - the technology of measuring defects, in CEGB Research - Structural Integrity. Central Electricity Generating Board, 1988. pp. 36-47.
Colombi Ciacchi, L., G. Gregori, V. Lughi, A. Rossi and V. Sergo, Piezo-spectroscopy: A materials science perspective. Recent Research and Development in Applied Spectroscopy, 1999. Vol. 2: pp. 243-272.
Cullity, B.D. and S.R. Stock, Elements of X-Ray Diffraction. Third Edition 2001, Prentice Hall.
Dassios, K.G. and C. Galiotis, Fluorescence studies of polycrystalline Al_2O_3 composite constituents: Piezo-spectroscopic calibration and applications. Applied Physics a-Materials Science and Processing, 2004. Vol. 79(3): pp. 647-659.
Day, J.C.C., Personal communication, University of Bristol, 2006. Program written in 2000.
Decker, R.F., The evolution of wrought age-hardenable superalloys. Journal of the Minerals, Metals and Materials Society, 2006. Vol. 58(9): pp. 32-36.
Delhez, R., T.H. Dekeijser, E.J. Mittemeijer, B.J. Thijsse, M.A. Hollanders, O.B. Loopstra and W.G. Sloof, Structure and properties of surface layers – X-ray diffraction studies. Australian Journal of Physics, 1988. Vol. 41(2): pp. 261-282.
Deng, D. and H. Murakawa, Prediction of welding residual stress in multi-pass butt-welded modified 9Cr-1Mo steel pipe considering phase transformation effects. Computational Materials Science, 2006. Vol. 37(3): pp. 209-219.
Denton, A.A., Determination of residual stresses. Metallurgical Reviews, 1966. Vol. 11: pp. 1-23.
De Wolf, I., Micro-Raman spectroscopy to study local mechanical stress in silicon integrated circuits. Semiconductor Science and Technology, 1996. Vol. 11(2): pp. 139-154.
Dieter, D.E.J., Mechanical Metallurgy. 1961: McGraw-Hill.
Di Rocco, H.O., D.I. Iriarte and J. Pomarico, General expression for the Voigt function that is of special interest for applied spectroscopy. Applied Spectroscopy, 2001. Vol. 55(7): pp. 822-826.
Doig, P. and P.E.J. Flewitt, Nondestructive stress measurement using X-ray diffraction methods. NDT International, 1978. Vol. 11(3): pp. 127-131.
Doig, P. and P.E.J. Flewitt, A theoretical consideration of the influence of surface profile on the measurement of stress using the X-ray diffraction method. Journal of Applied Crystallography, 1981. Vol. 14: pp. 321-325.
Doig, P., D. Lonsdale and P.E.J. Flewitt, An assessment of instrumental parameters which control the accuracy of stress measurement using the X-ray diffractometer method. Journal of Applied Crystallography, 1981. Vol. 14: pp. 124-130.

Dolby, R.E., R.H. Leggatt, I.C. Howard, D.J. Smith and A.H. Sherry, Some changes in the treatment of residual stress in flaw tolerance calculations – A TAGSI view. International Journal of Pressure Vessels and Piping, 2008. Vol. 85(3): pp. 166-174.
Dong, P. and J. Zhang, Residual stresses in strength-mismatched welds and implications on fracture behavior. Engineering Fracture Mechanics, 1999. Vol. 64(4): pp. 485-505.
Dong, P., J. Zhang and P.J. Bouchard, Effects of repair weld length on residual stress distribution. Journal of Pressure Vessel Technology-Transactions of the ASME, 2002. Vol. 124(1): pp. 74-80.
Doosan Babcock, personal communication, 2006.
Dugdale, D.S., Elements of elasticity. Commonwealth and International Library. Structures and Solid Body Mechanics Division. 1968, Pergamon Press.
Dunnwald, J. and A. Otto, An investigation of phase-transitions in rust layers using Raman-spectroscopy. Corrosion Science, 1989. Vol. 29(9): pp. 1167-1176.
Duong, P.H., H.K. Phan, N.T.T. Tam, D.X. Thanh, N.X. Nghia, and P. Lavallard, Influence of thermal and laser heating effects on the Raman spectra of luminescent yellow silicon fiber. Journal and Luminescence, 2000. Vol. 87-89: pp. 353-356.
El-Turki, A., G.C. Allen, C.M. Younes and J.C.C. Day, An investigation of the effect of thermal cycling on plasma-sprayed zirconia/NiCoCrAlY thermal barrier coating. Materials and Corrosion - Werkstoffe Und Korrosion, 2004. Vol. 55(1): pp. 24-29.
Evans, A.G., D.R. Mumm, J.W. Hutchinson, G.H. Meier and F.S. Pettit, Mechanisms controlling the durability of thermal barrier coatings. Progress in Materials Science, 2001. Vol. 46(5): pp. 505-553.
Evans, H.E., Cracking and spalling of protective oxide layers. Materials Science and Engineering A, 1989. Vol. 120: pp. 139-146.
Evans, H.E., Stress effects in high-temperature oxidation of metals. International Materials Reviews, 1995. Vol. 40(1): pp. 1-40.
Evans, H.E. and R.C. Lobb, Conditions for the initiation of oxide scale cracking and spallation. Corrosion Science, 1984. Vol. 24(3): pp. 209-222.
Fitzpatrick, M.E., A.T. Fry, P. Holdway, F.A. Kandil, J. Shackleton and L. Souminen, Determination of residual stresses by X-ray diffraction. Measurement Good Practice Guide. 2005, National Physical Laboratory.
Flewitt P.E.J. and R.K. Wild, Physical methods for materials characterisation. Second Edition. Series in Materials Science and Engineering. 2003, Institute of Physics.
Flinn, R.A. and P.K. Trojan, Engineering materials and their applications. Third Edition. 1986, Houghton Mifflin.
Forman, R.A., S. Block, J.D. Barnett and G.J. Piermari, Pressure measurements using ruby sharp-line luminescence. Bulletin of the American Physical Society, 1972. Vol. 17(3): pp. 351-357.
Francis, J.A., H.K.D.H. Bhadeshia and P.J. Withers, Welding residual stresses in ferritic power plant steels. Materials Science and Technology, 2007. Vol. 23(9): pp. 1009-1020.
Galerie, A., F. Toscan, M. Dupeux, J. Mougin, G. Lucazeau, C. Valot, A.M. Huntz and L. Antoni, Stress and adhesion of chromia-rich scales on ferritic stainless steels in relation with spallation. Materials Research, 2004. Vol. 7(1): pp. 81-88.
Garrod, R.I. and G.A. Hawkes, X-ray stress analysis on plastically deformed metals. British Journal of Applied Physics, 1963. Vol. 14(7): p. 422-427.

Gell, M., S. Sridharan, M. Wen and E.H. Jordan, Photoluminescence piezospectroscopy: A multi-purpose quality control and NDI technique for thermal barrier coatings. International Journal of Applied Ceramic Technology, 2004. Vol. 1(4): pp. 316-329.
George D. and D.J. Smith, Through-thickness measurement of residual stresses in a stainless steel cylinder containing shallow and deep weld repairs. International Journal of Pressure Vessels and Piping, 2005. Vol. 82: pp. 279-287.
Giannuzzi, L.A. and F.A. Stevie, A review of focused ion beam milling techniques for TEM specimen preparation. Micron, 1999. Vol. 30: pp. 197-204.
Goldfine, N., D. Schlicker, Y. Sheiretov, A. Washabaugh, V. Zilberstein and T. Lovett, Conformable eddy-current sensors and arrays for fleetwide gas turbine component quality assessment. Journal of Engineering for Gas Turbines and Power. Transactions of the ASME, 2002. Vol. 124(4): pp. 904-909.
Gooch, D.J., Plant-life extension - Remanent-life assessment of high temperature components. Power Engineering Journal, 1988: pp. 323-331.
Goudar, D.M., S. Hossain, C.E. Truman and D.J. Smith, Uncertainty in residual stress measurements. Proceedings of the ASME Pressure Vessels and Piping Division Conference, 2008. pp. 1-7.
Grabner, L., Spectroscopic technique for measurement of residual-stress in sintered Al_2O_3. Journal of Applied Physics, 1978. Vol. 49(2): pp. 580-583.
Grant, P.V., J.D. Lord and P.S. Whitehead, The measurement of residual stresses by the incremental hole drilling technique. Measurement Good Practice Guide. 2002, National Physical Laboratory.
Gurney, T.R., Residual stresses in a large circular disc caused by local heating and cooling at its centre. Journal of Strain Analysis 1971. Vol. 6(2): pp. 89-98.
Haigh, I.T., Lighter fuel - The gas-turbine comes of age. IEE Review, 1991. Vol. 37(3): pp. 97-102.
Hawkes, G.A., The measurement of surface residual stress by X-rays. British Journal of Applied Physics, 1957. Vol. 8(6): pp. 229-232.
He, J. and D.R. Clarke, Polarization dependence of the Cr^{3+} R-line fluorescence from sapphire and its application to crystal orientation and piezospectroscopic measurement. Journal of the American Ceramic Society, 1997. Vol. 80(1): pp. 69-78.
He, J. and D.R. Clarke, Determination of the piezospectroscopic coefficients for chromium-doped sapphire. Journal of the American Ceramic Society, 1995. Vol. 78(5): pp. 1347-1353.
He, M.Y., A.G. Evans and J.W. Hutchinson, The ratcheting of compressed thermally grown thin films on ductile substrates. Acta Materialia, 2000. Vol. 48(10): pp. 2593-2601.
Hill, M.R., A.T. De Wald, J.E. Rankin and M.J. Lee, Measurement of laser peening residual stresses. Materials Science and Technology, 2005. Vol. 21(1): pp. 3-9.
(a)Hilson, G., K.R. Hallam and P.E.J. Flewitt, The measurement of stresses within oxides produced on austenitic and ferritic steels using Raman spectroscopy. Materials Science Forum, 2006. Vol. 524-25: pp. 957-962.
(b)Hilson, G., C. Truman, D. Smith, and P. E. J. Flewitt, Through section measurements of residual stresses and their applications to repair welds. Presented at 8th International Conference on Engineering Structural Integrity Assessment, October 2006, Manchester.

Hilson, G., S. Simunjuntak, P.E.J. Flewitt, K.R. Hallam, M.J. Pavier and D.J. Smith, Spatial variation of residual stresses in a welded pipe for high temperature applications. Submitted to International Journal of Pressure Vessels and Piping, 2008.
Holden, T.M., H. Suzuki and D.G. Carr, Macroscopic stress measurements by neutron diffraction and the part played by the "stress-free" reference. Iron Steel Institute Japan, 2006. Vol. 46(7): pp. 959-965.
Holden, T.M., H. Suzuki, D.G. Carr, M.I. Ripley and B. Clausen, Stress measurements in welds: Problem areas. Materials Science and Engineering A, 2006. Vol. 437(1): pp. 33-37.
Hopkins, B. and F. Rogers, The elastic properties of steel at high temperatures. Proceedings of the Royal Society of London A, 1905. Vol. 76(514): pp. 419-425.
Hossain, S., C.E. Truman, D.J. Smith and P.J. Bouchard, Measurement of residual stresses in a Type 316H stainless steel offset repair in a pipe girth weld. Transactions of the ASME, 2006. Vol. 128: pp. 420-426.
Hsueh, C.H. and A.G. Evans, Oxidation induced stresses and some effects on the behavior of oxide-films. Journal of Applied Physics, 1983. Vol. 54(11): pp. 6672-6686.
Huntz, A.M., J.L. Lebrun and A. Boumaza, Relation between the residual-stresses and the high-temperature oxidation resistance of superalloys protected by plasma-sprayed coatings II. Oxidation of Metals, 1990. Vol. 33(3-4): pp. 321-355.
Hurst, R.C., M. Davies and P. Hancock, Determination of fracture strains of growing surface oxides on mild steel at high temperatures. Oxidation of Metals, 1975. Vol. 9(2): pp. 161-169.
James, M.N., D.J. Hughes, Z. Chen, H. Lombard, D.G. Hattingh, D. Asquith, J.R. Yates and P.J. Webster, Residual stresses and fatigue performance. Engineering Failure Analysis, 2007. Vol. 14(2): pp. 384-395.
James, M.R. and J.B. Cohen, Geometrical problems with a position sensitive detector employed on a diffractometer including its use in the measurement of stress. Journal of Applied Crystallography, 1979. Vol. 12: pp. 339-345.
Ji, S.D., H.Y. Fang, X.S. Liu, and Q.G. Meng, Influence of a welding sequence on the welding residual stress of a thick plate. Modelling and Simulation in Materials Science and Engineering, 2005. Vol. 13: pp. 553-565.
Johnston, C., M.A. Cooper, and R.J. Martin, An approach to power station boiler and turbine life management. Insight, 2004. Vol. 46(10): pp. 606-609.
Jones, C.P., Personal communication, University of Bristol 2008.
Jones, W.J., Molecular structure and properties from high resolution Raman spectra of gases. Philosophical Transactions of the Royal Society of London A, 1979. Vol. 293(1402): pp. 249-256.
Kadlecikova, M., J. Breza, M. Vesely and I. Cerven, A study of synthetic sapphire by photoluminescence and X-ray diffraction. Microelectronics Journal, 2003. Vol 34(2): Vol. pp. 95-97.
Kagawa, A., T. Okamoto and S. Goda, Young's moduli of iron-carbon-chromium alloy castings. Journal of Materials Science, 1987. Vol. 22: pp. 4165-4172.
Kassner, M.E. and T.A. Hayes, Creep cavitation in metals. International Journal of Plasticity, 2003. Vol. 19(10): pp. 1715-1748.
Kawasaki, M., T. Yoshioka and M. Shiojiri, A new specimen preparation method for cross-section TEM using diamond powders. Journal of Electron Microscopy, 1999. Vol. 48(2): pp. 131-137.
Khoi, P.H., N.T.T. Tam, P.H. Duong and N.X. Nghia, Investigation of vibrational and photoluminescence spectra of nanocrystaline silicon by micro-Raman

spectroscopy using various laser powers. Journal of Raman Spectroscopy, 1999. Vol. 30(5): pp. 385-389.
Kimball, A.L. Jr. and D.E. Lovell, Vibration measurements of Young's modulus with temperature from vibration measurements. Physical Review, 1925. Vol. 26: pp. 121-124.
Klug, H.P. and L.E. Alexander, X-ray diffraction procedures for polycrystalline and amorphous materials. 2nd Edition, 1974, Wiley-Interscience.
Klueh, R.L. and A.T. Nelson, Ferritic/martensitic steels for next-generation reactors. Journal of Nuclear Materials, 2007. Vol. 371: pp. 37-52.
Kouteva-Arguirova, S., T. Arguirov, D. Wolfframm and J. Reif, Influence of local heating on micro-Raman spectroscopy of silicon. Journal of Applied Physics, 2003. Vol. 94(8): pp. 4946-4949.
Kraus, I., N. Ganev, G. Gosmanova, H.D. Tietz, L. Pfeiffer and S. Bohm, Residual stresses in plasma-sprayed coatings Al_2O_3. Advanced Performance Materials, 1997. Vol. 4(1): pp. 63-69.
Kubel, C., A. Voigt, R. Schoenmakers, M. Otten, D. Su, T.C. Lee, A. Carlsson and J. Bradley, Recent advances in electron tomography: TEM and HAADF-STEM tomography for materials science and semiconductor applications. Microscopy and Microanalysis, 2005. Vol. 11(5): pp. 378-400.
Krishnan, R., S. Dash, R. Kesavamoorthy, C.B. Rao, A.K. Tyagi, B. Raj and M.M. Grp. Laser surface modification and characterization of air plasma sprayed alumina coatings. Surface and Coatings Technology, 2006. Vol. 200(8): pp. 2791-2799.
Lacaze, J., M. Lupker, N. Vialas and D. Monceau, Application of image analysis and image simulation for quantitative characterization of scale spallation during cyclic oxidation of a Pt-aluminide coating. Intermetallics, 2006. Vol. 14(4): pp. 423-434.
Layne, A.W., Next-generation turbine systems. IEEE Power Engineering Review, 2000: pp. 18-23.
Leggatt, R.H., Residual stresses in welded structures. International Journal of Pressure Vessels and Piping, 2008. Vol. 85(3) pp. 144-151.
Lehnert, G. and H. Meinhardt, A new protective coating for nickel alloys. Electrodeposition and Surface Treatment, Vol. 1972. 1: pp. 189-197.
Lipkin, D.M. and D.R. Clarke, Sample-probe interactions in spectroscopy - Sampling microscopic property gradients. Journal of Applied Physics, 1995. Vol. 77(5): pp. 1855-1863.
Lipkin, D.M., H. Schaffer, F. Adar and D.R. Clarke, Lateral growth kinetics of alpha-alumina accompanying the formation of a protective scale on (111)NiAl during oxidation at 1100°C. Applied Physics Letters, 1997. Vol. 70(19): pp. 2550-2552.
Liu, Y., C. Persson and S. Melin, Numerical Modeling of short crack behavior in a thermal barrier coating upon thermal shock loading. Journal of Thermal Spray Technology, 2004. Vol. 13(4): pp. 554-560.
Logan, D.L., A first course in the finite element method. Third Edition. 2002, Wadsworth Group.
Lonsdale, D., The accuracy of stress measurement using the X-ray diffraction method. Journal of Applied Crystallography, 1986. Vol. 19: pp. 300-307.
Lonsdale, D., P. Doig and P.E.J. Flewitt, The measurement of stress in engineering components using a transportable X-ray diffractometer. Central Electricity Generating Board, 1981.

Lonsdale, D. and P.E.J. Flewitt, Statistical considerations for accelerated test program design to optimize data extrapolation. Materials Science and Engineering, 1985. Vol. 69(2): pp. 15-20.
Luo, M.F., P. Fang, M. He and Y.L. Xie, Fluorescence spectroscopic study of the phase transformation of gamma-Al_2O_3 at high temperatures. Physica Status Solidi A, 2006. Vol. 203(8): pp. 2065-2072.
Luthra, K.L. and C.L. Briant, Mechanism of adhesion of alumina on MCrAlY alloys. Oxidation of Metals, 1986. Vol. 26(5-6): pp. 397-416.
Ma, Q. and D.R. Clarke, Stress measurement in single-crystal and polycrystalline ceramics using their optical fluorescence. Journal of the American Ceramic Society, 1993. Vol. 76(6): pp. 1433-1440.
Ma, Q. and D.R. Clarke, Piezospectroscopic determination of residual-stresses in polycrystalline alumina. Journal of the American Ceramic Society, 1994. Vol. 77(2): pp. 298-302.
Macherauch, E., X-ray stress analysis. Experimental Mechanics, 1966. Vol. 6(3): pp. 140-153.
Martena, M., D. Botto, P. Fino, S. Sabbadini, M.M. Gola and C. Badini, Modelling of TBC system failure: Stress distribution as a function of TGO thickness and thermal expansion mismatch. Engineering Failure Analysis, 2006. Vol. 13(3): pp. 409-426.
Massey, M.J., U. Baier, R. Maerlin and W.H. Weber, Effects of pressure and isotopic substitution on the Raman-spectrum of alpha-Fe_2O_3 – Identification of 2-magnon scattering. Physical Review B, 1990. Vol. 41(11): pp. 7822-7827.
Matteson, T.L., S.W. Schwarz, E.C. Houge, B.W. Kempshall and L.A. Giannuzzi, Electron backscattering diffraction investigation of focused ion beam surfaces. Journal of Electronic Materials, 2002. Vol. 31(1): pp. 33-39.
Mazza, T., E. Barborini, P. Piseri, P. Milani, D. Cattaneo, A.L. Bassi, C.E. Bottani and C. Ducati, Raman spectroscopy characterization of TiO_2 rutile nanocrystals. Physical Review B, 2007. Vol. 75(4) pp. 45416-45421.
McCumber, D.E. and M.D. Strurge, Linewidth and temperature shift of R lines in ruby. Journal of Applied Physics, 1963. Vol. 34(6): pp. 1682-1687.
McDonald, E.J., K.R. Hallam, W. Bell and P.E.J. Flewitt, Residual stresses in a multi-pass CrMoV low alloy ferritic steel repair weld. Materials Science and Engineering a-Structural Materials Properties Microstructure and Processing, 2002. Vol. 325(1-2): pp. 454-464.
McDonald, E.J., K.R. Hallam and P.E.J. Flewitt, A strategy for accommodating residual stresses in the assessment of repair weldments based upon measurement of near surface stresses. International Journal of Pressure Vessels and Piping, 2005. Vol. 82(4): pp. 339-346.
(a)McLean, M., L.M. Pan and R.N. Ghosh, Mechanisms and modeling of creep in superalloys. Sadhana-Academy Proceedings in Engineering Sciences, 1995. Vol. 20: pp. 287-300.
(b)McLean, M., G.A. Webster, F.R.N. Nabarro and A. Cottrell, Nickel-base superalloys - Current status and potential. Philosophical Transactions of the Royal Society of London Series A, 1995. Vol. 351(1697): pp. 419-433.
Meier, R.J., On art and science in curve-fitting vibrational spectra. Vibrational Spectroscopy, 2005. Vol. 39(2): pp. 266-269.
Meier, S.M. and D.K. Gupta, The evolution of thermal barrier coatings in gas-turbine engine applications. Journal of Engineering for Gas Turbines and Power-Transactions of the ASME, 1994. Vol. 116(1): pp. 250-257.

Menig, R., L. Pintschovius, V. Schulze and O. Vohringer, Depth profiles of macro residual stresses in thin shot peened steel plates determined by X-ray and neutron diffraction. Scripta Materialia, 2001. Vol. 45(8): pp. 977-983.
Mennicke, C., M.Y. He, D.R. Clarke and J.S. Smith, The role of secondary oxide inclusions ("pegs") on the spalling resistance of oxide films. Acta Materialia, 2000. Vol. 48(11): pp. 2941-2949.
Mirzaee-Sisan, A., Personal communication, University of Bristol, 2005.
Mirzaee-Sisan, A., D.J. Smith and C.E. Truman, Characterizing residual stress in rectangular beam specimens following thermomechanical loading. Journal of Strain Analysis for Engineering Design, 2007. Vol. 42(2): pp. 79-93.
Misture, S.T., Large-volume atmosphere-controlled high-temperature X-ray diffraction furnace. Measurement Science and Technology, 2003. Vol. 14(7): pp. 1091-1098.
Mochizuki, M., M. Hayashi and T. Hattori, Numerical analysis of welding residual stress and its verification using neutron diffraction measurement. Journal of Engineering Materials and Technology-Transactions of the ASME, 2000. Vol. 122(1): pp. 98-103.
Moore, J.C., Measurement of surface stress in austenitic steel. British Journal of Applied Physics, 1960. Vol. 11(6): pp. 242-244.
Mougin, J., M. Dupeux, L. Antoni and A. Galerie, Adhesion of thermal oxide scales grown on ferritic stainless steels measured using the inverted blister test. Materials Science and Engineering A, 2003. Vol. 359: pp. 44-51.
Mougin, J., A. Galerie, M. Dupeux, N. Rosman, G. Lucazeau, A.M. Huntz and L. Antoni, In-situ determination of growth and thermal stresses in chromia scales formed on a ferritic stainless steel. Werkstoffe und Korrosion, 2002. Vol. 53(7): pp. 486-490.
(a)Mougin, J., A. Galerie, G. Lucazeau and L. Abello, Raman spectroscopy determination of residual stresses at room temperature in chromia scales grown on pure chromium in oxygen and in water vapour. High Temperature Corrosion and Protection of Materials, 2001. Vol. 369-303: pp. 841-848.
(b)Mougin, J., T. Le Bihan and G. Lucazeau, High-pressure study of Cr_2O_3 obtained by high-temperature oxidation by X-ray diffraction and Raman spectroscopy. Journal of Physics and Chemistry of Solids, 2001. Vol. 62(3): pp. 553-563.
(c)Mougin, J., G. Lucazeau, A. Galerie and M. Dupeux, Influence of cooling rate and initial surface roughness on the residual stresses in chromia scales thermally grown on pure chromium. Materials Science and *Engineering A*, 2001. Vol. 308(1-2): pp. 118-123.
(d)Mougin, J., N. Rosman, G. Lucazeau and A. Galerie, In situ Raman monitoring of chromium oxide scale growth for stress determination. Journal of Raman Spectroscopy, 2001. Vol. 32(9): pp. 739-744.
Mu, N., J. Liu, J.W. Byeon, Y.H. Sohn and Y.L. Nava, Long-term oxidation and phase transformations in aluminized CMSX-4 superalloys. Surface and Coatings Technology, 2004. Vol. 188-89: pp. 27-34.
Mumm, D.R., A.G. Evans and I.T. Spitsberg, Characterization of a cyclic displacement instability for a thermally grown oxide in a thermal barrier system. Acta Materialia, 2001. Vol. 49(12): pp. 2329-2340.
Munro, R.G., G.J. Piermarini, S. Block and W.B. Holzapfel, Model line-shape analysis for the ruby R lines used for pressure measurement. Journal of Applied Physics, 1985. Vol. 57(2): pp. 165-169.

Murphy, K.S., K.L. More and M.J. Lance, As-deposited mixed zone in thermally grown oxide beneath a thermal barrier coating. Surface and Coatings Technology, 2001. Vol. 146: pp. 152-161.
Nagl, M.M. and W.T. Evans, The mechanical failure of oxide scales under tensile or compressive load. Journal of Materials Science, 1993. Vol. 28(23): pp. 6247-6260.
Nagl, M.M., W.T. Evans, D.J. Hall and S.R.J. Saunders, An in-situ investigation of the tensile failure of oxide scales. Oxidation of Metals, 1994. Vol. 42(5-6): pp. 431-449.
Nicholson, R.B., Nickel-base materials developments for high-temperatures. Philosophical Transactions of the Royal Society of London Series A, 1976. Vol. 282(1307): pp. 389-397.
Nychka, J.A. and D.R. Clarke, Damage quantification in TBCs by photo-stimulated luminescence spectroscopy. Surface and Coatings Technology, 2001. Vol. 146: pp. 110-116.
Nychka, J.A., D.R. Clarke, S. Sridharan, E. Jordan, M. Gell, M.J. Lance, C.J. Chunnilall, I.M. Smith, S.R.J. Saunders, R. Pillan, V. Sergo, A. Selçuk, A. Atkinson and K.S. Murphy, NDE assessment of TBCs: an interim report of a photo-stimulated luminescence 'round-robin' test. Surface and Coatings Technology, 2003. Vol. 163: pp. 87-94.
Ogden, S.L., Personal communication, Loughborough University 2007.
Park, J.B., J.Y. Hwang, D.S. Seo, S.K. Park, D.G. Moon and J.I. Han, Position dependent stress distribution of indium-tin-oxide on polymer substrate by applying external bending proce. Japanese Journal of Applied Physics 1, 2004. Vol. 43(5): pp. 2677-2680.
Parsley, M.C.J., Personal communication, University of Bristol 2005.
Padture, N.P., M. Gell and E.H. Jordan, Materials science - Thermal barrier coatings for gas-turbine engine apptications. Science, 2002. Vol. 296(5566): pp. 280-284.
Peng, X. and D.R. Clarke, Piezospectroscopic analysis of interface debonding in thermal barrier coatings. Journal of the American Ceramic Society, 2000. Vol. 83(5): pp. 1165-1170.
Perram, J.W., Interpretation of spectra. Journal of Chemical Physics, 1968. Vol. 49(9): pp. 4245-4247.
Phillips, J.R., D.P. Griffis and P.E. Russel, Channeling effects during focused ion beam micromachining of copper. Journal of Vacuum Science and Technology A, 2000. Vol. 18(4): pp. 1061-1065.
Pickard, L.K., Synthesis and characterisation of group 15 materials and transition metal spinel oxides. 2000, University of Bristol.
Price, A.T. and P.J. Alberry, Welding - The critical link, Research – Structural Integrity. Central Electricity Generating Board, 1988. pp. 15-26.
R6: Assessment of the integrity of structures containing defects. 2001, Revision 4, British Energy Generation Ltd.
Rabiei, A. and A.G. Evans, Failure mechanisms associated with the thermally grown oxide in plasma-sprayed thermal barrier coatings. Acta Materialia, 2000. Vol. 48(15): pp. 3963-3976.
Ragan, D.D., R. Gustavsen and D. Schiferl, Calibration of the ruby R_1 and R_2 fluorescence line shifts as a function of temperature from 0 to 600K. Journal of Applied Physics, 1992. Vol. 72(12): pp. 5539-5544.
RS Catalogue. Electrical automation cables, 2005. Vol. 1: pp. 1465.

Saint-Ramond, B., M. Carlin, M. Silva and J.R. Nickolls, Low mass bondcoat for robust thermal barrier coatings. High Temperature Corrosion and Protection of Materials 6, Part 1 and 2, 2004. Vol. 461-464: pp. 265-272.
Scherer, A., O.T. Inal and R.B. Petit, Modelling of degradation of nickel-pigmented aluminium oxide photothermal collector coatings. Journal of Materials Science, 1988. Vol. 23: pp. 1934-1942.
Schutze, M., Deformation and cracking behaviour of protective oxide scales on heat resistant steel under tensile strain. Oxidation of Metals, 1985. 24(3-4): p. 199-232.
Schwalbe, K.-H., Welded joints with non-matching weld metal-crack driving force considerations on the basis of the Engineering Treatment Model (ETM). International Journal of Fracture, 1993. Vol. 62: pp. 1-24.
Selcuk, A. and A. Atkinson, Analysis of the Cr^{3+} luminescence spectra from thermally grown oxide in thermal barrier coatings. Materials Science and Engineering A, 2002. Vol. 335(1-2): pp. 147-156.
Selcuk, A. and A. Atkinson, The evolution of residual stress in the thermally grown oxide on Pt diffusion bond coats in TBCs. Acta Materialia, 2003. Vol. 51(2): pp. 535-549.
Shebanova, O.N. and P. Lazor, Raman study of magnetite (Fe_3O_4): laser-induced thermal effects and oxidation. Journal of Raman Spectroscopy, 2003. Vol. 34(11): pp. 845-852.
Shillington, E.A.G. and D.R. Clarke, Spalling failure of a thermal barrier coating associated with aluminum depletion in the bond-coat. Acta Materialia, 1999. Vol. 47(4): pp. 1297-1305.
Shim, S.H. and T.S. Duffy, Raman spectroscopy of Fe_2O_3 to 62GPa. American Mineralogist, 2002. Vol. 87(2-3): pp. 318-326.
Shin, D.I., F. Gitzhofer and C. Moreau, Thermal property evolution of metal based thermal barrier coatings with heat treatments. Journal of Materials Science, 2007. Vol. 42(15): pp. 5915-5923.
Silvera, I.F. and R.J. Wijngaarden, Diamond anvil cell and cryostat for low-temperature optical studies. Review of Scientific Instruments, 1985. Vol. 56(1): pp. 121-124.
Singha, A., P. Dhar and A. Roy, A non-destructive tool for nanomaterials: Raman and photoluminescence spectroscopy. American Journal of Physics, 2005. Vol. 73(3): pp. 224-233.
Smith, D.J., P.J. Bouchard and D. George, Measurement and prediction of residual stresses in thick-section steel welds. Journal of Strain Analysis for Engineering Design, 2000. Vol. 35(4): pp. 287-305.
Smith, E. and G. Dent, Modern Raman spectroscopy - A practical approach, 2006. John Wiley and Sons.
(a)Sohn, Y.H., J.H. Kim, E.H. Jordan and M. Gell, Thermal cycling of EB-PVD/MCrAlY thermal barrier coatings: I. Microstructural development and spallation mechanisms. Surface and Coatings Technology, 2001. Vol. 146: pp. 70-78.
(b)Sohn, Y.H., K. Vaidyanathan, M. Ronski, E.H. Jordan and M. Gell, Thermal cycling of EB-PVD/MCrAlY thermal barrier coatings: II. Evolution of photo-stimulated luminescence. Surface and Coatings Technology, 2001. Vol. 146: pp. 102-109.
Sosa, A.D., M.D. Echeverria, O.J. Moncada and J.A. Sikora, Residual stresses, distortion and surface roughness produced by grinding thin wall ductile iron plates. International Journal of Machine Tools and Manufacture, 2007. Vol. 47: pp. 229-235.

Stefanescu, D., C.E. Truman, and D.J. Smith, An integrated approach for measuring near-surface and subsurface residual stress in engineering components. Journal of Strain Analysis for Engineering Design, 2004. Vol. 39(5): pp. 483-497.
Stefanescu, D., C.E. Truman, D.J. Smith and P.S. Whitehead, Improvements in residual stress measurement by the incremental centre hole drilling technique. Experimental Mechanics, 2006. Vol. 46(4): pp. 417-427.
Stone, H.J., P.J. Withers, T.M. Holden, S.M. Roberts and R.C. Reed, Comparison of three different techniques for measuring the residual stresses in an electron beam-welded plate of WASPALOY. Metallurgical and Materials Transactions a-Physical Metallurgy and Materials Science, 1999. Vol. 30(7): pp. 1797-1808.
Stott, F.H., The protective action of oxide scales in gaseous environments at high-temperature. Reports on Progress in Physics, 1987. Vol. 50(7): pp. 861-913.
Supergen2: Plant life extension consortium, technical annex. Engineering and Physical Sciences Research Council. Grant Number: EPSRC GR/S86334/01.
Suzuki, H. and T.M. Holden, Neutron diffraction measurements of stress in an austenitic butt weld. Journal of Strain Analysis for Engineering Design, 2006. Vol. 41(8): pp. 575-582.
Takano, Y., K. Fujii, M. Yoshinako, K. Hirota and O. Yamaguchi, Microstructure and mechanical behaviour of Cr_2O_3/10vol%W composites fabricated by spark plasma sintering. Journal of Materials Science, 2001. Vol. 20: pp. 73-75.
Teixeira, V., M. Andritschky, W. Fischer, H.P. Buchkremer and D. Stover, Effects of deposition temperature and thermal cycling on residual stress state in zirconia-based thermal barrier coatings. Surface and Coatings Technology, 1999. Vol. 121: pp. 103-111.
Theocaris, P.S. and D.P. Sokolis, Spectral decomposition of the linear elastic tensor for monoclinic symmetry. Acta Crystallographica Section A, 1999. Vol. 55: pp. 635-647.
Thermo Fisher Scientific, GRAMS32 Software, 2000.
Tolpygo, V.K. and D.R. Clarke, Temperature and cycle-time dependence of rumpling in platinum-modified diffusion aluminide coatings. Scripta Materialia, 2007. Vol. 57(7): pp. 563-566.
(a)Tolpygo, V.K. and D.R. Clarke, On the rumpling mechanism in nickel-aluminide coatings - Part I: an experimental assessment. Acta Materialia, 2004. Vol. 52(17): pp. 5115-5127.
(b)Tolpygo, V.K. and D.R. Clarke, On the rumpling mechanism in nickel-aluminide coatings - Part II: characterization of surface undulations and bond coat swelling. Acta Materialia, 2004. Vol. 52(17): pp. 5129-5141.
Tolpygo, V.K. and D.R. Clarke, Tensile cracking during thermal cycling of alumina films formed by high-temperature oxidation. Acta Materialia, 1999. Vol. 47(13): pp. 3589-3605.
Tolpygo, V.K., D.R. Clarke and K.S. Murphy, Oxidation-induced failure of EB-PVD thermal barrier coatings. Surface and Coatings Technology, 2001. Vol. 146: pp. 124-131.
Utke, I., P. Hoffmann and J. Melngailis, Gas-assisted focused electron beam and ion beam processing and fabrication. Journal of Vacuum Science Technology B, 2008. Vol. 26(4): pp. 1197-1276.
Verble, J.L., Temperature-dependent light-scattering studies of verwey transition and electronic disorder in magnetite. Physical Review B, 1974. Vol. 9(12): pp.5236-5248.

Vickers, T.J., R.E. Wambles and C.K. Mann, Curve fitting and linearity: Data processing in Raman spectroscopy. Applied Spectroscopy, 2001. Vol. 55(4): pp. 389-393.
Vij, D.R., Luminescence of solids. 1998, Plenum Press.
Vishay Micro-Measurements, Measurement of residual stresses by the hole-drilling strain gauge method, 2007.
Viswanathan, R., Life assessment and improvement of turbo-generator rotors for fossil plants: Seminar : Papers and discussions. 1985, Pergamon Press.
Viswanathan, R., Damage mechanisms and life assessment of high-temperature components. 1989: ASM International.
Viswanathan, R. and W. Bakker, Materials for ultrasupercritical coal power plants - Turbine materials: Part II. Journal of Materials Engineering and Performance, 2001. Vol. 10(1): pp. 96-101.
Voutchkov, I., A.J. Keane, A. Bhaskar and T.M. Olsen, Weld sequence optimization: The use of surrogate models for solving sequential combinatorial problems. Computer Methods in Applied Mechanics and Engineering, 2005. Vol. 194(30-33): pp. 3535-3551.
Walton, J. and N. Fairley, Noise reduction in X-ray photoelectron spectromicroscopy by a singular value decomposition sorting procedure. Journal of Electron Spectroscopy and Related Phenomena, 2005. Vol. 148(1): pp. 29-40.
Watkins, J.L. and A.S. Brierley, A post-processing technique to remove background noise from echo intergration data. Ices Journal of Marine Science, 1996. Vol. 53(2): pp. 339-344.
Wang, F.H., H.Y. Lou, S.L. Zhu and W.T. Wu, The mechanism of scale adhesion on sputtered microcrystallized CoCrAl films. Oxidation of Metals, 1996. Vol. 45(1-2): pp. 39-50.
Webster, G.A. and R.C. Wimpory, Development of procedures for the measurement of residual stress by neutron diffraction. Applied Physics A, 2002. Vol. 74: pp. 1227-1229.
Wen, M., E.H. Jordan and M. Gell, Evolution of photo-stimulated luminescence of EB-PVD/(Ni, Pt)Al thermal barrier coatings. Materials Science and Engineering A, 2005. Vol. 398(1-2): pp. 99-107.
Wen, Q.Z., D.M. Lipkin and D.R. Clarke, Luminescence characterization of chromium-containing theta-alumina. Journal of the American Ceramic Society, 1998. Vol. 81(12): pp. 3345-3348.
West, G., Microstructure and mechanical performance of SiC/BMAS glass-ceramic matrix composite. 1997, University of Warwick.
Withers, P.J., Residual stress and its role in failure. Reports on Progress in Physics, 2007. Vol. 70(12): pp. 2211-2264.
(a)Withers, P.J. and H.K.D.H. Bhadeshia, Overview - Residual stress part 1 - Measurement techniques. Materials Science and Technology, 2001. Vol. 17(4): pp. 355-365.
(b)Withers, P.J. and H.K.D.H. Bhadeshia, Overview - Residual stress part 2 - Nature and origins. Materials Science and Technology, 2001. Vol. 17(4): pp. 366-375.
Withers, P.J., M. Turski, L. Edwards, P.J. Bouchard, and D.J. Buttle, Recent advances in residual stress measurement. International Journal of Pressure Vessels and Piping, 2008. Vol. 85(3): pp. 118-127.
Wolfel, E.R., A novel curved position-sensitive proportional counter for X-ray diffractometry. Journal of Applied Crystallography, 1983. Vol. 16: pp. 341-348.

(a)Wu, X.M., J.Y. Yu, T.L. Ren and L.T. Liu, Micro-Raman spectroscopy measurement of stress in silicon. Microelectronics Journal, 2007. Vol. 38(1): pp. 87-90.
(b)Wu, X.M., J.Y. Yu, T.L. Ren and L.T. Liu, Micro-Raman measurement of thickness in microelectromechanical silicon structures. Journal of Micromechanics and Microengineering, 2007. Vol. 17(6): pp. 1114-1120.
Wu, X.Q., H. Guan, E.H. Han, W. Ke and Y. Katada, Influence of surface finish on fatigue cracking behavior of reactor pressure vessel steel in high temperature water. Werkstoffe und Korrosion, 2006. Vol. 57(11): pp. 868-871.
Wunder, S.L. and P.E. Schoen, Pressure measurement at high-temperatures in the diamond anvil cell. Journal of Applied Physics, 1981. Vol. 52(6): pp. 3772-3775.
Xu, Y.F., H.J. Zhang, H.Y. Li, S.N. Bao and P. He, Photoluminescence spectroscopy study on tris (8-hydroxyquinoline) aluminum film. Applied Surface Science, 2006. Vol. 252(6): pp. 2328-2333.
Yadav, V., V.K. Jain, P.M. Dixit, Thermal stresses due to electrical discharge machining. International Journal of Machine Tools and Manufacture, 2002. Vol. 42: pp. 877-888.
Yaghi, A.H., T.H. Hyde, A.A. Becker and W. Sun, G. Hilson, S. Simunjuntak, P.E.J. Flewitt, M.J. Pavier and D.J. Smith, A comparison between measured and modelled residual stresses in a circumferentially butt-welded P91 pipe. Submitted to the Journal of Pressure Vessel Technology, 2008.
Yaghi, A.H., T.H. Hyde, A.A. Becker and W. Sun, Numerical simulation of P91 pipe welding including the effects of solid-state phase transformation on residual stresses. Proceedings of the Institution of Mechanical Engineers L, 2007. Vol. 221(4): pp. 213-224.
Yaghi, A.H., T.H. Hyde, A.A. Becker, J.A. Williams and W. Sun, Residual stress simulation in welded sections of P91 pipes. Journal of Materials Processing Technology, 2005. Vol. 167(2-3): pp. 480-487.
Yanar, N.M., G. Kim, S. Hamano, F.S. Pettit and G.H. Meier, Microstructural characterization of the failures of thermal barrier coatings on Ni-base superalloys. Materials at High Temperatures, 2003. Vol. 20(4): pp. 495-506.
Yen, J. and M. Nicol, Temperature depencence of the ruby luminescence method for measuring high-pressures. Journal of Applied Physics, 1992. Vol. 72(12): pp. 5535-5538.
Ziegler, J., Particle interactions with matter, 2003. Available from www.srim.org.

14 Appendix

The following macro was written for photoluminescence spectroscopic background removal. This program enabled a recorded background to be removed from a defined series of spectra. Explanations of the program steps are written in italics. See Figure 4.28 for an example of the effect of background removal.

```
Program defines variables.
Sub MergeSheets()
    Dim SrcBook As Workbook
    Dim fso As Object, f As Object, ff As Object, f1 As Object
    Dim title As String
    Dim i As Integer

Program doesn't keep updating screen.
    Application.ScreenUpdating = False

Program sets directory from which to obtain files.
    Set fso = CreateObject("Scripting.FileSystemObject")
    Set f = fso.Getfolder("E:\excel")
    Set ff = f.Files
    i = 3

Program cycles through files with background noise and adds correct file extensions.
    For Each f1 In ff
        title = f1
        filname = Retfilename(title)
        'opens file
        Set SrcBook = Workbooks.Open(f1)

Program finds background scan.
        If f1 = "E:\excel\b.xls" Then
```

Program places background scan in EXCEL spreadsheet.

```
Range(Cells(1, 1), Cells(574, 2)).Copy
ThisWorkbook.Worksheets(1).Activate
Range(Cells(579, 1), Cells(1153, 2)).PasteSpecial
  Else
Range(Cells(1, 2), Cells(574, 2)).Copy
```

Program copies raw data (with background) into spreadsheet.

```
ThisWorkbook.Worksheets(1).Activate
Range(Cells(579, i), Cells(1153, i)).PasteSpecial
Cells(1, i) = filname
Application.CutCopyMode = False
SrcBook.Close
i = i + 1
End If
```

Program subtracts background from raw data.

Module 1

```
Function Retfilename(title)
Dim sPath As String
  Dim sList() As String
  Dim sAns As String
  Dim iArrayLen As Integer
  Dim Final As String
  FullPath = title
  sList = Split(FullPath, "\")
  iArrayLen = UBound(sList)
  sAns = IIf(iArrayLen = 0, "", sList(iArrayLen))
  NameFromFullPath = sAns
  Retfilename = Left(NameFromFullPath, Len(NameFromFullPath) - 4)
End Function
```

Clears worksheet for new data

Module 2

```
Sub ClearData()'
' ClearData Macro'
    Rows("579:1152").Select
    Range("F579").Activate
    Selection.ClearContents
End Sub
```

Program plots graphs.

Module 3

```
Sub PlotGraph()
    Dim ColNum As Integer
    ColNum = InputBox("Final Column NUMBER")
    Range(Cells(1, 1), Cells(575, ColNum)).Select
    Sheets("Sheet1").Select
    Charts.Add
    ActiveChart.ApplyCustomType ChartType:=xlUserDefined, TypeName:="Raman"
    ActiveChart.SetSourceData Source:=Sheets("Sheet1").Range("A1:G575"), PlotBy_
      :=xlColumns
    ActiveChart.Location Where:=xlLocationAsNewSheet
End Sub
```

Module 4

```
Sub Main()
    ClearData
    ThisWorkbook.MergeSheets
    PlotGraph
End Sub
```